9-3-2019 2:30 PM

The Effect of Stiffness Anisotropy of a Glacial Clay on the Behaviour of a Shallow Wind Turbine Foundation

Jesús A. González-Hurtado
The University of Western Ontario

Supervisor
Dr. Timothy A. Newson
The University of Western Ontario

Graduate Program in Civil and Environmental Engineering
A thesis submitted in partial fulfillment of the requirements for the degree in Doctor of Philosophy

Recommended Citation

González-Hurtado, Jesús A., "The Effect of Stiffness Anisotropy of a Glacial Clay on the Behaviour of a Shallow Wind Turbine Foundation" (2019). *Electronic Thesis and Dissertation Repository*. 6772.
https://ir.lib.uwo.ca/etd/6772

Abstract

Shallow wind turbine foundations are designed based on investigations of the ultimate, serviceability and fatigue limit states. The serviceability limit state design approaches in particular are based on simple isotropic elastic half-space analyses that ignore coupling between loading directions, and soil non-linearity and elastic anisotropy. Many of the wind farms in Ontario are constructed around the Great Lakes basin and a number of these areas are characterized as stiff clayey glacial tills. It is recognized that many of these glacial materials exhibit some degree of strength, stiffness and fabric anisotropy. This research aimed to characterize the anisotropic geotechnical properties of a specific glacial till deposit that underlies a 2.3 MW *onshore* wind turbine at a commercial wind farm in Port Alma, Ontario, and also assess the anisotropic elastic soil-foundation interaction between the underlying glacial till and the shallow foundation that supports the wind turbine. Additionally, the small-strain and anisotropic stiffness properties of a number of well-known Canadian clays of glacial origin were measured to provide bounds on the range of elastic behaviour that these forms of foundation may be subjected.

High quality laboratory samples of the Port Alma glacial till, as well as the other glacial clays studied, were tested in their intact state using consolidated isotropic undrained (CIU) triaxial tests with locally measured axial strains, CIU tests fitted with orthogonal bender element transducers and resonant column tests on vertically and horizontally trimmed samples. The critical state properties and stress-strain behaviour under monotonic loading of the Port Alma till showed similarities to those exhibited by other glacial clay tills found in the literature. The behaviour of the clay tills was also investigated at very small-strains. Results from bender element and resonant column tests showed that: the small-strain stiffness of the till material increases with increasing confining pressure according to a power law relationship; the stiffness of the material is strain dependent and the elastic stiffness of the material is higher in its horizontal direction than vertical. The effects of the stiffness anisotropy on the soil-foundation interaction for the wind turbine was investigated using a finite element model. The outcomes of the modelling were compared against analytical models found in the literature and measured field responses of the turbine foundation. The results indicate that the vertical and horizontal translations of the working wind turbine foundation are affected by the stiffness anisotropy, while its influence on the rocking behavior can be considered to be smaller.

Keywords

Wind turbine, shallow foundation, glacial till, glacial clay, critical state, small-strain, stiffness degradation, soil anisotropy, anisotropic stiffness, damping ratio, shear modulus, shear wave velocity, bender elements, resonant column, static triaxial.

Summary for Lay Audience

Shallow wind turbine foundations are designed based on investigations of the ultimate, serviceability and fatigue limit states. The serviceability limit state design approaches in particular are based on simple isotropic elastic analyses that ignore coupling between loading directions, soil non-linearity and elastic anisotropy. Many of the wind farms in Ontario are constructed around the Great Lakes basin and a number of these areas are characterized as stiff clayey glacial tills. It is recognized that many of these glacial materials exhibit some degree of strength, stiffness and fabric anisotropy. This research aimed to characterize the anisotropic geotechnical properties of a specific glacial till deposit that underlies a 2.3 MW onshore wind turbine at a commercial wind farm in Port Alma, Ontario, and also assess the anisotropic elastic soil-foundation interaction between the underlying glacial till and the shallow foundation that supports the wind turbine. Additionally, the small-strain and anisotropic stiffness properties of a number of well-known Canadian clays of glacial origin were measured to provide bounds on the range of elastic behaviour that these forms of foundation may be subjected.

High quality laboratory samples of the Port Alma glacial till, and the other glacial clays studied, were tested in their intact state using consolidated isotropic undrained (CIU) triaxial tests with locally measured axial strains, CIU tests fitted with orthogonal bender element transducers and resonant column tests on vertically and horizontally trimmed samples. Results from bender element and resonant column tests showed that the small-strain stiffness of the till increases with increasing confining pressure, the stiffness of the material is strain dependent and the elastic stiffness of the material is higher in its horizontal direction than vertical. The effects of the stiffness anisotropy on the soil-foundation interaction for the wind turbine was investigated using a finite element model. The outcomes of the modelling were compared against analytical models found in the literature and measured field responses of the turbine foundation. The results indicate that the vertical and horizontal translations of the wind turbine foundation are affected by the stiffness anisotropy, while its influence on the rocking behavior can be considered to be smaller.

Co-Authorship Statement

This thesis is prepared in accordance with the regulation for monograph thesis stipulated by the School of Graduate and Post Graduate Studies (SGPS) of Western University. All the laboratory testing, interpretation of results and writing of the draft and the final thesis were performed by the candidate himself, under the supervision of Dr. Timothy A. Newson. The supervisor's contribution consisted of providing advice throughout the research program and reviewing the draft and the final thesis and results from this investigation. The results of all the laboratory tests presented will be used in journals and conferences publications, which will be co-authored with Dr. Timothy Newson.

The results of the tests presented in Chapters five and six were submitted as conference papers and are still under review. Similarly, these results will be submitted as a journal paper to the Canadian Geotechnical Journal. The papers are co-authored with Dr. Timothy Newson. The candidate did all the laboratory work, interpretation of results and writing of the papers. The co-author provided advice on this work, reviewed the drafts and the results.

The results presented in Chapter seven were submitted as a conference paper and is still under review. Likewise, these results will be also submitted as a technical note to the Canadian Geotechnical journal co-authored by Pengpeng He and Dr. Timothy Newson. The candidate did all the laboratory work and interpretation of results. The co-author Pengpeng He prepared the numerical model and carried out the numerical analysis presented in the aforementioned Chapter. The co-author Dr. Timothy Newson provided advice on this work, reviewed the results and paper draft.

Acknowledgments

First and foremost, I would like to thank my beloved parents, Jesús and Georgina, for their endless love, patience, continuous support and encouragement to start this journey. They favoured me over themselves, have given me everything within their reach, and have greatly contributed to my achievements and success in life. I owe them my life, needless to say, and I fall short of words to express my deepest gratitude to them. Also, thanks to the rest of my family for cheering me up when I needed it the most.

To my dearly loved wife, Yanina, thanks for helping me and giving me your unconditional support while I was doing my research and when I was spending most of my weekends/nights writing my thesis. I admire your patience and resilience, you are a fundamental part of my life and the greatest soulmate I could have ever asked for. I love you with all my heart.

To my supervisor, Dr. Timothy Newson, thanks for giving me the opportunity of continuing my graduate studies, you saw a potential in me when we met in your Advanced Soil Mechanics course that I honestly did not know that I had. You have exposed me to challenges that have helped me to shape my character as a scientist and engineer. I am very grateful for your continuous support and friendship.

To my colleagues, and friends, Jordan Kiss, Colin Schmidt, Venkatesh Deshpande and Muhammad Safdar, thanks for your support while we were working together in the *Lab 16-A* solving many challenges while discussing our research results and talking about life. Special thanks to my colleague and friend Pengpeng He for helping me to complete some of the analysis for this investigation.

Thanks to Western University for granting me the Western Graduate Research Scholarship (WGRS) at the beginning of my doctoral studies in 2013. Many thanks to the Geotechnical Research Centre (GRC) for awarding me with the *William E. & Ruth Lardner Award* in 2017 as this helped me to continue and complete my doctoral studies. My most sincere gratitude to all the professors and staff of the Civil and Environmental Engineering (CEE) department at Western University, as well as to the people from the University Machine Services (UMS). To everyone else that I met at Western that provided me with their support and help throughout the past years, thanks. You all played an important role towards the completion of this work.

Table of Contents

List of Symbols and Abbreviations

Symbol		**Description**	**Units**
K	=	Bulk modulus	MPa
G	=	Shear modulus of shear stiffness	MPa
E	=	Elastic modulus or Young's modulus	MPa
e	=	Void Ratio	
f	=	Frequency	Hz
f_n	=	Natural frequency	Hz
f_r	=	Resonant frequency	Hz
k_R	=	Rocking stiffness	kN/radians
R	=	Radius	Meters
M	=	Moment loading	kN
G_{max}, G_0	=	Small-strain or maximum shear moduli	MPa
M_{max}, M_0	=	Small-strain or maximum constrained moduli	MPa
θ	=	Angle of rotation	Radians
V	=	Vertical loading	kN
K_0	=	Coefficient of earth pressure at rest	
$K_{0(NC)}$	=	K_o during normal consolidation	
w, u	=	Vertical and horizontal foundation responses	Meters
K_V, K_H, K_M, K_{MH}	=	Dimensionless elastic stiffness coefficients	
D	=	Damping ratio	%
I_p	=	Plasticity or plastic index	%
A	=	Soil activity	

p'	=	Effective Cambridge stress or mean effective stress	kPa
p'_0	=	Effective consolidation pressure at shear	kPa
p'_c	=	Pre-consolidation pressure	kPa
q	=	Deviator Stress	kPa
M	=	Slope of the critical state line	kPa
ϕ'	=	Effective angle of friction	Degrees
ϕ'_{cs}	=	Critical state effective friction angle	Degrees
CSL	=	Critical state line	
NCL	=	Normal compression line	
Γ	=	Specific volume on the intrinsic CSL	
λ	=	Slope of the isotropic compression line	
κ	=	Slope of the isotropic recompression line	
N	=	Void ratio of the isotropic normal compression line	
e_κ	=	Void ratio of the recompression line	
url	=	Unload/reload line	
w_c, w_L, w_p	=	Moisture content, liquid limit, plastic limit	%
E_v	=	Elastic modulus in the vertical direction	MPa
E_h	=	Elastic modulus in the horizontal direction	MPa
s_u	=	Undrained shear strength	kPa
tf	=	Time to failure	Sec
Δu	=	Excess pore pressure	kPa
ε_a, ε_r	=	Axial strain, radial strain	%
C_c	=	Compression index	

V_s = Shear wave velocity m/s

V_p = Compression wave velocity m/s

γ_{bulk} = Bulk unit weight kN/m^3

ε, γ = Shear strain %

ε_{avg} = Average flexural strain %

γ_{ref} = Reference shear strain at $G/G_{max} = 0.5$ %

ρ = Density kg/m^3

ε_f = Target failure strain %

θ_{max} = Maximum rotation Degrees

μ, μ_{vh} = Poisson's ratio for vertical strains due to horizontal strains

μ_{hv} = Poisson's ratio for horizontal strains due to vertical strains

μ_{hh} = Poisson's ratio for horizontal strains due to horizontal strains

G_{vh}, G_{hv} = Shear moduli in the vertical plane MPa

G_{hh} = Shear moduli in the horizontal plane MPa

V_{svh} = Shear wave velocity vertically polarized horizontally propagated m/s

V_{shv} = Shear wave velocity horizontally polarized vertically propagated m/s

V_{shh} = Shear wave velocity horizontally polarized horizontally propagated m/s

V_{pvh} = Compressional wave velocity vertically polarized horizontally propagated m/s

V_{phv} = Compressional wave velocity horizontally polarized vertically propagated m/s

V_{phh} = Compressional wave velocity horizontally polarized horizontally propagated m/s

M_{vh}, M_{hv} = Constrained moduli in the vertical plane MPa

M_{hh} = Constrained moduli in the horizontal plane MPa

σ_1', σ_v' = Effective vertical stress kPa

σ_3', σ_h' = Effective horizontal stress kPa

Y_1, Y_2, Y_3 = Yield kinematic surfaces

α = Anisotropy degree, Anisotropic ratio, Anisotropy factor

E^* = Modified elastic modulus equal to E_v MPa

G^* = Modified shear modulus equal MPa

K^* = Modified bulk modulus equal MPa

J = Cross-coupling parameter

μ^* = Associated Poisson's ratio equal to μ_{hh}

H, L = Height of sample m

CF = Clay fraction < 2µm %

BE = Bender element

CIU = Consolidated isotropically undrained test

RC, RCA = Resonant column, resonant column apparatus

VHM = Vertical-horizontal-moment loading

WT = Wind turbine

LVDT, LDT = Linear variable differential transformer, local deformation transducer

OCR = Over consolidation ratio

TX = Triaxial test

DMR = Detrital remanent magnetization

AMS = Anisotropy of magnetic susceptibility

List of Tables

List of Figures

List of Appendices

Chapter 1

1 Introduction

1.1 Overview

Renewable sources of energy constitute a significant part of the energy supplies of different countries around the world. Wind is a major source of renewable energy and is the fastest-growing major source of new energy in Canada (CanWEA, 2018). By the end of 2018 Canada finished with over 12,800 MW of total installed capacity placing the country in eight position in the world for wind energy capacity. Currently, Ontario is Canada's leader in clean wind energy and it accounts for 40% of the country total installed capacity. Wind energy supplies approximately 8% of Ontario's electricity demand today and is projected to keep on growing at a rapid rate in the years to come (CanWEA, 2018). To maintain the pace of expansion, the Canadian wind sector must address some major technical and policy issues. Some of these issues are associated with the construction and design of foundations for wind turbines. Recent research output for the foundations of offshore wind turbines has been significant (e.g. Byrne and Houlsby, 2003). In contrast, the literature for *onshore* foundation systems is still relatively sparse. Consequently, despite there being similar design issues for turbine foundations across the industry, there is often a diverse interpretation of design codes and understanding of the behavior of these foundations.

The present research focuses on the study of a shallow gravity base that serves as the foundation for a 2.3MW *onshore* wind turbine and its underlying soil, a glacial clay till deposit. Glacial clays are ubiquitous across the great lakes basins and wind farms are often placed on these stiff materials. These materials were laid down in the Port Bruce Stade (c. 15,000 years bp.) during the re-advance of the Laurentide Ice Sheet of the Late Wisconsin (Chapman and Putnam, 1966; Kelly, 1995). These subglacial lodgment tills are calcareous and fine-grained, suggesting that the ice overrode and incorporated fine-grained glaciolacustrine sediments deposited during the previous Erie Interstade. Large shallow gravity foundations are widely used for many of the wind farms in Southwestern Ontario due to the nature of these soils. The loading states for wind turbine foundations are atypical with low vertical loads (*V*) and high stochastic wind horizontal (*H*) and moment (*M*) loads, and even torsion (*T*). Design approaches for serviceability and ultimate limit states for shallow wind turbine foundations are typically based on European codes (e.g. DNV, 2002; IEC 61400-1, 2005) and engineering judgment to identify design requirements. Whilst these codes are updated regularly to include state-of-the-art knowledge, they still employ simple uncoupled isotropic elastic analyses of half-spaces (e.g. Borrowicka, 1943) and empirical modifications of the traditional bearing capacity equations for near-surface founded shallow foundations (e.g. Meyerhof, 1953) that are thought to be relatively conservative. In addition, the effect of anisotropy on serviceability limit states (SLS) is currently ignored.

Assessment of the ultimate limit state (ULS) and serviceability limit state (SLS) is of great importance for all construction projects. In contrast to offshore oil and gas foundations, with similar loading states, wind turbine foundations are still designed relatively conservatively and there is currently a lack of problem specific state-of-the art design approaches. These foundations are subjected to complex *VHMT* (Vertical-Horizontal-Moment-Torsion) loading and traditional ultimate limit state analytical approaches (e.g. Terzaghi, 1943; Meyerhof; 1963; Hansen; 1970; Green, 1954) often fail to accurately predict bearing capacities. Some researchers have emphasized the conservative nature of bearing capacity envelopes deduced from conventional methods, e.g. Bransby and Randolph, 1998; Taiebat and Carter, 2000; Gourvenec and Randolph, 2003; Randolph et al., 2005. Likewise, serviceability limit states (which are generally the primary design criteria) are based on very simple isotropic elastic half-space analyses that ignore coupling between loading directions, anisotropy, non-linearity, etc. Due to the nature of most soils, this assumption can be considered to be conservative because it is most likely that soils will exhibit some degree of stiffness anisotropy in response to the applied stresses. Although the characterization of an isotropic elastic material is attractive, since it only requires the determination of two material parameters out of four possible measurements (i.e. shear modulus *G* and bulk modulus *K* or Poisson's ratio *v* and Young's modulus *E*), for highly anisotropic soils it can lead to overconservative designs.

It is now well accepted that the working strains of many geostructures are much smaller than traditional measurement ranges in triaxial, oedometer and penetrometer tests in soils. The concept of small strain (non-linear) theory is beginning to be adopted in geotechnical practice (e.g. Burland, 1982; Clayton, 2011). More recently the anisotropy of small strain stiffness has been investigated by researchers and as indicated by Bishop and Hight (1977), most soils will likely be anisotropic or at least transversely isotropic (cross-anisotropic). The stress-strain response of these glacial clays soils is known to be complex and non-linear, and is dependent on the mode of loading, fabric anisotropy, rate and time effects, over-consolidation ratio, stress state and strain history. A number of studies have been carried out to assess the anisotropic stiffness behaviour of cohesive glacial deposits. Well known examples are non-carbonate heavily overconsolidated London clay (Jovicic and Coop, 1998; Gasparre et al., 2007b; Yimsiri and Soga, 2011), carbonate heavily overconsolidated Gault clay (Ng et al., 1995; Pennington et al., 1997; Lings et al., 2000; Yimsiri and Soga, 2011), and low plasticity overconsolidated Wallaceburg clay from Ontario (Becker, 1981). In addition, a number of authors have investigated the strength and stiffness behaviour of glacial soils in light of the potential mechanical effects of glaciers upon those soils, e.g. (Boulton and Paul, 1976; Bell, 1998; Sane et al., 2007; Tyldesley and Newson, 2016; and Kiss, 2016).

Although the effects of anisotropy on soil-structure interaction have not been widely investigated, some studies of anisotropic, homogeneous and non-homogeneous half spaces have been published, e.g. Barden (1963), Gerrard and Harrison (1970a, 1970b and 1971), Milovic and Touzot (1970), Milovic (1970), Gibson (1974), Hooper (1975), Rowe and Booker (1980b) and Gazetas (1981a, 1981b, 1981c, 1981d, 1981e and 1983). The work of Hooper (1975), Rowe and Booker (1981) and Gazetas (1981) suggest that predicted foundation displacements that do not take into account cross-anisotropy can be up to 50% in error for highly anisotropic materials like glacial clays. Of equal importance in the design of foundations subjected to dynamic loads, such as those from supported machinery and wind, is the necessity of understanding of the dynamic interaction of foundations. The operating cyclic strains for these types of foundation are in the range of 10^{-4} to 10^{-2}, leading to reductions in shear modulus of 30-70% of the very small strain (G_{max}) values. This appears to be more critical for low plasticity clays, such as the glacial till involve in this study. The majority of testing reported by researchers has been for relationships between shear modulus in the vertical direction (G_{vh}) versus static and cyclic strain; the degradation for stiffness in the horizontal plane has rarely been investigated (although it should be anticipated that the effect is coupled).

Moreover, the majority of the research reported in the literature for Canadian soils has mainly focused on the general classification and monotonic properties of these materials. More detailed study has been considered for some of the materials and limited analysis of the dynamic properties for the small and very small strain range has been conducted (e.g. Kim and Novak, 1981). However, the study of the anisotropic stiffness behaviour of glacial tills and how this can contribute to the overall stability of the foundation-soil systems is still sparse in the literature. Studies of this type will help with validation and calibration of state of design approaches for wind farms, leading to more efficient and economical designs, and potentially extending the life-cycles and investments made by wind turbine owners and operators in Canada. The rapid pace of expansion of the industry, the need for higher capacity foundations with larger turbines and the placement of wind farms on sub-optimal sites (as new land becomes more scattered) will lead the industry to optimize the design and construction of these foundations. Improvement of current methodologies could therefore very important for the success of the industry.

This thesis forms part of a comprehensive study designed to help the understanding of the short and long-term soil-structural interaction behavior of shallow wind turbine foundations on stiff clays and develop more appropriate engineering and numerical tools for their design. To that end, high quality laboratory and in-situ tests were conducted to fully characterize an appropriate glacial clay soil profile that underlies a shallow foundation of a commercial wind turbine located in a wind farm in the southwestern part of Ontario. The site that has been selected for this PhD study is mainly composed of a carbonate-rich glacial clay till deposit and is known to have an anisotropic fabric and associated mechanical behaviour. To complement the overall study of the turbine-foundation-soil behaviour, a full-scale monitoring system has been implemented on the site. All the aforementioned elements were used to validate a more appropriate design tool for wind turbine foundations optimized for some of Canada’s particular types of glacial soil.

1.2 Objectives and methods

1.2.1 Objectives

The main objective of the proposed research is to study the soil-foundation interaction between a wind turbine shallow foundation and a carbonate-rich glacial clay till in an Ontario site. To achieve the desired overall aim of this research, several specific objectives have been proposed. They are as follows:

1. To characterize the small-strain and anisotropic stiffness characteristics of the soil and the degradation of vertical and horizontal stiffness under increasing strain levels;
2. To characterize the small-strain and anisotropic stiffness characteristics of a number of other well-known Canadian clays of varying stress history and plasticity;
3. To measure and characterize representative working displacements of the chosen wind turbine foundation under loading in the field;
4. To assess the effects of anisotropy on the serviceability limit states of this wind turbine foundation; and
5. To conduct a parametric finite element study of the effects of anisotropy on shallow wind turbine foundations.

1.2.2 Methods

To accomplish the proposed objectives, the following milestones have been completed:

- A critical review of the literature on the current design practices and available guidelines for wind turbine foundations in Canada;
- A review of the literature on the mechanical behaviour and geology of glacial clay till soils of Ontario;
- A comprehensive laboratory testing program was completed using the resonant column apparatus, hybrid triaxial tests equipped with vertical/horizontal bender elements and small-strain transducers and was performed for soils to investigate small-strain and anisotropic behaviour;

- A finite element analysis was used to study the effect of stiffness anisotropy on the soil-foundation interaction between the wind turbine shallow foundation and its underlying soil deposit through parametric study.

1.3 Organization of the thesis

This thesis consists of the following eight chapters:

Chapter 1 provides a brief introduction to the thesis and presents a summary of the objectives and methods used in this research study. The chapter closes with a concise description of the thesis content and organization.

Chapter 2 is a literature review that explores the available information on the different types of foundations and design guidelines and philosophies that are most commonly used for onshore wind turbines in Canada. Similarly, it addresses the importance of the non-linear and anisotropic elasticity of soils on their influence on the serviceability limit states and operating cyclic strains. A review on the geological formation of glacial till deposits of southern Ontario and their basic characteristics are presented. A detailed review on the different available techniques for the determination of the small-strain properties of cohesive soils and the determination of cross-anisotropic elastic parameters are discussed.

Chapter 3 presents detailed background information on the field and geological setting of the site selected for this study, along with a summary and discussion of results from previous field and laboratory investigations. The field monitoring methodologies implemented, and the data gathered from the wind farm site are addressed at the end of the chapter.

Chapter 4 describes the experimental program developed for this investigation, as well as the different materials selected for testing, the laboratory methodologies used, sample preparation procedures adopted and general testing conditions. A general description of the site location and geological setting of the areas from where the natural soil samples were retrieved are also presented. Likewise, basic index properties, and stress-strain characteristics of the materials investigated are reviewed and discussed.

Chapter 5 shows the results obtained from a series of small-strain laboratory tests performed on undisturbed samples from the glacial clay till deposit that underlies the wind turbine shallow foundation. The results from resonant column tests and consolidated undrained triaxial tests equipped with local strain instrumentation and vertical/horizontal bender elements are presented. The results were used to derive a full set of anisotropic elastic moduli parameters, find critical state parameters and to assess the degradation behaviour of the glacial clay till deposit.

Chapter 6 presents a summary of the results of different laboratory techniques to study the stress-strain behaviour and critical state soil parameters, the stiffness degradation behaviour across a range of strains from very small to large, and the small-strain stiffness anisotropic behaviour of six different cohesive soils that include five Canadian clays of glaciogenic origin with different stress history and plasticity. A discussion of the results and their implications are covered at the end of the chapter.

Chapter 7 describes the development and implementation of a numerical model for the wind turbine shallow foundation system and the underlying glacial clay till deposit. The finite element program ABAQUS has been used to develop the numerical model using anisotropic stiffness parameters. Results from the finite element model are presented in the form of a parametric study and are also compared with experimental and published data.

Chapter 8 summarizes the main conclusions from the investigation, discusses limitations of the work and outlines the potential scope for future research.

Chapter 2

2 Literature review

This chapter presents a broad theoretical background and literature review on most of concepts and topics covered in this thesis. The current practices for designing shallow onshore wind turbine foundations in Canada are described in Section 2.1. The typical assumptions and philosophies considered in their design are also discussed. A comprehensive review of the geological formation of glacial till deposits of southern Ontario and their basic characteristics are presented in Section 2.2. A review of the different techniques and studies available for the determination of small-strain properties of cohesive soils and the determination of cross-anisotropic elastic parameters are also discussed in Sections 2.3 and 2.4. A summary of the findings of these areas are provided at the end of the chapter.

2.3 Onshore Wind Turbine Foundation Design

There are several forms of wind turbine (WT) foundation design available for the North American market. Based on the geotechnical and geological characteristics of soil deposits and site-specific turbine loads, the most appropriate foundation type can be determined; typically a deep or shallow footing. Once the type of foundation is selected, the foundation dimensions and shape are then selected to optimize cost, whilst maintaining the overall stability and serviceability requirements of the structure throughout its service life. Shallow foundation designs comprise mainly octagonal gravity bases, shallow rock anchors, and short pier foundations. Deep foundations include pile and cap foundations, rock anchors and pile anchor foundations, and the patented Patrick and Herderson tensionless pier (e.g. Svensson, 2010; Tinjum and Christensen, 2010). The present research focuses on the study of a shallow octagonal gravity base that serves as foundation for a 2.3MW onshore wind turbine and its underlying soil, a carbonate glacial clay till. This shallow type of foundation is widely used by many of the wind farms in southwestern Ontario due to the stiff nature of the glacial soils. Unfortunately, the interaction between the complex loadings and its effect on the foundation system has not been previously studied in detail. This has led to a lot of empiricism and conservative design in the Canadian wind sector.

2.1.1 Current Codes and Design Guidelines

Due to the absence of specific onshore WT foundation design standards in Canada, previous efforts have relied on a mixture of foreign codes, standards, and engineering judgment to identify design requirements. With increasing wind energy demand and wind turbines developing higher rated power (with bigger towers and blades), the necessity for design standards that can optimize construction and operation for local conditions have become more important. The most common codes and guidelines for WT design that include some specific details for onshore machines are: Canadian Wind Turbine Codes and Standards (2008) superseded by CAN/CSA-C61400-1 (2014), DNV/ Risø (2nd Edition, 2002), IEC Standard 61400-1 (Third edition, 2005-08), and ASCE/AWEA RP (2011). Notably, the Canadian Foundation Engineering Manual (CFEM, 2006), does not cover WT foundations as a specific case. From the above-mentioned international bodies, Det Norske Vertitas and Risø National Laboratory (DNV/Risø) have published what is arguably the most complete set of guidelines and recommendations for wind turbine design, for both offshore and onshore types, including steps for designing their foundation systems.

A common design philosophy adopted by these codes is to rely on relatively conservative geotechnical assumptions (e.g. linear elasticity, isotropy, uncoupled bearing capacity factors, circular foundations, etc) to simplify the design process of the WT shallow foundations. Such simple assumptions can have an important impact on the final design of the WT foundation. Coupled with relatively sparse and cheap site investigations, this has the potential for overdesign and additional construction costs. Soil stiffness is often approximated as spring stiffness and can be defined as the ratio of load or moment to the deformation in the direction of the load or rotation, respectively. The foundation design must keep the deformations of the soil below threshold values defined by the serviceability limit state (SLS). Four types of uniaxial loading cases are considered: vertical, horizontal, moment, and torsion, resulting in 4 different types of elastic stiffness. DNV (2010) provides equations to estimate the foundation stiffness of circular surface foundations resting on a stratum over bedrock (or a half-space) and embedded circular foundations on a stratum over bedrock. Such equations can be seen in Figures 2.1 and 2.2.

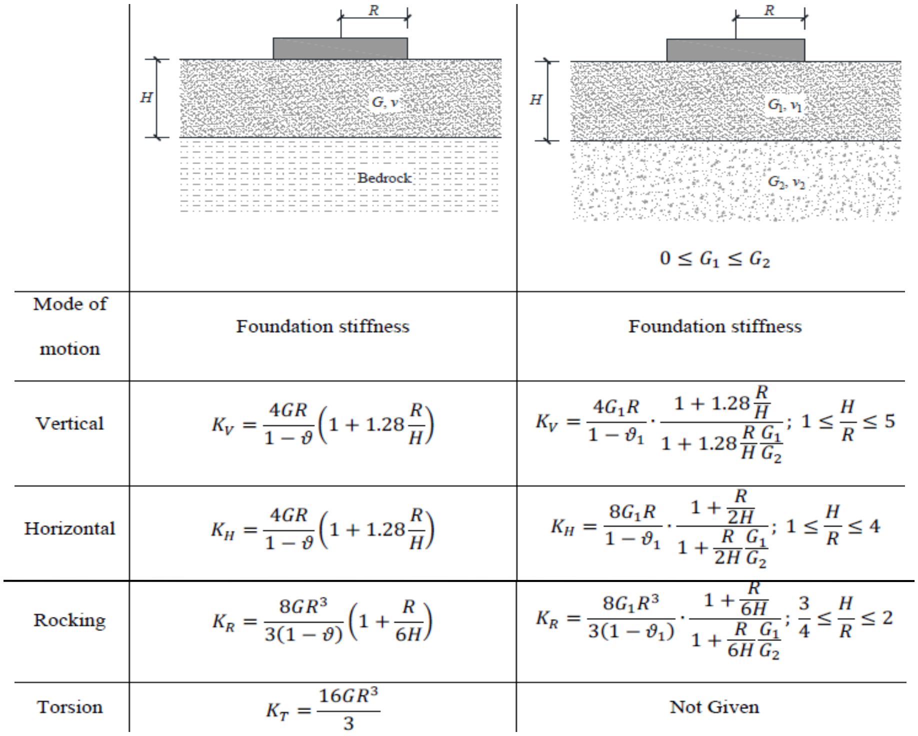

Mode of motion	Foundation stiffness	Foundation stiffness
Vertical	$K_V = \frac{4GR}{1-\vartheta}\left(1 + 1.28\frac{R}{H}\right)$	$K_V = \frac{4G_1R}{1-\vartheta_1} \cdot \frac{1 + 1.28\frac{R}{H}}{1 + 1.28\frac{R}{H}\frac{G_1}{G_2}};\ 1 \leq \frac{H}{R} \leq 5$
Horizontal	$K_H = \frac{4GR}{1-\vartheta}\left(1 + 1.28\frac{R}{H}\right)$	$K_H = \frac{8G_1R}{1-\vartheta_1} \cdot \frac{1 + \frac{R}{2H}}{1 + \frac{R}{2H}\frac{G_1}{G_2}};\ 1 \leq \frac{H}{R} \leq 4$
Rocking	$K_R = \frac{8GR^3}{3(1-\vartheta)}\left(1 + \frac{R}{6H}\right)$	$K_R = \frac{8G_1R^3}{3(1-\vartheta_1)} \cdot \frac{1 + \frac{R}{6H}}{1 + \frac{R}{6H}\frac{G_1}{G_2}};\ \frac{3}{4} \leq \frac{H}{R} \leq 2$
Torsion	$K_T = \frac{16GR^3}{3}$	Not Given

Figure 2.1: Foundation stiffness of circular foundations on stratum over bedrock or on stratum over half-space (DNV, 2010)

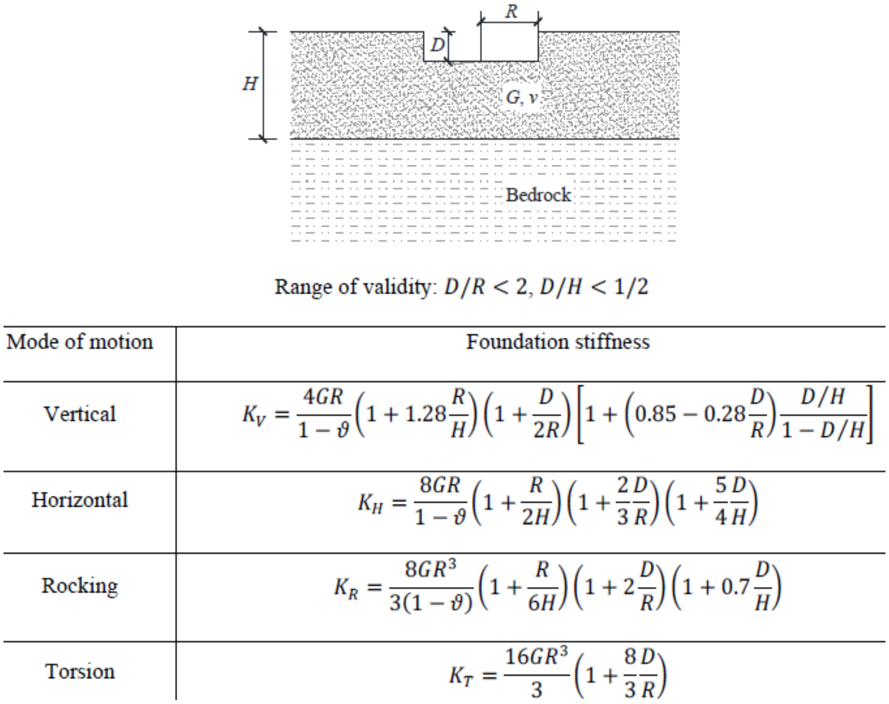

Range of validity: $D/R < 2$, $D/H < 1/2$

Mode of motion	Foundation stiffness
Vertical	$K_V = \frac{4GR}{1-\vartheta}\left(1 + 1.28\frac{R}{H}\right)\left(1 + \frac{D}{2R}\right)\left[1 + \left(0.85 - 0.28\frac{D}{R}\right)\frac{D/H}{1 - D/H}\right]$
Horizontal	$K_H = \frac{8GR}{1-\vartheta}\left(1 + \frac{R}{2H}\right)\left(1 + \frac{2}{3}\frac{D}{R}\right)\left(1 + \frac{5}{4}\frac{D}{H}\right)$
Rocking	$K_R = \frac{8GR^3}{3(1-\vartheta)}\left(1 + \frac{R}{6H}\right)\left(1 + 2\frac{D}{R}\right)\left(1 + 0.7\frac{D}{H}\right)$
Torsion	$K_T = \frac{16GR^3}{3}\left(1 + \frac{8}{3}\frac{D}{R}\right)$

Figure 2.2: Foundation stiffness of circular foundation embedded in stratum over bedrock (DNV, 2010)

For wind turbines, the rocking stiffness is considered to be a critical design parameter because it controls the location of the center of gravity with respect to the foundation of the WT system (Lang, 2012). Borrowicka (1943) developed the classic rocking stiffness equation, Equation 2.1, for circular foundations on isotropic elastic half-spaces:

$$k_R = \frac{8GR^3}{3(1-\mu)} = \frac{M}{\theta} \tag{2.1}$$

where G is the shear modulus, μ is Poisson's ratio of the soil below the foundation, R is the radius of the foundation, θ is the angle of rotation in radians, and M is the applied moment. G and μ will depend on the type of the soil underlying the foundation and the strain range associated with the applied loads. The stiffness equations embedded in current codes (e.g. DNV, 2010) are not coupled to each other, are applicable for only circular foundations on isotropic linear elastic homogeneous soils, and do not account for soil stiffness anisotropy or degradation. In reality, however, it is more likely that natural soil deposits may exhibit at least some degree of stiffness anisotropy and stiffness degradation due to the cyclic loading caused by the wind and regular operation of the wind turbine.

Coupled horizontal and rocking vibration of embedded foundations was first investigated by Baranov (1967), who formulated approximate analytical solutions and presented numerical results only for pure rocking, assuming that the foundation and the soil remained in full contact during vibrations. Later, Tajimi (1969) analyzed the response of a structure partially embedded and attached through its base to a rigid half-space underlying an elastic stratum. Beredugo and Novak (1972) investigated the coupled forced vibration in horizontal translation and rocking of partially embedded rigid footings to propose closed form formulas and graphs that could be used for design purposes. They suggested that the omission of coupling leads to some considerable errors in both resonant frequencies and amplitudes of the foundation system, and that the theory of surface footings considerably overestimates the resonant amplitudes. Gazetas (1983) and (1991) presented a summary of formulas to estimate static stiffnesses for vertical, horizontal, moment and torsion loads and coupled horizontal-moment for rigid embedded cylindrical foundations rigidly attached into a homogeneous soil stratum over bedrock. These formulas were developed by Kausel et al. (1975) and Elsabee et al. (1977).

Bell (1991) performed a series of three-dimensional finite-element analysis on surface and embedded rough rigid circular footings subjected to combined vertical, horizontal and moment loads. Bell (1991) observed the existence of cross-coupling when horizontal or moment loads act on a foundation; that is, for a compressible soil, when a foundation is subjected to pure horizontal load, it not only undergoes translation, but also rotation around a horizontal axis perpendicular to the direction of the load. Similarly, when a moment is applied, it produces both rotation and translation (see Figure 2.3). Gazetas (1991) explained that the coupling between the horizontal and moment forces is a consequence of the inertia of the foundation block as its center of gravity is often located above the center of pressure of the soil reactions.

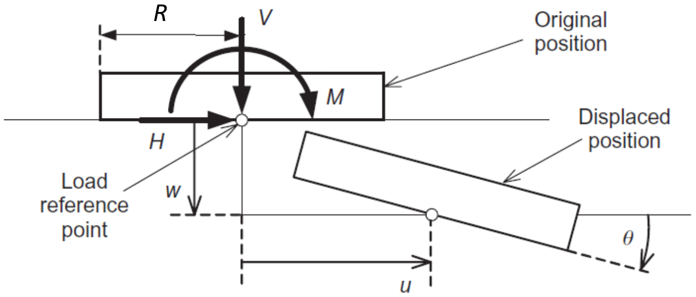

Figure 2.3: Nomenclature for foundation loading and geometry (adapted from Osman et al., 2007)

This cross-coupling is important since it is additive for the case when moment arises from a horizontal load applied at some distance above the footing, which is a typical case for wind turbine foundations. Bell (1991) expressed the stiffness of a footing using a matrix approach as defined by Equation 2.2:

$$\begin{Bmatrix} V/GR^2 \\ H/GR^2 \\ M/GR^3 \end{Bmatrix} = \begin{bmatrix} K_V & 0 & 0 \\ 0 & K_{HH} & K_{HM} \\ 0 & K_{MH} & K_M \end{bmatrix} \begin{Bmatrix} w/R \\ u/R \\ \theta_M \end{Bmatrix} \qquad (2.2)$$

where, K_V, K_H, K_M and K_{MH} are dimensionless elastic stiffness coefficients, G is the shear modulus, R is the foundation radius, V, H and M are the vertical, horizontal and moment loads, and w, u and θ_M are the vertical, horizontal and rotational responses. The dimensionless elastic stiffness coefficients depend only on the ratio of the foundation embedment to the radius of the foundation and the Poisson's ratio (μ). K_V, K_{HH} and K_M correspond to vertical, horizontal and moment degrees of freedom respectively. K_{MH} represents the cross-coupling of horizontal and moment degrees of freedom. For the case of surface circular rough footings resting on fully saturated soils (μ=0.5), Bell (1991) found that K_{MH} becomes zero, thus horizontal and moment loading become independent of each other. However, Bell (1991) demonstrated that $K_{MH} > 0$ with foundation embedment.

Doherty and Deeks (2003) extended the approach presented by Bell (1991). They used a scaled boundary finite-element method to evaluate semi-analytical solutions for the elastic coefficients for different embedment cases considering the effect of soil non-homogeneity in their analyses. They assumed that the shear modulus (*G*) varied with depth following a power law and, for non-homogeneous cases, to have a value of zero at the surface. Note that in the analyses of Bell (1991) and Doherty and Deeks (2003), the soil was considered to be linear elastic and isotropic. Thus, these methods fail to consider the variation of G with strain increments, and moreover they do not consider the stiffness anisotropy of the soil material.

DNV (2002) provides two empirical relationships to estimate the small-strain shear modulus (G_{max}) of clays; presented in Equations 2.3 and 2.4:

$$G_{max} = A\frac{(3-e)^2}{1+e}\sqrt{\sigma_o'}(OCR)^K \tag{2.3}$$

$$G_{max} = 2600 s_u \tag{2.4}$$

where *A* is a material constant that depends on the size and angularity of the soil grains, *e* is the void ratio, σ_o' is the mean effective stress, OCR is the overconsolidation ratio, *K* is a function of the plasticity index, and s_u is the undrained shear strength of the soil. DNV (2002) provides the expected shear strain levels associated with three of the most important sources of dynamic loading: earthquakes (large strains up to 10^{-2} to 10^{-1}); rotating machines (small-strains usually less than 10^{-5}); and wind and ocean waves (moderate strains up to 10^{-2}, typically 10^{-3}). As the value of G depends on the shear strain level, the DNV code also provides a typical range of shear modulus degradation (G/G_{max}) curves versus strain (see Figure 2.4). On the other hand, they do not give scientific reason nor cite a reference justifying where the degradation curves originate or to what type of soil these curves can be associated with. Figure 2.4 also shows G/G_{max} curves obtained by Vucetic and Dobry (1991) from a range of clays with different plasticity indexes. A comparison between the G/G_{max} range from DNV (2002) and the curves estimated by Vucetic and Dobry (1991), clearly shows that the proposed range do not account for the degradation behaviour of low plasticity clays for shear strains levels less than 10^{-3}.

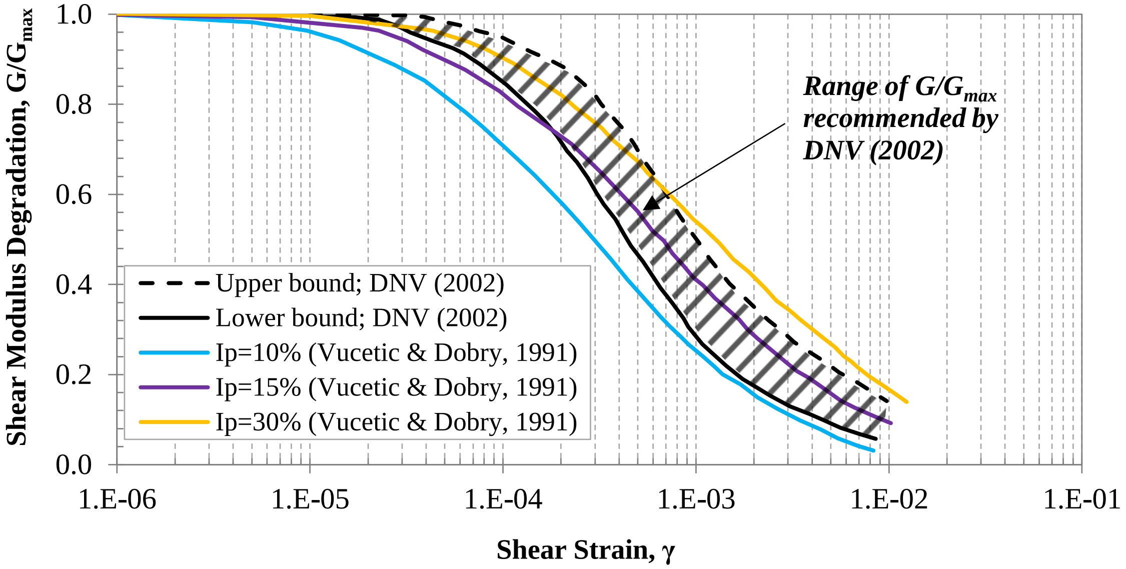

Figure 2.4: Shear modulus degradation with increasing of shear strain

2.1.2 Site-Specific Wind Turbine Design

The specific environmental conditions and founding soil can substantially differ from one site to another, which in turn may affect the assumptions adopted for the design of the WT foundation system. Recently, Fuglsang et al. (2002) considered terrain type (e.g. flat and complex mountainous terrain) and different wind conditions into the design process of WT from six different locations around Europe showing that the site-specific approach can be effective for optimizing the design process and minimizing the overall WT cost. Several aspects should be known to better understand the potential soil-foundation interaction, such as the soil conditions at the site, characteristics of the loading acting on the foundation system, and the foundation properties. DNV (2010) and IEC Standard 61400-1 (2005) recommend that for each specific site, the soil properties shall be assessed by qualified geotechnical engineers through a comprehensive soil investigation. Inevitably there will be some overdesign of foundations, since the soil properties will vary across any site, and the design will be essentially the same for dozens if not hundreds of wind turbines. In addition, soils subjected to cyclic loading during normal operation of wind turbines may exhibit stiffness degradation, and the values of shear modulus (*G*) and damping ratio (*D*) of the soil will depend on the induced strain levels and susceptibility of the soil to cyclic degradation.

The typical operating cyclic strains for foundations of supported rotating machines subjected to wind loads range between 10^{-4} to 10^{-3}, which can correspond to a reduction of approximately 30 to 70% in soil stiffness, as shown in Figure 2.5 (Gonzalez-Hurtado and Newson, 2016). Kiss (2016) compared the degradation behaviour of Port Alma glacial till, subjected to cyclic degradation at different levels of shear strains, with Venezuelan clay (VNP) material tested by Vucetic (1987), and found that the reduction in stiffness can be more significant in rich carbonate materials with low plasticity. Moreover, Figure 2.5 shows how the reduction in *G* varies for soils with different plasticity index at the same level of strain. For clays with plasticity index of 30% and 15%, at a shear strain level of 10^{-4} and 10^{-3}, G/G_{max} ranges from 0.95 to 0.75, and 0.55 to 0.40, respectively.

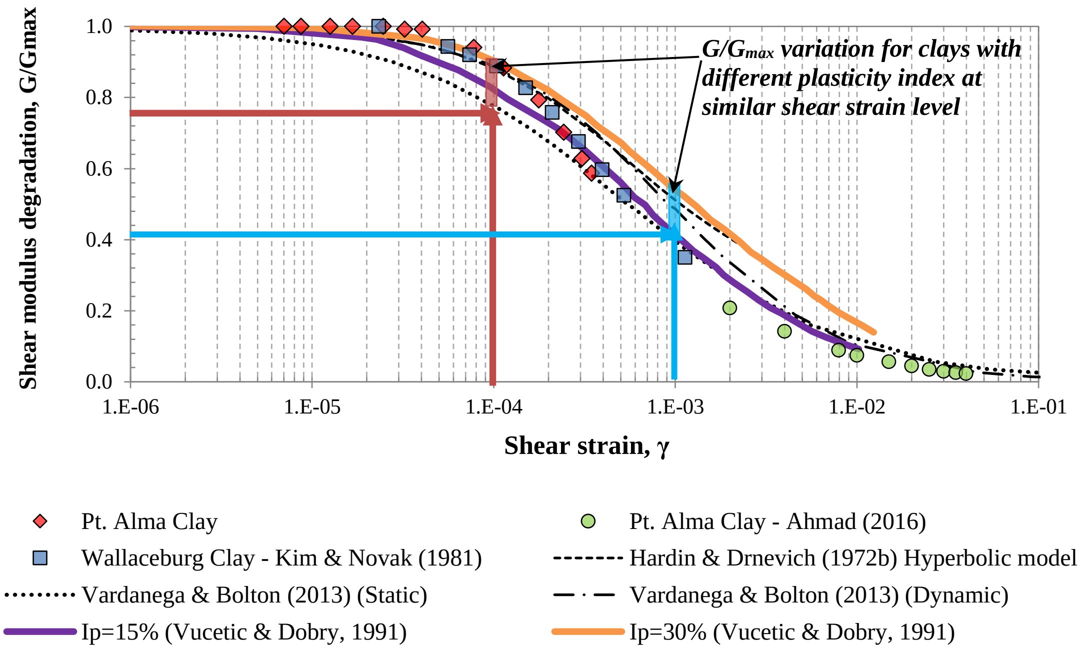

Figure 2.5: Shear modulus degradation of Port Alma material (adapted from Gonzalez-Hurtado & Newson, 2016)

Dynamic soil characteristics can facilitate the understanding of dynamic soil-foundation interactions. DNV (2010) specifies that the dynamic analysis of a gravity structure is necessary for soil-structure interactions, and the shear modulus and damping ratio of the soil used in the design process should be representative of the predominant strain level in the soil. Consequently, the necessity for detailed understanding of the soil conditions (e.g. soil homogeneity, dynamic properties, stiffness anisotropy characteristics) at a particular site is imperative for the site-specific design of wind turbines.

2.2 Glacial tills in Southern Ontario

The term till was defined by Geike (1863) as “a stiff clay full of stones varying in size up to boulders, produced by abrasion carried on by the ice sheet as it moved over the land”. It is also believed that the term till was originally used in Scotland to characterize a stiff hard clay soil that was unstratified and generally impervious (Dreimanis, 1976). Till is the most common glacial sediment found around the world and is ubiquitous in Canada, especially around the Great Lakes basin (see Figure 2.6).

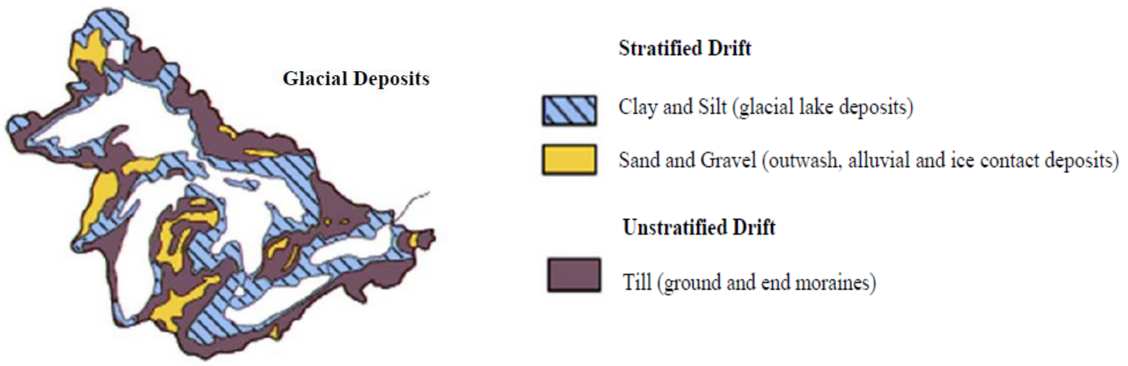

Figure 2.6: Dominant Glacial Deposits in the Great Lakes Basin (adapted from United States Environmental Protection Agency, 2008)

These tills were deposited from glacial ice during previous ice ages through two different mechanisms: a) the till formed from material that started to accumulate on the surface of the ice and was released from the surface as the ice melted, is referred to as “ablation till”; b) till deposited from the base of a glacier or ice sheet is generally known as basal till (Milligan, 1976). Equally important to the mode of deposition, is the geological origin of the till, which involves a sequence of actions that may have started with the erosion of rocks and minerals, or just merely deformation of them by a glacier or its melt-waters, followed by the transportation of this eroded material in or upon a glacier or ice sheet (Dreimanis, 1976).

Tills are often associated with other ‘till-like’ soils that have similar glaciogenic origin, such soils are: glaciomarine deposits, glaciofluvial deposits and glaciolacustrine deposits. Glaciomarine deposits are the result of the sediments deposited in a basin at the interface of a glacier and marine environment. Glaciofluvial deposits are sediments laid down by waters originating from glaciers and ice sheets, these are mainly composed of a mixture of gravel, sand and cobbles, and can be deposited proglacially, marginally and subglacially. Glaciolacustrine deposits are considered an extension of the glaciofluvial system and may occur whenever meltwater becomes ponded into lakes. On the other hand, glacial tills are glacioterrestial deposits product of poorly-sorted debris sediments released on land, these are also commonly known as ‘diamicton’ (Dreimanis, 1976, Trenter, 1999).

Dreimanis (1976) and Milligan (1976) classified glacial tills into basal and ablation tills according to their deposition mechanism. Figure 2.7 illustrates a comprehensive classification of tills presented by Dreimanis (1976), this shows the diverse genetic classifications applicable to tills by their way of transportation and subsequent deposition. Dreimanis (1976) added a third group of tills referred as waterlaid tills, this with the aim of describing a crudely stratified variety of till deposited in water, typically unsorted and originated from lacustrine sedimentation below floating ice. Other terms that are equivalent to or include waterlaid tills are waterlain till, subwater till, lacustrotill, marine or submarine till, among others (Dreimanis, 1976). Quigley (1979) described the main types of sedimentary deposits of glacial origin that are typical in Canada and may be encountered in geotechnical practice. The first three types are: waterlain tills, lacustrotills and mudflows, these may consist of coarse-grained material in a fine clayey matrix. The last two types are: varved clays and marine clays, which consist of more uniform, fine-textured, silty clays that are typically deposited distant form their main source.

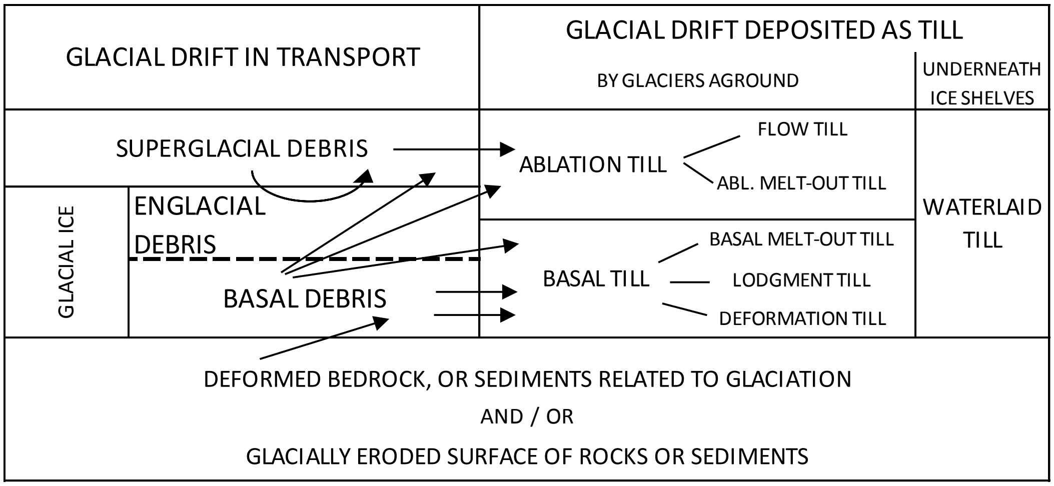

Figure 2.7: Genetic classification of tills (adapted from Dreimanis, 1976)

In Canada, the deglaciation period during the Late Wisconsin age, around 14,000 years before the present (B.P), dominated the formation of the surficial soils of the region. While the glaciers retreated in a northerly direction, subglacial lakes were formed by meltwater in low areas suppressed by topographic features, and glacial sediments were produced and deposited at the bottom. Approximate maximum boundaries of glacial lakes in southern Ontario and areas of the United States are shown in Figure 2.8. Many areas of southern Ontario that lie within the glacial lake boundaries are composed by formations of varved, or rhythmically laminated, silt and clay (e.g., Kenney 1976; Ashley et al. 1985, Morris and Kelly, 1997). Most of the sediments deposited within the basin of Lake Ontario were transported by local rivers and streams, glacial meltwaters and an extensive drainage from the Great Lakes before these started to discharge through the St. Lawrence river (Hough 1958; Flint 1971; LaFleur 1979; Muller et al. 1986; Cadwell 1988).

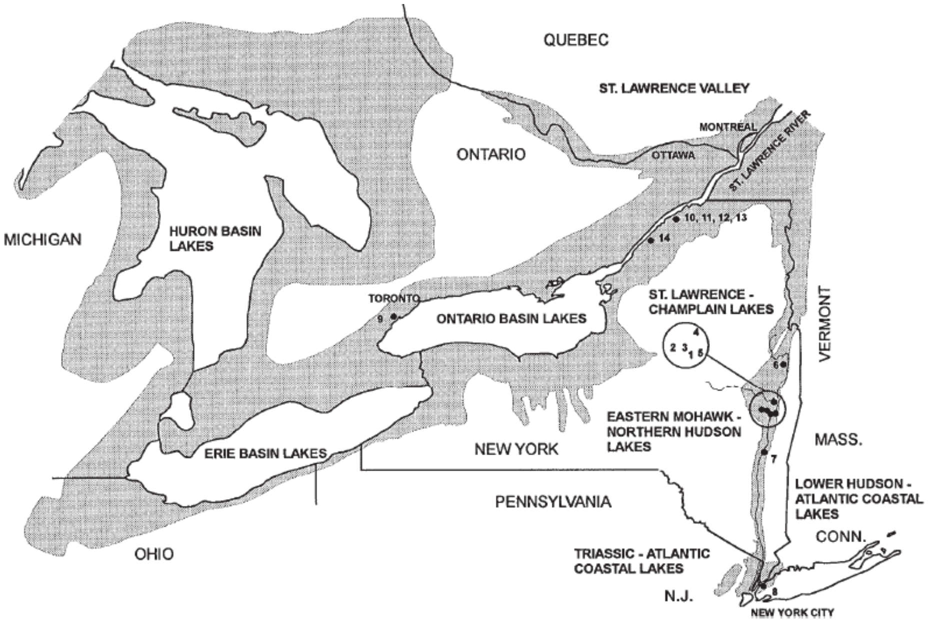

Figure 2.8: Maximum extent of glacial lakes in southern Ontario and New York State (shaded area; Boone and Lutenegger, 1997)

At the southern part of the province of Ontario and Lake Erie, most of the soft cohesive deposits are regarded as normally consolidated to lightly over-consolidated waterlain tills mainly composed of a silt and clay matrix with coarser materials randomly distributed within the unstratified mass (Quigley and Ogunbadejo 1972a; Quigley 1980). In general, these cohesive soils are composed of silt- and clay-size particles with activity ($A= I_p$/clay particles (<2 μm)) ranging between 0.6 and 0.4. The sediment minerals present primarily consist of illite, chlorite, quartz, feldspar, and carbonates; swelling minerals such as montmorillonite or vermiculite are rarely present (Torrance 1975; Quigley 1969, 1980; Quigley et al. 1982, 1985). Typical Atterberg limits test results indicate that the plasticity of these soils often ranges from low to medium ($2 < I_p < 30$).

The Quaternary stratigraphic section along the north shore of Lake Erie from Port Talbot to Plum Point has been described previously by Evenson et al. (1977). Detailed investigations on the Quaternary sediments of this area have been conducted since 1950, with special emphasis on the stratigraphy of the last ice age deposits and properties of the till deposits. A report by Kelly (1995), stated that in proximity to the Chatham-Wheatley area two tills units are exposed at the surface, and that both tills were deposited during the

Late Wisconsinan Substage (13,000 to 14,000 years B.P). The first till unit, called Tavistock Till, is considered to be the oldest of the two till units and was derived from glacial ice that advanced from the Lake Huron Basin. The second deposit, called Port Stanley Till, was derived from glacial ice that entered the Chatham-Wheatley area from the Lake Erie Basin. These two units are underlain by a third much older till unit called Catfish Creek Till. This unit was first called the 'lower till' by Dreimanis (1951), and later renamed after the locality on the north shore of Lake Erie (de Vries and Dreimanis, 1960). Catfish Creek Till was deposited during the beginning of the Late Wisconsinan Substage at the Nissouri Stade (21,000 years B.P) and is common over the interlake region of southern Ontario (Karrow, 1984). Morris (1994) and Morris and Kelly (1997), described the Catfish Creek Till as a massive layer of diamicton that directly overlies the bedrock surface. It has a thickness that ranges from 0.3 to 3 m, except beneath the town of Essex were has a thickness of 10 m. The Till has is dark brown to greyish brown in color, and its characterized by a sandy silty to silty sand matrix.

Tavistock till is present over much of Southwestern Ontario and is often covered by a thin layer of fine-grained glaciolacustrine sediment. The maximum thickness of this till has been reported to be 19 m, it is considered to be a clast-poor, massive to faintly stratified, silty to clayey silt till (Kelly, 1995; Kelly and Morris, 1997). According to Karrow (1974) and Cowan (1976), Tavistock till represents the advancing of the glacial sheet during the early part of the Port Bruce Stadial by ice flowing south-southeast from the Lake Huron and Georgian Bay basins and is considered time equivalent with the Erie lobe Port Stanley Till. Port Stanley till has been observed along the margins of Lake Erie, at Wheatley and south of Blenheim. This till is also covered by glaciolacustrine clay to sand-rich sediments and it reaches an observed maximum thickness of 15 m in the Lake Erie bluffs at Port Alma (Kelly, 1995). Dreimanis and Karrow (1972) stated that the Port Stanley till represents a Port Bruce Stadial glacial advance out of the Erie-Ontario basin.

Figure 2.9 depicts examples of sonic borehole records obtained by Morris and Kelly (1997) through different landform and materials at different locations in the St. Clair Plain. Borehole W-89-03, drilled at the south of the town of Chatham, depicts a typical soil profile of the surrounding areas showing the occurrence of the Catfish Creek, Tavistock and Port

Stanley Tills. It can be seen how the Port Stanley overlies the Tavistock and Catfish Creek Tills, following the deposition order described by Kelly (1995). From boreholes E-89-08 and E-89-09, the Tavistock and Catfish Creek Tills can be observed along with other interbedded glacial materials such as weathered and unweathered glaciolacustrine deposits, and laminated silt and clay deposits. These glacial deposits are thought to have been deposited during the retreat and readvance of the Huron lobe. More information on the formation of these glacial deposits can be found in Morris and Kelly (1997).

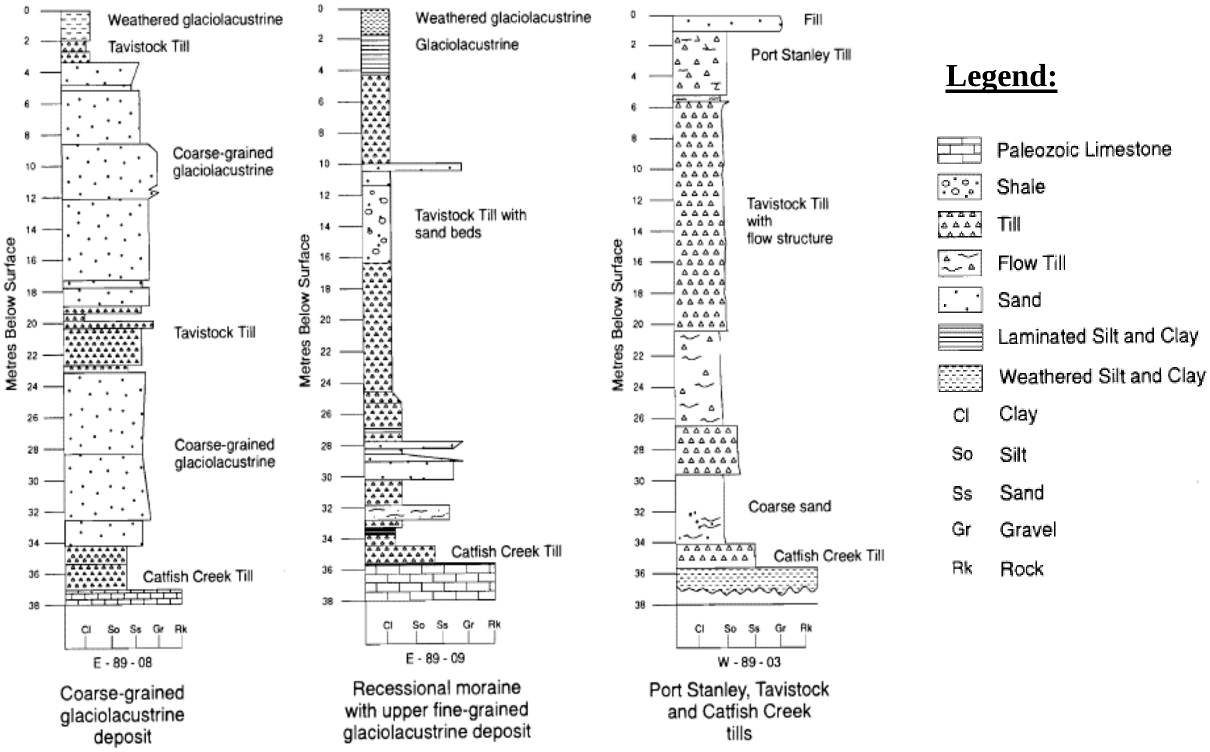

Figure 2.9: Examples of sonic borehole records at different locations within the St. Clair Plain (adapted from Morris and Kelly, 1997)

Gravenor et al. (1973) and Gravenor and Stupavsky (1974) carried out studies on the paleomagnetism and its relationship to till deposition and the magnetic susceptibility of the surface tills of southern Ontario. The aim of their work was to identify the source area of the tills and to characterize the direction of deposition through the study of magnetite particles contained in the Till. Gravenor et al. (1973) analyzed samples of clay till from Port Alma, Ontario. Their results showed that the clay till material, mainly characterized by Port Stanley Till, possessed a strong component of detrital remanent magnetization (DRM) that was produced when magnetic particles were released through a water or slurry layer at the base of the ice covering the Port Alma site. The till fabric analysis performed for the clay-rich till deposit showed that the ice flowed to the northwest out of the Erie basin confirming similar observations done by Chapman and Putnam (1951) and Dreimanis (1961). Kelly (1995) presented results of till-fabric analysis performed on soil samples from Port Alma; these showed that the preferred orientation of magnetic particles was towards north-northwest (348°) (Figure 2.10).

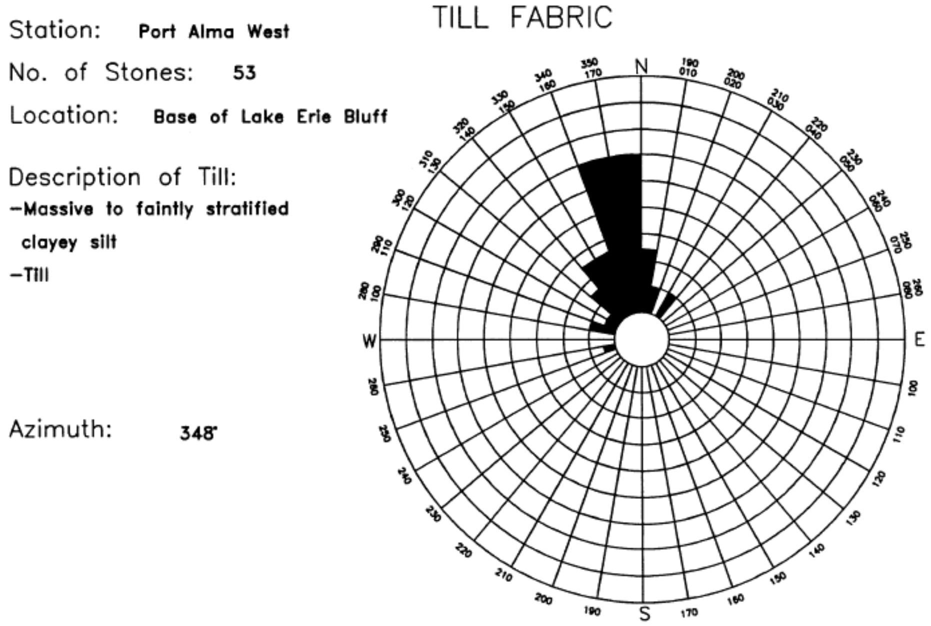

Figure 2.10: Till-fabric orientation at Port Alma section as reported by Kelly (1995)

Stupavsky et al. (1974) studied the anisotropy of magnetic susceptibility (AMS) of the Port Stanley Till at the Port Alma site. It was found that fine magnetite particles in the clay till were free to align themselves in the earth’s magnetic field, whereas coarser magnetite material was not affected by the earth’s field and retained their original alignment created by the ice flow. From the estimation of the ellipsoid of AMS of the analyzed Port Alma samples, the magnitude and direction of the principal susceptibilities were calculated using the method of successive approximations (Nye, 1960). These suggested that the minimum susceptibilities (particle short axis) were clustered close to the vertical direction parallel to the direction of deposition. This means that the plane of maximum and intermediate susceptibilities is nearly horizontal and that the long axes of the magnetite particles are preferentially arranged towards the horizontal plane and directed towards the northwest, as suggested by the till-fabric orientation in Figure 2.10. The average magnitude of AMS, defined as the ratio of the maximum and minimum susceptibilities, throughout the studied Port Stanley till deposit was about 1.14.

2.2.1 Basic geotechnical properties of glacial clay tills

There have been a considerable number of studies on low plasticity clay soils from across Ontario region over the last 50 years (e.g. Becker, 1981; Boulton, 1976; Cowan, 1976; Dreimanis and Karrow, 1972; Dreimanis, 1968 and 1976; Evenson et al., 1977; Graham and Houlsby, 1983; Gravenor and Stupavsky, 1974; Karrow, 1974; Kelly, 1995 and 1998; Kim and Novak, 1981; Kiss, 2016; Lo and Becker, 1979; Lo and Milligan, 1967; Lo, Adams and Seychuk, 1969; Milligan 1976; Quigley and Ogunbadejo, 1974 and 1976; Radhakrishna and Klym, 1974; Soderman and Quigley, 1965; Tyldesley et al., 2013; Kiss, 2016; Newson et al., 2019). Many of these have been glaciolacustrine and clayey glacial tills, which are the most common surficial deposits in the southwestern part of Ontario.

Glacial clay tills, and glacial deposits in general, have a complex formation history. Generally, they are over-consolidated, stiff, have low sensitivity, are primarily incompressible, and have relatively low moisture content (Bell, 2002). However, they are highly variable and cannot be identified by following traditional soil mechanics models based on clay or sand, but by studying their particular history. The geotechnical parameters and behaviour of glacial clay tills will specifically depend on the composition of the till (e.g. texture, density, and structure), and on their consolidation stress levels (Lutenegger et al., 1980; Graham & Houlsby, 1983). The composition of the till depends on several factors, such as the materials that the glacier transported, how they were incorporated, as well as the effect of the transportation mechanism and the mode of deposition (Lindsay, 1970; Stephenson et al., 1988; Trenter, 1999). For clayey glacial tills, its basic engineering properties are also affected by their clay fraction. When finer particles are dominant within the till matrix, the properties of the till will depend upon the variation of the fine particles content.

Bell (2002) explained that even though clayey tills are composed of clay particles, they usually do not exhibit ideal cohesive behaviour due to particle content variations. Variation in the fine grain fraction also can affect the Atterberg limits of tills, which are often used to estimate other geotechnical parameters of soils (e.g. strength, degree of consolidation). Bell (2002) claimed that the lower the clay fraction is, then the lower are the liquid and plastic limits. This will affect the liquid limit more than the plastic limit; thus, the result is that the plasticity index is reduced. For instance, Bell (2002) explained that Cromer till from the Norfolk area has lower Atterberg limits than other British clays. The significant difference being that the Cromer till has a lower clay fraction than the other tills. Milligan (1976) and Chung and Finno (1988) reported on Atterberg limits for different North American clayey glacial tills, such as Chicago clay, and other from Ontario, Saskatchewan, and Alberta. Plastic limits and liquid limits varied between 12% and 30%, and from 19% to 30%, respectively. These ranges of Atterberg limits corresponded favorably with those reported by Bell (2002) for a series of British till deposits.

The consolidation stress levels of a glacial clay till are usually high, due to the thickness of the ice sheet and the porewater pressures developed beneath the glacier (Bell, 2002), and some authors claim that the maximum ice overburden pressure can be determined from the pre-consolidation pressure (Boulton, 1976). As the glaciers advanced and retreated, this type of soil was also subjected to cycles of drying and wetting, erosion, weathering and deposition (Chandler, 2007). Taken together, the combination of the mineral composition and degree of consolidation determine the stiffness of the clayey till, usually yielding a small plasticity index. This stiffness and high shear strength of many glacial clay tills render them largely incompressible, experiencing small amounts of settlement under loading. For example, the Dublin Boulder Clay and London Clay have shear strengths over 100 kPa. However, the degree of over-consolidation of clay tills depends on their composition. For example, Chicago clays are much more compressible due to their basal and ablation till mixture (Chung and Finno, 1992). For New Liskeard clay, its higher fractions of swelling clays, Montmorillonite and Vermiculite, cause it to be susceptible to significant secondary consolidation and long-term creep (Soderman and Quigley, 1965).

Proper understanding of the structure and fabric of a natural soil, such as glacial tills, is paramount for better understanding of their properties and the behaviour that will manifest. The fabric development of till will depend on all of the processes that led to its formation (e.g. transport of debris, depositions of the sediment, intricated post-depositional history), and at the same time these will determine the preferred orientation of the soil particles within the till structure (Lindsay, 1970). From different till-fabric investigations (e.g. Fuller, 1964; Gravenor et al., 1973; Stupavsky et al, 1974) it has been found that the dominant fabric mode for tills deposited at glacier beds (e.g. basal tills, lodgment tills) tends to lie parallel to the flow direction of the ice during deposition and parallel to the direction of shearing (Shumway and Iverson, 2009; Benn and Evans, 2009; Iverson, 2017). The fabric developed in these types of tills is prone to be especially strong due to highly clustered orientation distributions that are a product of high bed shear strains (Iverson et al., 2008; Iverson, 2017).

Geotechnical properties of soils depend mainly on the arrangement of particles. Due to the preferred orientation of the long axes of the particles towards the horizontal plane of bedding, this rarely makes tills isotropic materials. Any anisotropy in the fabric of the soil material produces a directional dependence of geotechnical properties (e.g. strength, stiffness). It has been long recognized that natural soils exhibit some degree of anisotropy, and any added load or change in stresses causes the anisotropy to change (Kuganenthira et al., 1996; Clayton, 2011). In the past few years, several studies have looked at the influence of fabric anisotropy on shear strength and stress-strain behaviour of clays (e.g. Duncan and Seed, 1966; Ting, 1968; Mitchell, 1972; Banerjee et al., 1984; Saada and Bianchini, 1975; Kirkgard and Lade, 1993). More information on this topic will be presented in Section 2.4.

A database of basic geotechnical properties of different glacial clay tills has been compiled and is presented in Table 2.1, summarizing the sources of the published data. The soils presented in the database are generally low to medium plastic cohesive soils with plastic indices (I_p) ranging from 12% to 30% and are slightly to heavily overconsolidated range. Low plasticity and overconsolidation are two prominent features usually exhibited by glacial tills, and they are typically related to the clay content within the soil matrix and to the depositional environment of the glacial clay till deposit. From Table 2.1, it is clear that the majority of the research reported in the literature for Canadian soils has mainly focused on general classification and monotonic properties of these materials. However, the study of the anisotropic and small-strain stiffness behaviour of glacial tills and how this can contribute to the overall stability of the foundation-soil systems is still sparse in the literature.

Table 2.1: Summary of geotechnical properties of some glacial clayey tills

Soil Type	Sample Depth (m)	Clay Content (%)	Water Content, w_c (%)	Atterberg limits (%)	Plastic Index, I_P (%)	Stress History	Undrained Shear Strength, S_u (kPa)	Anisotropic parameters; (α) [n]	Reference strain parameter (γ_{ref})
Windsor Silty Clay (Kim & Novak, 1981)	4.6	70	50.6	$w_L = 51.3$ $w_P = 21.0$	30.3	P_c'=140 kPa OCR = 2.7	23.3	-	0.00067
Wallaceburg Silty Clay (Kim & Novak, 1981)	4	46	38.1	$w_L = 42.2$ $w_P = 17.6$	24.6	P_c'=273.6 kPa OCR = 5.1	39.3	-	0.00054
Chatham Clayey Silt (Kim & Novak, 1981)	4.2	33	27.8	$w_L = 29.0$ $w_P = 15.0$	14.0	P_c'=170 OCR = 2.1	46.0	-	0.00031
Port Stanley Silty Clay (Kim & Novak, 1981)	8	45	2i2.5	$w_L = 35.0$ $w_P = 15.5$	19.5	P_c'= 700 kPa OCR = 6.8	55.0	-	0.00043
Sarnia Silty Clay (Kim & Novak, 1981)	10.7	46	22.5	$w_L = 29.6$ $w_P = 15.4$	14.2	P_c'= 267 kPa OCR = 1.8	76.0	-	0.00031
Hamilton Clayey Silt (Kim & Novak, 1981)	6.4	32	17.2	$w_L = 25.0$ $w_P = 13.0$	12	P_c'= 510 kPa OCR = 5.8	126.6	-	0.00026
Iona Silty Clay (Kim & Novak, 1981)	2.1 (Elevation)	63	19.2	$w_L = 27.0$ $w_P = 14.3$	12.7	P_c'= 400 kPa OCR = 6.4	268.3	-	0.00028
Winnipeg Clay (Graham & Houlsby, 1983)	6-12	70-80	54-63	$w_L = 65-85$ $w_P = 25-30$	35-60	P_c'=150-250kPa OCR = 3-2	50-75	(1.8-1.9) [-]	-
Wellesville Dense Till (Radhakrishna & Klym, 1974)	10.7	30-10	6-8.5 (non-plastic)	-	-	P_c'= 580 kPa OCR = -	1442 (Block sample)	-	-
Tilbury clay till (Bedel, 1967)	10	42	20-24	$w_L = 30.0$ $w_P = 18.0$	12.0	P_c'= - OCR = 3	144-240	-	-
Windsor Clayey Silt Till (Trow, 1965)	-	-	18	$w_L = 26.0$ $w_P = 14.0$	12.0	P_c'= - OCR = -	240	-	-
Sarnia Glacial Clayey Soil (Quigley & Ogunbadejo, 1974)	4-7.1	40-50	20-27	$w_L = 35-40$ $w_P = 10-20$	25-20	P_c'= - OCR = -	100-300	-	-
Wallaceburg Clay (Becker, 1980)	2.61	-	23	$w_L = 35.0$ $w_P = 19.0$	16.0	P_c'= 520 kPa OCR = 16	96.0	(0.40) [0.70]	-
	3.90	-	38	$w_L = 42.0$ $w_P = 20.0$	22.0	P_c'= 315 kPa OCR = 7	47.0	(1.50) [0.75]	-
Port Alma Clay Till (Tyldesley and Newson, 2016)	0-1.5	40	22-32	$w_L = 46.0$ $w_P = 21.0$	25.0	P_c'= - OCR = 2-5	100-150	(-) [-]	-
	1.5-4.5	29	16-20	$w_L = 34.0$ $w_P = 19.0$	15.0	P_c'=- OCR = 2-3	60-200	(0.56-0.84) [-]	-
	4.5-40	31	16-24	$w_L = 30.0$ $w_P = 17.0$	13.0	P_c'= 360 kPa OCR = 1-1.5	60-80	(0.64-0.81) [-]	-
Port Alma Clay Till (Gonzalez-Hurtado, 2016)	4-5	29	18.0	$w_L = 34.0$ $w_P = 19.0$	15.0	P_c'=- OCR = 2-3	60-200	(0.36-1.16) [-]	0.00033
Cromer Till (Kazi & Knill. 1694)	7	20-25	11.5-13	$w_L =28.0$ $w_P =13.0$	15-20	P_c'=400 kPa OCR =7-2	176-224	-	-
Dublin Boulder clay (Long & Menkiti, 2007)	7.5	20.0	14.0	$w_L =29.0$ $w_P =16.0$	13.0	P_c'=650 OCR =2.5	350.0	-	-
Holderness till (Bell, 2002)	-	15-35	20-25	$w_L =38-27$ $w_P =23-16$	22-12	P_c'=- OCR =-	20-100	-	-

S_u: in-situ undrained shear strength; γ_{ref}: reference strain equal to the shear strain at 0.5 $G_{max;}$ w_L: liquid limit in percentage (%); w_P: plastic limit in percentage (%); Pc': pre-consolidation pressure (kPa); OCR: overconsolidation ratio; α: stiffness anisotropy (E_h/E_v; Young's modulus in horizontal direction/Young's modulus in vertical direction); n: strength anisotropy ($S_uTX_{compresion}/S_uTX_{extension}$; Undrained shear strength from triaxial compression/ Undrained shear strength from triaxial extension)

2.3 Measurement of small-strain stiffness

The maximum shear modulus, G_{max} (also found in the literature as G_o), is broadly considered to be a fundamental soil stiffness property and is important to geotechnical engineers for several reasons. It is a parameter for practical geotechnical problems both in earthquake engineering and for the prediction of soil-structure interaction. Reliable determination of G_{max} and estimating complete stress-strain curves, especially for small and very small strains ($\varepsilon < 10^{-5}$), offer the possibility of determining the functional relationship between shear modulus degradation and strain as seen in Figure 2.11. Many researchers have attempted to investigate the stiffness properties of different natural soils (e.g. Kim and Novak, 1981), and have focused on the estimation of the maximum shear modulus along the vertical axis of the samples ($G_{max} = G_{vh}$). In the present research, the study of anisotropy is also included, hence $G_{max(ij)}$ is measured in different planes within the soil specimens. The suffix ij refers to the plane in which the shear modulus is measured, and from here on the suffix "max" will be omitted (G_{vh}, G_{hv}, G_{hh}) (Jamiolkowski et al., 1995). More details on the calculation of G_{max} will be presented in the following sections.

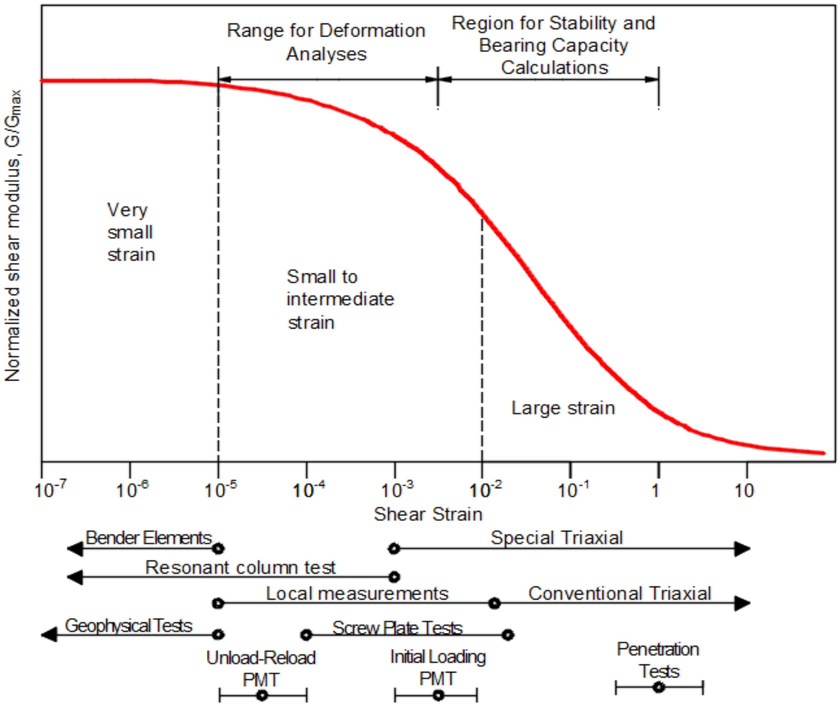

Figure 2.11: Stiffness degradation curve and strain range of different structures and testing methods (adapted from Ishihara, 1996; Atkinson, 2000; and Mayne, 2001)

The strain levels shown in Figure 2.11 have been sub-divided previously into three zones (Atkinson, 2000): *very small-strain*, where stiffness is constant and elastic, *small-strain*, where stiffness varies non-linearly with strain, and *large strain*, where the soil approaches failure and the stiffness is relatively low. The majority of geotechnical structures have operating conditions within intermediate strains from 10^{-5} to 10^{-2}. Different methods of determining the stiffness also provide a wide range of applicable strain levels and hence stiffness estimates, from very small strains to large strains, as shown in Figure 2.11. These methods encompass *in-situ* and laboratory techniques that can be used to measure soil stiffness directly (e.g. triaxial tests with local strain measurement) or indirectly through the measurement of propagating waves (e.g. resonant column, bender elements, geophysical tests). More information on these techniques will be provided in the next sections.

2.3.1 Static local strain measurement of small-strain stiffness

Precise determination of soil stiffness is difficult to achieve in routine laboratory testing. Conventionally, the determination of the axial stiffness of a specimen in a triaxial test is based on external measurements of displacement, which include a number of extraneous movements. For instance, the true soil strains developed in triaxial tests can be masked by deflections that originate in the compliance of the loading system and load measuring system. Such equipment compliance errors occur in addition to a variety of sample bedding effects, to give a poor definition of the stress-strain behaviour of the material under test, particularly over the small strain range. Most triaxial tests therefore tend to give apparent soil stiffnesses lower than those inferred from field behaviour (Jardine et al., 1984). However, this has been found to be less problematic for stiffer soils. Throughout the Rankine lecture “small is beautiful”, Burland (1989) provided evidences showing that the soil mass beneath and around structures (e.g. excavations, foundations, tunnels) can experience level of strains smaller than 0.1% under working load conditions. Moreover, Burland (1989) also added that if the strains are measured locally to a high accuracy, triaxial tests on high-quality samples could give accurate and consistent measurements of the *in-situ* small-strain stiffness.

Atkinson and Sällfords (1991) estimated the limits of reliable local strain measurements to be around a strain level of $5x10^{-5}$. Nevertheless, this limit was later modified to an improved level of 1.5×10^{-5} by Atkinson et al. (1993), as depicted in Figure 2.11. Local strain systems can be used to measure both axial and radial strains. These local axial strain systems can be classified as fixed-type or floating-type. The fixed-type instrument is attached to a fixed support and measures an absolute movement on a target mounted on the sample surface, while the floating-type instrument is attached to the specimen surface allowing the measurement of the gauge length deformation directly from one instrument (Yimsisi and Soga, 2002).

Cuccovillo & Coop (1997) developed a floating-type local system to measure local axial strains using a linear variable differential transformer (LVDT) to give reliable resolutions of about 2×10^{-7} with a working range of up to 10%. Goto et al. (1991) developed a local axial strain measuring system using a local deformation transducer (LDT), capable of measuring local axial strains to a resolution of $7x10^{-6}$ and working range of up to 2%. Clayton and Khatrush (1986) and Clayton et al. (1989) developed the classic Hall-Effect gauges by using a semiconductor sensor. The system was able to measure strains of around $2x10^{-5}$ with a working range between 2% to 7%.

Scholey et al. (1995) reviewed instrumentation for measuring local strains in triaxial testing. This paper shows the advantage and disadvantage of each device. Among their findings, they pointed out that measuring deformations externally in triaxial tests is inadequate when investigating the small-strain stiffness of soil materials, due to errors arising from the accuracy and resolution of the instruments. Moreover, Scholey et al. (1995) stated that the errors from local deformation measurements can be eliminated by measuring strains internally and locally over the central one third of the specimen. More recently Yimsiri and Soga (2002) revisited the review presented by Scholey et al. (1995) and supplemented their work including updated information on developments of the local strain instrumentation and additional discussions on the subject. They suggested that among the commercially available local axial strain measurement systems, the miniature water-submersible LVDT had the most promising features (e.g. robustness, large working range), but the high cost associated with their fabrication made the in-house made systems such as the Local deformation transducer (LDT) (Tatsuaoka, 1988) a cost-effective viable option.

2.3.2 Dynamic methods for measuring very small-strain stiffness

Dynamic techniques to determine stiffness in elastic media are based on velocity measurements of body waves: shear waves (s-waves) and compressional waves (p-waves) as depicted in Figure 2.12. S-waves have the motion of an individual particle perpendicular to the direction of the s-wave travel. These are also known as secondary, shear or transverse waves. P-waves have the motion of an individual particle parallel to the direction of travel, they are also known as primary, compressional, or longitudinal waves (Kramer, 1996; Ishihara, 1996). The links between the velocities of the body waves and stiffness assume that soil behaves as an isotropic homogeneous elastic medium. Equations 2.5 and 2.6 can be used to derive the maximum or small-strain shear stiffness and the compressional (or constrained) modulus:

$$G_{max} = \rho . V_s^2 \tag{2.5}$$

$$M_{max} = \rho . V_p^2 \tag{2.6}$$

where G_{max} (or G_o) is the maximum shear modulus, M_{max} (or M_o) is the maximum constrained modulus, ρ is the mass density of the material, V_S is the shear wave velocity, and V_P is the primary wave velocity. Equations 2.5 and 2.6 were originally derived from elastic theory (Hardin and Blandford, 1989).

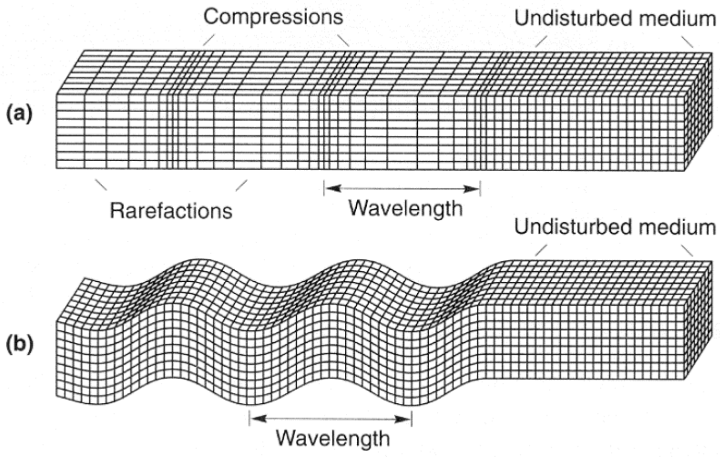

Figure 2.12: Deformations produced by body waves: a) p-wave; b) s-wave (adapted from Kramer, 1996)

2.3.2.1 Laboratory measurements

2.3.2.1.1 Bender elements

The bender element (BE) test provides the small-strain stiffness properties of a soil (e.g. G_{max}, E_{max}) by determining the velocity propagation of a shear or compressional wave through the soil sample (e.g., Sanchez-Salinero et al., 1986; Dyvik and Madshus, 1985; Clayton, 2011). Bender elements are electro-mechanical transducers that can either bend when a certain amount of voltage is applied through them or will produce voltage as they bend. In general, bender elements consist of two piezoceramic plates firmly fused to an inner metallic plate. A thorough explanation of the concept and fabrication of the bender elements have been presented by different authors (e.g., Shirley and Hampton, 1978; Dyvik and Madshus, 1985; Lee and Santamarina, 2005). Figure 2.13 shows a general schematic and the types of bender elements. Depending on the orientation of polarization, BE can be classified into two types: in series (Figure 2.13(b)) or parallel (Figure 2.13(c)). In the series type BE, the polarization direction of the two piezoelectric layers are opposite to each other and the BE is connected at the outer electrodes. In the parallel type, the two piezoelectric layers have the same polarization direction. Manufacturers often recommend the use of series-type BE as receiver and the parallel-type as source (Lee and Santamarina, 2005).

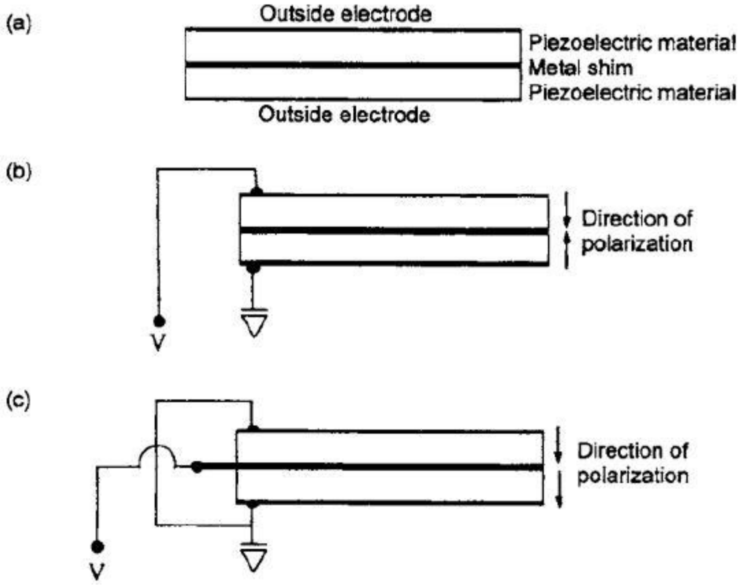

Figure 2.13: Bender elements: a) schematic representation of bender element; b) series type, and c) parallel type (Lee and Santamarina, 2005)

Typically, BE are fitted in the top cap and pedestal of a triaxial cell and act as miniature cantilever beams. When excited by an input voltage, the source element bends, producing a wave that travels through the soil sample at an assumed wave velocity (V_s or V_p). The wave motion causes the receiver element to mechanically vibrate, inducing a voltage signal that is captured by an oscilloscope or high-speed digital data acquisition system. The shear wave velocity is then calculated by determining the travel time of the shear wave between the tips of the source and receiver elements. The same procedure is applied to determine V_p from the compressional wave. G_{max}, is then calculated using the one-dimensional wave propagation relationship presented in Equation 2.5. Figure 2.14 shows a typical bender element test setup.

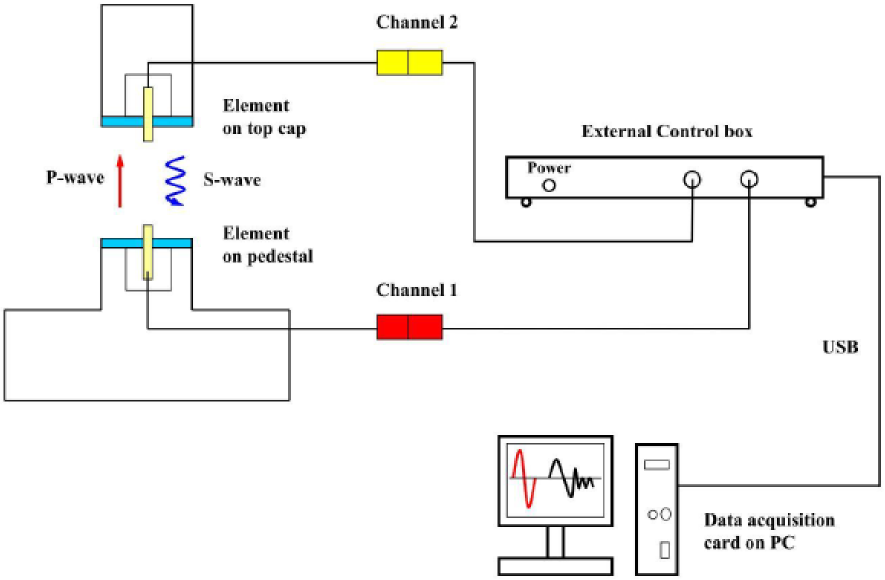

Figure 2.14: Typical setup of a bender element test (Gu et al., 2013)

Since the shear modulus is a direct function of shear wave velocity, the travel distance and the travel time for the velocity are the key parameters to be reliably determined. Viggiani and Atkinson (1995) performed a number of tests on samples of different heights in a triaxial cell, and from these tests they concluded that the tip to tip distance between the BE was the most appropriate measure for travel distance. That finding was supported by Brignoli et al. (1996) after carrying out laboratory measurements using bender elements and non-penetrating shear plates. Viggiani and Atkinson (1995) recommended the using of sinusoidal waves before square waves, as these are composed of different dominant frequencies that can result in near field effects. Besides reducing the near field effects, sinusoidal excitation allows the application of relatively simple methods of interpretation in the frequency and time domain (Viggiani and Atkinson,1995). As for the frequency of the propagated wave, it was found that the use of moderately high frequency waves (>3 kHz) was desirable since the near field effect was reduced and error in the interpretation methods was minimized (Sanchez-Salinero et al., 1986; Brignoli and Gotti 1992; Viggiani and Atkinson 1995). It was proved numerically and experimentally that near field effects are attenuated with distance and number of wavelengths (higher frequencies imply more wavelengths), so that the optimum number of wavelengths is around 3 to 5 (Sanchez-Salinero et al., 1986; Jovicic et al. 1996; Brignoli et al. 1996).

BE testing has been a useful tool to assess the small-strain stiffness anisotropy of different natural deposited cohesive materials, such as the stiff Gault clay, London clay, stiff Pietrafitta clay, and Chicago glacial clay (e.g., Pennington et al., 1997; Lings et al., 2000; Jovicic and Coop, 1998; Gasparre et al., 2007; Callisto and Rampello, 2002; Kim and Finno, 2012); and granular materials like Ticino sand and Ham River sand (Belloti et al., 1996; Kuwano and Jardine, 2002). Common BE orientations in the triaxial test apparatus produce shear waves that propagate vertically within the sample and generally are polarized in the horizontal direction, allowing for the measurement of G_{vh}, commonly regarded to be G_{max}.

Due to depositional history and induced stresses, most natural soils are inherently anisotropic, or at least cross-anisotropic. Hence, to properly describe the stiffness behavior of a cross-anisotropic soil, the bender element method can be used to evaluate anisotropic shear moduli, as the bender element orientations can be changed to induce shear waves that propagate in the horizontal direction. The shear modulus in the horizontal plane, G_{hh} and G_{hv}, can be evaluated by mounting bender elements on the side of a specimen or by cutting vertical and horizontal samples from blocks (Pennington et al. 1997; Jovicic and Coop 1998; Kuwano et al., 2000) as shown in Figure 2.15.

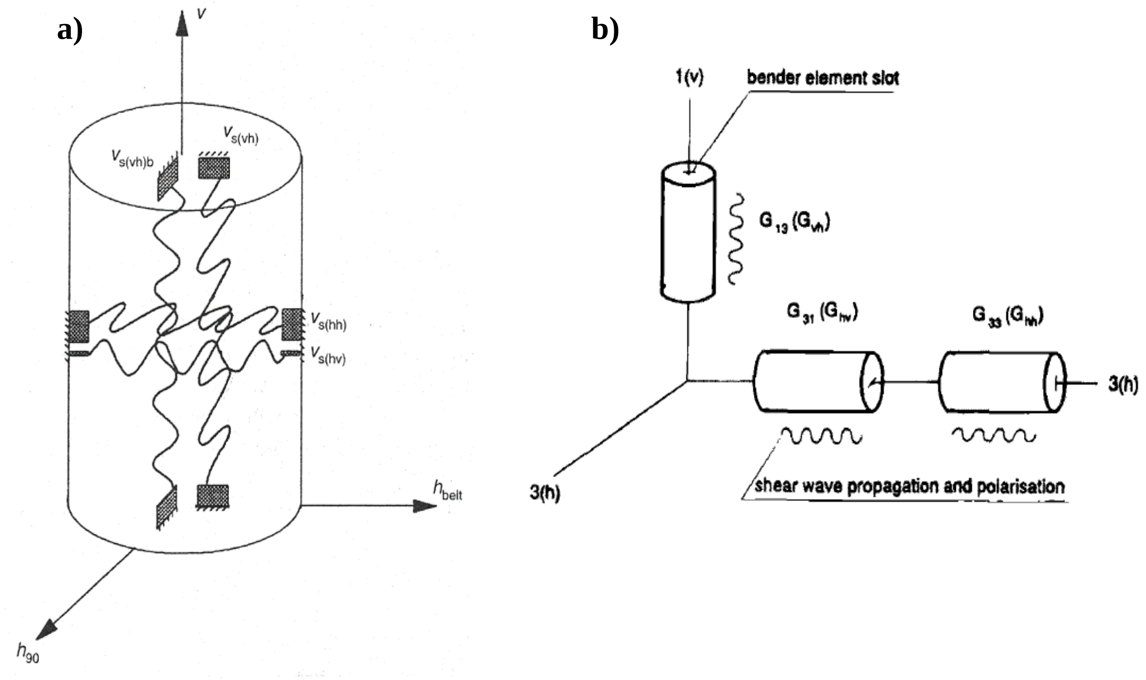

Figure 2.15: a) BE wave propagation and polarization directions scheme employed by Pennington et al. (1997); b) sample orientations used by Jovicic and Coop (1998)

2.3.2.1.1.1 Wave travel-time analysis

The methods to interpret the travel time of wave velocities can be divided into the time and frequency domain. Time domain methods are direct measurements based on the plots of the voltage amplitude signals versus time (e.g Viggiani and Atkinson, 1995; Arulnathan et al., 1998; Clayton et al., 2004). Frequency domain methods involve analyzing the spectral breakdown of the signals and comparing phase shifts of the components (e.g Viggiani and Atkinson, 1995; Brocanelli and Rinaldi, 1998; Arroyo, 2001). A number of issues have been identified when interpreting bender element test results, including the aforementioned near field effect (Sanchez-Salinero et al., 1986) and subjectivity in determining the arrival time of the propagated waves.

Due to those issues, satisfactory models or standards for test interpretation are still lacking (Viana da Fonseca et al., 2009; Alvarado and Coop, 2012). Moreover, Yamashita et al. (2009) reported that based on a review of various existing interpretation methods from different regions all over the world, no method proved to be superior to the others. However, this study identified three main approaches to determine wave travel-time, and these involved the observation of the source and received BE signals, cross-correlation of the signals, and a cross-power spectrum calculation of the signals (Yamashita et al., 2009). The first two approaches are considered to be techniques applied in the time-domain, and the latter regarded as a frequency-domain technique.

Figure 2.16 shows an example of visual analysis to measure travel-time using the first arrival (Fig. 2.16a) and peak-to-peak (Fig. 2.16b) methods. Visual inspection to determine arrival time is perhaps the most subjective approach, depending on the signal quality and the judgment exercised by the individual. However, it is the most commonly used method of interpretation because it is very straightforward (Chan, 2010). Using the peak to peak method may minimize the near field effects but is still affected by the criteria set for the first major peak (i.e when the first major peak does not have the largest magnitude). More information on these methods can be found in Viggiani and Atkinson (1995), Lee and Santamarina (2005), and Chan (2009). Additional signal processing procedures, such as cross-correlation and cross-power spectrum, have been explored to avoid "choosing" a travel time. Lee and Santamarina (2005) stated that such techniques must relate signals of the same nature or account for different frequency response functions. Use of cross-correlation and cross-power spectrum to provide travel time estimations have been extensively covered elsewhere (Viggiani and Atkinson, 1995; Arroyo, 2001; Leong et al. 2005).

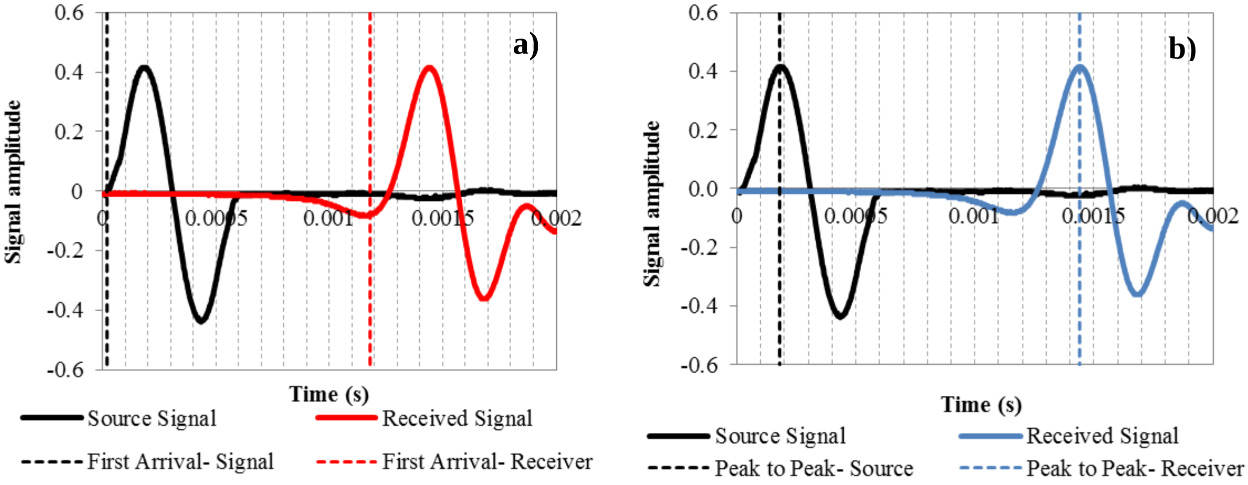

Figure 2.16:Typical waves measured with BE and suggestions of identification of travel-time: a) first arrival, and b) peak-to-peak

2.3.2.1.2 Resonant column test

The resonant column (RC) test is one of the most popular laboratory research techniques for measuring the stiffness properties of soils such, as the small-strain (or maximum) shear modulus (G_o or G_{max}) and small-strain (or maximum) elastic modulus (E_o or E_{max}), and damping ratio (D). This laboratory technique is now an ASTM standard test (ASTM D4015-15) and has been widely and successfully used for more than 40 years to study the dynamic response of soils in geotechnical engineering (Clayton, 2010), and throughout these four decades the RC technique has been continuously refined (Hall and Richart, 1963; Hardin and Black 1966; Drnevich, 1967; Anderson and Stokoe 1978; Kim and Stokoe 1994; Cascante et al., 1998). The RC apparatus has been used to study a wide range of soil materials, from cohesionless to cohesive materials, such as Toyoura and Ottawa sand (Iwasaki et al., 1978; Hardin and Kalinski, 2005), medium to high plastic clays (Idriss et al., 1977, 1978; Vucetic and Dobry, 1988), and low to medium plastic stiff clays (Kim and Novak, 1981; Gasparre et al., 2007; Reipas, 2012; Brosse et al., 2017).

Several RC devices have been developed by different researchers (Hardin & Music, 1963, 1965; Drnevich, 1966; Stokoe et al., 1980; Stoll, 1984; Avramidis & Saxena, 1990; Cascante et al., 1998; d'Onofrio et al., 1999; Menq & Stokoe, 2003). Some of these have created either free-free or fixed-free end conditions of the samples, however fixed-free configurations are most commonly used. The Stokoe fixed-free type apparatus is regarded as the most advantageous device compared to its counterparts, as it allows testing of stiff and hard geomaterials, testing on frozen soils, and it has relatively high available torque (Clayton et al., 2009).

The RC test in general consists of exciting a cylindrical soil specimen to identify the first-mode resonance. Torsional and longitudinal excitation can be used to estimate V_s and V_p for the waves propagating through the soil specimen. One of the important advantages of RC testing is that measurements can be performed for a range of strains between 10^{-4} % to 10^{-1} %. Figure 2.17(a) shows a simplified diagram of a typical fixed-free device. The test is usually performed while the soil specimen is under isotropic confinement. A cross-sectional view of a typical confining system is depicted in Figure 2.17(b). A sinusoidal torsional excitation is applied to the top of the specimen over a range of frequencies (e.g.

10 Hz to 200 Hz), and the acceleration amplitude is measured for the different frequencies with an accelerometer located at the top of the specimen (see Figure 2.18).

The output from the accelerometer is recorded along with the vibration frequency during a frequency sweep. The graph of accelerometer output versus vibration frequency is called the frequency response curve. A typical response curve is presented in Figure 2.19. The frequency at which the accelerometer output reaches a maximum during first-mode torsional resonance is denoted as the resonant frequency (f_r) and it is used to calculate V_s of the soil specimen. The output of accelerometer (A_r) at this frequency is used to estimate the shear strain amplitude during the test. The material damping can also be evaluated from the dynamic response using any of the following: the free-vibration decay curve, the half-power bandwidth method, or transfer-function method (Cascante and Santamarina, 1997). As an example, Figure 2.20 shows a typical data-set collected using the free-vibration decay approach. This curve is recorded by shutting off the driving force after the specimen is vibrating in a steady-state resonant motion.

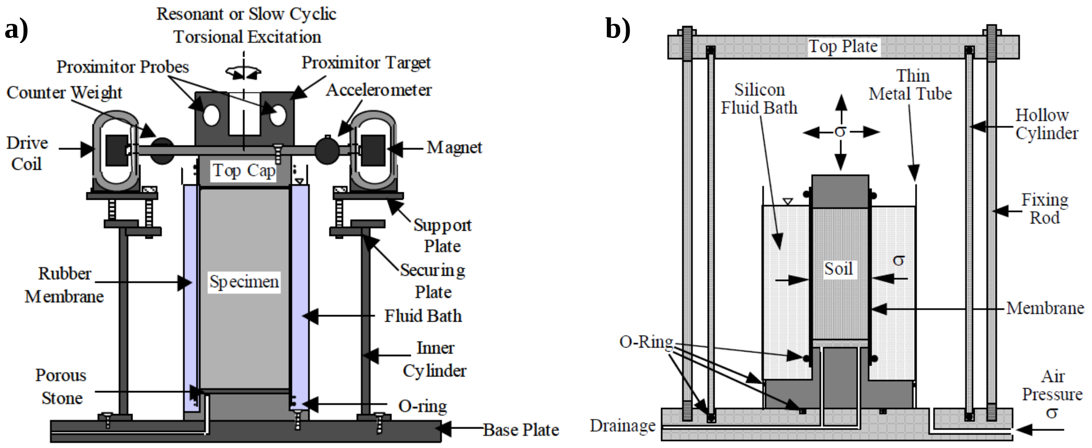

Figure 2.17: a) Simplified diagram of the RC device (Stokoe et al., 1999); b) simplified cross-sectional view of the confining system (Hwang, 1997)

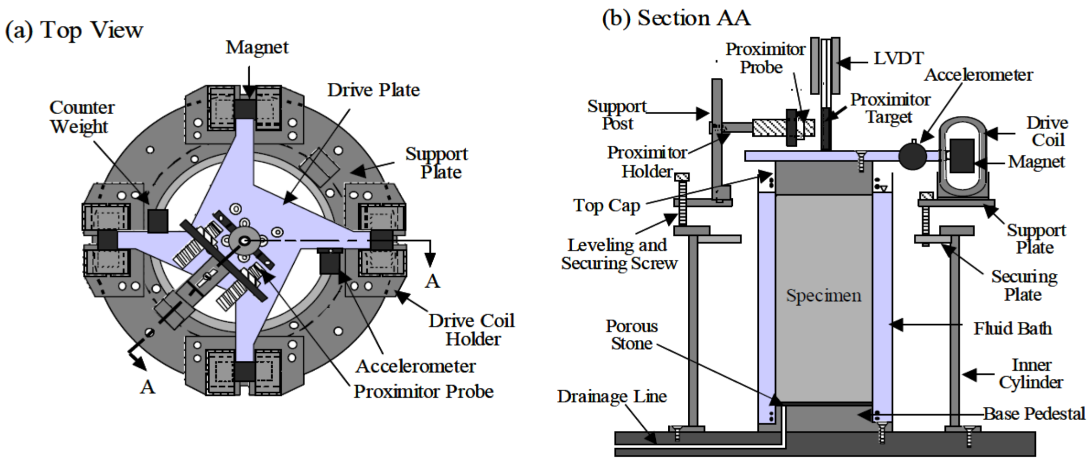

Figure 2.18: General configuration of the RC equipment (Hwang, 1997)

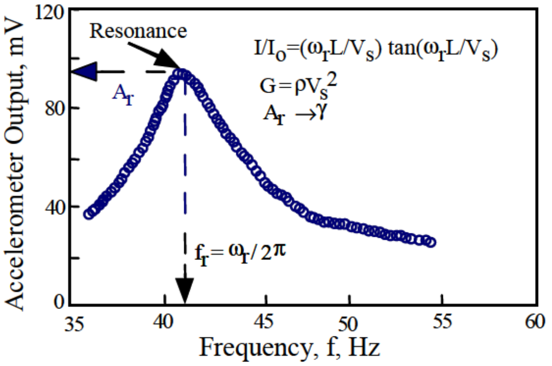

Figure 2.19: Dynamic response curve measured with a fixed-free RC (Stokoe et al., 1999)

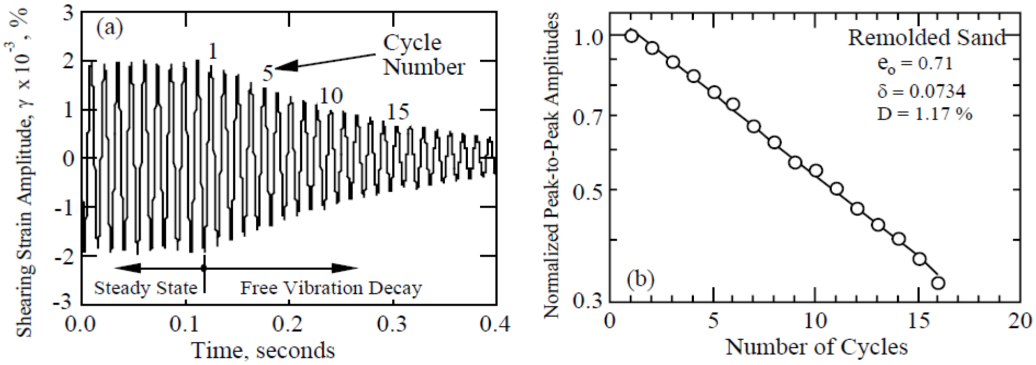

Figure 2.20: Material damping measurement in the RC test using the free-vibration decay curve (Stokoe et al., 1999)

2.3.2.2 In-situ measurements

2.3.2.2.1 Geophysical tests

The small-strain stiffness properties of the soil can be estimated in the field using *in-situ* geophysical techniques of wave propagation that induce strains of the same order as bender element tests ($<1\text{x}10^{-4}$ %). Previous research has shown that G_{max} measured *in-situ* is approximately equal to that measured in laboratory tests on very high-quality specimens (Clayton and Heymann 1999; Matthews et al. 2001; Clayton, 2011). Three of the most popular methods employed to measure G_{max} *in-situ* are the Seismic Down-Hole (Up-Hole) test, Seismic Cone Penetration Test (SCPT) and the Cross-Hole Seismic Test (CST). Campanella et al. (1986), Sully and Campanella (1995) and Clayton (2011) previously described both tests thoroughly.

The seismic down-hole (or up-hole) test can be performed in a single borehole. This uses a surface source adjacent to the borehole to induce seismic excitation to the ground (e.g. a sledgehammer striking a weighted beam). S-waves, polarized in the horizontal direction, can be generated by striking the source horizontally, whereas P-waves can be generated by hitting the source vertically or by dropping a weight onto it (Ishihara, 1996). Usually, a single receiver that can be moved to different depths, or a string of multiple receivers at different depths, is fixed to the walls of the plastic-cased borehole and single triggering receiver is placed at the energy source (Kramer, 1996, Ishihara, 1996) . The arrival of the seismic energy is detected at depth with geophones, Clayton (2011) stated that it is advantageous to two set of three orthogonally oriented geophones in each detector array, separated by 1 m in the vertical direction. Figure 2.21(a) depicts a typical set up for the down-hole test

The SCPT is conceptually similar to the down-hole test, except that it does not require a borehole. The SCPT is a modification of the CPT and is conducted using a conventional 10 or 15 cm^2 piezocone fitted with one or more accelerometers (Campanella et al., 1986). Seismic excitation is generated in the ground from surface impacts and the travel times are measured based on wave arrivals at the accelerometers fitted above the cone tip, as shown in Figure 2.21(b). True travel time will be estimated between two accelerometers approximately 1 m apart in the cone to eliminate dependence on trigger sensitivity. Stiffness anisotropy cannot be measured with the conventional SCPT, hence only estimations of G_v or G_{vh} can be made.

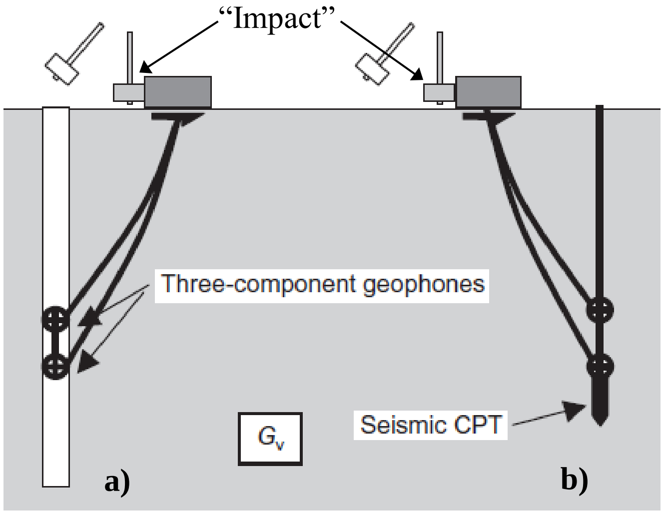

Figure 2.21: Typical set up of a) down-hole test and b) SCPT test (Clayton, 2011)

CST involves transmission of waves between three parallel boreholes and measurements of travel times between the source and two receivers. Figure 2.22 shows the typical configuration of the CST test. Shear and compression wave velocities can be determined from the measurement of the travel time between the source and receivers. P-waves induce volumetric strains (Fig. 2.12(a)), hence they travel at a speed related to the undrained volumetric stiffness. In saturated soils, values of V_p are typically found to be around 1500 m/s, therefore the calculated undrained bulk modulus is more similar to that of water rather than that of the volumetric skeletal stiffness of the soil (Clayton, 2011). S-waves induce changes in shape without changes in volume, thus the stiffness determined by this measurement is independent of the saturation of the soil. The source and receiver are typically located at the same depth and can be oriented to measure horizontally propagating-vertically polarized small-strain shear modulus (G_{hv}) and horizontally propagating-horizontally polarized small-strain shear modulus (G_{hh}) by changing the polarization of the propagated shear wave through the soil profile. Hence the anisotropy of G_{max} can be assessed using the modular ratio G_{hh}/G_{hv} also known as anisotropy degree or anisotropy ratio (α) (Clayton, 2011).

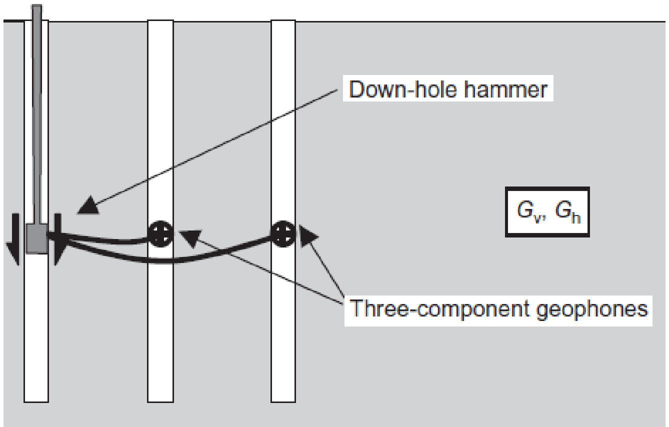

Figure 2.22: Cross-hole (CST) test typical set up (Clayton, 2011)

2.3.2.2.2 Conventional field tests

In-situ test results can be correlated to large strain measurements with a moderate degree of certainty. For example, conventional CPT results can be correlated to constrained moduli (Lunne et al. 1997). Pressuremeter tests (PMT) can be used to give estimates of the initial or unload-reload shear modulus at varying small to large strain levels (Mair and Wood 1987). PMT provide more reliable large strain moduli measurements and may be used to estimate moduli at the upper end of the small strain range (near 0.1%) in some geomaterials (Fahey 1999). Furthermore, several researchers have studied and presented empirical correlations to approximate the value of shear wave velocity using typical parameters obtained from *in-situ* penetration tests such as the standard penetration test (SPT) and CPT (Kramer, 1996). From SPT the typical values related to correlations are the standard penetration resistance (N) or the corrected penetration resistance (N_{60}). From CPT values of the cone tip resistance (q_t), sleeve friction (f_s), and measured cone penetration resistance (q_c). Different authors have compiled a large data base of the correlations between Vs-SPT and Vs-CPT; these can be found in Bellana (2009) and Weir et al. (2012).

2.3.3 Factors that influence the small-strain stiffness

Many factors have been identified as possible sources of influence over the elastic moduli of soils at very small and small strains. The most relevant factors affecting the elastic moduli of normally consolidated to overconsolidated clays have been identified as: state of the soil, time effects (creep/ageing), sample disturbance, recent stress history and anisotropy (Jardine et al., 1984; Atkinson and Sallfors 1991; Ishihara, 1996; Tatsuoka et al. 1997; Gasparre et al., 2007). The influence of anisotropy is addressed in more detail in Section 2.4.4.

2.3.3.1 Dependency on the soil-state

The stiffness of soils depends on multiple factors. Besides the intrinsic properties of the material (e.g. mineralogy and particle shape), the state and strain history of the soil, defined by parameters such as the over-consolidation ratio (OCR), void ratio (*e*), effective stress (*p'*), have been known to have an important influence on the stiffness of soils. To better describe the effect of these factors on stiffness, relationships of the form of Equation 2.7 have been adopted in many conventional stiffness models;

$$G = Sf(e)g(OCR)h(\sigma') \qquad (2.7)$$

where S is a material constant and the shear modulus, G, is expressed by multiplying individual functions of e, OCR, and σ' (σ' can be p' or, more generally, the mean normal effective stress or effective Cambridge stress). In previous concepts, such as the one proposed by Hardin and Black (1968), induced anisotropy was not explicitly considered and the contribution of the effective stress was expressed using $h(\sigma') = (p')^{0.5}$. Induced anisotropy is caused by the application of different effective stress in the vertical and horizontal directions of a soil material. Roesler (1979) observed that the shear wave velocities propagating in sand were a function of only the normal effective stresses acting on the planes of propagation and polarization of the waves. Based on these results, Hardin and Blandford (1989) proposed a more generalized equation considering the effective principal stresses acting on the plane of the wave propagation as follows:

$$G_{max_{ij}} = S_{ij} f(e)(OCR)^k (p_r)^{1-n_i-n_j} (\sigma_i')^{n_i} (\sigma_j')^{n_j} \qquad (2.8)$$

where G_{maxij} is the elastic shear modulus in the *i-j* plane, S_{ij} is a non-dimensional material constant (or fabric constant), p_r is a reference constant pressure usually taken as the atmospheric pressure (101.3 kPa), σ'_i and σ'_j are the effective principal stresses acting on the plane in which G_{max} is measured (*i* and *j* directions correspond to propagation and and particle motion directions, respectively), k is an empirical exponent that depends of the plasticity index of the soil, *n*i and *n*j are non-dimensional soil empirical exponents, and OCR is the soil overconsolidation ratio, respectively. With regard to the void ratio function (*f*(e)), different expressions have been proposed in the literature. However, Equations 2.9 and 2.10 are two of the most common expressions used for *f*(e). Equation 2.9 was proposed by Hardin and Black (1968), and Equation 2.10 was assumed by Jamiolkowski et al. (1995) when studying different natural cohesive materials.

$$f(e) = \frac{(2.973 - e)^2}{(1 + e)} \qquad (2.9)$$

$$f(e) = e^{-x}, \qquad x = 1.2\sim1.6 \qquad (2.10)$$

Rampello et al. (1994) and Viggiani and Atkinson (1995) pointed out that at least one of the three parameters (*e, p'*, and OCR) of the isotropic model proposed by Eq. (2.7) was redundant. They argued, at least for clays, that there is a unique link between these parameters under the conventional framework of bilinear elasto-plastic behaviour in *e-log p'* space. After a series of tests on six Italian clays, Jamiolkowski et al. (1995) determined that the OCR does not influence the shear modulus when the void ratio function described by Eq. (2.7) is used. Thus, showing experimentally the redundancy of using OCR within the formulation. Following the form of Eq. (2.8), Jamiolkowski et al. (1995) proposed Equations 2.11 and 2.12 to estimate the elastic shear modulus of anisotropic clays:

$$G_{vh} = S_{vh} f(e)(p_r)^{1-n_v-n_h}(\sigma'_v)^{n_v}(\sigma'_h)^{n_h} \qquad (2.11)$$

$$G_{hh} = S_{hh} f(e)(p_r)^{1-2n_{hh}}(\sigma'_h)^{n_h}(\sigma'_h)^{n_h} \qquad (2.12)$$

where n_v was equal to n_h. More recently Yimsiri and Soga (2011) used a relationship of a similar form to that proposed by Hardin and Black (1968) to fit the data obtained from a series of analyses performed on the anisotropic Gault clay and London clay:

$$G_{ij} = S_{ij} f(e)(p')^n \qquad (2.13)$$

where p' is the isotropic mean effective stress or effective Cambridge, S_{ij} and n are material constants, and *f*(e) is the void ratio function defined by Eq. (2.6).

G_{max} is believed to reflect contact-level deformation and exhibits a Hertzian-type power relation with the effective stress (Santamarina and Cascante, 1996; Cha et al., 2014). Thus, due to the intrinsic link between G_{max} and shear wave velocity, Eq. (2.13) may adopt the following form in terms of V_s (Hardin and Drnevich, 1972; Knox et al., 1982; Lee and Stokoe, 1986; Santamarina and Cascante, 1996, Cha et al., 2014):

$$V_s = \sqrt{G_{max}/\rho} \ = \alpha_s(p')^{\beta} \qquad (2.14)$$

where p' is the mean effective stress acting in the direction of particle motion and the direction of wave propagation, the α_s factor (m/s) is the shear wave velocity at a mean effective stress (p') equal to 1 kPa; and β is an exponent that captures or describes the sensitivity of the skeletal shear stiffness to the applied stress. The void ratio function used in Eq. (2.13) is implicitly included in the α_s factor of Eq. (2.14) (Cha et al., 2014). The velocity-stress power relationship described by Eq. (2.14) is particularly useful, since it captures the contact behaviour of the soil particles and fabric changes due to change in effective stress.

2.3.3.2 Sample disturbance

Sample disturbance can play a major role in the characterization of very small and small-strain behavior of clays. Many factors cause disturbance; amongst the most common are: borehole instability, reduction of effective stress, shear strains induced by tube penetration, sample extrusion and trimming, fast increments of pressures during testing (Clayton and Heymann, 2001; Hight, 2001). Disturbance causes a variety of different effects on soft soils, but in general, leads to a much flatter modulus reduction curve due to progressive destructuring and shrinkage of the limit state surface (Clayton et al. 1992). This makes it even more difficult to capture the real behaviour of the soil material being tested. Using high quality block samples and trimming the triaxial specimens with a fine wire saw can minimize the effects of disturbance to some extent. Nevertheless, even block samples can suffer from some measure of disturbance due to excavation method, stress relief, sample preparation, and saturation and consolidation methods used during testing.

Since the mid-1990s, the Norwegian Geotechnical Institute (NGI) has used a method proposed by Lunne et al. (1997) to evaluate sample disturbance on different offshore and onshore consulting projects (Lunne et al, 2006). This method is based on the quantification of the sample disturbance using the change in pore volume relative to the initial pore volume, or in other words, the ratio of the initial void ratio to consolidated void ratio ($\Delta e/e_o$). Table 2.2 shows the proposed criteria for evaluation of sample disturbance as quantified by the value of $\Delta e/e_o$ and over-consolidation ratio (OCR).

Table 2.2: Criteria for evaluation of sample disturbance (after Lunne et al., 1997)

OCR	**$\Delta e/e_o$**			
1 to 2	< 0.04	0.04-0.070	0.070-0.14	> 0.14
2 to 4	< 0.03	0.03-0.050	0.050-0.10	> 0.10
4 to 6	< 0.03	0.02-0.035	0.035-0.07	> 0.07
Quality:	1: *very good to excellent*	2: *good to fair*	3: *poor*	4: *very poor*

Note: the description of sample quality refers to use of samples for measurement of mechanical properties

2.3.3.3 Recent stress-history

Atkinson et al. (1990) defined “recent stress-history” as the existing stress-path direction in relation to its previous stress-path direction and noted that this can affect the small-strain stiffness. Likewise, Finno and Cho (2011) suggested that the main effect of the recent stress-history is that the stiffness depends on the angle between the current stress-path and its previous loading-path, with the largest stiffness occurring when the angle approaches 180° (i.e. complete reversal of direction of loading). Figure 2.23(a) shows the results obtained by Finno and Kim (2012) supporting the hypothesis drawn by Finno and Cho (2011) depicted in Figure 2.23(b). It is clear that the curves with the small rotation angles exhibit a softer degradation response compared to those with the large rotation angles. A number of studies on “recent stress-history” of different natural clays have been carried out, among those are: London clay (Atkinson et al. 1990; Gasparre et al., 2007), Bothkennar clay (Smith et al. 1992), Gault clay (Lings et al. 2000), Pietrafitta clay (Callisto and Rampello 2002), Boston blue clay (Santagata et al. 2005) and Chicago clay (Finno and Cho 2010).

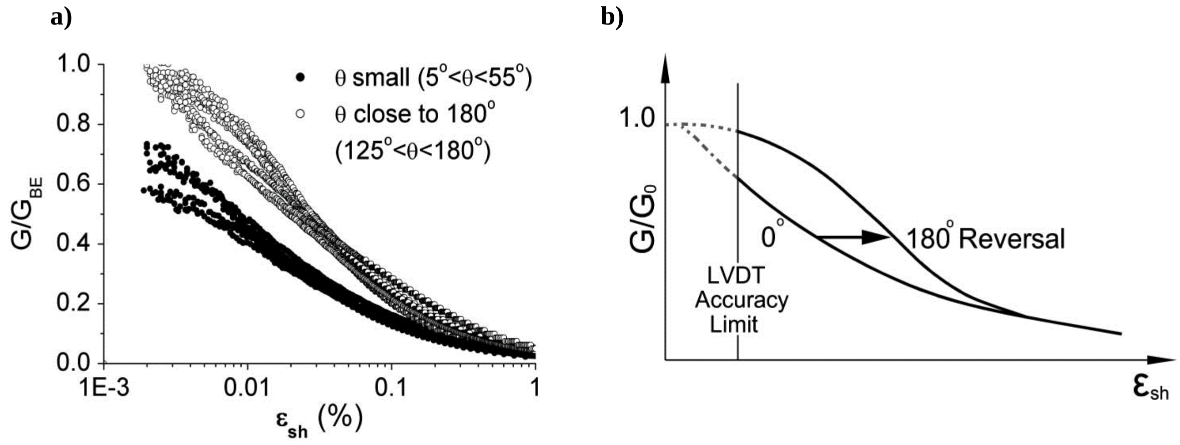

Figure 2.23: a) Normalized stiffness degradation of Chicago clay (Finno and Kim, 2012); b) Hypothesized effects of recent-stress history (Finno and Cho, 2011)

2.4 Anisotropy in soils

2.4.1 Anisotropy in geophysics

Anisotropy in soils refers to the variations in physical and mechanical properties when these are measured in different directions within the soil mass. Such differences are often attributed to depositional processes and layering (Woods, 2004). Over the course of the past decades, different studies have been conducted on wave propagation through layered-media to better understand the nature of anisotropy. Most of these studies have been published extensively in the geophysical literature, even though these relate to seismological problems, they have a relevance to this study and for the understanding of the anisotropy of natural clay deposits.

Crampin (1981) indicated that the anisotropy is a rather common phenomenon occurring in nature and can be related to different mechanisms including, lithological alignments, stress-induced effects, crystal alignments, regular sequences of fine layers, aligned cracks and other two-phase configurations. These mechanisms may cause effective anisotropy in the earth and in many man-made structures. Crampin (1971, 1975, and 1977) studied the effects of anisotropic layering on the propagation of seismic waves and observed that the propagation of both body and surface waves in anisotropic media differed from their propagation in isotropic media. Similarly, it was found that two of the most significant features of both body and surface waves in anisotropic media were the variation with direction of the velocity and the particle-motion polarization.

Anisotropy can be divided into two types: the first type is known as transverse anisotropy (also known as cross-anisotropy or hexagonal anisotropy), where there is a single vertical axis of symmetry and is mainly due to stratifications or horizontal alignments of structural nature. The second type is known as azimuthal anisotropy and is due to preferential alignments of crystals, cracks or structures along a particular azimuth.

2.4.2 Anisotropic elasticity

The small-strain stiffness anisotropy is another property of soil materials that is important. Bishop and Hight (1977) indicated that most soils will likely be anisotropic or at least transversely isotropic (cross-anisotropic) due to their depositional environment and complex stress history. To describe an anisotropic elastic material, 21 independent elastic constants are required (Green, 1828). If cross-anisotropy is assumed, then only 7 parameters are necessary to define the horizontal plane of isotropy (Graham and Houlsby, 1983). These parameters are the Poisson's ratios (μ_{vh}, μ_{hv}, *and* μ_{hh}) and the stiffness moduli (G_{vh}, G_{hh}, E_{hh}, E_{vh}), where the subscripts h and v relate to horizontal or vertical directions in which the stiffness is measured. Due to thermodynamic energy strain considerations, the compliance matrix of an elastic material must be symmetrical (Love, 1927), therefore:

$$\frac{\mu_{vh}}{E_{vh}} = \frac{\mu_{hv}}{E_{hv}} \tag{2.15}$$

$$G_{hh} = \frac{E_h}{2(1+\mu_{hh})} \tag{2.16}$$

These constraints reduce the number of parameters needed from 7 to 5 (μ_{vh} and μ_{hh}, *and* G_{vh}, E_{hh}, E_{vh}). The relationship between stress and strain increments in terms of the five independent parameters is expressed by the compliance equation, in matrix form (Love, 1944):

$$\begin{Bmatrix} \Delta\varepsilon_v \\ \delta\varepsilon_h \\ \delta\varepsilon_h \\ \delta\gamma_{vh} \\ \delta\gamma_{hv} \\ \delta\gamma_{hh} \end{Bmatrix} = \begin{bmatrix} \frac{1}{E_v} & -\frac{\mu_{hv}}{E_h} & -\frac{\mu_{hv}}{E_h} & 0 & 0 & 0 \\ -\frac{\mu_{vh}}{E_v} & \frac{1}{E_h} & -\frac{\mu_{hh}}{E_h} & 0 & 0 & 0 \\ -\frac{\mu_{hv}}{E_v} & -\frac{\mu_{hh}}{E_h} & \frac{1}{E_h} & 0 & 0 & 0 \\ 0 & 0 & 0 & \frac{1}{G_{vh}} & 0 & 0 \\ 0 & 0 & 0 & 0 & \frac{1}{G_{hv}} & 0 \\ 0 & 0 & 0 & 0 & 0 & \frac{1}{G_{hh}} \end{bmatrix} = \begin{Bmatrix} \delta\sigma'_v \\ \delta\sigma'_h \\ \delta\sigma'_h \\ \delta\tau_{vh} \\ \delta\tau_{hv} \\ \delta\tau_{hh} \end{Bmatrix} \tag{2.17}$$

in which $\delta\varepsilon$ and $\delta\gamma$ are incremental normal and shear strains; and $\delta\tau$ and $\delta\sigma'$ are incremental effective shear ad normal stresses.

Although all 5 cross-anisotropic parameters are independent, there are limits to the values that they can take, due to the thermodynamic requirement that strain energy be positive in an elastic material (Love, 1927; Pickering, 1970). E_v, E_h and G_{vh} should all be positive and must satisfy the conditions presented by Equations 2.18, 2.19 and 2.20 (Pickering, 1970; Raymond, 1970; Hooper, 1975; Lings, 2001):

$$-1 < \mu_{hh} < 1 \tag{2.18}$$

$$\frac{E_v}{E_h}(1-\mu_{hh}) - 2\mu_{vh}{}^2 \geq 0 \tag{2.19}$$

$$G_{vh} \leq \frac{E_v}{2\mu_{vh}(1+\mu_{hh}) + 2\sqrt{\left(\frac{E_v}{E_h}\right)(1-\mu_{hh}{}^2)\left(1-\frac{E_h}{E_v}\mu_{vh}{}^2\right)}} \tag{2.20}$$

Crampin (1981) described different types of axisymmetric anisotropy, ranging from orthorhombic (nine parameters), through tetragonal (six parameters), and hexagonal (five parameters), to cubic (three parameters). There is no direct evidence for which of the aforementioned types of anisotropy models is more correct. Consequently, the adoption of a five-parameter cross-anisotropy (hexagonal anisotropy) to explore soil behaviour is, strictly speaking an assumption, but is one commonly made by different researchers when studying the anisotropy of natural cohesive soil deposits (e.g. Jamiolkowski et al., 1995; Pennington et al., 1997; Lings et al., 2000; Gasparre et al., 2007; Nishimura, 2006 and

2014). Elastic anisotropy can be categorized as either stress-induced anisotropy or inherent anisotropy. Stress-induced anisotropy is caused by strain or stress changes after material deposition, particularly those resulting from post-depositional application of different effective stresses in the vertical and horizontal directions. Inherent anisotropy is intrinsically related to the grain characteristics and depositional process of the material. It was described by Casagrande and Carillo (1944) as ‘a physical characteristic inherent in the material and entirely independent of the later applied stresses and strain’.

2.4.3 Investigating anisotropy through laboratory tests

A group of researchers have attempted to study the stiffness anisotropy behaviour of soil materials with different laboratory techniques, e.g. torsional hollow cylinder, true triaxial, bender elements, and advanced triaxial with local strain measurements (Graham and Houlsby, 1983; Hardin and Blandford, 1989; Belloti et al., 1996; Pennington et al., 1997; Kuwano et al., 2000; Lings et al., 2000; Kuwano and Jardine, 2002; Gasparre et al., 2007; Yimsiri and Soga, 2011; Nishimura, 2014). From these studies, a series of methodologies have been developed to assess the anisotropy behavior of soils using different experimental techniques.

Graham and Houlsby (1983) stressed the difficulty of finding five parameters using standard laboratory equipment. They proposed a simplified version of the cross-anisotropic model. Their model consisted of only three independent parameters instead of the five for the classic cross-anisotropic models. The three independent parameters are defined in Equations 2.21 to 2.23:

$$\text{Anisotropy degree: } \alpha = \sqrt{E_h/E_v} = G_{hh}/G_{vh} \tag{2.21}$$

$$\text{Modified Poisson's ratio: } \mu^* = \mu_{hh} \tag{2.22}$$

$$\text{Modified Elastic modulus: } E^* = E_v \tag{2.23}$$

By substituting the three independent parameters into Eq. (2.17), the compliance matrix can be re-written in terms of the new parameters as follows:

$$\begin{Bmatrix} \delta\varepsilon_v \\ \delta\varepsilon_h \\ \delta\varepsilon_h \\ \delta\gamma_{vh} \\ \delta\gamma_{hv} \\ \delta\gamma_{hh} \end{Bmatrix} = \frac{1}{E^*} \begin{bmatrix} 1 & -\frac{\mu^*}{\alpha} & -\frac{\mu^*}{\alpha} & 0 & 0 & 0 \\ -\frac{\mu^*}{\alpha} & \frac{1}{\alpha^2} & -\frac{\mu_{hh}}{E_h} & 0 & 0 & 0 \\ -\frac{\mu^*}{\alpha} & -\frac{\mu^*}{\alpha^2} & \frac{1}{\alpha^2} & 0 & 0 & 0 \\ 0 & 0 & 0 & \frac{2(1+\mu^*)}{\alpha} & 0 & 0 \\ 0 & 0 & 0 & 0 & \frac{2(1+\mu^*)}{\alpha} & 0 \\ 0 & 0 & 0 & 0 & 0 & \frac{2(1+\mu^*)}{\alpha^2} \end{bmatrix} = \begin{Bmatrix} \delta\sigma'_v \\ \delta\sigma'_h \\ \delta\sigma'_h \\ \delta\tau_{vh} \\ \delta\tau_{hv} \\ \delta\tau_{hh} \end{Bmatrix} \qquad (2.24)$$

Now, by assuming that the horizontal plane is isotropic and from the compliance matrix symmetry, the links between the elastic parameters are defined as $\alpha^2 = E_h / E_v = \mu_{hv} / \mu_{vh}$, $\mu_{vh} = \mu_{hh} / \alpha$, and $G_{vh} = G_{hh} / \alpha = \alpha E^* / 2(1+\mu^*)$. Consequently, all of the cross-anisotropic elastic parameters can be calculated using the three-independent model as follows:

$$E_v = E^* \qquad (2.25)$$

$$E_h = \alpha^2 E^* \qquad (2.26)$$

$$G_{vh} = \alpha E^*/2(1+\mu^*) \qquad (2.27)$$

$$G_{hh} = \alpha^2 E^*/2(1+\mu^*) \qquad (2.28)$$

$$\mu_{hh} = \mu^* \qquad (2.29)$$

$$\mu_{vh} = \mu^*/\alpha \qquad (2.30)$$

$$\mu_{hv} = \alpha\mu^* \qquad (2.31)$$

Wood (1990) rewrote the stiffness matrix of a transversely isotropic material in terms of the triaxial stress-strain parameters:

$$\begin{Bmatrix} \delta p' \\ \delta q \end{Bmatrix} = \begin{bmatrix} K^* & J \\ J & 3G^* \end{bmatrix} \begin{Bmatrix} \delta\varepsilon_p \\ \delta\varepsilon_q \end{Bmatrix} \qquad (2.32)$$

where G^* and K^* are modified values of shear and bulk modulus, and J is a cross-coupling parameter accounting for the distortional and volumetric effects. For isotropic elastic soil, $J = 0$, and there is no such coupling. The parameters G^*, K^* and J can be written in terms of α, v and E^* by using Equations 2.17 and 2.32:

$$G^* = E^* \left[\frac{2 - 2\mu^* - 4\alpha\mu^* + \alpha^2}{6(1+\mu^*)(1-2\mu^*)} \right] \qquad (2.33)$$

$$K^* = E^* \left[\frac{1 - \mu^* - 4\alpha\mu^* + 2\alpha^2}{9(1 + \mu^*)(1 - 2\mu^*)} \right] \tag{2.34}$$

$$J = E^* \left[\frac{1 - \mu^* + \alpha\mu^* + \alpha^2}{3(1 + \mu^*)(1 - 2\mu^*)} \right] \tag{2.35}$$

Graham and Houlsby (1983) found that after using the inverse of Equation 2.32, a relationship between the direction of stress-path and volumetric and distortional effects in an undrained triaxial tests could be drawn:

$$\frac{\delta_q}{\delta_{p'}} = \frac{3G^*}{J} \tag{2.36}$$

Equation 2.36 can be re-written in terms of α and v^* by substituting Eq. (2.33) and (2.35) into Eq. (2.36):

$$\frac{\delta_q}{\delta_{p'}} = \frac{3G^*}{J} = \frac{3(2 - 2\mu^* - 4\alpha\mu^* + \alpha^2)}{2(1 - \mu^* + \alpha\mu^* - \alpha^2)} \tag{2.37}$$

The ratio of $\delta_q/\delta_{p'}$ $(3G^*/J)$ has bounds between -3/2 to +3 for α values very large or very small (α between 0.7 to 1.40, respectively) [Graham and Houlsby, 1983]. Likewise, α will determine the direction of the stress-path. If $\alpha < 1$, the soil is stiffer vertically than horizontally, thus an increase of p' is expected to be reflected in the undrained effective stress-path. On the other hand, if $\alpha > 1$, then the soil is stiffer horizontally than vertically, and a decrease in p' will be reflected in the undrained effective stress-path. Graham and Houlsby (1983) used their three-parameter model successfully to derive the anisotropic properties of Winnipeg clay. More details on their findings will be provided in the next section.

A more sophisticated approach to assess the cross-anisotropy behaviour of soil materials was employed by Hardin and Blandford (1989), Stokoe et al. (1991), Dellinger and Vernik (1992), Lee (1993), Jamilowski et al. (1995), Belloti et al. (1996), Pennington et al., (1997), Lings et al., (2000), Jovicic and Coop, (1998), Gasparre et al., (2007), Callisto and Rampello, (2002), Yimsiri and Soga (2011), Kim and Finno, (2012). They investigated the propagation of body waves through different particulate materials to obtain information on their small-strain anisotropy behaviour. It was found that the use of propagated compressional and shear waves, on the vertical and horizontal directions of the tested soil samples, allowed the assessment of the constrained (or compressional) modulus (M_{max}) and shear modulus (G_{max}) at very small strains (<0.001%). Assuming cross-anisotropy, Equations 2.3 and 2.4 can be used to calculate the stiffness properties using the propagated wave velocities in different directions of the tested samples.

Belloti et al. (1996) described a cross-anisotropic elastic medium following the stiffness matrix described by Love (1959) in terms of multiple constants:

$$[C] = \begin{bmatrix} C_{11} & C_{12} & C_{13} & 0 & 0 & 0 \\ C_{12} & C_{11} & C_{13} & 0 & 0 & 0 \\ C_{13} & C_{13} & C_{33} & 0 & 0 & 0 \\ 0 & 0 & 0 & C_{44} & 0 & 0 \\ 0 & 0 & 0 & 0 & C_{44} & 0 \\ 0 & 0 & 0 & 0 & 0 & C_{66} \end{bmatrix} \tag{2.38}$$

where $C_{11} = M_h$ (horizontal constrained modulus); $C_{33} = M_v$ (vertical constrained modulus); $C_{44} = G_{vh}$ (shear modulus in a plane including the axis of symmetry); $C_{66} = G_{hh}$ (shear modulus in the plane of isotropy); $C_{12} = M_h - 2G_{hh}$. C_{13} is the fifth independent material constant of the model. It was found by Stokoe et al. (1991) and Lee (1993) that the determination of C_{13} was not straightforward, since the parameter needed to be determined using oblique seismic body waves or measuring a modulus at an oblique direction. Once the five independent elastic constants (C_{11}, C_{33}, C_{44}, C_{66} and C_{13}) are known, the remaining material parameters (e.g., the elastic modulus and Poisson's ratio) that define a transversely isotropic elastic medium can be computed using the following equations (Stokoe et al., 1991; Belloti et al., 1996):

$$\mu_{hh} = \frac{C_{12}M_v - {C_{13}}^2}{M_h M_v - {C_{13}}^2} \tag{2.39}$$

$$\mu_{vh} = \frac{C_{13}M_h - C_{12}C_{13}}{{M_h}^2 - {C_{12}}^2} \tag{2.40}$$

$$\mu_{hv} = \frac{C_{13}M_h - C_{12}C_{13}}{M_v M_h - {C_{13}}^2} \tag{2.41}$$

$$E_v = \frac{|C|}{{M_h}^2 - {C_{12}}^2} \quad (2.42)$$

$$E_h = \frac{|C|}{M_h M_v - {C_{13}}^2} \quad (2.43)$$

where:

$|C| = \begin{vmatrix} C_{11} & C_{12} & C_{13} \\ C_{12} & C_{11} & C_{13} \\ C_{13} & C_{13} & C_{33} \end{vmatrix}$; μ_{hh} = Poisson's ratio in the horizontal plane (plane of isotropy); $\mu_{vh} = \mu_{hv}$ = Poisson's ratio in the vertical plane; E_v = elastic modulus in the vertical plane; and E_h = elastic modulus in the horizontal plane.

More recently, Sultaniya et al. (2010) reported findings from a series of numerical analyses of physical tests in the resonant column apparatus (RCA). These were performed to model the RCA for isotropic and transversely isotropic (cross-anisotropic) soil specimens. Sultaniya et al. (2010) adopted a finite element model of a Stokoe type RCA developed by Clayton et al. (2009). They found that using the resonant column apparatus with sample rotation (vertical and horizontal-cut soil samples), provides a maximum of four independent parameters to assess small-strain cross-anisotropy.

The shear and elastic modulus in the vertical plane (G_{vh} and E_v) can be estimated from torsional and flexural excitation of a vertical-cut sample. In addition, the shear and elastic modulus in the horizontal plane (G_{hh} and E_h) can be obtained from the torsional and flexural excitation of a horizontal-cut sample. However, Sultaniya et al. (2010) noted that when the elastic modulus was calculated using flexural vibration in RCA for samples with an aspect ratio of 2:1, an estimated maximum error of about 10% was introduced into the estimation, for both elastic moduli in the vertical and horizontal plane (E_v and E_h).

Additionally, Sultaniya et al. (2010) observed that although the shear modulus in the vertical direction (G_{vh}) could be obtained directly from a vertical-cut sample after applying torsional vibration, the shear modulus in the horizontal plane of the sample (G_{hh}) was not exactly the same as that estimated after inducing torsional vibration on a horizontal-cut sample. They argued that this discrepancy arises from the fact that the shear properties of the soil specimen are not uniform in the plane of torsional shear excitation, and that the estimated shear modulus was the result of a combination between G_{hh} to G_{vh}. Based on their analyses, they proposed an equation to calculate G_{hh} using the estimated shear modulus in the vertical and horizontal direction:

$$G_{hh} = \frac{{G_{hc}}^2}{G_{vh}} \tag{2.44}$$

where G_{hc} = shear modulus from horizontal-cut sample RC test; G_{vh} = shear modulus from vertical-cut sample RC test.

2.4.4 Previous studies on anisotropic stiffness of clays

Glacial deposits are a product of a complex depositional history and have undergone stress-strain histories throughout their creation (e.g. glaciation and deglaciation, erosion, lowering of ground water, desiccation, etc.). The predominantly one-dimensional consolidation strain history of these soils means that the soil behaviour is likely anisotropy, showing at least cross-anisotropy (Lings, 2001). Kirkpatrick and Rennie (1972) showed that the anisotropy of soils can be investigated using values of stiffness. They found that consolidation stresses influence the microstructure of clay when comparing electron micrographs from isotropically and anisotropically consolidated Kaolin clay samples. Since then, there have been a number of studies of the stress-strain responses of natural clays in terms of stiffness anisotropy using different laboratory techniques.

Graham and Houlsby (1983) showed that the ratio $J/3G^*$, defined by Eq. (2.36) where $J/3G^*$ represents the slope of the stress-path ($p':q$) from standard consolidated isotropically undrained (CIU) triaxial tests, can indicate if the soil is anisotropic. They studied the anisotropic elasticity of Winnipeg clay material underlying the University of Manitoba. Such material is lightly overconsolidated medium to high plasticity lacustrine clay laid down in pro-glacial Lake Agassiz during the Pleistocene epoch (Quigley, 1980). After performing a series of undrained triaxial tests on the natural clay, Graham and Houlsby (1983) quoted a range of slopes of the effective stress paths between -15.8 and -4.45. They also reported average values of elastic moduli for Winnipeg clay normalized by the consolidation pressure (σ_{vc}'): μ^*=0.22, K^*/σ_{vc}'=14.5, G^*/σ_{vc}'=8.5, and J/σ_{vc}'=-5.5. The data set was further analyzed using the same three-parameter formulation explained in the previous section; values of normalized anisotropic moduli are presented in Table 2.3. From their findings it was concluded that Winnipeg clay was anisotropic with an anisotropic ratio (α) equal to 1.37. Although the reported values were calculated pre-yield or within the elastic region of deformations of the material, the level of strain where the parameters were calculated ranged between 2% and 3%, thus these set of parameters may not be considered to be purely elastic.

Table 2.3: Normalized parameters obtained using anisotropic formulations on Winnipeg clay (interpreted from set B, Table 3, Graham and Houlsby, 1983)

Equivalent moduli		Anisotropic parameters	
K^*/σ_{vc}'	14.50	$E_v/\sigma_{vc}'=E^*$	15.29
G^*/σ_{vc}'	8.50	E_h/σ_{vc}'	28.59
J/σ_{vc}'	-5.50	μ_{vh}	0.17
μ^*	0.23	$\mu_{hh}=\nu^*$	0.23
α^2	1.87	G_{vh}/σ_{vc}'	8.50
		G_{hh}/σ_{vc}'	11.62
		$\alpha=G_{hh}/G_{vh}$	1.37

Becker (1981) studied the stiffness anisotropy of Wallaceburg clay. This material is believed to be a “water-lain” glacial till, deposited during the Late Wisconsin Substage of glaciation, of medium plasticity and overconsolidated clay (Becker, 1981; Kim, 1979). Wallaceburg clay was analyzed through a series of drained and undrained cyclic triaxial tests, using vertically and horizontally trimmed soil samples. The level of strain for the analyzes were reported to range between 0.5% and 1%. Stiffness parameters were calculated directly from drained and undrained probes (e.g. E_v, E_h, G_{vh}, μ_{vh}, and μ_{hh}). Values of G_{hh} were not reported. Becker (1981) used a parameter called modular ratio, ‘n’, to define the stiffness anisotropy of the Wallaceburg material. The parameter ‘n’ is equal to the ratio of E_h/E_v or E'_h/E'_v, where the superscripts refers to drained condition. This ‘n’ value can be used to compare it with the anisotropy factor proposed by Graham and Houlsby (1981) and showed in Eq. (2.37), where $\alpha^2 = E_h/E_v$, making $n = \alpha^2$. Becker (1981) reported that Wallaceburg clay was anisotropic, estimating values of α ($\sqrt{n}$) of 1.14 and 1.22 for drained and undrained conditions, respectively. Table 2.4 summarizes the drained parameters reported by Becker (1981). These drained parameters can be used to estimate a new set of cross-anisotropic parameters using the Graham and Houlsby (1981) three-parameter formulation. It can be seen that the estimations made of E'_h and μ'_{vh} using the reported values and the employed Graham and Houlsby (1981) equations, agree reasonably well with the measured values by Becker (1981), presenting a difference of 1.3% for E'_h and 6.8% for μ'_{vh}.

Table 2.4: Reported and estimated cross-anisotropic parameters for Wallaceburg clay (interpreted from Table 6.6, Becker, 1981)

Reported values		Parameter	Estimated[1]	Measured[2]	Difference (%)
E'_v	12.30	$E'_v=E^*$	12.30	-	-
G_{vh}/E'_v	0.40	E'_h	15.99	16.20	-1.30%
μ'_{vh}	0.16	μ'_{vh}	0.15	0.16	-6.81%
μ'_{hh}	0.18	$\mu'_{hh}=\mu^*$	0.17	-	-
$\alpha^2=E_h/E_v$	1.30	G_{vh}	4.92	-	-
		G_{hh}	5.61	-	-
		$\alpha=G_{hh}/G_{vh}$	1.14	-	-

1: Estimated using Graham & Houlsby three-parameter formulation
2: Measured by Becker (1981)

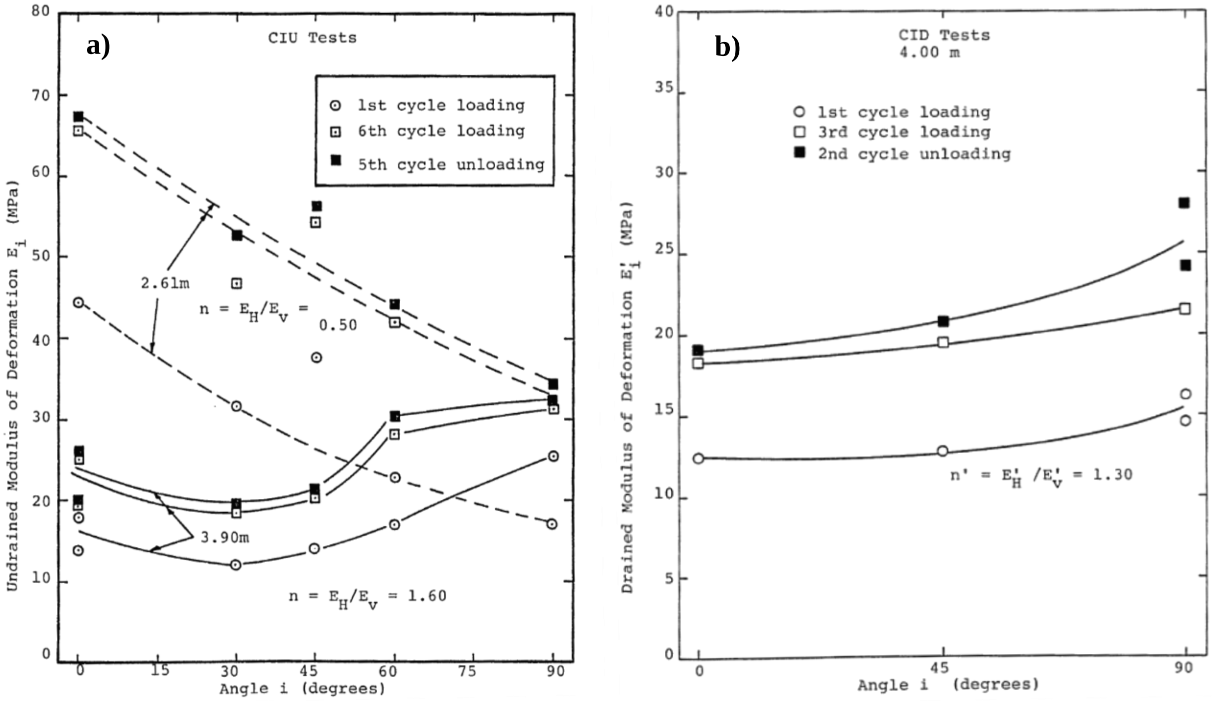

Figure 2.24: Effect of anisotropy on undrained and drained elastic modulus of Wallaceburg clay (adapted from Becker, 1981)

Doran et al. (2000) used the simplified cross-anisotropic elastic model proposed by Graham and Houlsby (1983) when developing an approach to estimate in-situ stresses using anisotropic elasticity and suction measurements. They gathered stress-path data from undrained CIU tests on overconsolidated clays taken from different published studies. From such stress-paths data Doran et al. (2000) estimated the ratio of $J/3G^*$ various natural clays, and these are depicted in Figure 2.25. Those materials are of glacial origin and were formed under different environments (e.g. marine and glacial). It is clear from Figure 2.25 that the direction of the stress-paths continuously inclines to the left, while q increases and p' decreases. The same behaviour was reported by Graham and Houlsby (1983) for lightly overconsolidated Winnipeg glacial clay and was attributed to the stiffness anisotropy, where the horizontal stiffness was higher than the vertical stiffness ($\alpha > 1$).

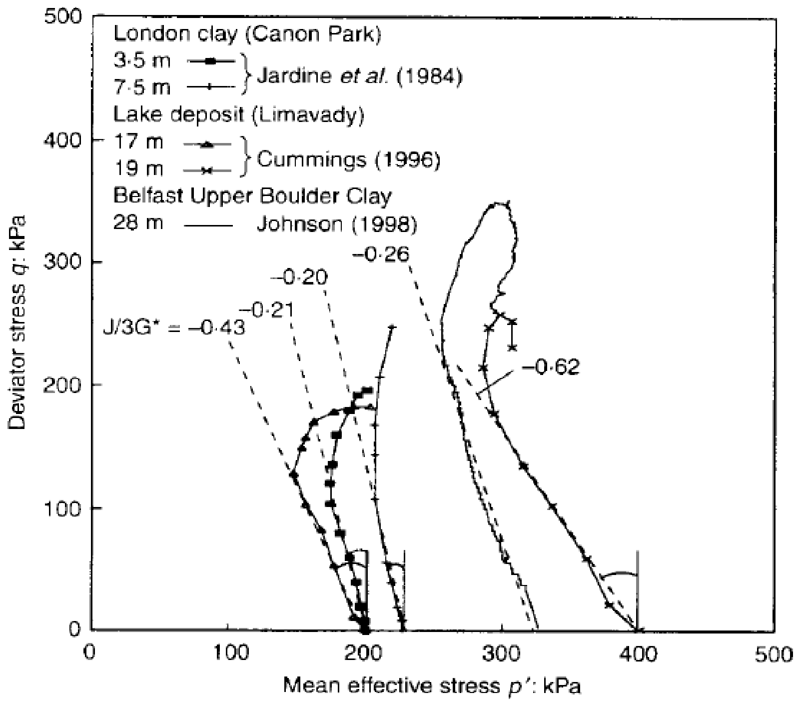

Figure 2.25: Undrained stress-paths of various overconsolidated natural clays (Doran et al., 2000)

A further analysis of the estimated values of $J/3G^*$ quoted in Figure 2.25 was carried out here using Equation 2.37 presented in Section 2.4.3. Table 2.5 shows the results from this analysis. Assuming μ^* between 0.2 and 0.33 (Nishimura, 2014), the calculated anisotropic ratios (α) of the glacial soil are larger than the unity, ranging between 1.2 to 2, respectively, confirming the hypothesis outlined by Graham and Houslby (1983).

Table 2.5: Anisotropic ratios for glacial clays reported by Doran et al. (2000)

Soil material	Sample depth (m)	$J/3G^*$	α^+	α^{++}
London clay (Jardine et al., 1984)	3.5	-0.21	1.23	1.34
	7.5	-0.20	1.22	1.32
Lake deposit (Cummings, 1996)	17	-0.43	1.56	1.87
	19	-0.63	1.92	2.08
Belfast Upper Boulder clay (Johnson, 1998)	28	-0.26	1.30	1.44

$^+$: using μ^* equal to 0.2; $^{++}$: using μ^* equal to 0.3

Jamiolkowski et al. (1995) studied the small-strain stiffness anisotropy of six Italian natural cohesive soils of low to medium-high plasticity, whose geological ages ranged from Holocene to Pliocene, and deposited under different sedimentation mechanisms (i.e. lacustrine, marine, estuarine and alluvial) G_{max} was measured using resonant column (RC) and oedometer apparatuses equipped with vertical and horizonal BE. The observed anisotropy, expressed as the ratio of G_{hh}/G_{vh}, showed the combined effect of fabric and stress induced anisotropy. The ratio of G_{hh}/G_{vh} can also be regarded as α. Fabric anisotropy was evaluated under isotropic stress-state, and α for the six clays ranged between 1.4 and 1.5.

Pennington et al. (1997) studied the elastic anisotropy behaviour of Gault clay, which is a glaciomarine deposit of medium to high plasticity, heavily overconsolidated and rich in carbonates (up to 30% of $CaCO_3$), laid down during the late Cretaceous epoch (Ng et al., 1995; Brosse et al., 2017). They found that Gault clay is cross-anisotropic based on shear moduli measured from two sets of vertical bender elements, both for horizontally polarized waves, and two pairs of horizontal bender elements for horizontally propagating waves polarized vertically and horizontally, as shown in Figure 2.15a. They suggested that the cross-anisotropy of this clay arises from the depositional structure of the clay. Pennington et al. (1997) also reported on field measurements of G_{vh} and G_{hh} performed by Butcher and Powell (1995) on Gault clay. These results showed that the horizontal stiffness was higher than the vertical stiffness when measured *in-situ*. The laboratory and field geophysical data were consistent and suggested that G_{hh}/G_{vh} ranged between 1.6 to 2. Similarly, results reported by Abbiss (1981) showed that the ratio of G_{hh} to G_{vh}, obtained *in-situ* using geophysical tests, was approximately 2. Lings et al. (2000) later confirmed these findings, and they estimated a ratio of G_{hh}/G_{vh} equal to 2.25 and E_h/E_v equal to 3.97 under anisotropic stresses. More recently, Yimsiri and Soga (2011) further confirmed the anisotropy behaviour of Gault clay by carrying out small-strain measurements using BE on soil specimens under isotropic stresses. They estimated ratios of G_{hh}/G_{vh} and E_h/E_v equal to 1.68 and 2.32, respectively

Jovicic and Coop (1998) investigated the stiffness anisotropy of London clay. This material is also a medium to high plasticity, heavily overconsolidated glaciomarine deposit that dates from the Eocene epoch (Brosse et al., 2017). They found that London clay is a cross-anisotropic material based on triaxial tests with bender elements. They tested a series of specimens trimmed in three different axial directions to evaluate the anisotropy using the method shown in Figure 2.10b. Similarly, Gasparre et al. (2007) performed tests on anisotropically consolidated specimens of London clay using a combination of triaxial with BE and torsional shear hollow cylinder tests on vertically and horizontally cut samples. From this study it was found that the modular ratios G_{hh}/G_{vh} and E_h/E_v were equal to 1.86 and 1.95. Yimsiri and Soga (2011) further investigated the anisotropy of London clay using a similar experimental procedure as that for the Gault clay. They estimated values of G_{hh}/G_{vh} and E_h/E_v equal to 1.20 and 2.18. Figure 2.26 shows a comparison between the normalized shear modulus measured in the vertical and horizontal planes of Gault clay and London clay by Yimsiri and Soga (2011) and these previous studies.

Assessments of the cross-anisotropy behaviour of other natural clays such as Pietrafitta stiff clay, Bangkok clay, and Chicago clay have also been made by other researchers and more information on their studies can be found in Callisto and Rampello (2002), Yimsiri et al. (2009), and Cho (2007). In an effort to summarize some of the information provided throughout the section, Table 2.6 was created to illustrate the range of the anisotropy behaviour of various natural and reconstituted clays materials. It can be seen that most of the work has been carried out on soils outside of North America and limited information is given on Canadian soils. Moreover, the data available on Canadian soils was obtained at levels of strain higher than 0.5%, thus these are not representative of the purely elastic behaviour (small-strain) of such materials. Additionally, complete information about the five independent elastic constants necessary to study the small cross-anisotropy behaviour is still scarce for most of the reviewed materials.

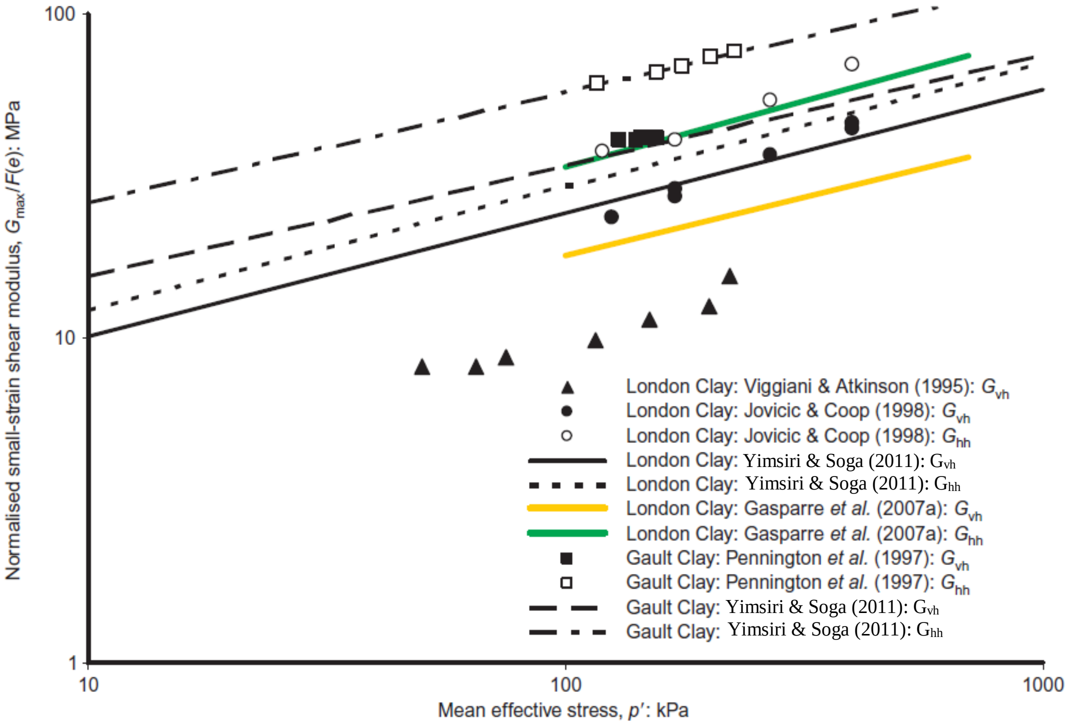

Figure 2.26: Normalized G_{max} measured in the vertical and horizontal planes of Gault clay and London clay vs. effective Cambridge p' (Yimsiri and Soga, 2011)

Table 2.6: Review of cross-anisotropic parameters of natural and reconstituted clays

				Cross-anisotropic parameters				
Reference	**Soil**	**Test type**	**Strain level (%)**	G_{hh}/G_{vh}	μ_{vh}	μ_{hv}	μ_{hh}	E_h/E_v
Ward et al. (1959)	London Clay	TX (CIU), V-H	0.2 - 0.6	-	-	-	-	1.2 - 1.4
Kirkpatric and Rennie (1972)	Reconstituted Kaolin	PS-TX (CID-U), V-H-I	very large	-	-	-	-	0.6 - 0.84
Franklin and Mattson (1972)	Reconstituted Kaolin	Compression wave velocity	very small	-	-	-	-	1.8 - 4.0
Saada and Ou (1973)	Reconstituted Edgar Kaolin	THCS, V-H	large	-	-	-	-	0.90 - 1.35
Atkinson (1975)	London Clay	PS-TX (CID-U), V-H	1	-	0.00	0.19	-	2
Lo et al. (1977)	Leda clay	TX (CIU-U), cubic specimen V-H-I	0.4 - 0.6	0.59	0.08	0.08	0.10	0.55
Saada et al. (1978)	Reconstituted Edgar Kaolin	Longitudinal RC (V-H)	0.0001 - 0.007	-	-	-	-	1.25 - 1.35
Yong and Silvestri (1979)	Champlain clay	TX (CID), V-H	0.5 - 1	-	0.35	0.24	0.20	0.62
Abbiss (1981)	Boulder clay London clay Gault clay	Seismic refraction Rayleigh wave	< 0.0001	2 - 3	-	-	-	-
Becker (1981)	Wallaceburg clay	CyTX (CIU - CID), V-H-I	0.5 - 1	-	0.16	-	0.18	1.29 - 1.48
Graham and Houlsby (1983)	Winnipeg clay	TX (CK$_o$D)*, V	2 - 3	-	-	-	0.23	1.87
Stokoe et al. (1992)	Bolson fill, site A and (site B)	Cross-hole	< 0.0001	0.79 - 1.23, (0.60)	-	-	-	-
Jamiolkowski et al. (1994)	Montealto di Castro site	Cross-hole	< 0.0001	0.99 - 1.21	-	-	-	-
Jamiolkowski et al. (1995)	Six Italian clays	OED-BE$_{V/H}$, Ko=0 and (Ko=1)	< 0.0001	1.4 - 1.5, (0.86 - 1.62)	-	-	-	-
Lings et al. (2000)	Gault clay	TX and BE	< 0.0001	2.25	0.00	-	-0.04	3.97
Gasparre et al. (2007)	London Clay	TX and BE, TSHC	< 0.0001	1.86	0.1	0.71	-0.02	1.95
Yimsiri and Soga (2011)	London Clay (Gault clay)	TX and BE	< 0.0001	2.18 (2.32)	0.07 (0.13)	0.15 (0.30)	0.18 (0.21)	1.20 (1.68)

TX= triaxial test; BE=bender element test; RC=resonant column test; THCS=torsional shear test and hollow cylinder; CID=isotropically consolidated drained test; CIU=isotropically consolidated undrained test; CKoD=Ko-consolidated; I=inclined specimen; V=vertically cut specimen (axial stress normal to bedding planes); H=horizontally cut specimen (stress parallel to bedding planes)

2.4.5 Some implications of considering stiffness anisotropy of soils in geotechnical problems

Even though the effects of anisotropy on soil-structure interaction can be important, they have not been widely investigated. Some studies of anisotropic, homogeneous and non-homogeneous half spaces have been published, e.g. Barden (1963), Gerrard and Harrison (1970a, 1970b and 1971), Milovic and Touzot (1970), Milovic (1970), Gibson (1974), Hooper (1975), Rowe and Booker (1980b) and Gazetas (1981a, 1981b, 1981c, 1981d, 1981e and 1983). Hooper (1975) found that if cross-anisotropy is considered, total and differential foundation settlements may be reduced about 40% and between 5-20% under undrained and drained conditions respectively. Rowe and Booker (1981) and Gazetas (1981) came to similar conclusions. Rowe and Booker (1981), after comparing the settlements for a cross-anisotropic soil with those determined assuming isotropic soil, found that the assumption of isotropy may lead to overestimates of settlement by up to 45% or underestimates of settlement by up to 16% for a range of cases.

Moreover, Gazetas (1981 and 1982) suggested that soil anisotropy can greatly influence both static and dynamic foundation displacements under undrained conditions and that those soils presenting a large degree of anisotropy are likely to experience settlement values 50% smaller than those computed using classical isotropic theories. Furthermore, Gazetas (1983) indicated that the anisotropy will exert an influence through the static stiffness of a half-space, with compressional modes (vertical and rocking) having greater stiffness as the anisotropic ratio ($\alpha=E_h/E_v$) increases. Dynamic behaviour will also be affected; the dynamic displacement functions (compliances) for low frequencies will reduce with increasing α.

More recently, a group of researchers have brought awareness on the importance of anisotropy and its implications in geotechnical problems such as the computation of ground movements arising from different construction activities (e.g., Simpson et al., 1996; Hashash and Whittle; 1996; Addenbrooke et al., 1997; Lee and Ng, 2002; Wongsaroj et al., 2004; Masin and Herle, 2005; Finno and Tu, 2006; Simpson, 2016). Simpson et al. (1996) carried out numerical analyses of ground movements above a trial tunnel in London clay using both isotropic and anisotropic models. It was found that shear modulus anisotropy greatly influences the calculated surface settlement trough. Figure 2.27 shows the computed and observed settlement troughs of the trial tunnel in London clay. Line A shows results for a non-linear but isotropic model, line B is for a linear elastic and cross-anisotropic model with G_{hh}/G_{vh} = 1.66, and line C is for a non-linear and cross-anisotropic model with $G_{hh}/G_{vh} = 2$. The cross-anisotropic models showed a much closer response to the observed settlement trough shape compared to that of the isotropic model. These findings show the conservatism of analyses performed considering soil isotropy. Addenbrooke et al. (1997) later concluded that adding anisotropy to a strongly non-linear elastic model can produce realistic settlement trough shapes.

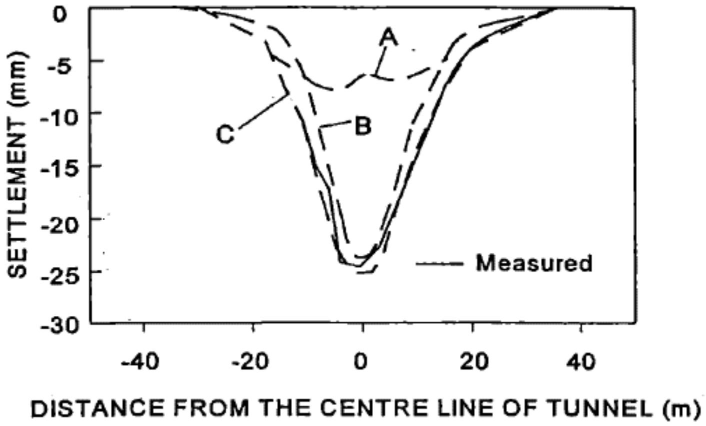

Figure 2.27: Computed settlement troughs of trial tunnel in London clay (Simpson et al., 1996)

Wongsaroj et al. (2004) also carried out numerical simulations using 2D and 3D models to simulate a tunnel excavation in London clay as Simpson et al. (1996). Besides examining the effect of anisotropy in surface deformation, they also investigated the generation of excess pore pressures from the tunnel construction. For both models, isotropy and anisotropy was considered. G_{hh} was assumed to be $1.5G_{vh}$. It was found that the anisotropic 3D model produced the narrowest settlement trough at the ground surface, the least horizontal movement around the axis level of the tunnel and the largest excess pore pressures above the tunnel. Figure 2.28 shows results of the 2D and 3D models for the settlement trough and excess pore pressures in the plane perpendicular to the axis after tunnel excavation.

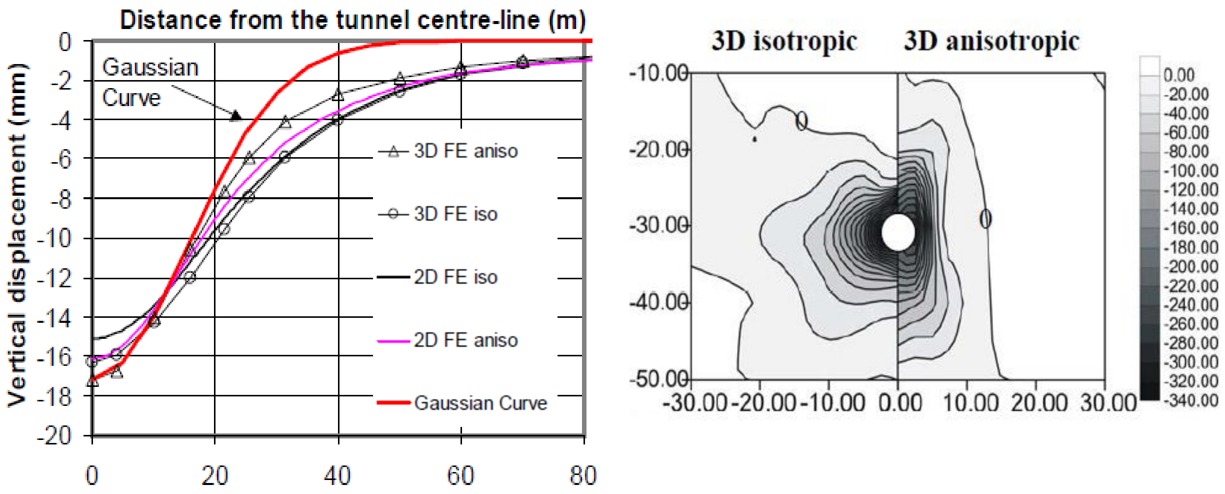

Figure 2.28: Predicted vertical displacements and predicted excess pore pressures contours in the plane perpendicular to tunnel axis (adapted from Wongsaroj et al., 2004)

Studies on tunneling in London clay material showed that the width and depths of the settlement troughs could be influenced strongly by small-strain stiffness anisotropy presented in the material. However, as pointed out by Masin and Herle (2005), to properly predict the behaviour of soils with small-strain stiffness anisotropy there is a need to use proper constitutive models that consider: non-linearity of the stress-strain curve (Gunn, 1993), path-dependent stiffness (Masin and Herle, 2005), and anisotropic behavior with different responses in at least two perpendicular directions (Addenbrooke et al., 1997).

Considering this, to properly produce and calibrate constitutive models capable of simulating the real behaviour of a particular soil material such as the Canadian glacial tills, there is a great necessity of obtaining appropriate laboratory and field data that will lead to the development of such models. Simply incorporating soil anisotropy into geotechnical characterization, analysis, and design of wind turbines shallow foundation systems may be a simple but important step towards the effective expansion of the Canadian wind energy sector.

2.5 Summary

The onshore wind turbine foundations type that are regularly used in the North American market were described. The selection between shallow or deep foundation system will be dictated by the geotechnical and geological characteristics and site-specific turbine loads. This thesis concentrates on the study of the soil-foundation interaction of an onshore wind turbine shallow foundation system resting on a glacial clayey till deposit at a wind farm in southwestern Ontario.

The most common codes and guidelines available for wind turbine foundations design were identified (e.g DNV/Risø, 2002; IEC 61400-1, 2005). No specific Canadian wind turbine foundation design standard was found, most of the designs carry out locally rely on a mixture of foreign codes, standards, and engineering judgment. Furthermore, whilst most of the international codes typically used are updated regularly with state-of-the-art knowledge, they often rely on conservative geotechnical assumptions such as linear elasticity and isotropic behaviour of the soil material. These assumptions may not be suitable for Canadian soils, which are product of glacial sediments and have undergone through complex formation, transportation and deposition histories. Also, it was determined that the stiffness of cohesive soils from southern Ontario is strain-dependent and they exhibit strength and stiffness anisotropy (Lo et al., 1971; Becker, 1981; Kim and Novak, 1981; Gonzalez-Hurtado and Newson, 2016).

A summary of the approaches used to experimentally determine anisotropy and theoretical concepts used to describe its characteristics for small-strain elasticity are described in this chapter. The review highlights the use of wave propagation transducers (bender elements) in the vertical and horizontal directions on soil specimens to measure propagated wave velocities with different polarization (e.g. V_{svh} and V_{shh}) at very small strains (ε <0.001%). This allows for the estimation of the small-strain stiffness of soil samples in their vertical and horizontal directions (G_{vh} and G_{hh}), enabling the calculation of the anisotropy ratio ($\alpha = G_{hh}/G_{vh}$) to assess the level of anisotropy of the material. Other approaches such as the analysis of the stress-path behavior from undrained triaxial tests and using the resonant column to test vertically and horizontally trimmed samples were also found in the literature and seem promising for the evaluating elastic anisotropy.

Data compiled from different stiffness anisotropy investigations showed that the majority of these studies have been conducted outside of North America and limited information is available for Canadian soils. In addition, the anisotropy studies performed on Canadian soils were carried out at level of strain that is not representative of purely elastic behaviour (ε >0.5%). The small-strain stiffness anisotropy ratio (α) data found in the literature for different overconsolidated soils, shows a wide range of α varying from 0.8 to 2.2. Most of these results suggest that such materials are predominantly stiffer in the horizontal direction, which seems reasonable given the expected changes is stress ratio (K_o) during unloading. Some evidence was found from theoretical and numerical approximations, that stiffness anisotropy can greatly influence the estimation of ground deformations (Lee and Rowe, 1989; Simpson et al., 1996). These suggest that numerical models using stiffness anisotropy could exhibit closer estimations to that measured in the field, and also in some cases the assumption of isotropy could potentially lead to settlement overestimations of up to 45% (Rowe and Booker, 1981).

Chapter 3

3 Port Alma wind farm site description

In this chapter, detailed background information on the field and the geological setting of the wind farm is presented. Moreover, the results of *in-situ* and laboratory testing on the Port Alma soil material conducted previously are reviewed and discussed. An overview of a field monitoring system implemented during this investigation to measure the shallow foundation vibration, ground monition and wind data are shown in Appendix A.

3.1 Introduction

The Port Alma wind farm forms part of the energy portfolio of South-western Ontario. The wind farm is owned and operated by Kruger Energy, and began its power production in November of 2008 with an installed capacity of 101.2 MW; able to produce enough energy to power around 30,000 households per year. With a total of 44 turbines, the wind farm is located approximately 3.1 km north of Lake Erie in the Municipality of Chatham-Kent, Ontario, Canada. This thesis focuses on the study of one of the wind turbines within the Port Alma commercial wind farm, specifically turbine T4, also known as KEPA 4. The approximate site location and boundaries of the wind farm site are shown in Figure 3.1 and Figure 3.2, respectively.

Figure 3.1: Approximate location of the wind farm study site (Google Earth, 2018)

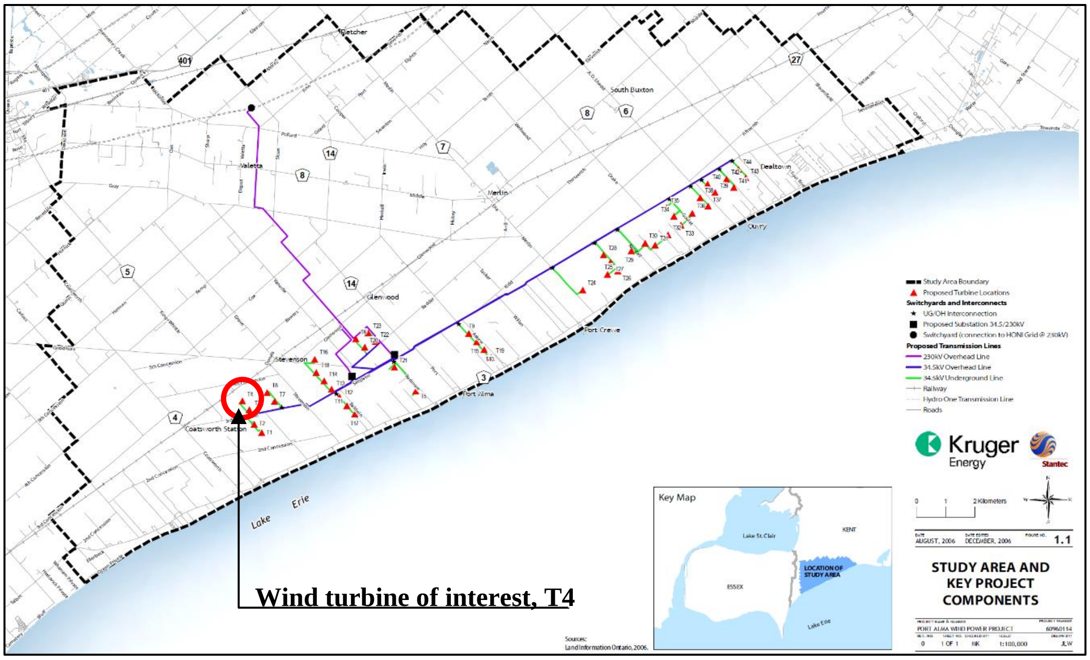

Figure 3.2: Wind farm site, boundary denoted by dashed line. The wind turbine in study number T4 inside the red circle. (adapted from Stantec, 2007)

3.2 Wind turbine description

The specific turbine model (Siemens MK II) produces nominal power of 2.3 MW and has a hub height of 80 m and triple bladed rotor with a 93 m diameter. The minimum and maximum elevations reached by the swept rotor area of the blades are 34 m and 127 m, respectively. The total mass of the tower and rotor is approximately 2860 tons. The wind turbine and its tower are supported by a shallow octagonal foundation, with a 19 m diameter and 3 m depth at the center (Figure 3.3). A meteorological (MET) tower, instrumented and monitored by the power generation company (Krueger Energy), is located 150 m North-West of the wind turbine. The meteorological tower features five cup anemometers at different heights (from 35 to 80 m), capable of recording wind speed and direction. A north-facing view of the site showing the wind turbine T4 and its relative position to the MET tower is presented in Figure 3.4.

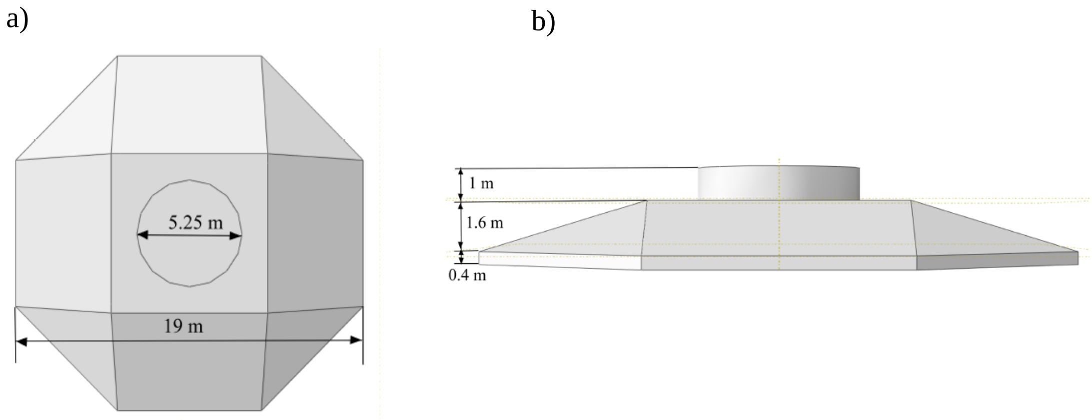

Figure 3.3: Foundation geometry; a) top view and b) cross-section (adapted from Deshpande, 2016)

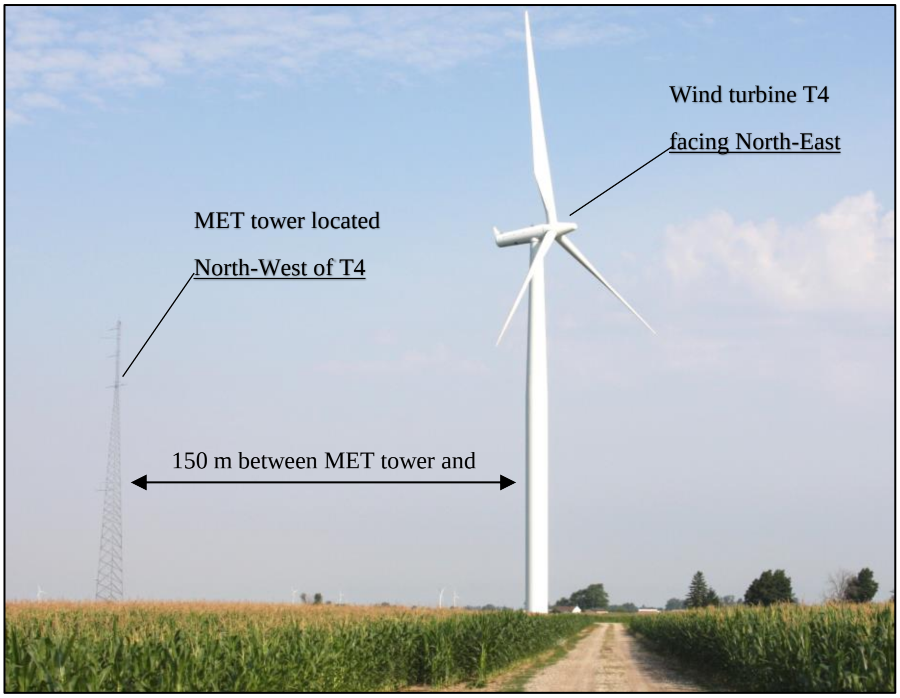

Figure 3.4: Relative position between wind turbine T4 and meteorological tower

3.3 Geological setting of the wind farm site

Geologically, this site sits in a physiographic region of South Western Ontario known as St. Clair clay plain, and within the sub-region called the Essex clay plain (Chapman and Putnam, 1966). Figure 3.5 shows the Chatham-Wheatley area map with information on the

Quaternary geological deposits of the area. From the site investigation performed by Tyldesley et al. (2013), it was found that the wind farm site area is comprised of a carbonate-rich clayey silt tills and is situated at the union of four major geological deposits: The Port Stanley and Tavistock tills, glaciolacustrine sand and gravel, and glaciolacustrine clayey silt. These materials were deposited in the Port Bruce Stadial, about 15,000 years ago, during the Late Wisconsin due to the re-advance of the Laurentide Ice Sheet (Kelly, 1995).

The composition of these subglacial tills is calcareous and fine-grained, produced by the crushing and incorporation of fine-grained glaciolacustrine sediments that were lain down during the previous Erie Interstade. Consequently, a stratum between 40 to 45 m of clayey silt tills with interbedded glaciolacustrine sediments were created. The bedrock is shale with limestone-dolostone-shale interlayers. The material under the foundation is a Tavistock till with overlying glaciolacrustine soils. These findings are consistent with the information reported in the review of the glacial tills of Southern Ontario (Section 2.2.3).

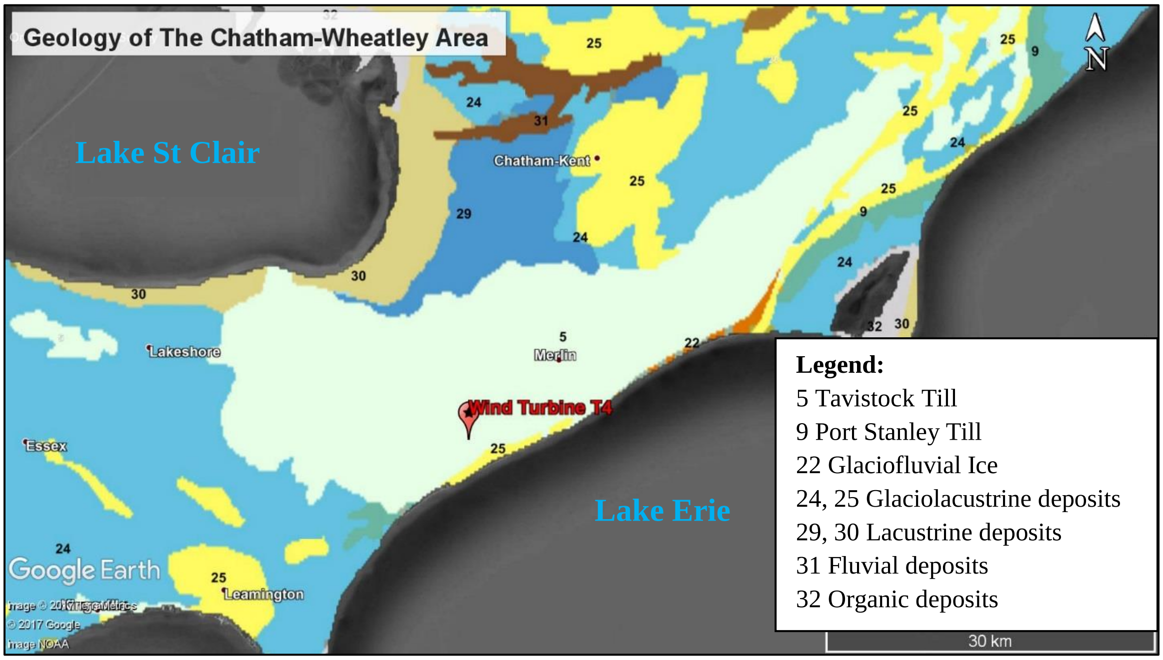

Figure 3.5: Geology of the Chatham-Wheatley area showing the position of the wind turbine site. (adapted from Ontario Geological Survey, 2012)

3.4 IEC classification and design wind speeds and loads

The wind farm is sited in predominantly open flat agricultural land with surrounding small trees and hedges (see Figure 3.4). The wind farm has been classified as an IEC 61400-1 Class IIb site; this categorizes the area as having medium level turbulence intensity and wind speeds (IEC 61400-1, 2005). The expected value of the turbulence intensity at a wind speed of 15 m/s for a class IIb is 14% and the reference 50-year return period 10-minute average wind speed is specified as 42.5 m/s. The project site specific extreme value 50-year 10-minute average wind speeds have been estimated to be 33.9 m/s. The annual average wind speed at hub height is 8.5 m/s and the 50-year return period 3 second gust wind speed is 59.5 m/s. The design loads of the foundation are shown in Table 3.1 below.

Table 3.1: Magnitude of design loads for the wind turbine foundation

Condition	Normal force*, V (kN)	Horizontal force, H (kN)	Overturning moment, M (kN m)	Torsional moment, T (kN m)
Normal operations[1]	2900	900	60000	7300
Highest overturning moment [2]	2900	1100	76200	4400

*; does not include mass of the foundation

1; Design load case normal operation (DCL1.1) according to IEC 61400-1 Ed.3

2; Design load case with highest overturning moment (DCL6.1) according to IEC 61400-1 Ed.3

An independent extreme value analysis was conducted by Kiss et al. (2014) using a pseudo superstation approach (Perterka, 1992). This was based on recorded site-specific data, where the analysis of extreme wind speed is performed and compared with the IEC classification of the site. The superstation approach differs from methods using long-term wind data in that it evaluates the peak wind gust speed for various return periods. This method establishes a single superstation with many station years of data by using short-term data measured at multiple stations in a region. In this approach, the extreme wind speeds recorded at different stations should be statistically independent.

An approximate single superstation was created using the 10-minute averaged wind speeds at hub height from all 44 turbines on the site over a 2-year period. The annual maxima were fit with a Type I extreme value Gumbel distribution which is plotted in Figure 3.6. The

Gumbel fit suggests that the 50-year 10-minute average wind speed at hub height is 26.9 m/s, which is noticeably less compared to the IEC class IIb value of 42.5 m/s and the site-specific manufacturer provided value of 33.9 m/s. The 50-year 10-minute average wind speed IEC class IIb value represents the average annual wind speed multiplied by a factor of 5 (Kiss, 2016). At an elevation of 10 meters, the NBCC specifies values of 23 and 27 m/s for 10-year and 50-year return periods respectively for Leamington Ontario (Kiss et al., 2014), these are shown as red circles in Figure 3.6.

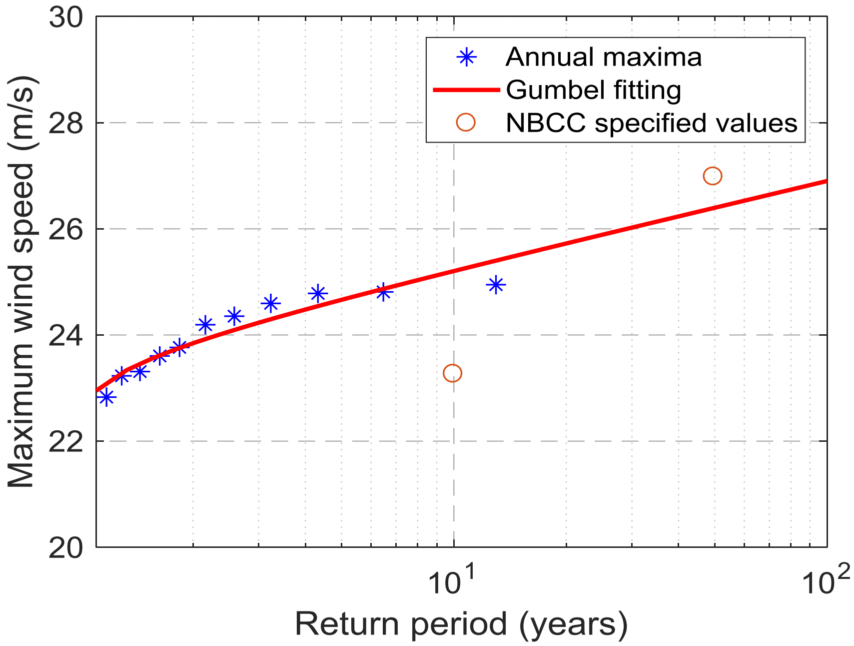

Figure 3.6: Gumbel Type I fit of extreme value wind data (adapted from Kiss et al., 2014)

3.5 Subsurface conditions beneath the foundation

The site investigation performed by Tyldesley et al. (2013) was designed to characterize the overburden stratigraphy and to obtain basic geotechnical properties of the materials below the wind turbine foundation. For that purpose, a series of boreholes were drilled adjacent to the turbine foundation to depths of twice the foundation diameter to evaluate the soil profile, perform *in-situ* tests and collect high-quality samples for laboratory testing. Figure 3.7 shows the approximate location of the drilled boreholes adjacent to the wind turbine. The boreholes were spaced at 3 m from each other to allow for later cross-hole geophysical testing. A track-mounted drill rig was used for the borehole drilling activities.

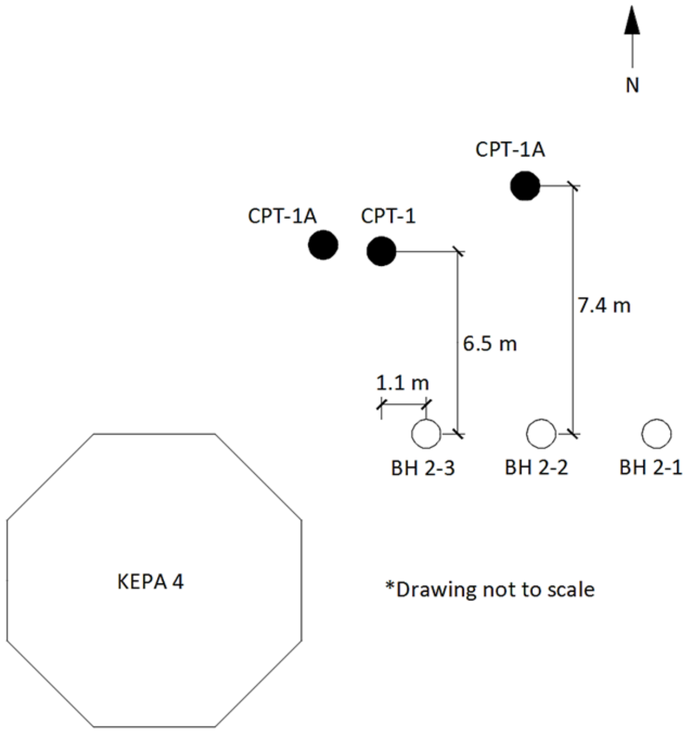

Figure 3.7: Borehole relative locations to foundation (adapted from Newson et al., 2019)

3.5.1 On-site stratigraphy

By using PQ core samples from the drilling operations, it was possible to characterize the generalized stratigraphic profile shown in Figure 3.8. Tyldesley et al. (2013) stated that the soil consistency was similar throughout the profile with distinctions mainly in color and plasticity. Furthermore, the soil profile on the site consists of three very distinct layers that can be separated as follows: from 0 to 1.5 m a heavily weathered oxidized upper crust with pronounced fissures, between 1.5 and 4.5 m a partially weathered lower crust that transitions from an oxidized to an unoxidized state, and from 4.5 m to depths greater than 40 m an unweathered clay till.

It was found that the upper crustal zone of this deposit is mottled brown-grey or brown-green with a stiff to very stiff consistency presenting fissures. The underlying lower crust has relatively lower natural moisture content, has a very stiff consistency, and is prevalently brown in color. At several locations, this layer is composed of clayey silt, sandy clay and silt seams. Between 3 and 4 m below the ground surface the soil changes color from brown to grey. A uniform grey appearance characterizes the lowest third layer, a stiff to very stiff consistency, low plasticity and relatively uniform moisture contents.

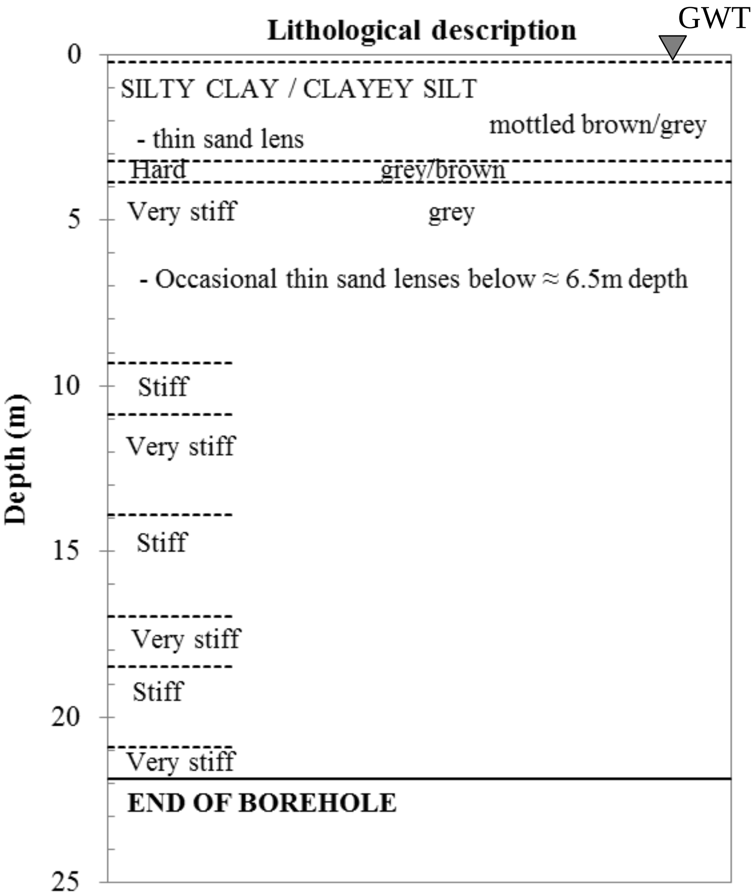

Figure 3.8: General stratigraphic profile

3.5.2 Available *In-situ* test data

As described by Tyldesley et al. (2013), the *in-situ* testing adjacent to the boreholes consisted of standard penetration test (SPT), cone penetration test (CPT), field shear vane (FSV), installation of vibrating wire piezometers, cross-hole seismic testing (CST) and seismic cone penetration test (SCPTu), and was conducted to depths of 30 m. The results of these *in-situ* tests on the Port Alma soil deposit are presented in this section and described. Figure 3.9 shows the results of the cone tip resistance (q_t), sleeve friction (q_s), pore water pressure (u_2), and friction ratio (FR) measurements for CPT-1.

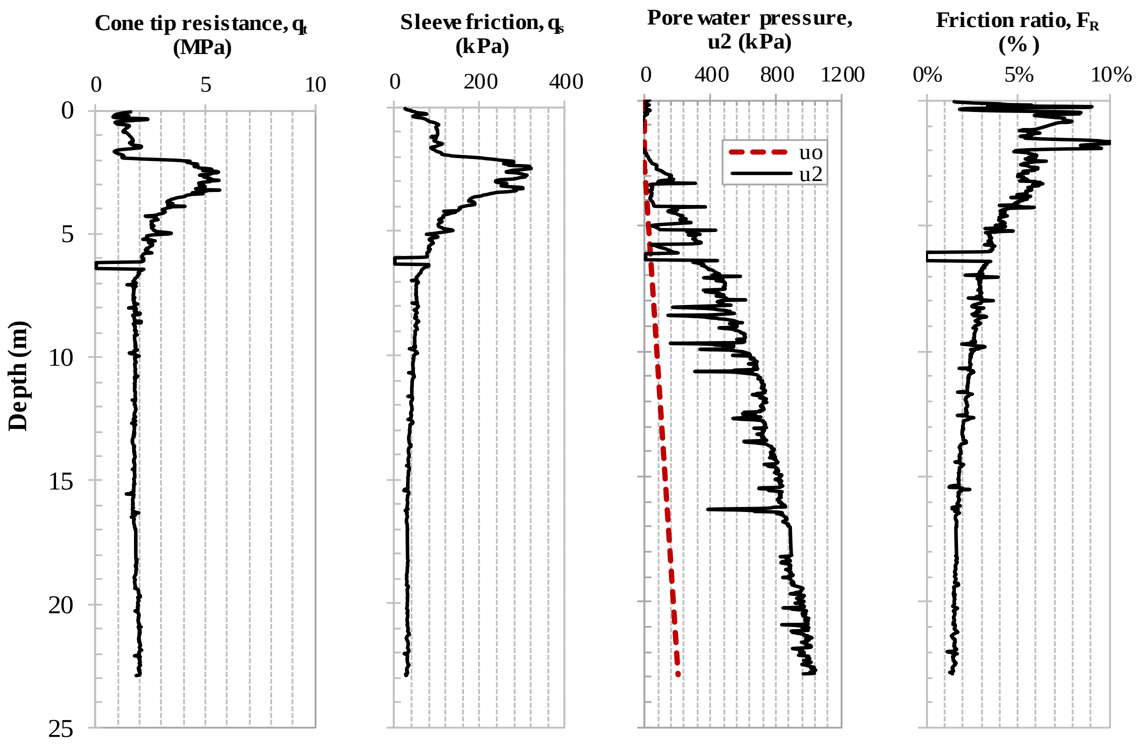

Figure 3.9: CPT-1 results; (a) cone tip resistance, (b) sleeve friction, (c) pore water pressure, (d) friction ratio (adapted from Newson et al., 2019)

Sleeve friction (q_S) increases from 0 to 300 kPa for the first 3 m, decreasing for the subsequent 7 meters to 25 kPa, where it remains constant for the rest of the profile. The tip resistance (q_t) readings show fluctuations between 1 MPa to 3 MPa for the first 1.5 m depth reaching a peak value of 4.5 MPa at 0.5 m (upper crust). Between 1.5 m and 2.5 m depth there is a steady increase of q_t from 2 MPa to 6 MPa and then a decrease from 6 MPa to 2 MPa for the subsequent 1.5 m (lower crust). Tyldesley et al. (2013) reported that some of the variations of q_t along the first 4.5 m depth are likely related to localized weathering and the presence of cracks and fissures. For depths below 4.5 m, the tip resistance remains around 2 MPa (unweathered till).

High values of q_t and F_R are usually associated with heavily overconsolidated very stiff to stiff fine-grained soils, as is the case for the upper and lower crust between 0.5 m to 4.5 m with the steady decreasing of q_t and F_R to almost constant low values, the soil behaviour type is likely associated with a clayey silt to silty clay soil with decreasing overconsolidation ratio (OCR), as is the case for the unweathered till. Using the normalized cone tip resistance along with the friction ratio, it was possible to produce normalized soil behaviour type plots from the CPT soundings. These plots and their description can be found in Appendix A.1. Notably, the pore water pressure (u_o) measurements were negative between 0 to 2.5 meters, this type of behaviour is associated with strongly dilative soils such as heavily overconsolidated stiff fine-grained soils. The development of excess pore pressure during cone penetration below 5 m depth is again characteristic of silty and clayey soil with low OCR (Robertson and Campanella, 1983; Robertson, 1990).

Results from standard penetration tests (SPT) showed that corrected N_1 values ranged from 14 to 15 for the till deposit indicating a stiff consistency. Only a single N_1 value for the weathered till of 43 was recorded indicating a hard consistency. The corrected N_1 values ranged from 11 to 20 for the unweathered till indicating a firm to stiff consistency. The variation of SPT blow count with depth is found in Appendix A.2. Porewater pressures at different depths were measured using vibrating wire piezometers. Interpretation from these data showed that the ground water table at the site was at around 0.70 m below the ground surface.

To characterize the small-strain stiffness properties of the soil deposit, seismic cone penetration testing (SCPTu) and cross-hole seismic testing (CST) were carried out. SCPTu was performed to obtain the shear wave velocity (V_s), and CST was performed to obtain both shear wave (V_s) and compressional wave velocity (V_p) with depth. For SCPTu the shear wave velocities measured correspond to vertically propagating waves with horizontal polarity (V_{svh}), and for CST, the shear wave measured is horizontally propagating and horizontally polarized (V_{shh}) (Newson et al., 2019). The measured wave velocities, from both tests, are shown in Figure 3.10a and b. Shear wave velocity (V_s) measurements from the SCPTu were not reported for the upper weathered till. The V_s reported for the lower weathered till was around 200 m/s, and for the unweathered till was between 195 m/s and 260 m/s. Similarly, the V_s measurements from the CST in the upper till were between 294 m/s and 257 m/s, and in the lower till were between 258 m/s and 244 m/s. The measured V_s range for the unweathered till was between 240 m/s and 320 m/s. Similar measured values of V_s from *in-situ* testing have been reported by Burghignoli (1994), AGI (1991), and Jamiolkowski and Lo Presti (1994) on a range of Italian naturally deposited stiff clays, whose geological ages ranged from Holocene to Pliocene and were the products of different sedimentation processes in aqueous environments (i.e. lacustrine, alluvial, marine, estuarine).

Some discrepancies are shown between the shear wave velocity measurements from SCPTu and CST testing. These can be attributed to a partial soil variability between the boreholes used to perform the testing (e.g. presence of silt and sand lenses, fissures and discontinuities, soil disturbance) since the SCPTu test was carried out in borehole CPT-1 and the CST was performed in borehole BH12-2. Moreover, Robertson et al. (1986) reported a difference of 20% between measured V_s values obtained by CST and SCPTu. Such difference was attributed to the existence of anisotropy within the studied soil deposit that could have affected the wave propagation. This could be a significant contribution to the difference between the CST and SCPTu results; the shear wave velocities from both *in-situ* tests were measured in different propagation planes and Clayton (2011) reported on similar differences between vertically and horizontally propagated shear waves in the anisotropic London clay using down-hole and cross-hole *in-situ* techniques.

The compression wave velocity (V_p) varied throughout the profile ranging from 1200 m/s to 1600 m/s and does not exhibit a clear trend with depth. Generally, measurements of V_p in the field does not reflect the skeletal stiffness of the soil and is usually an indication of saturation as the V_p in water is approximately 1500 m/s (Clayton, 2011). Using the wave velocity results, estimations of the shear modulus (G_{max}), elastic modulus or Young's modulus (E_{max}), and Poisson's ratio (μ) were obtained with depth for the soil deposit., (see Figure 3.11). The estimated Poisson's ratio with depth ranged between 0.47 to 0.49; these values also indicate that the soil is saturated.

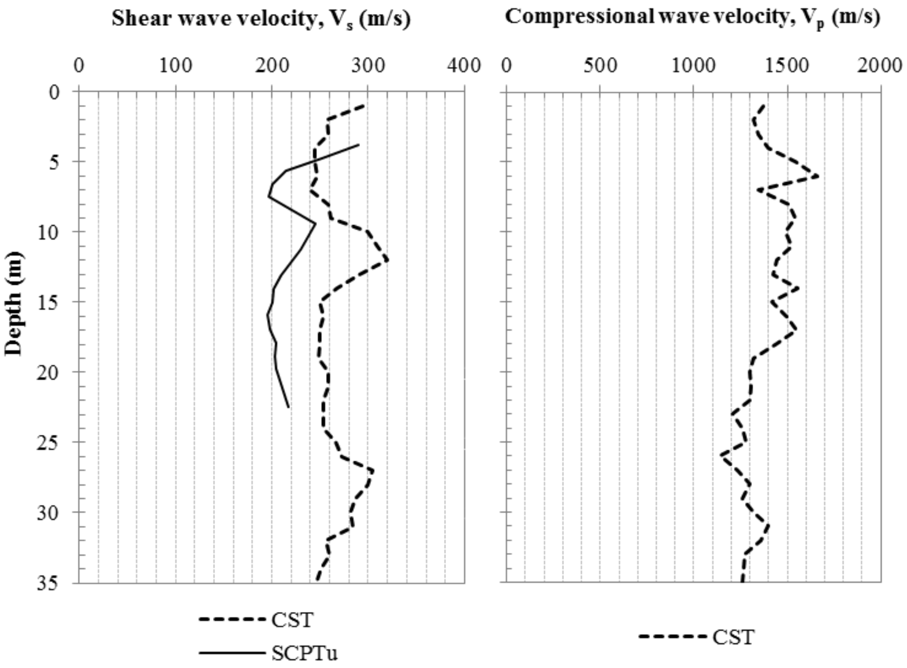

Figure 3.10: CST results; (a) shear wave velocity, (b) compressional wave velocity (adapted from Newson et al., 2019)

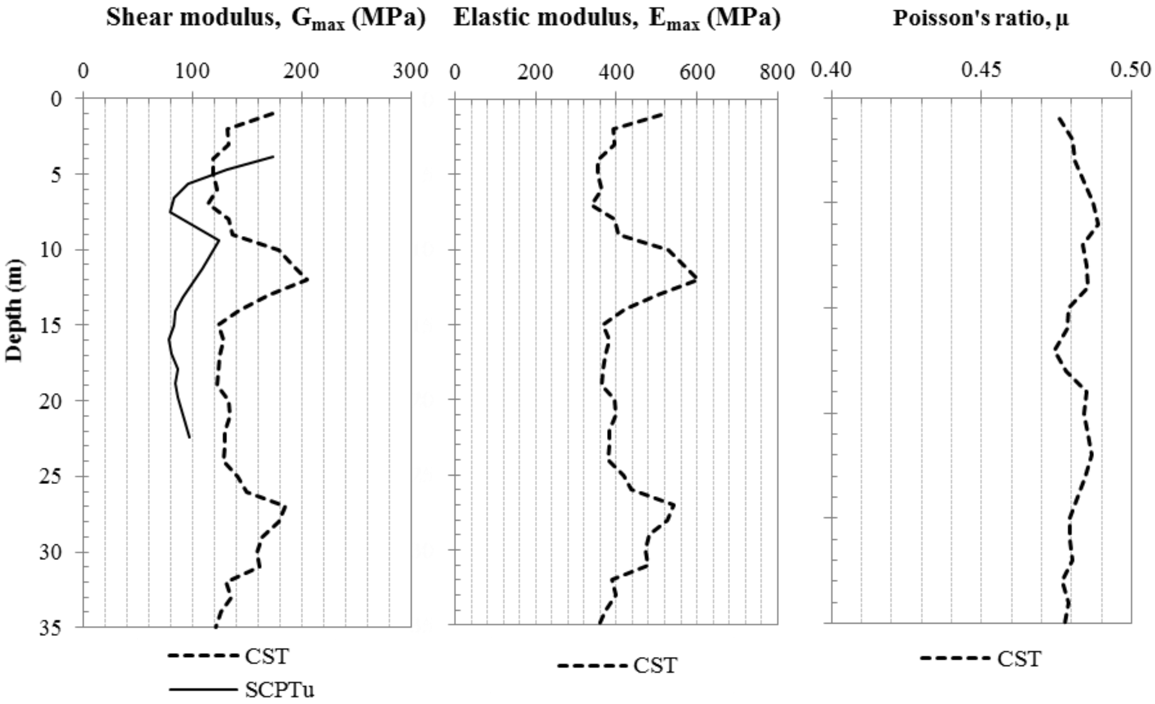

Figure 3.11: CST results; (a) shear modulus, (b) elastic modulus, and (c) Poisson's ratio (adapted from Newson et al., 2019)

3.5.3 Available laboratory test data

The existing laboratory test data on the Port Alma material has been divided into two groups herein. The first group covers the results from basic laboratory characterization tests, such as the calculation of carbonate content within the soil profile, natural moisture content and unit weight, Atterberg limits, and particle size distribution analysis. Unless otherwise indicated, the data reported in this group is from Newson et al. (2019). The second group covers the stress-strain behaviour from one-dimensional consolidation behaviour, and isotropic consolidation shear testing, and this is from a variety of sources as noted.

3.5.3.1 Basic laboratory testing

3.8.3.1.1 Carbonate content

Previous tests were performed to determine the total carbonate content and the individual amounts of calcite ($CaCO_3$) and dolomite ($MgCaCO_3$) within the Port Alma soil deposit using the Chittick test. Figure 3.12a and b show the percentages of calcite, dolomite and total carbonate content, and the ratio of calcite to dolomite with depth, respectively.

The results showed that for the first 1.5 m to 2 m depth there is an absence of carbonates. The carbonate content increases from nearly 0% to around 24% within the lower crust. This value then decreases to about 20% at the transition zone between the lower crust and the unweathered till (around 5 m depth). There is an increase in the carbonate content at around 9 m depth reaching a value of about 32%. The carbonate content then remains almost constant fluctuating between 23% to 25% within the unweathered till. Similar findings were reported by Quigley and Ogunbadejo (1974) when studying a natural stiff clay deposit from Sarnia Ontario. They proposed that downwards leaching removed soil carbonates from the near surface and were redeposited further down the soil profile at around 1.5 m depth.

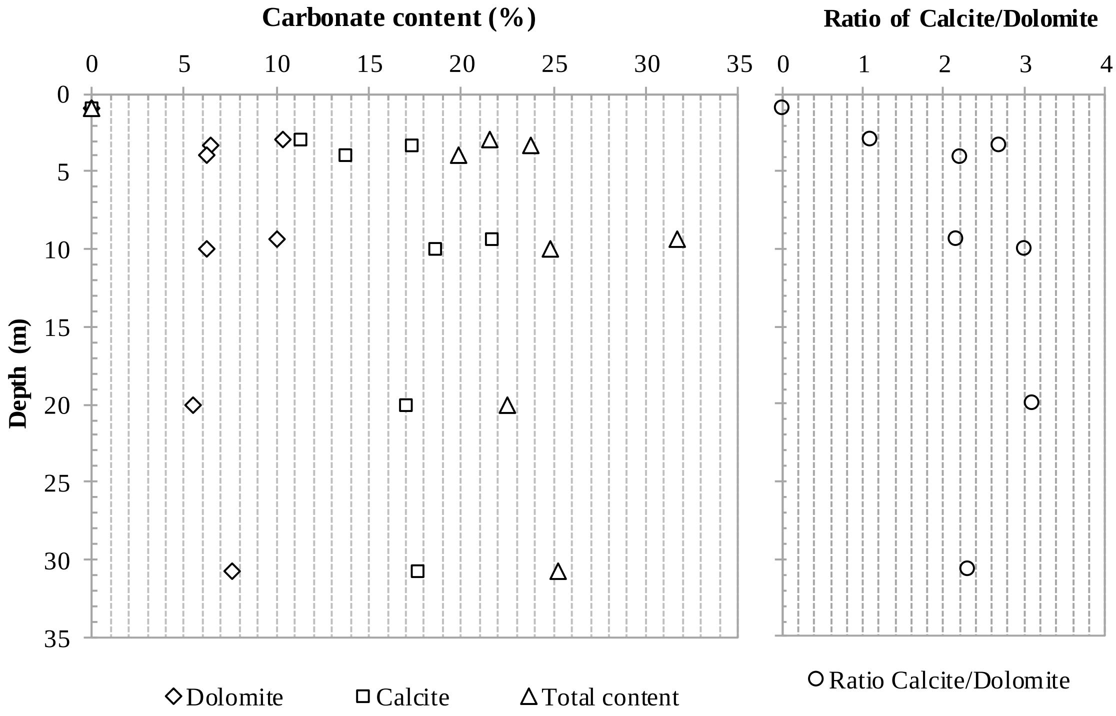

Figure 3.12: Chittick test results: (a) carbonate content percentages, (b) ratio of calcite/dolomite

3.8.3.1.2 Natural moisture content, unit weight, and Atterberg limits

Moisture content tests and Atterberg limits were carried out on split spoon samples, thin wall samples, and PQ core samples. Similarly, from cut samples selected for the triaxial and oedometer tests, the unit weight was determined as well. Figure 3.13 shows a summary from these tests with depth for the soil deposit. High values of moisture content, between 22% and 32%, were reported for shallow depths (0 m to 1 m) of the soil deposit, decreasing to 19% between 1 and 2 m depth. For the rest of the profile, between 2 m to 36 m below ground level, the moisture content is relatively constant with a value of approximately 20%. The calculated unit weight for the upper and lower weathered till, ranges between 20.3 to 21.6 kN/m^3. From 5 m downwards, the unit weight of the till deposit remained constant with a value of 20.5 kN/m^3. Between 1 m and 3 m depth, the liquid limit and plastic limit of the soil deposit ranged around 43% and 20% respectively (plasticity index, PI or I_p≈23-25%), indicating medium plasticity clay. From 3 m downwards, the liquid limit and plastic limit remained around 30.5% and 17% (I_p ≈ 13-15%) indicating low plasticity clay.

Similarly, the reported water contents of the lower weathered till and the unweathered till are very close to their plastic limits, which indicate stiff consistency and overconsolidation. Additionally, calculated values of liquidity index (*LI*) (Figure 3.13c) showed that the average for the upper weathered till is approximately 0.2, the lower weathered till is approximately -0.10 and the unweathered till is approximately 0.2. The liquidity index compares the current moisture content of a soil to its Atterberg limits. A liquidity index equal or less than 0 means the soil is at its plastic limits and indicates a heavily overconsolidated clay.

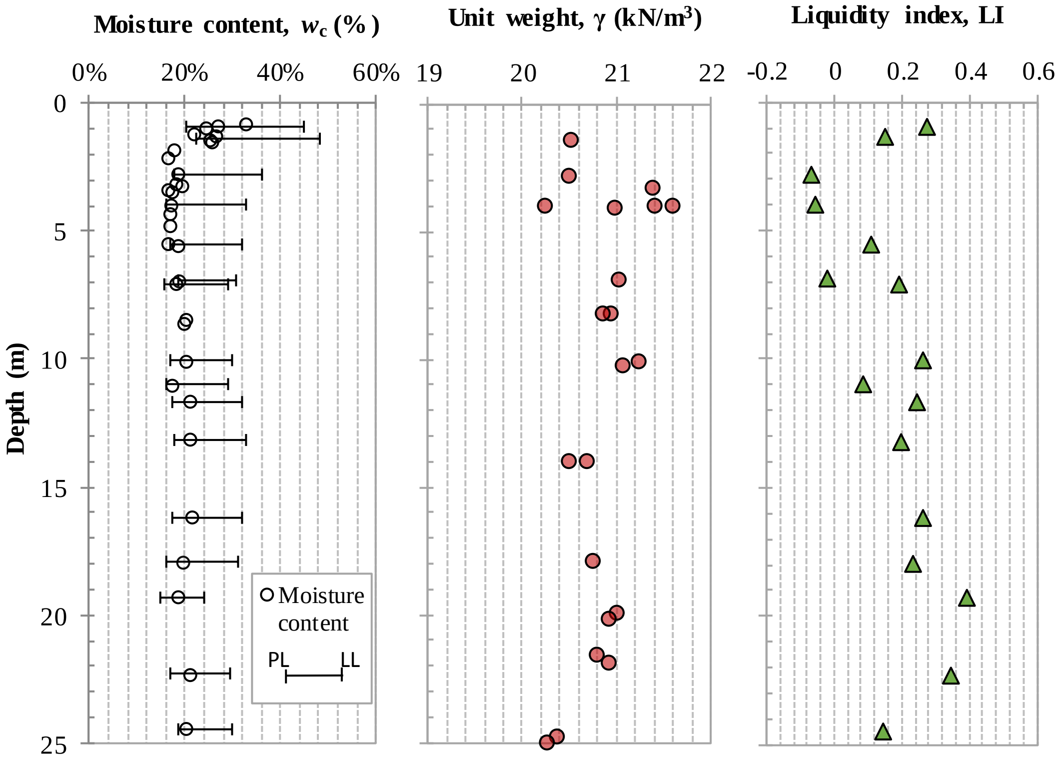

Figure 3.13: (a) moisture content and Atterberg limits, (b) unit weight, and (c) liquidity index

3.8.3.1.3 Grain size distribution

Figure 3.14, 3.15 and 3.16 present the grain size distribution for the upper weathered, lower weathered and unweathered till within the soil deposit. The upper weathered till is composed by 85% of fine-grain sized particles (< 0.075mm) and 15% of medium to fine sand sized particles. The lower weathered till and unweathered till have similar composition of particle sizes. The grain size distribution curves indicate that both layers, are composed of approximately 20% sand sized particle, less than 3% are gravel sized particles, and approximately 77% of a mixture of fine-grain sized particles with clay content that ranges from 26% to 40%.

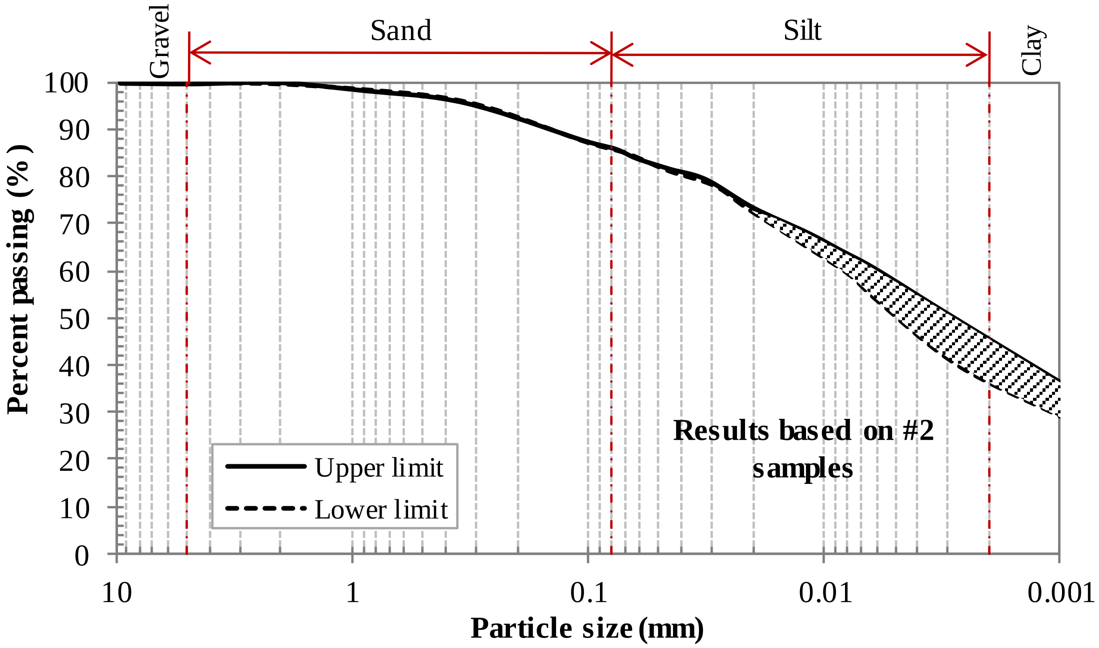

Figure 3.14: Grain size distribution - Upper weathered till

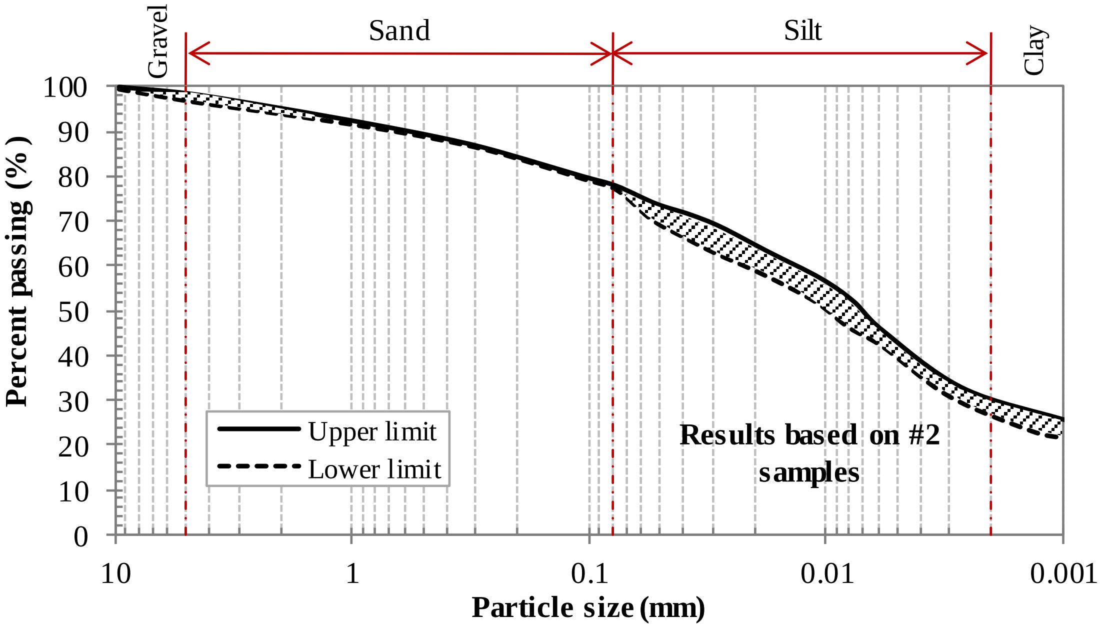

Figure 3.15: Grain size distribution - Lower weathered till

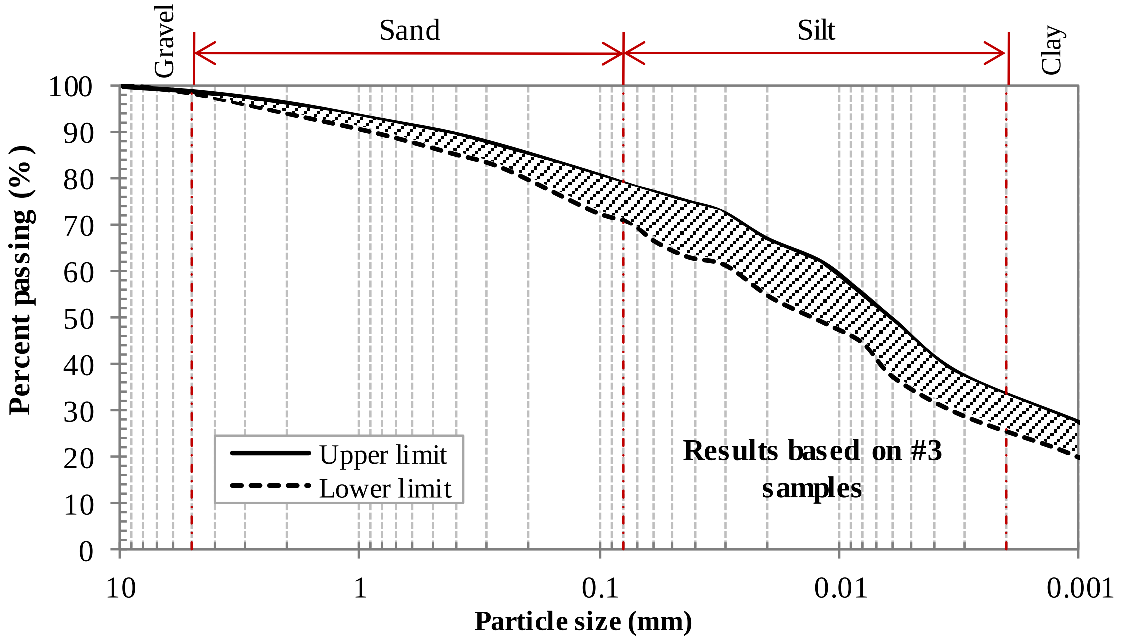

Figure 3.16: Grain size distribution - Unweathered till

3.5.3.2 Stress-strain behaviour

3.8.3.2.1 One-dimensional consolidation behaviour

The one-dimensional consolidation behaviour of the soil deposit was assessed using oedometer testing. From a wide range of parameters obtained by Newson et al. (2019), only the data describing void ratio (*e*), constrained modulus (E_o') and overconsolidation ratio (OCR) is shown here. Figures 3.17(a) to (c) show a summary of these data. The correspondent results of the coefficient of consolidation (C_v) and hydraulic conductivity (*k*) with depth are shown in Appendix A.4.

The void ratios of the samples at their *in-situ* vertical pressure are plotted in Figure 3.17(a). The upper weathered till layer exhibited the higher void ratio (e ≈ 0.62) compared to the other two lower soil layers. The void ratio in the lower weathered till ranged between 0.46 to 0.54 and the void ratio in the unweathered till ranged from 0.46 to 0.52. Figure 3.17(b) shows that the constrained modulus increases with depth. From 0 to 10 m below ground surface, E_o' ranges from about 5 to 10 MPa, and from 10 m onwards, E_o' ranges from about 11 to 18 MPa. The OCR presented in Figure 3.17(c) was estimated using a calculation method proposed by Boone (2010), as well as the Casagrande construction method for estimations of OCR. From these estimations, the OCR was found to vary between 2 to 5 on the upper weathered till, having the higher overconsolidation ratio within the soil deposit. Between 2 m and 4 m (lower weathered till) the OCR ranged from 2 to 4, and this decreased to an average constant value of approximately 1.5 from 4 m to 36 m below the ground surface (unweathered till). Within the first 10 m of the profile, the OCR values obtained with the CPT data and oedometer tests follow a similar trend, although they differ in magnitude. Below 10 m and as the depth increases, OCR values estimated from the CPT data show a general decrease and are similar to those estimated from the oedometer tests.

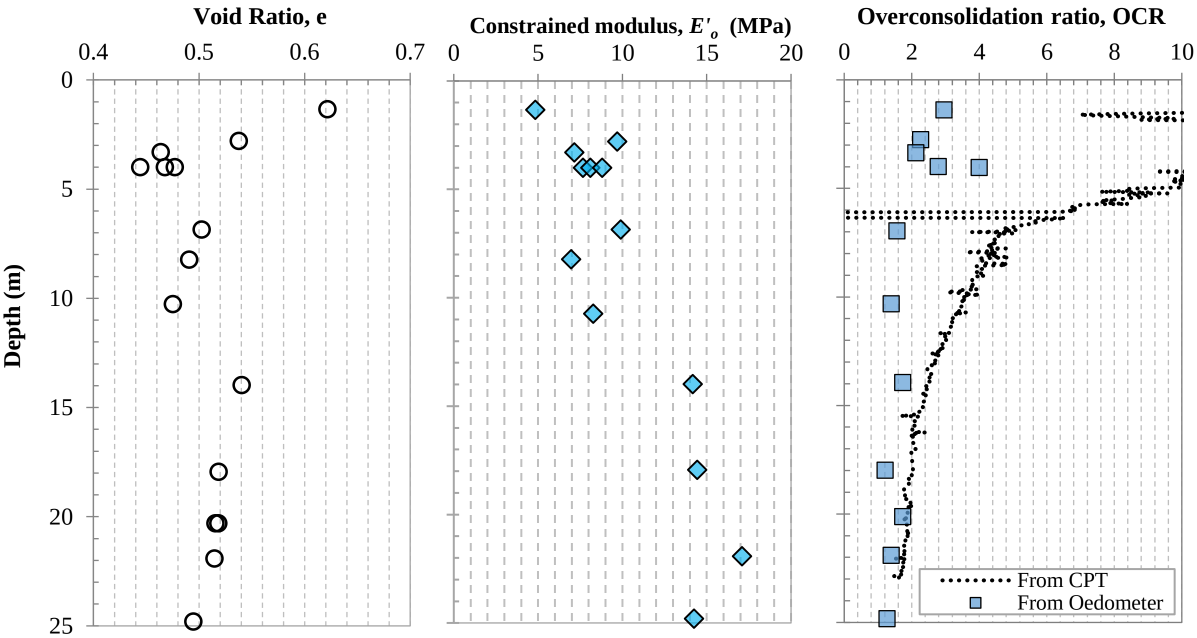

Figure 3.17: Summary of oedometer results; (a) void ratio, (b) constrained modulus, and (c) overconsolidation ratio

3.8.3.2.2 Isotropic and shear behaviour

Newson et al. (2019) and Kiss (2016) evaluated the isotropic and shear behaviour of the Port Alma soil deposit through a series of consolidated isotropic undrained (CIU) triaxial tests equipped with a pair of piezoelectric wave transducers (bender elements, BE). The CIU tests performed were used to determine the shear strength and shear stiffness of the soil, and to investigate the elastic-plastic response and critical state properties of the till deposit. Newson et al. (2019) performed tests on undisturbed samples from different depths within the soil deposit, thus allowing the characterization of the different soil layers. Kiss (2016) carried out CIU tests on soil samples that belonged to the unweathered till deposit, primarily from a depth twice of the foundation diameter (between 20 to 25 m below the ground surface). The CIU triaxial test results obtained by Newson et al. (2019) and Kiss (2016) will be presented later in Chapter 5.

As mentioned previously, the CIU triaxial tests performed by Newson et al. (2019) and Kiss (2016) also used BE transducers aligned with the vertical direction of the samples. The BE allowed for the measurement of vertically propagated and horizontally polarized shear and compressional wave velocities (Vs_{vh} and Vp_{vh}) through the Port Alma glacial till material, thus allowing the estimation of small-strain elastic properties in the vertical plane of the soil specimens (e.g. vertical shear modulus (G_{vh}), vertical constrained modulus (M_{vh}). Overall, the soil samples were subjected to isotropic compression and swelling and shear wave velocities and compressional wave velocities were measured at each stage. More detailed information on these test procedures and subsequent analyses can be found in Newson et al. (2019) and Kiss (2016). Newson et al. (2019) only reported findings on Vs_{vh} and G_{vh}, while Kiss (2016) reported findings for both $\mathrm{Vs}_{\mathrm{vh}}$ and $\mathrm{Vp}_{\mathrm{vh}}$ (G_{vh} and M_{vh}).

In general, the measured shear wave velocities by Newson et al. (2019) and Kiss (2016) showed good agreement. Figure 3.18 shows that V_{s} values increase with higher effective confining pressure. Similar behaviour for $\mathrm{G}_{\mathrm{max}}$ can be observed in Figure 3.19. The main reason behind the increase in the velocity propagation is the change in the sample density due to the increase effective stress at each stage. Shear waves travel at a velocity that is function of the shear stiffness and density (ρ) of the soil (Clayton, 2011). Moreover, Hardin (1961) and Hardin and Richart (1963) after performing resonant column tests on cohesionless soils concluded that, at very small strains ($<10^{-3}$ %), V_{s} depends essentially upon the void ratio (e) and the effective confining pressure (p'). Later, Harding and Black (1968) found that for cohesive soils V_s can be also influenced by the plasticity index (I_{p}) and the overconsolidation ratio (OCR) of the soil. Since the small-strain shear modulus of the soil (G_{max}) is a direct function of V_{s}, both exhibit a similar behaviour with increasing of effective pressure. The preconsolidation pressure (p_c') for this material is shown on the figures for reference. Similarly, the V_p and M_{max} values estimated by Kiss (2016) increased with higher effective pressures. V_p and M_{max} are also functions of the effective confining pressure and soil density, which can also explain the observed trend depicted in Figures 3.20 and 3.21.

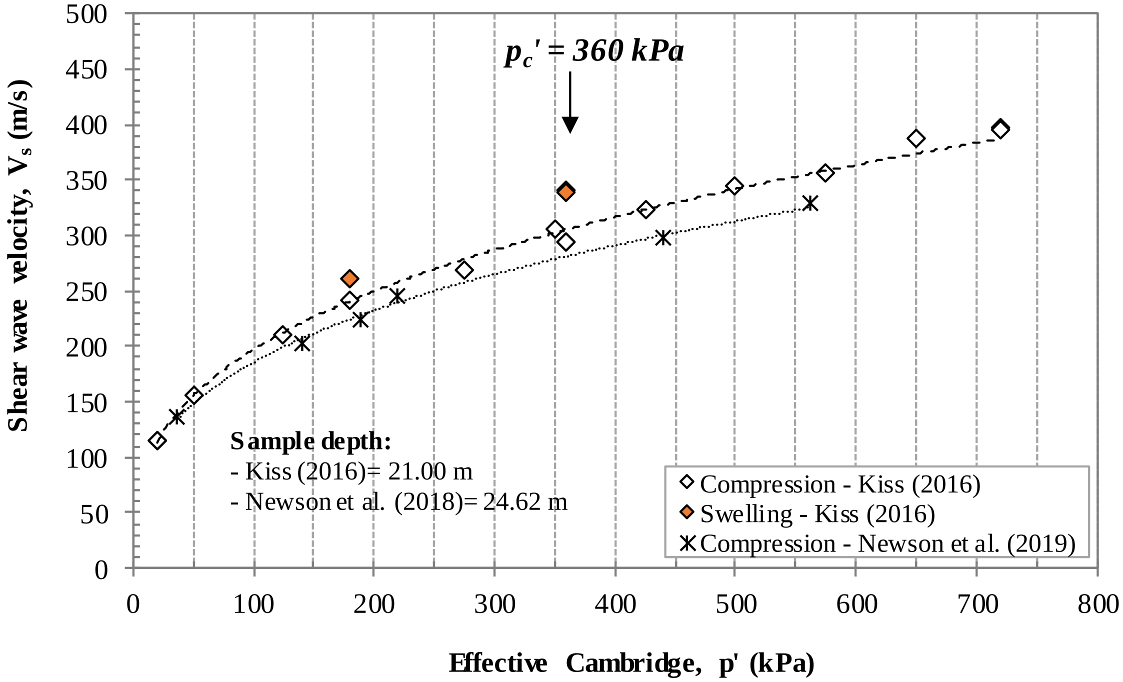

Figure 3.18: Shear wave velocity with effective confining pressure

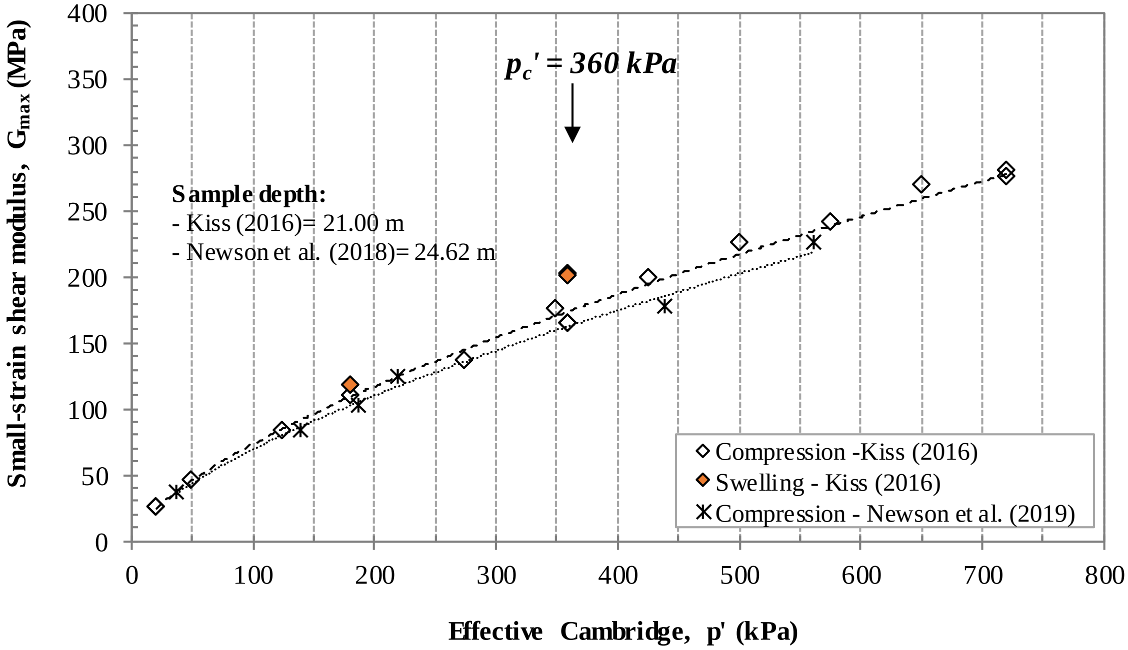

Figure 3.19: Small-strain shear modulus with effective confining pressure

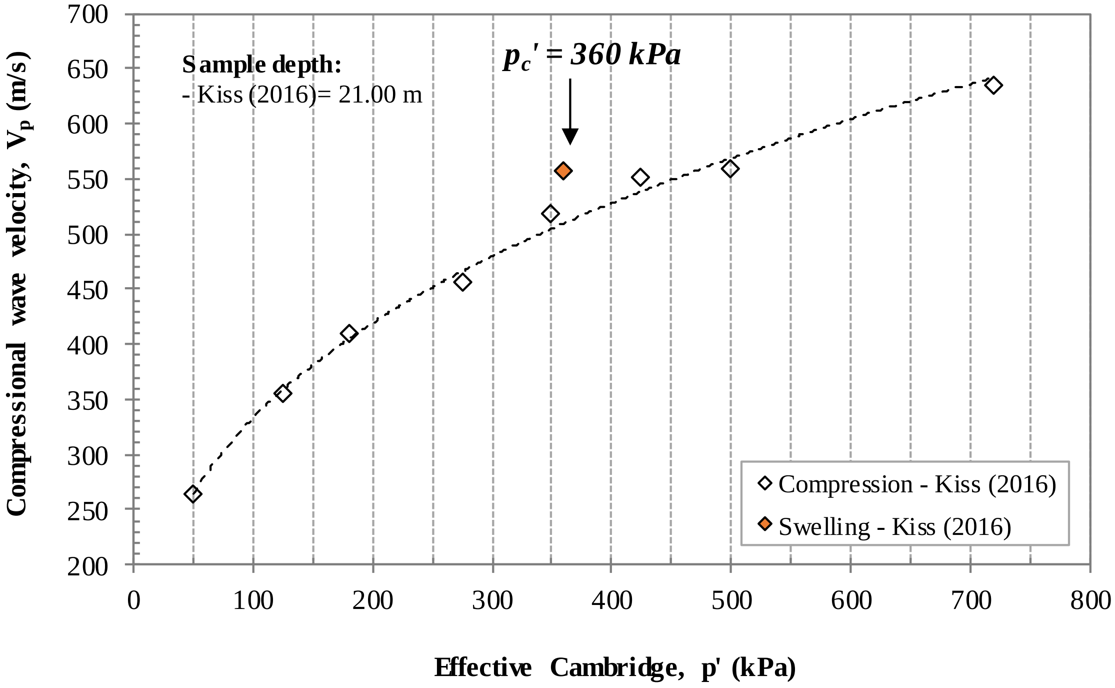

Figure 3.20: Compressional wave velocity with effective confining pressure

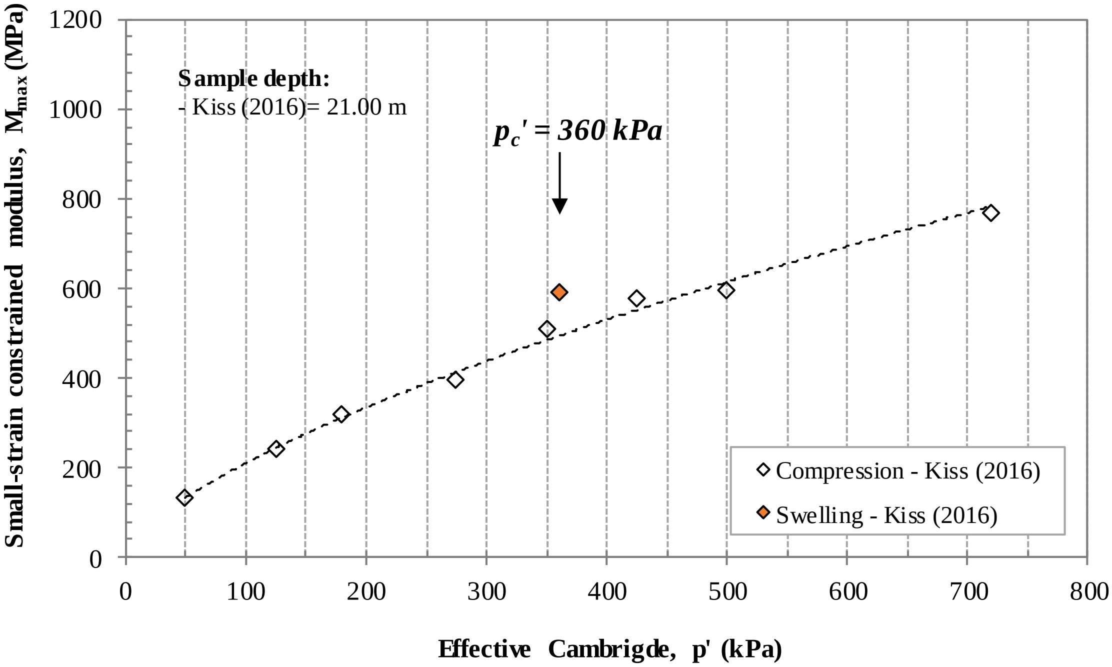

Figure 3.21: Small-strain constrained modulus with effective confining pressure

3.8.3.2.3 Summary of strength and stiffness data

Kiss (2016) used the ‘Stress History and Normalized Soil Engineering Properties (SHANSEP) approach, developed by Ladd and Foott (1974), to demonstrate that the unweathered till layer at Port Alma exhibits normalizable behaviour. This study supports the approach that comparison of triaxial tests from slightly different depths can be made and will allow future tests to be conducted on different samples that are from a wider range of depths; providing they are normalized using the SHANSEP procedure. This practice was used by Vucetic (1988, 1988 & 1990), while investigating the degradation of marine clays under repetitive loading. The test procedure and analysis for the SHANSEP method will not be explained herein; a more detail discussion can be found in Ladd and Foott (1974).

Based on the work of Kiss (2016), on the normalizable behaviour of the unweathered till layer and the feasibility of using samples from different depths to estimate the geotechnical properties of the till material from triaxial testing, the BE test results presented in the previous section have been used to compare with the small-strain properties measured *in-situ* using the CST and SCPTu tests. The effective Cambridge pressure (p') applied at each compression stage during the BE tests, were used to estimate an *in-situ* depth that corresponded to the effective stress state used in the tests. The effective Cambridge pressure (p') is estimated using the vertical and horizontal effective stresses representative of the *in-situ* condition experienced by a soil sample at each depth. Further discussion of the estimation of the *in-situ* stresses and p’ will presented in Chapter 4. Using this approach Figure 3.22 was produced, showing the distribution of the small-strain elastic parameters with depth obtained in the laboratory, along with the SCPTu and CST test results presented in Section 3.5.2. In a similar manner, a summary of the undrained shear strength (s_u) with depth obtained from *in-situ* and laboratory tests are illustrated below in Figure 3.23. Good agreement can be observed among the different methods used to characterize the undrained shear strength of the deposit.

It can be seen from Figure 3.22a and b that there is a good agreement between the measured values of the vertically propagated horizontally polarized shear wave velocities (V_{svh}) from the laboratory tests and those obtained from the SCPTu *in-situ* testing at depths between 10 m to 35 m. The V_s and G_{max} values estimated at lower effective stresses (depths between

1 m to 5 m) from BE test are consistently lower than the *in-situ* measured values. This difference could be attributed to sample disturbance, insufficient consolidation/creep times, and inadequate re-construction of the stress history of the specimen (Jardine et al., 1984; Gasparre et al., 2007). Disturbances are usually associated with the destructuring, loss of bonding, and yielding that happens at interparticle level during sampling and preparation of the specimens and cannot be totally recovered during reconsolidation (Clayton and Heymann, 2001). Another way to induce excessive disturbance is while stresses are applied during the reconsolidation of the sample. Fast increments of pressures during testing can induce excessive development of plastic strains inside the soil specimen that can affect the natural soil structure (Gasparre, 2005; Kim, 2011).

Based on resonant column tests performed on various natural clays, Anderson and Woods (1976) found that the small-strain shear modulus increased almost linearly with the logarithm of time after the end of the primary consolidation. They pointed out that it would be important to account for adequate increase in velocity due to time effects if shear wave velocities were to be estimated by laboratory means. In addition, Anderson and Stokoe (1978) suggested that for a certain soil deposit the stiffness will depend on its geological age. In terms of the reconstruction of the soil stress history, more recently Zapata-Medina et al. (2011) found that higher values of G_{max} are obtained when the laboratory stress path can model a field loading history of K_0 consolidation to the maximum past pressure and subsequent unloading to the initial effective vertical stress than if one merely uses a recompression technique to bring the soil to the *in-situ* stresses.

As explained in Chapter 2 and discussed in Section 3.5.2, the study of the inherent small-strain stiffness anisotropy of natural soil deposits, especially of heavily overconsolidated clays, helps to better understand the behaviour of soil materials and can be used to further characterize its elastic properties for use in geotechnical design. Thus, to further analyze the data obtained from the in-situ testing, the anisotropy ratio, was estimated and presented in Figure 3.22c. This modular ratio is also known as the anisotropy ratio ($\alpha = G_{hh}/G_{vh}$) and from its calculation it can be inferred whether the material is anisotropic or not. If $\alpha = 1$ the material is isotropic, if $\alpha > 1$ the material is anisotropic with a higher stiffness in its horizontal direction, and if $\alpha < 1$ the material is also anisotropic but stiffer vertically.

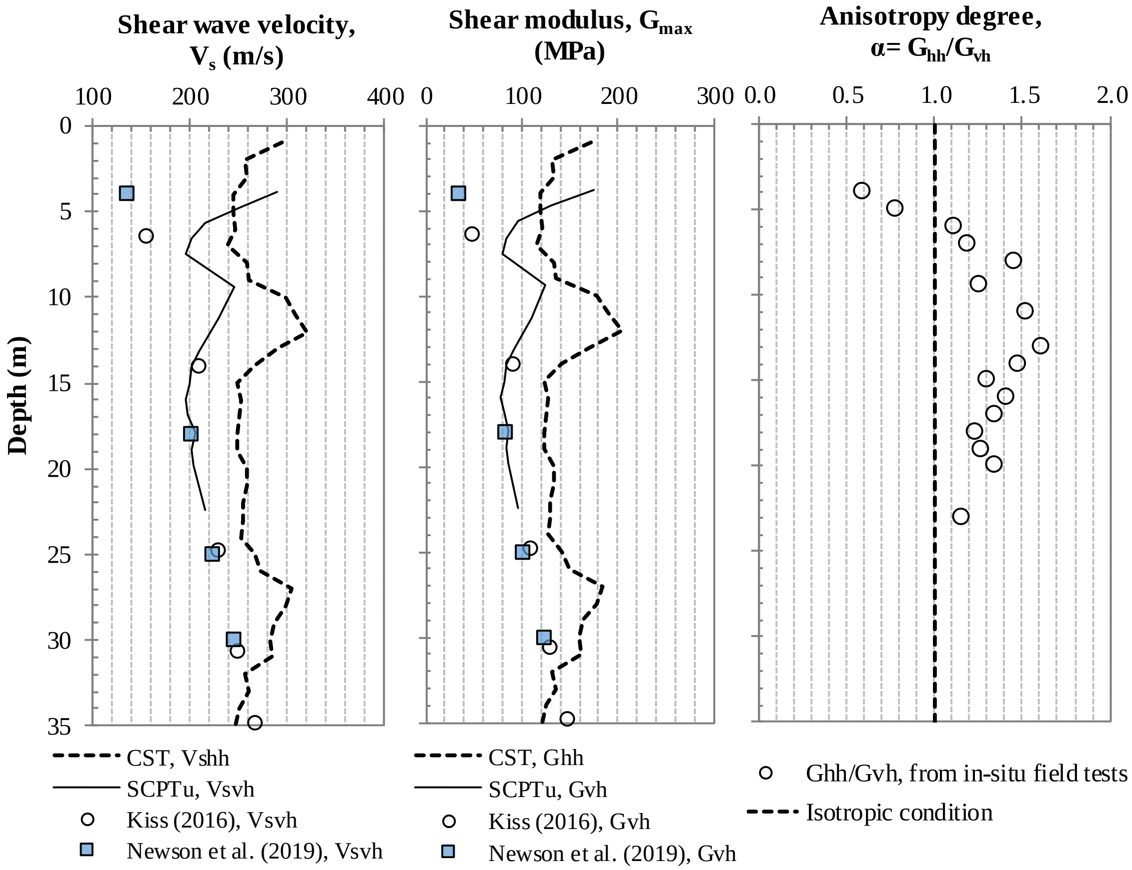

Figure 3.22: (a) shear wave velocity, (b) shear modulus, and (c) stiffness ratio

Different studies on the stiffness anisotropy of natural cohesive deposits were reviewed in Chapter 2. A number of those studies used geophysical techniques in the field to determine the small-strain soil stiffness in the vertical and horizontal directions (G_{vh} and G_{hh}) of stiff cohesive deposits such as London clay, Gault clay, Boulder clay and several Italian clays (e.g. Abbiss, 1981; Stokoe et al., 1992; Jamiolkowski et al., 1994; Butcher and Powell, 2016). All of these soils exhibited stiffness anisotropy at very small-strains with different α values. For London and Gault clay α ranged from 2.0 to 3.0, and for the Italian clays α ranged between 0.80 and 1.60. The α values estimated for the Port Alma deposit, shown in Figure 3.22c, ranged from 0.60 to 0.80 between 3 m and 4.5 m depth, suggesting that the material is anisotropic and vertically stiffer within the lower crust. The G_{hh}/G_{vh} ratio then ranges from 1.10 to 1.65 between 5 m and 13 m depth and starts to decrease with depth, reaching 1.20 at around 23 m. These results suggest that the unweathered till is also anisotropic but is stiffer in the horizontal direction.

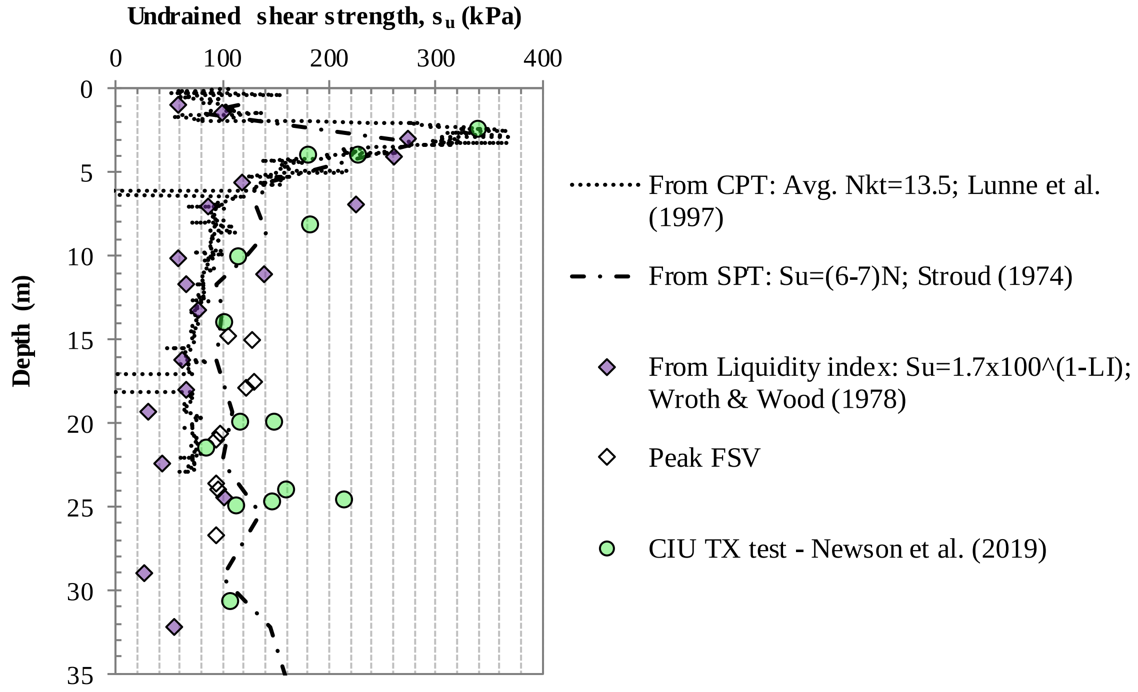

Figure 3.23: Undrained shear strength from in-situ and laboratory tests

Table 3.2 presents a summary of the geotechnical properties estimated and reported by Newson et al. (2019) and Kiss (2016) and discussed throughout this section.

Table 3.2: Summary of geotechnical properties of the Port Alma till deposit

Property	Upper Crust	Lower Crust	Unweathered Till
Natural Water Content, (%)	22-32	16-20	16-24
Unit Weight, (kN/m^3)	20.3	21	21.6
Liquid Limit (%)	46	34	30
Plastic Limit (%)	21	19	17
Carbonate Content (%)	0	23	24
Clay (%)	40	29	31
Silt (%)	45	49	45
Sand (%)	15	20	21
OCR	2-5	2-3	1-1.5
G_o (MPa)	100-120	60-200	60-80
Undrained Shear Strength (kPa)	100-150	150-250	100-130
$\alpha = G_{hh}/G_{vh}$ **(measured *in-situ*)**	-	0.60 – 0.80	1.10 – 1.65

3.6 Summary

The focus of this thesis is the study of the shallow foundation system that serves as support for an operating 2.3 MW wind turbine at a wind farm in Port Alma Ontario. This chapter presented an overview of the background information available on the site and geological setting of the Port Alma wind farm. Likewise, the existing wind conditions characteristic of the site are described. The results from *in-situ* and laboratory testing on the Port Alma soil material performed prior this investigation was reviewed and discussed. The Port Alma soil material can be categorized as a glacial till deposit product of an extensive and complex history of different major geological events. *In-situ* tests allowed the characterization of the glacial till deposit below the wind turbine shallow foundation. Three distinct soil layers were found, an upper and a lower weathered crust between 0 to 4.5 m depth, and an unweathered till of about 30 to 35 m thick. Most of the basic laboratory techniques helped to defined basic geotechnical properties and the stress-strain behaviour of the Port Alma soil material.

In general, the soil material is of low plasticity, lightly overconsolidated to heavily overconsolidated, rich in carbonates. The small-strain stiffness of the overburden material and its undrained shear strength were assessed by *in-situ* and laboratory means. The estimation of the undrained shear strength (s_u) from empirical correlations, field and laboratory results showed good agreement. This data allowed the characterization of s_u with increasing of depth for the Port Alma soil deposit. Measurements of shear wave velocity from SCPTu and CST tests indicate that the lower crust is vertically stiffer, while the unweathered till is horizontally stiffer. These results suggest that the small-strain stiffness of the Port Alma soil deposit is anisotropic. Till-fabric studies previously performed on glacial soils from around Port Alma, revealed that the soil fabric of these materials was mainly oriented in the direction of the ice flow during the deposition. These anisotropic fabrics can produce a directional dependence of the stiffness properties in a material. This concept could explain the anisotropy exhibited by the Port Alma till deposit. Similar behaviour has been exhibited by other materials of glacial origin (e.g. London clay and Chicago glacial clay) with similar formation history and mineralogy characteristics.

Chapter 4

4 Materials description and laboratory methods

4.1 Overview

This chapter describes the experimental program developed and carried out in the laboratory, including the materials selected for testing and the laboratory methods used. Some of these materials have been investigated previously (e.g. Lo and Becker, 1978; Kim and Novak, 1981; Kiss, 2016) and some of their basic geotechnical properties have been documented in the literature. A general description of the site location and geological setting of the areas where the natural soil samples were retrieved are presented in Section 4.2.2. Similarly, basic index properties, and stress-strain characteristics of the materials investigated are reviewed and discussed in Section 4.2.3, and a more detailed review of existing information can be found in Appendix B.2.

Section 4.3 describes the testing conditions and procedures followed in the laboratory. All of the laboratory tests described in the present study were performed under undrained conditions in either the resonant column apparatus or the stress-path triaxial system. The outline of the laboratory test program is introduced in Section 4.3.1, and the description of the basic laboratory tests used are presented in Section 4.3.2. The stress-paths followed during consolidation were determined based on the estimated current in-situ stresses and geological events in the past, and the approach for their calculation is explained in Section 4.3.4. The procedures for the undrained triaxial tests procedures and bender element test are described in Sections 4.3.6 and 4.3.7, respectively. Lastly, the resonant column test is described in Section 4.3.8.

4.2 Cohesive materials

4.2.1 Introduction

Glacial clay materials are abundant across the Great Lake basins and wind farms are often placed on these stiff geomaterials. The behaviour of glacial clay soils has been shown to be highly non-linear and strain dependent, and at the same time such behaviour is governed by intrinsic features of the soil structure, such as fabric anisotropy and current stress state.

A limited number of studies of the stiffness anisotropy behaviour of Canadian glacial clays at large strain levels ($\varepsilon > 0.5\%$) has been conducted and suggest that these natural cohesive materials present differences in their stiffness properties (e.g. G and E) when measured in the vertical and horizontal directions, as reported by Becker (1981). However, little is known about the small-strain stiffness anisotropy of such glacial materials. In this investigation, six different cohesive materials were selected for testing.

Five of these soils were naturally deposited, and the sixth material was created under controlled laboratory conditions. Four of the glacial materials belong to areas located in southwestern Ontario, specifically from Port Alma, Windsor, Wallaceburg and Blenheim; whereas the remaining material was retrieved from a site near Winnipeg, Manitoba. The sixth material is a manufactured clay called Edgar plastic kaolin 'EPK' clay. Some of the properties of these soils have been previously studied by different researchers and are documented in the literature, such as Port Alma clay (Gonzalez-Hurtado and Newson, 2016; Kiss, 2016; Newson et al., 2019), Wallaceburg clay (Lo & Becker, 1978; Kim & Novak, 1981), Blenheim clay and EPK clay (Reipas ,2012), and Windsor clay (Kim and Novak, 1981).

During this research, it was possible to get access to stored soil samples from previous investigations conducted at the Western University (e.g. Kim & Novak, 1981). To check the condition of the samples, several basic laboratory tests (e.g. moisture content, Atterberg limits, unit weight) as well as more advanced testing (e.g. consolidated isotropic undrained (CIU) triaxial testing, one-dimensional consolidation test) were performed to assess the quality of the materials. Additionally, to further evaluate the quality of the samples, the method suggested by Lunne et al. (1997) [used by the Norwegian Geotechnical Institute] was employed. This method is based on the quantification of the sample disturbance using the change in pore volume relative to the initial pore volume, or in other words, the ratio of the initial void ratio to the consolidated void ratio ($\Delta e/e_o$). This ratio was calculated for all the different samples, using the one-dimensional consolidation test, and CIU triaxial tests. Lunne et al. (1997) defined different quality categories depending on the over-consolidation ratio (OCR) and the values of $\Delta e/e_{o.}$ Results showed that the samples used in this investigation fell within the categories of 'very good to excellent' and 'good to fair'.

Moreover, the reported values of moisture content, void ratio and unit weight for each of the samples found in the literature were compared against values estimated throughout this investigation, these results can be found in Appendix B.1.

4.2.2 General geological and geotechnical characteristics of the investigated materials

The materials obtained from Port Alma, Wallaceburg and Blenheim belong to the physiographic region known as the St. Clair clay plains (Chapman and Putnam, 1966). The clay deposits of this area generally consist of normally consolidated “water-lain” tills with relatively low shear strength, below a very stiff to hard oxidized surface crust. These deposits are calcareous and fine-grained, suggesting that the ice overrode and incorporated fine-grained glaciolacustrine sediments deposited during the previous Erie Interstade. This has created approximately 40 to 45 m thickness of clayey silt tills with interbedded glaciolacustrine sediments.

Further to the west of Ontario, Windsor clay is known to be overlain by fine-to-coarse lacustrine sand (Hudec, 1998), and has a lacustrine origin, laid down by inundation from a series of glacial lakes which formed during the retreat of the last ice sheets. Winnipeg clay belongs to the physiographic region of Red River Valley plain (Johnston, 1946; Corkery, 1996). This area consists mainly of offshore glaciolacustrine sediments, such as clay, silt with minor sand; 1 to 20 m thick; very low relief massive and laminated deposits deposited from suspension in the offshore, deep water of glacial Lake Agassiz; commonly scoured and homogenized by icebergs (Matile and Keller, 2004).

The properties of the soils tested vary from highly overconsolidated glacial clays to soft clays, according to their geological environments during and after formation. Table 1 presents a summary of the geotechnical properties of the studied materials. The geotechnical properties that were previously estimated and reported by other researchers were reviewed and discussed. This section presents, in tabular form, a summary of the geotechnical properties of the soils used in this investigation (see Table 4.1 and 4.2). More information on the site locations where samples were obtained, geological history, sampling techniques for material recovery, and geotechnical characteristics can be found in Appendix B.2

Table 4.1: Basic geotechnical properties of testing materials

Material	γ_{bulk} (kN/m^3)	e_o	w_n (%)	w_p (%)	w_L (%)	I_p (%)	I_L	C_c
Wallaceburg silty clay	18.50	1.05	38.1	17.6	42.2	24.60	0.83	0.210
Windsor silty clay	17.40	1.36	50.6	21.0	51.3	30.30	0.98	0.289
Winnipeg clay	18.50	1.05	55.4	30.0	90.0	60.00	0.42	0.560
Blenheim clay	21.14	0.47	19.2	16.7	23.1	6.40	0.39	0.092
EKP Kaolin clay	17.02	1.30	49.3	36.2	61.6	25.40	0.52	0.361
Port Alma clay	21.60	0.56	18.0	17.0	30.0	13.0	0.08	0.110

e_o, void ratio; w_n (%), moisture content; w_p (%), plastic limit; w_L (%), liquid limit; I_p (%), plasticity index; I_L, liquidity index; C_c, compression index

Table 4.2: Stress-strain characteristics of testing materials for *in-situ* conditions

Material	Depth (m)	c_u (kPa)	p_c' (kPa)	OCR	V_{svh} (m/s)	G_{vh} (MPa)	V_{pvh} (m/s)	E_v (MPa)	α=G_{hh} /G_{vh}
Wallaceburg silty clay	4.2	39.3	274	4.0	129.3	30.9	225.9	94.4	-
Windsor silty clay	5.0	25.1	140	2.7	93.8	15.3	184.6	59.3	-
Winnipeg clay	11.0	87.9	280	2.3	-	-	-	-	-
Blenheim clay	3.0	75.1	345	5.4	196.8	81.9	-	-	0.9
EKP Kaolin clay	-	32.4	150	2.5	130.7	29.1	-	-	-
Port Alma clay	21.0	80.2	360	2.5	200.0	90.0	390.0	-	1.15

c_u, undrained shear strength; p_c', pre-consolidation pressure; OCR, over-consolidation ratio; V_{svh}, shear wave velocity at in-situ pressure from laboratory testing; G_{vh}, shear modulus at in-situ pressure from shear wave velocity; V_{pvh}, compressional wave velocity at in-situ pressure from laboratory testing; E, elastic modulus at in-situ pressure from compressional wave velocity; α, anisotropic ratio.

4.3 Laboratory methodologies

4.3.1 Outline of experimental program

The laboratory experimental program was designed to characterize the small-strain stiffness behaviour and the linear-elastic characterization at medium to large strains of the different intact natural cohesive materials described in Section 4.2. Furthermore, the characterization of the soil response using critical state soil mechanics and the small-strain stiffness anisotropy behaviour of the testing materials were also considered when designing the experimental program.

Basic laboratory tests (e.g., moisture content, unit weight, Atterberg limits, etc.) were performed on every material tested. Detailed descriptions of the basic laboratory tests used during this investigation are presented in Section 4.3.2. A series of more advanced tests: consolidated isotropically undrained (CIU) triaxial tests with local axial displacement measurement, bender element (BE) tests equipped with bender element transducers in the vertical and horizontal directions of the testing specimens, and resonant column (RC) tests with sample rotation, were performed according to the programs outlined in Tables 4.3, 4.4, and 4.5.

Table 4.3: CIU triaxial tests with local axial strain measurement

Sample name	Sample ID	Pre-consolidation pressure, p_c' (kPa)	Consolidation pressure, p' (kPa)	OCR
Port Alma (PA) clay	PA-CIU-Sa#1 PA-CIU-Sa#2	360	160	2.3
Wallaceburg (WB) silty clay	WB-CIU	274	140	2.0
Windsor (WIN) silty clay	WIN-CIU	140	55	2.5
Blenheim (BL) clay	BL-CIU	345	345	1
	BL-CIU		60	5.8
EPK clay	EPK-CIU-Sa#1 EPK-CIU-Sa#2	150	60	2.5

Table 4.4: Bender element tests (vertical and horizontal)

Sample name	Sample ID	Pre-consolidation pressure, p_c' (kPa)	OCR range
Port Alma (PA) clay	PA-$BE_{V/H}$	360	14 to 1
Wallaceburg (WB) silty clay	WB-$BE_{V/H}$	274	11 to 1
Windsor (WIN) silty clay	WIN-$BE_{V/H}$	140	3 to 1
Winnipeg (WN) clay	WN-$BE_{V/H}$	280	11 to 1
Blenheim (BL) clay	BL-$BE_{V/H}$	345	11 to 1
EPK clay	EPK-$BE_{V/H}$	150	5 to 1

Table 4.5: Resonant column tests (with sample rotation)

Sample name	Sample ID	Pre-consolidation pressure, p_c' (kPa)	OCR range
Port Alma (PA) clay	PA-RC$_{0°}$ PA-RC$_{90°}$	360	9 to 1
Wallaceburg (WB) silty clay	WB-RC$_{0°}$ WB-RC$_{90°}$	274	5 to 1
Windsor (WIN) silty clay	WIN-RC$_{0°}$ WIN-RC$_{90°}$	140	2.5 to 1
Winnipeg (WN) clay	WN-RC$_{0°}$	280	5.5 to 1
Blenheim (BL) clay	BL-RC$_{0°}$ BL-RC$_{90°}$	345	11.5 to 1
EPK clay	EPK-RC$_{0°}$	150	5 to 1

0° rotation sample: Vertically cut sample; 90° rotation sample: Horizontally cut sample

4.3.2 Basic laboratory tests

Basic soil index laboratory tests were performed on the soil samples used in this investigation. The undisturbed soil samples were obtained by means of PQ cores, Shelby tubes (e.g. Port Alma clay, Winnipeg clay), and block samples (e.g. Blenheim clay, Wallaceburg clay, Windsor clay). The basic laboratory tests consisted of the following:

- natural moisture contents (ASTM D2216-10);
- unit weights (ASTM D4318-17);
- Atterberg limits (ASTM D4318-17);
- Carbonate content by Chittick test (Dreimanis, 1962);
- One-dimensional consolidation (ASTM D2435-11);

Natural moisture content and unit weight calculation were performed to all the soils used in this investigation. Atterberg limits were performed only on Winnipeg clay material, and chemical testing was performed only on the Port Alma clay material, due to the number of samples available for this purpose. The determination of total carbonate content and the individual amounts of calcite ($CaCO_3$) and dolomite ($MgCaCO_3$) in soils was made using the Chittick Apparatus (Dreimanis, 1962), which is based on the volumetric evolution of carbon dioxide when carbonates react with dilute hydrochloric acid. Table 4.6 presents the carbonate content testing program used.

The study of one-dimensional consolidation was carried out on samples from the Winnipeg clay material and Wallaceburg silty clay. One-dimensional consolidation tests were completed to estimate the preconsolidation pressure (p_c') and the overconsolidation ratio (OCR) of the soils investigated. A seating load of 5 kPa was applied to ensure adequate contact between the loading piston and the soil sample. Load increments were added to the sample by doubling its previous load. The preconsolidation pressure of each studied material was then calculated using the semi-logarithmic method proposed by Boone (2010).

Table 4.6: Carbonate content (Chittick test) testing program

Depth (m)	Borehole ID	Sample number	Test ID
0.50	12-2	1a	1
1.00	12-2	1d	2
1.50	12-2	2b	3
2.00	12-2	2c	4
2.50	12-2	3c	5
3.00	12-1	3a	6
3.50	12-2	3e	7
4.00	12-2	3i	8
4.50	12-2	4b	9
5.50	12-1	7	10
7.00	12-1	9	11
10.00	12-2	7b	12
14.00	12-1	18	13
16.00	12-1	20	14
18.00	12-2	10a	15
20.00	12-1	24	16
22.00	12-1	26	17
24.00	12-2	14d	18
28.00	12-2	17	19
32.00	12-1	34	20
36.00	12-1	36	21

4.3.3 General procedure for soil specimen preparation

The following sample preparation procedure was used (with minor modifications) for all of the RC, CIU triaxial with local transducer, and CIU triaxial with vertical and horizontal bender element tests of this investigation. Testing materials were obtained from waxed block samples, or Shelby sample tubes or PQ core samples that were relatively undisturbed. The waxed block samples were opened and cut into small pieces to obtain multiple rectangular soil specimens for the different testing procedures. Similarly, for the thin wall samples tubes or PQ core samples, the soil material was extruded first, and carefully cut. The exposed materials were sealed first with layers of plastic wrap, a layer of aluminum foil, cheese cloth, and lastly covered by wax. These smaller block/cylinders were stored until testing was required.

When the soil materials were used for testing, the following steps were taken to make the testing specimens. Firstly, the waxed material was carefully opened to avoid puncture of the material and minimize disturbance. Then the small block/cylinder sample was placed in a soil lathe. The sample was trimmed down carefully with a wire saw to form a nominally 50 mm diameter solid cylinder. After reaching the desired diameter, the trimmed specimen was placed inside a split metal mold of 100 mm height to cut any excess soil on the top and bottom of the soil cylinder. Subsequently, once the specimen was ready, moisture content samples were taken from the material trimmings, and the final cylinder dimensions (e.g. diameter, height) as well its weight were recorded. Figure B.24, found in Appendix B, shows small waxed block and cylinder samples, as well as the wire-saw and soil lathe used for sample trimming. Likewise, Figure B.25 shows a photographic sequence of the sample preparation in the laboratory.

4.3.4 Consolidation scheme and reconstruction of stress history

Samples for the CIU triaxial and RC tests were reconsolidated isotropically at, or close to, their effective *in-situ* stress states. For this simulation, the effective *in-situ* stresses for each material were approximated with the effective Cambridge (p') confining stress, as suggested by Anderson (1974):

$$p' = \frac{(\sigma_1' + 2\sigma_3')}{3} \tag{4.1}$$

where σ_1' is the vertical effective stress; and σ_3' is the horizontal effective stress. The vertical and horizontal stresses determine the coefficient of earth pressure at rest, K_o:

$$K_o = \frac{\sigma_3'}{\sigma_1'} \tag{4.2}$$

By substituting Eq. (4.2) into Eq. (4.1):

$$p' = {\sigma_1}' \frac{(1+2K_o)}{3} \tag{4.3}$$

Therefore, using Equation 4.3, the effective Cambridge confining stress could be obtained through the vertical effective pressure and the coefficient of earth pressure at rest. The natural cohesive soils used in this investigation are considered to have experienced different major geological events; normal K_o-consolidation during their deposition, and K_o-unloading due to the melting of glaciars, erosion, dessication, etc. Jaky (1944) proposed an equation that models the effective stress path expected during K_o-consolidation:

$$K_{o(NC)} = 1 - \sin\phi' \tag{4.4}$$

where ϕ' is the effective angle of friction of the soil. Mayne and Kulhawy (1982) proposed another empirical equation to estimate the K_o-unloading stress path:

$$K_o = K_{o(NC)} OCR^{\sin\phi'} \tag{4.5}$$

where $K_{o(NC)}$ is the K_o value during normal consolidation, and OCR is the oversocolidation ratio. By substituting Eq. (4.4) into Eq. (4.5):

$$K_o = (1 - \sin\phi')OCR^{\sin\phi'} \tag{4.6}$$

and by substituting Eq. (4.6) into Eq. (4.3):

$$p' = \sigma_1' \frac{\left[1+2\left((1-\sin\phi')OCR^{\sin\phi'}\right)\right]}{3} \tag{4.7}$$

Thus, using Eq. (4.7), the effective Cambridge confining stress can be estimated taking into consideration K_o-loading/unloading processes.

4.3.5 Specimen saturation, consolidation, and shearing procedures

The procedures presented here were used for testing specimens in both the stress-path triaxial system and resonant column (RC) apparatus. Once the soil specimen was fully fitted inside the triaxial system or RCA, and the standard cell or chamber was in place, this was filled with de-aired water. Once the cell was full, water around the soil sample was pressurized to achieve full saturation of the specimen. The difference between the cell pressure and back pressure was kept within 10 kPa; in general, a cell pressure of 200 kPa and back pressure of 190 kPa, at the saturation stage of each test. Those 10 kPa of effective saturation pressure were maintained for a minimum of 48 hours to achieve full saturation of the soil specimens.

To check the degree of saturation of the specimens, the Skempton's pore water pressure parameter 'B' (known as B-check) was calculated for each specimen before moving to the consolidation phase of the test. The B-check requires the specimen drainage to be closed, to keep the volume of the sample constant, whilst the cell pressure was increased to 100 kPa. The B values were calculated for each test as follows:

$$B = \frac{\Delta u}{\Delta \sigma_c} \tag{4.8}$$

The value of 'B' should be between 0.95 and 1.0 (95% to 100 % of saturation reached) for clay specimens (ASTM D4767). However, this theoretical value was found to vary depending on the soil type as reported by Black and Lee (1973). All the samples tested herein reached values of 'B' greater than 0.95. Figure 4.26 shows the specimen saturation by increasing of back pressure and the subsequent B-check to confirm the sample saturation.

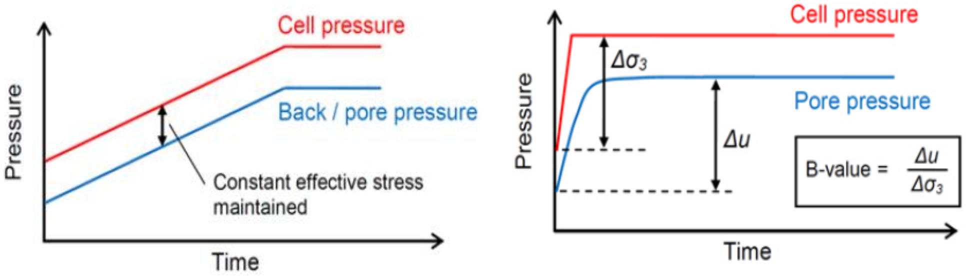

Figure 4.1: a) Specimen saturation by increasing of back pressure (left); b) B-check to confirm saturation (right) (adapted from GDS instruments Ltd., 2012)

Once the saturation stage was completed, the next step was the consolidation stage, which was used to bring the soil specimens to the desired effective stress state. As mentioned in Section 4.3.4, all of the soil specimens were reconsolidated isotropically following the programs outlined in Table 4.3, 4.4, and 4.5. Samples for consolidated isotropically undrained (CIU) triaxial tests with local strain measurements were consolidated to their estimated in-situ stress states, whilst soil specimens used with CIU triaxial tests with vertical/horizontal bender elements and resonant column (RC) tests were consolidated to different stress states less than their estimated original *in-situ* condition.

To ensure no significant plastic strains occurred that could disrupt the natural soil structure, the soil specimens were consolidated at a stress rate of around 2 to 4 kPa/hour until the desired effective pressure was reached. From that point onwards, the consolidation stage was continued until the volume change (ΔV) of the specimen was no longer significant, and at least 95% of the excess pore pressure was dissipated. The consolidation stage took between 1 to 4 days, depending on the desired effective confining pressure value for each sample. At this point soil samples were allowed to creep for 24 hours (1440 minutes), before moving forward to another test stage. After the required consolidation was reached, the specimen was subsequently subjected to shear or simply to a new consolidation stage, depending on the test.

In the case of the CIU triaxial tests with local strain measurements, at the end of the consolidation stage of these tests, samples were sheared in compression by applying an axial strain (ε_a) to the specimens at a constant rate under undrained conditions (specimen drainage was kept close, and excess pore water pressure (Δu) recorded). The rate of axial strain was slow enough to allow adequate equalization of excess pore pressures during the shearing stage. The shearing rate was calculated using Equations 4.9 and 4.10 proposed by Head (1998):

$$Strain\ rate = \frac{\varepsilon_f L}{100 t_f} \frac{mm}{minute} \qquad (4.9)$$

$$t_f = 1.8\ x\ t_{100};\ with\ side\ drains \qquad (4.10)$$

where ε_f is the strain at failure, L is the sample length in mm, t_f is time to failure, and t_{100} is the time intercept obtained from the volume change versus square-root time from consolidation stage. The strain at failure used for the specimens was typically 15-20%, and the average strain rate used throughout the CIU tests in this investigation was about 0.0085 mm/min (≈0.5 mm/hr).

4.3.6 Consolidated isotropically undrained (CIU) triaxial test with local axial displacement transducers

Compressive CIU triaxial tests were carried out in accordance with ASTM D4767-11, using a GDS Instrument Ltd. triaxial testing system (GDSTTS), designed for stress-path testing (Figure 4.2). The GDSTTS is based on the classic Bishop & Wesley type stress-path triaxial cell. The system consisted of a hydraulically pressurized cell with an internal load transducer of 5 kN, accurate to 0.1% of the full-scale output with a resolution of 0.0001 kN; a pore-water pressure transducer on the base accurate to +/- 2 kPa up to a maximum of 3450 kPa with a resolution of 0.01 kPa. The back and cell pressures were controlled using the GDS pressure-volume controllers with maximum volumetric capacity of 1000 cm3 and volume measuring accuracy of 1 mm^3, and pressurizing capacities of up to 2 MPa with an accuracy of 1 kPa. The global axial displacement was measured with an external linear variable differential transformer (LVDT), accurate to 0.5% of full range (50 mm) with a resolution of 0.0001 mm.

A pair of local axial displacement transducers (or small LVDT) manufactured by GDS Instrument Ltd. (Figure 4.3), were used to measure local deformation on the soil specimens when subjected to axial compression. The small LVDTs had a range of ± 5mm, an accuracy of 0.1% of the full range output (10 mm) with a resolution of 0.0002 mm.

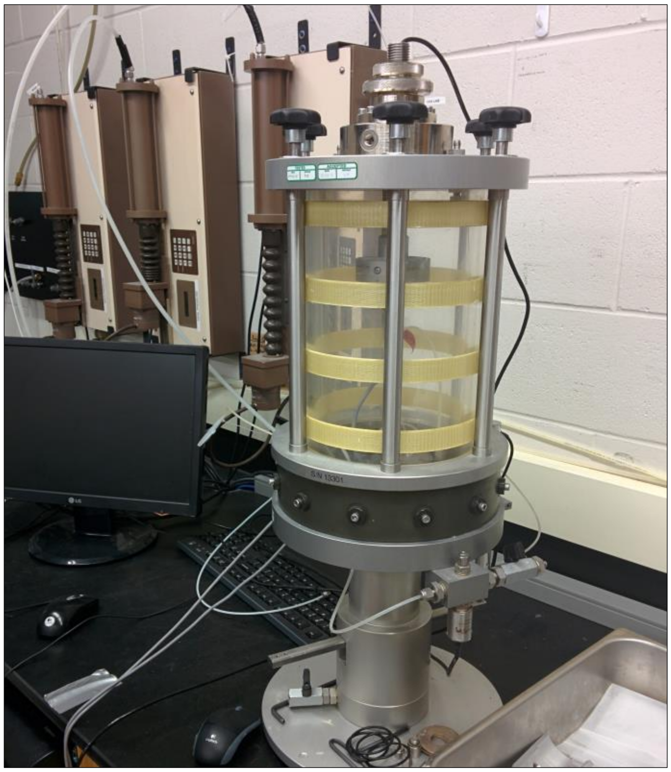

Figure 4.2: Bishop & Wesley stress-path type triaxial equipment and pressure/volume controllers at Western University soils laboratory

Figure 4.3: GDS local displacement transducers available at Western University soils laboratory

Soil specimens were prepared following the guidelines from Section 4.3.3. After the specimen was created, radial filter paper was placed around the sample, as well as at the top and bottom of the specimen. Porous discs, saturated under vacuum pressure, were placed between the bottom of the sample and the pedestal of the triaxial apparatus, and between the top part of the sample and the top cap. A rubber membrane was placed around the sample and sealed with two O-rings on the top and bottom of the specimen. Once the soil specimen was set up and placed inside the triaxial apparatus, the small LVDT were attached to the specimen.

Figure B.26 (see Appendix B), shows the procedure of mounting the small axial transducers right outside the soil specimen. The first step was to mark with a soft pen the desired position for the axial mounts (usually at the center of the specimen). Once the position was marked, a water-resistant and rubber-friendly adhesive was applied to the mounting pads and were placed against the specimen, where pins were subsequently inserted through the mount pads to ensure full fixity of the axial caliper to the specimen. Once the mounting procedure was done, the spacer arms at the sides of the mounting blocks were removed, the cell was filled with de-aired water and all of the transducers were zeroed.

Two different lengths of spacer arms were available in the laboratory: 29.81 mm and 42.50 mm. These lengths corresponded to the gauge length that was used to calculate axial strain at the end of the shearing stage of the soil specimen using Equation 4.11:

$$\varepsilon_a = \frac{small\ LVDT\ reading\ (mm)}{Gauge\ lentgh\ (mm)} x\ 100\% \qquad (4.11)$$

The specimen saturation, consolidation, and subsequent shearing was done as outlined in Section 4.3.5 and following the test program summarized in Table 4.3. The parameters recorded during the CIU triaxial tests included: cell pressure (CP), back pressure (BP), time, volume change (ΔV), axial load (P), axial displacement (d), and porewater pressure (u). The monitoring of the test and the recording of the testing parameter were done with the software GDSLAB v2.5.3 provided by GDS instruments Ltd. ASTM D4767-11 presents the different equations for the calculation of standard triaxial parameters for undrained tests. Correction for the use of vertical filter-paper strips and rubber membrane were considered, however, these were not applied because the error in deviator stress due to the strength of the filter-paper strips and rubber membrane did not exceeded 5%, as outlined by the standard.

4.3.6.1 Data analysis for CIU tests

4.3.6.1.1 Stress-strain parameters:

To describe the progression and development of stresses and strains in the triaxial test, the following parameters were calculated at the end of the test: the effective Cambridge or mean effective stress (p'), deviator stress (q), volumetric strain (ε_p) and distortional strain (ε_q). Wood (1990) described thoroughly the relationship of these parameters with the principal effective stresses ($\sigma'_1, \sigma'_2, \sigma'_3$) and strains ($\varepsilon'_1, \varepsilon'_2, \varepsilon'_3$). The equations relating p', q', ε_p and ε_q to the axial stress (σ'_a), radial stress (σ'_r), axial strain (ε'_a), and radial strain (ε'_r) are provided below:

$$p' = \frac{(\sigma'_a + 2\sigma'_r)}{3} \tag{4.12}$$

$$q = \sigma'_a - \sigma'_r \tag{4.13}$$

$$\Delta\varepsilon_p = \delta\varepsilon_a + 2\delta\varepsilon_r \tag{4.14}$$

$$\Delta\varepsilon_q = \frac{2(\delta\varepsilon_a - \delta\varepsilon_r)}{3} \tag{4.15}$$

These parameters were used to determine characteristics of the soil related to elastic behaviour, shear strength, critical state, isotropic normal compression behavior, and anisotropy.

4.3.6.1.2 Stiffness properties:

The undrained elastic parameters for Young's modulus (E_u) and the shear modulus (G_{sec}) are determined from Equations 4.16 and 4.17. The values of E_u and G_{sec} are non-linear with strain:

$$E_u = \frac{\mathrm{d}q}{\mathrm{d}\varepsilon} \tag{4.16}$$

$$G_{sec} = \frac{E_u}{3} \tag{4.17}$$

4.3.6.1.3 Soil critical state parameters:

The stablished relationships for the critical state line are defined by Equations (4.18) and (4.19) (Schofield and Wroth, 1968):

$$q = Mp \quad (4.18)$$

$$\Gamma = e + \lambda lnp \quad (4.19)$$

where the constants M, Γ *and* λ represent basic properties of the soil materials, q is the deviator stress, p is the Cambridge effective stress parameter, and e is the void ratio. The critical state is a point of reference that describes a soil's current state. Figure 4.4 illustrates the critical state concept as depicted by Schofield and Wroth (1968).

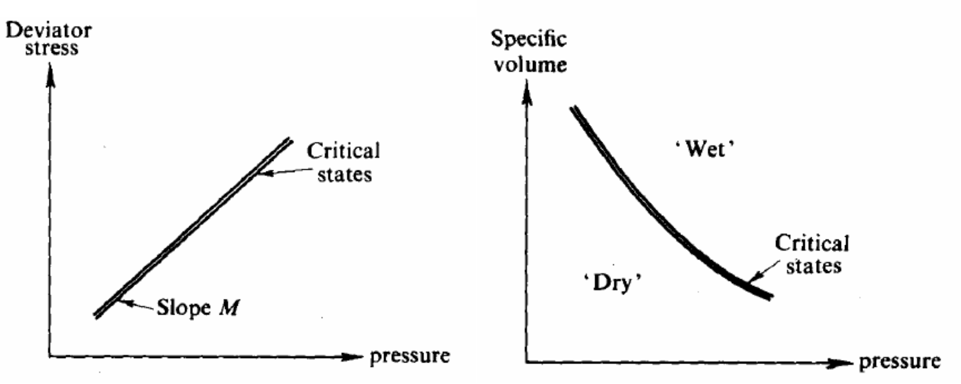

Figure 4.4: Critical State (adapted from Schofield and Wroth, 1968)

The slope of the critical state line (M) is given by Equation (4.20):

$$M = \frac{6 \sin \phi'_{cs}}{3 - \sin \phi'_{cs}} \quad (4.20)$$

where ϕ'_{cs} is the critical state friction angle.

The parameters N, λ, e_κ and κ characterize the isotropic normal compression line in e - ln p' space as defined in Equations 4.21 and 4.22. Figure 4.5 shows the critical state line and the isotropic normal compression line.

$$e = N - \lambda lnp' \quad (4.21)$$

$$e = e_\kappa - \kappa lnp' \quad (4.22)$$

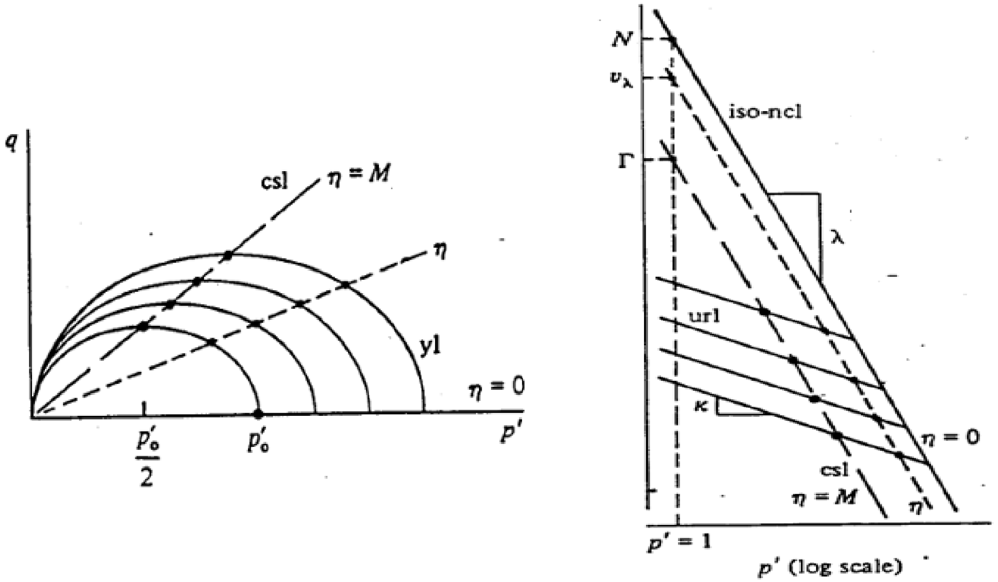

Figure 4.5: Relationship between critical state and isotropic normal compression line (adapted from Wood, 1990)

in which λ is the slope of the isotropic compression line, κ is the slope of the isotropic recompression line, N is the void ratio of the isotropic normal compression line at p'= 1 kPa, and e_κ is the void ratio of the recompression line at p'=1 kPa. The critical state line runs parallel to the normal compression line. The parameter Γ, which is the specific volume of the point on the critical state line corresponding to p'=1 kPa can be determined from the following equation:

$$\Gamma = N - (\lambda - \kappa)\ln(2) \tag{4.23}$$

4.3.7 Bender element (BE) test

The same stress-path triaxial testing system described in Section 4.3.6, was used to carry out the BE tests. The three pairs of bender elements used in this study manufactured by GDS Instruments Ltd., were fitted together inside the triaxial system. The BE used can produce both shear (V_s) and compressional (V_p) waves, and this feature enables the possibility of estimating G_{max} and E_{max} using the same soil specimen. Moreover, when using multiple pairs of BE for the same test on different directions (vertical or horizontal) within the same soil sample, a more advanced characterization of the small-strain stiffness properties of the soil material can be done. Also, depending of the direction of propagation and polarization of the BE, different types of waves can be measured.

The three pairs of BE transducers used in this investigation were arranged as follows: one pair of BEs were placed on the top and bottom of the soil specimen (vertical direction), while the other two pairs were laterally mounted (horizontal direction) on the soil specimen. The vertical pair of BE allowed the measurement of vertically propagating and horizontally polarized wave velocities (V_{svh} and V_{pvh}). The horizontal pairs of BE allowed the measurement of horizontally propagating and vertically polarized waves velocities (V_{shv} and V_{phv}), and horizontally propagating and horizontally polarized waves velocities (V_{shh} and V_{phh}). Figure 4.32 shows in schematic form the convention adopted for the BE pairs used in this research.

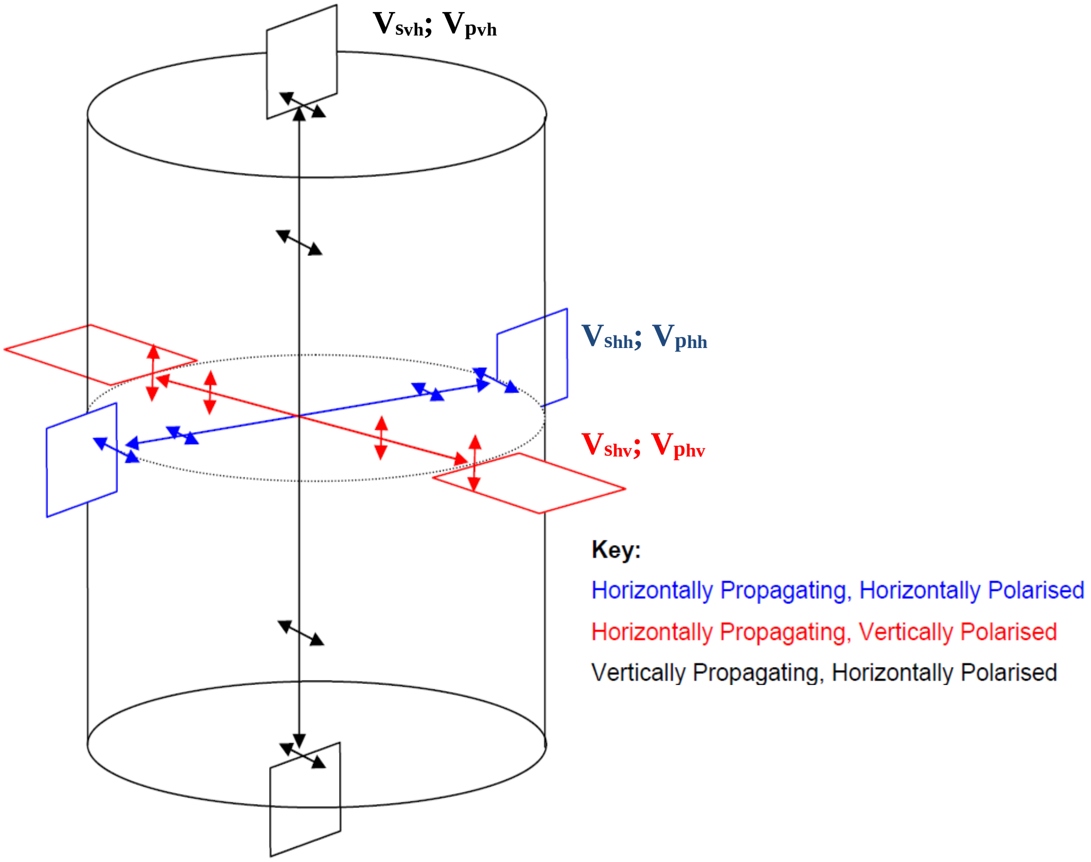

Figure 4.6: Bender elements orientation (adapted from GDS, 2015)

In general, each of the GDS BE has approximate dimensions of 13 mm length, 11 mm width, and 1 mm thickness, after being coated with a water-resistant epoxy. Then, the BE is positioned inside a steel insert such that the length of the BE protruding from the insert towards the soil sample is approximately 2 mm. Figure 4.7 depicts the BE available at Western University soils laboratory and used for this investigation.

Figure 4.7: Vertical bender elements attached to pedestal and top cap (left); Typical horizontal bender element (right)

To prepare soil specimens and set-up the samples for the BE test inside the triaxial apparatus, the methods outlined by the ASTM D4767-11 were adopted, which are summarized in Sections 4.3.3 and 4.3.6. However, some variations were introduced. The first step was to make sure that before installing the bottom and top BE in the vertical direction, a small groove of approximately 10 mm long, 2 mm wide and 2 mm deep was cut on the top and bottom of the sample. Both cuts were done parallel to each other, to ensure that both BE were in line and facing each other.

Once the vertical pair of BE were in place, the next step was to carry out the installation of the horizontal bender elements. Two pairs of holes in diametrically opposite locations were cut in the sample membrane at around mid-height of the specimen. The holes were made by pinching a small piece of the membrane with a flat nose plier; once the membrane was stretched, a small cut of approximately 5 mm diameter was made. Before positioning the BE insert on each hole, the alignments and corresponding polarization of each horizontal

BE pair was carefully checked. Each BE was equipped with a blue hard-rubber grommet and a small O-ring, to facilitate the insertion and contact with the sample, and to ensure a good seal pushing the joint between the membrane and the grommet of the BE transducer. To further aid the sealing of the joint, a water-resistant and rubber-friendly adhesive was used. The minimum set time for the adhesive was around 2 hours, and total recommended curing time was 24 hours. After that, the cell was filled with de-aired and distilled water, and all of the transducers were zeroed. The specimen saturation and subsequent consolidation stages were done as outlined in Section 4.3.5 and following the test program summarized in Table 4.4. Figure 4.34 shows the successful installation of the three pairs of BE on a soil specimen before the start of a test and the conditions of the sample at the end of the test.

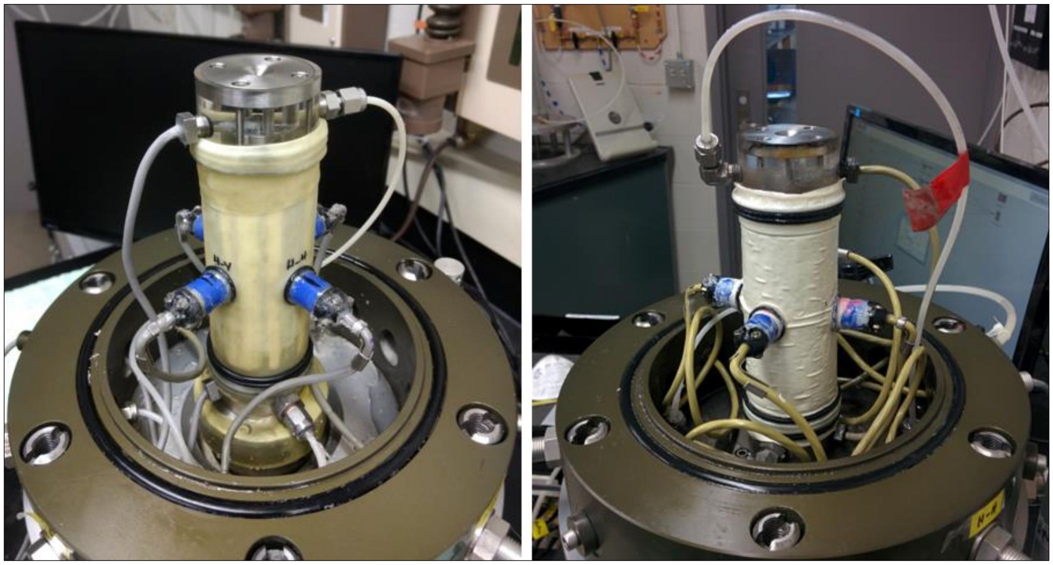

Figure 4.8: Soil specimen with bender elements installed prior testing (left); soil specimen at the end of the testing (right)

4.3.7.1 Data analysis from the bender element (BE) test

As was previously described, the adopted polarization of the BE transducers allowed for the measuring of body waves (shear and compressional waves) velocities on different planes within the soil specimen. The shear and compressional wave velocities measured were V_{svh}, V_{shv}, V_{shh}, and V_{pvh}, V_{phv}, V_{phh}, respectively, where the first letter of the subscripts refers to the type of wave (s for shear, p for compressional), and the two last subscript letters refer to the direction of propagation and polarization, respectively (v for vertical, h for horizontal); For example, V_{shh} is a shear wave velocity horizontally propagated and horizontally polarized. From the measurement of these propagating waves through the soil, the maximum or small-strain shear stiffness (*G*) and compressional or constrained modulus (*M*) of the soil material can be estimated using the following set of equations derived from elastic theory (Hardin and Blandford, 1989):

$$G_{vh} = \rho {V_{svh}}^2;\ G_{hh} = \rho {V_{shh}}^2;\ G_{hv} = \rho {V_{shv}}^2 \tag{4.24}$$

$$M_v = \rho {V_{pvh}}^2;\ M_h = \rho {V_{phh}}^2;\ M_v = \rho {V_{phv}}^2 \tag{4.25}$$

where ρ represents the bulk density of the soil material.

The small-strain stiffness properties are functions of the wave velocities, and at the same time, the estimated propagating velocities depend on the travel time and travel distance. Hence, these last two parameters, travel time and travel distance, are key properties that need to be determined from the tests in a reliable way. Sine wave input signals were applied with a frequency range of 10 kHz to 12.5 kHz for the bender elements in the vertical direction, and a frequency range of 15 kHz to 20 kHz for the bender elements in the horizontal direction. These ranges of frequencies for both directions of propagation were chosen to ensure at least 4 wave lengths of travel (Sanchez-Salinero et al., 1986; Jovicic et al., 1996). The recording of the time histories was done using the GDS Bender Elements software (GDS BES) v2.2.4. The GDS BES software allowed the signal stacking to minimize electrical noise. In general, 5 to 12 waves were stacked with 1 second delay between each wave.

The analysis of the recorded time histories of the transmitted waves was carried out by direct inspection of the raw data using Microsoft Excel and using the GDS Bender Element Test Analysis Tool (GDS BEAT) (Rees et al., 2013). One of the advantages from the GDS BEAT software is that it allows for the analysis of the wave propagation travel times by three common methods, such as the observation of points within the received element signal (e.g., first arrival, first deflection, zero crossing, peak to peak), cross-correlation of the source and received signals, and cross-power spectrums of the source and received signals. The method of signal analysis chosen in this investigation was 'peak to peak' due to its simplicity, ease of verification, and the ability of producing consistent results throughout the analyses (Jovicic et al., 1996; Chan, 2010; Hasan and Wheeler, 2015). After the estimation of the wave travel time, the value of the velocities can be calculated as:

$$V_{s(vh,hv,hh)}\ or\ V_{p(vh,hv,hh)} = \frac{D_{1-2}}{t_{pp}}\left(\frac{m}{s}\right) \tag{4.26}$$

where D_{1-2} is the distance between the tip of the source bender element and the tip of the receiving bender element and t_{pp} is the time between the source wave peak and the receiving wave peak. Figure 4.9 shows an example of a typical shear wave velocity-time history obtained from different input frequencies for one of the tested materials.

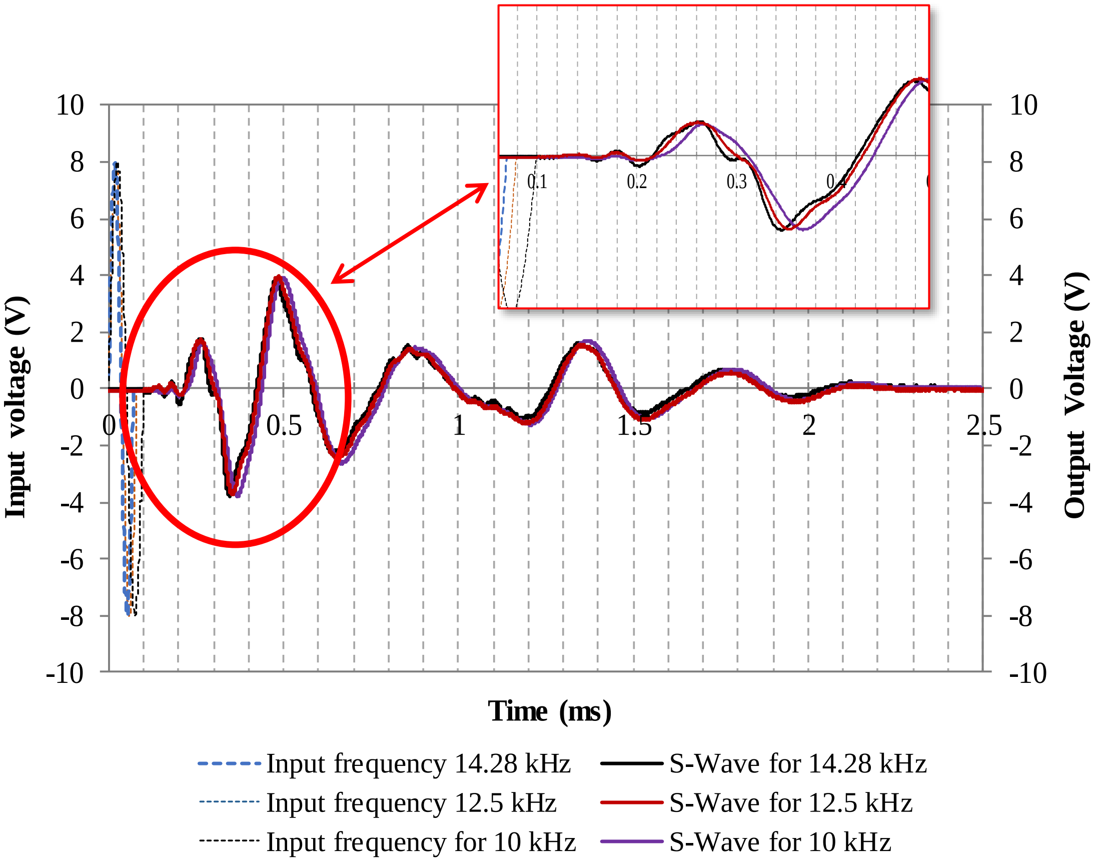

Figure 4.9: Typical shear wave signal recorded during bender element test

4.3.8 Resonant column (RC) test

RC tests were carried out in accordance with ASTM D4015-15. The resonant column apparatus (RCA) used in this investigation is a Stokoe fixed-free type, designed and constructed by GDS Instruments Ltd. This RCA allows for testing shear stiffness (torsional excitation) and longitudinal stiffness (flexural excitation) on the same soil specimen. The set-up consists of a standard cell/chamber , where the back and cell pressures are controlled using a GDS pressure/volume controllers. This chamber is capable of 1 MPa gaseous cell pressure, with a volume measuring accuracy of 1 mm^3, and pressurizing capacity up to 1MPa, with an accuracy of 1kPa. Inside the chamber, an LVDT is used to measure sample deformation, and one water inner cell is placed to aid membrane sealing. In addition, an electromagnetic drive system is placed inside the chamber, which is comprised by precision wound coils, composite Sintered Neodymium Iron Boron (NdReB) “rare-earth” magnets, and one internal mounted counter-balanced accelerometer.

The soil specimens for testing were prepared according to the ASTM D4767-11 guidelines, and by following the procedure explained in Section 4.3.3. However, a variation to the sample preparation was introduced for the RC test specimens. The variation consisted of trimming test specimens from the same material at different orientations with respect to the sample *in-situ* vertical axis (e.g. 0° equal to vertical cut samples, 90° to horizontally cut samples). This preparation method was employed by Lo et al. (1971), Yong and Silvestri (1979), and Becker (1981) for anisotropy studies on natural deposited cohesive materials.

The overall procedure of setting up the soil specimen inside the RCA is very similar to what was done for setting up the samples inside the triaxial system, previously explained in Section 4.3.6. Once the soil specimen is mounted on the system’s fixed bottom (or pedestal), the next step was to place the support cylinder around the sample, which goes rigidly screwed into the bottom plate/platform of the unit. The drive system is on top of the soil sample, connected through its top cap by using four bolts, and on top of the support cylinder, through a drive clamp with four bolts that will make them rigidly connects them.

The drive system is the core part of the RCA, used to apply sinusoidal excitation for the RC test. A flat aluminum four-armed drive plate integrates the drive system, with four permanent magnets encased by a pair of drive coils at each end. For best results, the drive system should be carefully aligned to ensure free movement of each magnet within the coils before starting each test. Once the drive system is in place, aligned, and tightened, each of the coils is connected to the drive box. Final step is to place and screw the RCA top plate into place, which besides increasing the stiffness of the drive system, serves as the specimen LVDT holder. The 1 MPa standard cell top was placed around the assembled system, which was connected to an air compressor allow changes to the cell pressure within the available range. This was done using a computer-controlled valve which regulates the cell pressure from the GDS LAB software. Figure B.27 (see Appendix B.3) shows a photographic sequence of the setting up of a soil specimen inside the RCA, as well as the placing of the rest of the equipment in the system (e.g., support cylinder, drive system, RCA top plate, standard cell).

Once the RCA system was assembled, soil specimens were tested under saturated state and isotropic confining, following the determined testing plan outlined in Table 4.5. The saturation and consolidation procedures were as described in Section 4.3.5. Different studies reported that once the primary consolidation takes place, the stiffness properties (G_{max}, E_{max}) tend to increase with the logarithm of time, and the damping ratio (D) tends to decrease (Afifi, 1970; Kim and Novak, 1981). Hence, once the soil samples reached 90% consolidation, the time and volume change at that stage was recorded, and then the soil sample was left consolidating for 24 additional hours to allow creep to take place before starting the dynamic excitation of the specimen (ASTM 4015-15). Past the additional 24 hours the final volume change and LVDT reading were recorded to calculate the change in the dimensions and void ratio of the test specimen at a particular stress state.

Generally, soil specimens were tested from low to high stress states. At each stress state, the specimens were subjected to a certain range of dynamic strains starting from low to high strain levels, usually from 0.001% to 0.1%. At each strain level, one torsional resonant frequency test, one torsional damping test, and one flexural resonant frequency test were performed. These tests were repeated until the full range of strains were covered at the same confining pressure. Once the strains range was completed with a certain confining pressure, this pressure was increased to the next level. The same sequence of procedures was repeated for each confining pressure until the highest confining pressure was reached.

4.3.8.1 Data analysis from resonant column (RC) test

The basic principle of the resonant column test is based on the theory of wave propagation in prismatic rods and the aim of the test is to vibrate (e.g. in torsion or flexure) a cylindrical soil specimen in a fundamental mode of vibration. Once the fundamental mode is established, measurements of the lowest natural frequency (resonant frequency) and vibration amplitude are made, from which the respective velocities (V_s or V_p) and modulus (G or E) can be computed. As was pointed out in the previous section, test specimens from the same material were prepared at different orientations with respect to the sample *in-situ* vertical axis. Table 4.7 and Table 4.8 present a summary of the properties to be obtained from both vertical (0° rotation) and horizontal-cut (90° rotation) samples.

Table 4.7: Estimated properties from vertical-cut samples (0° rotation)

	Velocities (m/s)	**Elastic parameters**	**Damping ratio (%)**
Torsional mode	V_s	G_{vh}	D
Flexural mode	V_p	E_v	-

Table 4.8: Estimated properties from horizontal-cut samples (90° rotation)

	Velocities (m/s)	**Elastic parameters**	**Damping ratio (%)**
Torsional mode	V_s	G_{hh}	D
Flexural mode	V_p	E_h	-

Analogous to the conventions adopted on the bender element data analysis (Section 4.3.7.1), the subscripts employed in both Tables 4.7 and 4.8 refer to the vertical or horizontal direction of the shear or compressional wave in which the stiffness property was measured.

In order to carry out the RC test, the GDS RCA software provided by GDS Instruments Ltd. was used. This software allows the user to run different frequency sweeps to find the resonant frequency of the soil sample at a certain level of strain. The data processing and calculations were performed in Microsoft Excel using a dedicated spreadsheet created for this investigation. A typical test consisted of an initial sweep of frequencies from 20 Hz to

100 Hz with a frequency increment of 2 Hz. Then the following fine sweep consisted of a ± 5 Hz with an increment of 0.2 Hz. An accelerometer attached to the drive plate measured the acceleration amplitude of the drive system at each frequency. At the end of the test, values of the natural frequency of the sample and the output voltage of the accelerometer were recorded. These last two parameters are key for the estimation of the propagated velocities and shear strain level induced on the test specimen.

4.3.8.1.1 Shear wave velocity and shear modulus calculation:

The shear wave velocity (V_s) can be obtained using the measured n^{th} natural frequency of torsional vibration f_n from this basic relationship:

$$V_s = \frac{2\pi f_n H}{\beta} \tag{4.27}$$

in which f_n = natural frequency of the sample as found from the RC test (Hz), H = the sample height (m) and β = square root of the frequency equation (Richart et al., 1970):

$$\beta \, \tan\beta = \frac{I}{I_o} \tag{4.28}$$

where I = mass polar moment of inertia of the specimen in (kg.m^2), and I_o = mass polar moment of inertia of the drive system (kg.m^2). The I_o value of the drive system was obtained experimentally by calibrating the RCA (refer to Appendix B.4 for calibration procedures and results). The I_o value obtained from the calibration procedure was approximately 0.0038 kg.m^2.

Using the shear wave velocity computed from Equation 4.27 and the mass density of the soil specimen (ρ), the shear modulus (G) can be calculated as (Richart et al., 1970):

$$G = V_s^{\,2}.\rho \tag{4.29}$$

4.3.8.1.2 Torsional shear strain (γ) calculation:

The torsional shear strain (γ) was computed from the angle of twist of the specimen by Equation 4.30:

$$\gamma = \frac{r.\theta_{max}}{H} \tag{4.30}$$

$$\theta_{max} = \frac{y_a}{l_a} \tag{4.31}$$

where r = radius of tested specimen; H = height of specimen; θ_{max} = angle of twist; y_a = displacement of accelerometer mounted on the drive plate; and l_a = offset of accelerometer from axis of the tested specimen (provided by GDS and equal to 0.04325 m).

The angle of twist (θ_{max}) was obtained by using the acceleration amplitude recorded by the accelerometer installed in the drive plate, the natural frequency of the sample, and the sample geometry (GDS, 2006; Drnevich et al., 2015). To calculate the angle of twist of the specimen, initially the voltage output of the accelerometer was converted from the peak output of +/- G into m/s^2:

$$a_{cc} = a_{volts}\left(\frac{9.81}{Gain}\right) \tag{4.32}$$

where a_{cc} = output acceleration in m/s^2; a_{volts} = output acceleration in Volts as obtained from GDS RCA software; Gain = 1000 mV/G. After the output acceleration was converted to m/s^2, the displacement of the accelerometer was estimated by relating this to the angular acceleration:

$$y_A = \frac{{a_{cc}}^2}{\omega} \tag{4.33}$$

$$\omega = 2\pi f_r \tag{4.34}$$

where y_A = displacement of the accelerometer, w = angular velocity, and f_r = resonant frequency of vibration system (Hz). Hence the maximum displacement of the accelerometer is defined as:

$$y_a = \frac{a_{cc}}{4\pi^2 {f_r}^2} = \frac{0.00981.a_{volts}}{39.4784.{f_r}^2} = \frac{2.48x10^{-4}.a_{volts}}{{f_r}^2} \tag{4.35}$$

By substituting Eq. (4.35) into Eq. (4.31):

$$\theta_{max} = \frac{2.48x10^{-4}.a_{volts}}{l_a.{f_r}^2} \tag{4.36}$$

By substituting Eq. (4.36) into Eq. (4.30):

$$\gamma = \frac{r.2.48x10^{-4}.a_{volts}}{H.l_a.{f_r}^2} = \frac{0.005745.r.a_{volts}}{H.{f_r}^2} \tag{4.37}$$

Equation 4.37 can be used to calculate the torsional shear strain of a discretionary point within the top section of a test specimen (GDS, 2006). However, the average torsional shearing strain was assumed to be equal to that of a point whose distance to the axis is 0.8 times the radius of the specimen as ASTM D4015-15 recommends:

$$\gamma_{avg} = 0.8.\left(\frac{0.005745.r.a_{volts}}{H.{f_r}^2}\right) = \frac{0.004596.r.a_{volts}}{H.{f_r}^2} \tag{4.38}$$

4.3.8.1.3 Compressional wave velocity and elastic modulus calculation:

For the calculation of the compressional wave velocity (V_p) and elastic modulus (E), ‘Rayleigh’s method’ outlined by Cascante et al. (1998) was employed. Only the equations used for that purpose are presented herein. For more detailed information on the derivation of the equations refer to Cascante et al. (1998).

As pointed out by Cascante et al. (1998), the longitudinal wave velocity (V_{LF}) in a rod can be calculated from measuring the elastic modulus in flexural excitation (E_{flex}). Equation 4.39 was used to link the longitudinal wave velocity (V_{LF}) and the elastic modulus in flexural excitation (E_{flex}):

$$V_{LF} = \frac{\sqrt{E_{flex}}}{\rho} \tag{4.39}$$

in which ρ = mass density of the soil specimen. This relationship ensures that both the diameter of specimen and any internal scale in the material (e.g., particle size) are significantly shorter than the wavelength of the travel velocity (Cascante et al., 1998).

The flexural excitation (E_{flex}) of the testing soil specimen can be estimated using Equation 4.40:

$$E_{flex} = \frac{(2\pi f_r)^2 \left[L^3 \left(\frac{33}{140} m_t + m_a + m_b + m_x\right)\right]}{3I_b} \qquad (4.40)$$

where f_r = resonant frequency as obtained from GSD RCA software (Hz); L = height of soil specimen (m); I_b = mass polar moment of inertia of soil specimen (kg.m^2); m_t = mass of the soil specimen (kg); m_a = mass of top cap (kg); m_b = mass of porous disc on top of specimen (kg); m_x = mass of drive system (kg). The mass of the drive plate was obtained through a calibration process outlined by Cascante et al. (1998) and within the GDS RCA system manual. The longitudinal wave velocity (V_{LF}), obtained from Eq. (4.39), relates to the compressional wave velocity (V_p) by Equation 4.41:

$$\boldsymbol{V_p = V_{LF}\sqrt{\frac{1-\mu}{(1+\mu)(1-2\mu)}}} \qquad (4.41)$$

$$\boldsymbol{\mu = \left(\frac{1}{2}\frac{{V_{LF}}^2}{{V_s}^2}\right) - 1} \qquad (4.42)$$

where μ = Poisson's ratio; V_s = shear wave velocity (Eq. 4.27) (m/s).

4.3.8.1.4 Flexural shear strain (ε) calculation:

Under flexural excitation, the flexural strain imposed on the test specimen is related to the deflection curve formed when the specimen is under load. Hence, the average strain can be defined in terms of the tension or compression side by Equation 4.43 (Cascante et al., 1998):

$$\varepsilon_{avg} = \frac{4}{\pi}.r.H.\alpha \qquad (4.43)$$

$$\alpha = \frac{y_a}{H^2[2H + 3(x_{acc} - H)]} \qquad (4.44)$$

in which r = specimen radius (m); H = specimen height (m); y_a = displacement of the accelerometer (Eq. 4.35); x_{acc} = distance from the base of the sample to the base of accelerometer (for GDS RCA this is equal to 0.005 m).

By substituting Eq. (4.35) into Eq. (4.44), and then by substituting Eq. (4.44) into Eq. (4.43), the average flexural strain (ε_{avg}) can be calculated as:

$$\varepsilon_{avg} = \frac{4.r.(2.48x10^{-4}.a_{volts})}{H.\pi.{f_r}^2.[2H + 3(x_{acc} - H)]} \tag{4.45}$$

4.3.8.1.5 Damping ratio calculation:

After the resonant frequency of the specimen was found, the damping testing was initiated. Viscous damping ratio (*D*), is measured from the shape of free vibration decay curve (Figure 4.37). This curve is measured using the accelerometer mounted on the resonant column drive plate. A sinusoidal wave, whose amplitude and frequency are of the same characteristics as those of the system resonance in torsional excitation, is applied to the soil specimen and then ceased shortly after, so that the resulting free vibrations can be measured.

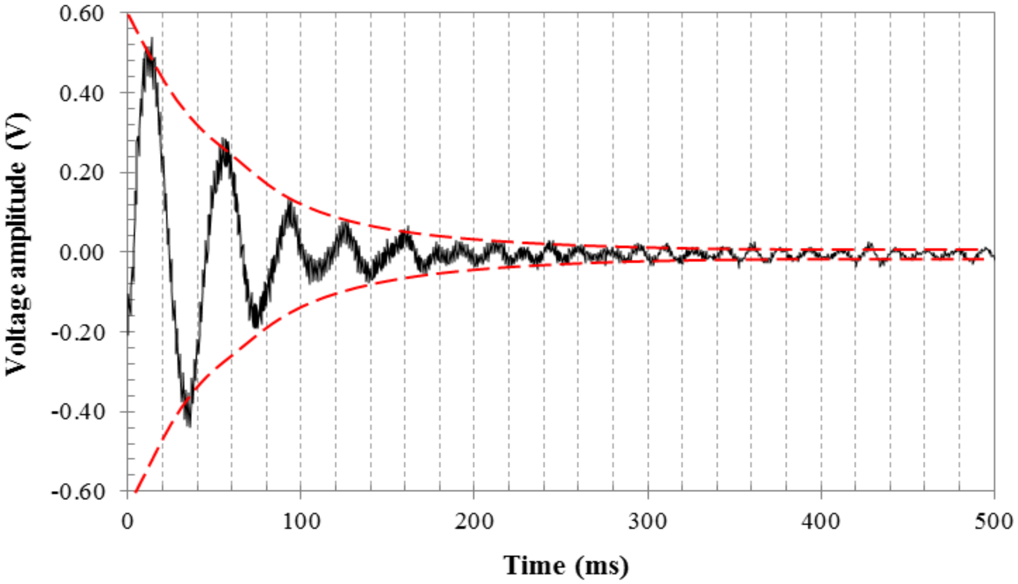

Figure 4.10: Typical free vibration decaying curve for measurement of material damping ratio from RC test

Once the response of the specimen in free vibration was measured, the damping ratio of the soil material was evaluated using the logarithmic decay method. The logarithmic decrement (δ) of the decaying curve is calculated using Equation 4.46 (Richart et al.,1970):

$$\delta = \frac{1}{n} \ln \left(\frac{A_1}{A_{n+1}} \right) \tag{4.46}$$

where, A_1/A_{n+1} = ratio of peak amplitudes of response; and n = cycles apart (10 or less as per ASTM D4015-15). The damping ratio (D) is calculated as:

$$D = \sqrt{\frac{\delta^2}{4\pi + \delta^2}} \tag{4.47}$$

4.4 Summary

This chapter presents a review of the general geological and geotechnical characteristics of the cohesive materials studied in this investigation and the laboratory methodologies employed for the characterization of the materials. Out of six clays selected for testing, five of these are naturally deposited overconsolidated glacial clays of low to medium plasticity sampled from areas around southwestern Ontario and Manitoba. The remaining sixth material was artificial and created under controlled laboratory conditions. Different researchers studied some of these materials previously (e.g. Kim and Novak, 1983; Becker, 1981; Kiss, 2016). The available data show good characterization of the basic geotechnical properties and existing data on certain small-strain properties (e.g. V_s, G_{max}). Notably, such small-strain properties were obtained only in the vertical direction of the materials. The laboratory techniques selected for this investigation allow for the study of dynamic soil properties in different directions of the soil samples (e.g. vertical and horizontal directions) at very small to small strain ranges, thus enabling the anisotropic characterization of the materials and the critical state and stress-strain behaviour from small to large strains. These laboratory techniques are CIU triaxial tests with orthogonal bender elements, resonant column testing on vertically and horizontally trimmed samples, and CIU triaxial tests with local strain measurements. The results from the different laboratory tests will be presented and discussed in the following chapters.

Chapter 5

5 Experimental results on the Port Alma glacial till material

This chapter presents the results obtained from a comprehensive laboratory study carried out on the Port Alma unweathered glacial till material. The laboratory study encompassed as series of CIU triaxial tests with locally measured axial strains, CIU tests fitted with vertical and horizontal bender element transducers and resonant column tests on vertically and horizontally trimmed samples. The aim of the laboratory study was to: further characterize the critical state properties and stress-strain behaviour of the Port Alma material under static loading (from *in-situ* pressures), to assess the very small-strain stiffness properties in the vertical and horizontal directions with confining pressure, to measure the stiffness degradation of vertically and horizontally trimmed samples and assess the small-strain stiffness anisotropy. The next sections present the results and analysis of these experimental studies, and a discussion of their implications. The results from determination of total carbonate content and the individual amounts of calcite ($CaCO_3$) and dolomite ($MgCaCO_3$) on the Port Alma clay till deposit are shown in Appendix C.

5.1 Consolidated isotropic undrained (CIU) triaxial test results

5.1.1 Stress-strain behaviour and critical state soil parameters

Undrained compression triaxial tests were performed on isotropically consolidated soil samples. The tested specimens were from depths between 20 to 21 m below the ground surface, specifically within the unweathered till zone, and were recovered from borehole BH12-2 (see Figure 3.7). The samples were re-consolidated to pressures equal to their *in-situ* effective stresses. The calculation of the *in-situ* effective stresses was addressed in Section 4.3.4. The *in-situ* overconsolidation ratio (OCR) of the samples was approximately 2.3. The pre-consolidation pressure (p_c') of the till deposit was approximately 360 kPa and was estimated by Newson et al. (2019) using high quality one-dimensional consolidation test on samples. Following the elasticity investigations, the soil samples were sheared in undrained compression at strain rates 0.6%/hr to allow for suitable equalization of excess pore pressures during the shearing. The tested specimens were fitted with a pair of local axial transducers to improve the quality of the deformation measurements and to resolve strains from low levels (> 0.001%).

The test results were interpreted using deviatoric and effective Cambridge stress parameters q and p' and void ratio e; more detailed description on the calculation of these parameters was presented in Section 4.3.6.1. Plots of deviator stress (q) vs. effective Cambridge stress (p'), deviator stress (q) vs. axial strain (ε_a), excess pore water pressure (Δu) vs. axial strain (ε_a), and isotropic compression and swelling in q-p' space were created to assess the stress-strain response and to obtain fundamental critical state soil parameters of the tested unweathered till soil specimens. The deviator stress (q), effective Cambridge (p') and excess pore water pressure (Δu) parameters were normalized by the effective consolidation pressure at shear (p_o') to compare with previous results obtained by Newson et al. (2019) and Kiss (2016), and to account for any variations that resulted from the sample preparation and re-consolidation effects. The same normalization procedure has been adopted by other researchers previously (Ladd and Foot, 1974; Ladd et al, 1977; Atkinson and Little, 1998; Kiss, 2016).

Figure 5.1 shows the stress-paths in normalized $q{:}p'$ space of the tested undisturbed samples from the unweathered till layer. Along with the stress-path curves, the estimated location of the critical state line (CSL) obtained in this investigation and the others reported by Newson et al. (2019) and Kiss (2016) are also shown. The normalized deviator stress (q/p_o') increased with decreasing mean effective stress while, the soil specimens were subjected to shear during the triaxial compression tests. Once the specimens reached critical state, all of the specimens showed an increase in the deviator stress with the increasing of the mean effective stress. The critical state line defined by the tested specimens in this investigation, PA-CIU$_{160}$-1 and PA-CIU$_{160}$-2, had an M value equal to 1.14, which is equivalent to a friction angle (ϕ') of about 28.62°. This value lies within the range of values of M (1.15 to 1.03) and ϕ' (28.85° to 26.08°) previously reported by Newson et al. (2019) and Kiss (2016).

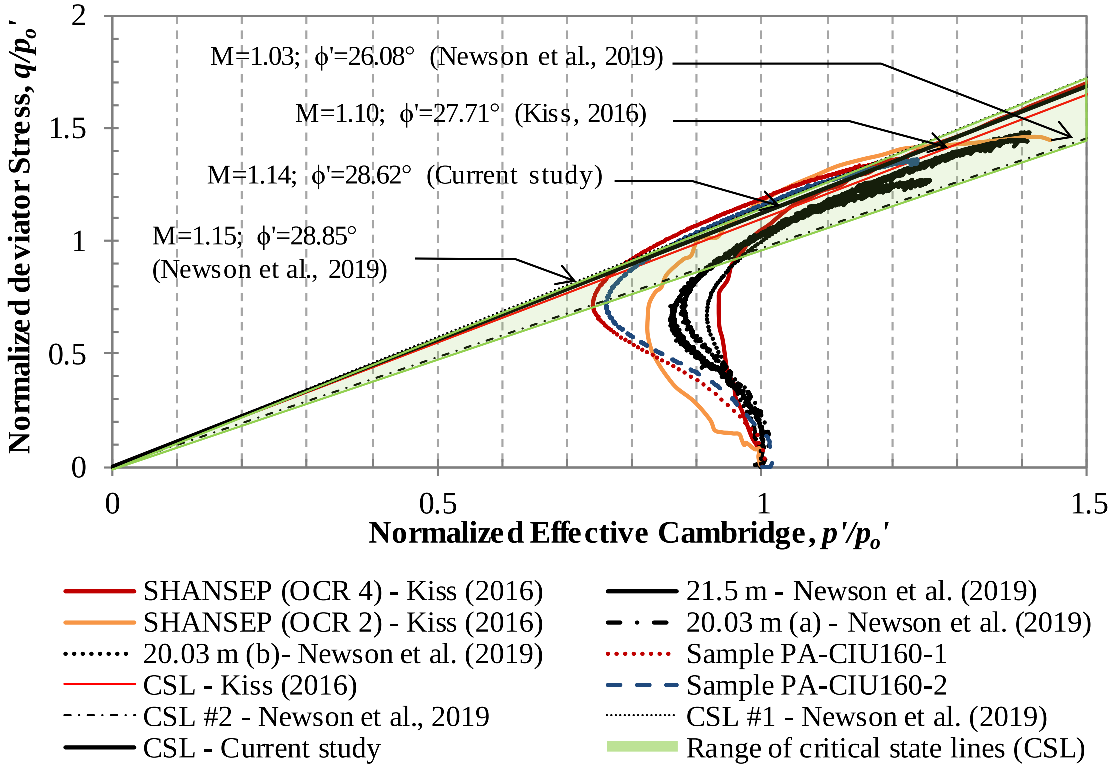

Figure 5.1: Normalized effective Cambridge stress (p'/p_o') vs. normalized deviator stress (q/p_o') of Port Alma till from CIU tests

The normalized deviator stress (q/p_o') versus the axial strain (ε_a) curves are presented in Figure 5.2. The samples tested exhibited similar behaviour throughout the shearing stages and compare closely to the previous results reported by Kiss (2016) and Newson et al (2018). The soil samples exhibited strain-hardening with the increasing of the axial strain during the shearing stage. The same feature can be observed in Figure 5.1 as well, once the samples reached the CSL they showed increase in deviatoric stress with increasing p'. This type of behaviour is typical of overconsolidated (OC) samples in undrained CIU triaxial tests (Atkinson and Little, 1983). OC samples appeared to strain uniformly at a constant state for strains higher than 10% and up to 15% to 20% strain. Newson et al. (2019) and Kiss (2016) estimated that the undrained shear strength (s_u) of the unweathered till ranged between 100 to 120 kPa. Similar values were obtained from samples PA-CIU$_{160}$-1 and PA-CIU$_{160}$-2, of 105.5 kPa and 110 kPa, respectively.

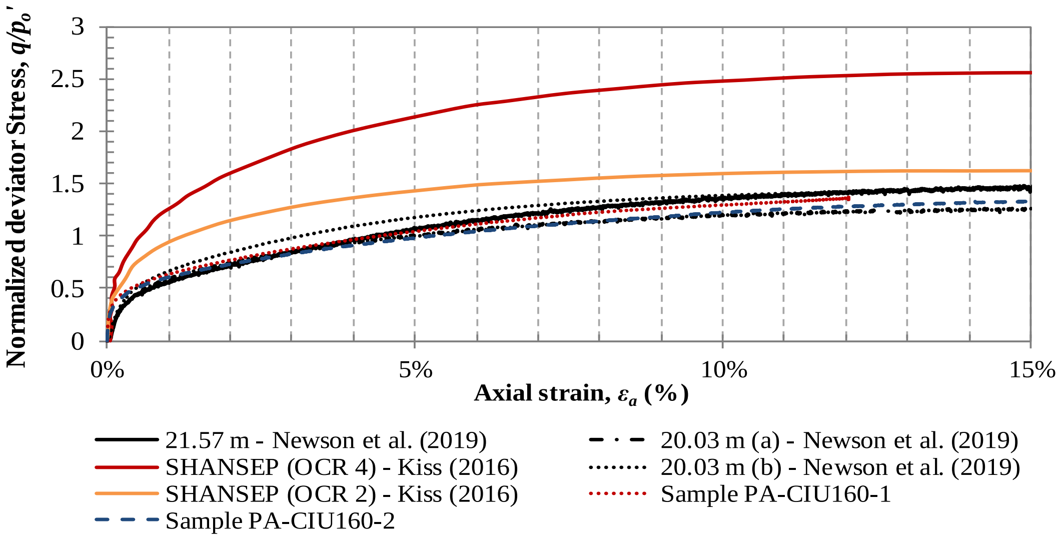

Figure 5.2: Axial strain (ε_a) vs. normalized deviator stress (q/σ_c') of Port Alma till

Figure 5.3 depicts the normalized excess pore water pressure (Δ_u/p_o') versus the axial strain (ε_a). The excess pore water pressure-strain relationship experienced by the samples tested for the *in-situ* conditions is typical of over-consolidated clays. The pore pressures started to build up once the shearing was initiated and kept increasing until they peaked between 1% and 2% of the induced axial strain. After that, the excess pore water pressure started to steadily decrease with increasing strain. This type of behavior is due to attempted dilatancy of the soil skeleton, and is typical response exhibited by overconsolidated cohesive soil materials in undrained shearing.

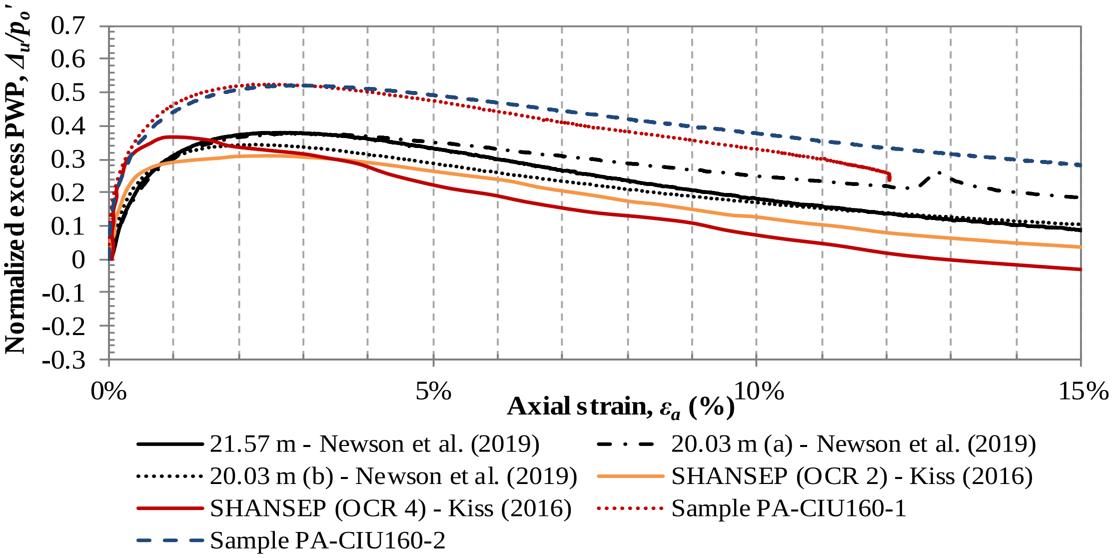

Figure 5.3: Axial strain (ε_a) vs. normalized excess pore pressure of Port Alma till

Figure 5.4 shows the results from the isotropic compression and swelling test of the unweathered till in void ratio-ln (*p'*) space. From this plot of the isotropic consolidation stages of different samples, it was possible to define the normal compression lines (NCL) and the unloading-reloading lines (URL), to estimate the critical state parameters (*N*, λ, κ, Γ and Λ) of the unweathered till material. The estimated slopes of the NCL (λ) and the URL (κ) in this investigation, fell within the previously established range of slopes found by Newson et al. (2019) and Kiss (2016). The values of λ and κ were approximately 0.041 and 0.011 respectively. The value of the reference volume for the normal compression line, *N*, was 0.646 and the critical state line, Γ, was approximately 0.625. The corresponding value of Λ was estimated to be 0.732 using Equation 5.1 (Schofield and Wroth, 1968):

$$\Lambda = \frac{(\lambda - \kappa)}{\lambda} \tag{5.1}$$

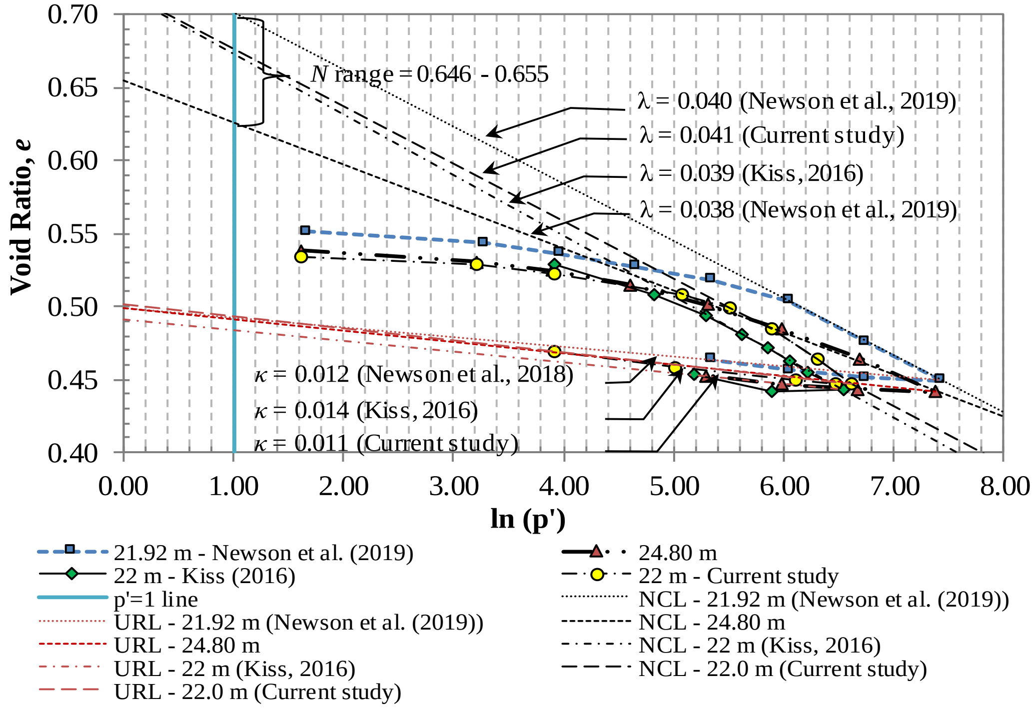

Figure 5.4: Void ratio-ln (p') space for isotropic compression and swelling of Port Alma till

Table 5.1 provides a summary of the soil critical state parameters of the unweathered clay till zone of the glacial deposit, gathered from the present investigation and previous studies (Newson et al., 2018; and Kiss, 2016), and shows the soil to be a stiff overconsolidated material of low plasticity, low activity and low compressibility. Similar behaviours have been reported for other glacial soil deposits found around the Port Alma area that were previously studied by Soderman et al, (1960), Kim and Novak (1981) and Lo and Becker (1979). Table 5.2 presents a compilation of critical state parameters of other natural low plasticity clay soils, previously studied by other researchers. These cohesive materials have similar geotechnical characteristics to the Port Alma glacial clayey till deposit, such as mineralogy, stress-strain response, and formation and deposition history.

Table 5.1: Summary of critical state parameters of the unweathered till zone

	Newson et al. (2019)	Kiss (2016)	Current study
M	1.00-1.15 (ϕ'=28.85°-26.08°)	1.10 (ϕ'=27.71°)	1.14 (ϕ'=28.62°)
I_p	13.0 %	13.0 %	13.0 %
$\boldsymbol{\lambda}$	0.038 to 0.040	0.039	0.041
κ	0.012	0.014	0.011
Λ	0.68 to 0.70	0.636	0.732
N	0.585 to 0.655	0.653	0.646
Γ	0.567 to 0.635	0.636	0.625

Table 5.2: Critical state parameters from other natural clay materials

	Marto (1996)	Atkinson (1993)	Pestana et al. (2002)	Toll & Ong (2003)
	Keuper Marl silt	*Glacial till*	*Lower Cromer till*	*Residual sandy clay*
M	1.16 (ϕ'=29°)	1.18 (ϕ'=29°)	1.2 (ϕ'=30°)	1.23 (ϕ'=31°)
I_p	19.0 %	18.0 %	13.0 %	15.0 %
$\boldsymbol{\lambda}$	0.083	0.090	0.073	0.080
κ	0.020	0.014	0.017	0.020^*
Λ	0.759	0.844	0.767	0.750
N	1.062	0.980	0.786	1.060^*
Γ	1.023	0.810	0.730^*	1.000

5.1.2 Deviatoric stress-strain behaviour

To investigate the stiffness degradation behaviour of the Port Alma unweathered till from triaxial tests, the tested soil specimens were fitted with a pair of local displacement transducers, as well as a vertical pair of bender element transducers to measure shear wave velocities along the vertical axis of the samples. Axial strains were resolved from each transducer using Equation 4.11. The secant shear modulus (G_{sec}), shear strain (ε_s) and undrained elastic modulus (E_u) are defined as:

$$\boldsymbol{G_{sec}} = \frac{\boldsymbol{\Delta_q}}{\boldsymbol{3\Delta\varepsilon_s}} \tag{5.2}$$

$$\boldsymbol{\varepsilon_s} = \frac{\boldsymbol{2}}{\boldsymbol{3}}(\boldsymbol{\varepsilon_a} - \boldsymbol{\varepsilon_r}) \tag{5.3}$$

$$\boldsymbol{E_u} = \boldsymbol{G_{sec}2(1 + \mu)} \tag{5.4}$$

where Δ_q = change in deviator stress; ε_a = axial strain; ε_r = radial strain; μ = Poisson's ratio (equal to 0.5 under undrained conditions). The stiffness properties and resultant strains from each test were calculated as the average from the pair of local transducers. Figure 5.5 and Figure 5.6 show the secant shear modulus degradation and undrained secant elastic modulus, respectively. Both stiffness parameters (G_{sec} and E_u) were obtained by means of local and external displacement measurements for samples PA-CIU$_{160}$-1 and PA-CIU$_{160}$-2. The soil specimens were tested to effective pressures similar to their original *in-situ* conditions as previously described in Table 4.3.

In addition to the estimation of G_{sec}, Figure 5.5 also displays the small-strain shear modulus estimated by means of shear wave velocity propagation using the bender element transducers (G_{BE}) right before commencement of the shearing stages of each sample. G_{BE} from the shear wave propagation ranged between 108 to 110 MPa at a strain levels around 0.001%. G_{sec} calculated from the monotonic undrained compression of samples PA-CIU$_{160}$-1 and PA-CIU$_{160}$-2, showed good agreement in terms of stiffness values and in the degradation behaviour with increasing strain. The estimated maximum G_{sec} for both samples ranged between 100 to 104 MPa at shear strain levels of approximately 0.0015%. Similar shear strain values using equipment manufactured by GDS were reported by Finno and Kim (2012) after measuring the degradation behaviour of Chicago clay.

G_{sec} obtained using external instrumentation was about 50 MPa at a shear strain level of approximately 0.01%. The difference between the readings of the local and external displacement transducers are obvious, and these can be attributed to the lower resolution provided by the external transducer, irregular contact between sample top cap and load cell, compliance in load system, etc. (Yimsiri and Soga, 2002). Similar trends for the undrained elastic modulus (E_u) degradation curves can be observed in Figure 5.6, compared to those from Figure 5.5. From the measured strains using local transducers, E_u ranged from 310 to

315 MPa at a strain level close to 0.001%, whereas the E_u estimated by external means started at approximately 150 MPa at around 0.01% of shear strain. E_u steadily degrades to similar values (around 10 MPa) between 0.1% and 1% from both local and external measurements. The stiffness degradation behaviour of Port Alma till is comparable to other glacial materials found in the literature; this will be discussed in a later section.

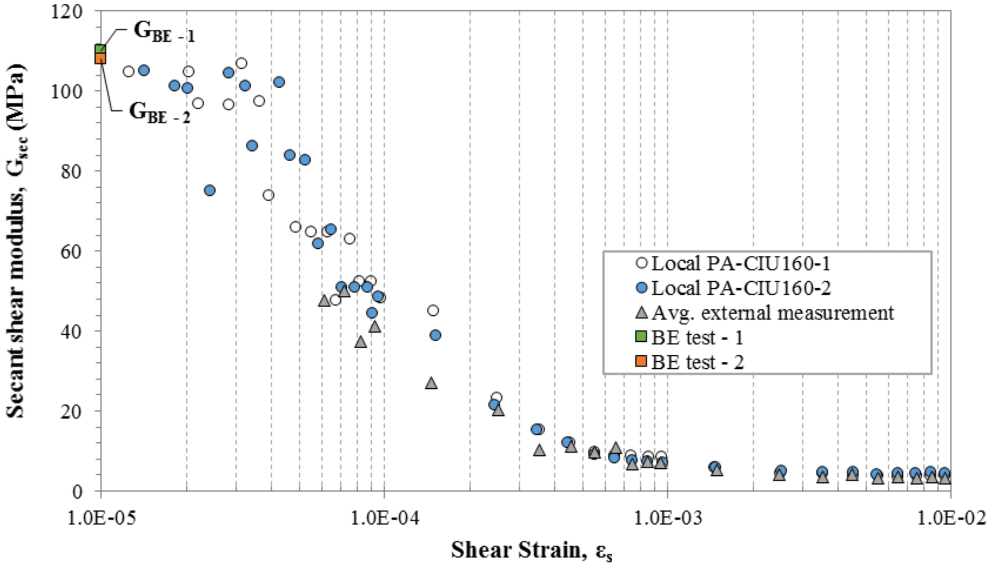

Figure 5.5: Secant shear modulus degradation curves from samples PA-CIU$_{160}$-#1 and PA-CIU$_{160}$-#2 measured with locally and externally, and with bender elements

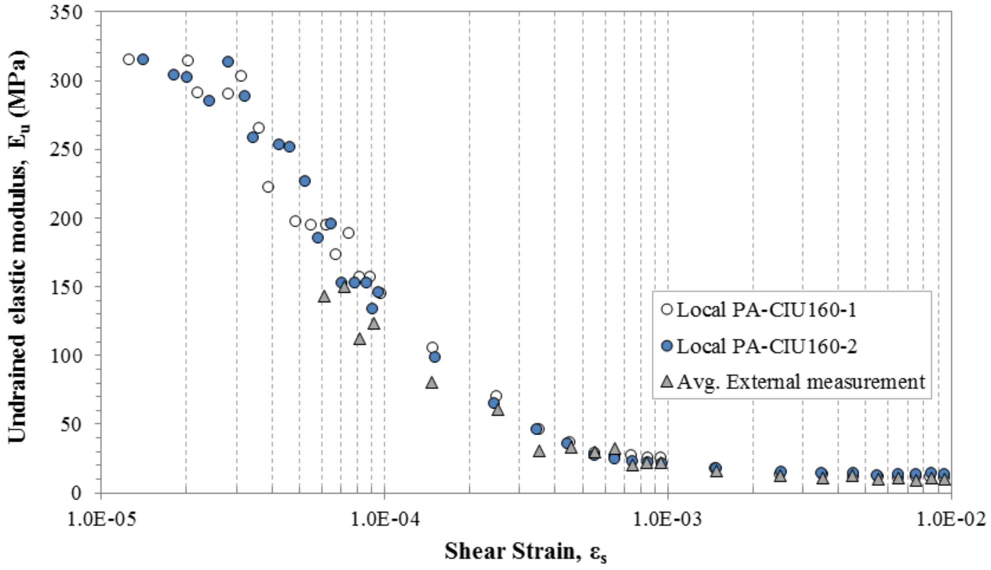

Figure 5.6: Undrained elastic modulus degradation curves from samples PA-CIU$_{160}$-#1 and PA-CIU$_{160}$-#2 as measured by local and external displacement transducers

5.2 Bender elements (BE) test results

Undisturbed material obtained from borehole BH12-2, (from 20 to 21 m depth), were tested under isotropic compression and swelling pressures with a stress-path triaxial system (see Section 4.3.6) fitted with vertical and horizontal bender element (BE) transducers to measure vertically and horizontally propagated shear and compressional waves. The pre-consolidation pressure (p_c') of the test specimen was approximately 360 kPa, and the soil specimen was subjected to different confining pressures that ranged from 25 to 750 kPa. The overconsolidation ratio (*OCR*) of the sample changed from 7 to 1 once confining pressures exceeded p_c'. The *in-situ* stress condition of the soil was estimated to be approximately 160 kPa (thus the *OCR* = 2.25). BE tests were carried out as described in Section 4.3.7 and the testing program outlined in Table 4.4 conducted for sample PA-$BE_{V/H}$. Due to the different modes of excitation and directions of polarization of the BE transducers, shear waves (S-wave) and compressional waves (P-wave) can be obtained in all of the vertical or horizontal planes of the test specimen (i.e. V_{svh}, V_{shv}, and V_{shh} *or* V_{pvh}, V_{phv}, and V_{phh}). Knowledge of the travel time and distance traveled by the propagated wave, allows the velocity of the body wave to be estimated. BE tests were performed using stacked sinusoidal input signals to obtain the propagation velocities. More information on the procedures adopted for the velocity calculations can be found in Section 4.3.7.

BE testing has previously been used to estimate small-strain elastic properties of different natural cohesive materials (e.g. Jovicic and Coop, 1998; Lings et al., 2000; Clayton, 2011). The calculation of elastic body wave velocities (shear and compressional waves) in different planes of the test specimen, enables estimates of the small-strain shear stiffness and compressional modulus (e.g. G_{vh}, G_{hv}, and G_{hh} *or* M_{vh}, M_{hv}, and M_{hh}) to be made in the corresponding planes of propagation employing Equations 2.2 and 2.3. The relative magnitudes of the shear stiffnesses in the vertical and horizontal directions enables the small-strain elastic anisotropy to be assessed. The BE tests from this investigation were designed to measure the small-strain stiffness and inherent stiffness anisotropy of the Port Alma clay material. In Section 2.4.2 of the literature review, the inherent anisotropy was defined as that which results from the anisotropic fabric of soils (grain characteristics and orientation). An attempt has therefore been made to measure the degree of inherent anisotropy of the Port Alma unweathered till. The use of isotropic stresses ensured that any differences in the measured stiffnesses resulted only from the current fabric and structure of the soil (and assumes no significant changes in fabric occur over this stress range).

Figures 5.7 and 5.8 show the variation of the measured propagated wave velocities with increasing effective confining pressure and different direction and polarization of the BE transducers. Along with these measurements, the data reported by Kiss (2016) is also shown. Both shear wave (V_s) and compressional wave (V_p) velocities, increased with increasing confining pressure. This trend is expected as S-waves and P-waves travel at velocities (V_s or V_p) that are function of the stiffness and density of the soil (Clayton, 2011; Hardin and Richart, 1963). Moreover, for cohesive materials, the overconsolidation ratio (OCR) and the plasticity (I_p) of the soil can also influence V_s (Hardin and Black, 1968; Kim and Novak, 1981). Kiss (2016) only employed vertical BE transducers, which can only measure vertically propagated-horizontally polarized body waves (V_{svh} and V_{pvh}). The values reported by Kiss (2016) show a good agreement with the ones measured in this investigation, where an average difference of around 3% and 4% was obtained when comparing data sets of V_{svh} and V_{pvh}.

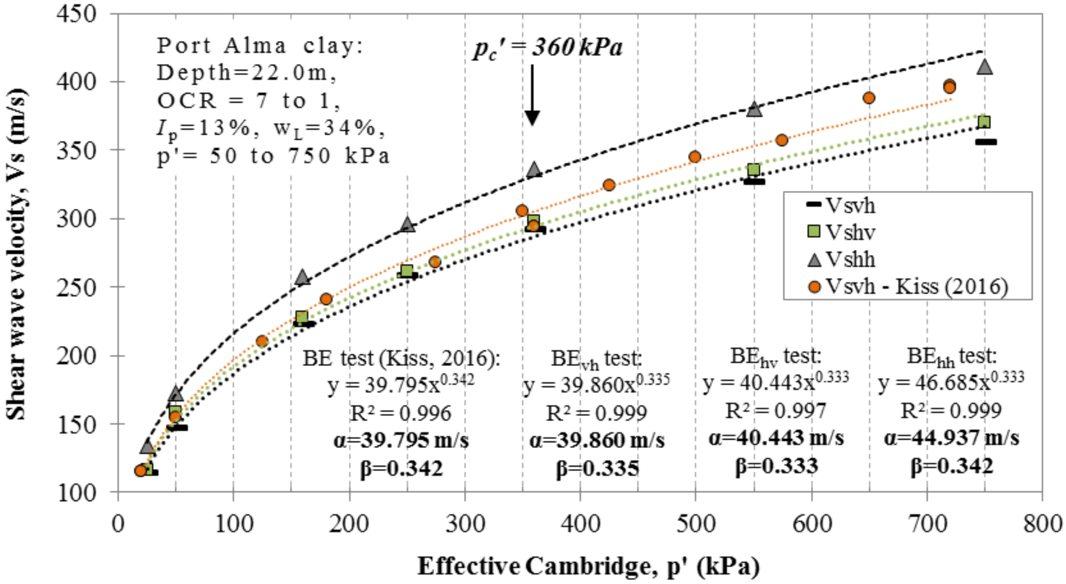

Figure 5.7: Shear wave velocities measured from propagating shear waves with increasing effective pressure on Port Alma clay

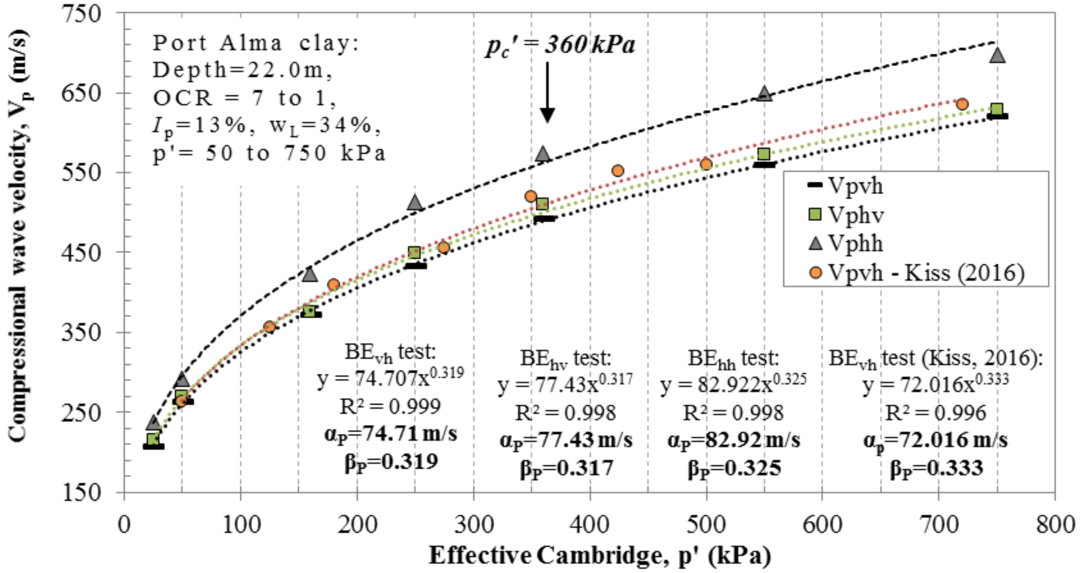

Figure 5.8: Compressional wave velocities measured from propagated compression waves with increasing of effective pressure on Port Alma clay

The measured vertically propagated-horizontally polarized (VH-mode) and horizontally propagated-vertically polarized (HV-mode) shear wave (V_{svh} and V_{shv}) and compressional wave (V_{pvh} and V_{phv}) velocities, were similar throughout the test. However, values of V_{shv} and V_{pvh} are approximately 2.7% and 2.4% higher compared to the V_{svh} and V_{phv} measurements. The ratios of V_{svh}/V_{shv} and V_{pvh}/V_{phv} are on average equal to 0.97 and 1.02, respectively. The measured values of horizontally propagated-horizontally polarized (HH-mode) shear wave velocities, V_{shh}, were about 16% higher than V_{svh} and V_{shv}. Similarly, HH-mode compressional wave velocities, V_{phh}, were consistently higher, approximately 14% on average, when compared to V_{pvh} and V_{phv}. The ratio of V_{shh}/V_{svh} for S-waves is on average equal to 1.16, and the ratio of V_{phh}/V_{pvh} for P-waves is around 1.14. The results have implications for higher stiffness in the horizontal direction of the material and cross-anisotropy, and these will be discussed later.

Figure 5.9 better depicts the relationship between velocity ratios for the Port Alma material. Crampin (1977) examined the effects of soil anisotropy on the seismic wave propagation. It was found that the measurements of body and surface waves in anisotropic media differed from their propagation in isotropic media and varied with the direction of the velocity and the particle-motion polarization. Similar findings were obtained by

Jamiolkowski et al. (1995) and Belloti el al. (1996) when studying the inherent anisotropy of 5 different natural cohesive soils and medium dense Ticino sand using BE tests, respectively.

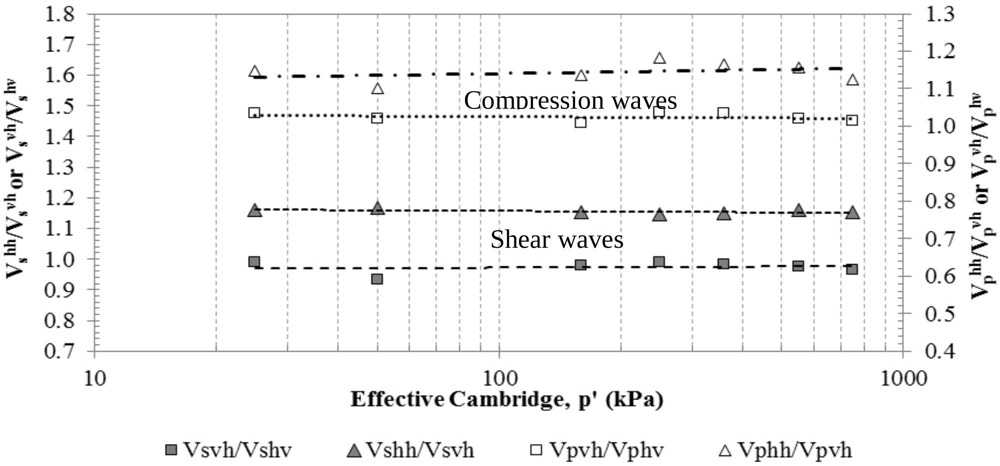

Figure 5.9: Velocity ratios obtained from BE testing on Port Alma glacial till

Power law curves were fitted using the least squares methods to the results showed in Figures 5.7 and 5.8, and the resultant velocity-stress power relations are shown in the figures. The power law equations follow the form of Equation 2.11 (defined in Section 2.3.3.1). Such equations can be used to explain changes in both contact stiffness and inherent soil fabric (Cha et al., 2014), which are described by the wave velocity factors α and β shown in Equation 5.5 as follows:

$$V_s = \alpha_s \, (p'/1\,kPa)^{\beta} \qquad (5.5)$$

Where α_s (m/s) is the wave velocity in the soil mass when the mean effective stress is equal to 1 kPa. This has been named α_s and α_p here, where the subscript corresponds to the propagated wave either S- or P-wave. The factor β describes the stress sensitivity of P- and S-wave velocities. Table 5.3 shows a summary of the factors α and β as obtained from BE tests on Port Alma glacial till material. Notably, values of β_s and β_p for both VH and HH-modes are similar and lie in a narrow range between 0.32 to 0.35. Moreover, α_s and α_p in the VH-mode differ from the ones estimated in the HH-mode by a difference of around 17% and 10%, respectively. It is worth mentioning that α_s and α_p in HH-mode are consistently higher than those estimated in VH-mode. The R^2 of the power regressions show a strong significance between p' and the propagated velocities (V_s and V_p).

Table 5.3: $\alpha_{s\ or\ p}$ and $\beta_{s\ or\ p}$ factors obtained from BE tests on Port Alma glacial till

Vs_{ij} or Vp_{ij}	α_s or α_p (m/s)	β_s or β_p	R^2
Vs_{vh}	36.974	0.354	0.999
Vs_{hv}	39.711	0.347	0.997
Vs_{hh}	44.937	0.342	0.999
Vs_{vh} - Kiss (2016)	37.599	0.357	0.996
Vp_{vh}	74.707	0.319	0.999
Vp_{hv}	77.430	0.317	0.998
Vp_{hh}	82.922	0.325	0.998
Vp_{vh} - Kiss (2016)	72.016	0.333	0.996

S-waves: α_s *and* β_s; P-waves: α_p *and* β_p; i: propagation direction; j: polarization

Figures 5.10 and 5.11 show the variation of the small-strain shear modulus (G_{max}) and constrained modulus (M_{max}) with confining pressure, estimated using the measured wave velocities for different directions and polarizations within the soil specimen. Both G_{max} and M_{max} are functions of the soil density, and V_s and V_p respectively. Thus, Figures 5.10 and 5.11 present similar trends to those in Figures 5.7 and 5.8. Values of G_{max} and M_{max} in HH-mode (G_{hh} and M_{hh}) are consistently higher than those estimated for VH/HV-modes (G_{vh} and G_{hv}; M_{vh} and M_{hv}). G_{hh} is on average 33% higher than G_{vh} and G_{hv}. Both G_{vh} and G_{hv} are approximately equal, with G_{hv} just 5% higher than G_{vh}. Similarly, M_{hh} was 31% higher than M_{vh} and M_{hv} throughout the test, and M_{vh} was 5% higher than M_{hv}.

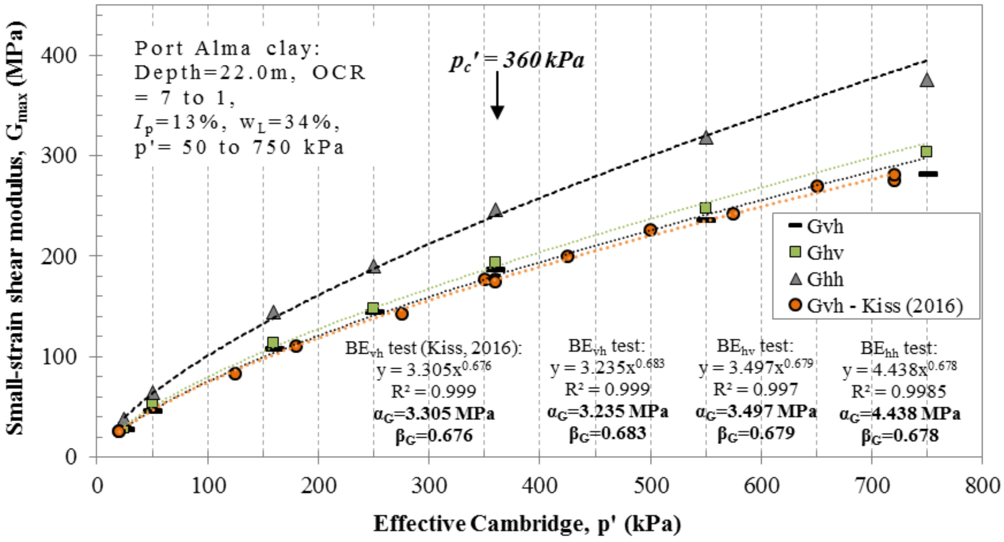

Figure 5.10: Small-strain shear modulus with increasing effective pressure of Port Alma clay

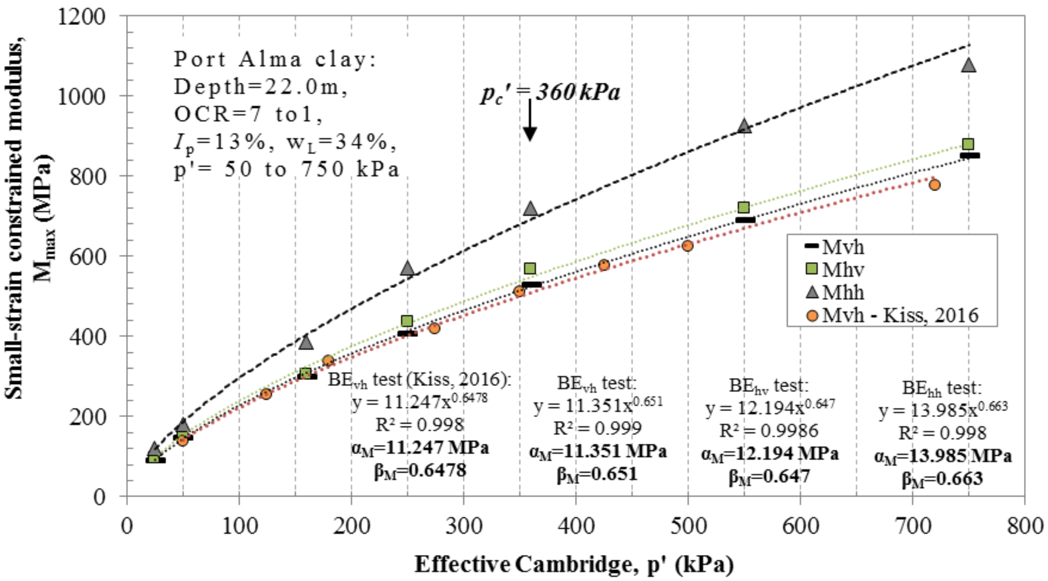

Figure 5.11: Small-strain constrained modulus with increasing effective pressure of Port Alma clay

Figure 5.12 shows comparison of different moduli ratios with increasing isotropic effective stresses. The ratio of M_{vh}/M_{hv} is equal to 1.05 and the ratio of M_{hh}/M_{vh} is 1.31. The ratio of G_{vh}/G_{hv} is close to unity, with an average of around 0.95, and G_{hh}/G_{vh} is approximately equal to 1.34. As discussed in Section 2.4 of the literature review, a cross-anisotropic soil has the feature that the values of G_{vh} and G_{hv} (or M_{vh} and M_{hv}) are equal. It should be noted that the values of G_{vh} and G_{hv} are not necessarily defined for a single plane, as might be implied from the notation, but are for different planes which are determined on the same vertical axis but different horizontal axes. These also applies when analyzing M_{max} from both VH- and HV-modes.

It therefore appears that assuming the Port Alma unweathered till material to be a cross-anisotropic can be a justifiable assumption since the ratio of G_{hv}/G_{hv} is close to 1; this is indicative that the soil might have experienced one-dimensional deposition and unloading (Pennington et al., 1997; Jovicic and Coop, 1998). Graham and Houlsby (1983) represented the degree of soil anisotropy with the ratio of stiffnesses of G_{hh} to G_{vh}, which in our case is equal to 1.34. Values of G_{hh}/G_{vh} have been previously reported for different natural cohesive soils clays including Panigglia and Pisa clays (Jamiolkowski et al., 1994), Gault clay (Pennington et al. 1997; Lings et al. 2000), London clay (Jovicic and Coop 1998) and

Chicago clays (Cho and Finno 2010). In these studies, the anisotropy degree for normally to lightly overconsolidated clays ranged from 1.2 to 1.7 and those for the heavily overconsolidated clays were higher than 2.2.

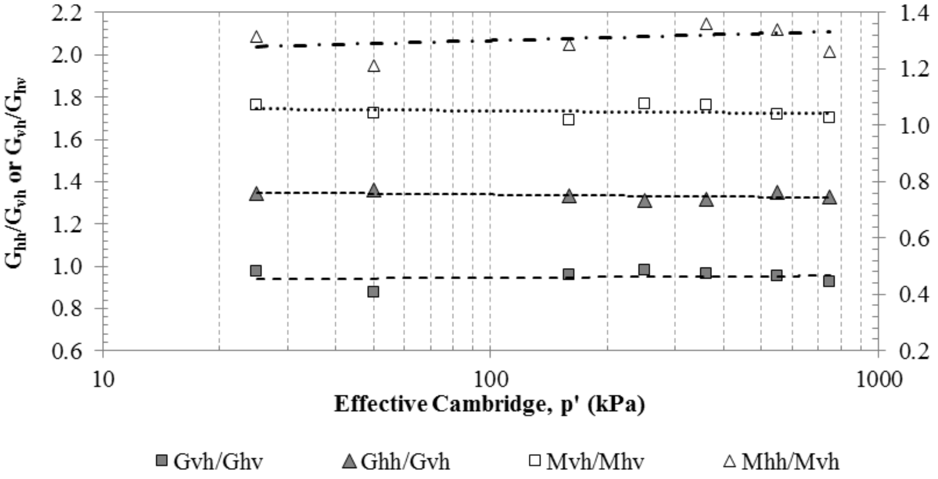

Figure 5.12: Moduli ratios estimated from BE testing in different propagation direction and polarization on Port Alma glacial till

Similar to the velocity-stress power relations obtained for Figures 5.7 and 5.8, a new set of stiffness-stress power relations were obtained and shown in Figures 5.10 and 5.11. Table 5.4 shows a summary of the factors *α* and *β* obtained from power regression of Figures 5.10 and 5.11. The factors were regarded as α_{Gij} and β_{Gij}, α_{Mij} and β_{Mij} for shear modulus and constrained modulus, respectively. The subscripts *i* and *j* refer to the direction of propagation and polarization, respectively.

Table 5.4: α and β factors obtained from the stiffness-stress power relations for Port Alma glacial till

G_{ij} or M_{ij}	α_{Gij} or α_{Mij} (MPa)	β_{Gij} or β_{Mij}	R^2
G_{vh}	3.235	0.683	0.999
G_{hv}	3.497	0.679	0.997
G_{hh}	4.438	0.678	0.999
G_{vh} - Kiss (2016)	3.305	0.676	0.999
M_{vh}	11.351	0.651	0.999
M_{hv}	12.194	0.647	0.998
M_{hh}	13.985	0.663	0.998
M_{vh} - Kiss (2016)	11.247	0.648	0.996

Shear modulus: α_G and β_G; Constrained modulus: α_M and β_M; i: propagation direction; j: polarization

Table 5.5 summarizes the small-strain elastic properties that were obtained using vertical and horizontal bender elements, under isotropic confining pressures during consolidation of the Port Alma unweathered glacial till material. In particular, the results for the estimated *in-situ* and pre-consolidation pressures are highlighted within the table.

Table 5.5: Summary of small-strain elastic properties obtained from BE test on Port Alma glacial unweathered till material

Propagation and polarization directions	p' (kPa)	V_s (m/s)	V_p (m/s)	G_{max} (MPa)	M_{max} (MPa)
Vertically propagating, horizontally polarized (VH-mode)	25	115.31	207.75	28.20	91.56
	50	147.97	264.41	46.76	149.31
	160*	**223.13**	**372.74**	**108.18**	**300.30**
	250	258.66	433.01	145.39	407.44
	360**	**292.64**	**492.49**	**187.09**	**529.88**
	550	327.72	560.42	236.49	691.56
	750	356.81	620.65	282.15	853.71
Horizontally propagating, vertically polarized (HV-mode)	25	116.62	214.98	28.85	98.04
	50	158.31	269.79	53.53	155.44
	160*	**227.82**	**375.90**	**112.78**	**305.41**
	250	261.15	448.90	148.20	437.88
	360**	**297.82**	**509.83**	**193.77**	**567.85**
	550	335.50	571.73	247.84	719.74
	750	370.30	629.02	303.89	876.89
Horizontally propagating, horizontally polarized (HH-mode)	25	133.82	238.29	37.99	120.45
	50	172.47	291.34	63.52	181.26
	160*	**257.43**	**423.09**	**144.01**	**386.90**
	250	296.08	512.69	190.50	571.17
	360**	**335.95**	**574.49**	**246.57**	**721.03**
	550	380.40	648.47	318.63	925.93
	750	411.44	697.39	375.17	1077.88

*: p’=160 kPa (estimated in-situ pressure); OCR=2.25

**: p’=p_c’=360 kPa (estimated pre-consolidation pressure); OCR=1

5.3 Resonant column (RC) test results

Resonant column (RC) tests were also performed on undisturbed soil specimens of the Port material (depth between 20 to 21 m from borehole BH12-2). Soil specimens for the RC tests, were prepared from PQ core samples, which were large enough to produce vertically and horizontally trimmed 50 x 100 mm cylindrical specimens. Soil specimens were prepared as described in Section 4.3.5, and the test was carried out as outlined in Section 4.3.8. The samples were subjected to increments of isotropic confining pressures following the testing program presented in Table 4.5. Soil specimens were trimmed considering the sample original *in-situ* vertical axis. Vertically cut specimens were labeled as ‘0° rotation sample’, and horizontally cut specimens as ‘90° rotation sample’.

Both, vertically and horizontally cut samples, were tested at low and high stress levels, and at each stress state the specimen was subjected to low and high strain amplitudes (approximately from 10^{-5} to 10^{-3}). At each strain amplitude, one torsional, one damping, and one flexural resonant frequency test were performed. Small-strain shear wave velocity and shear modulus were determined at approximately 24 hours after the soil sample reached 90% of primary consolidation. The RC test results were evaluated following the data analysis procedure shown in Section 4.3.8.1. Plots of shear wave velocity (V_s) vs. log-shear strain (γ), shear modulus (G) vs. log-shear strain (γ), normalized shear modulus (G/G_{max}) vs. log-shear strain (γ), damping ratio (D) vs. log-shear strain (γ), elastic modulus (E) vs. log-shear strain, and normalized elastic modulus (E/E_{max}) vs. log-shear strain (γ), were produced for both 0° and 90° rotation samples. For brevity only, a complete set of plots will be presented for the 0° rotation sample in this section. Plots for the 90° rotation sample can be found in Appendix D.1.

Figures 5.13 to 5.16 show the results from the torsional test on the 0° rotation sample (vertical). Low and high strain amplitude tests were carried out to assess the dynamic response of the Port Alma till material with increasing shear strain amplitude, and to assess the effect of high shear straining on the small-strain shear modulus (G_{max}). This information is useful particularly for analysis of seismic effects (Kim and Novak, 1981), or to evaluate the soil stiffness degradation due to machinery induced strains (soil-structure interaction problems) such as for wind turbine structures. Figures 5.13 and 5.14 show the variation in shear wave velocity (V_s) and shear modulus (G) with the logarithm of shear strain at different confining pressures. As can be seen, both V_s and G decreases as shear strain amplitude increases, once strain amplitudes exceed a threshold level. Furthermore, the magnitude of V_s and G at low strain amplitudes ($< 2\times10^{-5}$) increases with increasing confining pressures.

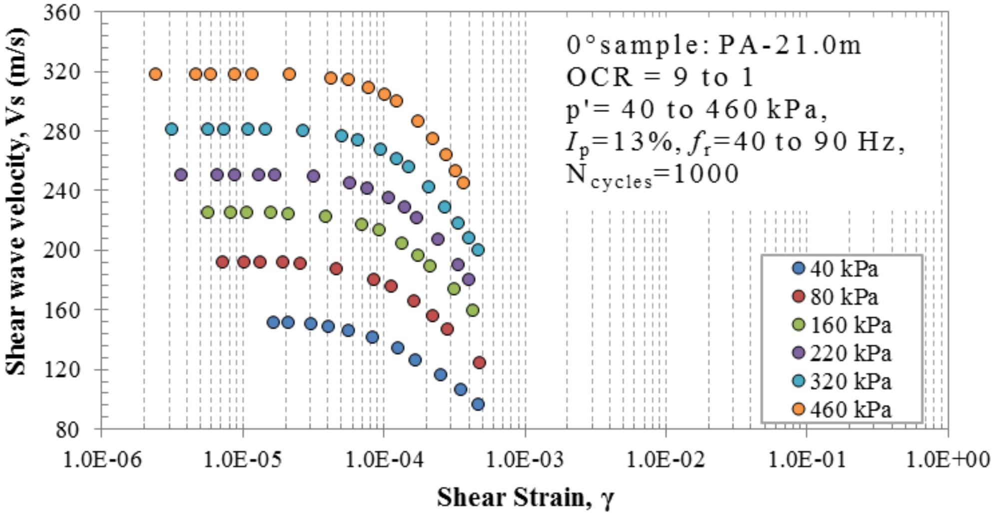

Figure 5.13: Shear wave velocity variation with strain amplitude of Port Alma clay

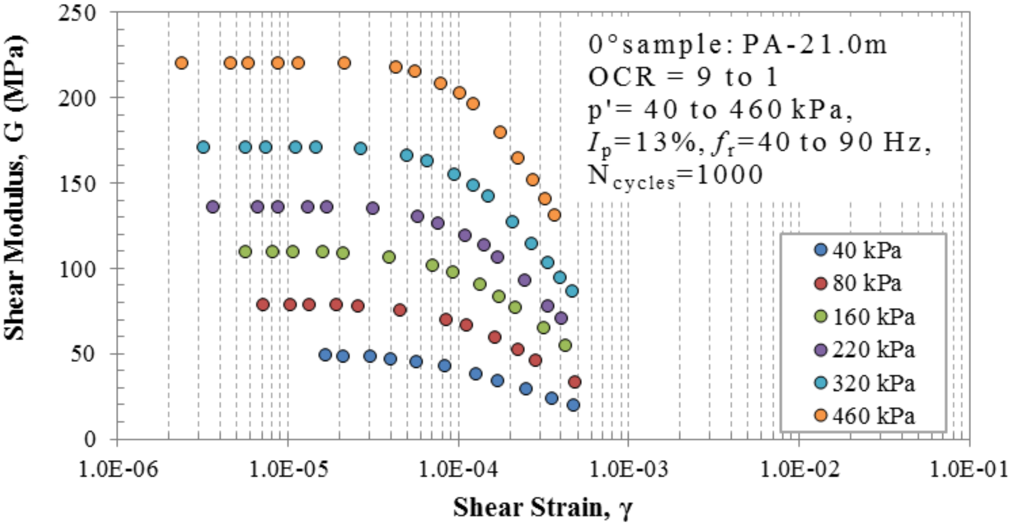

Figure 5.14: Shear modulus variation with strain amplitude of Port Alma clay

The relative reduction in G due to increasing strain amplitude can be better seen from a plot of the normalized shear modulus (G/G_{max}) at a given time versus the logarithm of the shearing strain amplitude. G is the shear modulus at high strain, and G_{max} is the maximum shear modulus measured at very small strain amplitudes just before the high strain amplitude test. The value of G/G_{max} defines the reduction in percentage of G due to high strain amplitude. In this investigation, G was determined for a constant number of 1000-cycles to eliminate the cyclic effect. These results are shown in Figure 5.15 for different confining pressures and OCR values. It can be seen from the figure that G/G_{max} starts to decrease once the shearing strains reach between $3x10^{-5}$ to $4x10^{-5}$, whereas for shear strain levels below $3x10^{-5}$, G/G_{max} remains almost constant or linear. G/G_{max} decreases more significantly once shear strain amplitudes exceed approximately $4x10^{-4}$; at this level of strain G/G_{max} varies from 45 to 59 percent for 40 and 460 kPa, respectively.

Another general trend that appears in Figure 5.15 is the difference in strain dependency of G for different confining pressures. The effect of high amplitude straining for higher confining pressures is less than for low pressures in the strain range from $5x10^{-5}$ to $4x10^{-4}$. In other words, G/G_{max} degrades faster at lower confining stresses than at much higher stresses. Also, the normalized modulus curves have a general tendency of shifting somewhat to the right as confining pressures increases, with the shape of the curve remaining constant. The average reference strain (γ_{ref}) for the unweathered till is approximately $3x10^{-4}$ (≈ 0.03%). γ_{ref} is the shear strain level where the degradation of G is about 50%, or G/G_{max} equal to 0.5 (Vardanega and Bolton, 2014).

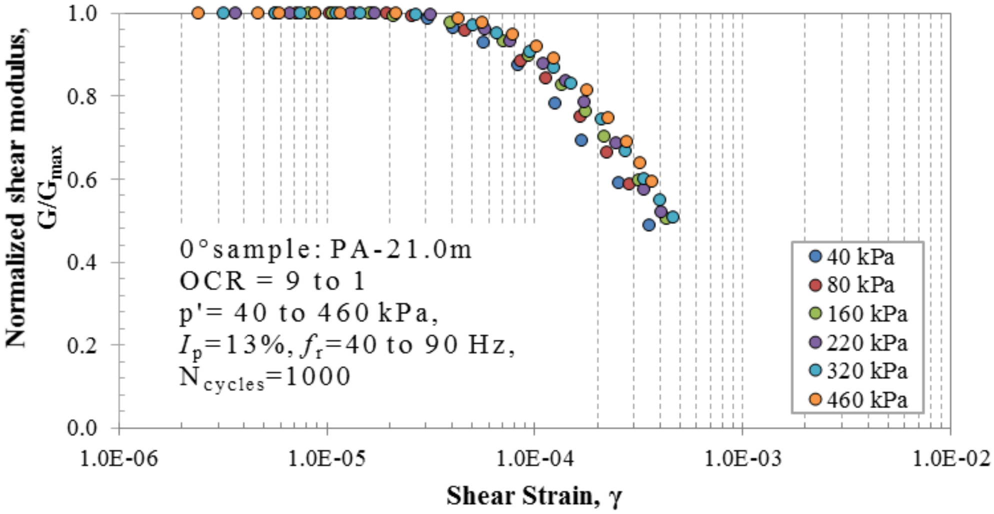

Figure 5.15: Normalized shear modulus variation with strain amplitude of Port Alma clay

The damping ratio (*D*) of the soil specimens was measured after completing every resonant frequency test and after each increment of strain, until the completion of the desired range of shearing strain amplitudes. The effect of high amplitude straining on low amplitude damping ratio was evaluated. The general trend shown in Figure 5.16 is that *D* constantly increases as the amplitude of straining increases above 4x10^{-5}; below this level of strain *D* remains almost constant. This threshold strain amplitude is nearly equal to that exhibited in the degradation of *G*. Another general trend is that the low strain amplitude damping ratio decreases with increasing confining pressures. For the unweathered till, *D* decreases from 2.8 to 1.5 at a shear strain level of about 1.3x10^{-5}, for 40 and 460 kPa of confining stresses, respectively.

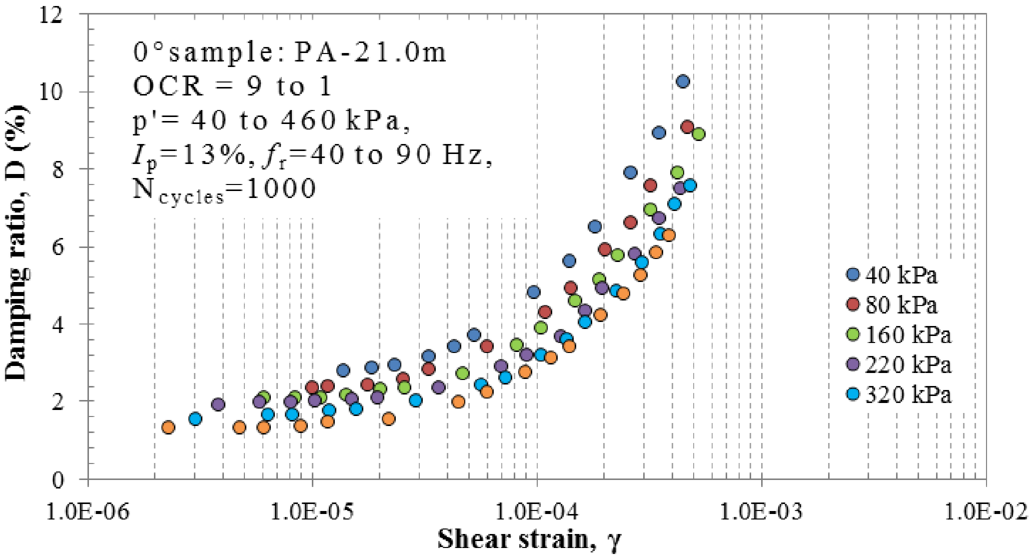

Figure 5.16: Damping ratio variation with strain amplitude for Port Alma clay

Resonant column measurement of the elastic modulus or Young's modulus (*E*) of soil materials is less common compared to the measurement of V_s and *G*, as very little information is reported in the literature. To complete the description of the small-strain stiffness properties of the Port Alma soil material, E was also measured using the flexural excitation mode of the RC apparatus. The flexural test was carried out following the torsional test. Similar testing conditions and procedures required to perform the torsional test were used for the flexural test. The variation of E with increasing shear strains and confining pressures follows a similar behaviour at low strain amplitudes, when compared to *G* in Figure 5.14, also E remains almost constant for strains below 10^{-5}. For shearing strains above 10^{-5}, E starts to decrease abruptly and tends to degrade faster compared to G. The behaviour of the normalized elastic modulus (E/E_{max}) versus shear strain amplitude, shows that E/E_{max} reduces faster at lower confining stresses than at much higher stresses, and the normalized curves also have a general tendency to shift slightly to the right. The plots for these results can be found in Appendix D.1.

Figures 5.17 to 5.19 show a comparison between values of G vs. γ, G/G_{max} vs. γ, and D vs. γ, obtained from the RC test on 0° and 90° rotation samples, respectively, consolidated to *in-situ* effective stress (160 kPa). From Figure 5.17 is evident that the shear modulus obtained for the 90° rotation sample at low strain amplitudes ($<10^{-5}$), is around 16% higher than the G values for the 0° rotation sample at very small-strain levels. These results suggest that the small-strain stiffness of the Port Alma unweathered till for its *in-situ* condition is anisotropic. This same trend is observed during the progression of the test, as the shearing strain amplitudes are increased up to $6\text{x}10^{-5}$. From this point onwards, the difference in G for both samples starts to decrease, becoming negligible at shearing strains of about $5\text{x}10^{-4}$, where the shear modulus of the 90° and 0° rotation samples are almost equal. The decrease in magnitude of G for the 90° rotation sample could be due to loss of fabric or alterations in the particle arrangements within the soil skeleton with increasing shear strain. Moreover, total carbonates (dolomite and calcite) have been found in the Port Alma clay. The presence of these minerals could create bonding between soil particles through cementation causing an increase in the stiffness properties of the soil material. Once the bonding breaks (e.g. due to shearing) it could lead to a drastic decrease in stiffness as exhibited by the 90° rotation sample.

From the G/G_{max} curves shown in Figure 5.18, for 0° and 90° samples, it can be seen than both specimens present similar degradation behaviour with increasing shearing strain. The approximate value of γ_{ref} for both samples is about $4\text{x}10^{-4}$, and the threshold strain is between $4\text{x}10^{-5}$ to $5\text{x}10^{-5}$. Likewise, the damping ratio variation presented in Figure 5.19 shows a similarity in damping for both tested samples. However, this also suggests that D_r for the 0° sample increases more rapidly than the 90° sample for strains above the threshold strain.

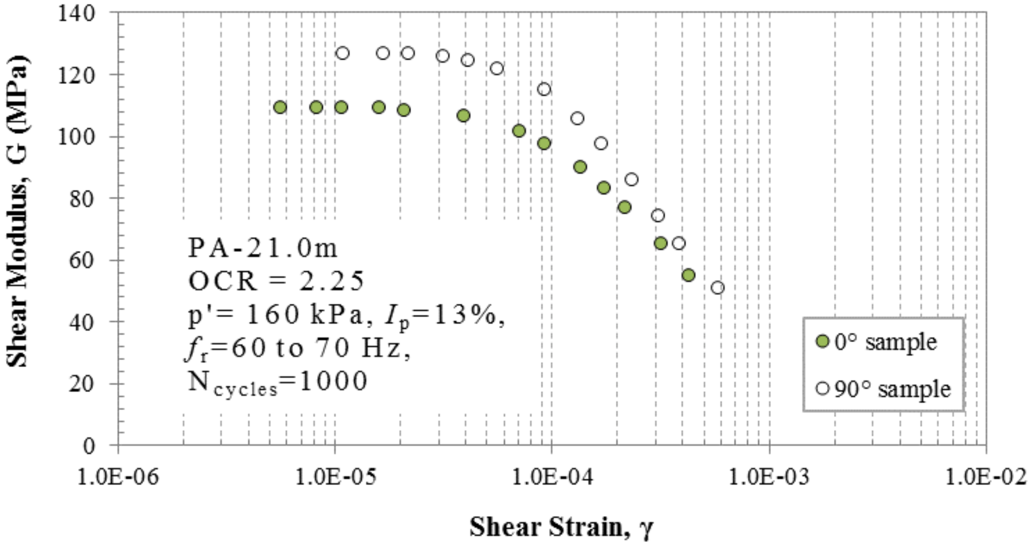

Figure 5.17: Shear modulus variation with strain amplitude, of 0° and 90° samples at *p'*=160 kPa for Port Alma clay

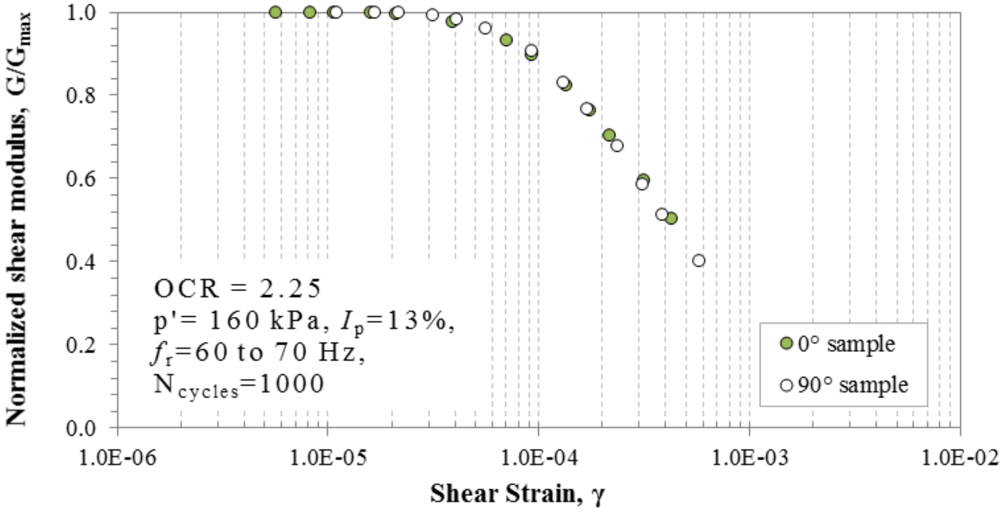

Figure 5.18: Normalized shear modulus variation with strain amplitude, of 0° and 90° samples at *p'*=160 kPa for Port Alma clay

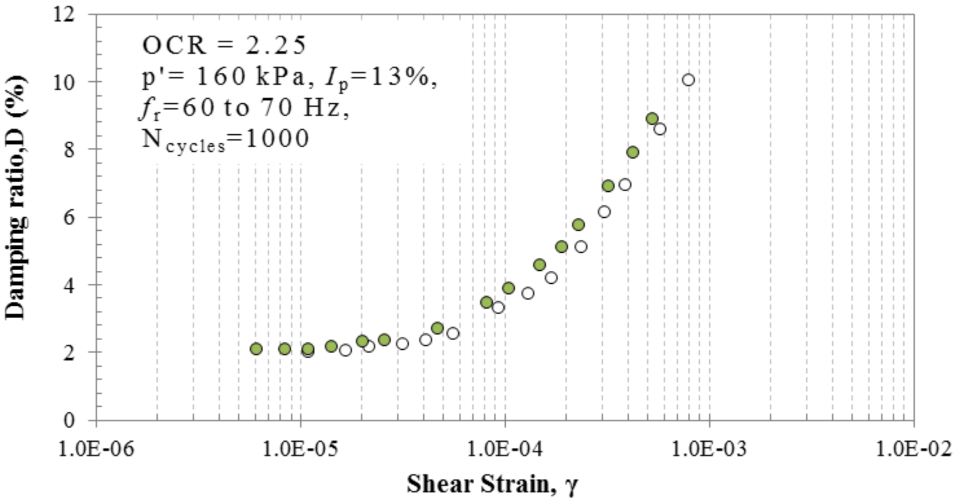

Figure 5.19: Damping ratio variation with strain amplitude, of 0° and 90° samples at p'=160 kPa for Port Alma clay

5.4 Summary of results

Comparisons between the shear wave velocities measured from BE tests and RC tests, and the estimated small-strain shear modulus, were carried out and are presented in Figures 5.20 and 5.21, respectively. From both figures, it is possible to see good agreement between the measured and estimated values of V_S and G between the 0° rotation sample and BE test in VH- and HV-mode, and the 90° rotation sample with respect the BE test in HH-mode. To better compare the results between BE and RC tests, power law curves were fitted to the results obtained from the RC test. The factors α_S and β_S, and α_G and β_G for the 90° rotation sample, are consistently higher compared to those estimated for the 0° rotation sample. Such results are in good agreement to what was obtained in the BE tests These results confirm the trends observed from the BE test in Section 5.2.

Table 5.6 shows a summary of the factors α_S / α_G and β_S / β_G obtained from the power law fitting for both RC and BE tests. The comparison between both tests shows that for the propagated waves in the VH- and HV-mode and the 0° sample, the factor α_S and β_S were very similar, with average values of 40.116 and 0.336, respectively. Likewise, for the propagated waves in HH-mode and the 90° rotation sample, α_S and β_S were similar with average values of 47.089 and 0.329, respectively. Similar behaviour is observed for the factors α_G and β_G for the aforementioned cases.

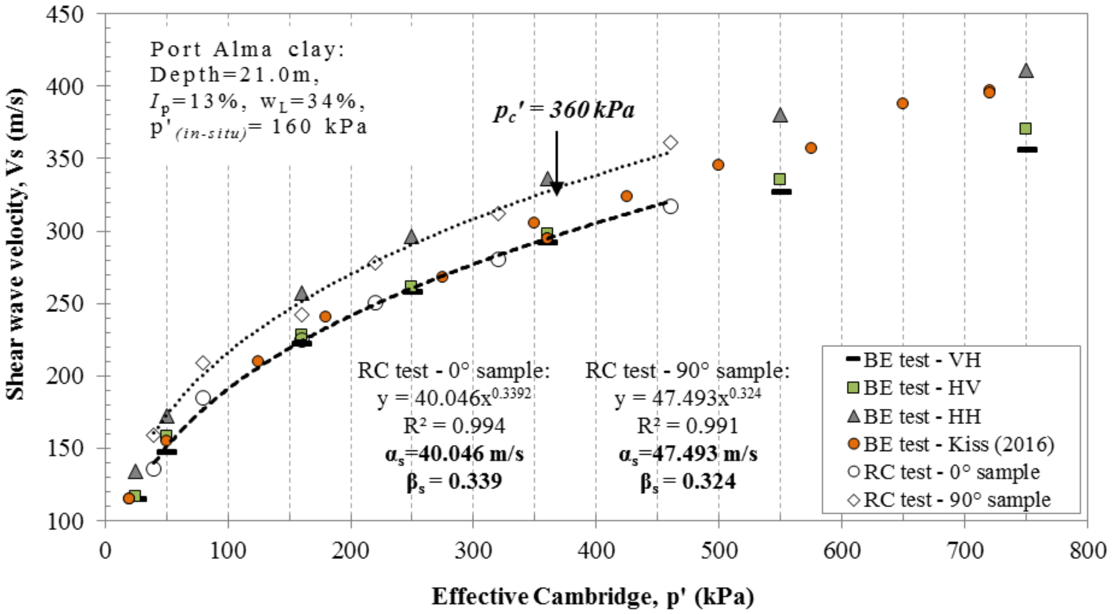

Figure 5.20: Shear wave velocity with increasing effective pressure from the RC and BE tests for Port Alma clay

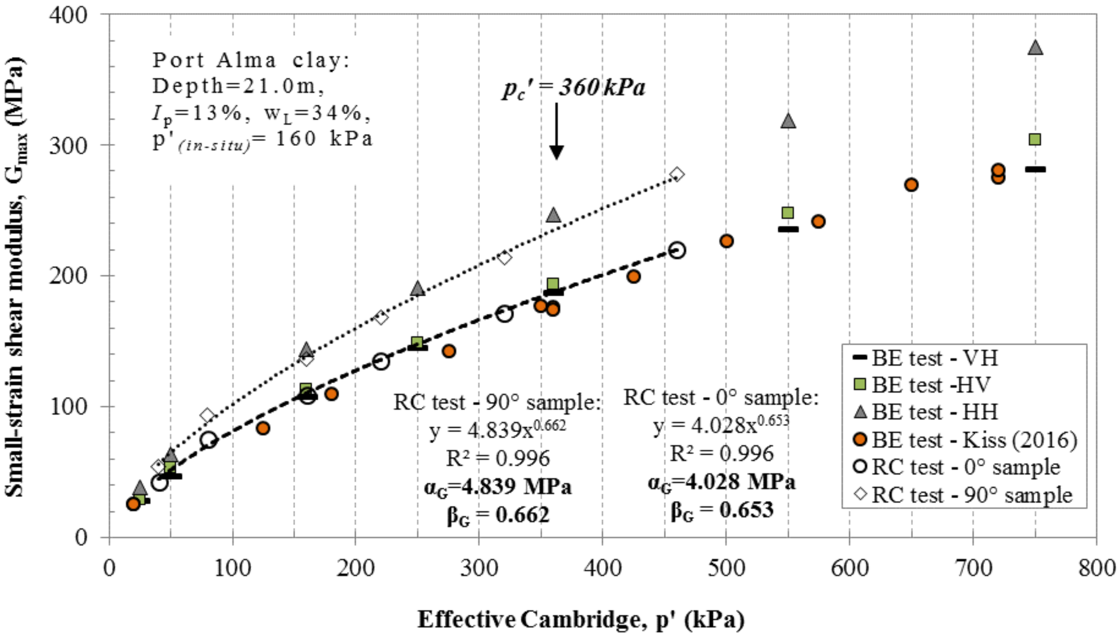

Figure 5.21: Small-strain shear modulus with increasing effective pressure from the RC and BE tests for Port Alma clay

Table 5.6: α and β factors obtained from BE and RC tests on Port Alma glacial till

Vs_{ij}	α_s or α_G (m/s)	β_s or β_G	R^2
Vs_{vh} - BE test	39.860	0.335	0.999
Vs_{hv} - BE test	40.443	0.333	0.997
Vs_{hh} - BE test	46.685	0.333	0.999
$Vs_{0°}$ - RC test	40.046	0.339	0.994
$Vs_{90°}$ - RC test	47.493	0.324	0.991
G_{vh} - BE test	3.235	0.683	0.999
G_{hv} - BE test	3.497	0.679	0.997
G_{hh} - BE test	4.438	0.678	0.999
G_v - RC test	4.028	0.653	0.996
G_h - RC test	4.839	0.662	0.996

To further analyze the results from the resonant column testing on the 0° and 90° samples, the anisotropy degree defined by Graham and Houlsby (1983) was estimated employing the relationships $\alpha=(G_h/G_v)$ and $\alpha=(E_h/E_v)^{0.5}$. These were calculated at different levels of shear strain amplitude for the *in-situ* condition (p'=160 kPa), and at different confining pressures as depicted in Figures 5.22 and 5.23, respectively. The small-strain stiffness anisotropy is estimated at very low strain levels, Figure 5.22 shows that for the Port Alma unweathered till material the anisotropy degree, obtained from either G_h/G_v or $(E_h/E_v)^{0.5}$, remains almost constant for shear strains between $3x10^{-6}$ and $2x10^{-5}$. For strains above $2x10^{-5}$, the anisotropy degree starts to decrease quickly with increasing shear strains. Notably, the relationship $\alpha=(E_h/E_v)^{0.5}$, decreases faster than $\alpha=G_h/G_v$ with the same shear strain increments. Figure 5.22 shows evidence of the susceptibility of the small-strain anisotropy to incremental shear strains. In contrast, Figure 5.23 shows how little the small-strain anisotropy degree varies with increasing isotropic effective stresses. These finding suggest that, under the testing conditions adopted, the induced shear strain increments exert a more important effect on the variation of the small-strain stiffness anisotropy than volumetric changes. Furthermore, Figure 5.23 confirms the good agreement of the estimation of the anisotropy degree, defined by G_h/G_v, from both BE and RC tests. These shows that the *in-situ* anisotropy degree of the Port Alma unweathered till ranges between 1.25 to 1.33.

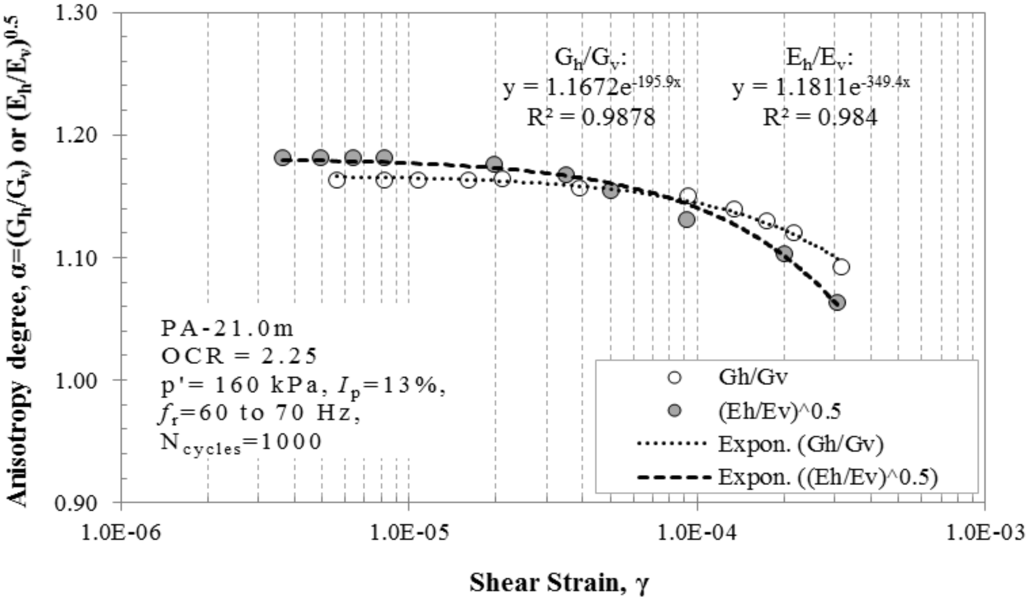

Figure 5.22:Anisotropy degree variation with increasing of shear strain amplitude of Port Alma clay

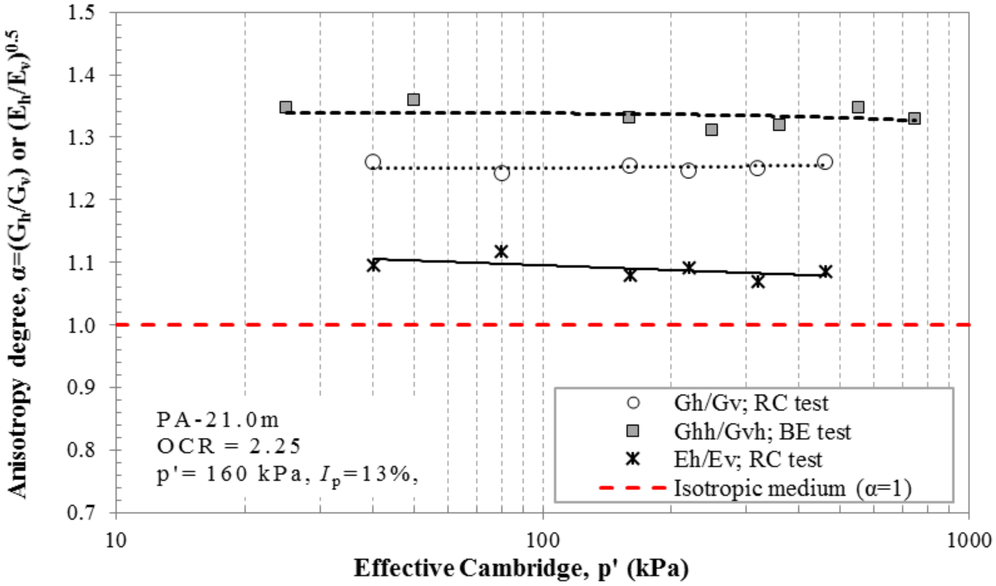

Figure 5.23: Small-strain anisotropy degree variation with increasing of isotropic effective stress of Port Alma clay

5.5 Discussion of the results

5.5.1 Shear modulus degradation from static tests with small to large strains

Internal measurements of strains using locally mounted miniature water-submersible LVDTs or small LVDTs provide a much stiffer and more realistic estimation of soil stiffness than the typical external axial strain measurements (see Figure 5.5) and are therefore fundamental to properly understand the small-strain stiffness degradation obtained from static triaxial compression tests. Ever since Burland (1989) indicated that the typical working strain levels beneath and around structures in stiff soils were less than 0.1%, a number of different experimental studies on the stress-strain behaviour at strains below 0.1% have been carried out.

Many of these experimental studies have focused on characterizing naturally deposited cohesive soils, such as the heavily over-consolidated marine deposits of London and Gault clays, the lightly over-consolidated of medium plasticity Bangkok clay, various UK glaciomarine tills of low plasticity and slightly over-consolidated such as Magnus till, Cowden till and Northumberland till, and the slightly over-consolidated Chicago glacial clay of low plasticity. All of these materials have been used to compare the shear modulus obtained for the Port Alma glacial till material using local instrumentation during the CIU triaxial tests. Figure 5.24 shows the normalized secant shear modulus degradation (G_{sec}/p'_o) of the Port Alma material, as well of other natural cohesive soils. Normalizing G_{sec} with p'_o is a technique used by different researchers, where p'_o is the effective stress to which the samples were consolidated (e.g. Pantelidou and Simpson 2007; Hight et al. 2007; Grammatikopoulou et al. 2008, Simpson and Rouainia, 2012; Vardanega and Bolton, 2013).

Stiffness is shown to be related to p'_o, as samples consolidated to a high p'_o exhibit higher stiffness than samples of similar composition consolidated to lower p'_o values (e.g. Chicago glacial clays, UK Tills). Jardine (1992) reported that the stiffness of Magnus Till was about 10 times higher for small strains close to 0.002% than for large strains of around 1%. Likewise, the referenced fine-grained materials shown in Figure 5.24, exhibit a drop in secant shear modulus (G_{sec}) by an order of magnitude between shear strains of 0.002% and 1%; similar behaviour is displayed by the Port Alma till material. Moreover, both Port Alma till and Chicago glacial clay, show similar stiffness and shear degradation behaviour between shear strains of 0.002% and 1%. These matching responses could be due to both materials having similar geotechnical properties and geological formation history, as Chung and Finno (1992) reported that Chicago glacial clays are lightly overconsolidated with OCR between 1.2 to 1.4 and have liquid limits and plasticity index of 33% and 15%, respectively, and were deposited subglacially during the Wisconsin stage of the Pleistocene epoch. Overall, although the natural fine-grained materials presented in Figure 5.24 have different composition and formation history, they all degrade at similar rates with normalized stiffness coinciding at shear strains between 0.5% to 1%.

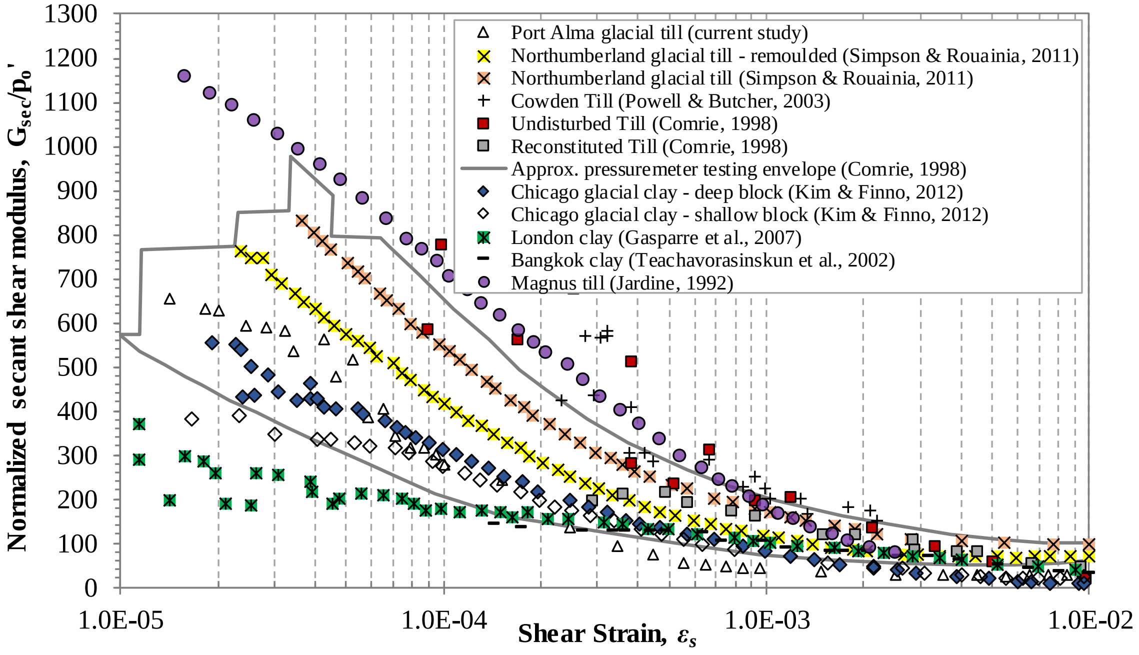

Figure 5.24: Normalized secant shear modulus with increasing of shear strain

5.5.2 Shear modulus degradation and damping ratio at very small to medium strains

To investigate the validity of the laboratory tests used in this investigation, comparisons between published data and the laboratory results have been conducted. Figure 5.25 presents a set of curves of shear modulus degradation (G/G_{max}) with strain.

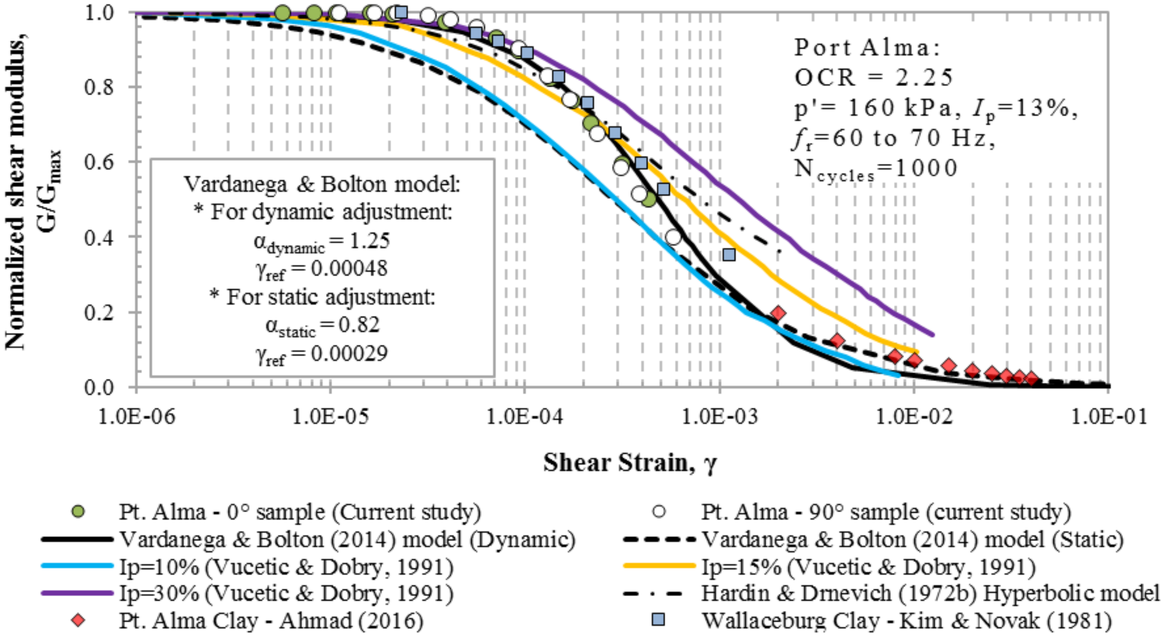

Figure 5.25: G/G_{max} from RC test at p'=160 kPa for 0° and 90° rotation samples, compared to empirical models

The white and green dotted curves show the G/G_{max} of the carbonate unweathered glacial till in this study (Port Alma Clay) at very small to small strains obtained with the RC test using 0° and 90° rotation samples, respectively. The blue squares represent the G/G_{max} of Wallaceburg Clay at very low to low strains previously studied by Kim and Novak (1981) using the RC, which it is believed to have a similar geological formation history as the Port Alma Clay. The red diamond curve also characterizes the behaviour of Port Alma Clay, this time at medium to large strain levels from a study performed by Ahmad (2016), using a radial piezoelectric device for measuring shear wave velocity.

Also shown in Figure 5.25 are five analytical methods proposed by 3 different investigators. The dash dotted line is the Hardin and Drnevich hyperbolic model (1972b), dashed and solid lines the Vardanega and Bolton hyperbolic model (2013) (static and dynamic, respectively), and blue, yellow and purple lines for the Vucetic and Dobry (1991) modulus reduction as function of plasticity index (I_p) equal to 10%, 15% and 30%, respectively. Hardin and Drnevich (1972b) suggested an empirical modified hyperbolic relationship. The modified hyperbolic relationship describes the shear modulus (G) at strain level (γ) with the equation:

$$G/G_{max} = 1/(1 + \gamma_h) \tag{5.6}$$

$$\gamma_h = \gamma/\gamma_r \left[1 + \alpha_{cyc}.exp\left(-b.\left(\gamma/\gamma_r\right)\right)\right] \tag{5.7}$$

Where γ_h is the hyperbolic strain, $\gamma_r = \tau_{max}/G_{max}$ with τ_{max}= the shearing strain at failure; α_{cyc}=the cycle factor= 1.0+0.25 log(N) for clays with N = the number of cycles; finally, b = the soil coefficient taken as 1.3 for saturated cohesive soils.

Vardanega and Bolton (2013) conducted a meta study of a wide variety of laboratory studies of cohesive soils. The database includes soils with different stress history and basic soil index parameters, from normally consolidated to heavily overconsolidated soils, and from non-plastic to highly plastic soils, including those studied in Ontario by Kim and Novak (1981). The gathered data was used to calibrate functions to describe the modulus reduction (G/G_{max}) of clays and silts and prediction of the reference strain parameter (γ_{ref}). The equations deduced are as follow:

- With static test adjustment applied:

$$G/G_{max} = 1\Big/\left(1 + \left(\gamma/\gamma_{ref}\right)^{0.74}\right) \tag{5.8}$$

$$\gamma_{ref} = 2.2.\left(I_p/1000\right) \tag{5.9}$$

- With dynamic test adjustment applied:

$$G/G_{max} = 1\Big/\left(1 + \left(\gamma/\gamma_{ref}\right)^{0.94}\right) \tag{5.10}$$

$$\gamma_{ref} = 3.7\left(I_p/1000\right) \tag{5.11}$$

where I_p is the plasticity index expressed numerically.

The laboratory results for the soils presented (for the Port Alma and Wallaceburg clay) in Figure 5.25 compare very favorably with the studied empirical models. The Hardin-

Drnevich relationship can be used to fit the data in most situations, however the modified hyperbolic model seems to overestimate G/G_{max} for these soils at shear strain levels greater than 0.3%. On the other hand, the Vardanega-Bolton model, with the static test adjustment, underestimates the shear modulus degradation at levels below 0.03%. Whereas, in the case of the dynamic test adjustment, better estimates G/G_{max} occur for shear strains below 0.02%. Test results from Ahmad (2016) exhibit good agreement with the Vardanega-Bolton model, laying right below the two adjustments at strain levels between 0.2% and 0.4%, and approaching the estimated values by the aforementioned model for strains above 0.4%.

The shear modulus degradation of the Port Alma Clay was compared to a relationship proposed by Vucetic and Dobry (1991) in Figure 5.25. At very small strains, the soil behaves as a medium plasticity clay, and after passing the threshold strain of about 0.008% the stiffness starts to decrease rapidly and the behaviour of the soil shifts from medium plastic to a low plasticity clay. The same observations can be found for the Wallaceburg Clay studied by Kim and Novak (1981). The presence of total carbonates (around 20%) in the Port Alma clay, which may act as a cementing agent between soil particles, suggests the existence of a bonded structure and thus an extra component of strength and stiffness. When this bonded structure breaks down the stiffness starts to decrease drastically. This might explain why the carbonate till exhibits a stiffer response at strains below the observed threshold and behaves more like a medium plasticity clay, compared to the response at higher levels of strains when it changes to that of low plasticity clay. Ng et al. (1995) reported similar observations when studying the small-strain stiffness of heavily overconsolidated Gault Clay which was found to have up to 30% of calcium carbonate content.

The damping ratio curves obtained from the RC test on 0° and 90° rotation samples at p'=160 kPa are shown in Figure 5.26. These were compared against three different models to assess their validity. Two of the empirical models used were proposed by Darendeli (2001) and Zhang et al. (2005). The third one, was obtained from the well-known family of damping ratio curves developed by Vucetic and Dobry (1991). Darendeli (2001) used a broad soil database from different research projects to develop his model. The databased comprised of a combination of RC and cyclic torsional shear (CTS) tests carried out on intact soil samples. The tested soils ranged from natural clean sands to clays from sampling depths (3-263 m), confining pressures (0.3-27.2 atm), I_p (0-132%) and OCR (1-8). A statistical analysis of the database was undertaken to calibrate all of the required parameters for the empirical model. The model takes into consideration the influence of: number of cycles, loading frequency, overconsolidation ratio, mean confining pressure and plasticity.

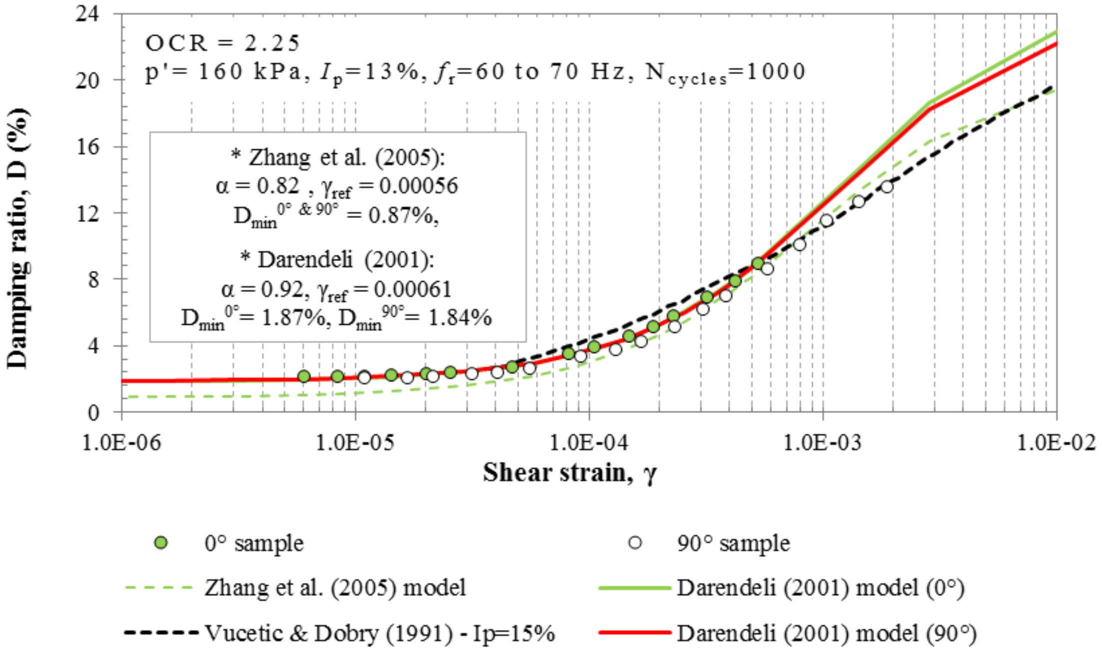

Figure 5.26: Damping ratio obtained from RC test at p'=160 kPa for 0° and 90° samples, compared to empirical models

Likewise, Zhang et al. (2005) developed a series of predictive equations to estimate the damping ratio of Quaternary, Tertiary and older residual soils. The equations are based on a modified hyperbolic model and a series of statistical analysis of existing RC and CTS tests results from 122 soil specimens obtained from the southeastern United States. Factors considered in the development of the model were restricted to shear-strain amplitude, confining stress, and plasticity index. The equations to estimate the damping ratio are expressed in terms of a polynomial function of normalized shear modulus and a minimum damping ratio. On the other hand, Vucetic and Dobry (1991) performed a compilation of the results from an extensive number of studies that included a variety of soil types, testing equipment and cyclic test types. Representative G/G_{max} and damping ratio curved were graphically fitted to produce a family of curves for modulus reduction and damping ratio. Vucetic & Dobry (1991) indicated that the proposed charts are recommended for preliminary studies only due to high data scatter presented within their dataset. It is also stated that soil data ranges from clean sands to clays, encompassing wide overconsolidation ratios (1-15) and plasticity indexes (0-175%).

From Figure 5.26 it is clear how the damping ratio for both 0° and 90° samples are almost identical (0°=2.17; 90°=2.05) at very small to small strain levels between 6×10^{-6} to 6×10^{-5}, after which the damping ratio of the 0° sample starts to increase somewhat more rapidly than that of the 90° sample. The damping ratio estimated using the Darendeli (2001) model at very small to small strains is very similar to that obtained from the RC test for the tested Port Alma samples. Conversely, the minimum damping ratio obtained using the polynomial function of Zhang et al. (2005) underestimated the experimental values obtained from the RC test by around 40%. Due to the limitations presented by the Vucetic and Dobry (1991) model, comparisons between this model and the RC results could not be done for very small to small strain range. For shearing strains between 6×10^{-5} and 5×10^{-4}, the estimated damping ratios using both Darendeli (2001) and Zhang et al. (2005) models predict the rate of increase and values obtained from the RC tests reasonably well, whereas the Vucetic and Dobry (1991) exhibit an overestimation of the damping ratio values for similar shearing strains range. The Vucetic and Dobry (1991) and Zhang et al. (2005) models better predict the increasing of damping ratio for strains higher than 5×10^{-4}.

5.5.3 Stiffness with depth through the soil profile

As mentioned on Section 3.5.2, different *in-situ* tests were used to assess the stiffness of the Port Alma soil deposit with depth (e.g. SCPTu, CST). Figure 5.27 shows estimates of the shear wave velocity (V_s) and shear modulus (G) with depth. These include results from SCPTu, CST, BE, RC tests, and empirical correlations proposed by Hardin and Black (1969), and Kim and Novak (1981). These empirical correlations depend upon the soil properties such as the void ratio (e), overconsolidation ratio (OCR) and effective mean stress (σ_m'):

- Hardin and Black (1969):

$$V_s = (159 - 53e).OCR^{K/2}.\sigma_m{'}^{0.25} \qquad (5.12)$$

$$G = 1576\left(\frac{2.973 - e}{1 + e}\right).OCR^{K}.\sigma_m{'}^{n} \qquad (5.13)$$

- Kim and Novak (1981):

$$V_s = (73.03 - 33.86e).OCR^{K/2}.\sigma_m{'}^{0.25} \qquad (5.14)$$

$$G = 767\left(\frac{2.973 - e}{1 + e}\right).OCR^{K}.\sigma_m{'}^{n} \qquad (5.15)$$

where *K* is a function of plasticity index and *n* equal to 0.65.

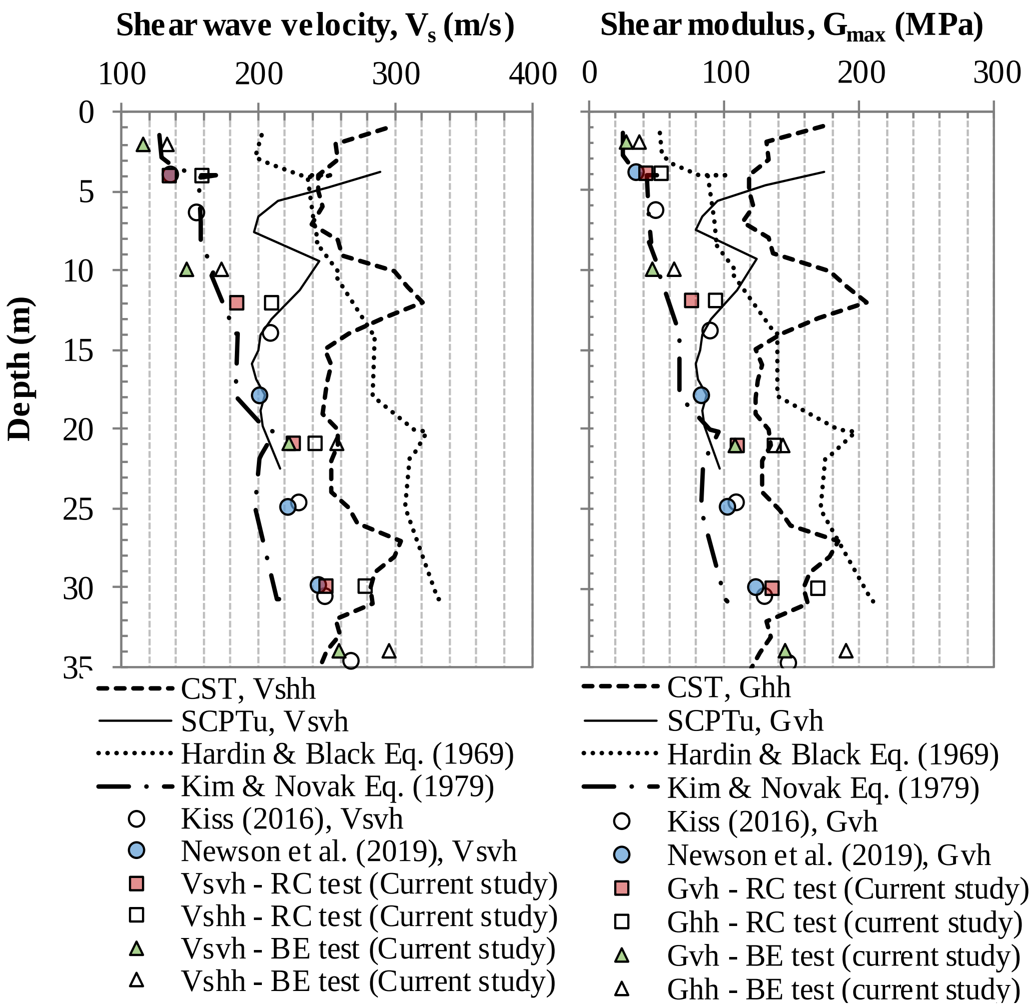

Figure 5.27: V_s and G_{max} variation with depth for Port Alma soil deposit estimated by *in-situ* and laboratory means, and empirical correlations

From the SCPTu, the measured shear wave velocity in the weathered zone was found to be between 210 to 300 m/s, while in the unweathered till it ranged between 200 to 250 m/s. From CST, the shear wave velocity in the upper crust was measured at 294 m/s and 255 m/s and in the lower crust was 257 m/s and 244 m/s. The shear wave velocity measured in the unweathered till ranged from 240 m/s to 320 m/s. The correlations have similar trends to each other, showing an increase of Vs and G with depth, however Equations 5.11 and 5.12 provide higher estimates compared to Equations 5.13 and 5.14, delimiting an upper and lower bound for the velocities and small-strain stiffness. Values of V_s and G from SCPTu and CST fall within the upper and lower limits set by the empirical correlations, as well as the values calculated by Kiss (2016), Newson et al. (2019) and the current investigation, by means of BE and RC tests. Laboratory measurements of V_s, and subsequent estimation of G, are in good agreement with the field data for depths below 10 m as shown in Figure 5.27.

Pennington et al. (1997) and Ng et al. (1995) reported values of shear wave velocity and shear modulus for Gault Clay and London Clay obtained by Butcher and Powell (1995) using geophysical methods such as seismic cone, Rayleigh method and Refraction method. Pennington et al. (1997) also performed bender element testing to estimate the shear wave velocity of Gault Clay samples to compare with the values found by Butcher and Powell (1995) from seismic cone. This comparison showed that the laboratory results were slightly higher than those from the field testing. Similarly, Ng et al. (1995) compared both Rayleigh and Refraction methods results by Butcher and Powell (1995) for Gault Clay and London Clay respectively. They concluded that the shear stiffness of the two stiff clays had some discrepancies and the measurements made by the refraction method were considerably higher than the measurements made using the Rayleigh method.

5.5.4 Small-strain stiffness anisotropy behaviour

Figure 5.28 presents comparisons between the previously shown Port Alma data and a study performed by Yimsiri and Soga (2011), where they investigated the cross anisotropic small-strain elastic parameters of London and Gault Clay proposing linear relationships for both clays as a function of void ratio. Even though the slope of the power relationships shown in Figure 5.28 are slightly steeper, the measured properties of the Port Alma unweathered till follow a similar trend that is comparable to both London and Gault Clays, which have also been reported to show stiffness anisotropy. Likewise, values of normalized G_{vh} and G_{hh} of Chicago glacial clay (Cho, 2007, Kim and Finno, 2012) are shown in Figure 5.28 and compared against the results of Port Alma unweathered till obtained from this study. Although the Chicago glacial clay exhibit a much stiffer response in the small-strain range compared to the Port Alma material, the comparison between these two showed a better correlation, since the slope of the power relationships of both materials are very similar.

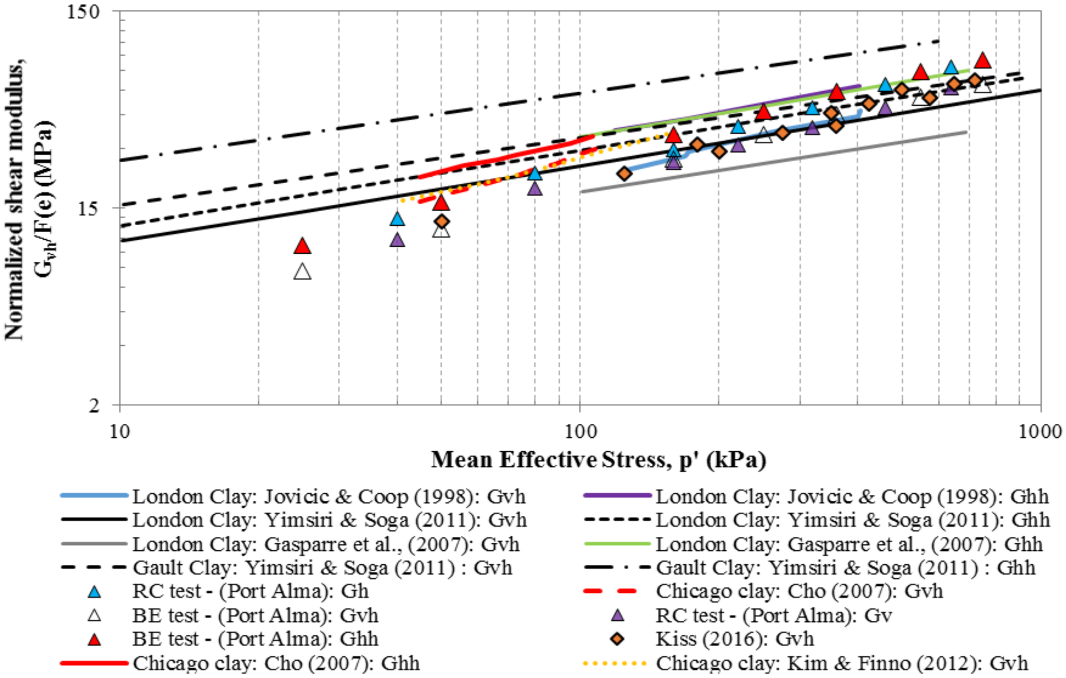

Figure 5.28: Normalized small-strain shear modulus with increasing of isotropic confining pressure

The small-strain shear modulus, in the vertical and horizontal directions, of the Port Alma unweathered clay can be represented by Equation 5.16 and 5.17. Both equations were obtained combining the results of from both the BE and RC tests, as well as using the data reported by Kiss (2016) on the values of G_{vh}. Likewise, Equations 5.18 and 5.19 represent the small-strain shear modulus in the vertical and horizontal directions of the Chicago glacial clay. These were obtained using the available data reported by Cho (2007) and Kim and Finno (2012) The relationships obtained by Yimsiri and Soga (2011) on the London and Gault clays are presented in Equations 5.20 to 5.23.

- Port Alma unweathered till:

$$G_{vh} = 1.035F(e)p'^{0.635} \quad [MPa] \tag{5.16}$$

$$G_{hh} = 1.324F(e)p'^{0.637} \quad [MPa] \tag{5.17}$$

- Chicago glacial clay (Cho, 2007; Kim and Finno, 2012):

$$G_{vh} = 1.522F(e)p'^{0.628} \quad [MPa] \tag{5.18}$$

$$G_{hh} = 2.791F(e)p'^{0.538} \quad [MPa] \tag{5.19}$$

- London clay (Yimsiri and Soga, 2012):

$$G_{vh} = 4.250F(e)p'^{0.380} \quad [MPa] \tag{5.20}$$

$$G_{hh} = 5.10F(e)p'^{0.380} \quad [MPa] \tag{5.21}$$

- Gault clay (Yimsiri and Soga, 2012):

$$G_{vh} = 7.150F(e)p'^{0.340} \quad [MPa] \tag{5.22}$$

$$G_{hh} = 12.00F(e)p'^{0.340} \quad [MPa] \tag{5.23}$$

Table 5.7 shows values of shear wave velocity and shear modulus in the vertical and horizontal directions from an unweathered till sample subjected to mean effective stress of 160 kPa (estimated *in-situ* condition). One measure of anisotropy is the ratio of $\alpha=G_{hh}/G_{vh}$. For Port Alma the ratio is equal to 1.26, suggesting a larger horizontal stiffness than vertical stiffness. This compares to London Clay with α =1.5-2.5 (Gasparre et al., 2007; Yimsiri and Soga, 2011), Gault Clay α =1.35-1.6 (Pennington et al., 1997; Yimsiri and Soga, 2011) and Chicago Glacial Clay α =1.1-1.4 (Finno et al., 2012; Kim and Finno, 2012), which all have higher horizontal than vertical stiffness. Figure 5.29 shows a comparison between values of α from these different materials. From this data, one can infer that the depositional environment and post-depositional stresses have had a significant effect on the anisotropic stiffness ratio α, and overall an the small-strain stiffness at different planes of the soil. For example, London and Gault Clays were deposited in glaciomarine environments during the late Cretaceous period and has been folded and eroded significantly since then, whereas the Chicago Glacial clay is a till deposited subglacially at the ice margin (basal till) with a complex post-depositional stress history during the Pleistocene epoch.

Table 5.7: Stiffness properties in the vertical and horizontal directions from RC test

Vertical direction	V_{svh}	225.17	m/s
(0° rotation sample)	G_{vh}	109.11	MPa
Horizontal direction	V_{svh}	242.05	m/s
(90° rotation sample)	G_{hh}	136.93	MPa

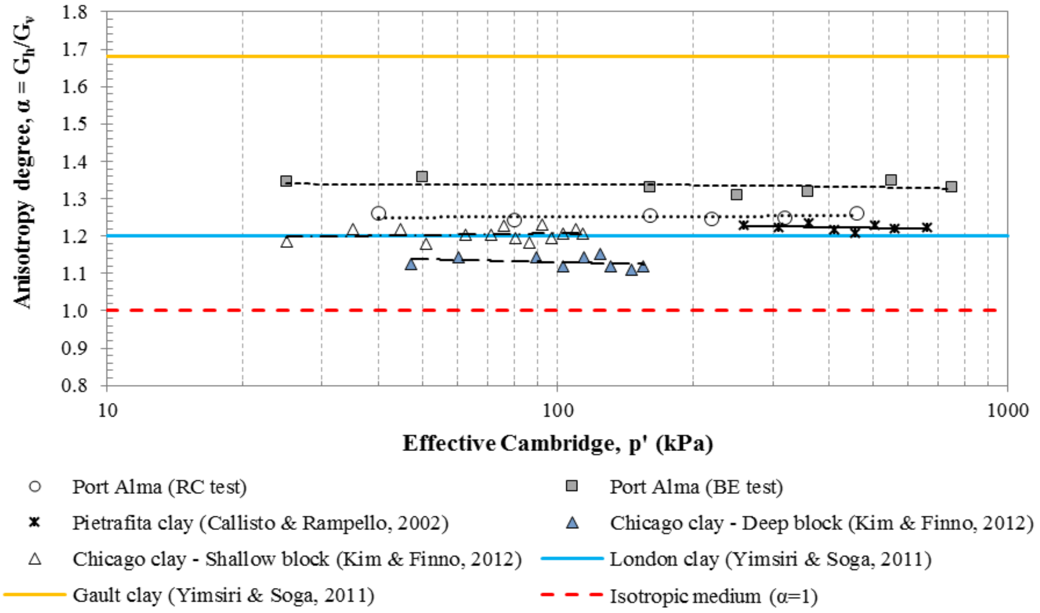

Figure 5.29: Anisotropy degree variation with increasing of isotropic confining pressure for different cohesive materials

The Port Alma material is believed to be a Tavistock Till and is understood to be a soft, waterlaid deposit occupying the boundary between glacial and glaciolacustrine sediments and is genetically a till, but has been deposited in an aqueous environment (likely as a slurry below an ice sheet). In general, these types of till can only be distinguished from glaciolacustrine sediments by their coarser textures (Dreimanis, 1976). This view is supported by previous paleomagnetic measurements made on this material, which show a strong component of detrital remanent magnetization formed when magnetic particles in the till were released through water or slurry at the base of an ice sheet. The anisotropic stiffness ratio (α) data found in the literature suggest that for soils with glaciogenic origin like the Port Alma glacial till, α values are bigger than 1 and therefore have higher stiffness in the horizontal than vertical direction.

5.6 Summary

This chapter presents a review of the results obtained from different advanced laboratory techniques employed to characterize the critical state parameters, stress-strain behaviour at small to large strains, and from very small to medium shear strains, and the small-strain stiffness anisotropy of soil samples recovered from the Port Alma wind farm. The soil material is characterized as a low plasticity glacial till rich in carbonates deposited during the late Wisconsin stage of the Pleistocene epoch. Previous paleomagnetic tests on soil material from the same area showed that the soil fabric had a preferred orientation with respect to that of the ice flow when the material was deposited.

Results from CIU tests showed that the critical state behaviour of the Port Alma unweathered glacial till material is comparable to that of similar tills found in the literature. Similarly, the normalized stiffness degradation measured using local measurement of strain during CIU tests under *in-situ* conditions, showed that the Port Alma till follows similar degradation rates when compared to other low plasticity glacial tills and ‘till-like’ materials found within the literature. Likewise, it was shown from results of the RC tests that the small-strain stiffness of the Port Alma material is almost constant at very small shearing strains, and after reaching a threshold strain of about 4×10^{-4} the stiffness becomes highly non-linear and starts decreasing with increasing strain, thus the stiffness of the material is shown to be strain dependent.

From results of multidirectional BE transducers and RC test on vertically and horizontally trimmed samples subjected to isotropic confining pressures, it was found that small-strain stiffness of the material is higher in the horizontal direction (direction perpendicular to deposition) than the one measured in the vertical direction of the soil specimens. From these it was noted that the small-strain stiffness of the Port Alma glacial till is anisotropic and dependent on the fabric characteristics of the material. The *in-situ* anisotropy ratio (α) of the unweathered till ranges from 1.2 to 1.35 and is believed to have been deposited subglacially in an aqueous environment. Similar α values have been reported in the literature for other cohesive soils of glacial origin (e.g. Pietrafitta clay, London clay, Gault clay and Chicago glacial clay).

Chapter 6

6 Summary of experimental results on *different cohesive* materials

A summary of the results obtained from a series of advanced laboratory stress-strain tests carried out in this investigation on a selection of *different cohesive* materials is presented in this chapter. This testing included the use of: consolidated isotropic undrained (CIU) triaxial tests with local strain measurements, CIU tests with vertical and horizontal bender elements to measure orthogonally propagated shear and compressional wave velocities, and resonant column tests on vertically and horizontally trimmed soil specimens. These laboratory techniques were employed to study the stress-strain behaviour and critical state soil parameters, the stiffness degradation behaviour across a range of strains from very small to large, and the small-strain stiffness anisotropic behaviour of these cohesive materials. The laboratory procedures used are discussed thoroughly in Chapter 4 with a detailed description of the testing programme (see Section 4.3.1).

From the materials selected for testing, five of these are natural cohesive soils of glacial origin, and one is a manufactured clay called Edgar plastic kaolin 'EPK' clay formed under controlled laboratory conditions. The natural glacial materials were found at different sites around southwestern Ontario and Manitoba; specifically from the localities of Windsor, Wallaceburg, Blenheim, Port Alma, and Winnipeg. The properties of these soils vary from soft glacial clays to highly overconsolidated clays of low to medium plasticity. The analyses performed on these materials are complementary with the available geotechnical data for Port Alma clay (Newson et al., 2019; Kiss, 2016), Wallaceburg clay (Lo & Becker, 1978; Kim & Novak, 1981), Blenheim clay (Reipas, 2012), Windsor clay (Kim and Novak, 1981), Winnipeg clay (Baracos et al., 1980; Graham & Houlsby, 1983), and 'EPK' kaolin clay (Reipas, 2012; Sasanian, 2011). A summary of basic geotechnical properties of these materials is presented in Chapter 4, whereas a more detailed review of existing information can be found in Appendix B.

6.1 Basic geotechnical characteristics of tested soils

6.1.1 Consistency limits, plasticity, mineralogy, and critical state

Values of consistency limit, plasticity and mineralogy as obtained by Newson et al. (2019), Kim and Novak (1981) and Reipas (2012) for the different natural clays tested in this investigation, and previously presented in Section 4.3, are shown in Figures 6.1 and 6.2. Figure 6.1 shows the Casagrande plasticity chart showing the range of plasticity values for glacial lake clays reported by Casagrande (1947) and an envelope obtained by Soderman et al. (1960) for different glacial clay soils from southern Ontario. Data published by Kim and Novak (1981) for other glacial materials from different parts of southern Ontario have also been plotted for reference. The Atterberg limits of Port Alma clay, Wallaceburg clay and Blenheim clay correspond well with the envelope reported by Soderman et al. (1960) and lie within the limits reported by Casagrande (1947). Very close to the right-hand side of the envelope lies Windsor clay, which also sits within the upper limit established by Casagrande (1947) known as the “T-line”. Winnipeg clay lies on top of the “A-line”, farther away from the envelope of the southwestern Ontario glacial clays suggesting that the matrix of the material is mainly clay, and that the sedimentary minerals present in the soil may differ from those of the other southwestern Ontario glacial soils due to the nature of its parent material. It is also noticeable that the Atterberg limit values indicate that the plasticity of the studied material ranges from low to medium ($6 < I_p < 33$), which corresponds to typical values of plasticity index reported in the literature for different glacial clay tills and ‘till-like’ materials (e.g. Trenter, 1999; Kim and Novak, 1981; Lo and Becker, 1983).

Values of activity (ratio of plasticity index to clay fraction) reflect the mineralogy of the clay fraction (Soderman et al., 1960) and for the studied soils, the activity ranges from 0.26 to 0.54. This suggests that these materials are within the range of inactive clays (activity < 0.75) and close or within the range for previously studied glacial soils (0.29 < activity < 0.49) as shown in Figure 6.2. These low values of activity indicate that the materials do not have a significant amount of active clay material, such as vermiculite or montmorillonite. Previous studies on the minerals present in different Ontario glacial clays showed the presence of carbonates, quartz, chlorite, feldspar and illite (Quigley 1980; Quigley et al.

1976, 1985). Similar findings were reported by Wu (1958) and Chung and Finno (1992) when studying local glacial deposits around the Chicago area in the United States.

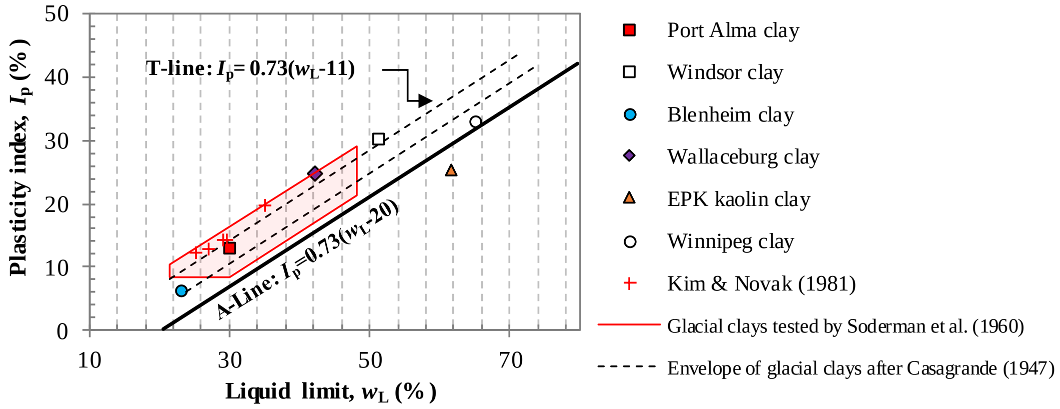

Figure 6.1: Relationship between plasticity index (I_p) and liquid limit (w_L) of different glacial clays

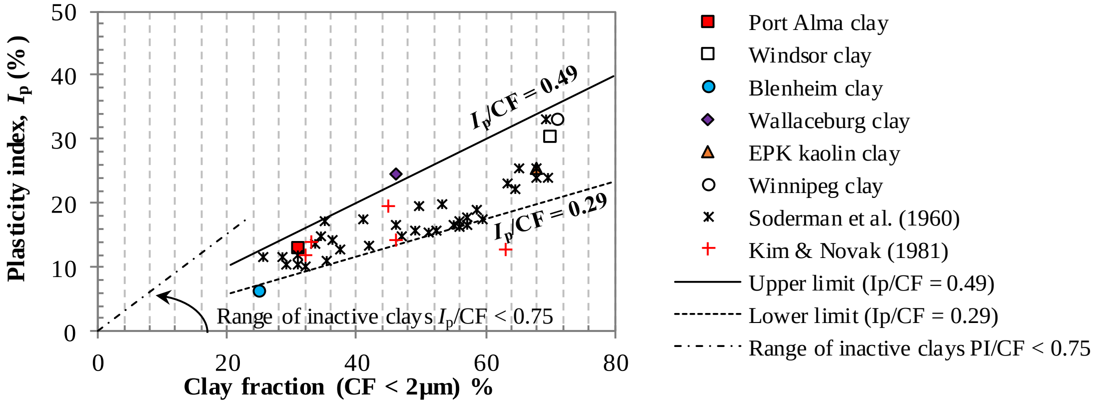

Figure 6.2: Activity of different glacial clays

Terzaghi and Peck (1967) recognized that decreasing angles of friction (ϕ'_{CS}) occur with increasing plasticity index (I_p) for different clay materials. The angle of friction can be linked to the slope of the critical state line in q:p' space (M) through Equation 6.1:

$$M = \left(\frac{6 \sin \phi'_{CS}}{3 - \sin \phi'_{CS}}\right) \qquad (6.1)$$

Values of M were obtained from consolidated isotropic undrained (CIU) triaxial tests for the different materials used in this investigation. These were plotted along with published data for different soils, including glacial clays and tills from Canada and the rest of the world (Trenter, 1999; Soderman et al., 1960; Mitchell, 1976; Ahmad, 2016) in Figure 6.3. It is clear that there is a reduction in M with increasing plasticity index and it can also be inferred that this reduction may also be associated with increasing clay fraction of the different materials. Stark et al. (2005) suggested that the angle of friction is actually a function of the clay mineralogy and clay fraction. The results shown in Figure 6.3 also suggest that M values for Canadian glacial soils may vary between 1.5 to 0.8 (approximately ϕ'= 35° to 20.5°) taking into consideration the data obtained from Soderman et al. (1960) and Ahmad (2016) for different cohesive soils of glacial origin and those used in this study.

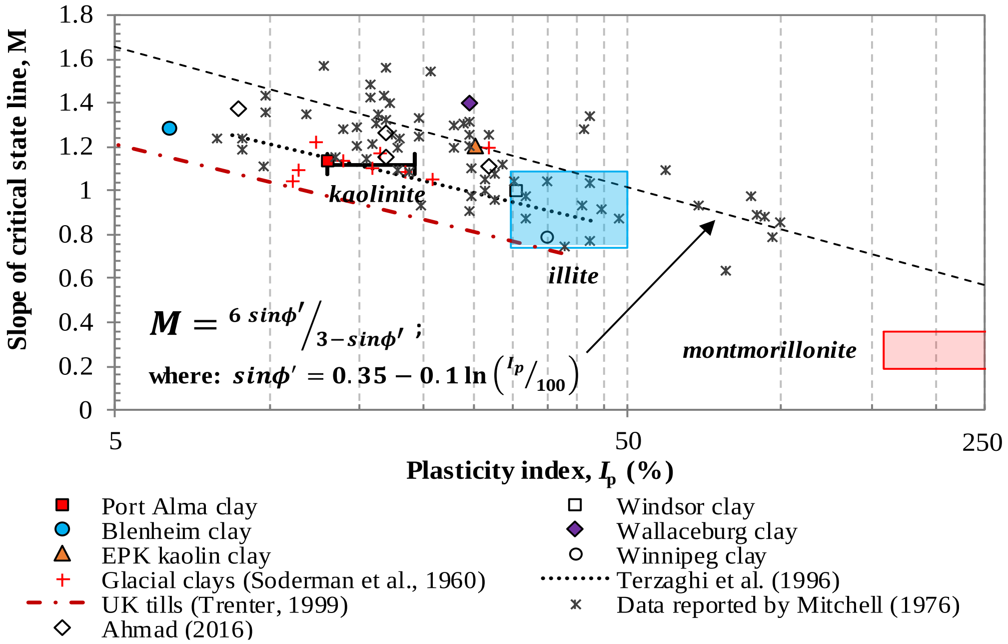

Figure 6.3: Relationship between plasticity index (I_p) and critical state parameter (M) for different glacial clays

A summary of the geotechnical properties of the materials obtained from the current investigation and gathered from previous studies, are presented in Table 6.1. Results from the triaxial tests carried out on the glacial clays show similarities in the critical state behaviour when subjected to undrained shearing under isotropic pressures. The soil samples exhibit strain-hardening with increasing of axial strain during the shearing stage as shown in Figure 6.4. This supports the hypothesis regarding the overconsolidated nature of these glacial clays (Atkinson and Little, 1983). Likewise, the measured stiffness degradation (G_{sec}) with local instrumentation for the tested soils follow similar degradation rates when compared to other low to medium plasticity glacial till and ‘till-like’ materials found in the literature. Further critical state soil mechanics interpretations and stress-strain results of the studied glacial clays are presented in Appendix D.1.

Table 6.1: Summary of critical state parameters and properties of the different glacial clay and cohesive materials tested

	Port Alma	*Windsor*	*Blenheim*	*Wallaceburg*	*EPK kaolin*	*Winnipeg*
I_p (%)	13.00^{1}	30.30^{2}	6.40^{3}	24.60^{2}	25.40^{3}	33.00
M (CSL)	1.14	1.00	1.28	1.40	1.21	0.793*
ϕ' (°)	28.62	25.41	31.90	34.67	30.33	20.50*
λ (NCL)	0.041	0.174	0.062	0.175	0.162	0.159
k (URL)	0.011	0.049	0.018	0.031	0.043	0.060
N	0.646	1.646	0.743	1.620	1.802	1.766
$\Lambda=1-(k/\lambda)$	0.732	0.718	0.714	0.821	0.735	0.621
Γ	0.625	1.559	0.712	1.520	1.720	1.697
CF (%) (<2µm)	31.0^{1}	70.0^{2}	25.0^{3}	46.0^{2}	68.0^{3}	71.0^{4}
Activity (I_p/CF)	0.419	0.433	0.256	0.535	0.373	0.465

CF: clay fraction; *Baracos et al. (1980); **Graham & Houlsby (1983); ^{1}Newson et al. (2019); ^{2}Kim & Novak (1981); ^{3}Reipas (2012); ^{4}Trek-Geotechnical

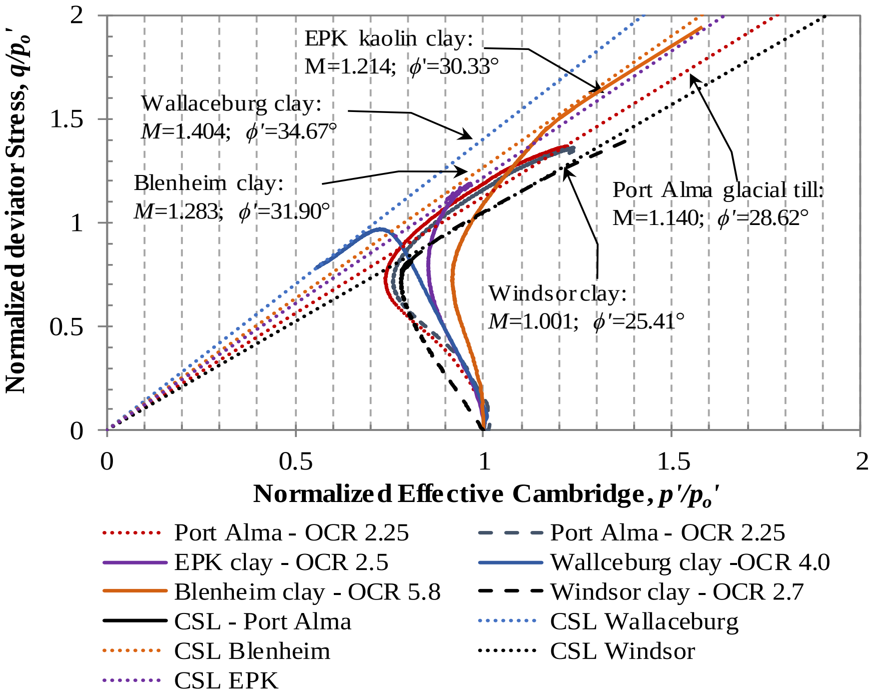

Figure 6.4: Effective Cambridge stress vs. deviator stress of the different glacial clays under CIU tests normalized by the effective consolidation pressure at shear

6.2 Small-strain behaviour from bender element and resonant column tests

The small-strain behaviour the cohesive materials was investigated using a combination of orthogonal plane bender elements (BE) and resonant column (RC) testing on vertically and horizontally trimmed samples. These results are presented in the following sections.

6.2.1 Summary of results from bender elements (BE) tests

Bender element (BE) tests were carried out following the procedures outlined in Section 4.3.7. In general, three pairs of orthogonal bender element (BE) transducers were arranged as follows: one pair of BEs were placed on the top and bottom of the soil specimens (vertical direction), while the other two pairs were laterally mounted (horizontal direction) on the soil specimens (see Figures 4.6 and 4.8). The vertical pair of BE allowed the measurement of vertically propagating and horizontally polarized shear wave velocities (V_{svh}), whereas the horizontal pairs of BE allowed the measurement of horizontally propagating and vertically polarized shear waves velocities (V_{shv}), and horizontally propagating and horizontally polarized shear waves velocities (V_{shh}). For each of the materials, the measurement of shear wave velocities was performed under isotropic compression and swelling pressures. A complete set of results showing the measured shear wave velocities and the estimated small-strain shear modulus for each material, in both vertical and horizontal directions of the samples, are presented in detail in Appendix D.2.

A summary of vertically propagated and horizontally polarized (V_{svh}) shear wave velocities measured with the increasing effective pressure (p') is shown in Figure 6.5. Similar trends are exhibited by the different materials, where propagating shear wave velocities (V_{svh}) increase with increasing p'. Such behaviour has been previously reported in the literature (e.g. Hardin and Richart, 1963; Ishihara,1996), and has been attributed to the relationship between the propagating velocities of the body waves (S-waves and P-waves) with respect to the stiffness and density of the soil. Similar observations were noted for horizontally propagated and horizontally polarized waves (V_{shh} and V_{phh}) as shown in Appendix D.2.

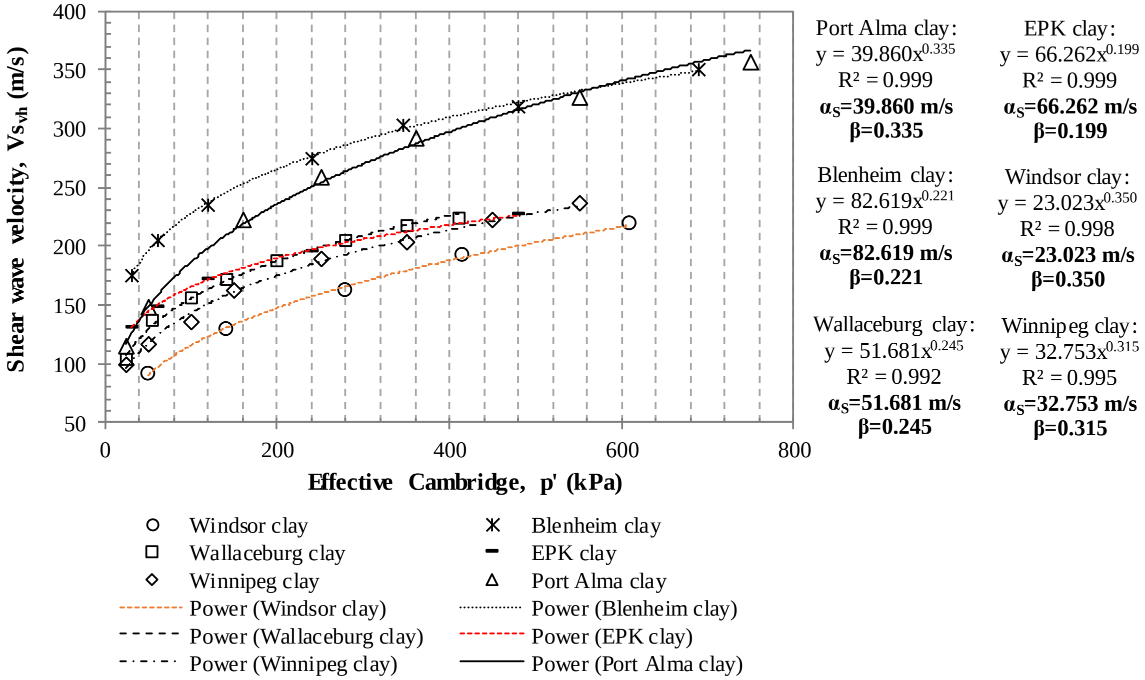

Figure 6.5: Shear wave velocities measured from vertically polarized-horizontally propagating shear waves (V_{svh}) with increasing effective pressure

Another noticeable feature in Figure 6.5 is the difference between measured values of V_{svh} at similar confining pressure between the materials; this also applies for V_{shh}. It can be seen how the soils with higher plasticity (I_p), such as Windsor clay and Winnipeg clay, have lower values of V_{shv} compared to the other soils with lower I_p, such as Port Alma and Blenheim clay. For cohesive soils, Hardin and Black (1968), Kim and Novak (1981) and Vucetic and Dobry (1991) found that I_p and the overconsolidation (OCR) ratio exert a great influence when measuring V_{svh}. Power law curves were fitted using the least squares method to the results and are shown in Figure 6.5, such equations follow the same form of the velocity-stress power relationship reported by Cha et al. (2009, 2014):

$$V_s = \alpha_s (p')^{\beta} \tag{6.2}$$

where α_s is the shear wave velocity at p' = 1 kPa and the β exponent captures the sensitivity of the skeletal shear stiffness to the applied stress. These parameters reflect the contact behaviour and fabric changes linked with changes in the effective stress (Cha et al., 2009). For the studied materials, α_s ranges from 23 m/s to approximately 82 m/s, while the exponent β ranges between 0.20 to 0.35, respectively. For the V_{shh} power law curves, α_s and β yielded ranges of 31 m/s to 73 m/s and 0.20 to 0.33, respectively. Notably, Vs_{hh} values were consistently higher than Vs_{vh} throughout the tests, for the Port Alma, Winnipeg, Windsor, Wallaceburg and EPK clays. The opposite situation was found for the Blenheim clay, where Vs_{vh} was slightly higher than Vs_{hh}.

Figure 6.6 shows the estimated small-strain shear modulus in the vertical direction (G_{vh}) for the various materials. Similar trends and behaviour to the results for V_{svh} can be observed for G_{vh} in Figure 6.6. This would be expected since as the shear modulus is a function of the shear wave velocity and soil density. The small-strain shear modulus in the horizontal direction (G_{hh}) for Port Alma, Winnipeg, Windsor, Wallaceburg and EPK clays was consistently higher than G_{vh} for the tests. The exception is Blenheim clay where G_{hh} was somewhat higher than G_{vh}.

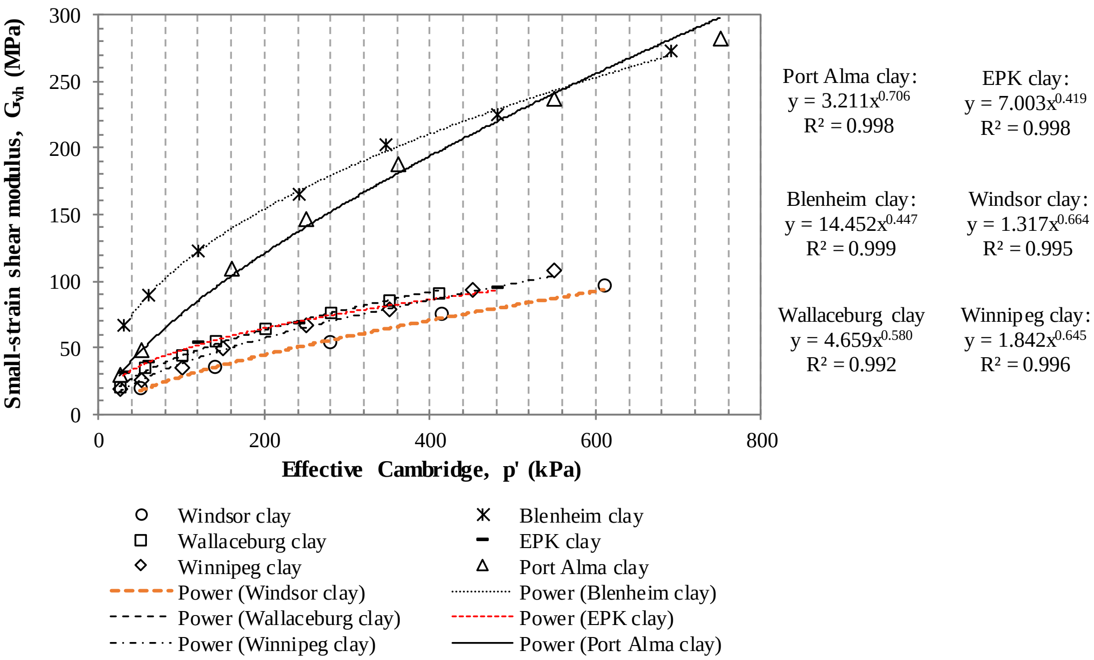

Figure 6.6: Small-strain shear modulus in the vertical plane (G_{vh}) with increasing effective pressure for different cohesive materials

6.2.2 Summary of results from resonant column (RC) tests

Resonant column (RC) testing was conducted in accordance with ASTM D4015-15 and following the procedures outlined in Section 4.3.8. In general, vertical (0° rotation) and horizontal-cut (90° rotation) specimens from the same material were tested. The shear modulus degradation curves from the resonant column tests for the different clay samples cut vertically cut (0° rotation samples) are shown in Figure 6.7. These indicates that the shear modulus (normalized by G_{max}) reduces with shear strain increment. The results show threshold shear strain values, where the modulus begins to reduce, that are similar to other clay soils (e.g. Ishihara, 1996). The threshold shear strain also seems to increase with increasing plasticity index and the OCR appears to have little effect on the observed results, as has been found previously (e.g. Vucetic and Dobry, 1991).

Likewise, damping ratio curves for the tested 0° rotation clay samples were obtained from the resonant column testing and are shown in Figure 6.8. The minimum damping ratio range for these soils lie between 1.8% and 2.2% and the magnitude starts to gradually increase with shear strain increments. Such ranges correspond well with those reported by Kim and Novak (1981) for other clay soils from Southern Ontario.

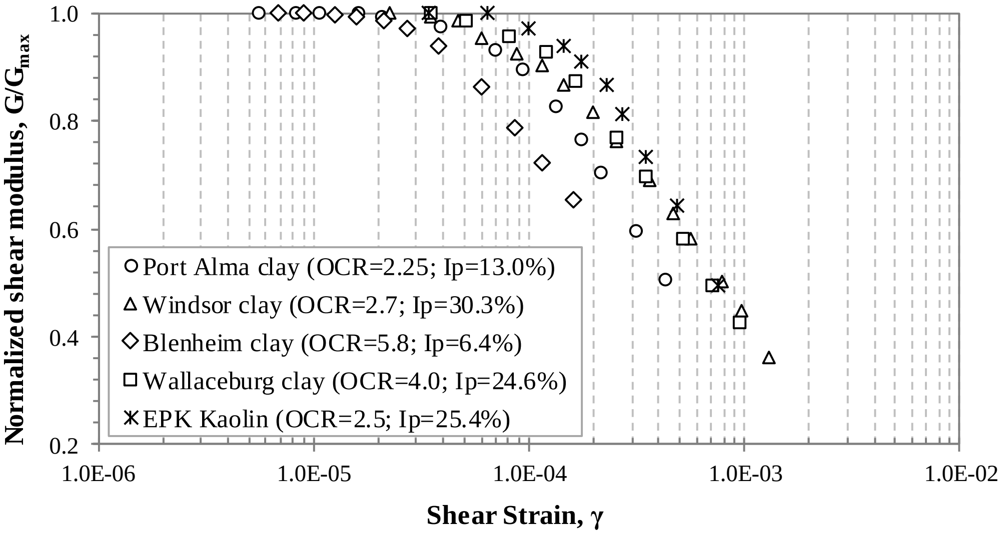

Figure 6.7: Normalized shear modulus degradation with increasing of strain for different cohesive soils tested

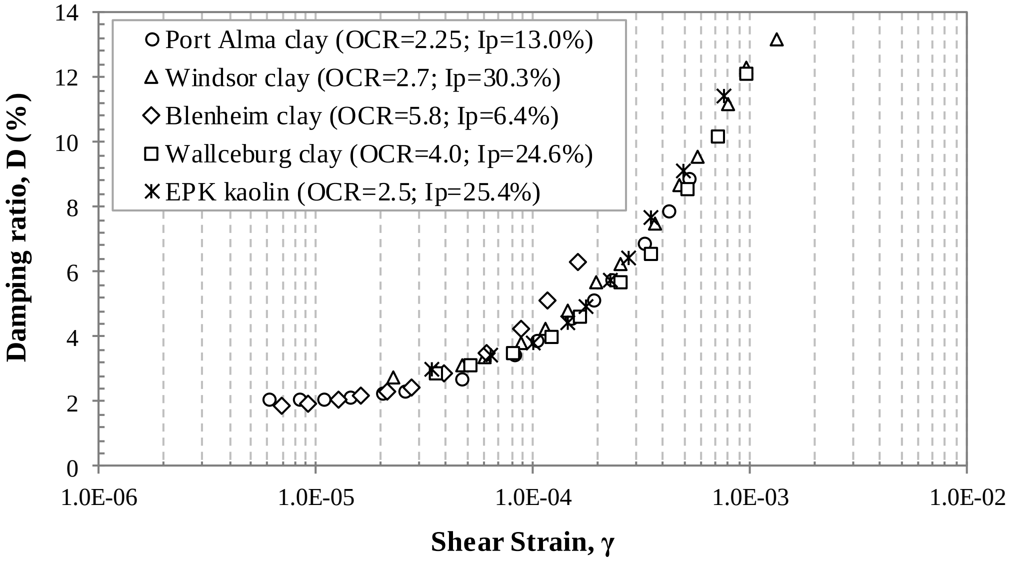

Figure 6.8: Variation of soil damping ratio with increasing of strain for different cohesive soils tested

Measurements of shear wave velocities (V_{svh} and V_{shh}), and estimation of small-strain shear modulus in the horizontal direction (G_h), damping ratio in the horizontal direction (D^h), and Young's modulus in both vertical and horizontal directions (E_v and E_h) were also performed for the different clay materials. These results are shown in more detail in Appendix D.3.

Figures 6.9 and 6.10 show a summary of the measured shear wave velocities (V_{svh}) and estimated small-strain shear modulus (G_{vh}) with increasing effective pressure for 0° rotation samples of Port Alma, Blenheim, Wallaceburg, Windsor, and EPK clay materials. The resonant column results have similar trends and behaviour with increasing of effective pressure, to those found using bender elements (presented in the previous section). Power law curves were again fitted to the data as shown in Figure 6.9, α_s yielded values between 25 m/s to 79 m/s, and β ranged from 0.20 to 0.33. Values of V_{shh} and G_{hh} for 90° rotation samples were consistently higher to those measured for 0° rotation samples. These results are presented in Appendix D.3

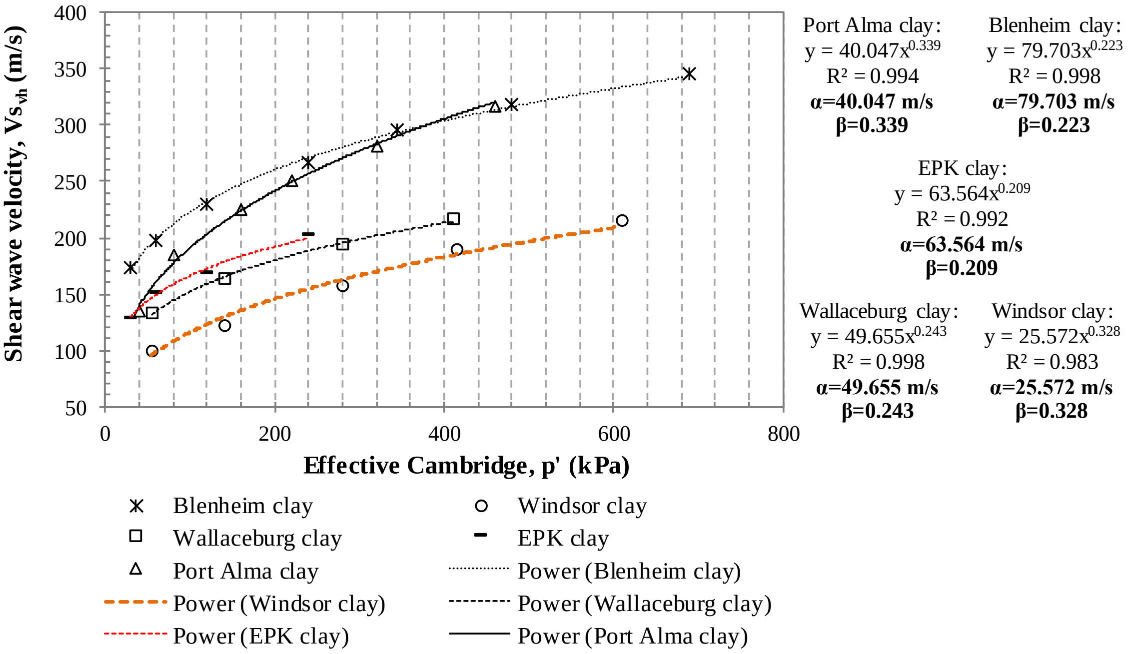

Figure 6.9: Measured shear wave velocity in the vertical direction (V_{svh}) with increasing effective pressure from 0° rotation samples

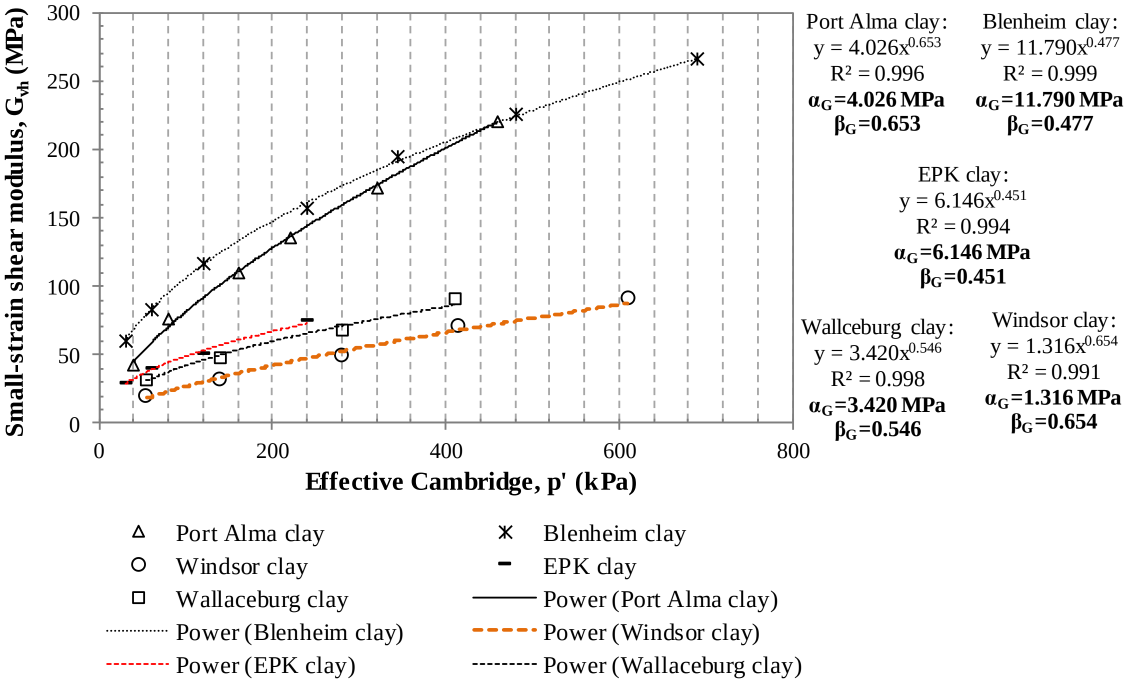

Figure 6.10: Small-strain shear modulus measured in the vertical direction (G_{vh}) with increasing effective pressure for 0° rotation samples

6.2.3 Small-strain stiffness anisotropy of the tested soils

The anisotropy of the small-strain stiffness can be assessed by comparing values of maximum shear modulus (G_{max}) measured in the vertical and horizontal directions of a soil material (Clayton, 2011). This can be characterized with the concept of modular ratio, also known as anisotropic ratio (α). The anisotropic ratio is defined as the ratio between G_{hh} and G_{vh} ($\alpha = G_{hh}/G_{vh}$). As described throughout sections 6.2.1 and 6.2.2, the small-strain shear modulus G_{vh} and G_{hh} of different clay materials were estimated using measurements of shear wave velocities in the vertical and horizontal planes of such materials (V_{svh} and V_{shh}). As described in the preceding sections, two types of tests were employed to measure shear waves: bender elements and resonant column. The data collected from both tests were compared and found to be very similar. Figures 6.11 and 6.12 show a summary of the calculated anisotropic ratio (α) of the different clay materials for the bender element and resonant column results. These suggest that the six overconsolidated clay materials tested are anisotropic, or at least cross-anisotropic. Moreover, five of the six materials are predominantly stiffer in the horizontal direction, with α ranging between 1.10 to 1.30, while the remaining sixth clay (Blenheim clay) had an average α of around 0.92 suggesting a stiffer behaviour in the vertical direction.

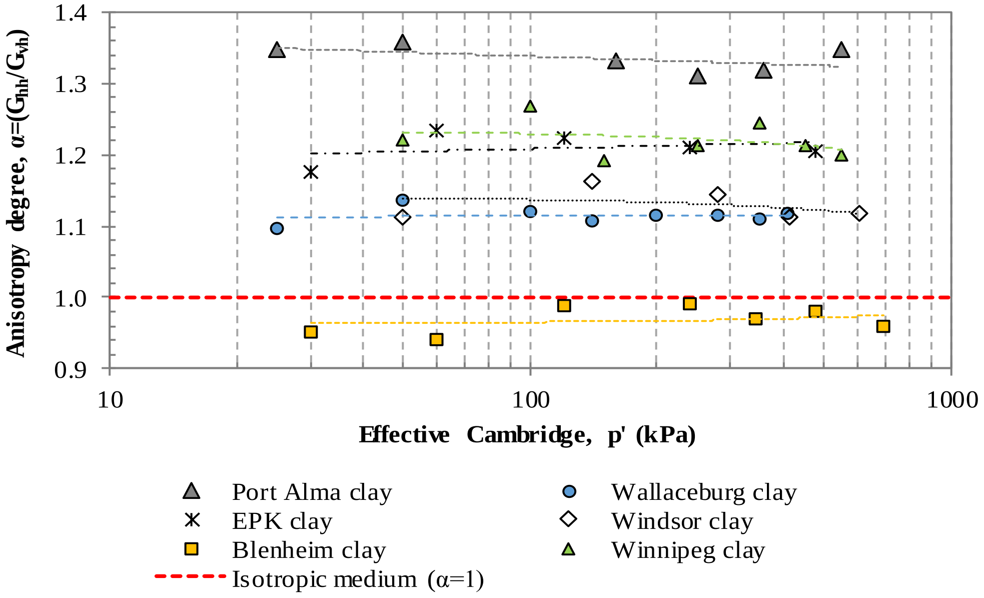

Figure 6.11: Anisotropy degree with increasing isotropic confining pressure for different cohesive materials as measured with the bender elements

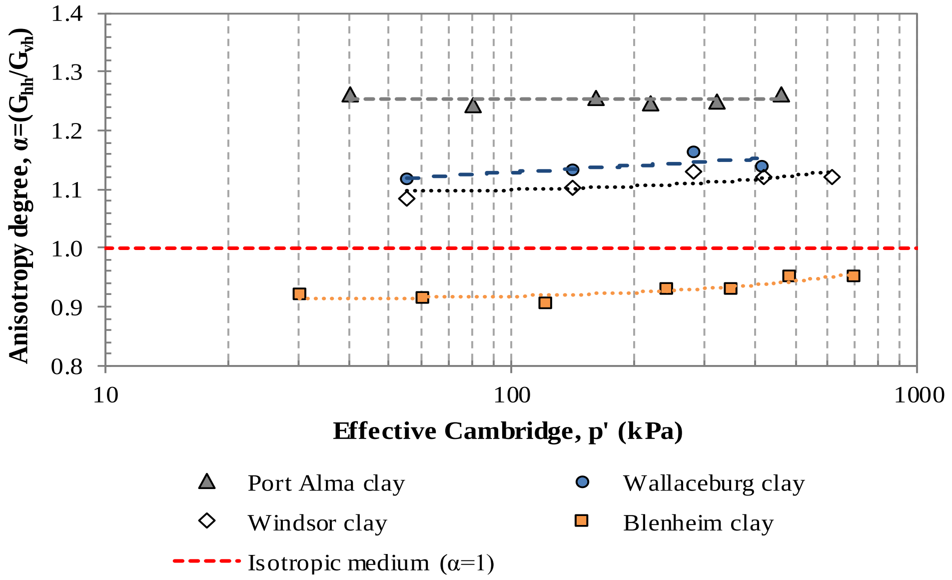

Figure 6.12: Anisotropy degree with increasing isotropic confining pressure for different cohesive materials as measured with the resonant column

To further interpret the change of the vertical and horizontal small-strain shear modulus (G_{vh} and G_{hh}) with pressure from both bender elements and resonant column, Figures 6.13 and 6.14 were created. The shear modulus, G_{vh} or G_{hh}, has been normalized by the void ratio function: $F(e) = (2.973 - e)^2/(1 + e)$, as recommended by Hardin and Black (1968). Best-fit lines for each of the materials were obtained and shown in Figures 6.13 and 6.14, respectively, and Table 6.2 shows a summary of these results. It can be seen that the slopes of the power relationships (*nv* and *nh*) are very similar for Blenheim, Wallaceburg, Windsor and Winnipeg clay ranging between 0.45 to 0.50, whereas Port Alma clay has the largest slope of around 0.65. EPK clay has the smallest of the slopes of approximately 0.26.

Table 6.2: Stiffness constants for different cohesive materials

Material	S_{vh}	S_{hh}	***nv***	***nh***	$\alpha = S_{vh}/S_{hh}$
Port Alma clay	0.955	1.242	0.650	0.645	1.301
Windsor clay	2.901	3.251	0.418	0.403	1.121
Wallaceburg clay	2.694	3.083	0.484	0.447	1.144
Winnipeg clay	2.037	2.562	0.492	0.494	1.258
Blenheim clay	3.653	3.505	0.422	0.444	0.959
EPK clay	9.288	11.22	0.261	0.265	1.208

S_{vh} & S_{hh} are material constants; *nv* & *nh* are empirical stress exponents (Jamiolkowski et al., 1995)

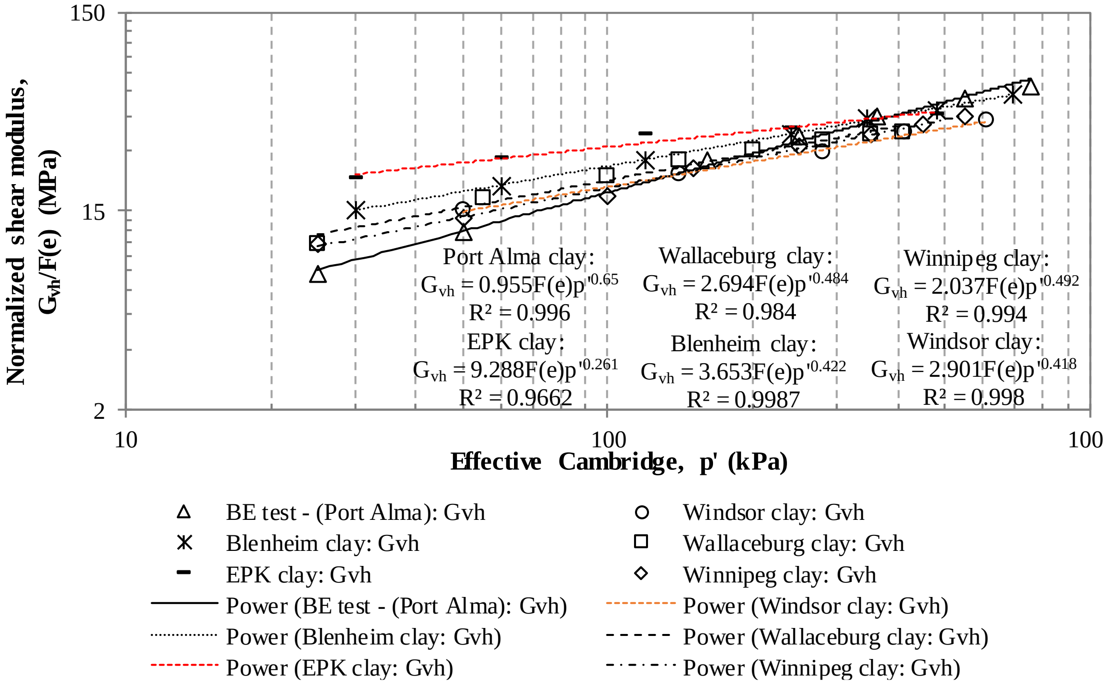

Figure 6.13: Normalized small-strain vertical shear modulus (G_{vh})

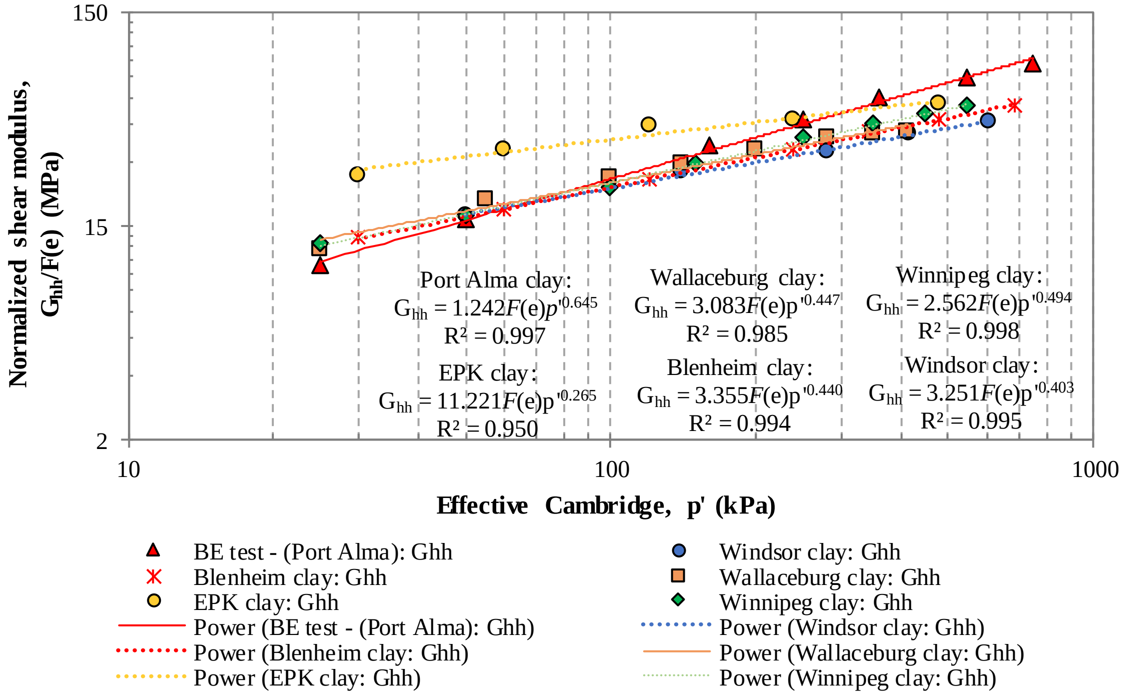

Figure 6.14: Normalized small-strain horizontal shear modulus (G_{hh})

6.3 Discussion of the results

6.3.1 Wave velocity parameters (α_s and β) and their relationship with basic soil properties

Measurements of shear wave velocity, *in-situ* and in the laboratory, have been shown to be a reliable way to determine the small-strain shear stiffness of natural soils (Ishihara, 1996; Cramer, 1996; Clayton, 2011). Throughout this investigation the shear wave velocity of different cohesive overconsolidated materials of low to medium plasticity, have been measured employing two different methods: bender elements (BE) and resonant column (RC) test. These tests have allowed the measurement of vertically propagating and horizontally polarized shear waves velocities (V_{svh}), and horizontally propagating and horizontally polarized shear wave velocities (V_{shh}). Results from both tests carried out under similar conditions were presented in Sections 6.2.1 and 6.2.2. Those results show that the data compiled using the bender elements and resonant column are comparable, further validating the laboratory measurement of the propagating waves and estimation of the stiffness properties of the materials studied herein.

The relationship between shear wave velocity (V_s) and effective confining pressure (p') can be characterized with a power law defined by $V_s = \alpha_s (p')^{\beta}$ (Cha et al., 2009). Both α_s and β were obtained for the different cohesive materials tested. Cha et al. (2014) compiled a database from published studies on wave velocity covering a wide range of soils (e.g. sandy and clayey soils, lightly cemented sands, high-specific surface clays). They proposed an empirical equation that relates β to α_s (see Equation 6.3), such relationship is plotted within Figure 6.15 as a solid red line, along with the data from this study, a compilation of different published wave velocity data of other Canadian clays, cohesive materials studied by Kim and Novak (1981) and those studied by Ahmad (2016). It should be noted that the wave velocity data gathered were obtained under *isotropic* effective stress conditions.

$$\beta = 0.73 - 0.27 \log\left(\frac{\alpha_s}{m/s}\right), 1\,m/s \le \alpha_s \le \sim 500\,m/s \qquad (6.3)$$

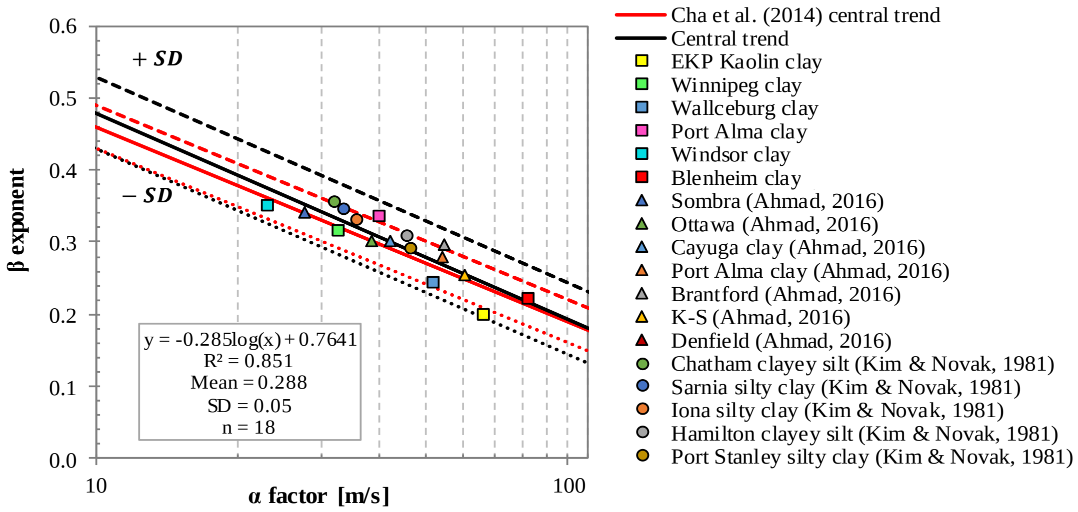

Figure 6.15: Relationship between the α-factor and the β exponent for different glacial and cohesive materials

The wave velocity parameters of the Canadian soils in the database were used to obtain a new empirical correlation of β as function of α_s, this is presented as a revised version of Equation 6.3 in Equation 6.4. The statistical analysis from the regression shown in Figure 6.15 suggests a high correlation (R^2 =0.851) for the proposed empirical correlation using the compiled data of Canadian soils.

$$\beta = 0.764 - 0.285 \log\left(\frac{\alpha_s}{m/s}\right), 10\ m/s\ \leq \alpha_s \leq {\sim}100\ m/s \qquad (6.4)$$

From Figure 6.15 is clear that β decreases with increasing α_s. Cha et al. (2014) attributed this to several factors: increasing soil density, decreasing plasticity, overconsolidation, and soil cementation. Blenheim clay, which has the highest OCR and lowest plasticity, exhibits the highest α_s (80 m/s) and lowest β (0.22) among the soils in Figure 6.15. In contrast, Windsor clay has the lowest α_s (23 m/s) and highest β (0.35) of the soils from Figure 6.15. This may be attributed to its high plasticity, high water content, and high initial void ratio. Cha et al. (2014) also studied the link between the wave velocity parameters α_s and β to a range of basic soil properties. They found the best correlations with soil compressibility (C_c) and they proposed expressions with α_s and β as a function of C_c:

$$\alpha_s = 13.5\ (m/s).(C_c)^{-0.63} \qquad (6.5)$$

$$\beta = 0.17 \log C_c + 0.43 \tag{6.6}$$

Figure 6.16 shows the correlation between the α and β exponents with compressibility (C_c) for the compiled data of Canadian soils shown in Figure 6.15. It can be seen that the data trend is well predicted by Equations 6.5 and 6.6. This is more evident for the data shown in Figure 6.16(a), where Equation 6.5 corresponds with the estimated trend for the compiled data. However, for the Figure 6.16(b) the estimated trend of the compiled data does not match with the trend from Equation 6.6. The regression analysis suggests a low correlation ($R^2 = 0.01$) between the compression index of the Canadian soils in the database and the β exponent.

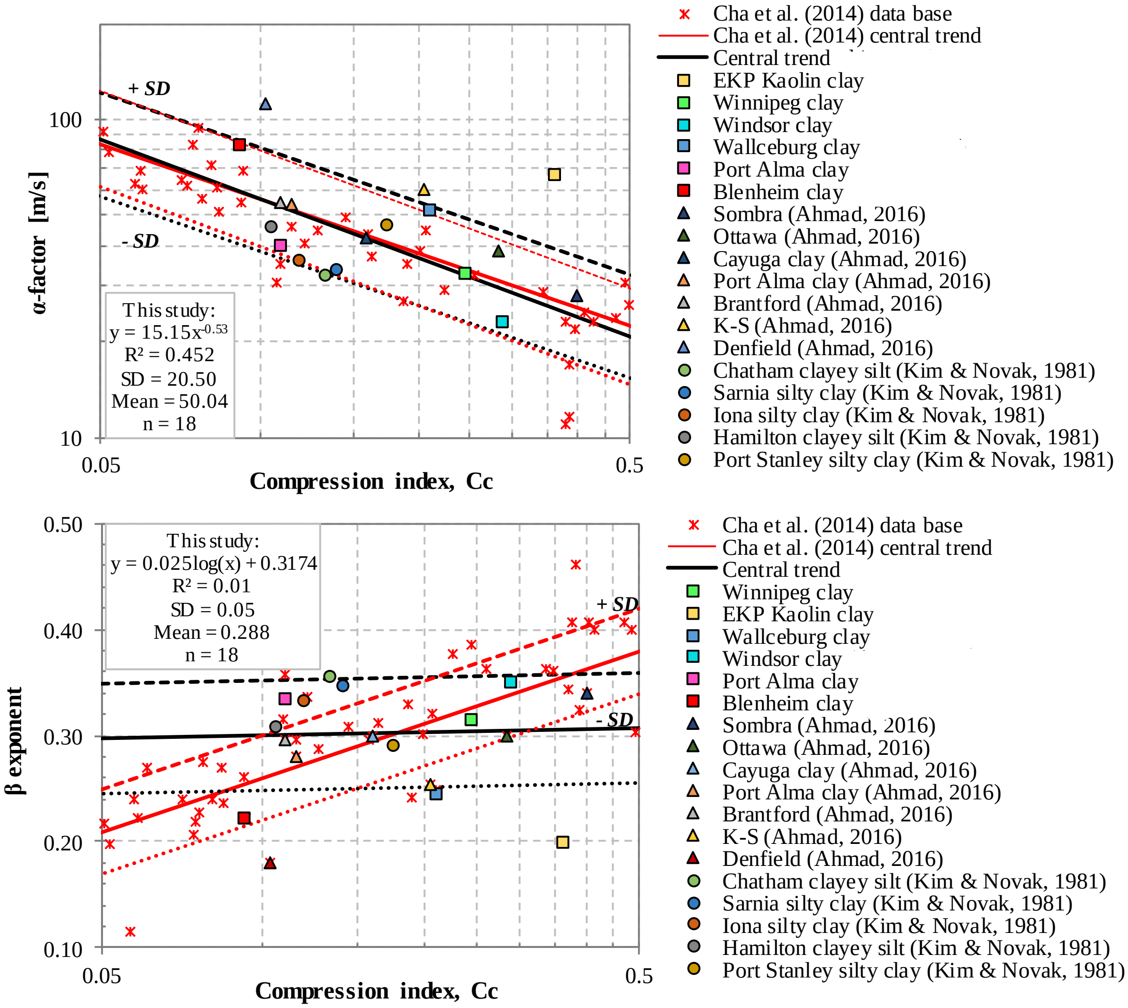

Figure 6.16: Relationship between: a) the α-factor and compression index (C_c) and b) the β exponent and compression index (C_c) for different cohesive materials

A similar analysis was carried out using different basic soil properties to further investigate the variations of the wave velocity parameters α_s and β for the compiled database of Canadian soils. The basic geotechnical properties included soil activity, plasticity index, and liquidity index. The results again suggest low correlations between the wave velocity parameters and the basic soil properties used in the analysis. Despite the low significance of the regressions, the trends show that α_s decreases and β increases with increasing of: soil activity, plasticity index and liquidity index. These results can be found in Appendix D.4.

6.3.2 Further analysis of the small-strain stiffness anisotropy

The small-strain stiffness anisotropy of the five Canadian cohesive soils has been discussed in the previous sections. These results suggest that the materials are anisotropic and generally exhibit stiffer responses in their horizontal directions. The soils are overconsolidated, medium to low plasticity glacial tills and have likely undergone a complex formation history that cannot easily be characterized following traditional soil mechanics approaches.

It has been noted in the literature that the behaviour of glacial tills is intimately related to their composition and on their consolidation stress levels. Among these, the transportation mechanism and mode of deposition of the glacial tills play an important role for the proper understanding of their structure and the fabric developed during their formation. From different till-fabric investigations it has been found that for tills deposited at the base of glacier (e.g. lodgment tills), the dominant fabric mode tends to lie parallel to the direction of the ice flow direction and parallel to the direction of shearing. These anisotropic fabrics lead to materials with directional dependence of their geotechnical properties, (e.g. strength and stiffness), such as the glacial clay tills tested in this investigation. This section tries to shed further light on the anisotropic characteristics of these materials and compares these results to similar studies.

Different researchers have investigated the small-strain anisotropy of other stiff overconsolidated clays with glaciogenic origin (e.g. Jamiolkowski et al., 1995). Figures 6.17 and 6.18 show the variation of the normalized vertical and horizontal small-strain shear modulus (G_{vh} and G_{hh}) with pressure of well characterized clays such as London clay, Gault clay and Chicago clay (Pennington et al., 1997; Jovicic and Coop, 1998; Gasparre et al., 2007; Cho,2007; Yimsiri and Soga, 2011) . These plots also incorporate the results obtained from this investigation.

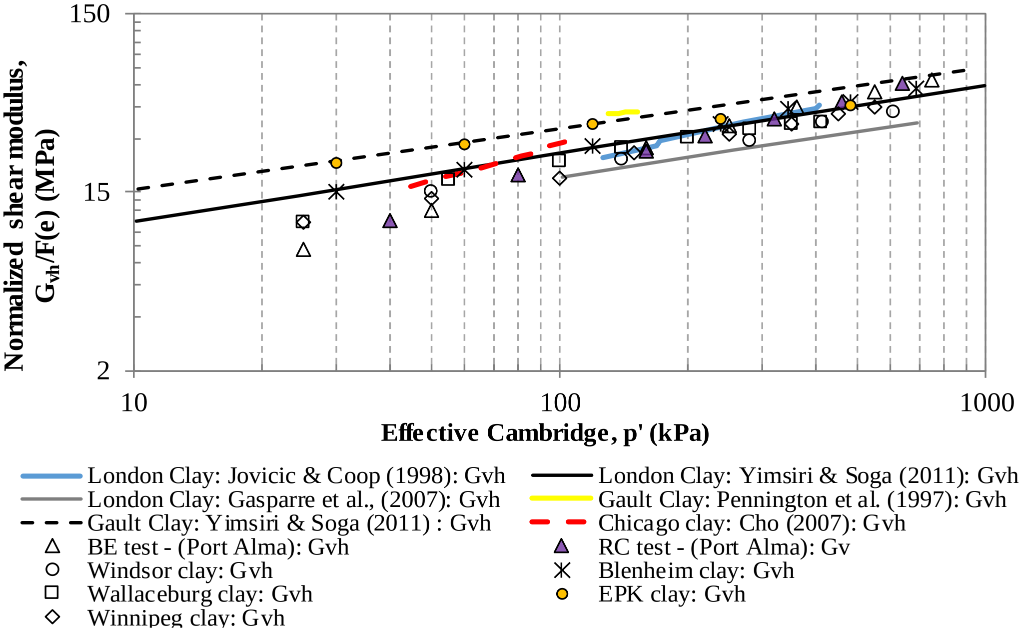

Figure 6.17: Comparison of obtained small-strain vertical shear modulus (G_{vh}) with published data

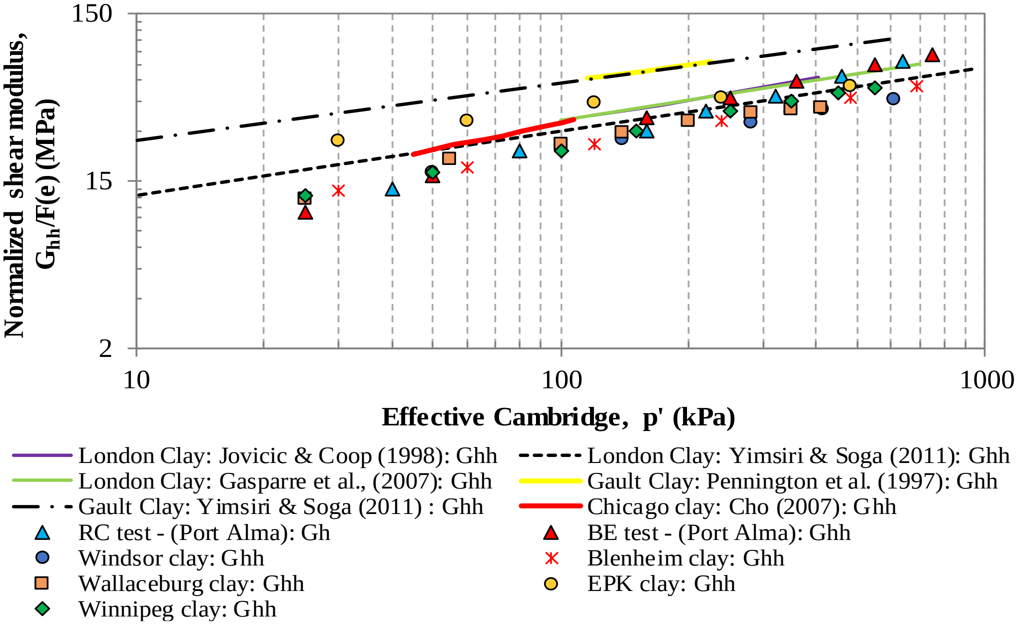

Figure 6.18: Comparison of obtained small-strain horizontal shear modulus (G_{hh}) with published data

It is clear that the normalized values of G_{vh} and G_{hh} with increasing of mean effective stress from all of the cohesive materials follow a comparable trend. Moreover, the slopes of the best-fit lines in both of the figures are very similar. One contrasting feature is that the UK clays (London and Gault clays) present a much stiffer response in the vertical and horizontal directions when compared to the Canadian soils. The UK clays, despite having a glacial origin, are heavily overconsolidated (OCR ≈ 6.5 to 40) of medium to high plasticity materials that have been deposited under marine environments between the Eocene and Cretaceous epochs and have likely undergone a much more complex formation history (Gasparre et al., 2007; Brosse et al., 2017). These could explain the stiffer responses when compared to Canadian clays and Chicago clay. Both Canadian and Chicago clays have very similar formation history that dates from the Pleistocene epoch, meaning that both are geologically ‘younger’ deposits compared to the UK clays, and were probably deposited under fresh water or similar environments around the Great Lakes Basins.

The data shown in Figures 6.17 and 6.18 show good agreement with the relationships implied by the equations proposed by Jamiolkowski et al. (1995), previously presented in Section 2.3.3.1 and reintroduced here:

$$G_{vh} = S_{vh} f(e)(p_r)^{1-n_v-n_h}(\sigma'_v)^{n_v}(\sigma'_h)^{n_h} \tag{6.7}$$

$$G_{hh} = S_{hh} f(e)(p_r)^{1-2n_{hh}}(\sigma'_h)^{n_h}(\sigma'_h)^{n_h} \tag{6.8}$$

The stiffness constants S_{vh}, S_{hh}, nv and nh from Equations 6.7 and 6.8 were deduced from Figures 6.17 and 6.18 for each of the different published materials and are summarized in Table 6.3. The same parameters were also obtained summarized in Table 6.2 for the Canadian clays. Jamiolkowski et al. (1995) suggested the use of the ratio S_{hh}/S_{vh} to estimate the soil anisotropy (α). The value of exponents nv and nh are approximately equal, this matches the observations reported by Jamiolkowski et al. (1995) and Nishimura (2014).

Figure 6.19 shows the variation of the anisotropic ratio (α) with consolidation pressure. Again, the data obtained for the Canadian soils from this investigation is compared with results of small-strain stiffness anisotropy with pressure from other materials reported in the literature. Where the pressure variation data is absent, a horizontal line is used. This shows the wide range of stiffness anisotropy for these overconsolidated clay soils, which are predominantly stiffer in the horizontal direction. The slight gradients of some of the curves, suggest that the pressure induced anisotropic fabric changes may be different in the horizontal and vertical directions. The materials tested in this investigation generally lie in a narrow band within α = 1.10 to 1.30, with slightly increasing gradients with pressure. It should be noted that these materials are all assumed to be cross-anisotropic, which may not necessarily be the case. They are also predominantly isotropically consolidated, which has been assumed not to have an effect on the observations of small-strain anisotropy but could be an area for further study.

Table 6.3: Stiffness constants for different published materials

Material	Author	S_{vh}	S_{hh}	*nv*	*nh*	$\alpha=S_{vh}/S_{hh}$
London clay	Yimsiri & Soga (2011)	4.21	5.082	0.38	0.38	1.21
	Jovicic & Coop (1998)	1.57	3.044	0.46	0.43	1.95
	Gasparre et al. (2007)	3.20	5.947	0.36	0.40	1.86
Gault clay	Yimsiri & Soga (2011)	7.03	11.89	0.34	0.34	1.69
	Pennington et al. (1997)	16.96	25.24	0.16	0.18	1.49
Chicago clay	Cho (2007)	1.75	2.391	0.54	0.59	1.37

S_{vh} & S_{hh} are material constants; *nv* & *nh* are empirical stress exponents (Jamiolkowski et al., 1995)

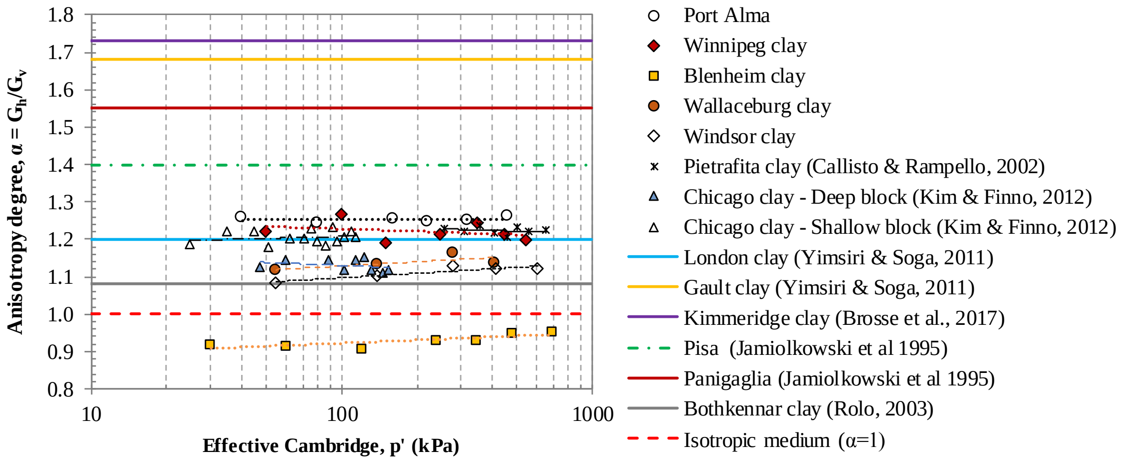

Figure 6.19: Comparison of obtained anisotropy degree with published data

Whilst Figure 6.19 shows the range of anisotropic ratios for stiff overconsolidated clays found in the literature, there is not an obvious trend for the interpretation of the data. However, following a study of the anisotropy of six Italian clays, Jamiolkowski et al. (1995) proposed the equation below to estimate the small-strain anisotropy (α):

$$\alpha = \frac{G_{hh}}{G_{vh}} = \frac{S_{hh}}{S_{vh}} {K_o}^{n} \qquad (6.9)$$

where K_o is the earth pressure at rest, n is an empirical exponent and S_{hh} and S_{vh} are material fabric parameters. This relationship is plotted in Figure 6.20 for the data and materials shown in Figure 6.19. The best-fit values for the equation are $n = 0.476$ and $S_{hh}/S_{vh} = 1.423$, which are a slightly higher than those found by Jamiolkowski et al. (1995) for their materials, but the R^2 value is still reasonably good and confirms the appropriateness of the obtained correlation. Equation 6.10 shows the proposed empirical correlation:

$$\alpha = 1.423. {K_o}^{0.476} \qquad (6.10)$$

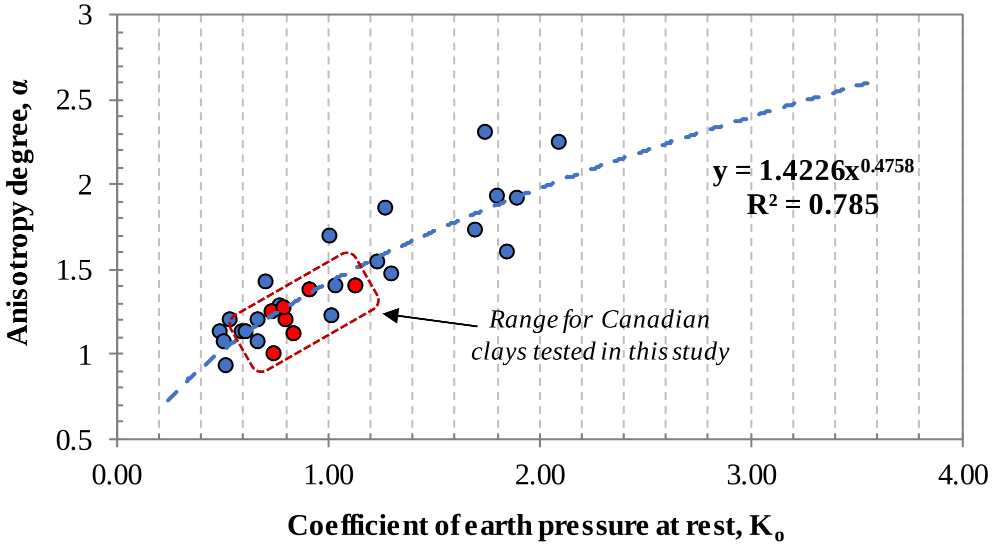

Figure 6.20: Relationship between anisotropy degree (α) and the coefficient of earth pressure at rest (K_o)

A clear trend given by Figure 6.20 is that α increases with the increasing values of K_o. This suggest a dependence between the anisotropic small-strain modulus G_{vh} and G_{hh} on the current soil state and stress history. Jamiolkowski et al. (1995) pointed out that when a soil sample is subjected to isotropic stress states, the ratio of G_{hh}/G_{vh} will directly reflect the initial anisotropy of the material, reflecting both stress-induced and fabric anisotropy. Thus, for a given soil, Equation 6.10 could be used to assess such initial anisotropy. The tested Canadian clays tend to lie towards the lower end of this curve and it should be noted that all of the plotted values are for the *in-situ* stress state. Whilst this relationship provides a reasonable fit to the current database, the small-strain anisotropy is complex and will likely be dependent upon the clay fraction, clay structure, mineralogy, depositional origin and post-depositional environment. In addition, the majority of the clays tested are likely to be cross-anisotropic, since they are waterlain tills, true glacial clay tills may display more complex anisotropic characteristics.

6.3.2.1 Summary of anisotropic stiffness moduli

To further characterize the stiffness anisotropy and small-strain behaviour of the cohesive materials, analysis of the data obtained from CIU triaxial, bender elements and resonant column tests was completed. This was performed to provide suitable data to create a comprehensive set of stiffness moduli assuming soil cross-anisotropy. For that purpose, the three-parameter formulation outlined by Graham and Houslby (1983) and Wood (1990), and previously explained in Section 2.4.3, was used. Additionally, a check of the estimated values of G_{hh} from resonant column testing was performed using the analysis proposed by Sultaniya et al. (2010) explained at the end of Section 2.4.3. The results of this analysis are shown in detail in Appendix D.5.

To successfully apply the three-parameter model of Graham and Houlsby (1983), the modified Poisson's ratio (μ*) needs to be estimated. For this purpose, Equation 2.40 was used and is reintroduced here in Equation 6.11 as follows:

$$\frac{\delta_{p'}}{\delta_q} = \frac{J}{3G^*} = \frac{2(1-\mu^* + \alpha\mu^* - \alpha^2)}{3(2-2\mu^* - 4\alpha\mu^* + \alpha^2)} \tag{6.11}$$

Additional information can be found from the $q{:}p'$ plots of the CIU triaxial tests (see Figure 6.4). The initial slopes of the stress-path curve for each of the materials were determined, $\delta_q/\delta_p{}' = J/3G^*$. The initial slope of each material was calculated for values of δq that fell within the strain range of 0.01% to 0.1%. This corresponds with the range reported by Smith et al. (1992) for Bothkennar clay, where they found that the deformations of the material are still fully recoverable (Jardine, 1992). Jardine (1992) proposed a general framework of soil behaviour that consisted on the definition of three main zones of stress-strain response. He recognized three surfaces or envelopes named Y_1, Y_2 and Y_3, surrounding the stress state at which the soil is located; where Y_1 is the limit of the zone of linear elastic response where strains might range between 0.002% to 0.006% and deformations are fully recoverable; Y_2 delimits a zone of non-linear stress-strain behaviour where plastic strains are produced but are still recoverable within the strain range from 0.01% to approximately 0.1%; and Y_3 is the zone of irrecoverable plastic strain that become more significant for strains higher than 0.1%.

A comparable strain range to that of Bothkennar clay was also reported by Jardine (1985) and Georgiannou (1988) when studying low plasticity tills and clayey sands, respectively. Calculating δ_q/δ_p' for that range of strains ensures that the analysis is carried out within the elastic zone of deformations (Jardine et al., 1991). The measurement of such low strain values was possible due to the use of local displacement transducers in the CIU triaxial tests. Figure 6.21 shows stress-paths obtained from undrained CIU triaxial tests for the different cohesive materials.

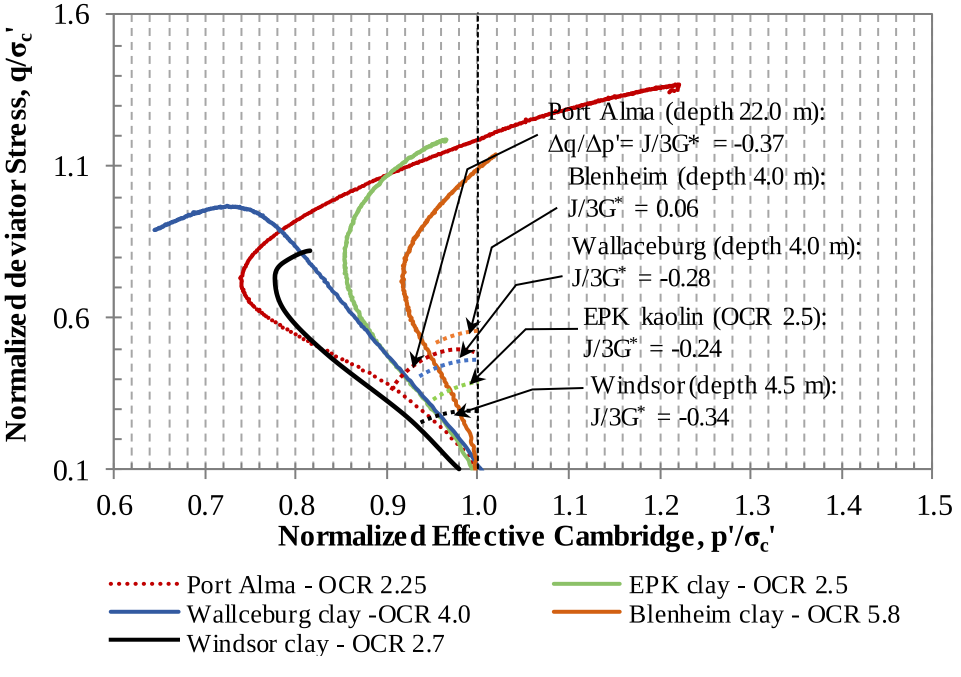

Figure 6.21: Normalized undrained stress-paths obtained for the various overconsolidated clays

Notably, the majority of the values of *J/3G** obtained are negative. The negative sign indicates the direction of the effective stress-path curve during pre-yield condition, and is indicative that the anisotropy degree, α, is bigger than 1 suggesting that the soil is stiffer horizontally than vertically (Becker, 1981; Graham and Houslby, 1983; Wood, 1990). This further confirms the results obtained from the bender elements and resonant column tests in the previous sections, where $\alpha = G_{hh}/G_{vh}$ for most of the cases was higher than 1. Using Equation 6.9 along with average values of α from Figure 6.11 and values of $J/3G^*$ from Figure 6.21, the modified Poisson's ratio (μ^*) can be obtained. Table 6.3 presents a summary of μ^* values estimated for each soil. By definition in the three-parameter formulation of Graham and Houlsby (1983), the modified Poisson's ratio is equal to the Poisson's ratio in the horizontal plane for each material ($\mu^* = \mu_{hh}$). Lings (2001) reported the following limiting condition to μ_{hh}: $-1 < \mu < 1$, which it is fully satisfied by the μ^* values shown in Table 6.4.

Table 6.4: Stress-path slopes and modified Poisson's ratio obtained on various overconsolidated clays

Soil sample	3G*/J	β (J/3G*)	α =(G_{hh}/G_{vh})	$\mu^* = \mu_{hh}$
Port Alma clay	-2.72	-0.37	1.15	0.24
Blenheim clay	17.54	0.06	0.92	0.22
Wallaceburg clay	-3.57	-0.28	1.08	0.45
Windsor clay	-2.99	-0.34	1.11	0.45
Winnipeg clay	-4.04	-0.25	1.19	0.37
EPK clay	-4.22	-0.24	1.23	0.33

Having estimated μ^* and by assuming $\alpha = G_{hh}/G_{vh}$, one remaining parameter is needed, and this is the modified elastic modulus E^*, which according to the Graham and Houlsby model is equal to the elastic modulus in the vertical direction of the material (E_v). E_v was estimated from the resonant column test for each soil and these results are presented in Appendix D.3. Using Equations 2.28 to 2.34, the remaining stiffness parameters of the simplified model (E_h, μ_{hv}, μ_{vh}) can be found. These results were compiled for each material and are presented in Table 6.5. The estimated cross-anisotropy parameters satisfy the conditions of the inequalities presented in Equations 2.21 to 2.23. Frequently in soil modeling practice, generic values of Poisson's ratio μ_{vh} (normally assumed to be isotropic) are taken between 0.2 to 0.33. From this point of view, it seems that the only values off that range are those obtained for Wallaceburg and Windsor clays. Nishimura (2014) pointed out that such large values of Poisson’s ratio (μ_{vh}) between 0.2 to 0.33 are suitable for problems with associated strains of 0.1%; and for very small strains, measured values of μ_{vh} may be lower than 0.2.

Table 6.5: Summary of cross-anisotropy parameters for different cohesive materials obtained using Graham & Houlsby (1983) three-parameter formulation

	Assuming $\alpha = G_{hh}/G_{vh}$ *	Port Alma clay	Blenheim clay	Wallaceburg clay	Windsor clay	Winnipeg clay	EPK clay
Drained parameters	G_{vh} (MPa)	108.18	84.77	53.68	18.41	48.64	38.13
	G_{hh} (MPa)	124.01	78.36	58.08	20.49	57.94	47.06
	G_{hh}/G_{vh}	1.15	0.92	1.08	1.11	1.19	1.23
	μ_{vh}	0.274	0.241	0.418	0.401	0.309	0.268
	μ_{hv}	0.208	0.262	0.387	0.361	0.259	0.218
	μ_{hh}	0.238	0.221	0.452	0.445	0.367	0.330
	$E^* = E_v$ (MPa)	270.81	225.08	144.34	47.94	111.78	82.46
	E_h (MPa)	355.66	190.51	168.35	59.07	158.29	124.75
	$(E_h/E_v)^{0.5}$	1.15	0.92	1.08	1.11	1.19	1.23
Undrained parameters	E_v^u (MPa)$^{++}$	326.10	262.74	160.37	55.24	143.72	112.08
	E_h^u (MPa)$^{++}$	359.30	240.55	170.33	59.67	205.58	132.26
	μ_{hh}^u	0.449	0.542	0.469	0.460	0.285	0.410
	μ_{hv}^u	0.551	0.458	0.531	0.540	0.715	0.590
	μ_{vh}^u	0.500	0.500	0.500	0.500	0.500	0.500

$^{++}$ Derived using Lings (2001) equations
*bender element data

6.4 Summary

This chapter presents a review of the results from a comprehensive testing program used to characterize the stress-strain properties of a group of cohesive materials. These materials were mainly Canadian clays with glaciogenic origin. Advanced testing techniques were used to study the critical state, stress-strain behaviour and the small-strain stiffness anisotropy of the cohesive materials. The basic geotechnical properties of the studied natural soils indicate that these are overconsolidated stiff glacial clays of low to medium plasticity ($6 < I_p < 33$) and low activity (0.29 < activity < 0.49). Such stress history and mechanical characteristics are typically found on glacial clay tills and ‘till-like’ materials.

To further interpret the nature of the tested materials, a database containing basic properties of other Canadian glacial soils was compiled from the literature and compared against the results for these soils. Such comparisons support the view that these natural cohesive soils are of glacial origin, more specifically ‘water-laid’ tills. Results from triaxial CIU tests showed that the critical state behaviour of the tested materials is very similar, yielding values of M (slope of critical state line) or effective angle of friction well within the range of other soils of a similar nature reported in the literature. Moreover, the normalized stiffness degradation obtained with local instrumentation is comparable to other low plasticity glacial materials found in the literature that present similar degradation rate with increasing shear strains.

The small-strain stiffness of the soils was evaluated using bender elements (BE) and the resonant column (RC) test. Such tests were used to obtain the stiffness of the materials in their vertical and horizontal directions through measurements of propagated wave velocities (shear and compressional waves). A particular focus was placed on the analysis of shear wave velocities in different propagation directions and polarization (e.g. V_{svh} and V_{shh}), that were later used to estimate the small-strain shear modulus of the soil samples in their vertical and horizontal directions (G_{vh} and G_{hh}). The BE and RC tests yielded comparable results, both in magnitude and trend with increasing effective stress. The close agreement between the results, from one type of test to the other, also helped to further validate the obtained stiffness properties. Moreover, the estimation of G_{vh} and G_{hh} suggests that five of the tested cohesive soils present a stiffer response in their horizontal direction ($G_{hh} > G_{vh}$), while the remaining material shows an opposite trend ($G_{hh} < G_{vh}$).

The difference between the stiffness moduli G_{vh} and G_{hh} indicate that the small-strain stiffness behavior of the materials is in fact anisotropic or at least cross-anisotropic, and that the anisotropy ratio (α) ranges between 1.10 to 1.30 for Wallaceburg, Windsor, Port Alma, Winnipeg and EPK clay, whereas for Blenheim clay α is around 0.92. Different empirical correlations were proposed to aid with the calculation of G_{vh} and G_{hh} for similar glacial clay materials as a function of void ratio and mean effective stress. Also, a new correlation to estimate the anisotropy ratio (α) as a function of the coefficient of earth pressure at rest (K_o) was developed after gathering data from different anisotropic materials found in the literature. A complete set of stiffness parameters for each soil were derived using the three-parameter model proposed by Graham and Houlsby (1983), and using the results from bender elements, resonant column, and undrained CIU tests.

Chapter 7

7 The effects of soil stiffness anisotropy on the responses of a shallow wind turbine foundation

7.1 Overview

Existing design codes incorporate uncoupled isotropic elastic analytical solutions for determining serviceability limit states (SLS) under complex (VHM) loading. However, most natural soil deposits exhibit some degree of stiffness anisotropy and stiffness degradation with cyclic straining. This chapter presents results obtained from a numerical analysis developed to assess the anisotropic elastic soil-foundation interaction between a shallow wind turbine foundation and the glacial till deposit found at the Port Alma wind farm site (KEPA 4). The numerical analysis was performed with a finite element (FE) model of the shallow wind turbine foundation and the founding soil, developed in ABAQUS (2016). A set of dimensionless coupled static stiffness equations were developed to predict the load-displacement response of surface and embedded foundations, founded on anisotropic soils with linear increase of stiffness with depth under complex loading. Furthermore, an example of the application of the proposed equations is presented at the end of the chapter, where the elastic vertical and horizontal displacements, and rotation of the KEPA 4 foundation subjected to pseudo-static loads are assessed and compared to existing analytical solutions and measured field responses.

7.2 Method

7.2.1 Numerical model development

A finite element model of the shallow wind turbine foundation of KEPA 4 (at Port alma) has been created with the software package ABAQUS (2016). The finite element model employed in this study was developed and used previously (He et al., 2019) to assess the load-displacement response of a surface circular foundation resting on an elastic anisotropic soil of uniform stiffness. The soil was represented by a mesh of approximately 180000 three-dimensional 8-noded continuum elements (C3D8R). To understand possible boundary effects, five model domain widths ($L = 5D_f$, $10D_f$, $20D_f$, $50D_f$ and $100D_f$) were examined (see Figure 7.1). These dimensions represent the horizontal distance from the foundation edge to either side of the domain and the vertical depth of the soil below the foundation (L), and the foundation diameter (D_f).

The horizontal displacement of the vertical sides was restricted, and the bottom of the model was kept fixed by restricting all six degrees of freedom. The base contact interface between the foundation and the soil was chosen to be fully rough. The wind turbine shallow foundation was idealized as a circular rigid body and was modelled with both surface and embedded conditions. Figure 7.1 shows the model geometry with a typical finite element mesh. Figure 7.2 shows the effect of the model dimensions on the different elastic stiffnesses [K_V, K_{HH}, K_{MM} & K_{MH} (see Equation 2.2)] for an isotropic soil (see Section 2.1.1) and Bell's finite element results (1991) with a $100D_f$ mesh for comparison. It can be seen that a domain size (L) of $50D_f$ to $100D_f$ is sufficiently accurate, thus a model dimension of $50D_f$ was adopted for the remaining analyses shown in this chapter.

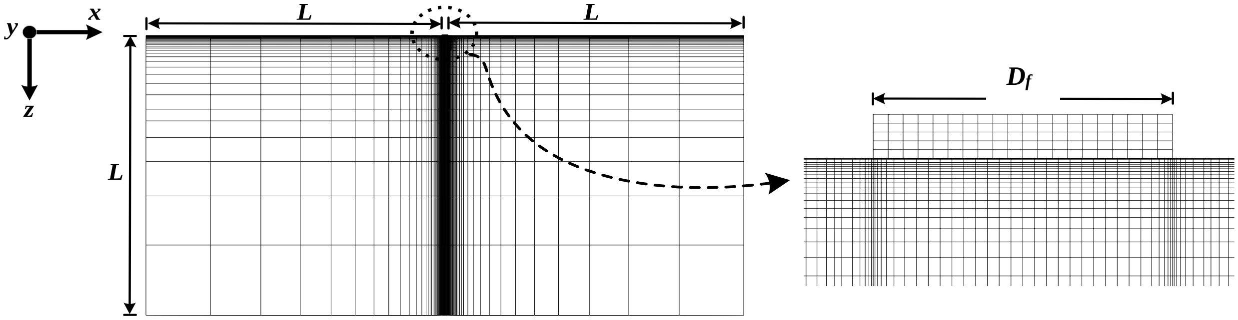

Figure 7.1: Finite element mesh representation

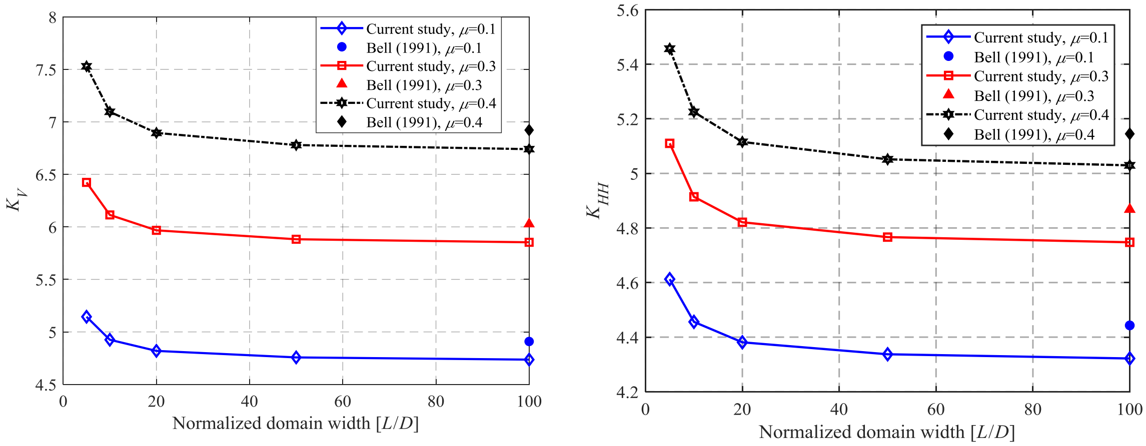

Figure 7.2 (a): Effect of model dimensions on elastic stiffnesses

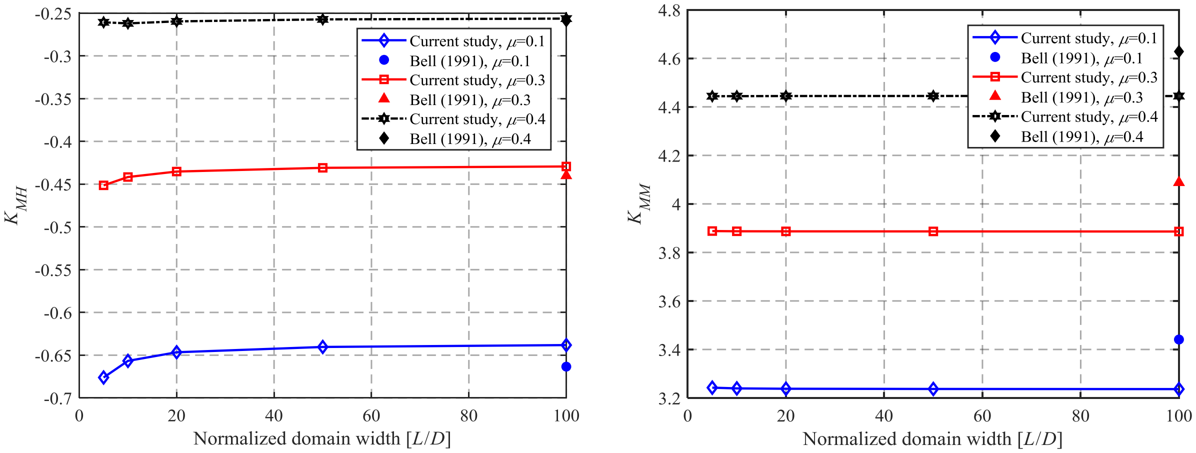

Figure 7.2 (b): Effect of model dimensions on elastic stiffnesses

7.2.2 Material and modelling assumptions

Graham & Houlsby (1983), proposed a simplified form of cross-anisotropic model that required only three independent parameters, rather than seven as utilized in classical cross-anisotropic models (e.g. Lings, 2001; Clayton, 2011). The founding soil used for the numerical analysis was modelled as an anisotropic linear elastic material adopting the aforementioned three-parameter formulation (α, μ^*, E^*) developed by Graham and Houslby (1983). where. Further details of the three independent anisotropic parameters are presented in Table 7.1 and in Section 2.4.3. Similarly, due to a thermodynamic requirement (Love, 1927), the summarized elastic parameters can only take certain bounds that were previously described by Lings (2001), these were shown in Section 2.4.2. Note that isotropy provides a special case, where $\alpha=\sqrt{E_h/E_v}=1$.

Table 7.1: Three independent parameters from Graham and Houlsby (1983) model

Anisotropy factor: $\alpha = \sqrt{E_h / E_v}$

Modified Poisson's ratio: $\mu^* = \mu_{hh}$

Modified elastic modulus: $E^* = E_v$

μ_{hh} is the Poisson's ratio relating to horizontal strain caused by imposed horizontal strain in normal direction (Lings, 2001); E_h and E_v are the soil elastic modulus in the horizontal and vertical directions, respectively

To assess the changes in the responses of the soil, the material beneath the foundation was assumed to be a homogeneous layer with constant stiffness with depth, and as a non-homogeneous layer with linearly increasing stiffness with depth (Gibson, 1967). The latter assumption better represents most natural deep soil deposits, as they often exhibit an increase of elastic stiffness with depth (Doherty & Deeks, 2003). In addition, many soil deposits have a stiffer weathered near surface layer, with a heavily overconsolidated crust underlain by the main deposit (Lo and Becker, 1980).

To accommodate the effect of a stiffer crust overlying a soil, the concept of a “surface” modulus G_o has been adopted. Rowe and Booker (1980) suggested that the direct determination of the surface modulus may be difficult, but could be estimated from the measured modulus G variations with depth Z. Moreover, they also suggested that the calculation of G_o in such way may not introduce additional error, since errors associated with the soil idealization are independent of the selection of this reference modulus. Figure 7.3 shows the stiffness distribution with depth assumed for the homogeneous and non-homogeneous soil profiles used herein.

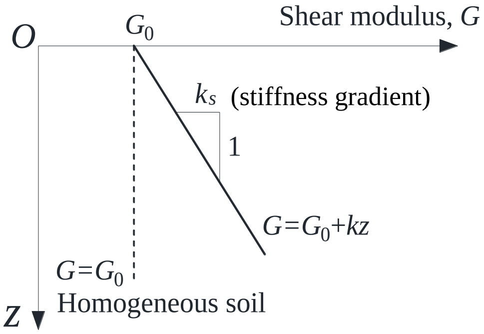

Figure 7.3: Stiffness distribution for homogeneous and non-homogeneous soils

7.2.3 Analytical approach

The effect of foundation embedment was also studied and was included by using different embedment ratios ($e = d/D_f$) from 0 to 0.16, [with foundation diameter (D_f) and embedment (d)]. The effect of different stiffness gradients ($0 \leq k_s \leq 1$) for the non-homogeneous soil stiffness increase with depth were considered using the Gibson factor $1/\beta$ (where $1/\beta = \frac{k_s D_f}{E_{v_o}}$), which varied from 0 to 0.08. Note E_{vo} is the vertical elastic modulus of the soil at the surface. Table 7.2 shows a summary of the different cases studied with the finite element analysis, as well as the range of parameters for the different models.

Table 7.2: Analytical cases used in the finite element model

Embedment ratio d/D_f	**Homogeneous soil**	**Gibson soil; $1/\beta = \frac{k_s D_f}{E_{v_o}}$**				
	$1/\beta = 0$	**0.015**	**0.030**	**0.047**	**0.060**	**0.080**
0	Case (1-1)	Case (1-2)	Case (1-3)	Case (1-4)	Case (1-5)	Case (1-6)
0.03	Case (2-1)	--	--	--	--	--
0.06	Case (3-1)	--	--	--	--	--
0.09	Case (4-1)	--	--	--	--	--
0.12	Case (5-1)	--	--	--	--	--
0.16	Case (6-1)	--	--	--	--	--

A parametric study was carried out to assess the variation of the elastic solutions due to changes in the anisotropic parameters α and μ_{hh}. Six values of α were adopted, varying from 0 to 2 (i.e. 0.2, 0.4, 0.6, 1.0, 1.5 and 2.0), and μ_{hh} was varied between 0 and 0.49 (i.e. 0, 0.10, 0.20, 0.30, 0.40 and 0.49). Therefore, each case shown in Table 7.4 includes 36 sub-cases (i.e. six values of α × six values of μ_{hh}).

7.3 Numerical model results

7.3.1 Calibration

To further verify the results of the finite analyses in this investigation, these were compared with the numerical solutions obtained by Bell (1991) and analytical solutions found in the literature for circular surface foundations resting on an isotropic homogeneous soil. Figures 7.4 and 7.5 show comparisons between the vertical (K_V), horizontal (K_{HH}), moment (K_{MM}) static stiffness and the cross-coupling term (K_{MH}) obtained from the current study, Bell (1991) and the analytical solutions of Spence (1968), Gerrard and Harrison (1970), and Poulos and Davis (1974). The analytical solutions are defined by the following Equations:

$$K_V = \frac{4\ln(3-4\mu)}{1-2\mu} \tag{7.1}$$

$$K_{HH} = \frac{8}{2-\mu} \tag{7.2}$$

$$K_{MM} = \frac{8}{3(2-\mu)} \tag{7.3}$$

These analytical solutions assume rough footings, which are characterized by the fact that the base of the footing is rigidly connected to the soil, hence allowing a full transmission of shear stress. In this instance, the application of vertical, horizontal and moment loading can be applied. Spence (1968) provides an exact solution that satisfies the boundary conditions for a rough footing through Equation 7.1. Gerrard and Harrison (1970) proposed Equation 7.2 which corresponds to a footing that displaces rigidly in the horizontal plane, while flexing in its vertical plane instead of rotating rigidly. Finally, Poulos and Davis (1970) derived an approximate elastic solution for a rigid rough circular footing subjected to an overturning moment through Equation 7.3.

Figures 7.4 and 7.5 show that the solutions of the current study compare well (with differences of less than 5%) with the approximate solutions of K_V, K_{HH} and K_{MM} from Bell (1991). The numerical solutions from this study and Bell's (1991) are in good agreement with the results obtained using Equation 7.1 for K_V (Figure 7.4a), while these are shown to be higher than those obtained with Equations 7.2 and 7.3 for K_{HH} and K_{MM} (Figures 7.4b and 7.5a) for Poisson's ratios (μ) between 0 to 0.4. It should be noted that the numerical and analytical solutions gradually increase with increasing μ. However, the current study's results lie closer to the analytical solutions due to the much finer mesh and improved numerical methods than those used by Bell (1991). Likewise, the cross-coupling term in Figure 7.5b obtained by Bell (1991) shows good agreement with that obtained in this study. Figure 7.5b also shows a decreasing coupling between horizontal displacement and body rotation with μ and no coupling when the soil media is incompressible (i.e. undrained case: μ=0.5), which makes the uncoupled analytical solutions of K_{HH} and K_{MM} approach the coupled results obtained from the current study as shown in Figures 7.4 and 7.5a.

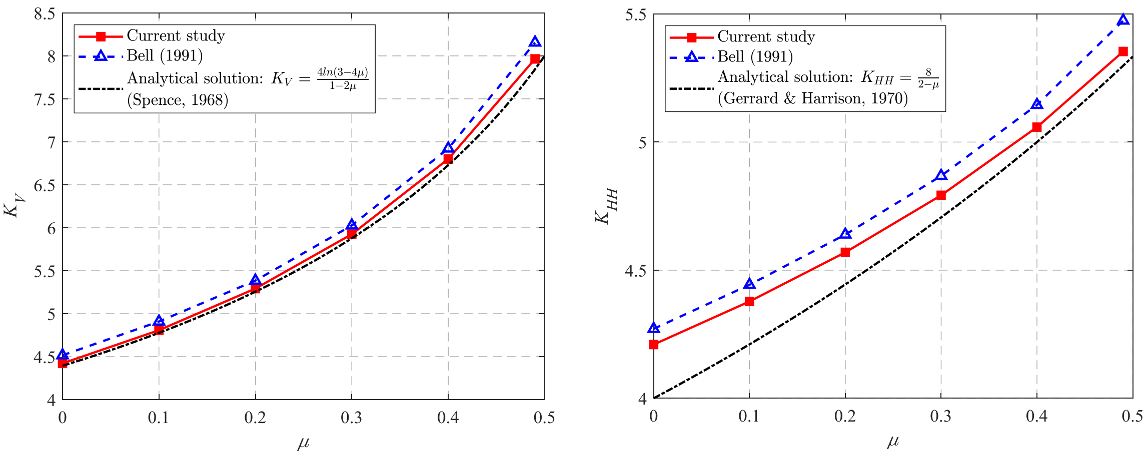

Figure 7.4: Vertical (K_V) and horizontal (K_{HH}) stiffnesses for surface circular foundations on isotropic homogeneous soils

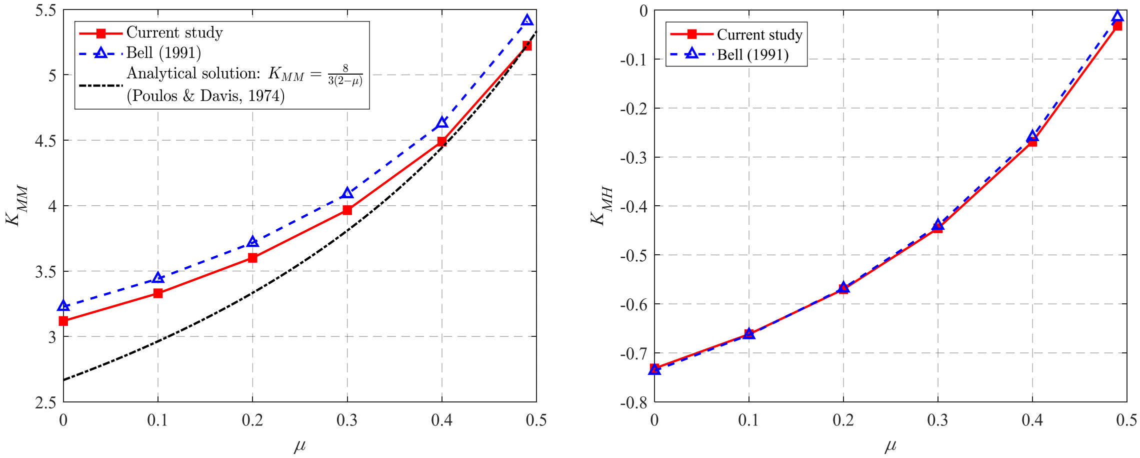

Figure 7.5: Moment (KMM) and cross-coupled (KMH) stiffnesses for surface circular foundations on isotropic homogeneous soils

7.3.2 Coupled elastic solutions obtained from parametric study

By analyzing surface foundations on homogeneous soils (i.e. Case (1-1) in Table 7.2), approximate stiffness equations can be obtained as a function of μ_{hh} and α, as shown below in the first term of Equation 7.4. If only the first term of the equation is considered, then when the soil material is isotropic (i.e. $\alpha = 1.0$), this then devolves to the equation commonly-used for isotropic stiffness values (see Figures 2.1 and 2.2), for example in DNV (2002, 2010). Equations 7.4a and 7.4c show that K_V and K_{MM} decrease with α, while K_{HH} exhibits the opposite trend. This is because $\alpha = \sqrt{E_h/E_v}$, and K_V and K_{MM} are influenced more by the vertical stiffness, E_v, ($\alpha < 1$), whilst K_{HH} is dominated by the horizontal stiffness, E_h, ($\alpha > 1$). It should also be noted that the cross-coupling parameter is not affected by α. In contrast, all of the stiffness coefficient values increase with larger μ_{hh}. Moreover, Equation 7.4d becomes zero when μ_{hh} is equal to 0.5, which indicates no coupling between horizontal and moment responses; this was also confirmed by Bell (1991). The soil anisotropic ratio (α) also shows no influence on the coupling term.

Cases (1-1) to (1-6) in Table 7.2 can also be used to obtain the responses for the Gibson soil on the foundation stiffness. Similarly, the effect of embedment on the foundation can be provided by analyzing Cases (1-1) to (6-1). The final stiffness equations including the Gibson and embedment correction factors are shown in Equation 7.4 (He, 2019; Gonzalez-Hurtado et al., 2019), where $0 \leq 1/\beta \leq 0.08$. It can be seen that the embedment ratios affect all four stiffness coefficients, while the Gibson factor, $1/\beta$, affects everything except for the coupling behavior between horizontal and moment responses. Equation 7.4 was obtained by performing least squares curve fitting and the statistical results obtained from the fitting show that $R^2 \approx 1$. The derivation of Equation 7.4, the correction factors and curve fitting can be found in Appendix E.3.

$$K_V = \left[\frac{1}{(1.1-\mu_{hh})(0.112\alpha+0.0937)}\right]\cdot\left[\left(\frac{1}{\beta}\right)\cdot 1.36+1\right]\cdot\left[\frac{1.03e}{0.90+4e}+1\right] \tag{7.4a}$$

$$K_{HH} = \left[\frac{5.375\alpha+4.58}{2.4-\mu_{hh}}\right]\cdot\left[\left(\frac{1}{\beta}\right)\cdot 0.63+1\right]\cdot\left[\frac{e}{0.32+e}+1\right] \tag{7.4b}$$

$$K_{MM} = \left[\frac{1}{(1.2-\mu_{hh})(0.145\alpha+0.125)}\right]\cdot\left[\left(\frac{1}{\beta}\right)\cdot 0.30+1\right]\cdot\left[\frac{1.93e}{0.88+e}+1\right] \tag{7.4c}$$

$$K_{MH} = K_{HM} = \left[\frac{-1.5(0.5-\mu_{hh})}{1-\mu_{hh}}\right]\cdot[-6.49e+1] \tag{7.4d}$$

where $1/\beta$ is the Gibson factor, defined as $1/\beta = \frac{k_s D_f}{E_{v_o}}$; E_{v0} is the vertical elastic soil modulus at ground level; e is the embedment ratio, defined as the ratio of the foundation diameter to the foundation depth ($e = d/D_f$).

7.4 Application of the proposed coupled anisotropic elastic stiffness equations

In this section, the serviceability limit state (elastic) behaviour of the KEPA 4 shallow foundation is investigated based on the stiffness equations from the current study, Gazetas (1983) and (1991), Bell (1991) and DNV (2016). The stiffness equations proposed by Gazetas can be found in Appendix E.6. A parametric study was also carried out to assess the effect of the changes in values of soil stiffness gradient (k_s), soil anisotropy (α^2), and Poisson's ratio (μ_{hh}) on the foundation responses. The approximate dimensions of the foundation and the properties of the anisotropic soil, as estimated in the previous sections and chapters, are summarized in Table 7.3. The estimation of the approximate value of soil anisotropy (α), small-strain shear modulus (G_{vh}), and soil stiffness gradient for the Port Alma glacial clay till deposit is shown in Appendix E.1. Note that the shear modulus used in the analysis was taken at a depth equal to the foundation radius following the recommendations of Whitman (1976) and DNV (1992).

The pseudo-static normal operation and rated power production loads considered for the estimation of the foundation responses are presented in Tables 7.4 and 7.5, respectively. Table 7.4 shows the normal operation design loads, provided by the manufacturer of the wind turbine, for normal wind conditions and normal operation determined from criterion IEC DLC1.1 (IEC 61400-1, 2005) for power production. Table 7.5 shows the rated power production loads acting of the foundation, estimated by He (2019) using the Blade Element Momentum Method (BEM) (after Hansen, 2015). More details on the application of this method may be found in Newson et al. (2018).

Table 7.3: Foundation and soil parameters

α^2	μ_{hh}	$G_{vh} = G_R$, [MPa]	k_s, [MPa/m]	R, [m]	*d/D_f*
1.30	0.24	82.0	2	9.5	0 & 0.16

α: anisotropic parameter; μ_{hh}: Poisson's ratio; G_{vh}: Small-strain shear modulus in the vertical direction; G_R: small-strain shear modulus at a depth equal to the foundation radius (Whitman, 1976); k_s: stiffness gradient; R: foundation radius; embedment ratio = d/D_f

Table 7.4: Design loads provided by manufacturer

Design loads	V [kN]	H [kN]	M [kN*m]
Normal operation loads (DCL 1.1)	21820	900	60000

Table 7.5: Rated power production loads (He, 2019)

H [kN], Mean ± Standard deviation	M [kN*m], Mean ± Standard deviation
261 ± 27	20567 ± 2157

V: same as described in Table 7.4; H and M were estimated for an average wind speed of 12 m/s and turbulence intensity of 14% (Newson et al., 2018)

Table 7.6 presents a summary of the calculated elastic stiffnesses using the different approaches. In addition to the case outlined in Table 7.3 (presented as Case (a) in Table 7.6), two more cases were studied to show the effects of variation of the anisotropic parameter and the change of the stiffness gradient on the elastic stiffnesses. In Case (b), α^2 was varied from 0.5 to 2, following the limits suggested by Lings (2001) and in Case (c), the normalized Gibson factor ($1/\beta$), was varied between 0 to 0.2 (see Gibson, 1967; Rowe and Booker, 1981).

The elastic stiffnesses estimated using Equation 9 for Case (a) are generally higher compared with the results given by the uncoupled isotropic solutions of the DNV (2016) and the coupled isotropic solutions of Bell (1991) and Gazetas (1983) and (1991), and both DNV (2016) and Gazetas are the same, and similar to Bell's (1991) solutions. Thus, it could be inferred that the anisotropic parameter and the stiffness increase with depth are of some importance for this scenario and can certainly affect the estimated foundation deformations. In addition, Cases (b) and (c) show that the variation of α^2 produces a range of values that generally span the isotropic values and increase considerably when the Gibson factor is changed from 0 to 5.

The translational responses of the foundation for the surface and embedded conditions under normal operation design loads and rated power production loads are shown in Tables 7.7 and 7.8 and in Tables 7.9 and 7.10, respectively. These responses were estimated using the recommendations of DNV (2016) that suggest a working value of shear strains for wind turbine foundations of 10^{-3} to estimate the reduction in stiffness. This corresponds to an approximately 70% reduction in the small-strain shear modulus (G_R) or G/G_{max} = 0.3 as shown in Figure 2.5 of Section 2.1.2. Further, an equivalent linear analysis was carried out with the finite element model to estimate the average equivalent shear strain at the centerline of the foundation at a depth equal to its radius (R = 9 m) resulting from the application of the normal operation design loads presented in Table 7.4. This was performed using the von Mises equivalent strain increment criterion presented in Shrivastava et al. (2012) and Pardis et al. (2017). The analysis yielded an average shear strain of approximately $3.4\text{x}10^{-3}$ and a reduction in the small-strain shear modulus of about 57% (G/G_{max} = 0.43). Contour plots showing the distribution with depth of the volumetric strain (ε_v), equivalent shear strain (ε_s), deviatoric stress (q) and mean stress (p) obtained from some of the finite element analysis using the pseudo-static normal operation loads from Table 7.4, are presented in Appendix E.7. These plots show the stress and strain concentrations at the corner of the footing, which attenuate with increasing depth.

The vertical translation, u_v, is seen to be overestimated if the soil stiffness anisotropy is neglected for both normal operation design and working loads condition. The horizontal translation, u_H, of the surface foundation is shown to be overestimated by DNV (2016) and

Gazetas (1981) and (1991), while for the embedded case the Gazetas solutions seem to underestimate the responses. These differences in the results could be attributed to a lack of consideration of the cross-coupling effect and soil non-homogeneity for the traditional solutions. The rocking angle, θ, exhibits a similar trend to u_V, but the differences between the different methods are smaller.

Table 7.6: Stiffness comparison for surface foundations

Normalized stiffness		K_V	K_{HH}	K_{MH}/K_{HM}	K_{MM}
Current study	Case (a): $\alpha^2 = 1.3$ & $\frac{1}{\beta} = 0.71$ (i.e. k_s=2)	6.96	7.18	-0.51	4.36
	Case (b): $\alpha^2 = 0.5 - 2.0$ & $\frac{1}{\beta} = 0.71$	7.77 - 6.63	4.96 - 8.77	-0.51	5.18 - 3.99
	Case (c): $\alpha^2 = 1.3$ & $\frac{1}{\beta} = 0 - 5$	5.36 – 7.47	4.96 - 20.57	-0.51	3.59 - 8.97
DNV (2016) - isotropic uncoupled		5.26	4.55	--	3.51
Bell (1991) - isotropic coupled		5.62	4.73	-0.52	3.85
Gazetas (1983) & (1991) - isotropic coupled		5.26	4.55	0	3.51

Table 7.7: Foundation responses under normal operation loads for *G/G_{max}* = 0.30

	u_V [mm]		u_H [mm]		θ [deg]	
	$d/D = 0$	$d/D = 0.158$	$d/D = 0$	$d/D = 0.158$	$d/D = 0$	$d/D = 0.158$
Case (a)	12.942	11.600	0.668	0.293	0.0315	0.0241
DNV (2016)	17.812	15.382	0.851	0.703	0.0466	0.0286
Bell (1991)	16.687	--	1.621	--	0.0438	--
Gazetas (1983)	17.812	15.381	0.851	0.105	0.0466	0.0285
Gazetas (1991)	17.812	15.174	0.851	0.149	0.0466	0.0285

Table 7.8: Foundation responses under normal operation loads for *G/G_{max}* = 0.43

	u_V [mm]		u_H [mm]		θ [deg]	
	$d/D = 0$	$d/D = 0.16$	$d/D = 0$	$d/D = 0.16$	$d/D = 0$	$d/D = 0.16$
Case (a)	9.178	8.225	0.573	0.240	0.0244	0.0186
DNV (2016)	12.427	10.731	0.594	0.490	0.0325	0.0199
Bell (1991)	11.642	--	1.131	--	0.0306	--
Gazetas (1983)	12.427	10.731	0.594	0.074	0.0325	0.0199
Gazetas (1991)	12.427	10.587	0.594	0.104	0.0325	0.0199

Table 7.9: Responses of the foundation under rated power production loads for G/G_{max} = 0.30

	u_H [mm], Mean ± Std.		θ [deg], Mean ± Std.	
	$d/D = 0$	$d/D = 0.16$	$d/D = 0$	$d/D = 0.16$
Case (a)	0.208±0.022	0.085±0.0089	0.0108±0.0011	0.0082±0.0001
DNV (2016)	0.246±0.026	0.204±0.0210	0.0160±0.0017	0.0098±0.0010
Bell (1991)	0.511±0.054	--	0.0150±0.0016	--
Gazetas (1983)	0.246±0.026	-0.002±0.0005	0.0160±0.0017	0.0098±0.0010
Gazetas (1991)	0.246±0.026	0.016±0.0015	0.0160±0.0017	0.0098±0.0010

Table 7.10: Responses of the foundation under rated power production loads for G/G_{max} = 0.43

	u_H [mm], Mean ± Std.		θ [deg], Mean ± Std.	
	$d/D = 0$	$d/D = 0.16$	$d/D = 0$	$d/D = 0.16$
Case (a)	0.179±0.019	0.0692±0.0072	0.0084±0.0008	0.0064±0.0006
DNV (2016)	0.172±0.018	0.142±0.015	0.0112±0.0011	0.0068±0.0008
Bell (1991)	0.357±0.037	--	0.0105±0.0011	--
Gazetas (1983)	0.172±0.018	-0.0013±0.0003	0.0112±0.0011	0.0068±0.0008
Gazetas (1991)	0.172±0.018	0.0114±0.0010	0.0112±0.0011	0.0068±0.0007

The results of the parametric study are presented in graphical form in Figures 7.6 to 7.8. The vertical (u_v) and horizontal (u_H) translations of the foundation were normalized by the foundation diameter (D_f) and are presented in Figures 7.6 and 7.7, respectively. The foundation rotation or rocking angle (θ) in degrees is presented in Figure 7.8. The translations and rotation were obtained using the rated power production design loads from Table 7.5, and by estimating the different elastic stiffnesses using Eq. 9 for μ_{hh} from 0 to 0.5, for α^2 between 0.2 to 2, and k_s from 0 to 2. Similar behaviour is seen in Figures 7.6, 7.7, and 7.8, where the translational and rotational responses of the foundation diminish with increasing Poisson's ratio and soil stiffness gradient. Similarly, for u_V and θ, these responses get smaller when α^2 decreases, which is a consequence of increasing the vertical stiffness of the soil (E_v or G_v) or decreasing horizontal stiffness (E_h or G_h). The opposite trend with respect α is observed in Figure 7.7 for u_h.

Additionally, measured field responses of the foundation are included where applicable for reference (see Figures 7.7 and 7.8), to compare with the estimated values from the parametric study. Such responses were obtained from the field monitoring system implemented and described in Appendix D.5. For more details on the measurements and results from this field study refer to Gonzalez-Hurtado et al. (2017). It is acknowledged that such field responses were measured under dynamic loading conditions for normal wind and normal operation conditions of the KEPA 4 wind turbine, and that the nature of this soil-structure interaction is actually frequency-dependent. Therefore, careful attention should be paid when comparing foundation responses obtained using static stiffness equations (stiffnesses for frequencies approaching to zero) and those obtained in a dynamic structural analysis considering a spectrum of frequencies as in the case of high-frequent vibrations.

For wind loading of wind turbine foundations, for both onshore and offshore, the peak frequencies of the loads can be relatively small (0.5 to 0.05 Hz) producing induced vibrations of such a nature that the static stiffnesses may be representative for the dynamic stiffnesses that are required in structural analysis (Whitman, 1976; DNV, 1992 and 2002), thus allowing for the estimation of the foundation responses under static loading. The measured field responses, u_h and θ, are shown to be smaller compared to the estimated responses using Equation 7.4. This can be attributed to simplifications in the assumed material behaviour compared to the field case and to the approach in the parametric study assuming no embedment [to allow comparison with the solutions of DNV (2016) and Bell (1991)]. Moreover, the field responses also do not account for the effects of foundation damping (soil material damping plus radiation/geometric damping) on the static stiffnesses. Additional figures showing the embedded case (e = 0.16) for u_h and θ were produced and are shown in Appendix E.8.

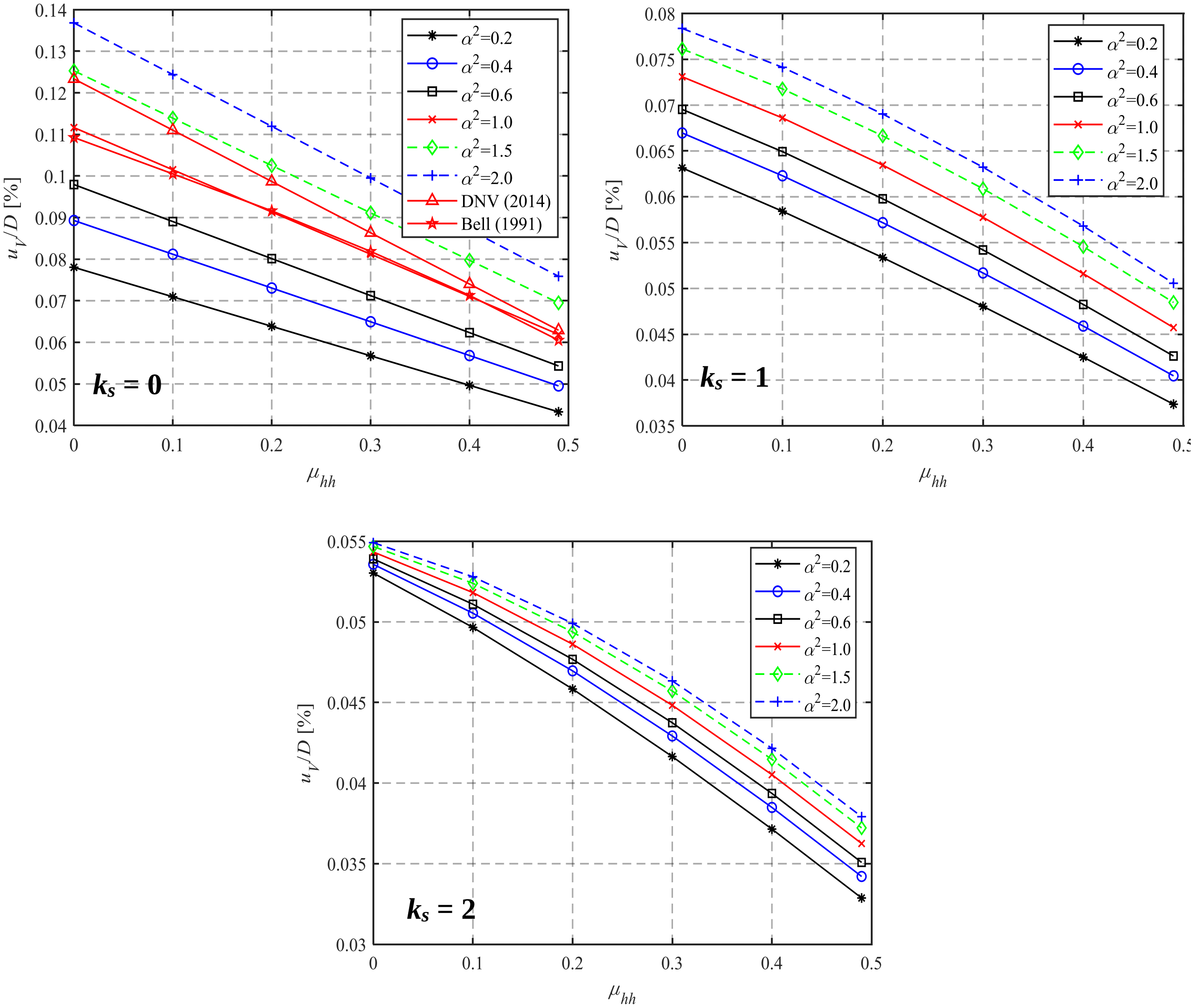

Figure 7.6 : Normalized vertical translation (u_V/D$_f$) for surface foundation as function of different soil parameters

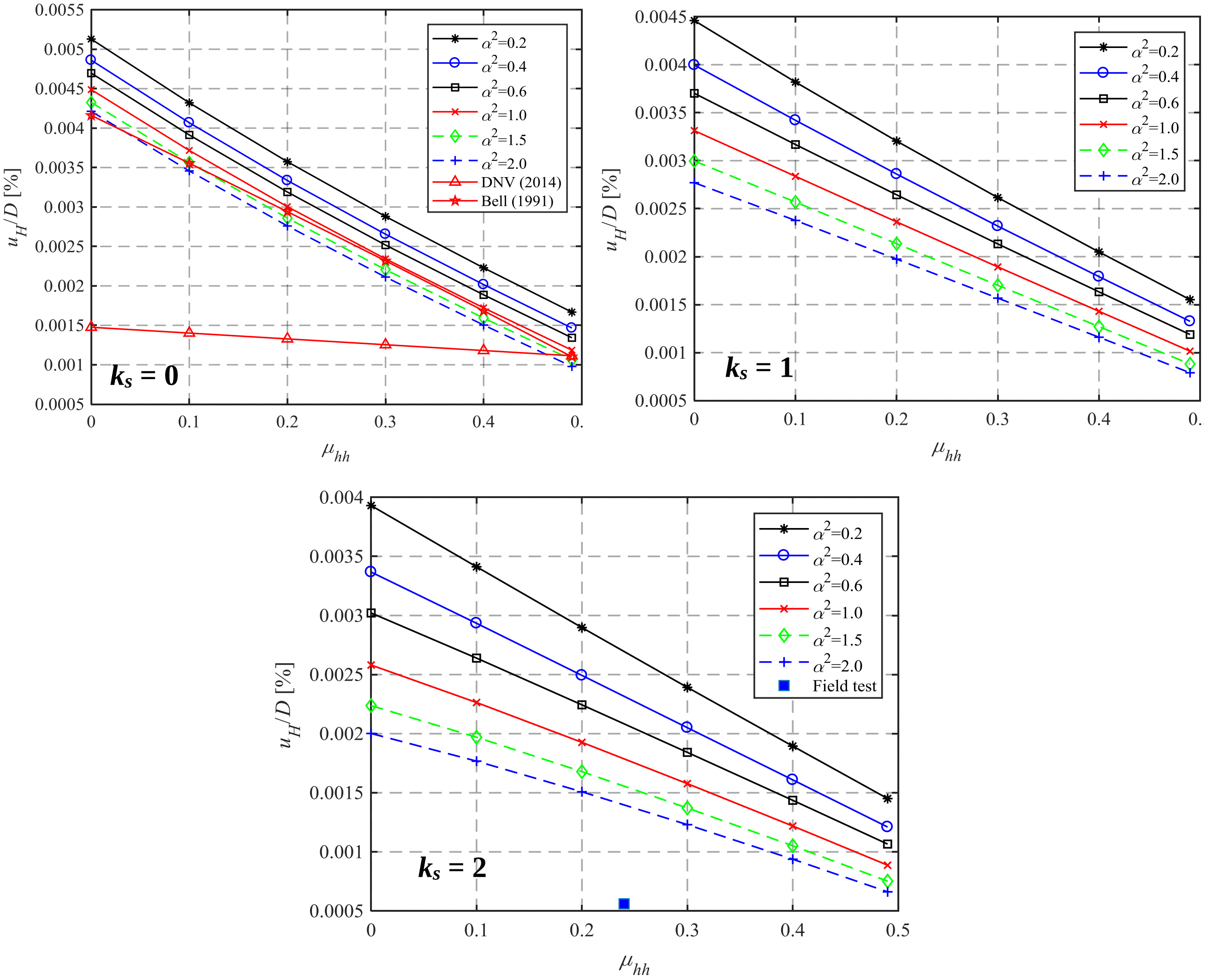

Figure 7.7: Normalized horizontal translation (u_H/D_f) for surface foundation as function of different soil parameters

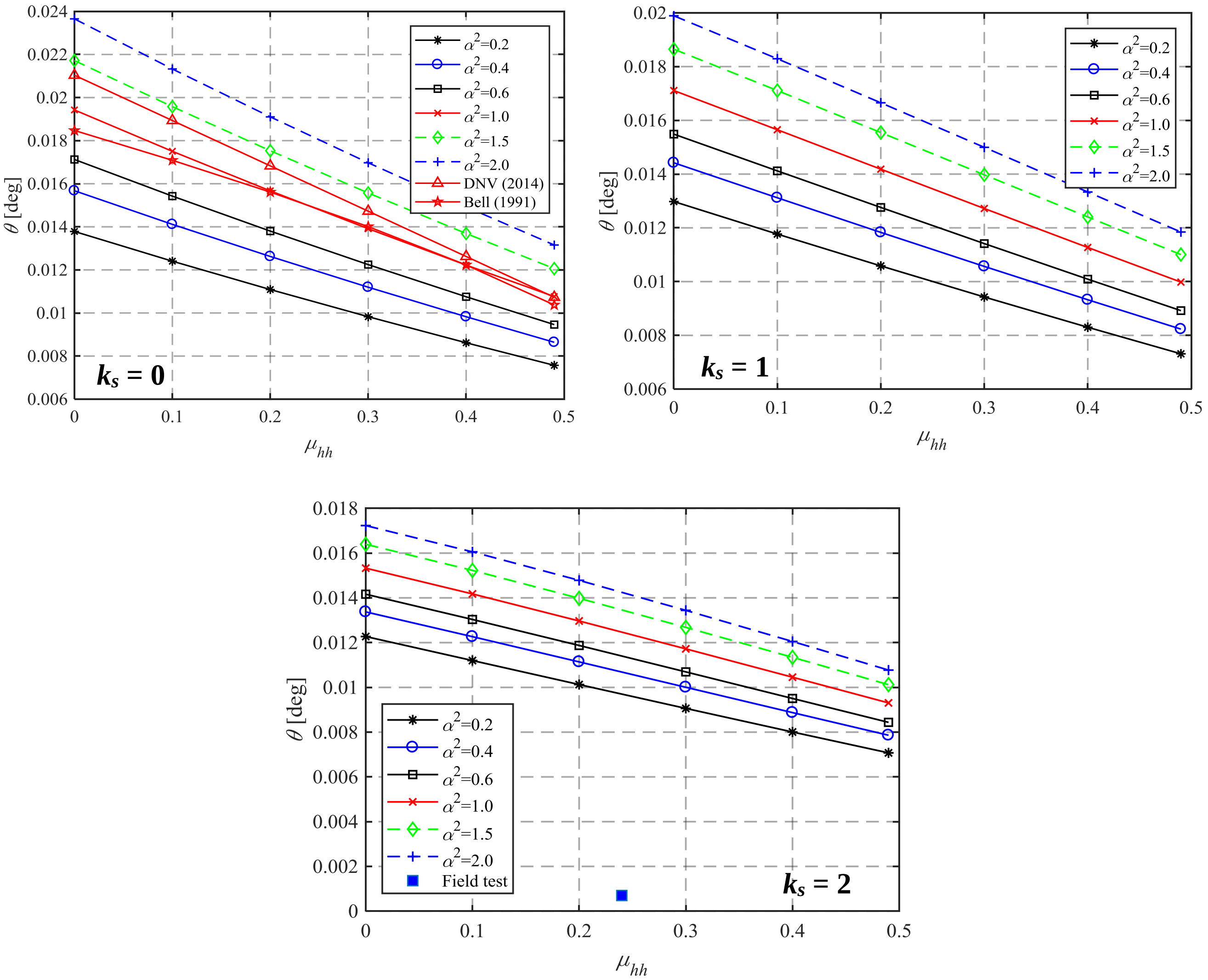

Figure 7.8: Foundation rotation (*θ*) for surface foundation as function of different soil parameters

7.5 Summary

Assessment of the ultimate limit state (ULS), serviceability limit states (SLS) and fatigue are of importance for the design of shallow wind turbine foundations. For wind turbines, serviceability limit states are often a significant design criterion since the location of the center of gravity with respect to the foundation of the wind turbine system can be controlled through the rocking stiffness. In this study coupled elastic deformations of a circular foundation founded on anisotropic soil under combined Vertical-Horizontal-Moment (VHM) loading have been studied using finite element analysis. A 3-parameter cross-anisotropic soil model was adopted. The effect of model dimensions was investigated, and the results show that domain widths of 50 times the foundation diameter are sufficiently accurate for finite element analysis. The results of the stiffness coefficients of surface foundations resting on a homogeneous isotropic soil compare favorably with currently available values. The vertical and rocking stiffness decrease with the anisotropic stiffness ratio (α), while the horizontal stiffness shows an increasing trend. On the other hand, the coupling stiffness showed no changes with varying values of α and seems to only depend on the Poisson's ratio.

To account for the effects of soil non-homogeneity and foundation embedment, Gibson soils and embedded foundations were considered. The Gibson and embedment correction factors were derived. The analysis shows that a higher Gibson modulus can increase the vertical, horizontal and moment stiffness, while it does not affect the coupling between horizontal and moment responses. To show the application of the derived stiffness equations, a field case was examined. The results indicate that the vertical and horizontal translations of the working wind turbine foundation can be affected by stiffness anisotropy, influenced by the soil stiffness in the vertical and horizontal directions of the soil, while its influence on the rocking behavior can be considered to be smaller. A set of normalized translation plots for surface foundations were also obtained from a parametric study. These plots further demonstrate the effect of different soil parameters, such as the soil stiffness gradient, Poisson's ratio and soil anisotropy, on the estimation of the elastic responses of a shallow surface foundation.

Chapter 8

8 Conclusions and Recommendations

8.1 Overview

For this thesis, a comprehensive experimental program was carried out to study the advanced geotechnical properties of a glacial till deposit that underlies the shallow foundation of a commercial wind turbine located in a wind farm at Port Alma, Ontario. The experimental study focused on the characterization of the critical state properties and stress-strain behaviour under monotonic loading for in-situ pressure conditions, assessment of the very small-strain properties in the vertical and horizontal directions with increasing confining pressure, measurement of the stiffness degradation of vertically and horizontally trimmed samples, and the evaluation of the small-strain stiffness anisotropy. The laboratory techniques included a series of consolidated isotropic undrained (CIU) triaxial tests with locally measured axial strains, CIU tests fitted with vertical and horizontal bender element transducers and resonant column tests on vertically and horizontally trimmed samples.

In addition, a number of well-known Canadian clays of glacial origin were also studied to further characterize their geotechnical properties. Similar testing techniques used for the Port Alma till material were employed to investigate the stress-strain and stiffness degradation from very small to large strains, and to assess the elastic anisotropy behaviour of these cohesive materials. A parametric study of the effect of changing stiffness anisotropy of the underlying material was also conducted based on the range of values found in the laboratory testing. A numerical analysis was conducted using a finite element (FE) model to assess the soil-foundation interaction between the shallow wind turbine foundation and the glacial clayey till at the Port Alma wind farm site. Results from the numerical analysis were used to compare with measured field responses of the shallow wind turbine foundation system.

This chapter summarizes the main outcomes and conclusions obtained from the laboratory investigations and numerical analysis. Similarly, limitations of the research are highlighted and used to propose future work.

8.2 Conclusions

8.2.1 Behaviour of Port Alma clayey till

1. The basic geotechnical properties of the unweathered clay till at the Port Alma wind farm showed that the soil is a low plasticity cohesive material rich in carbonates. A review of the literature on the geological formation of the deposit suggests that this material was deposited during the late Wisconsin stage of the Pleistocene epoch. Moreover, paleomagnetic test results found in the literature suggest that the preferred orientation of the Port Alma till fabric relates to the direction of ice flow when the material was deposited.

2. Chittick testing performed on Port Alma samples from different depths showed that the first 3 m of the soil deposit are absent of carbonates (e.g. calcite and dolomite). Between 3 m to 5 m the carbonate content increased from 0 to approximately 24% and then remained constant for the entire depth of the soil deposit. These results are in good agreement to that reported by Newson et al. (2019) for Port Alma and those reported by Quigley and Ogunbadejo (1976) when studying the mineralogy of a till deposit in Sarnia, Ontario.

3. Consolidated isotropic undrained (CIU) triaxial tests showed that the critical state behaviour of the Port Alma glacial till material is similar to that exhibited by other clay tills found in the literature, such as the Cromer till (Pestana et al., 2002), and that the critical state parameters obtained in this investigation are in good agreement with the results previously reported by Kiss (2016) and Newson et al. (2019). Similarly, the plots of the normalized deviator stress vs. axial strain and the normalized excess pore water pressure vs. axial strain showed that the response of the Port Alma material under estimated *in-situ* pressures is typical of overconsolidated cohesive soil materials described in the literature.

4. The normalized stiffness degradation measured using local strain transducers during CIU tests under *in-situ* pressure conditions indicate that the Port Alma till follows a similar stiffness degradation rate to that exhibited by other low plasticity glacial tills

and 'till-like' materials found within the literature (e.g. Magnus till, London clay, Chicago clay and Cowden till).

5. The results from isotropic compression tests using orthogonal bender elements (BE) transducers indicate that both vertically propagated-horizontally polarized (VH-mode) and horizontally propagated-horizontally polarized (HH-mode) shear and compressional wave velocities (V_{svh} and V_{shh}; V_{pvh} and V_{phh}) increase with higher confining pressure (p'). This trend is expected as S-waves and P-waves travel at velocities (V_s or V_p) that are function of the stiffness and density of the soil (Hardin and Richart, 1963; Clayton, 2011). Likewise, the small-strain shear moduli (G_{vh} and G_{hh}) and small-strain constrained moduli (M_{vh} and M_{hh}) also increase with greater pressures.

6. Measured shear and compressional waves with increasing confining pressure follow the velocity-stress power law relationship proposed by Cha et al. (2014). The wave velocity parameters α_s and α_p obtained in HH-mode are higher than those obtained in VH-mode. The factors β_s and β_p from both VH- and HH-modes are very similar and range between 0.32 and 0.35.

7. Values of G_{max} and M_{max} in HH-mode (G_{hh} and M_{hh}) are consistently higher than those estimated for VH/HV-modes (G_{vh} and G_{hv}; M_{vh} and M_{hv}). Whereas both G_{vh} and G_{hv}, and M_{vh} and M_{hv} are approximately equal. The ratio of G_{hh}/G_{vh} and M_{hh}/M_{vh} is equal to 1.34 and 1.31, respectively. This suggest that the Port Alma till is anisotropic and stiffer in the horizontal direction. The ratio of G_{vh}/G_{hv} and M_{vh}/M_{hv} ranges between 1.05 to 0.95, indicating that the material could be cross-anisotropic, since the ratios of G_{vh}/G_{hv} and M_{vh}/M_{hv} are close to 1.

8. Resonant column (RC) test results showed that the stiffness of the Port Alma till is strain dependent. The small-strain stiffness of the material is close to constant at very small shearing strains ($\gamma \leq 1\text{x}10^{-5}$) and the stiffness becomes highly non-linear and starts decreasing with strain increments once a threshold strain of about $4\text{x}10^{-4}$ is passed. Similar degradation behaviour was exhibited by both vertically and horizontally trimmed samples.

9. The obtained small-strain shear stiffness and elastic modulus from horizontally trimmed samples (90° sample) (G_{hh} and E_h) are consistently higher than those obtained from vertically trimmed samples (0° sample) (G_{vh} and E_h). These results are consistent with those obtained from the BE tests. The anisotropy degree estimated using the relationships presented by Graham and Houlsby (1983): $\alpha=(G_{hv}/G_{vh})$ and $\alpha=(E_h/E_v)^{0.5}$, yielded values of 1.25 and 1.15, respectively.

10. The anisotropy degree defined by $\alpha=(G_{hv}/G_{vh})$ and $\alpha=(E_h/E_v)^{0.5}$ were calculated at different strain levels for the estimated in-situ stress (p'=160 kPa) and different isotropic confining pressures. These results indicate that under the testing conditions adopted the induced shear strain increments exert a more important effect in the variation of the small-strain stiffness anisotropy than volumetric changes.

11. Comparisons between laboratory measurements of V_{svh} and V_{shh} (and G_{vh} and G_{hh}) on undisturbed samples of Port Alma till with *in-situ* tests (e.g SCPTu, CST) show that the laboratory measurements of the glacial till elastic properties underestimate the values obtained in the field for depths between 1 to 10 m, for depths below 10 m the laboratory measurements of V_s and G_{max} show good agreement with in-situ measurements. Possible reasons for differences between laboratory and field measurements can be attributed to voids ratio differences between the field and laboratory, scale effects with respect to natural fissuring, and the effects of layers in naturally deposited soils.

8.2.2 Behaviour of different Canadian glacial clays

1. The basic geotechnical properties of the studied natural soils (Port Alma clay, Wallaceburg clay, Windsor clay, Blenheim clay and Winnipeg clay) indicate that these are overconsolidated firm to stiff glacial clays of low to medium plasticity ($6 < I_p < 33$) and low activity ($0.29 <$ activity < 0.49). Such stress history and mechanical characteristics are typical of glacial clay tills and ‘till-like’ materials found in the literature.

2. Results from consolidated isotropically undrained (CIU) triaxial tests showed that the normalized critical state behaviour of the tested materials is very similar, yielding values of M (slope of critical state line) or effective angle of friction well within the range of other soils of a similar nature reported in the literature.

3. The normalized stiffness degradation obtained with local instrumentation is comparable to other glacial materials of low to medium plasticity found in the literature. These also show similar stiffness degradation rates with increasing shear strain.

4. Bender element (BE) testing showed that the propagating wave velocities (shear and compressional waves) for both vertical and horizontal directions for the studied cohesive soils increased with increasing of confining pressure, these follow the velocity-stress power law relationship proposed by Cha et al. (2014).

5. Resonant column (RC) results indicated that the normalized shear modulus (G/G_{max}) of the soils reduces with shear strain increment. The results show threshold shear strain values, where the modulus begins to reduce, that are similar to other clay soils found in the literature. The threshold shear strain also seems to increase with increasing plasticity index and the OCR appears to have little effect on the observed results, as has been found previously (e.g. Vucetic and Dobry, 1991). Additionally, the minimum damping ratio range for these soils lie between 1.8% and 2.2% and the magnitude starts to gradually increase with shear strain increments.

6. The small-strain stiffness anisotropy was assessed for each of the cohesive natural materials. Results obtained using sample rotation in the RC and orthogonal BE showed that Port Alma clay, Wallaceburg clay, Windsor clay and Winnipeg clay are horizontally stiffer ($G_{hh} > G_{vh}$), whereas Blenheim clay seems to be vertically stiffer ($G_{hh} < G_{vh}$).

7. The estimation of the anisotropic ratio (α) suggest that the materials are anisotropic or at least cross-anisotropic. α values ranged between 1.10 to 1.30 for the horizontally stiffer materials, while the vertically stiffer material had α value of 0.92. These results

are in good agreement with those reported in the literature for other glacial cohesive soils.

8. The wave velocity parameters α_s and β for the different soils were shown to be well predicted using the correlations proposed by Cha et al. (2014) that are function of soil compressibility (C_c). A new relationship between α_s and β was proposed using the data collected during this investigation.

9. The variation of the normalized vertical and horizontal small-strain shear modulus (G_{vh} and G_{hh}) with pressure followed similar trend to that exhibited by other anisotropic stiff overconsolidated clays with glaciogenic origin found in the literature (e.g. London clay, Gault clay and Chicago clay). The variation of normalized stiffness with pressure also showed good agreement with the relationships implied by the equations proposed by Jamiolkowski et al. (1995) for the estimation of G_{vh} and G_{hh}.

10. A new correlation to estimate the anisotropy ratio (α) as a function of the coefficient of earth pressure at rest (K_o) was developed after gathering data from different anisotropic materials found in the literature. This equation follows a similar form to that described by Jamiolkowski et al. (1995) in terms of an empirical exponent n and material constants S_{hh} and S_{vh}.

11. A complete set of stiffness parameters for each soil were derived using the three-parameter model proposed by Graham and Houlsby (1983), and using the results from bender elements, resonant column, and undrained CIU tests.

8.2.3 Effects of soil stiffness anisotropy on the serviceability limit state of a shallow wind turbine foundation

1. The coupled elastic deformations of circular foundations founded on anisotropic soils under combined Vertical-Horizontal-Moment (VHM) loading were studied using finite element analysis. The 3-parameter cross-anisotropic soil model proposed by Graham and Houslby (1983) was adopted for the models.

2. The effect of model dimensions was investigated, and the results showed that domain widths of 50 times the foundation diameter are sufficiently accurate for finite element analysis. Moreover, the estimates of the stiffness coefficients for surface foundations resting on a homogeneous isotropic soil compared favorably with results found in the literature.

3. A set of dimensionless coupled static stiffness equations were developed to predict the load-displacement response of surface and embedded foundations, founded on anisotropic soils with linear increase of stiffness with depth under complex loading.

4. To study the effect of soil stiffness anisotropy on foundation responses and to show the application of the derived stiffness equations, a field case was examined. The results showed that the vertical and horizontal translations of the wind turbine foundation under working loads are influenced by the stiffness anisotropy and the soil stiffness in the vertical and horizontal soil direction. However, the influence of anisotropy on the rocking behavior was found to be less significant.

5. Normalized translation plots for surface foundations were obtained from a parametric study. These plots further demonstrate the effect of different soil parameters, such as the soil stiffness gradient, Poisson’s ratio and soil anisotropy, on the estimation of the elastic responses of large shallow near surface foundations.

8.3 Recommendations for future work

The following points can be considered for potential improvements and further research work in the future:

1. During this research only 5 different natural glacial clays were studied, four of which belong to areas around southwestern Ontario. As pointed out previously throughout this investigation, the small-strain anisotropy data for Canadian soils is very scarce in the literature. It is strongly recommended to continue with of more studies that include the stiffness anisotropy assessment of other natural Canadian soils. These studies can greatly contribute to the characterization of these type of soils and to better understand their complex behaviour.

2. Here the majority of the testing was conducted under *isotropic* pressures on relatively undisturbed samples. *Anisotropic consolidation* could also be used to assess the variations on the small-strain anisotropic ratio.

3. Only the inherent anisotropy of the natural materials was studied in this study. The effect of stress-induced anisotropy could also be investigated by using reconstituted and intact samples of the same soils. This could help to evaluate any influence of soil microstructure on stiffness anisotropy.

4. Microstructure and fabric analysis of the natural materials could be carried out using scanning electron microscope (SEM) imagery and microstructural analysis. These can contribute to a better understanding of the link between the glacial clay mechanical behaviour and their anisotropic fabrics.

5. Considering that sample availability and time are not an issue, different stiffness parameters can be measured employing a series of advanced tests. Drained small-strain elastic modulus (E_{max}) can be measured using drained probes (with different directions $\Delta q/\Delta p'$ in stress space) with local strain measurements. Similarly, this parameter could be obtained for both vertical and horizontal directions (E_v and E_h) using sample rotation (for directions other than 0° and 90°). Moreover, measuring the stiffness degradation of horizontally cut samples under monotonic loading with local measurement of strains can further complete the characterization of the behaviour of Canadian glacial clays.

6. The measurement of local radial strains could facilitate the derivation of the Poisson's ratio in different directions (μ_{vh} and μ_{hh}) using sample rotation and directional drained probes.

7. Recent equipment development has allowed the integration of both bender elements and resonant column testing into one setup. This could help with reducing testing time as both tests can be carried out with the same soil sample and number of samples needed for testing. This test set up can also be used to study the stiffness anisotropy of the material by using sample rotation (vertically and horizontally cut samples).

8. Although the stiffness parameters used for the development of the numerical model were obtained using “working values” of shear strains for wind turbine foundations, the small-strain and soil degradation data obtained in this investigation could be used to develop a more complex constitutive model that can accurately predict the strain dependence and non-linear behaviour of glacial clays. Such a constitutive model could be implemented in a more sophisticated numerical model to produce more accurate numerical results.

9. The shallow wind turbine foundation was modelled as a circular rigid element, however in reality, this has an octagonal shape and it tapers towards the edges and flexes. Such assumptions could potentially impact the outcome of the numerical analysis. This can be further investigated by explicitly modelling the shape of the foundation.

10. A rigorous dynamic analysis is also required to better understand the frequency-dependent nature of the foundation system responses (supported by the field data measured by González-Hurtado et al, 2017) in light of the soil anisotropy.

11. The field work performed by González-Hurtado et al. (2017) can be improved by allowing extended periods of data collection. In this work it was shown that there was a relationship with the shape of the particle velocities of the propagated waves through the ground and the presence of anisotropy in the ground. Further work is necessary to better understand the form of the generated waves (surface and body) and the relative contributions of the foundation type, soil materials and heterogeneity, and strain levels.

References

Afifi, S. E. A., 1970. Effects of stress history on the shear modulus of soils. Ph.D. dissertation, The University of Michigan, Ann Arbor, MI.

Ahmad, S. (2016). Piezoelectric device for measuring shear wave velocity of soils and evaluation of low and high strain shear modulus, PhD Thesis, London, Ontario, Canada: Department of Civil and Environmental Engineering, Western University.

Anderson, D. G., 1974. Dynamic modulus of cohesive soils. PhD thesis, The University of Michigan, at Ann Arbor, Michigan.

Anderson, D. G., and Stokoe, K. H. 1978. Shear Modulus: A Time Dependent Soil Property. Dynamic Geotechnical Testing, ASTM STP 654. D. T. M. L. Silver. West Conshohocken: 66-90.

ASTM D2216-10 Standard Test Methods for Laboratory Determination of Water (Moisture) Content of Soil and Rock by Mass, ASTM International, West Conshohocken, PA, 2010.

ASTM D2435/D2435M-11 Standard Test Methods for One-Dimensional Consolidation Properties of Soils Using Incremental Loading, ASTM International, West Conshohocken, PA, 2011.

ASTM D4015-15e1 Standard Test Methods for Modulus and Damping of Soils by Fixed-Base Resonant Column Devices, ASTM International, West Conshohocken, PA, 2015.

ASTM D4318-17 Standard Test Methods for Liquid Limit, Plastic Limit, and Plasticity Index of Soils, ASTM International, West Conshohocken, PA, 2017.

ASTM D4767-11 Standard Test Method for Consolidated Undrained Triaxial Compression Test for Cohesive Soils, ASTM International, West Conshohocken, PA, 2011.

ASTM D7263-09 Standard Test Methods for Laboratory Determination of Density (Unit Weight) of Soil Specimens, ASTM International, West Conshohocken, PA, 2009.

Atkinson, J. H., and Little, J. A. (1988). Undrained Triaxial Strength and Stress-Strain Characteristics of Glacial till Soil, *Canadian Geotechnical Journal*, 25, 428-439.

Atkinson, J. H., Richardson, D., and Stallebrass, S. E. (1990). Effect of recent stress history on the stiffness of overconsolidated soil. *Géotechnique*, 40, 531-540.

Atkinson, J.H. (1993). An Introduction to The Mechanics of Soils and Foundations, McGraw-Hili Book Company (UK) Ltd.

Banerjee, P. K., Stipho, A. S., and Yosif, N. B. (1984). A theoretical and experimental investigation of the behaviour of anisotropically consolidated clays. In Developments in soil mechanics and foundation engineering, Vol. II (edited by P. K. Banerjee & R. Butterfield), pp. 1-41. London: Elsevier Applied Science.

Baracos, A. (1977). Compositional and structural anisotropy of Winnipeg soils-a study based on scanning electron microscopy and X-ray diffraction analysis. Canadian Geotechnical Journal, 14, 125-143.

Baracos, A., Graham, J., Kjartanson, B.H. and Shields, D.H.S., 1983. Geology and soil properties of Winnipeg. ASCE Special Publication on Geological Environment and Soil Properties. 39-56.

Barden, L. 1963. Stresses and displacements in a cross-anisotropic soil. *Géotechnique*, 13, 198-210.

Becker, D. E. (1981). Settlement analysis of intermittently-loaded structures founded on clay subsoils. (PhD Thesis). London, Ontario, Canada: Department of Civil and Environmental Engineering, Western University.

Bell, F. (2002). The geotechnical properties of some till deposits occurring along the coastal areas of eastern England. Engineering Geology, 63, 49-68.

Bell, F.G. (1998). The geotechnical properties and behavior of pro-glacial lake clay, and its cementitious stabilization. Geotechnical and Geological Engineering, 16, 167-199.

Bell, R.W. (1991). The analysis of offshore foundations subjected to combined loading. Master Thesis, University of Oxford.

Bellotti, R., Jamiolkowski, M., Lo Presti, D.C.F. and O'Neill, D.A. (1996). Anisotropy of small strain stiffness in Ticino sand. *Géotechnique*, 46(1): 115–131.

Benn, D. I., and Evans, D. J. A. (2010). Glaciers and Glaciation. Second Ed. Hodder-Arnold, London, 2010.

Bishop, A. W. & Hight, D. W., (1977). The value of Poisson’s ratio in saturated soils and rocks stressed under undrained conditions. *Géotechnique*, 27(3), 369–384.

Black, D. K., and Lee, K. L. (1973). Saturating laboratory samples by back pressure. *Journal of Soil Mechanics and Foundation Division*, ASCE, 99(1), paper 9484, 75-93.

Boone, S.J. (2010). A critical reappraisal of “preconsolidation pressure” interpretations using the oedometer test. *Canadian Geotechnical Journal*, 47(3): 281– 296.

Borowicka, H. (1943). Über ausmittig belastete, starre Platten auf elastisch-isotropem Untergrund. Ingenieur-Archiv, 14(1), pp. 1-8.

Boulton, G. S. (1976). The Development of Geotechnical Properties in Glacial Tills. In R.F. Legget, Glacial Tills: An Interdisciplinary Study (pp. 292-303). Ottawa: The Royal Society of Canada.

Boulton, G.S., and Paul M.A. 1976. The influence of genetic processes on some geotechnical properties of glacial tills. *Quarterly Journal Engineering Geology,* 9, 159-194.

Burland, J. B. (1989). Small is beautiful: the stiffness of soils at smalls-strains. Ninth Laurits Bjerrum Lecture. *Canadian Geotechnical Journal*, 26, 4, pp. 499-516.

Bransby, M. F., and Randolph, M. F. (1998, Jan). Combined loading of skirted foundations. *Géotechnique,* 48(5), 637–655.

Brinkgreve, R. B. J. 2005. Selection of soil models and parameters for geotechnical engineering application. Soil Constitutive Models: Evaluation, Selection, and Calibration, Geotechnical special publication 128, J. A. Yamamuro and V. N. Kaliakin, eds., ACSE, Reston, VA, 69–98

Brosse, A., Hosseini, R. K., Jardine, R. J., and Coop, M. R. (2017). The shear stiffness characteristics of four Eocene-to-Jurassic UK stiff clays. *Géotechnique,* 67 (3), 242-259.

Byrne, B.W. and Houlsby, G.T. (2003). Foundations for Offshore Wind Turbines. Philosophical Transactions of the Royal Society of London, Series A, Vol. 361, Dec., 2909–2930.

Callisto, L., and Rampello, S. (2002). Shear strength and small-strain stiffness of a natural clay under general stress conditions. *Géotechnique*, 52(8), 547–560.

Canadian Geotechnical Society (2006). Canadian Foundation Engineering Manual, 4th Ed., BiTech publications, Vancouver, BC.

Canadian Standards Association. (2008). CSA Guide to Canadian wind turbine codes and standards. Canada: CSA.

Canadian Standards Association. (2014). CAN/CSA-C61400-1 Wind turbines part1: design requirements. CSA.

Casagrande, A. & Carillo, N. (1944). Shear failure of anisotropic materials. Proc. Boston Soc. Civ. Engrs 31, 74–87.

Casagrande, A. (1947). Classification and Identification of Soils, American Society of Civil Engineers, 73[6], 783-810.

Cascante, G., Santamarina, C. and Yassir, N., (1998). Flexural excitation in a standard torsional-resonant column device. *Canadian Geotechnical Journal*, Vol. 35, 478-490.

Cha, M., Santamarina, J., Kim, H., and Cho, G. (2014). Technical Note. Small-Strain Stiffness, Shear-Wave Velocity, and Soil Compressibility. Journal of Geotechnical and Geoenvironmental Engineering., 140 (10), 06014011.

Chan, C. M. (2010). Bender element test soil specimen: Identifying the shear wave arrival time. *Electronic Journal of Geotechnical Engineering*, 15 (1), 1263–1276.

Chandler R. (2010). Stiff sedimentary clays: geological origins and engineering properties. *Géotechnique*, 60[12], 891-902.

Chapman, L. J., and Putnam, D. F. (1966). The Physiography of Southern Ontario. Second edition, University of Toronto Press.

Chung, C. K., and Finno, R. J. (1992). Influence of depositional processes on the geotechnical parameters of Chicago glacial clays. Engineering Geology, 32, 225-242.

Clarke, B. G. (2018). The Engineering Properties of Glacial Tills, Geotechnical Research, 5[4], 262-277.

Clayton, C. R. I. (2011). Stiffness at small strain: research and practice. *Géotechnique*, 61(1), 5-37.

Clayton, C. R. I., Priest, J. A., Bui, M. and Kim, S. G., (2008). The Stokoe Resonant Column Apparatus: Effects of Stiffness, Mass and Specimen Fixity. *Géotechnique*, Vol. 59, 429-437.

Corkery, M.T., (1996). Geology and landforms of Manitoba. The Geography of Manitoba: Its land and its People. The University of Manitoba Press: Manitoba, pp. 11-30.

Coulomb, C. 1976. Essai sur une applicationde regles de maximis et minimis a quelques problemas de statique relatifs a l’archetecture. Memoires de Mathematique et de Physique Presentes a l’Academie Royale des Sciences. Paris 7, 343-382.

Cowan, W. R. Quaternary geology of the Orangeville area, southern Ontario. Ontario Division of Mines, Geoscience. Report 141, p. 98.

Cuccovillo, T. & Coop, M. R. (1997). The measurement of local axial strains in triaxial tests using LVDTs. *Géotechnique*: 47, No. 1, 167–171

D. G. Toll and B. H. Ong. (2003). Critical-state parameters for an unsaturated residual sandy clay. *Géotechnique*, 2003, 53(1), 93-103.

Darendelli, M. H. (2001). Development of a new family of normalized modulus reduction and material damping curves. (PhD Thesis). Austin, Texas, US. The University of Texas at Austin.

Dassault Systèmes (2016). Abaqus analysis user’s manual. Simulia Corp, Providence, RI, USA.

Davies, M. C. R., and Newson, T. A. 1993. A crirical state constitutive model for anisotropic soil. Proceedings of the Wroth Memorial Symposium, Oxford, pp. 192-229.

Dellinger, J., and Vernik, L.. (1994). Do travel times in pulse-transmission experiments yield anisotropic group or phase velocities? Geophysics, 59, No. 11, 1774–1779.

Deshpande, V. (2016). Numerical modelling of wind turbine foundations subjected to combined loading. MESc Thesis. Western University.

Det Norske Veritas. (2007). DNV-OS-J101, Design of offshore wind turbine structures. DNV.

DNV, (2002). Guidelines for design of wind turbines (2nd edition, technical report). Oslo, Norway: Det Norske Veritas.

DNV, GL, DNVGL-ST-0126 (2016). Design of support structures for offshore wind turbines.

Doherty, J.P., & Deeks, A.J. (2003). Elastic response of circular footings embedded in a non-homogeneous half-space. Géotechnique, 53(8), pp. 703-714.

Dora, I. G., Sivakumar, V., Graham, J., and Johnson, A. (2000). Estimation of in-situ stresses using anisotropic elasticity and suction measurements. Géotechnique: 50 [2], 186-196.

Dreimanis, A. (1962). Quantitative gasometric determination of calcite and dolomite by using Chittick apparatus. Journal of Sedimentary Petrology, 32 (3), 520-529.

Dreimanis, A. (1976). Tills: Their origin and properties. In glacial till: An Interdisciplinary Study. Ed. R.F Legget, Royal Society of Canada, Special publication. 12, 11-49.

Dreimanis, A., and Karrow, W. R. (1972). Glacial history of the Great Lakes-St. Lawrence Region, the classification of the Wisconsinan Stage, and its correlatives; 24th international Geological Congress (Montreal). Section 12, 5-15.

Drnevich, V. P. (1967). Effect of Strain History on the Dynamic Properties of Sand Michigan, University of Michigan. PhD: 151.

Drnevich, VP., Werden, S., Ashlock, JC., Hall, JR. (2015). Applications of the new approach to resonant column testing. Geotechnical Testing Journal, 38(1), 23–39.

Drucker, D.C., and Prager, W. 1952. Soil mechanics and plastic analysis or limit design. Quarterly of Applied Mathematics,10, 2, 157-165.

Duncan, J. M. & Seed, H. B. (1966). Anisotropy and stress reorientation in clay. *Journal of Soil Mechanics and Foundation Engineering Division*. American Society of Civil Engineers, 92[5], 21-50.

Duncan, J. M., and Chang, C.Y. (1970). Nonlinear analysis of stress and strain in soils. *Journal of Soil Mechanics and Foundations Division*, 96, 5, 1629–1653.

Dyvik, R., and Madshus, C. (1985). Lab measurements of Gmax using bender element. Proceedings, ASCE Convention on Advances in the Art of Testing Soils under Cyclic Conditions, 186–196.

Evenson, E. B., Dreimanis, A., and Newsome, J. W. 1977. Subaquatic flow tills: a new interpretation for the genesis of some laminated till deposits. Boreas. Vol. 6, 115-133.

Fuller, M. D. (1962). A magnetic fabric in till: Geological Magazine, 99[3], 233-237.

Gasparre, A., Nishimura, S., Anh-Minh, N., Coop, M. R., and Jardine, R. J. (2007b). The stiffness of natural London Clay, *Géotechnique*, 57 [1], 33–47.

Gazetas, G. 1981a. Deformational soil cross-anisotropy: experimental evaluation and mathematical modeling. Case Western Reserve Univ. Res. Rep.8102, Cleveland, Ohio.

Gazetas, G. 1981b. Dynamic compliance matrix of rigid strip footing bonded to a viscoelastic cross-anisotropic half-space. *International Journal of Mechanical Sciences*.

Gazetas, G. 1981c. Strip foundations on cross-anisotropic soil layer subjected to dynamic loading. *Géotechnique*, 31, 2.

Gazetas, G. 1981d. Stresses and displacements in cross-anisotropic soils. *Journal of Geotechnical Division*, ASCE.

Gazetas, G. 1981e. Indentation of anisotropic half-space by yielding circular foundation. *Journal of the Engineering Mechanics Division*, ASCE, 107, 4.

Gazetas, G. 1983. Analysis of machine foundation vibrations: state of the art. International Conference on Soil dynamics and Earthquake Engineering, 2, 1.

GDS Instruments. (2006). Resonant Column System Handbook. Hook, UK: GDS Instruments Ltd.

GDS Instruments. (2015). Bender Elements Handbook. Hook, UK: GDS Instruments Ltd.

Geike, A. 1863. On the phenomena of the glacial drift of Scotland. Transactions of the Geological Society of Glasgow. 1, 1-190.

Georgiannou, V. N. (1988). The behaviour of clayey sands under monotonic and cyclic loading. PhD thesis, University of London.

Gerrard, C. M. & Harrison, W. J. (1970a). Circular loads applied to a cross-anisotropic half-space. Paper 8. Commonwealth Scientific and Industrial Research Organization: Div. Appl. Mech.

Gerrard, C. M. & Harrison, W. J. (1970b) Stresses and displacements in a loaded orthorombic half-space. Canberra: Commonwealth Scientific and Industrial Research Organization: Div. Appl. Mech.

Gerrard, C. M. & Harrison, W. J. 1971. The analisys of a loaded half-space comprised of anisotropic layers. CSIRO Australia, Division of Applied Geomechanics, Technical Paper #10.

Gibson, R. E. (1974). The analytical method in soil mechanics. Geotechnique 24, No. 2, 115-140.

Gibson, R.E. (1967). Some results concerning displacements and stresses in a non-homogeneous elastic half-space. *Géotechnique*, 17(1), pp. 58-67.

Gonzalez-Hurtado, J. and Newson, T. 2016. Small-strain behaviour of a carbonate clay till underlying a wind turbine shallow foundation by different in-situ and laboratory tests, Canadian Geotechnical Society: Geo Vancouver, Vancouver, Canada. Paper # 3653.

Gonzalez-Hurtado, J., He, P., Newson, T., Hong, H., Postman, M., and Molnar, S. (2017). “Field monitoring and analysis of an onshore wind turbine shallow foundation system”. Canadian Geotechnical Society: Geo Ottawa, Ottawa, Canada. Paper # 406.

Gourvenec, S., and Randolph, M. 2003. Effect of strength non-homogeneity on the shape of failure envelopes for combined loading of strip and circular foundations on clay. *Géotechnique*, 53(6), 575–586.

Graham, J. and Shields, D.H., (1985). Influence of geology and geological processes on the geotechnical properties of a plastic clay. Engineering Geology, 22: 109--126.

Graham, J., and Houlsby, G. T. (1983). Anisotropic elasticity of a natural clay. *Géotechnique*, 33 [2], 165–180.

Gravenor, C. P., and Stupavsky, M. 1974. Magnetic susceptibility of the surface tills of Southern Ontario. *Canadian Geotechnical Journal*, 11, 5, 658-663.

Gravenor, C. P., Stupavsky, M., and Symons, D. T. A. (1973). Paleomagnetism and Its Relationship to Till Deposition, *Canadian Journal of Earth Sciences*, 10, 1068-1078.

Green, A. (1954). The plastic yielding of metal junctions due to combined shear and pressure. *Journal of the Mechanics and Physics of Solids*, 2(3), 197–211.

Green, G. (1828). An essay on the application of mathematical analysis to the theories of electricity and magnetism. Published by the author.

Gu, X., Yang, J. and Huang, M., (2013). “Laboratory measurements of small strain properties of dry sands by bender element.” Soils and Foundations, 53(5), 735-745.

Hall, J. R. and Richart, F. E. 1963. Dissipation of Elastic Wave Energy in Granular Soils." *Journal of the Soil Mechanics and Foundations Division*, ASCE 89(6): 27-56.

Hansen, J. B. (1970). A revised and extended formula for bearing capacity. Bulletin No. 28.

Hardin, B. O. & Kalinski, M. E. (2005). Estimating the shear modulus of gravelly soils. *Journal of Geotechnical and Geoenvironmental Engineering*, 131(7), 867–875.

Hardin, B. O. and Drnevich, V. P., (1972). Shear modulus and damping in soils: Design equations and curves. *Journal of Soil Mechanics and Foundations Division*, ASCE 98, No. SM7, 667–692.

Hardin, B. O., and Black, W. L. (1966). Sand Stiffness under Various Triaxial Stresses." *Journal of the Soil Mechanics and Foundations Division-ASCE*, 92(SM2): 27-42.

Hardin, B. O., and Blandford, G. E. (1989). Elasticity of particulate materials. *Journal of Soil Mechanics and Foundations Division*. 115[2], 1449-1467.

Hardin, B., and Black, W. (1968). Vibration modulus of normally consolidated clay. *Journal of Soil Mechanics and Foundations*, 353-369.

Hasan, A. M., and Wheeler, S. J. (2015). Measuring travel time in bender/extender element tests. Geotechnical Engineering for Infrastructure and Development. January 2015, 3171-3176.

Head, K. (1998). Manual of soil laboratory testing, effective stress tests. Wiley

Hooper, J. A., (1975). Elastic settlement of a circular raft in adhesive contact with a transversely isotropic medium. *Géotechnique*, 25 (4), 691-711.

House, A.R., Oliveira, J.R.M.S., and Randolph, M.F. (2001). Evaluating the coefficient of consolidation using penetration tests. International Journal of Physical Modelling in Geotechnics, 3, 17-26.

Hudec, P.P. (1998). Geology and geotechnical properties of glacial soils in Windsor. In P.F. Karrow & O.L. White (Eds.), Urban geology of Canadian cities, GAC Special Publication, 42, pp. 225–236.

Idriss, I. M., Dobry, R., and Singh, R. D. (1978). Nonlinear behavior of soft clays during cyclic loading. *Journal of Geotechnical Engineering Division*, ASCE, 104(GT12), 1427-1447.

Idriss, I. M., Moriwaki, Y., and Dobry, R. (1977). Stress-strain behavior of soft clay in level ground deposits during and after cyclic earthquake loading, normal marine clay, Icy Bay area, Gulf of Alaska. Final report for Shell Development Company, Woodward-Clyde Consultants, San Francisco, California.

IEC 61400-1. (2005). IEC 61400-1: Wind Turbines–Part 1: Design Requirements. International Electrotechnical Commission, Geneva.

Ishihara, K. (1996). Soil behaviour in earthquake geotechnics. New York: Oxford.

Iverson, N. R. (2017). Determining Glacier Flow Direction from Till Fabrics, Geomorphology, 299, 124-130.

Iverson, N. R., Hooyer, T. S., Thomason, J. F., Graesch, M., and Shumway, J. R. (2008). The Experimental Basis for Interpreting Particle and Magnetic Fabrics of Sheared Till, Earth Surface Processes and Landforms, 33, 627–645.

Iwasaki, T., Tatsuoka, F., and Takagi, Y. (1978). Shear Moduli of Sands Under Cyclic Torsional Shear Loading. Soils and Foundations, 18 (1): 39-56

Jaky, J. (1944). The coefficient of earth pressure at rest. In Hungarian (A nyugalmi nyomas tenyezoje). *Journal of the Society of Hungarian Architects and Engineering*, 78 (22), 355–358.

Jamiolkowski, M., Lancellotta, R., and Lo Presti, D. C. F. (1995). Remarks on the stiffness at small-strains of six Italian clays, proceedings of the 1st international symposium of pre-failure deformation characteristics of geomaterials, 817-836.

Jardine R.J. (1995), One perspective of the pre-failure deformation characteristics of some geomaterials. Proc. of the Int. conference on the pre-failure deformation characteristics of geomaterials, Hokkaido, Japan, Vol.2, pp. 855-885.

Jardine, R. J. (1985). Investigations of pile-soil behaviour, with special reference to the foundations of offshore structures. PhD thesis, University of London.

Jardine, R. J. (1992). On the kinematic nature of soil stiffness. Soils and Foundations, Vol. 32 [2], pp. 111-124.

Jardine, R. J., St. John, H. D., Hight, D. W. and Potts, D. M. (1991). Some practical applications of a non-linear ground model. Proc. 10th ECSMFE, Florence, Vol. 1, pp. 223-228.

Johnston, W. A. (1946). Glacial Lake Agassiz with special reference to the mode of deformation of the beaches. Geological Survey of Canada. Bulletin 7, 20 p.

Jovicic, V., and Coop, M. R. (1998). The measurement of stiffness anisotropy in clays with bender element tests in the triaxial apparatus. *Geotechnical Testing Journal*, 21 [1], 3-10.

Jovicic, V., Coop, M.R., and Simic, M. (1996). Objective criteria for determining Gmax from bender element tests. *Géotechnique*, 46 (2), 357–362.

Karrow, P. F. 1974. Till stratigraphy in parts of southwestern Ontario. Geological Society of American Bulletin. 85, 761-768.

Kausel, E., Whitman, R.V., Morray, J.P., & Elsabee, F. (1978). The spring method for embedded foundations. Nuclear Engineering and design, 48(2-3), pp. 377-392.

Kelly, R. I. 1998. Map 2557, Chatham and Wheatley Areas. Ontario Geological Survey. Ontario, Canada: Queen's Printer for Ontario.

Kelly, R.I. (1995). Quaternary geology of the Chatham – Wheatley area, southern Ontario. Ontario Geological Survey, Open File Report 5925.

Kim, D. S., and Stokoe, K. H. (1994). Torsional Motion Monitoring-System for Small-Strain Soil Testing. *Geotechnical Testing Journal*, 17 (1), 17-26.

Kim, T. C. (1979). Dynamic properties of cohesive soils of southwestern Ontario. M.E.Sc. thesis, The University of Western Ontario, London, Ontario.

Kim, T. C., and Novak, M. (1981a). Dynamic properties of some cohesive soils of Ontario. *Canadian Geotechnical Journal*, 18, 371-389.

Kim, T. C., and Novak, M. (1981b). Resonant column technique for dynamic testing of cohesive soils. *Canadian Geotechnical Journal*, 18, 448-455.

Kim, T., and Finno, R. J. (2011). Anisotropy Evolution and Irrecoverable Deformation in Triaxial Stress Probes. *Journal of Geotechnical and Geoenvironmental Engineering*. ASCE, 138(2), 155-165.

Kirkgard, M. M., and Lade, P. V. (1991). Anisotropy of Normally Consolidated San Francisco Bay Mud, *Geotechnical Testing Journal*, 14 [3], 231-246.

Kiss, J. (2016). Evaluation of the response of carbonate clay beneath a wind turbine foundation. (MESc. Thesis). London, Ontario, Canada: Department of Civil and Environmental Engineering, Western University.

Kiss, J., Newson, T. and Miller, C. (2014). The effect of wind-structure interaction on the behavior of a shallow wind turbine foundation, Canadian Geotechnical Society: Geo Regina. Regina, Canada. Paper # 231.

Kondner, R.L. 1963. Hyperbolic stress-strain response: cohesive soil. *Journal of Soil Mechanics and Foundations Division*, 89, 1, 115-143.

Kramer, S.L., (1996). “Geotechnical Earthquake Engineering” (Vol. 80). Upper Saddle River, NJ: Prentice Hall.

Kuganenthira, N., Zhao, D., and Anandarajah, A. (1996). Measurement of fabric anisotropy in triaxial shearing. *Géotechnique*, 46[4], 657–670.

Kuwano, R. and Jardine, R. J. (2002). On the applicability of cross-anisotropic elasticity to granular materials at very small strains. *Géotechnique,* 52[10], 727-749.

Kuwano, R., Connolly, T M., and Jardine, R. J. (2000). Anisotropic stiffness measurements in a stress-path triaxial cell. *Geotechnical Testing Journal*, 23[2], 141–157.

Ladd, C. C, and Foott, R. (1974). New design procedure for stability of soft clays. *Journal of Geotechnical Engineering Division*, ASCE, 100(GT7), 763-786.

Ladd, C. C., Foote, R., Ishihara, K., Schlosser, F., and Poulos, H. G. (1977). Stress-deformation and strength characteristics. State-of-the-Art Report, IX International Conference on Soil Mechanics and Foundation Engineering, Tokyo, 421-494.

Lang, P. J. (2012). Sensitivity of shallow wind turbine foundation design and soil response to geotechnical variance with construction cost implications. M.Sc, University of Wisconsin-Madison.

Lee, J. N. K., (1993). Experimental study of body wave velocities in sand under anisotropic conditions. Ph.D thesis, Department of Civil Engineering, The University of Texas at Austin.

Lee, J-S, and Santamarina, C. (2005). Bender elements: performance and signal interpretation. *Journal of Geotechnical and Geoenvironmental Engineering*, 131(9), 1063-1070.

Lindsay, J. F. (1970). Clast Fabric of Till and Its Development, Journal of Sedimentary Petrology, 40 [2], 629-641.

Lings, M. L., Pennington, D. S., and Nash, D. F. T. (2000). Anisotropic stiffness parameters and their measurement in a stiff natural clay. *Géotechnique*, 50 [2], 109–125.

Lings, M.L., (2001). Drained and undrained anisotropic elastic stiffness parameters. *Géotechnique*, 51 (6), 555–565.

Lo, K. Y. (1965). Stability of slopes in anisotropic soils. *Journal Soil Mechanics and Foundations Division*, ASCE, 94 (4), 85-106.

Lo, K. Y., Adams, J. I., and Seychuk, J. L. (1969). The Shear Behaviour of a Stiff Fissured Clay. Proceedings of the Seventh International Conference on Soil Mechanics and Foundation Engineering, (pp. 249-255). Mexico.

Lo, K. Y., and Becker, D. E. (1979). Pore-pressure response beneath a ring foundation on clay. Canadian Geotechnical Journal, 16, 551-566.

Lo, K. Y., and Becker, D. E.(1978). Tower silo foundations in Southern Ontario, Research Report, GEOT-1-78, 1978.

Lo, K. Y., and Milligan, V. (1967). Shear Strength Properties of Two Stratified Clays. *Journal of the Soil Mechanics and Foundations Division*, 353-367.

Lo, K. Y., Seychuk, J. L., and Adams, J. I. (1971). A study of the deformation characteristics of a stiff fissured clay. ASTM symposium on sampling of soil and rock, STP 483, 60-76.

Love, A. E. H. (1927). A treatise on the mathematical theory of elasticity, 2 vols. Cambridge: Cambridge University Press.

Lunne, T., Berre, T., and Strandvik, S. (1997). Sample disturbance effects in soft low plastic Norwegian clay. Proceedings of the international symposium on recent developments in soil and pavement mechanics, Rio de Janeiro, Brazil (ed. M. S. S. Almeida), pp. 81–102. Rotterdam, the Netherlands: Balkema.

Lutenegger, A. J., Kemmis, T. J., and Hallberg, G. R. (1983). Origin and properties of glacial till and diamictons. ASCE Geological Environment and Soil Properties, Special Publication, Geotechnical Engineering Division, pp. 310-331.

Marto, A. (1996). Critical state of Keuper marl silt. Jurnal Kejuruteraan Awam, 9(2), 34-58.

Matile, G.L.D., and G.R. Keller. (2004). Surficial geology of southern Manitoba (south of 53°); Manitoba Industry, Economic Development and Mines, Manitoba Geological Survey, Surficial Geology Compilation Map Series, SG-SMB, scale 1:500 000.

Mayne, P.W., Kulhawy, F.H., (1982). K0–OCR relationship in soil. Journal of the Geotechnical Engineering Division, ASCE, 108 (GT6), 851–872.

Meyerhof, G. G. (1953). The bearing capacity of foundations under eccentric and inclined loads. Proc. 3rd ICSMFE, 440-445.

Meyerhof, G. G. (1963). Some recent research on the bearing capacity of foundations. Canadian Geotechnical Journal, 1(1), 16–26.

Milligan, V. (1976). Geotechnical aspects of glacial tills. In glacial till: An Interdisciplinary Study. Ed. R.F Legget, Royal Society of Canada, Special publication. 12, 11-49.

Milovic, D. M. (1970). Contraintes et deplacernents dans une couche elastique d'epaisseur Iimitee, produits par une fondation circulaire. Le Genie Civil, 147(5), pp. 281-295.

Milovic, D.M., and Touzot, G. 1970. Bi-dimensional stress distribution in an anisotropic layer of finite thickness. Géotechnique, 20, 2, 1051-1072.

Mitchell, J. K. (1976). Fundamentals of Soil Behaviour, New York, John Wiley and Sons.

Mitchell, R. J. (1972). Some deviations from isotropy in lightly overconsolidated clay, Géotechnique, 22[3], 459-467.

Moayerian, S., (2012). Effect of Loading Frequency on Dynamic Properties of Soils Using Resonant Column. Master Thesis. University of Waterloo.

Morgan, K., and Ntambakwa E. (2008). “Wind turbine foundation behavior and design considerations.” Garrad Hassan American Inc., Huston: AWEA Wind Conference, 1-14.

Morris, T. F., and Kelly, R. I. (1997). Origin and physical and chemical characteristics of glacial overburden in Essex and Kent counties, southwestern Ontario. Canadian Journal of Earth Sciences, 34, 233-246.

Morris, T.F. (1994). Quaternary geology of Essex County, southwestern Ontario. Ontario Geological Survey, Open File Report 5886.

Muir Wood, D., (1990). Soil behaviour and critical state soil mechanics. Cambridge: Cambridge University Press.

Newson, T. A, Tyldesley, M, Gonzalez-Hurtado, J. A., and He, P. 2019. Private communication.

Ng, C., Bolton, M., and Dasari, G. 1995. The small strain stiffness of a carbonate stiff clay. Japanese Geotechnical Society. Soils and foundations, 35, 4, 109-114.

Nishimura, S. (2014). Cross-anisotropic deformation characteristics of natural sedimentary clays. Géotechnique, 64 [12], 981–996.

Ohde, J. 1939. Zur Theorie der Druckverteilung im Baugrund. Bauingenieur 20: 93–99.

Osman, A. S., and Bolton, M. D. 2005. Simple plasticity-based prediction of the undrained settlement of shallow circular foundations on clay. Géotechnique 55, No. 6, 435–447.

Osman, A. S., White, D. J., Britto, A. M., & Bolton, M. D. (2007). Simple prediction of the undrained displacement of a circular surface foundation on non-linear soil. Géotechnique, 57 (9), pp. 729-737.

Pardis, N., Ebrahimi, R., & Kim, H. (2019). Equivalent strain at large shear deformation: Theoretical, numerical and finite element analysis. Journal of Applied Research and Technology, 15(5).

Pennington, D. S., Nash, D. F. T., and Lings, M. L. (1997). Anisotropy of G0 shear stiffness in Gault Clay. Géotechnique, 47 [3], 391–398.

Pestana, J. M, Whittle A. J, Gens A. (2002). Evaluation of a constitutive model for clays and sands: Part II—Clay behaviour. International Journal for Numerical and Analytical Methods in Geomechanics. 26(11), 1123–1146.

Peterka, J. (1992). Improved extreme wind prediction for the United States. Journal of Wind Engineering and Industrial Aerodynamics, 41, 533-541.

Pickering, D.J. (1970). Anisotropic elastic parameter for soil. Géotechnique, 20 (3), 271–276.

Poulos, H.G., & Davis, E.H. (1974). Elastic solutions for soil and rock mechanics, John Wiley, New York.

Prashant, A., and Penumadu, D. (2005). A laboratory study of normally consolidated kaolin clay. Canadian Geotechnical Journal, 42(1), 27-37.

Quigley, R. M. (1980). Geology, mineralogy, and geochemistry of Canadian soft soils: a geotechnical perspective. Canadian Geotechnical Journal, 17, 261–285.

Quigley, R. M., and Ogunbadejo, T.A. (1976). Till geology, mineralogy and geotechnical behaviour, Sarnia, Ontario. In glacial till: An Interdisciplinary Study. Ed. R.F Legget, Royal Society of Canada, Special publication. 12, 336-345.

Quigley, R.M, and Ogunbadejo, T.A. (1974). Soil weathering, soil structure and engineering properties, Sarnia clay crust. Soil Microscopy, 165-178.

Radhakrishna, H.S, and Klym, T.W. (1974). Geotechnical properties of a very dense glacial till. Canadian Geotechnical Journal, 11, 3, 396-408.

Rampello, S., Viggiani, G.M.B. and Amorosi, A. (1997). Small-strain stiffness of reconstituted clay compressed along constant triaxial effective stress ratio paths. Géotechnique 47 (3), 475–489.

Randolph, M., Cassidy, M., Gourvenec, S., & Erbrich, C. (2005). Challenges of offshore geotechnical engineering. In Proceedings of the international conference on soil mechanics and geotechnical engineering, Vol. 16, pp. 123–176.

Randolph, M.F. (1981). Piles subjected to torsion. Journal of the Geotechnical Engineering Division, 107(8), pp. 1095-1111.

Raymond, G.P. (1970). Discussion on 'Stresses and displacements in a cross-anisotropic soil' by Barden, L. Géotechnique, 20 (4), 456–458.

Rees, S., Le Compte A., and Snelling, K. (2013). A new tool for the automated travel time analyses of bender element tests. Proceedings, 18th ICSMGE, Paris. 2843-2846.

Reipas, L. K. (2012). Effect of heterogeneous soil structure of the small strain dynamic properties of soils. M.E.Sc. thesis, The University of Western Ontario, London, Ontario.

Richart, F., Hall, J. and Woods, R. (1970). Vibrations of soils and foundations. Prentice-Hall Inc., Englewood Cliffs, New Jersey.

Roscoe, K. H., and Burland, J. B. (1968). On the generalized stress-strain behavior of wet clay. Engineering plasticity, J. Heyman and F. A. Leckie, eds., Cambridge University Press, Cambridge, U.K., 535–609.

Roscoe, K. H., Schofield, A. N., and Thurairjah, A. (1963). Yielding of clays in states wetter than critical. Geotechnique, 13, 3, 211-240.

Rowe, K. R. & Booker, J. R. (1981). The behaviour of footings resting on a non-homogeneous soil mass with a crust. Part I: Strip footings. Canadian Geotechnical Journal, 18 (2), pp. 250-264.

Rowe, R. K., And Booker, J. R. 1980. Finite layer analysis of non-homogeneous soils. University of Western Ontario Research Report GEOT-2-80.

Saada, A. S., and Bianchini, G. F. (1975). Strength of one-dimensionally consolidated clays, Journal of Geotechnical Engineering Division. American Society of Civil Engineers, 101[11], 1151-1164.

Saada, A. S., and Bianchini, G. F. (1992). Crack propagation and fabric control on the static and dynamic strength of cohesive soils. Final report submitted to the Air Force Office of Scientific Research. Washington, DC: Boiling Air Force Base.

Sanchez-Salinero, I., Roesset, J. M., Stokoe, I., and Kenneth, H. (1986). Analytical studies of body wave propagation and attenuation. GR-86-15, University of Texas, Austin, Texas.

Sane, S. M., Desai, C. S., Jenson, J. W., Contractor, D. N., Carlson, A. E., and Clark, P. U. 2008. Disturbed state constitutive modeling of two Pleistocene tills. Quaternary Science Reviews, 27, 3-4, 267-.

Schofield, A. N. & Wroth, C. P. (1968). Critical state soil mechanics. London: McGraw-Hill.

Shilts, W. 1976. Glacial till and mineral exploration. In glacial till: An Interdisciplinary Study. Ed. R.F Legget, Royal Society of Canada, Special publication. 12, 11-49.

Shirley, D. J., and Hampton, L. D. (1978). Shear wave measurements in laboratory sediments. Journal of the Acoustical Society of America, 63 (2), 607–613.

Shumway, J. R., and Iverson, N. R. (2009). Magnetic fabrics of the Douglas Till of the Superior lobe: exploring bed-deformation kinematics. Quaternary Science Reviews 28, 107–119, 2009.

Sivakumar, V., Doran, I., & Johnson, A. (2001). The effect of anisotropic elasticity on the yielding characteristics of oversonsolidated natural clay. Canadian Geotechnical Journal, 125- 137.

Skempton, A. (1970). First-time studies in over-consolidated clays. Géotechnique, 20(4), 320- 324.

Smith, I. M., and Griffith, D. V. 1982. Programming the finite element method. 2nd edition. J. Wiley & Sons.

Smith, Jamie C. (2014). Effects of Inflow Parameters and Operating Conditions on the Structural Response and Power Production of a Commercial Wind Turbine. (MESc. Thesis). Windsor, Ontario, Canada: Department of Civil and Environmental Engineering, University of Windsor.

Smith, P. R., Jardine, R. J., and Hight, D. W. (1992). The yielding of Bothkennar clay. Géotechnique, 42 [2], 257-274.

Soderman, L. G., Kenney, T. C., and Loh, A. K. (1960). Geotechnical properties of glacial clays in Lake St. Clair region of Ontario. Proceedings of 14th Canadian Conference on Soil Mechanics, pp. 55-89.

Spence, D.A. (1968). Self similar solutions to adhesive contact problems with incremental loading. Proc. R. Soc. Lond. A, 305(1480), pp. 55-80.

Stantec. (2007). Port Alma Wind Power Project Environmental Screening Report/Environment Impact Statement, Stantec Consulting Ltd. Available at http://www.kruger.com/assets/uploads/EnviroScreeningRpt.pdf [Accessed October 17, 2017]

Stark, T. D., Choi, H., and McCone, S. (2005). Drained Shear Strength Parameters for Analysis of Landslides, Journal of Geotechnical and Geoenvironmental Engineering, 131[5], 575-588.

Stephenson, D. A., Fleming, A. H., and Mickelson, D. M. (1988). Glacial Deposits. In: The Geology of North America, W. Back, J. S. Rosenshein, and P. R. Seaber (Editors). Geological Society of North America, Boulder, Colorado, Vol. 0-2, pp. 273-382.

Stokoe, II, K.H., Lee, J.N.-K. and Lee, S.H.-H. (1991). Characterization of soil in calibration chamber with seismic waves. In: A.B. Huang, ed. Calibration Chamber Testing. Elsevier Science Publishing, New York, USA, 363–376.

Stupavsky, M., Symons, D. T. A., and Gravenor, C. P. (1974). Paleomagnetism of the Port Stanley Till, Ontario, Geological Society of America Bulletin, 85, 141-144.

Sultaniya, A. K., Clayton, C. R. I., and Priest J. (2010). Assessing cross anisotropy of small-strain stiffness using the resonant column apparatus. 5th International Conference on Recent Advances in Geotechnical Earthquake Engineering and Soil Dynamics, May 24th-29th May, San Diego, USA, Paper No. 1.14b.

Suresh Shrivastava , Chiradeep Ghosh & John J. Jonas (2012) A comparison of the von Mises and Hencky equivalent strains for use in simple shear experiments, Philosophical Magazine, 92:7, 779-786

Svensson, H. 2010. Design of Foundations for Wind Turbines. Master's Dissertation, Lund University. Sweden

Taiebat, H., & Carter, J. (2000). A semi-empirical method for the liquefaction analysis of offshore foundations. International Journal for Numerical and Analytical Methods in Geomechanics, 24(13), 991-1011.

Teller, J. T., and Bannatyne, B. (1976). Geology and topography of the buried bedrock surface of southern Manitoba. Manitoba Mineral Resource Division, Surficial Map 76-3.

Teller, J. T., and Fenton, M. M. (1980). Late Wisconsinan glacial stratigraphy and history of southeastern Manitoba. Canadian Journal of Earth Sciences, 17, 19-35.

Terzaghi, K., and Peck R. B. (1967). Soil Mechanics in Engineering Practice, 2nd Edition, J. Wiley, New York, USA.

Ting, W. H. (1968). Some effects of history on the stress-strain behavior of kaolin. PhD thesis, University of Cambridge.

Tinjum, J.M., and Christensen, R.W. (2010). "Site investigation, characterization and assessment for wind turbine design and construction." In Wind Energy Systems, edited by John D. Sorensen and Jens N. Sorensen, 26-45. Woodhead Publishing.

Trenter, N. A. (1999). Engineering in Glacial Tills, Construction Industry Research and Information Association, London, UK.

Tyldesley, M., Newson, T., Boone, S., and Carriveau, R. 2013. Characterization of the geotechnical properties of a carbonate clayey silt till for a shallow wind turbine foundation, 18th International Conference on Soil Mechanics and Geotechnical Engineering, CFMS, Paris, France, 1: 2407-2410.

Vardanega, P. J., and Bolton, M. D. 2013. Stiffness of clays and silts: normalizing shear modulus and shear strain. Journal of Geotechnical and Geoenvironmental Engineering, ASCE, 139(9):1575–1589.

Viggiani, G., and Atkinson, J.H. (1995). Interpretation of bender element tests. Géotechnique, 45 (1), 149–154.

Vucetic, M. (1988). Normalized behavior of offshore clay under uniform cyclic loading. *Canadian Geotechnical Journal*, 25(1), 33-41.

Vucetic, M. (1990). Normalized behaviour of clay under irregular cyclic loading. *Canadian Geotechnical Journal*, 27, 29-46.

Vucetic, M., and Dobry, R. (1988). Degradation of marine clays under cyclic loading. Journal of Geotechnical Engineering., ASCE, 114(2), 133-149.

Vucetic, M., and Dobry, R. (1991). Effect of soil plasticity on cyclic response. Journal of Geotechnical Engineering, 117[1], 89-107.

Whitman, R.V. (1976). Soil-platform interaction. In Proc. Conf. on Behavior of Offshore Structures.

Yimsiri, S., and Soga, K. (2011a). Cross-anisotropic elastic parameters of two natural stiff clays, *Géotechnique*, 61 [9], 809-814.

Young, R. N., and Silvestri, V. (1979). Anisotropic behaviour of a sensitive clay. Canadian Geotechnical Journal, 16 (2), 335-350.

Zhang, J., Andrus, R., and Juang, C. H. (2005). Normalized Shear Modulus and Material Damping Ratio Relationships. ASCE, *Journal of Geotechnical and Geoenvironmental Engineering*, Vol. 131 [4], 453-464.

Appendix A

Appendix A presents the results obtained from a series of geotechnical *in-situ* and laboratory tests performed at the Port Alma wind farm for the characterization of the glacial clay deposit. A detailed analysis of these results, and a discussion of their implications, can be found in Sections 3.5.2 and 3.5.3 of Chapter 3, respectively.

A.1 *In-situ* and laboratory testing results for Port Alma clay deposit

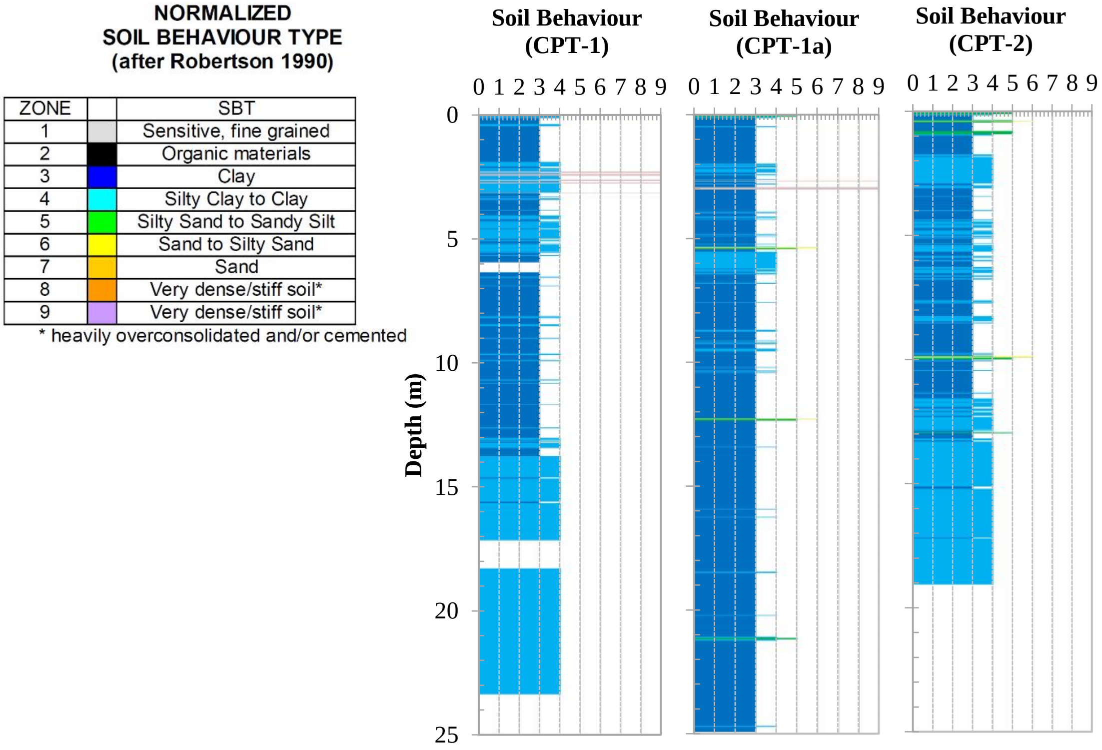

ZONE		SBT
1	⬜	Sensitive, fine grained
2	⬛	Organic materials
3	🟦	Clay
4	🟦	Silty Clay to Clay
5	🟩	Silty Sand to Sandy Silt
6	🟨	Sand to Silty Sand
7	🟧	Sand
8	🟧	Very dense/stiff soil*
9	🟪	Very dense/stiff soil*

* heavily overconsolidated and/or cemented

Figure A.1: Cone penetration test (CPT) results with depth for Port Alma clay deposit (after Newson et al., 2018)

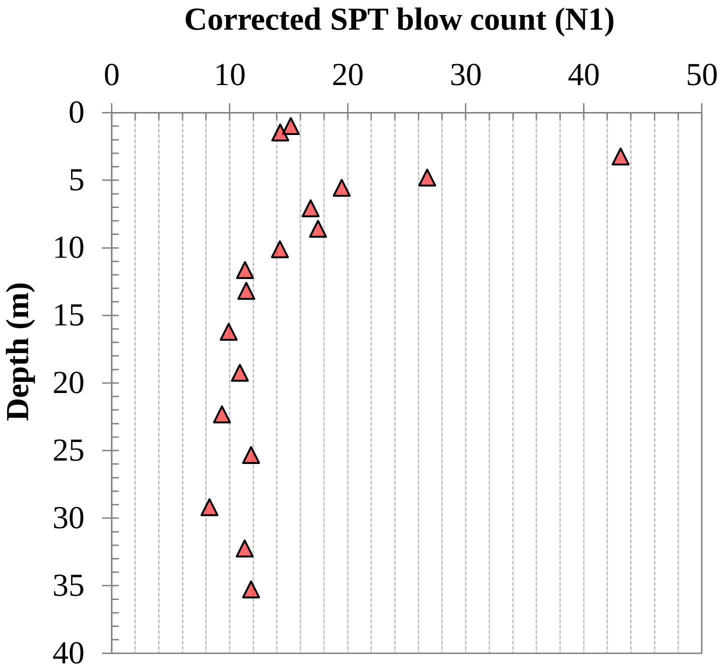

Figure A.2: SPT blow count with depth for Port Alma clay deposit (after Newson et al., 2019)

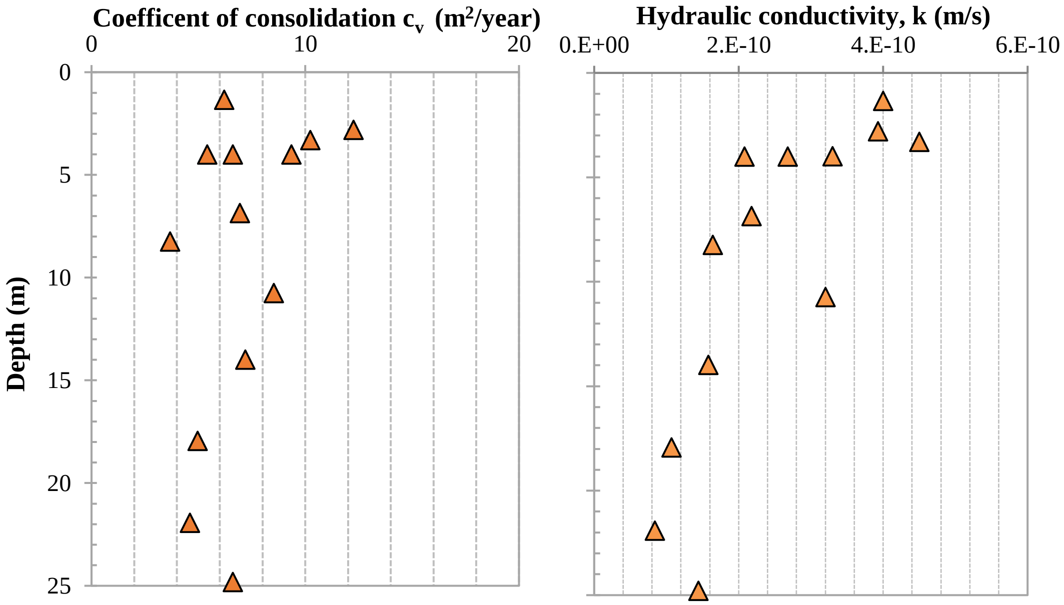

Figure A.3: Coefficient of consolidation (a) and hydraulic conductivity for Port Alma clay deposit (after Newson et al., 2019)

A.2 Field methodologies

In order to assess the behaviour of the wind turbine foundation system and its energy transmission to the surrounding soil, a field monitoring system was designed and previously installed in the field. This monitoring system was created with the aim of measuring the foundation vibration, ground motion, and wind data. The system was installed in November 2016 and the data has been reported previously by Gonzalez-Hurtado et al. (2017). The next sub-sections present an overview of the field monitoring system employed during this investigation.

A.2.1 Field monitoring system and foundation monitoring

The foundation monitoring system employed included four uniaxial tiltmeters and three portable high frequency triaxial seismometers (known as Tromino®), and one triaxial accelerometer (see Figure 3.24). The sampling rates of the tiltmeter, Trominos and accelerometer are 20, 128 and 20 Hz, respectively. The Trominos can capture velocities in 3 directions simultaneously, with an accuracy of ±1.2 mm/s at full scale, that can be recorded in a frequency range between 0.1 Hz to 200 Hz. The tiltmeters (denoted as TM1, 2, 3 and 4) were placed at the four cardinal directions to measure the rotation of the foundation in the N-S and E-W directions.

The triaxial accelerometer, located at N0, can measure accelerations between ±3g with a bandwidth range of 0.5 Hz to 50 Hz. The triaxial accelerometer was installed at the same position as TM2 (see Figure 3.24), and the three Trominos were located at 30 (N1), 130 (N2) and 300 m (N3) to the North of the foundation edge, respectively. Vibrations towards the N and E cardinal directions have been taken as positive. In this research, only the data obtained from N0 to N3 were used to analyze the wave propagation induced by the vibration of the wind turbine foundation. The wind direction, θ, was measured clockwise from the North, as shown in Figure A.4. For more details on the measurements, data gathered, analyzes and results from this field study refer to Gonzalez-Hurtado et al. (2017).

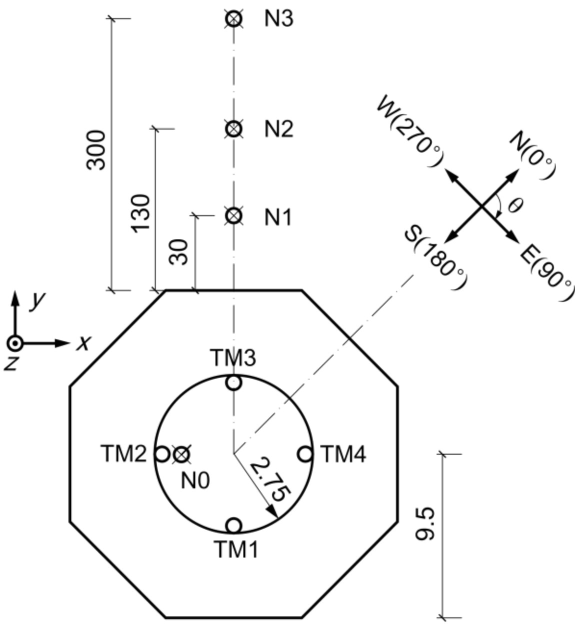

Figure A.4: Diagram of foundation and location of the instrumentation (all dimensions in meters) – not to scale

A.2.2 Wind monitoring

Wind speed and direction variation over the study period was characterized to relate the response of the foundation to the incoming wind field. The speed and direction of the wind was measured from 5 ultrasonic anemometers located on a meteorological tower (MET) tower (at 34, 61, 70, 77 and 80 m above ground level) located 150 m to the North-West of the wind turbine and the turbine nacelle (80 m). The wind data was collected at 1 Hz. Only the wind data measured at the nacelle (80 m) is reported in this study.

Kiss (2016) carried out field measurements to assess the wind behaviour and its influence on the foundation using uniaxial seismic accelerometers placed on top of the shallow wind turbine foundation. Likewise, Bas et al (2013) performed an analysis of the strain response of the wind turbine tower using Fiber Bragg Grating (FBG) strain sensor array. For more detailed information on the instrumentation and field measurements, data analysis and processing, refer to Bas et al. (2013) and Kiss (2016). Figures A.5a and b show typical plots of the normalized spectral densities vs. normalized frequencies for wind and accelerometer data as obtained by Kiss (2016). Figure A.6 depicts the spectral density vs. frequency obtained using the recorded data from one accelerometer as reported by Kiss

(2016). Similarly, Figure A.7 presents the spectral density estimate generated by Bas et al. (2013) using the data from the strain gauges array on the wind turbine tower.

The normalized spectral density of the wind data plotted in log-log space (Figure A.5a) follows a classic pattern (Kiss, 2016). The von Karman spectrum was fitted to the wind data obtained in the field and the fit coefficients were estimated as a=9.38 and b=17.07. The maximum value of the von Karman spectrum is about 0.18 at a non-dimensional frequency of 0.09. From Figure A.5b two picks were observed at non-dimensional frequencies of 0.3 and 60. Both peaks can be seen in Figure A.6 and they correspond to frequencies of approximately 0.011 Hz and 2.29 Hz. An additional peak occurring at about 6.5 Hz was captured and shown in Figure A.6. The spectral density generated by Bas et al (2013) shows similar findings as those reported by Kiss (2016). Figure A.7 shows two clear peaks corresponding to the natural frequencies (approximately 0.322 Hz and 2.73 Hz) of the wind turbine tower as reported by Bas et al. (2013). They did not report any additional frequency peaks. Kiss (2016) attributed the additional frequency captured in his study to a potential blade crossing frequency that could not have been identified by Bas et al. (2013), as their study was conducted while the blades of the wind turbine were locked out.

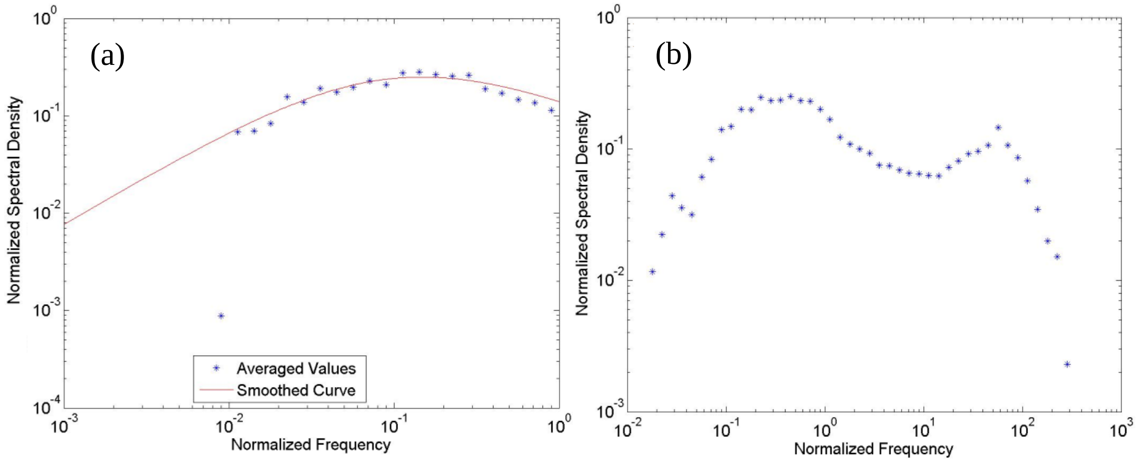

Figure A.5: Typical plots of normalized spectral densities vs. normalized frequencies for (a) wind data and (b) accelerometer data (adapted from Kiss, 2016)

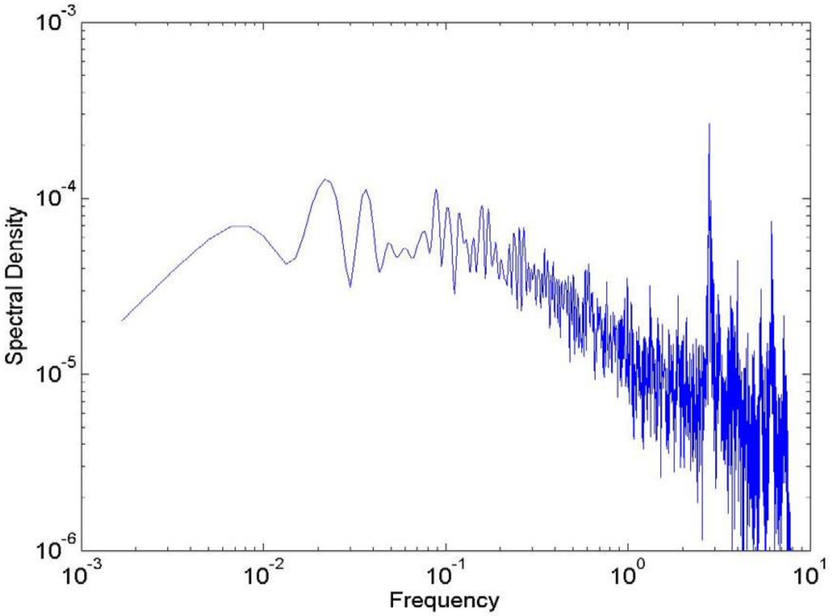

Figure A.6: Spectral density estimate data from one accelerometer (Kiss, 2016)

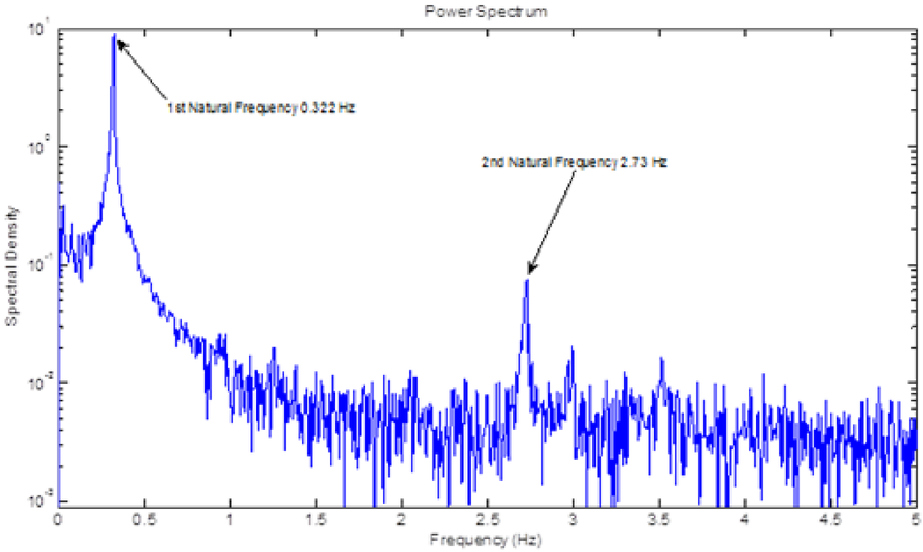

Figure A.7: Spectral density estimate from strain gauge readings on turbine tower (adapted from Bas et al, 2013)

Appendix B

This appendix presents the results obtained from the quality assessment of the soil materials tested in this investigation; a review of the geological features, location and index properties of the cohesive materials investigated; a photographic sequence of the sample preparation for the different laboratory testing used and covered in Chapter 4; and the procedures and calibration results of the resonant column apparatus used for the investigation, as well as the results from a benchmark testing using Barco #49 sand.

B.1 Sample quality assessment

Soil disturbance can occur during sampling, transportation and storage, also during handling and preparation of the material before testing. Moreover, damage to soil 'structure' can also occur due to poor saturation or reconsolidation procedures. To evaluate the quality (or level of disturbance) of the samples used in the laboratory tests of this investigation, the method suggested by the Norwegian Geotechnical Institute (NGI) and developed by Lunne et al. (1997) was used. The proposed method by Lunne et al. (1997) for sample quality evaluation uses the change in volume a sample undergoes during re-consolidation to *in-situ* effective stresses. This can be done by calculating the ratio between the change in void ratio at the start of the test with the void ratio of the sample when consolidated to the in-situ pressure (Δe) and in-situ void ratio of the sample (e_o). The criteria proposed by Lunne et al. (1997) in terms of $\Delta e/e_o$ is indicated in Table B.1.

Table B.1: Sample quality assessment based on the ratio $\Delta e/e_o$ (Lunne et al., 1997)

OCR	Normalized change in void ratio, $\Delta e/e_o$			
1 to 2	< 0.04	0.04-0.070	0.070-0.14	> 0.14
2 to 4	< 0.03	0.03-0.050	0.050-0.10	> 0.10
4 to 6	< 0.03	0.02-0.035	0.035-0.07	> 0.07
Quality:	**1: very good to excellent**	**2: good to fair**	**3: poor**	**4: very poor**

Note: the description of sample quality refers to use of samples for measurement of mechanical properties

Here, the ratio $\Delta e/e_o$ for each of the sample used was estimated from one-dimensional consolidation testing, consolidated undrained triaxial testing and bender element testing. These results are shown on Figure B.1, along with the quality classification from Table

B.1. Results suggest that the samples are 'very good to excellent' and 'good to fair'. Moreover, Figures B.2 to B.4 show the comparison between the estimated and reported values of moisture content, void ratio and unit weight for each of the samples, respectively.

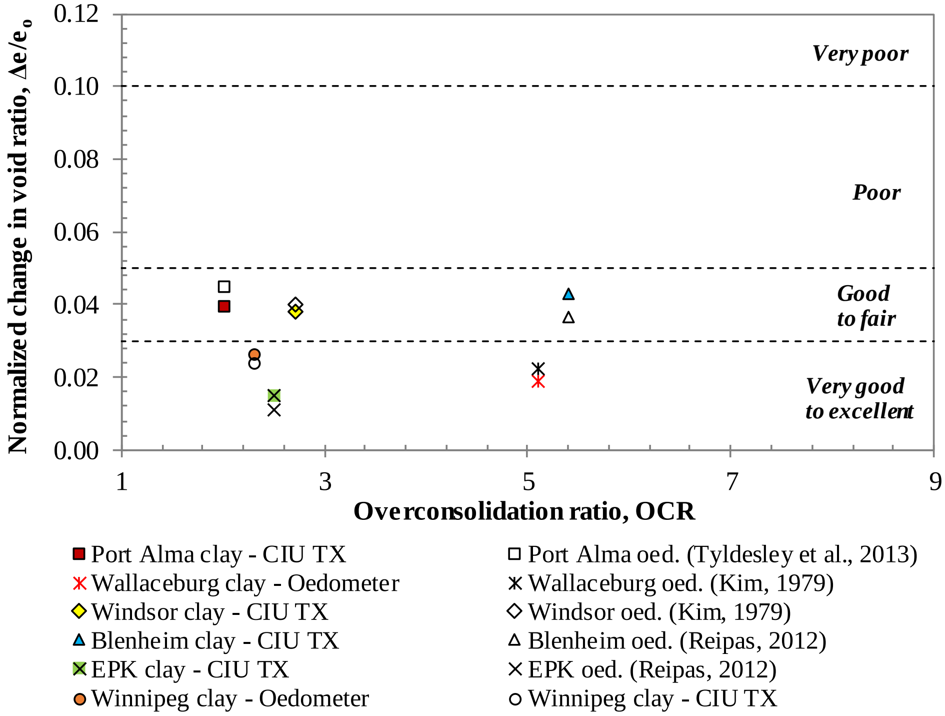

Figure B.1: Sample quality assessment of studied materials

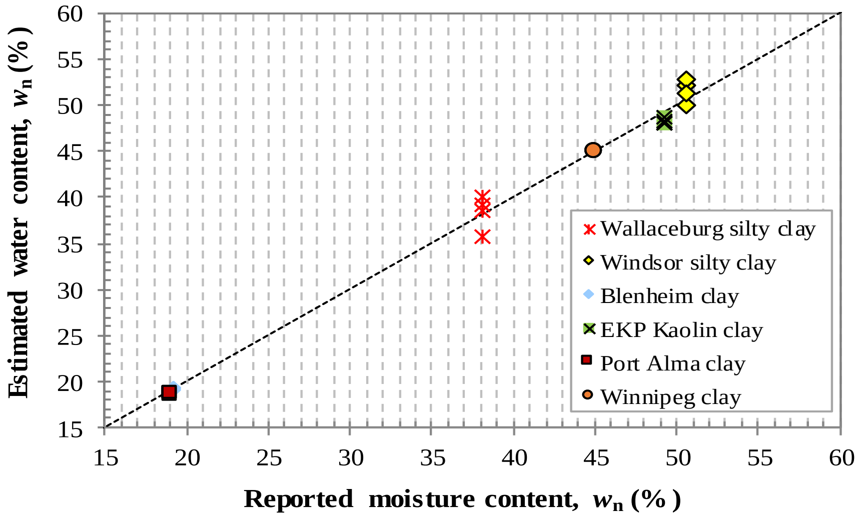

Figure B.2: Comparison of estimated vs. reported moisture content for studied materials

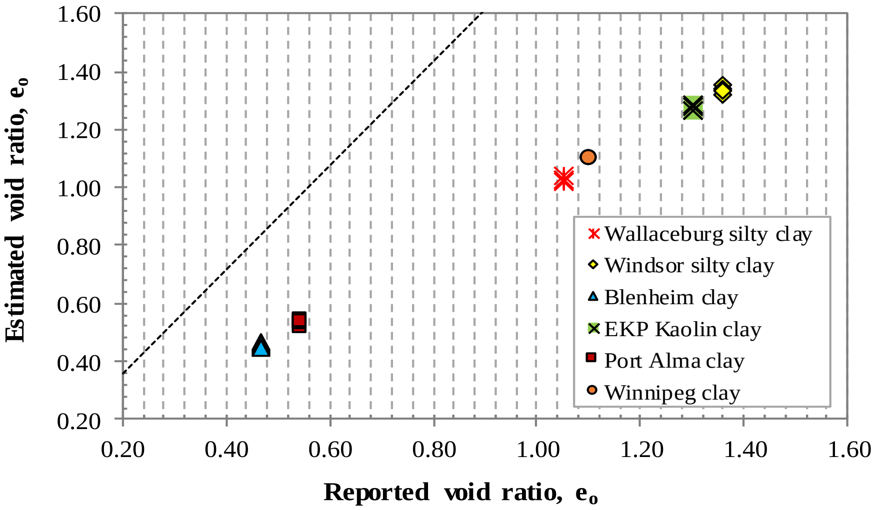

Figure B.3: Comparison of estimate vs. reported void ratio for studied materials

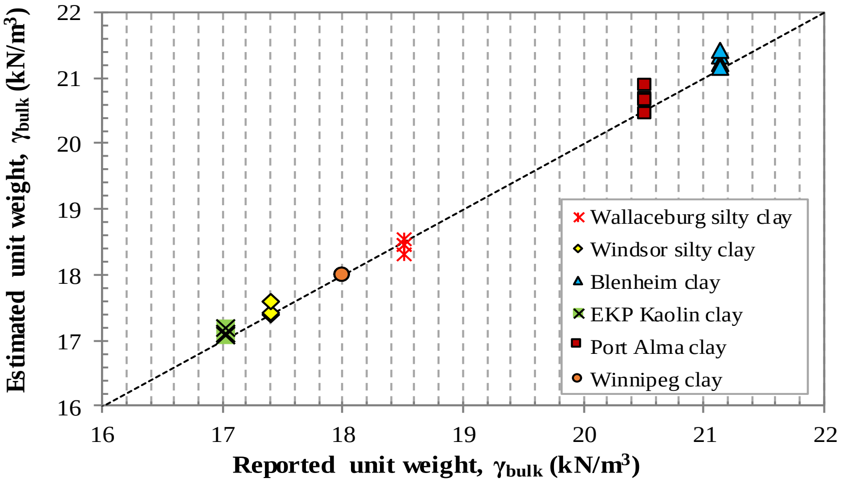

Figure B.4: Comparison of estimate vs. reported unit weight for studied materials

Table B.2: Summary of results for the estimated and reported properties

	Reported			**This study***			**Difference (%)**		
Material	**γ_{bulk} (kN/m^3)**	**e_o**	**w_n (%)**	**γ_{bulk} (kN/m^3)**	**e_o**	**w_n(%)**	**γ_{bulk} (kN/m^3)**	**e_o**	**w_n**
Port Alma clay	20.50	0.54	19.00	20.69	0.54	18.83	0.93	-0.33	-0.89
Wallaceburg silty clay	18.50	1.05	38.10	18.46	1.03	38.37	-0.24	-1.87	0.71
Windsor silty clay	17.40	1.36	50.60	17.51	1.34	51.58	0.65	-1.60	1.94
Winnipeg clay	18.00	1.10	45.00	18.00	1.10	45.00	0.00	0.00	0.00
Blenheim clay	21.14	0.47	19.20	21.29	0.46	19.24	0.71	-1.44	0.21
EKP Kaolin clay	17.02	1.30	49.30	17.13	1.28	48.25	0.63	-1.85	-2.13

*the average values from this study were obtained from different samples used for various laboratory test such as: resonant column testing (vertical and horizontal samples), CIU triaxial tests, bender element tests and oedometer test

B.2 Review of cohesive materials investigated

B.2.1 Site locations, geology and sampling

B.2.1.1 Port Alma clay

The site sits in a simple geographical and environmental area in the Great Lakes region of Southern Ontario known as Port Alma. The area is underlain by carbonate-rich clayey silt tills and is located at the convergence of four major geological deposits. These consist of the Port Stanley and Tavistock tills, glaciolacustrine sand and gravel, and glaciolacustrine clayey silt. These materials were laid down in the Port Bruce Stade (c. 15,000 years bp.) during the re-advance of the Laurentide Ice Sheet of the Late Wisconsin (Chapman and Putnam, 1966; Kelly, 1995). These subglacial lodgment tills are calcareous and fine-grained, suggesting that the ice overrode and incorporated fine-grained glaciolacustrine sediments deposited during the previous Erie Interstade. This has created approximately 40 to 45 m thickness of clayey silt tills with interbedded glaciolacustrine sediments. The bedrock is shale with limestone-dolostone-shale interlayers.

Samples from this site were retrieved from three different boreholes (BH12-1, BH12-2, and BH12-3). The boreholes were drilled using the PQ coring technique to retrieve relatively undisturbed samples for the length of the borehole. Once the subsurface exploration was completed, it was reported that the Port Alma site was underlaid by a glacial till deposit composed of three characteristic layers: a heavily weathered oxidized upper crust from 0 to 1.5 m, a partially weathered lower crust that transitions from an oxidized to an unoxidized state between 1.5 and 4.5 m and an unweathered clay till from 4.5 m to a depth greater than 40 m (Newson et al. 2019).

B.2.1.2 Wallaceburg silty clay

The Wallaceburg clay material has been previously studied at the soil's laboratory of Western University. Such studies have contributed significantly to our current knowledge of the cohesive soil of Southern Ontario. The Wallaceburg clay material used in this study belongs to a portion of samples used by Lo & Becker (1978), Becker (1981), and Kim &

Novak (1981) research that was stored and preserved in the soil's laboratory of Western University.

The material was obtained from a site located approximately 1.6 km east of highway 40 at Wallaceburg, and about 0.4 km north of Base Line Road, Kent County Road 15 (Kim, 1979). Geologically, this site sits within the physiographic region known as the St. Clair clay plains (Chapman and Putnam, 1966). The clay deposits of this area are generally considered to consist of normally consolidated, "water-lain" tills with relatively low shear strength below a very stiff to hard, brown surface crust. These deposits are considered products of the Late Wisconsin Substage of glaciation. The bedrock of the area in known to be either black shale or limestone of the Paleozoic area. More details on the geological formation and origin of these clay deposits may be found elsewhere (Soderman et al., 1960; Chapman and Putnam, 1966; Kim, 1970; Lo and Becker, 1978; Kim and Novak, 1981; Becker, 1981; Morris and Kelly, 1997).

Sampling from this site was done in an open excavation at a depth of 4 m below the ground surface. Kim (1979) described that several block samples were recovered, carefully wrapped in plastic and waxed in the field to prevent them from drying out. After the site investigation was carried out, Kim (1979) and Becker (1981) reported that the soil of the site was found to generally possess the following characteristics: approximately 0.15 m of a black clayey topsoil overlying a 3 m layer of stiff to very stiff silty clay brown crust. The brown silty clay crust was underlain by a deposit of about 18 m in thickness of stiff to soft grey silty clay. The gray silty clay in turn overlies a thin veneer of hard grey silty clay till, about 0.46 m in thickness. The bedrock is a black shale and was encountered at about 22 m below the ground surface.

B.2.1.3 Windsor silty clay

The Windsor clay material was also previously studied at the soil's laboratory of Western University. The Windsor soil material used in this research belonged to a group of samples retrieved by Kim (1979) and Kim and Novak (1981) for their research work that was stored and preserved within the soil laboratory of Western University.

As reported by Kim (1979), the Windsor clay material was retrieved from a site located south of the Morton Terminal on the east bank of the Detroit river, in the west end of the city of Windsor. The site sits in the physiographic region of South Western Ontario known as the St. Clair clay plain (Chapman and Putnam, 1966). Devonian shale and carbonate bedrock underlie the site and surrounding areas. The overburden around this area is mainly composed of quaternary deposits that consist of brown, weathered and desiccated lacustrine clay, normally consolidated lacustrine clay, silty Tavistock Till, glaciolacustrine clay and coarse catfish creek till, and range between 15 to 50 m in thickness (Morris and Kelly, 1997, Morris, 1994). The clay strata of this area are known to be overlay by fine-to-coarse lacustrine sand (Hudec, 1998), and to be of lacustrine origin and were laid down by inundation from a series of glacial lakes. More detailed information on the geological formation and origin of the clay deposits may be found elsewhere (Chapman and Putnam, 1966; Kim, 1979; Kim and Novak, 1981; Morris and Kelly, 1997, Hudec, 1998).

Kim (1979) described that the sampling was performed from an open excavation and the samples were retrieved from a depth of around 4.6 m below the ground surface. After retrieving the samples, they were wrapped in plastic and waxed in the field to prevent them from drying out. Kim (1979) reported that the subsurface conditions at the site generally consisted of top soil overlaying surficial deposits of sand and gravel of approximately 3 m thick. Below this, an extensive deposit of cohesive soil was found. The cohesive soil deposit consisted of two different layers; a layer of clayey silt of around 1 m, laminated with random silt partings and fine sand; and an extensive stratum of silty clay of around 4 m with occasionally sand and silt partings. The water table was found at a depth of 1.5 below the ground surface by the time of the soil exploration.

B.2.1.4 Blenheim silty clay

The Blenheim clay material selected for this research was retrieved and stored by Reipas (2012). Reipas (2012) also reported on some basic geotechnical properties of the Blenheim material, these properties will be presented and discussed in the Section 4.2.3. The town of Blenheim is in the Southwestern region of Ontario, specifically in the south-central Chatham-Kent area. This area sits in the physiographic region of South Western Ontario known as St. Clair clay plain, and within the sub-region called Essex clay plain (Chapman and Putnam, 1966). It is characterized by sandy silt to silt matrix and silty clay matrix, with moderate to high carbonate content. The bedrock is shale with limestone-dolostone-shale interlayers (Morris and Kelly, 1997).

Not much information was provided by Reipas (2012) on the exact location from where the soil samples were retrieved. Although it was reported that block samples of Blenheim clay were obtained from a construction site near Blenheim Ontario using an excavator from a depth of about 2.5 to 3.0 m below ground level. Subsequently, the samples were stored in wax and stored until needed for testing. The description of the subsurface conditions found at the site by the time of the excavation was not reported by Reipas (2012).

B.2.1.5 Winnipeg clay

The site where this material was retrieved is located approximately at the south side of the City of Winnipeg Deacon Reservoir; limiting with Suthwyn Road to the north, by the Red River floodway to the west, and by the Manitoba Provincial Road 207 to the east. The site sits in the physiographic region of Red River Valley plain (Johnston, 1934; Corkery, 1996). This area consists meanly of offshore glaciolacrustine sediments. Clay, silt minor sand; 1 to 20 m thick; very low relief massive and laminated deposits deposited from suspension in offshore, deep water of glacial Lake Agassiz; commonly scoured and homogenized by icebergs (Matile and Keller, 2004). The bedrock of this area is known to be predominantly Paleozoic limestone (Teller and Bannantyne, 1976). A more detailed explanation on the geological formation and origin of the clay deposits of the area can be found on: Johnston, 1934; Baracos, 1977; Teller and Fenton, 1979; Baracos et al., 1983; Graham and Shields, 1985; and Corkery, 1996.

Trek-Geotechnical Inc. reported that a track-mounted drill rigs equipped with 125 mm diameter solid stem augers and 225 mm diameter hollow stem auger with a continuous sampler were used for most of the drilling activities. All soils observed during test hole drilling were reported to be visually classified on site according to the Modified Unified Soil Classification System (USCS). Undisturbed samples were obtained at regular intervals during drilling while undisturbed (Shelby tube) samples were obtained at select depths within the test holes. High plasticity clay fill was encountered at depths between 1.2 to 4.5

m below ground surface. High plasticity lacustrine clay can was found below the clay fill and extended to depths ranging from 13.7 m to 20.6 m. The lacustrine clay was stiff at shallower depths near the ground surface and became firm with increasing depth. Silt till was identified beneath the lacustrine clay. The lacustrine clay/silt till boundary varied between 13.7 and 20.6 m across the site. The silt till was low plasticity, dense and contained sand, gravel and cobbles and boulders. Frequent cobbles and boulders were encountered, with increasing depth, in the silt till. Dolomitic/ limestone bedrock was encountered at depths ranging from 21.2 to 28.6 m.

B.2.1.6 Edgar plastic kaolin 'EPK' clay

EPK Kaolin clay was selected as the manufactured clay due to its uniformity, great commercial availability, its relatively quick rate of consolidation, and the existing information from previous studies (e.g. Reipas, 2012). The EPK clay samples used in this study were prepared by Reipas (2012). The preparation of the sample involved mixing of powdered clay with certain amount of distilled water in a mixer to create a slurry that has a moisture content of 120%, twice the liquid limit of Kaolin clay (LL=61.6%). A consolidometer apparatus was used to consolidate the EPK mixtures, for this purpose the consolidometer allowed for drainage of excess water. More detailed information on this material and the preparation procedure adopted can be found on: Saada and Bianchini (1992), House et al (2001), Prashant and Penumadu (2005), and Reipas (2012).

B.2.2 Index properties and stress-strain characteristics

B.2.2.1 Port Alma clay

Besides the conventional sampling technique, mentioned in Section 4.2.2.1, *in-situ* testing adjacent to the drilled boreholes consisted of standard penetration test (SPT), cone penetration test (CPT), field shear vane (FSV), cross-hole seismic testing (CST) and seismic cone penetration test (SCPTu). Likewise, different basic laboratory tests were carried out as well. These included, the calculation of carbonate content within the soil profile, natural moisture content and unit weight, Atterberg limits, one-dimensional consolidation, and consolidated isotropic undrained (CIU) triaxial tests.

From the analysis of the field and laboratory tests described in Chapter 3, it was found that the upper crust layer of the till deposit had a mottled brown-grey color, with very pronounced fissures, and a stiff to very stiff consistency. Its average natural moisture content (w_n) was reported as approximately 26%, average liquid (LL) and plastic limits (PL) of about 46% and 21%, over-consolidation ratio (OCR) values decreasing from 5 to 2, undrained shear strength (C_u) between 55 and 150 kPa, and maximum shear modulus (G_{max}) ranging from 100 to 150 MPa. The lower crust was found to has relatively lower natural moisture content, has a very stiff consistency, and is prevalently brown in color. The average natural moisture content was of 17%, average liquid and plastic limits of 34% and 19%, OCR values between 2 and 3, average undrained shear strength (C_u) of about 200 kPa, and maximum shear modulus (G_{max}) ranging from 120 to 150 MPa. The unweathered till layer is characterized by a uniform grey appearance, a stiff to very stiff consistency, low plasticity and relatively uniform moisture contents of around 13% and 20 %, respectively. The overconsolidation ratio was found to be around 1.5 throughout the whole stratum, with an average undrained shear strength of approximately 100 kPa, and a maximum shear modulus that ranged between 100 to 130 MPa. A more detailed information on the field and laboratory test results from previous studies on the Port Alma clay till can be found in Section 3.5.

B.2.2.2 Wallaceburg silty clay

In addition to the conventional sampling, field shear vane (FSV) testing to determine *in-situ* undrained shear strength (S_u) of the clay deposits was conducted by Lo and Becker (1979). The FSV results showed that the undrained shear strength, increased from 74 to 144 kPa within the first 2 to 3 m below the ground surface, revealing the presence of a brown silty clay crust. The natural water (w_n) content of this layer varied from 21 to 27% with an average of about 23%. Plastic limit (PL or w_p) was about 19% and the liquid limit (LL or w_L) ranged from 32% to 42%. Plastic index (PI or I_p) ranged from 13% to 23%, and liquidity index varied from 0.15 to 0.57. The average unit weight of the crust was around 20.44 kN/m^3. From one-dimensional consolidation test, it was found that pre-consolidation pressure ($P_c^{'}$) ranged between 670 to 527 kPa. Consequently, the overconsolidation ratio ($OCR=p_c^{'}/\sigma'_{vo}$) varied from around 33 to 17.

Underlying the brown crust, a grey silty clay deposit was found. The deposit can be divided into two different layers, one between 3 m to 12 m, and another layer from 12 m to 21 m. From the field shear vane testing, S_u of the crust layer was found to decrease in value between 3 m and 8 m, from 58 kPa to 19 kPa, then gradually increased to 34 kPa at 12 m. S_u of the soil layer between 3m and 8m was relatively constant throughout the entire depth, as it only increases from 35 kPa to 40 kPa at around 21 m. The natural water content (w_n) of the deposit ranged from 30% to 55% with an average of 42%. Plastic limit (PL or w_p) of the deposit varied between 17% and 23%, with an average of 20%. The liquid limit (LI or w_L) ranged from 28% to 50% with an average of 40%. The average Plastic index (I_p) was about 20%, and liquidity index was generally around 1.0. The average unit weight of the deposit was around 17.6 kN/m^3. From the consolidation testing, the pre-consolidation pressure ($p_c^{'}$) was found to decrease within the upper 6 m of the deposit, and it ranged between 244 to 105 kPa. Thus, the overconsolidation ratio (OCR=$\sigma'_{pc}/\sigma'_{vo}$) varied from around 5 to 1.1. Below 10.7 m the clay deposit becomes normally consolidated.

Becker (1981) also reported findings on the study of the effect of anisotropy on the undrained deformation of the Wallaceburg clay material. To carry out the anisotropy study, Becker (1981) employed a technique previously used by Lo et al. (1971) and Yong and Silvestri (1979) to examine the anisotropic stiffness of a stiff fissured clay and the strength anisotropy of a sensitive clay, respectively. The method consisted on trimming portions of block samples from the same material at different orientations or inclination angles with respect the sample *in-situ* vertical axis (e.g. 0° equal to vertical cut samples, 90° horizontally cut samples). Using cyclic undrained (CIU) triaxial undrained tests on samples cut at 0°, 30°, 45°, 60°, and 90°, it was found that the deformation behaviour of the Wallaceburg clay was somewhat anisotropic.

To quantify the level of anisotropy, Becker (1981) based his findings on the calculation of a modular ratio ‘$n = E_h/E_v$’ using the elastic modulus of the soil in the horizontal direction (E_h) and the modulus in the vertical direction (E_v). It was determined that ‘n’ for the brown crust, at 2.6 m depth, was about 0.4, and at 3.6 m depth within the clay deposit ‘n’ was around 1.5. Becker (1981) attributed this to an inherent anisotropy linked principally to the environmental conditions during which the soil was deposited as well as the stress changes after deposition (Lo, 1965; Ladd et al., 1977). Table B.3 shows a summary of the cross-anisotropic elastic parameters of Wallaceburg clay estimated by Becker (1981).

Table B.3: Summary of cross-anisotropic elastic parameters of Wallaceburg clay (Becker, 1981)

	First cycle					Subsequent cycles				
Layer	E_v (MPa)	n	G_{vh}/E_v	μ_{vh}	μ_h	E_v (MPa)	n	G_{vh}/E_v	μ_{vh}	μ_h
Crust (2.61 m)	44.40	0.40	0.27	0.50	0.80	65.40	0.50	0.31	0.50	0.75
Firm clay (3.90 m)	16.40	1.50	0.25	0.50	0.50	23.00	1.60	0.28	0.50	0.20

Kim (1979) and Kim and Novak (1981) also reported on the index properties, strength characteristics and consolidation behaviour of Wallaceburg clay samples as well. Soil samples from a depth of 4 m below the ground surface, and from the same site investigation described by Becker (1981), were used in their study. The natural moisture content was determined to be around 38% and void ratio equal to 1.05. The liquid and plastic limits were around 42.2% and 17.6 % respectively. The preconsolidation pressure (Pc'), from one-dimensional consolidation test, was calculated as 273.6 kPa using the Casagrande method. From CIU triaxial tests, the undrained shear strength (S_u) value was approximately 41.6 kPa. Figure B.5 show results from one-dimensional consolidation tests performed by Kim (1979).

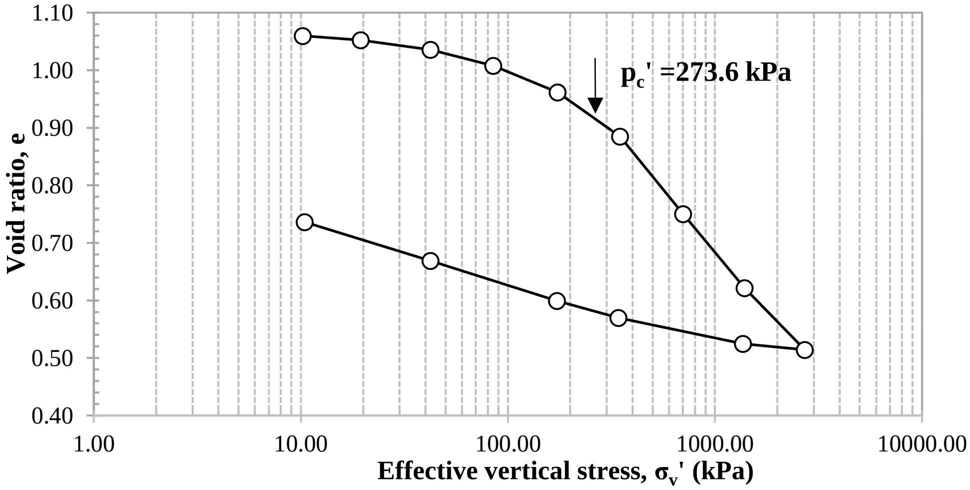

Figure B.5: Consolidation testing results for Wallaceburg clay (adapted from Kim, 1979)

Additionally, Kim and Novak (1981) studied the small-strain behaviour of Wallaceburg clay using a Stokoe type resonant column (RC) apparatus. Shear wave velocity (V_s) and shear modulus (G) degradation curves with increasing of shear strain (γ) were obtained. Similarly, damping ratio (D_r) with increasing of strain and compressional wave velocity (V_P) with increasing of confinement were reported. The soil samples tested by Kim and Novak (1981), were subjected to increasing of effective confining pressures, starting with pressures equal to the original *in-situ* pressure condition of the samples (e.g. 55 kPa, 140 kPa, 280 kPa, and 410 kPa).

In general, Kim and Novak (1981) observed that the elastic properties estimated (e.g. V_s, G) using the RC technique were independent of the shear strain amplitude when this was less than 0.01%, but the elastic parameters tend to decrease rapidly once the strain amplitude exceeded the 0.01% threshold level. Also, the low strain amplitude shear wave and shear modulus tended to increase with increasing of confining pressure and decrease with increasing of void ratio. More details on the testing methodologies adopted, and test results and discussion can be found in Kim (1979), Kim and Novak (1981a) and Kim and Novak (1981b). Figures B.6 to B.9 show a summary of results of the RC testing on the Wallaceburg clay material performed by Kim (1979) and Kim and Novak (1981).

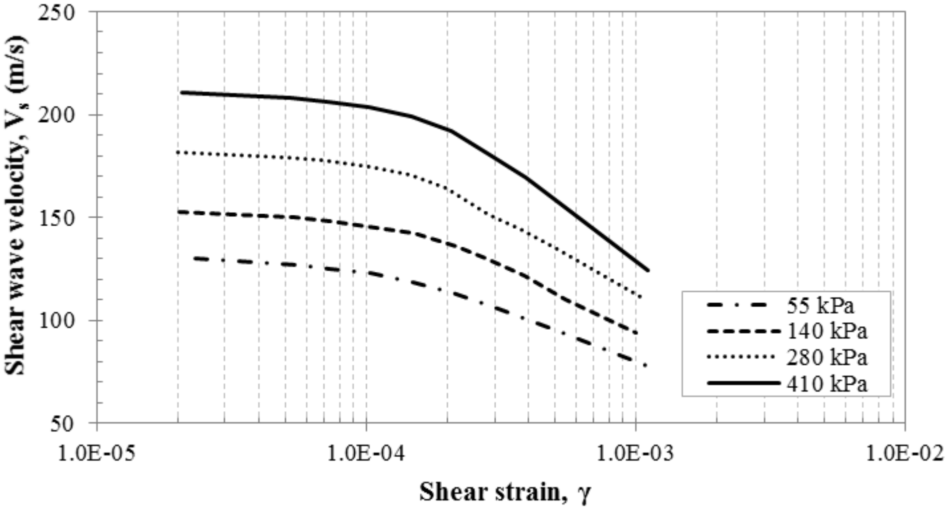

Figure B.6: Variation of shear wave velocity of Wallaceburg clay with strain amplitude and confining pressure (adapted from Kim, 1979)

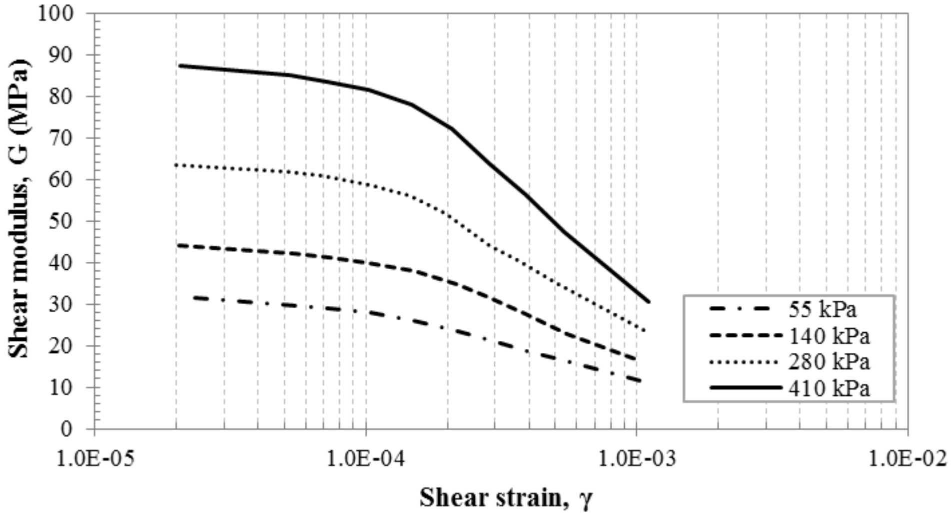

Figure B.7: Variation of shear modulus of Wallaceburg clay with strain amplitude and confining pressure (adapted from Kim, 1979)

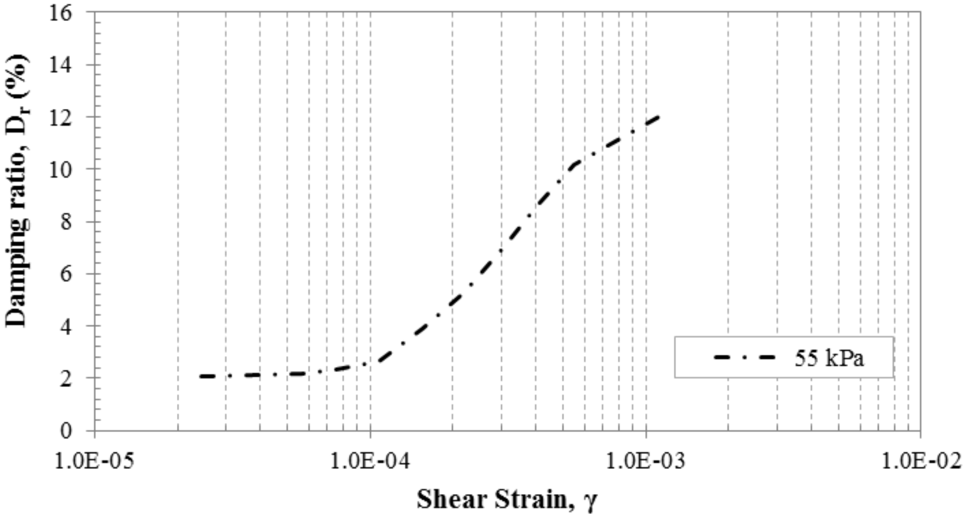

Figure B.8: Variation of damping ratio with increasing of strain at 55 kPa for Wallaceburg clay (adapted from Kim, 1979)

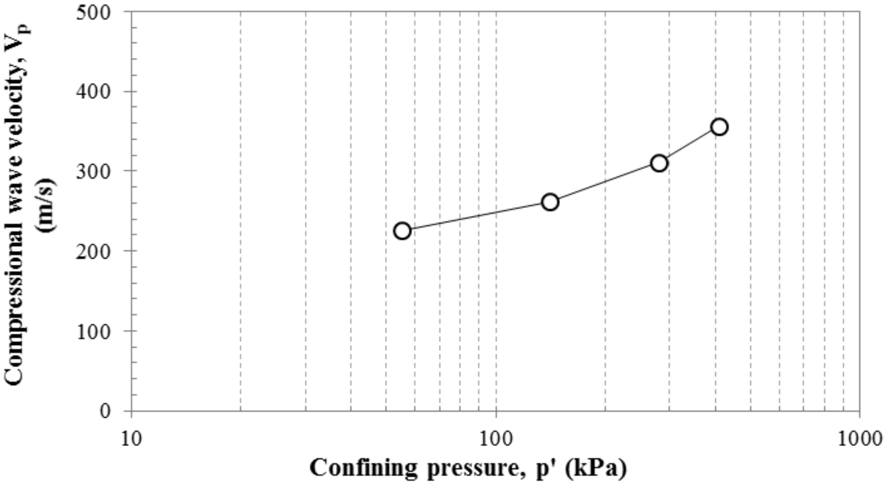

Figure B.9: Variation of compressional wave velocity with increasing of confining pressure for Wallaceburg clay (adapted from Kim, 1979)

B.2.2.3 Windsor silty clay

The Windsor clay material was previously studied at the soil's laboratory of Western University by Kim (1979) and Kim and Novak (1981). According to Kim (1979), the consistency of the silty clay stratum found at the site varied from soft to stiff. Results from *in-situ* vane shear testing indicated that the undrained shear strength of the silty clay varied from 17.2 kPa to greater than 143.6 kPa. Below about 4 m depth, the reported average in-situ undrained shear strength and the average remolded undrained shear strength were approximately 28.7 kPa and 19.2 kPa respectively.

Results from one-dimensional consolidation testing showed that the preconsolidation pressure at the in-situ sample level was equal to 140 kPa (see Figure B.10). The natural moisture content of the clay was around 51%, the liquid limit and plastic limit were about 51.3% and 21% respectively. The void ratio was estimated to be approximately 1.36, and unit weight equal to 17.05 kN/m^3. More details on the results of the Windsor clay material can be again found in Kim (1979), Kim and Novak (1981a) and Kim and Novak (1981b). Figures B.11 to B.14 show a summary of results of the RC testing on the Wallaceburg clay material performed by Kim (1979) and Kim and Novak (1981).

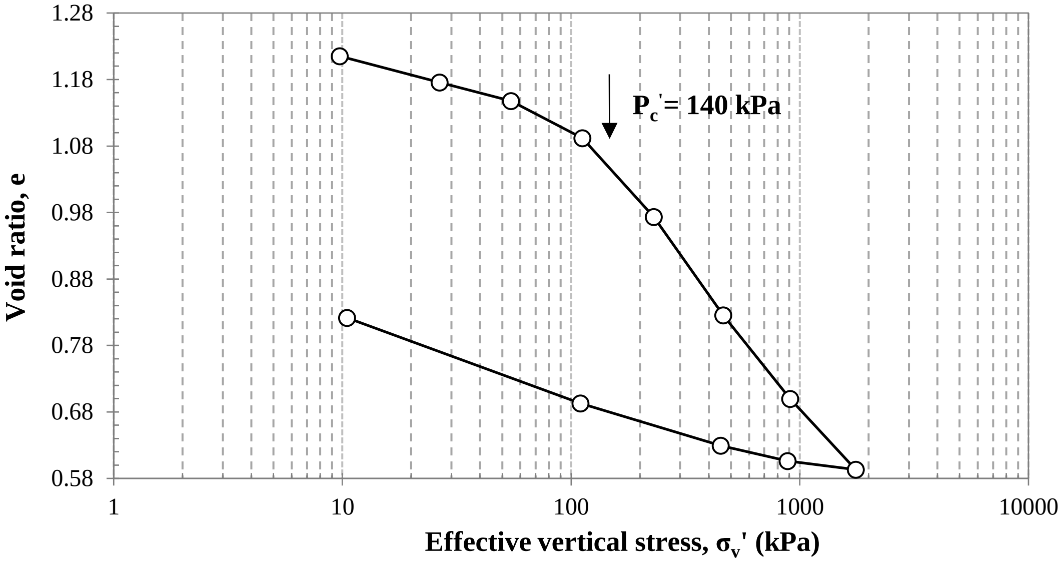

Figure B.10: Consolidation testing results for Windsor clay (adapted from Kim, 1979)

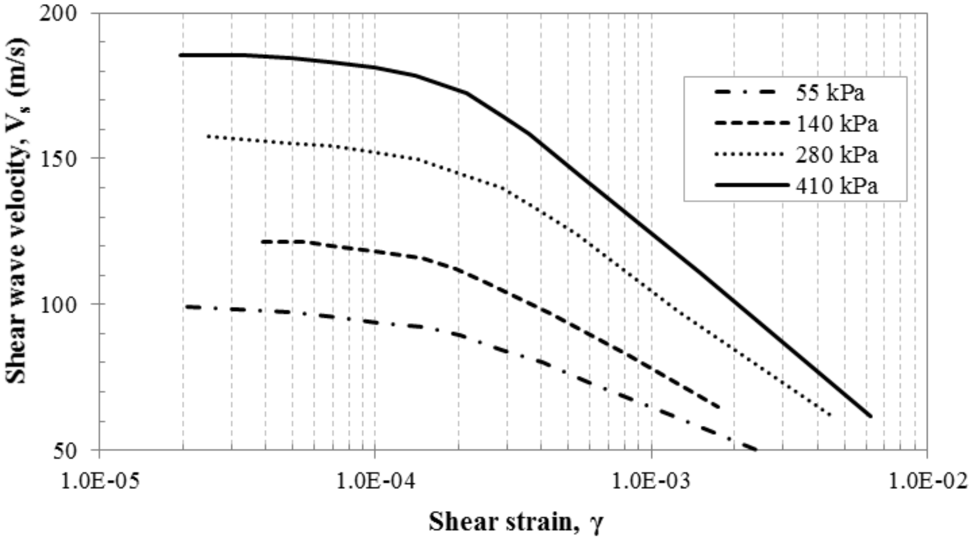

Figure B.11:Variation of shear wave velocity of Windsor clay with strain amplitude and confining pressure (adapted from Kim, 1979)

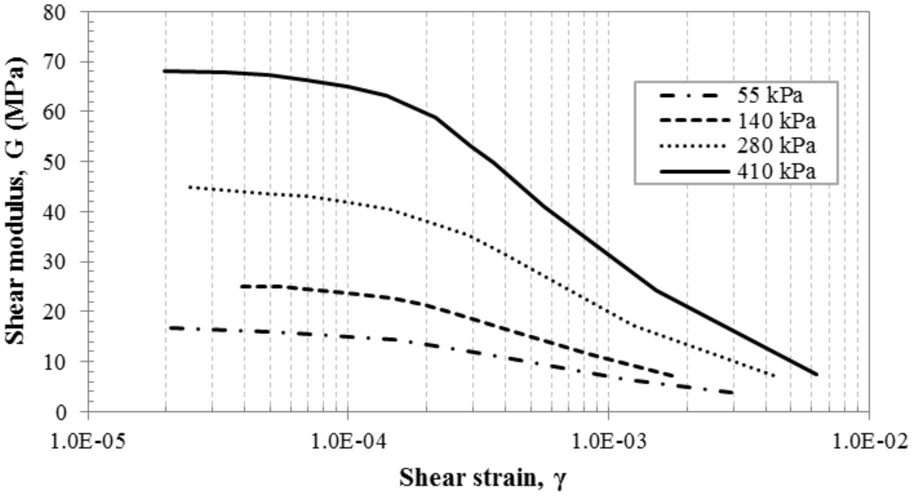

Figure B.12:Variation of shear modulus of Windsor clay with strain amplitude and confining pressure (adapted from Kim, 1979)

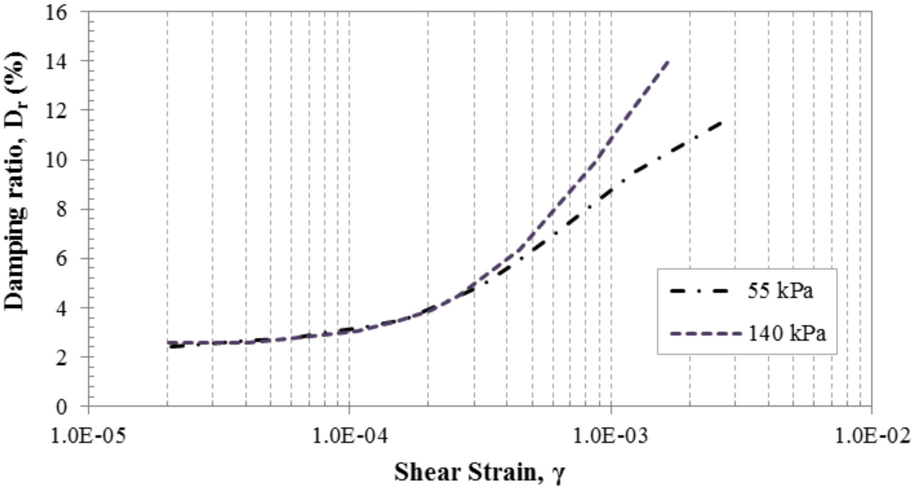

Figure B.13:Variation of damping ratio with increasing of strain at 55 kPa and 140 kPa for Windsor clay (adapted from Kim, 1979)

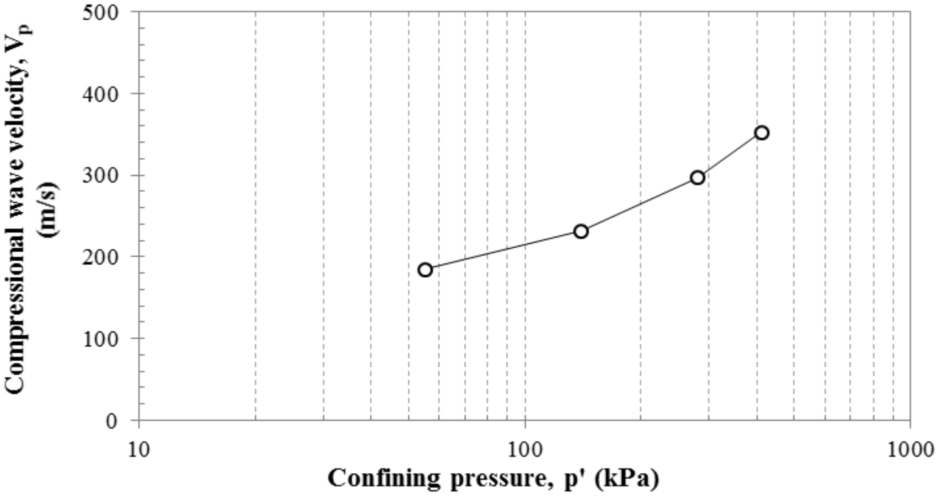

Figure B.14:Variation of compressional wave velocity with increasing of confining pressure for Windsor Clay (adapted from Kim, 1979)

B.2.2.4 Blenheim silty clay

Reipas (2012) performed a series of laboratory tests on Blenheim silty clay samples to characterize the basic geotechnical properties of the material. Among the laboratory tests carried out by Reipas (2012), results were found of the following properties: natural moisture content and Atterberg limits, unit weight, specific gravity, percent of fine content from sieving and hydrometer test, pre-consolidation pressure from one-dimensional consolidation, and small-strain elastic properties from resonant column (RC) test. The natural moisture content (w_c) ranged between 18.5% to 19.2%, while the liquid limit (LL) and plastic limit (PL) were approximately 23.1% and 16.7% (plasticity index or PI≈6.4). The unit weight (γ_{bulk}) was reported to be about 21.13 kN/m^3 and the specific gravity (G_s) around 2.65. Figure B.15 show the typical curve obtained by Reipas (2012) from one-dimensional consolidation.

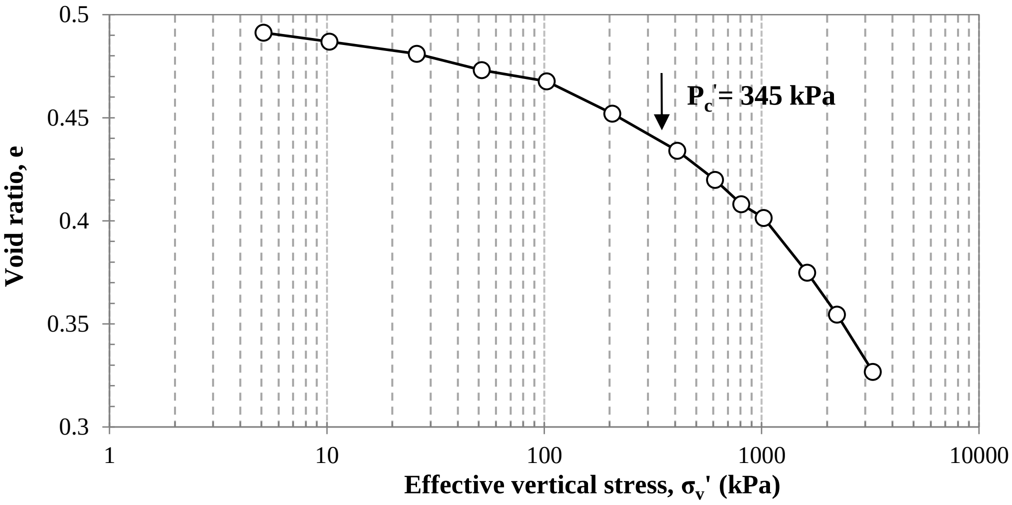

Figure B.15:Consolidation testing results for Blenheim silty clay (adapted from Reipas, 2012)

The resonant column (RC) tests performed by Reipas (2012) were used mainly to estimated shear wave velocity (V_s), shear modulus (G) and damping ratio (D_r) with increasing of strain amplitude (γ) and increasing of confinement (p’). Furthermore, Reipas (2012) analyzed vertical (0° rotation) and horizontal (90° rotation) cut samples, following a similar procedure used by Becker (1981), Lo et al. (1971) and Yong and Silvestri (1979), to examine the anisotropic stiffness of Blenheim clay. The procedure was briefly explained in Chapter 4.

The RC test results reported by Reipas (2012), showed that the elastic properties exhibited an independence of the shear strain amplitude when this was less than 0.005%. Once the shear strain amplitude exceeded the 0.005% threshold level, the elastic parameters decreased rapidly. Also, Reipas (2012) noticed that the shear wave velocity and shear modulus at very low strain amplitudes, increased with increasing of confining pressure and decreased with increasing of void ratio. Reipas (2012) tested the horizontal cut samples (90° rotation) only at confining pressures of 60 kPa and 240 kPa. Similar behaviour as that of the vertical cut samples was observed on the horizontal cut samples. Although, Reipas (2012) found that the elastic properties exhibited by Blenheim clay in the horizontal direction differed in value to that in the vertical direction, thus reporting an anisotropic ratio of 0.925 and 0.971 at 60 kPa and 240 kPa respectively. Instead of using ‘n’ as Becker (1981) did, Reipas (2012) used ‘α’ to refer to the anisotropic ratio, where $\alpha=G_{hh}/G_{vh}$.

In terms of the obtained damping ratio, all samples were reported to follow a similar trend. The damping ratio increased with increasing shear strain, and the damping ratio tended to decrease as confining pressure increases. The damping ratio was measured for both samples (0º rotation and 90º rotation) at 60 kPa and 240 kPa confining pressures and was found to be the same for both. Figures B.16, B.17, and B.18 show a summary of the RC test plotted results reported by Reipas (2012).

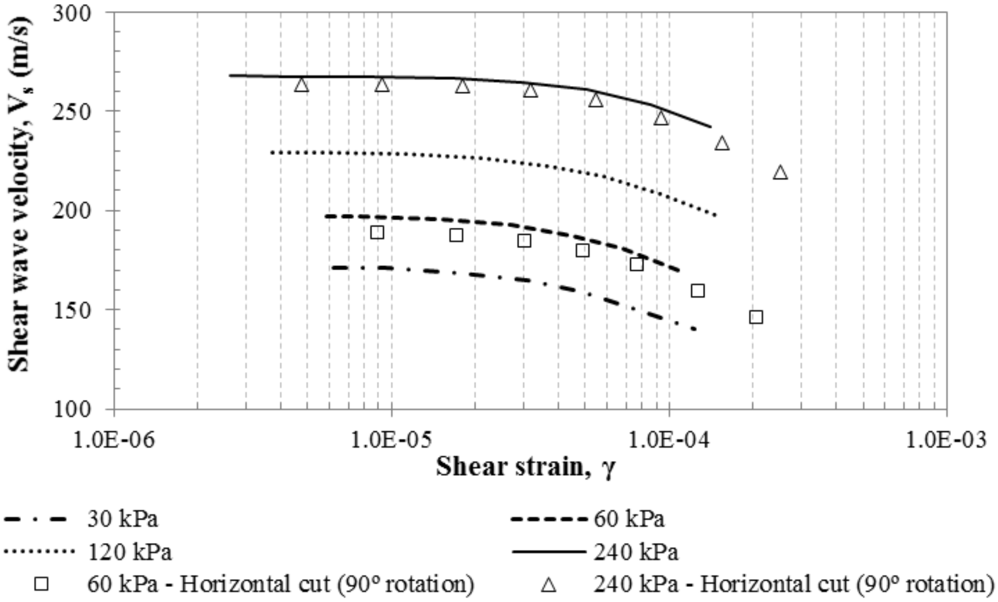

Figure B.16:Variation of shear wave velocity with strain amplitude and confining pressure for vertical and horizontal Blenheim clay samples (adapted from Reipas, 2012)

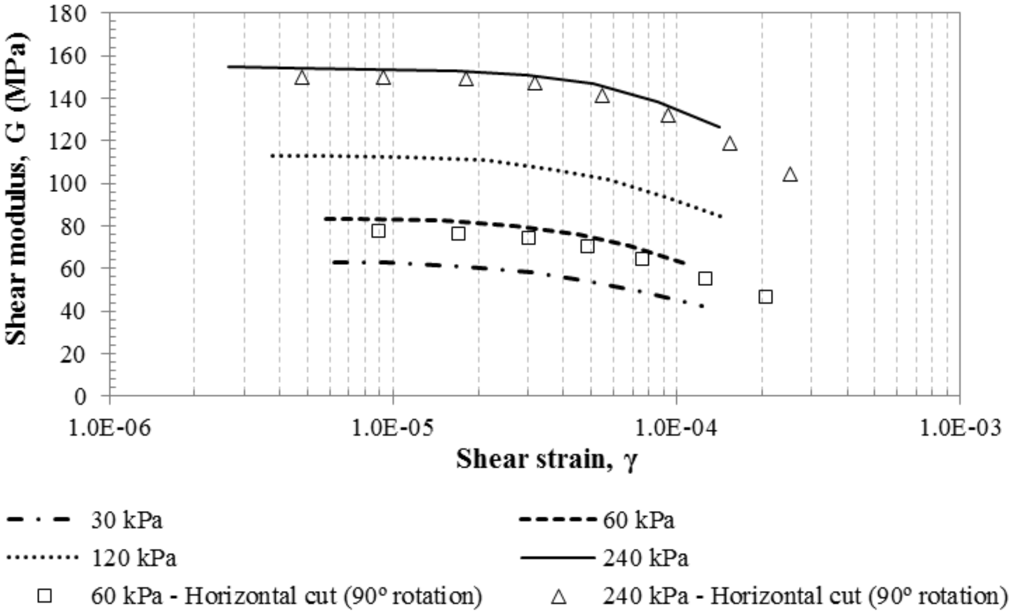

Figure B.17:Variation of shear modulus with strain amplitude and confining pressure for vertical and horizontal Blenheim clay samples (adapted from Reipas, 2012)

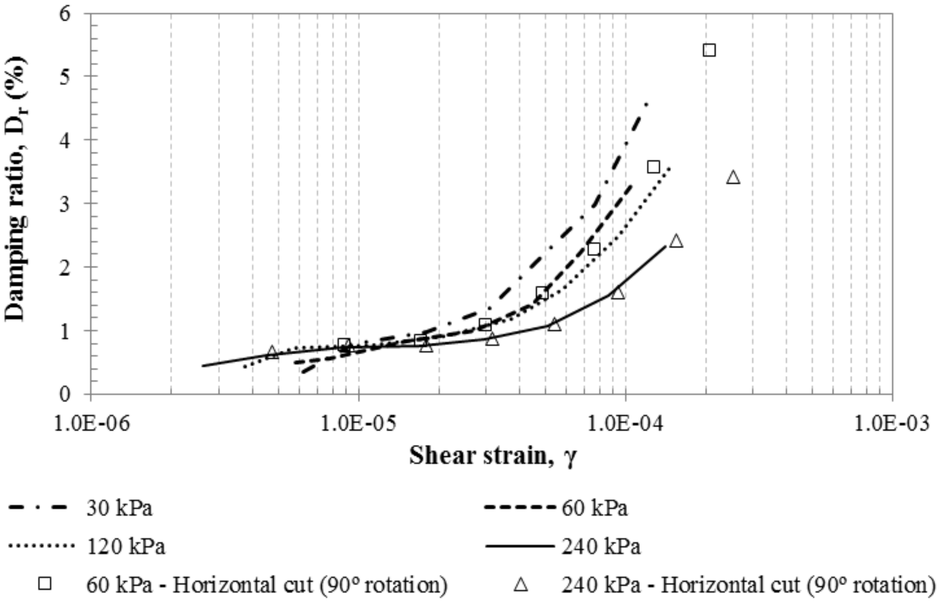

Figure B.18:Variation of damping ratio with strain amplitude and confining pressure for vertical and horizontal Blenheim clay samples (adapted from Reipas, 2012)

B.2.2.5 Winnipeg clay

Selected samples were tested for soil index properties. A series of laboratory tests to determine strength and consolidation characteristics were completed during the laboratory work conducted by TrekGeotechnical Inc.. Soil moisture tests and Atterberg limits were completed from samples within the clay fill, brown lacustrine clays, grey lacustrine clays and the silt till. The average moisture content of the clay fill was about 34.4%, for the brown clay around 42.2%, 50.5% for the grey clay, and 14.8% for the silt till. Average Atterberg limit values were found as follow: clay fill, PL equal to 23.8% and LL equal to 73.1%; brown clay, PL equal to 25.4% and LL equal to 79.1%; grey clay, PL equal to 25.9% and LL equal to 80.8%, and the silt till, PL equal to 12.1 and LL equal to 22.2%. Average void ratio of the clay fill was about 0.89,1.25 for the brown clay, and 1.34 for the grey clay.

Results from consolidated isotropic undrained (CIU) triaxial tests on samples from around 9.5 m depth, showed that for effective confining pressures of 75 kPa, 150 kPa, and 225 kPa, undrained shear strength values were about 26 kPa, 65 kPa, and 75 kPa respectively. In addition, consolidation testing results showed that the average pre-consolidation pressure (p_c') for the clay fill was about 115 kPa, for the brown lacustrine clay was around 240 kPa, and for the grey lacustrine clay p_c' ranged between 257 kPa to 200 kPa (See Figure B.19).

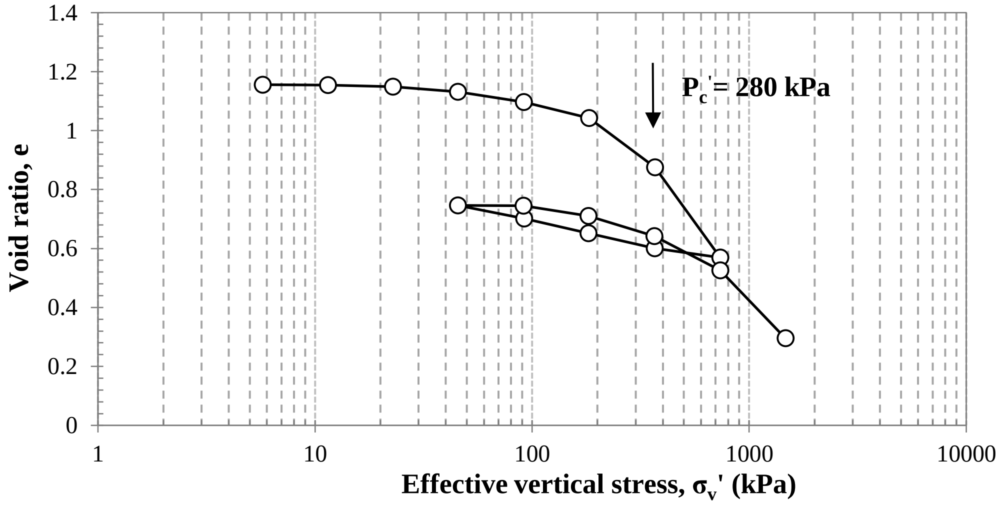

Figure B.19:Consolidation testing results for Winnipeg clay (adapted from private report)

B.2.2.6 Edgar plastic kaolin ‘EPK’ clay

Reipas (2012) calculated and reported on a different number of geotechnical properties of the EPK samples reconstituted in the Western University soils laboratory. The natural moisture content of the samples was around 50%, and the liquid limit (LL) and plastic limit (PL) were about 61.6% and 36.2% respectively. From one-dimensional consolidation testing, results showed that the pre-consolidation pressure ($p_c{}'$), determined using the Casagrande method, was around 150 kPa (see Figure B.20).

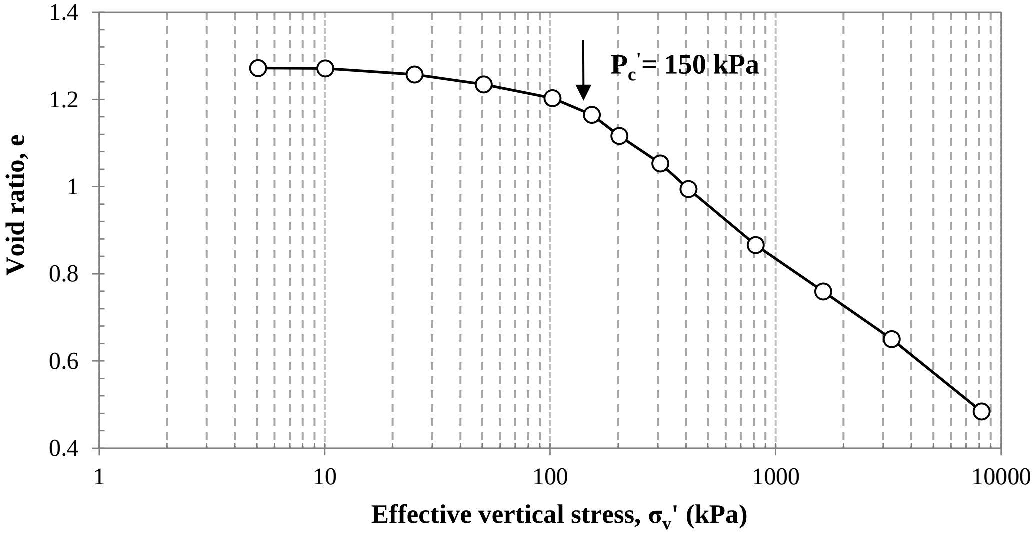

Figure B.20: Consolidation testing results for EPK clay (adapted from Reipas, 2012)

In addition to the basic characterization of the EKP material, Reipas (2012) performed resonant column (RC) tests on several EPK samples. The RC test focused mainly on estimating the shear wave velocity (V_S), shear modulus (G), and damping ratio (D_r) with increasing of shear strain amplitude and increasing of confining pressure, out of the selected EPK samples. RC results showed that the maximum shear wave velocity and maximum shear modulus at very small strain amplitudes, increased with the increasing of confinement. The maximum shear waves velocities obtained at 30, 60, 120, and 240 kPa were around 130 m/s, 145 m/s, 166 m/s, and 204 m/s respectively. Similarly, the maximum shear modulus at 30, 60, 120, and 240 kPa were about 30 MPa, 36 MPa, 48 MPa, and 75 MPa respectively. The shear strain amplitude threshold was observed at around 0.02%, once the shear strain amplitude exceeded the 0.02% threshold level, the elastic parameters decreased rapidly. In terms of damping ratio (D_r), Reipas (2012) observed that all samples followed a similar trend of having damping ratio increased with increasing shear strain. Also, the samples showed the damping ratio to decrease as confining pressure increases. For shear strains less than 0.02%, the damping ratios were very similar between the tested samples. For shear strains greater than 0.02%, the difference between samples increases. Figures B.21, B.22, and B.23 show a summary of the RC test plotted results reported by Reipas (2012).

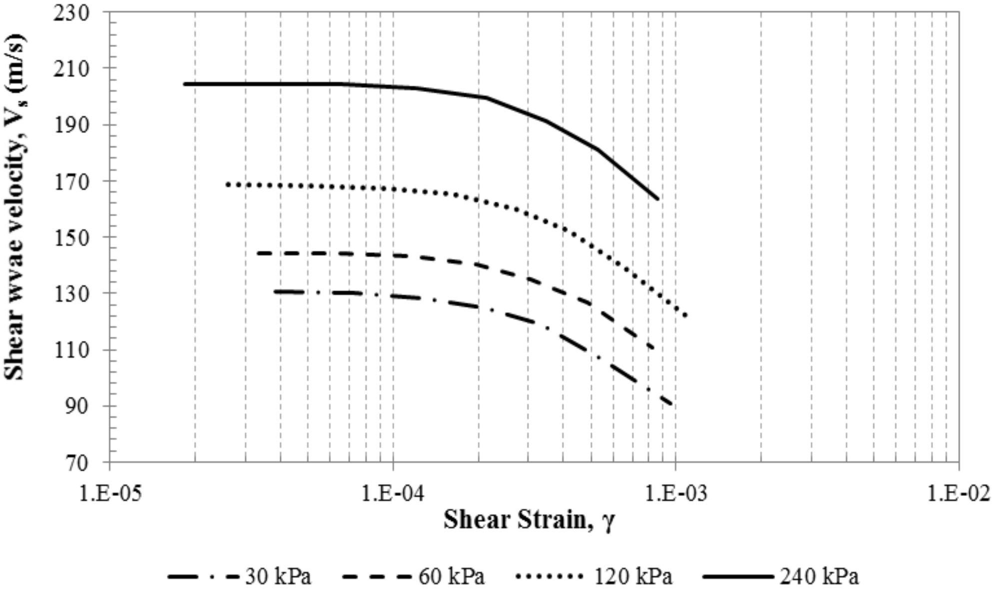

Figure B.21: Variation of shear wave velocity of EPK clay with strain amplitude and confining pressure (adapted from Reipas, 2012)

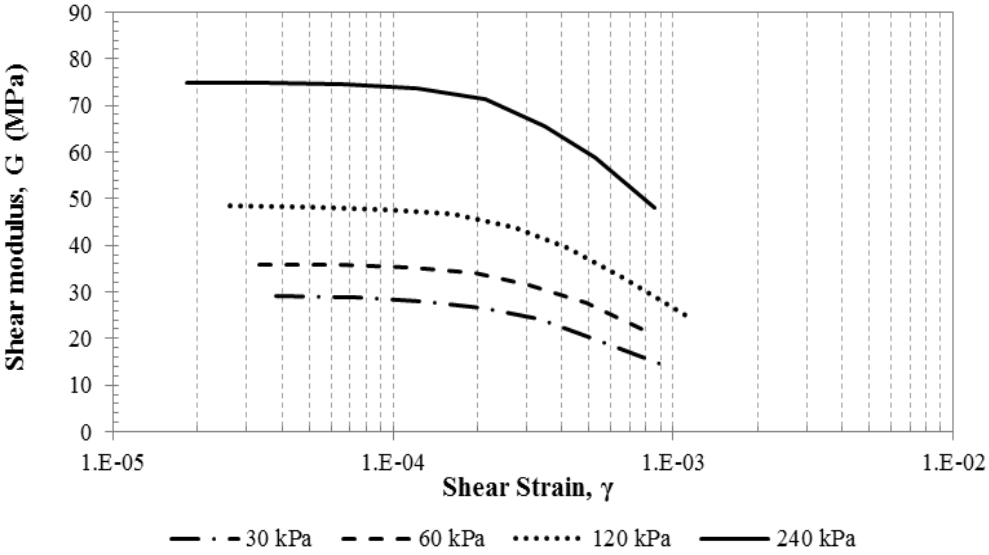

Figure B.22: Variation of shear modulus of EPK clay with strain amplitude and confining pressure (adapted from Reipas, 2012)

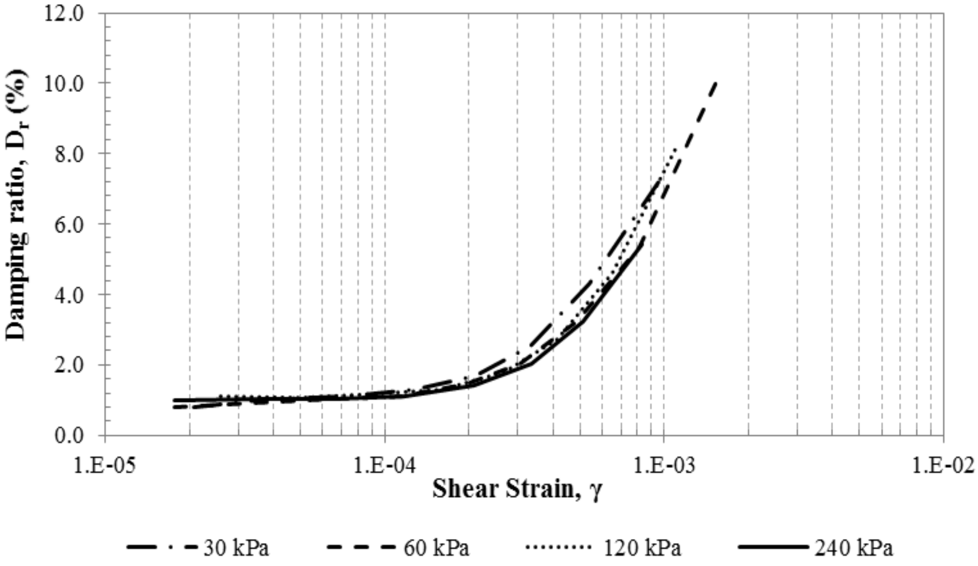

Figure B.23: Variation of damping ratio of EPK clay with strain amplitude and confining pressure (adapted from Reipas, 2012)

B.3 Photographic sequence of sample preparation for different tests

The sample preparation procedures were presented and discussed in Chapter 4

Figure B.24:Waxed block and cylinder samples, wire saw, and soil lathe

Figure B.25: Sample preparation sequence: a) waxed soil sample; b) opening of waxed sample; c) soil sample placed in soil lathe; d) trimmed sample; e) sample placed inside split metal mold; f) 50 x 100mm cut sample with radial filter paper

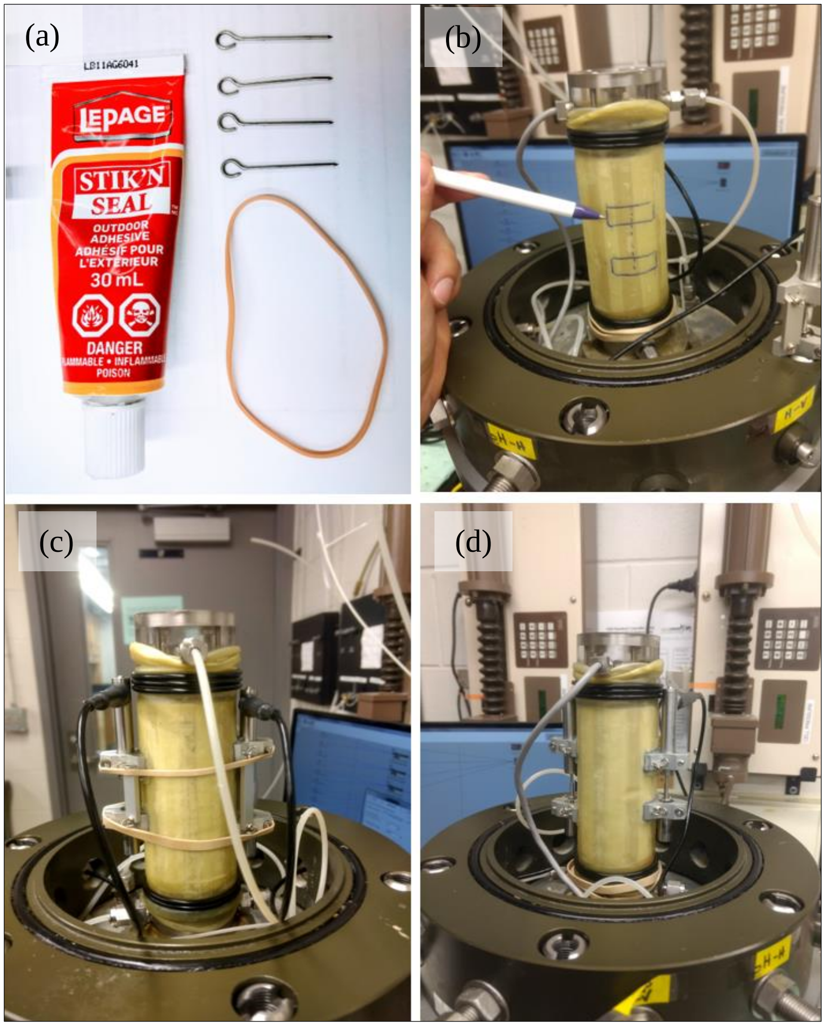

Figure B.26: Local displacement transducers mounting sequence, a) adhesive and pins used; b) placing area for mounting pads; c) soil specimen with small LVDT in place; d) final look of specimen with small LVDT

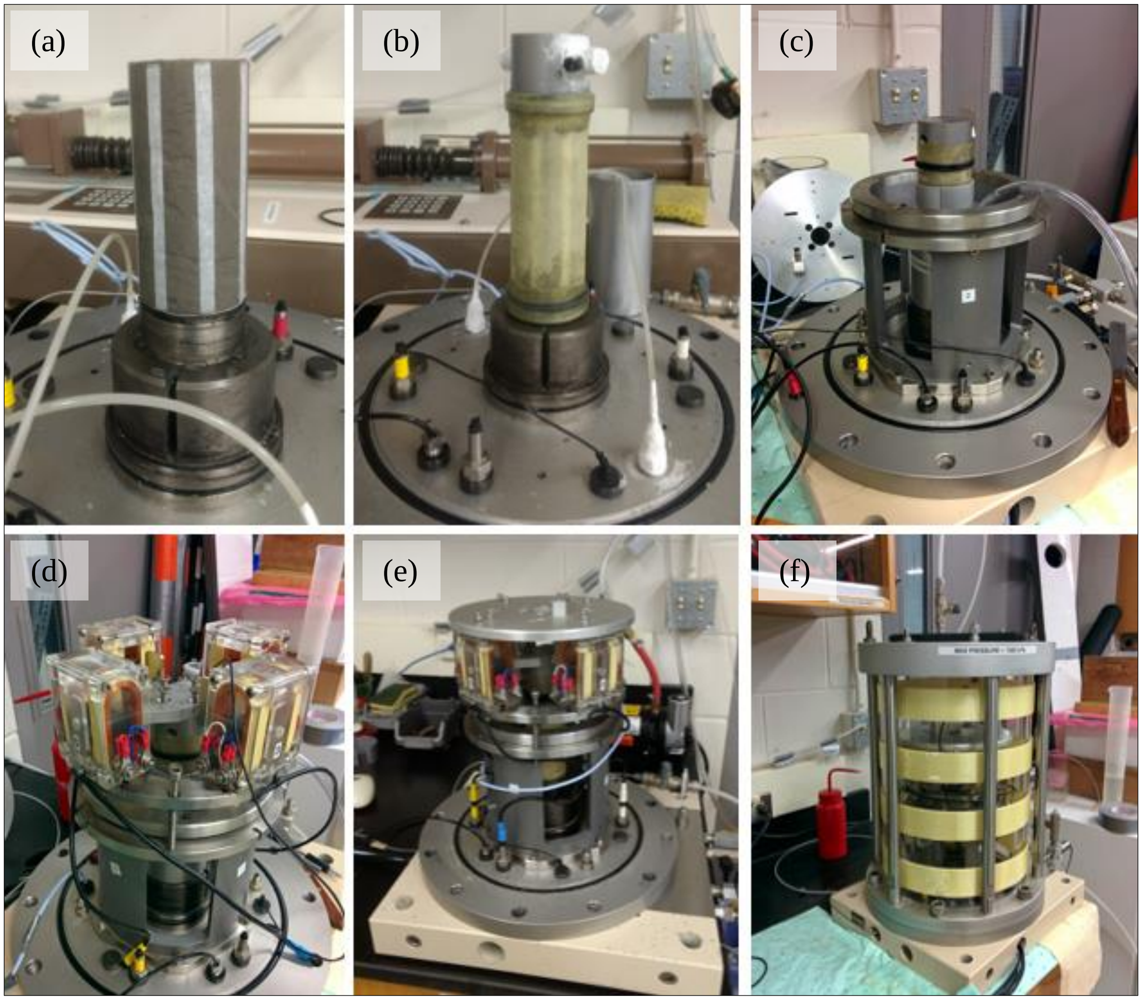

Figure B.27: Setting up process of a soil specimen and assembly of the essential RCA parts: a) placing of 50 mm x 100 mm soil specimen on pedestal; b) soil specimen covered with rubber membrane, fixed to pedestal with O-rings and attached to the top cap; c) support cylinder in place; d) drive system fixed to support cylinder and top plate screwed in place; e) standard cell covering the RCA system and ready for testing

B.4 Resonant column calibration

The standard analysis of RC results is based on the continuum theory of elastic wave propagation. The solution for the equation of motion for a fixed-free type resonant column (RC) is given by Equation B-1 as follows (Richart et al., 1970):

$$\frac{I}{I_o} = \frac{\omega_o H}{V_s} \tan\left(\frac{\omega_o H}{V_s}\right) = \beta \tan \beta \qquad \text{(B-1)}$$

where I = mass polar moment of inertia of the specimen in (kg.m^2), I_o = mass polar moment of inertia of the drive system (kg.m^2), H = height of the soil sample (m), ω_o = circular resonant frequency (rad/s), and β = resonant column test calibration factor. From the theory of wave propagation, the velocity of the shear wave propagation is computed using measured value of resonant frequency, specimen dimension, and the mass polar moment of inertia of drive system using Equation B-2 (ASTM D4015-15):

$$V_s = \frac{2\pi f_n H}{\beta} \qquad \text{(B-2)}$$

where V_s = shear wave velocity (m/s), and f_n = natural frequency of the specimen obtained from RC test (Hz). Due to the complex geometry of the drive system, its mass polar moment of inertia (I_o) is normally obtained experimentally through a calibration process (Drnevich, 1978; GDS, 2006; Kumar and Clayton 2007; Clayton et al. 2009, Khan et al., 2007; ASTM D4015-15).

A calibrated mass and a calibration specimen are used to measure I_o assuming the system as a torsional pendulum with a single-degree-of-freedom (SDOF) with total mass equal to the added masses of the driving system itself and any additional mass or masses attached to the system (Clayton et al, 2009; GDS, 2006). The equation of motion for such described system can be written as follows:

$$\omega_n = \sqrt{\frac{k}{I_o}} \qquad \text{(B-3)}$$

where w_n = the natural circular frequency of vibration of the sample, k = torsional stiffness of the specimen, and I_o = mass polar moment of inertia of all masses added at the top of the specimen. During the calibration procedure *f* is remeasured using additional masses on top of the drive system, a linear equation expressing the additional masses in terms of w_n can be written as follows:

$$I_{am} = \frac{k}{\omega_n^2} - I_o \tag{B-4}$$

where I_{am} = mass polar moment of inertia of the added mass. By plotting values I_{am} against $1/\omega_n^2$ for each test, I_o is defined by the y-axis intercept, and the torsional stiffness of the bar (k) is represented by the gradient. In this study, three calibration bars made of aluminum with different torsional stiffnesses were used. This made possible to cover an ample range of frequencies by varying the thickness of each calibration bar. Figure B.28 depicts the calibration bars and added masses used during the calibration procedure. Table B.4 shows a summary of the calibration bars properties measured in the laboratory, such as the bars dimensions and masses.

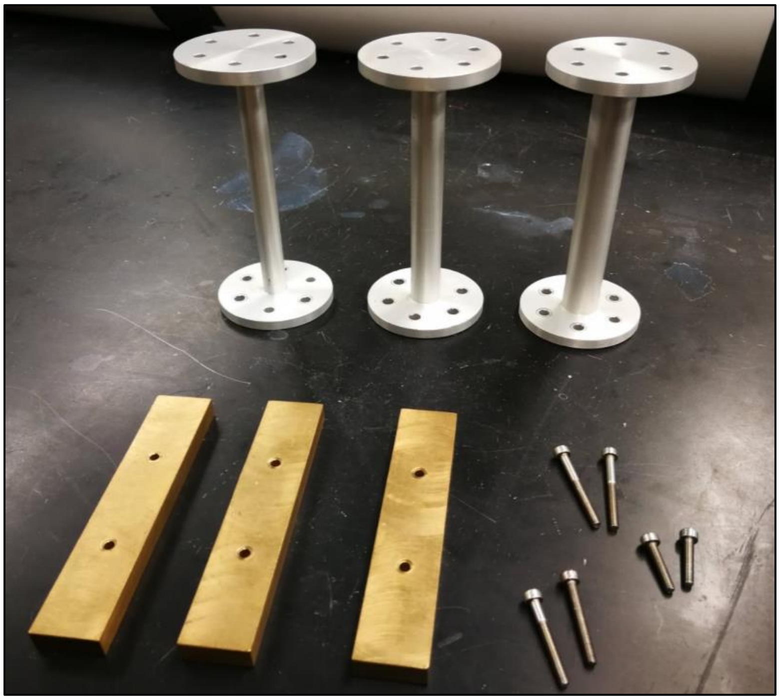

Figure B.28: Calibration bars and added masses

Table B.4: Dimensions and Masses of the Calibration Bars

	Bar section	Mass (kg)	Diameter (mm)	Height (mm)
10 mm Bar	Flange	0.0254	50.0	5.0
	Middle Bar	0.0213	10.0	100.0
12.5 mm Bar	Flange	0.0255	50.0	5.0
	Middle Bar	0.0333	12.5	100.0
15 mm Bar	Flange	0.0254	50.0	5.0
	Middle Bar	0.0479	15.0	100.0

Figure B.29 shows the results of calibration tests on the Stokoe type resonant column apparatus used in this investigation. This was obtained by plotting Equation B-4 for three different calibration bars. Along with the results obtained herein, calibration data obtained by Reipas (2012) is also shown in plot for comparison. Results from both calibration data show good agreement and the average value of the mass polar moment of inertia of the drive system (I_o) obtained was equal to 0.00392 kg.m^2.

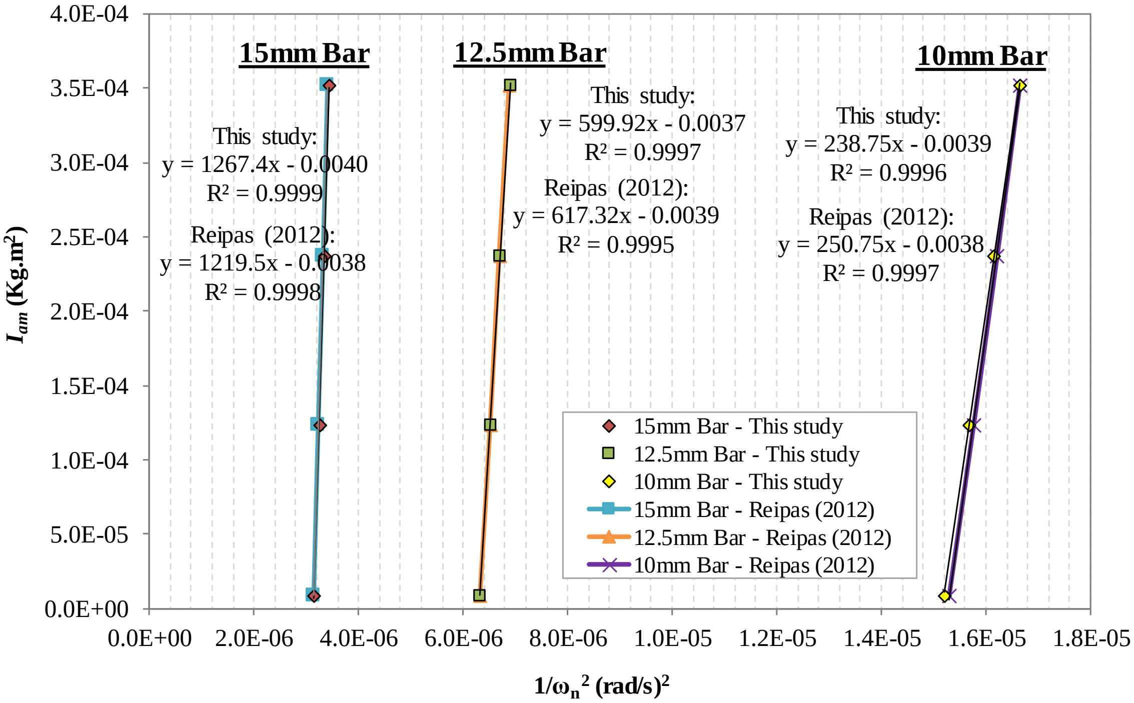

Figure B.29: Results of calibration of a Stokoe type resonant column apparatus with bars of different stiffnesses

Table B.5 shows the calculated properties (torsional stiffness and resonant frequency) of the calibration bars by assuming shear modulus of aluminum equal to 27 GPa (Clayton et al., 2009) and the mass polar moment of inertia of the drive system equal 0.004 Kg.m^2. Similarly, Table B.6 shows a summary of the results obtained from the calibration procedure using the resonant column apparatus. The obtained frequencies from the RC test for each calibration bar are in good agreement with the calculated frequencies in Table B.5. the difference between the assumed and estimated shear modulus of the aluminum bar is of approximately 5%.

Table B.5: Calculated properties of calibration bars

Calibration bar	Dimensions of central rod		Calculated torsional stiffness* (kN.m)	Calculated resonant frequency** (Hz)
	Height (mm)	Diameter (mm)		
1	100	10	0.265	40.59
2	100	12.5	0.647	63.42
3	100	15	1.342	91.33

*Based on shear modulus of aluminum G=26.5 GPa (Clayton et al., 2009); **Assuming I_{drive}=0.004 Kg.m^2

Table B.6:Summary of results of calibration procedure using the RC apparatus

Calibration bar	Resonant frequency, f (Hz)	Dynamic torsional stiffness, k_d (N.m)	Estimated mass polar moment of inertia of drive, I_o (Kg.m^2)	Estimated shear wave velocity of calibration bar from RC test (m/s)	Estimated shear modulus of calibration bar from RC test (GPa)
1	40.6	0.239	0.0039	3055.1	25.18
2	63.3	0.600	0.0037	3047.8	25.06
3	89.6	1.267	0.0040	3003.8	24.95

Figure B.30 shows a comparison between the obtained shear wave velocities (V_s) of each calibration bar using the RC apparatus, along with data obtained by Reipas (2012) using the same set up from this investigation, data obtained by Moayerian (2012) using a Stokoe type RC apparatus fabricated at the University of Waterloo (Cascante et al., 2003). V_s values obtained experimentally by De Billy (1980) and Lambe and Whitman (1979), both previously reported by Kumar and Clayton (2007), are also shown in Figure B.30. V_s data obtained from the calibration procedure for the aluminum bars fall within the limits reported by Lambe and Whitman (1979) and are in good agreement with the V_s value reported by the De Billy (1980) of 3086 ± 20 m/s. One trend observed from Figure B.30 is that the measured shear wave velocities slightly decrease with the increasing of resonant frequency. Similar behaviour was reported by Kumar and Clayton (2007) where they observed similar slight decrease up to a frequency of 175 Hz, thereafter the computed values of V_s decreased significantly. Drnevich (1978) mentioned that an imperfect coupling between the specimen and the end platen could lead to a decrease in the magnitude the shear wave velocity, especially for very stiff materials (f > 200 Hz).

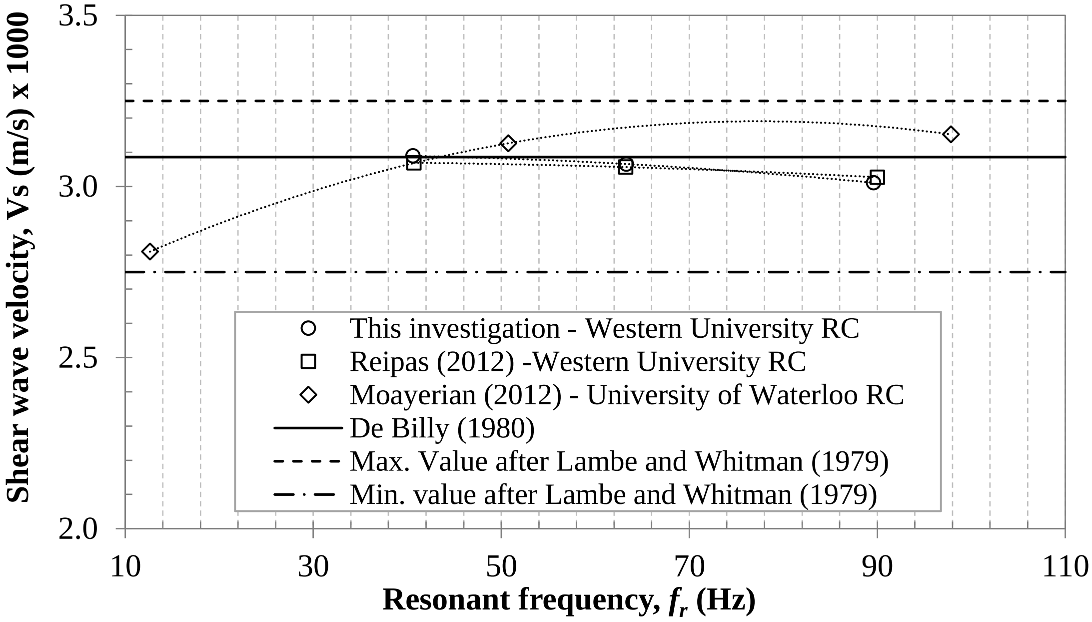

Figure B.30: Variation of obtained shear wave velocity for aluminum with resonant frequency and its comparison with published data.

The damping ratio (D) of the aluminum bars was also measured throughout the calibration exercise. This was obtained using the free decay and logarithmic decrement method (see Chapter 4, Section 4.3.8). Figures B.31, B.32 and B.33 show the variation of damping ratio with increasing of shear strain for the 10 mm, 12.5 mm and 15 mm diameter bars, respectively. Also, data obtained by Reipas (2012) and Moayerian (2012) are shown for reference. Moayerian (2012) computed the damping ratio by curve fitting the measured transfer function between the applied torque and induced angle of twist with the theoretical equations (e.g. Cascante et al. 2003).

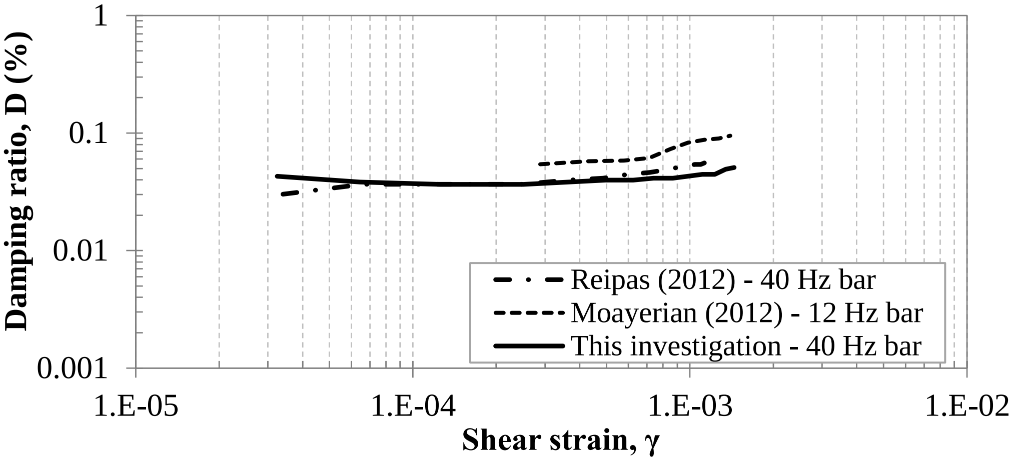

Figure B.31: Damping ratio vs. shear strain for 10 mm bar (40 Hz)

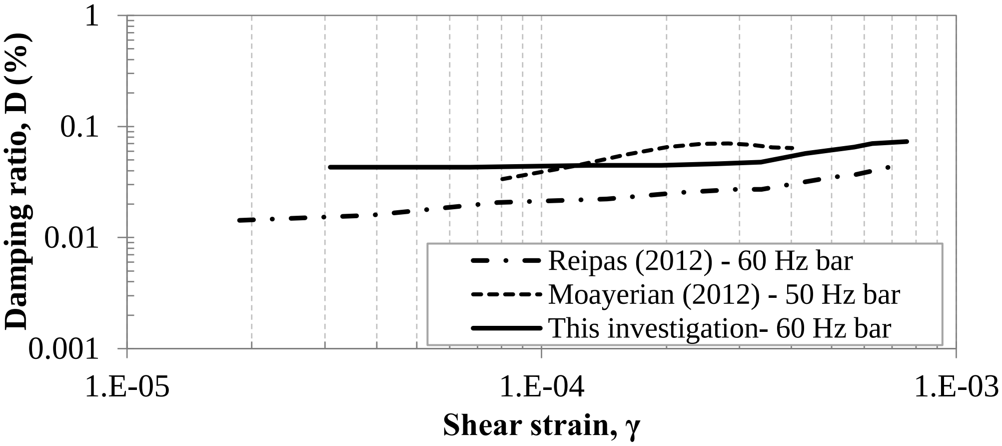

Figure B.32:Damping ratio vs. shear strain for 12.5 mm bar (60 Hz)

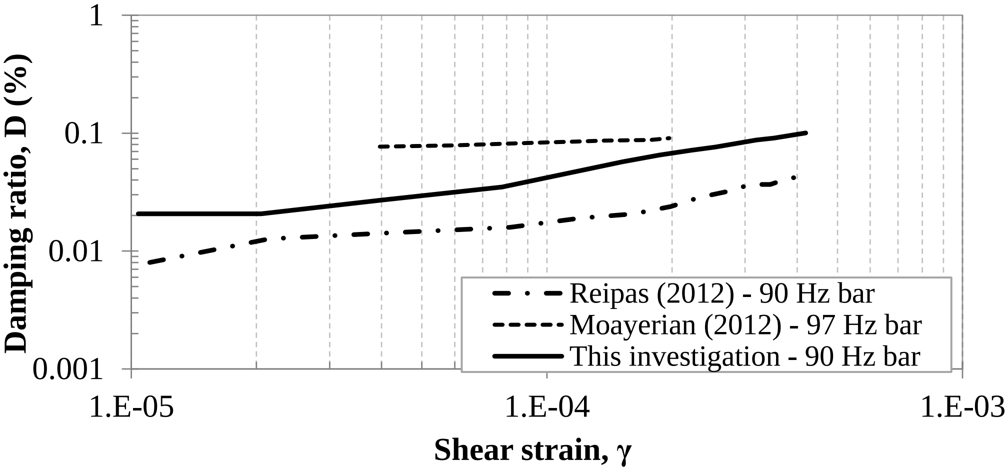

Figure B.33: Damping ratio vs. shear strain for 15 mm bar (90 Hz)

From Figures B.31, 32 and 33 can be inferred that the damping ratio of the aluminum bars falls between 0.01% and 0.1%. Such values are also similar to the ones reported by Moayerian (2012) and Reipas (2012). Khan et al. (2007) reported *D* values for aluminum close to 0% as well, whereas Kumar and Clayton (2007) computed *D* values of as low as 0.12%. Both Khan et al. (2007) and Kumar and Clayton (2007) reported increase of damping ratio with the increasing of resonant frequency, especially for frequencies higher than 175 Hz, such behavior was not observed here as the maximum resonant frequency for a calibration bar used was 90 Hz.

B.4.1 Small-strain characterization of Ottawa silica sand samples

To further assess the measurements of dynamic properties and consistency in the results of the Stokoe type resonant column (RC) apparatus used in this investigation, a series of RC tests were conducted on a benchmark standardized laboratory sand also known as Ottawa silica sand or Barco sand #49. The Ottawa silica sand was selected as benchmark material for testing due to its well characterized properties found in the literature and is uniformly graded, which should aid with reproducibility of samples and repeatability of results. Figure B.34 shows the grain size distribution of the material and Table B.7 presents a summary of the geotechnical properties estimated in the laboratory by Reipas (2012).

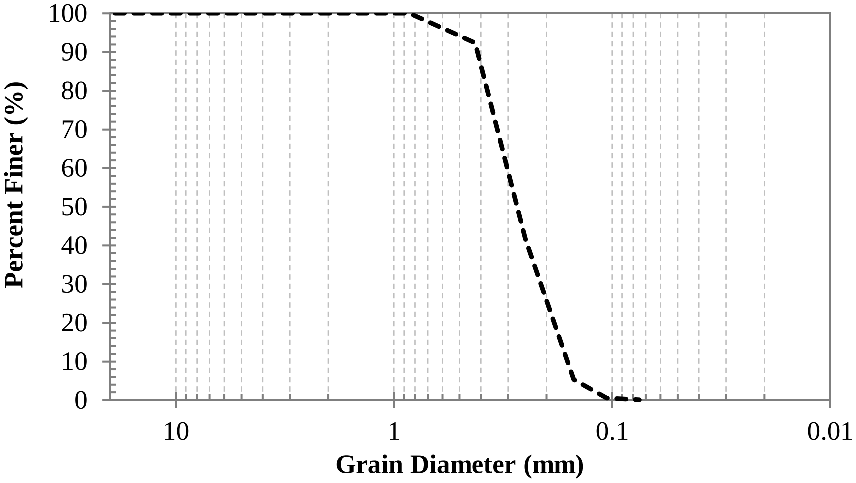

Figure B.34: Grain size distribution of Ottawa silica sand (Barco #49) (adapted from Reipas, 2012)

Table B.7: Geotechnical properties of Ottawa silica sand

Property	Ottawa silica sand (Barco 49)
e_{min}	0.476
e_{max}	0.727
G_s	2.66
D_{10}	0.16
D_{50}	0.26
D_{60}	0.30

Sand samples were prepared inside a split mold using dry pluviation and tamping technique. Vacuum pressure was applied to hold the samples once the split mold was removed. The driving plate system and LVDT were place around and on top of the sample, respectively, and the chamber was assembled. The vacuum pressure to hold the sample was progressively released while increasing the cell pressure. All the sand samples were tested under isotropic confinement with increasing pressures from 30 kPa to 240 kPa. At each confining pressure, the resonant frequency and damping ratio of the samples were measured over a range of shear strains from 10^{-6} to 10^{-3}. Table B.8 shows a summary of the properties of the Ottawa sand samples tested in this study. Two samples were created, sample #1 with relative density of 60% and void ratio of 0.577, and sample #2 with relative density and void ratio of 70% and 0.552, respectively.

Table B.8: Summary of properties for the Ottawa sand samples tested

Properties	Sample # 1	Sample # 2
Sample Mass (g)	328.12	328.12
Initial Sample Height, h_o (mm)	99.00	96.93
Initial Sample Diameter (mm)	50.00	50.14
Density, ρ (kg/m^3)	1687.97	1714.44
Void Ratio, e	0.577	0.552
Relative density, D (%)	60.00	69.70

Figures B.35 to B.38 show typical results for the dynamic properties measured at confining pressures of 60 kPa and 240 kPa. Data obtained by Reipas (2012) and Moayerian (2012) on different Barco #49 samples were included for comparison. Figures B.35 and B.36 show the variation of the normalized shear modulus (G/G_{max}) of the samples with the increasing of shear strain. Results from the different studies show good agreement and follow the hyperbolic model proposed by Oztoprak and Bolton (2013). From Figures B.35 and 36 can be seen that the sample exhibit a stiffer response with the increasing of confining pressures as the degradation curves start to shift from ~~right to left~~. Figures B.37 and B.38 show the variation of the damping ratio with shear strain. Results are in good agreement with the published data and these follow similar behaviour with increasing of strain. It can be seen that the damping ratio somewhat decreases with the increasing of confining pressures.

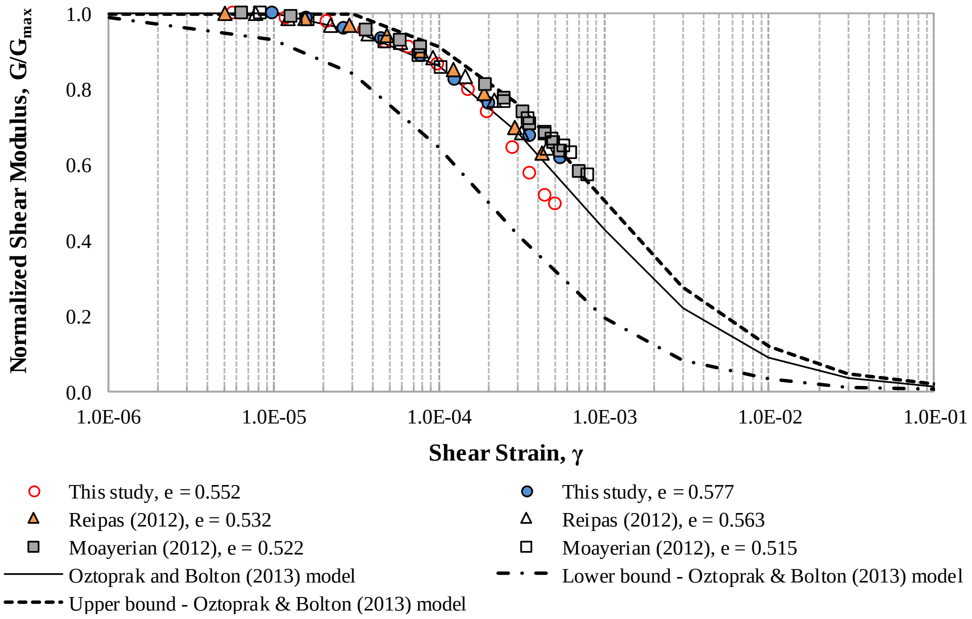

Figure B.35: Normalized shear modulus G/G_{max} vs. shear strain at σ'=60 kPa

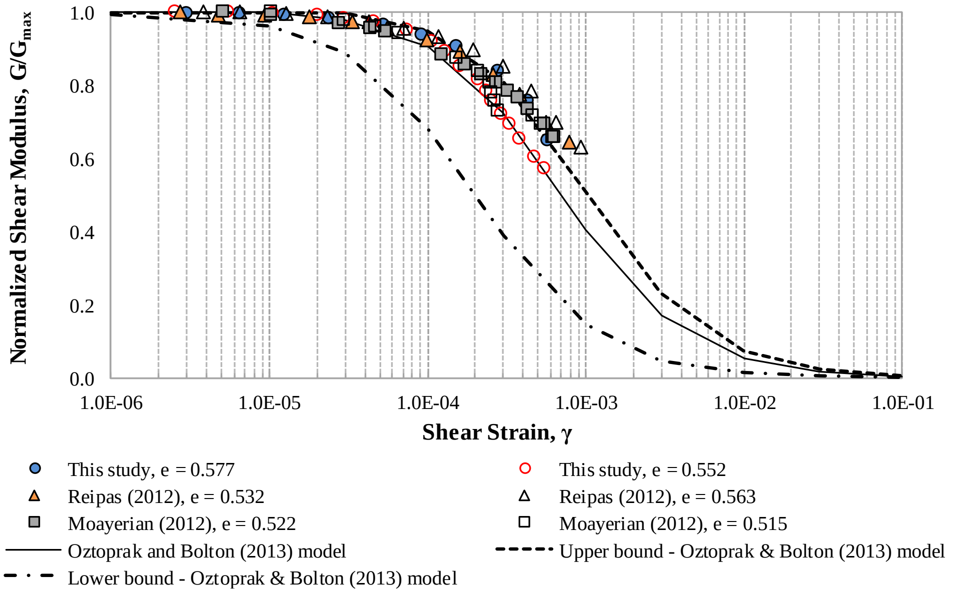

Figure B.36: Normalized shear modulus G/G_{max} vs. shear strain at σ'=240 kPa

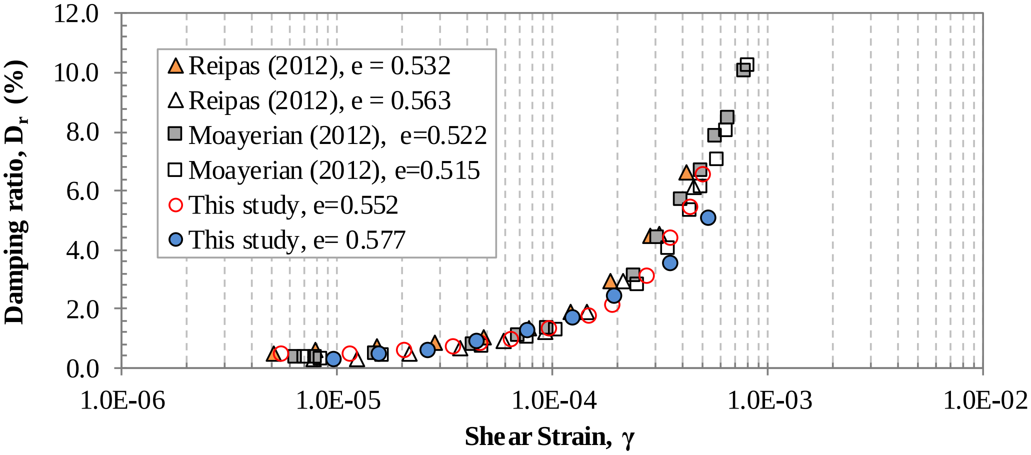

Figure B.37: Damping ratio vs shear strain at σ'= 60 kPa

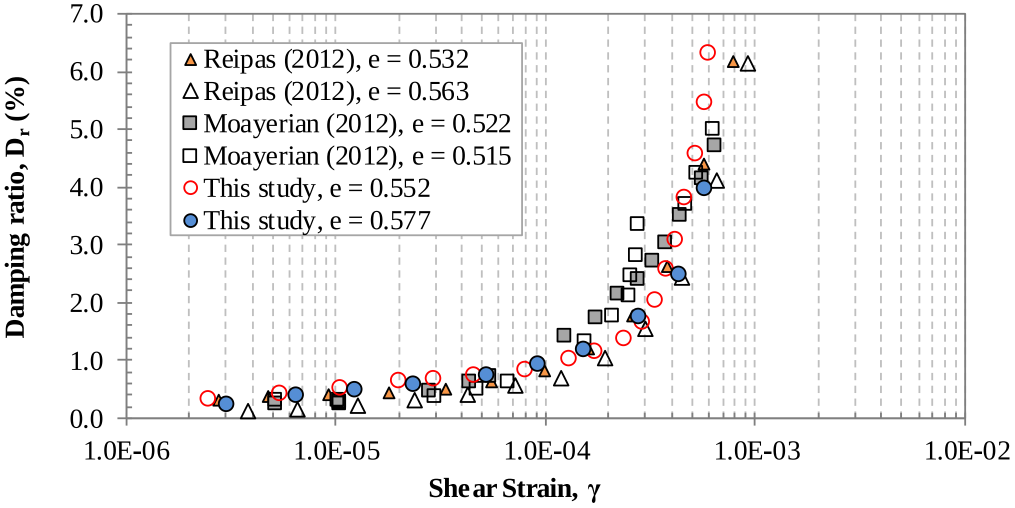

Figure B.38: Damping ratio vs shear strain at σ'= 240 kPa

Appendix C

Appendix C presents the results obtained from resonant column tests on vertically (0° rotation) and horizontally (90° rotation) trimmed samples of Port Alma clay. The majority of the results for the vertically cut samples are shown in Section 5.3 of Chapter 5. A complete set of results for the horizontally cut samples are presented in Section C.1.2. A detailed analysis of these experimental studies, and a discussion of their implications, can be found in Sections 5.3 and 5.4 of Chapter 5, respectively.

C.1 Chittick test results for Port Alma clay till deposit

Figure C.1 shows the results from determination of total carbonate content and the individual amounts of calcite ($CaCO_3$) and dolomite ($MgCaCO_3$) for the Port Alma clay till deposit. The results from the Chittick test are compared to that obtained by Newson et al. (2019).

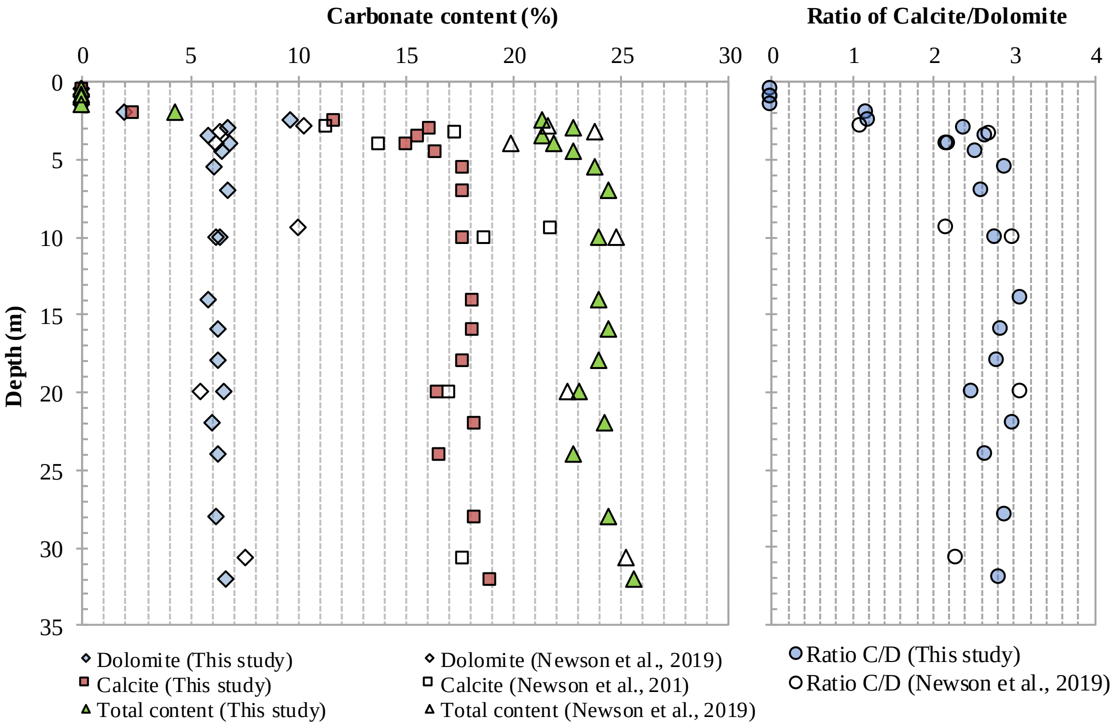

Figure C.1: Elastic modulus variation with strain amplitude of Port Alma clay

C.2 Resonant column test results for Port Alma clay

C.2.1 Vertically-cut sample (0° rotation)

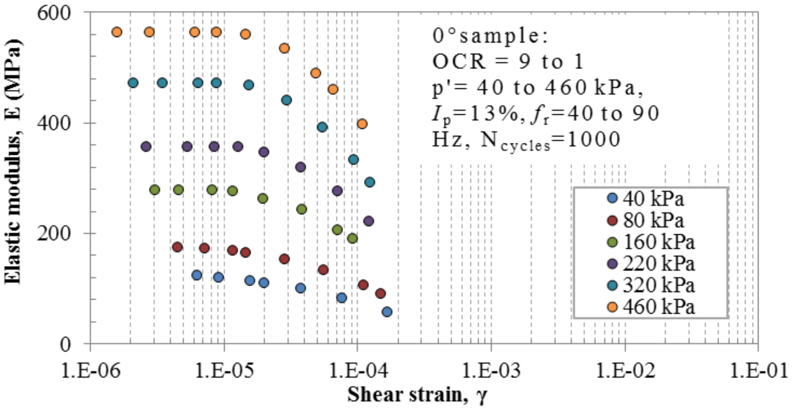

Figure C.2: Elastic modulus variation with strain amplitude of Port Alma clay

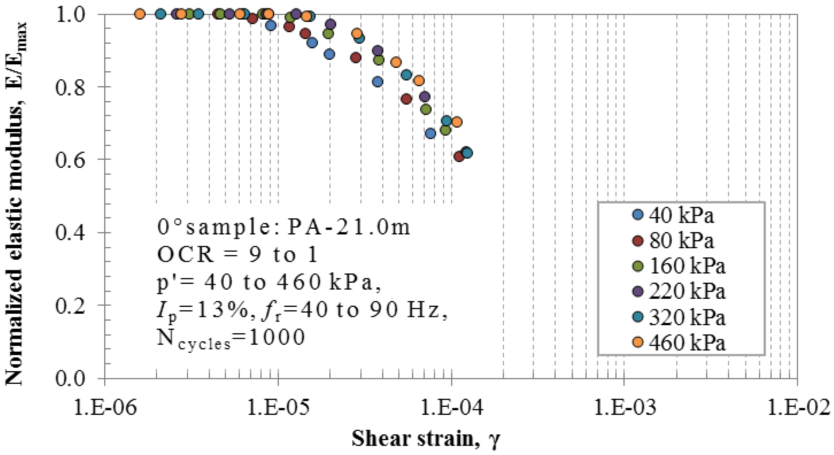

Figure C.3: Normalized elastic modulus variation with strain amplitude of Port Alma clay

C.2.2 Horizontally-cut sample (90° sample)

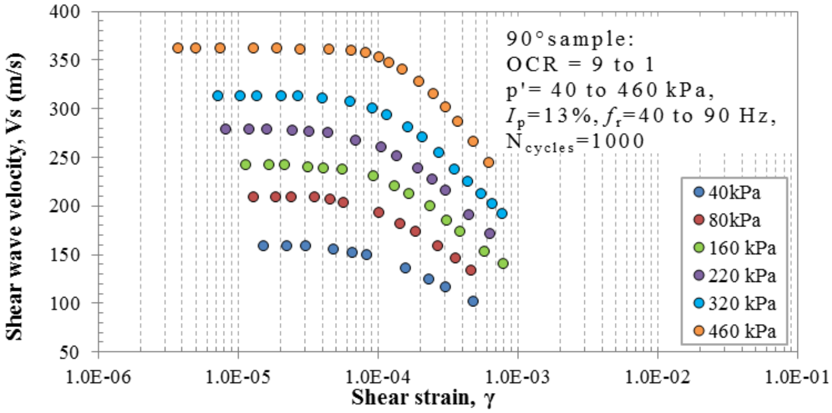

Figure C.4: Shear wave velocity variation with strain amplitude of Port Alma clay

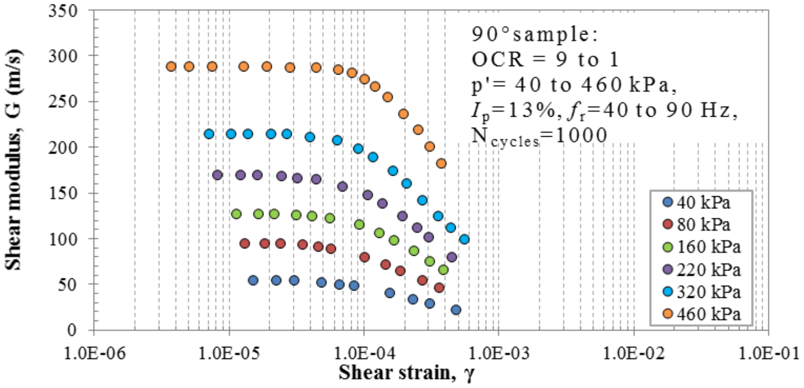

Figure C.5: Shear modulus variation with strain amplitude of Port Alma clay

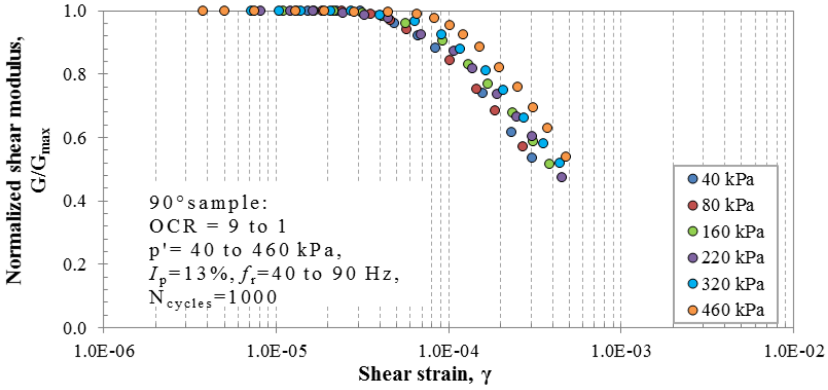

Figure C.6: Normalized shear modulus variation with strain amplitude of Port Alma clay

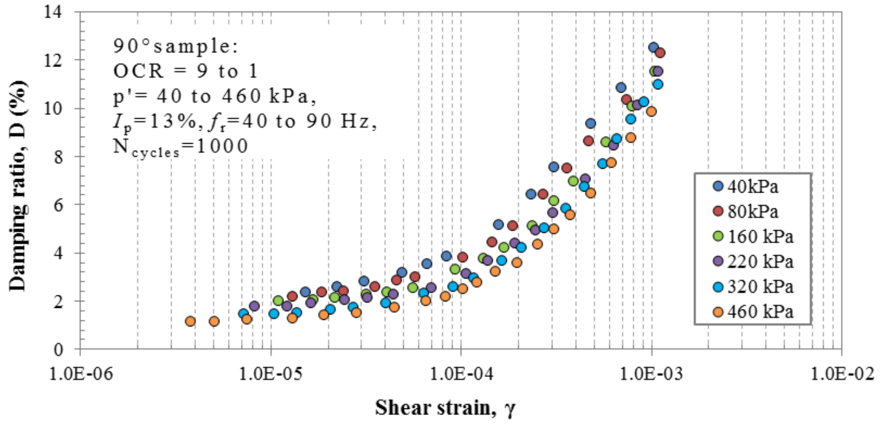

Figure C.7: Damping ratio variation with strain amplitude of Port Alma clay

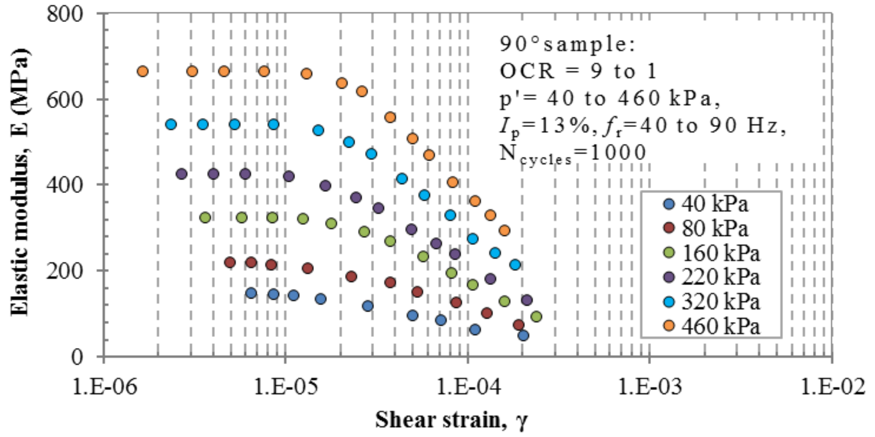

Figure C.8: Normalized elastic modulus variation with strain amplitude of Port Alma clay

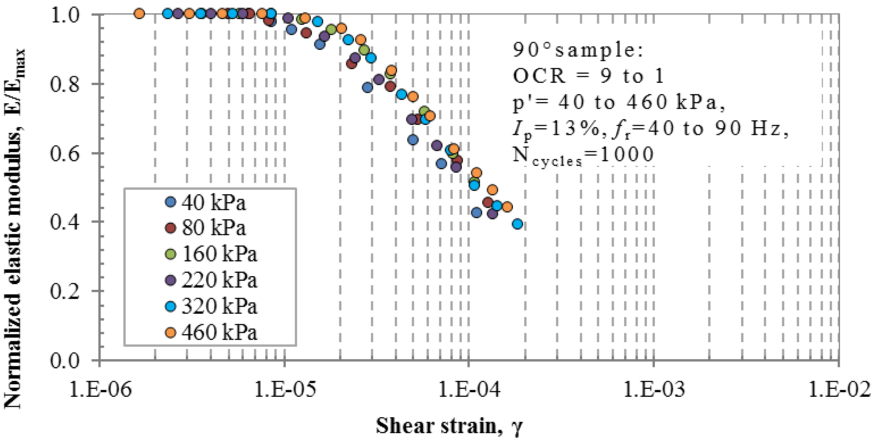

Figure C.9: Normalized elastic modulus variation with strain amplitude of Port Alma clay

Appendix D

Appendix D presents a summary of the results from consolidated isotropic undrained (CIU) triaxial tests with local strain measurements, bender elements and resonant column testing on the different cohesive materials (Port Alma clay, Windsor clay, Wallaceburg clay, Blenheim clay, Winnipeg clay, and EPK clay). Comprehensive analyses of these results were done throughout Chapter 5 and 6. Section D.1 shows a summary of the critical state and deviatoric stress-strain behavior of these cohesive soils.

Section D.2 presents detailed measurements of propagated shear waves in the vertical and horizontal directions of the samples (V_{svh} and V_{shh}) and the estimation of the small-strain shear modulus for the same materials (G_{vh} and G_{hh}).

Results from the resonant column tests are shown in Section D.3, these include plots for shear wave velocity (V_s), shear modulus (G), damping ratio (D), elastic modulus (E) and normalized shear modulus and elastic modulus (G/G_{max} and E/E_{max}) against shear strain (γ) for both 0° and 90° rotation samples. Different empirical models for G/G_{max} and damping ratio were included in some of the plots to further verify the validity of the results. Such models were explained further in Section 5.4.2 of Chapter 5.

Section D.4 shows the results from a further analysis carried out on the shear waves measured in the vertical direction of each cohesive material. Different empirical correlations to estimate shear wave velocity were used for comparison with the data obtained in this investigation. Various analyses of the estimated wave velocity parameters (α_s and β_s) for the materials following the approach of Cha et al. (2014) are shown at the end of the section. Additionally, a check of the estimated values of G_{hh} from resonant column testing was performed using the analysis proposed by Sultaniya et al. (2010) explained at the end of Section 2.4.3. The results of this analysis are shown in detail in Section D.5.

D.1 Critical state and deviatoric stress-strain behaviour of studied cohesive soils

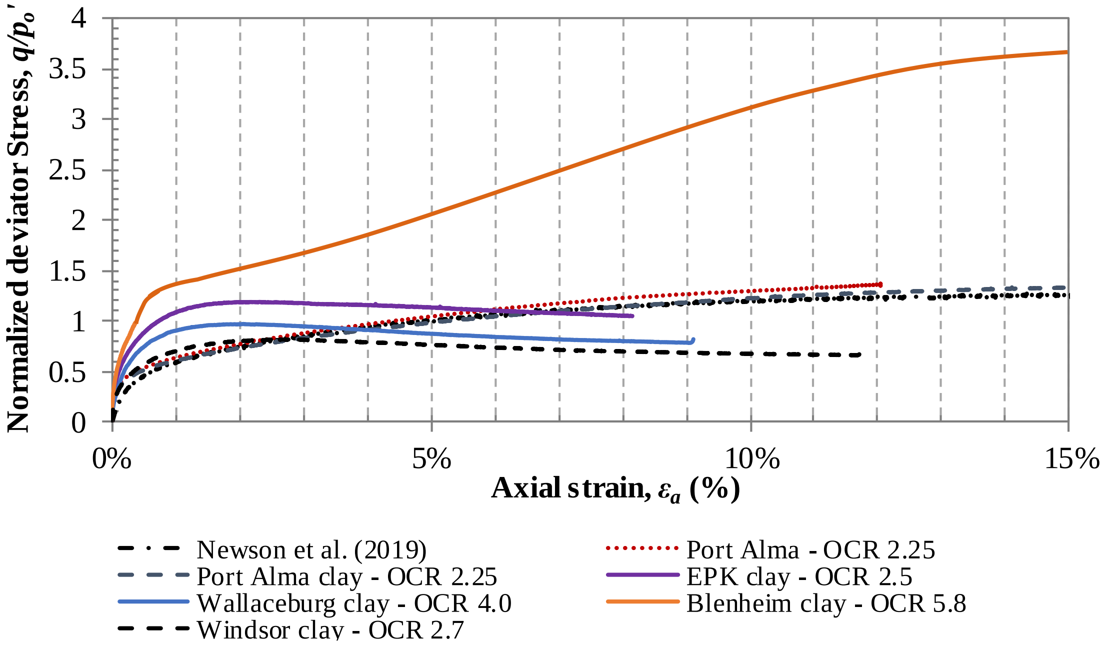

Figure D.1: Axial strain (ε_a) vs. normalized deviator stress (q/p_o') of different tested cohesive materials from CIU tests

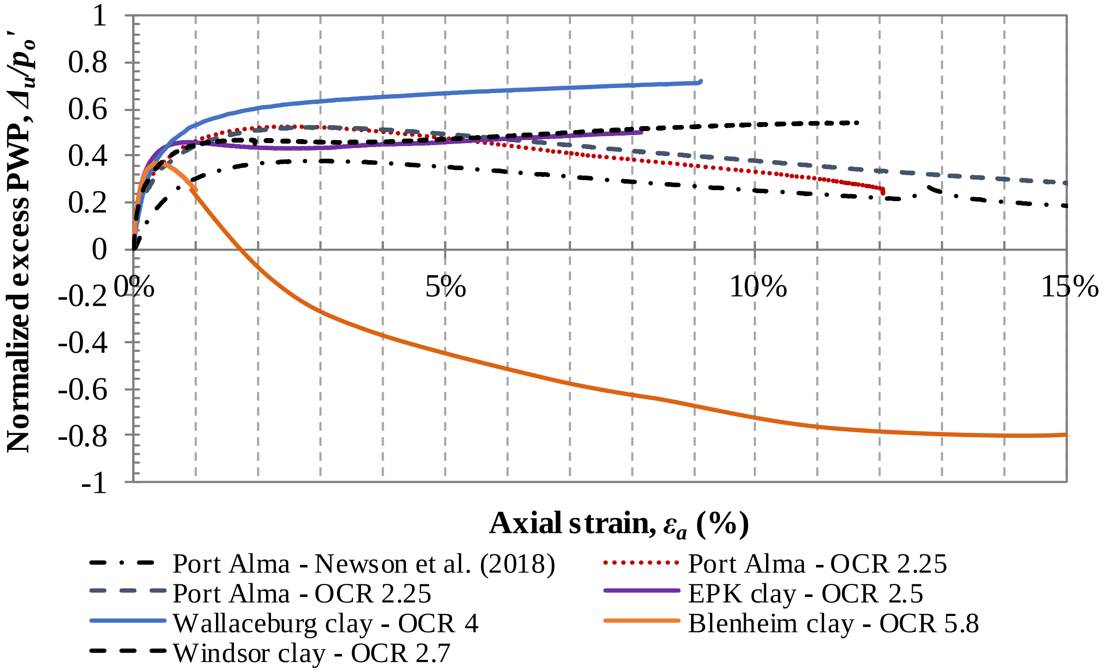

Figure D.2: Axial strain (ε_a) vs. normalized excess pore water pressure (Δ_u/p_o') of different cohesive materials from CIU tests

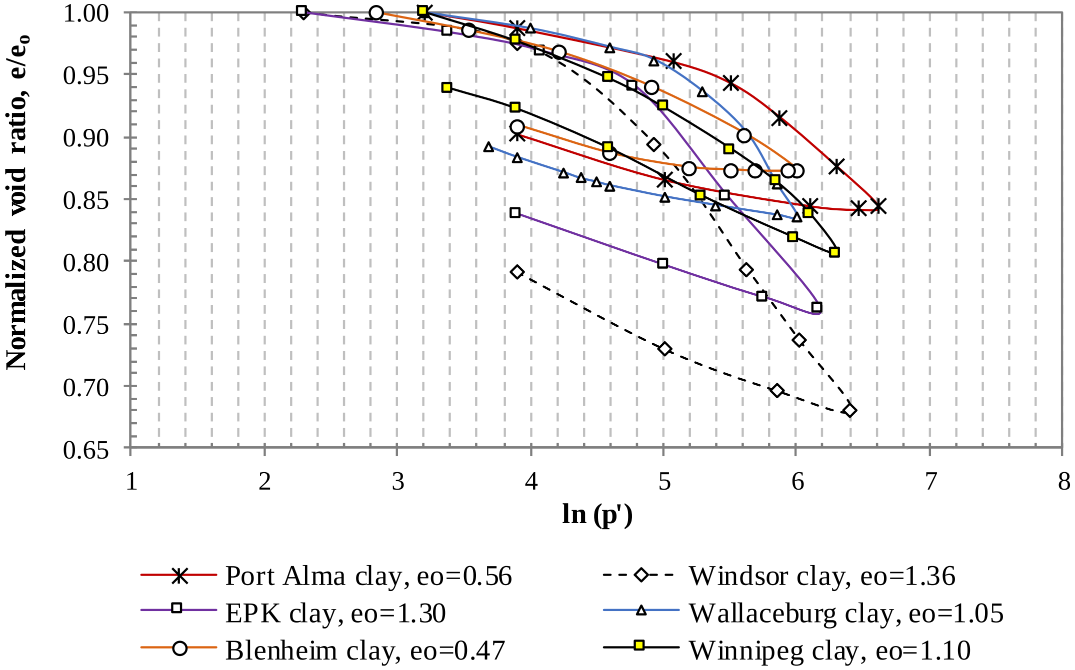

Figure D.3: Normalized void ratio-ln (p') space for isotropic compression and swelling of different cohesive materials from CIU tests

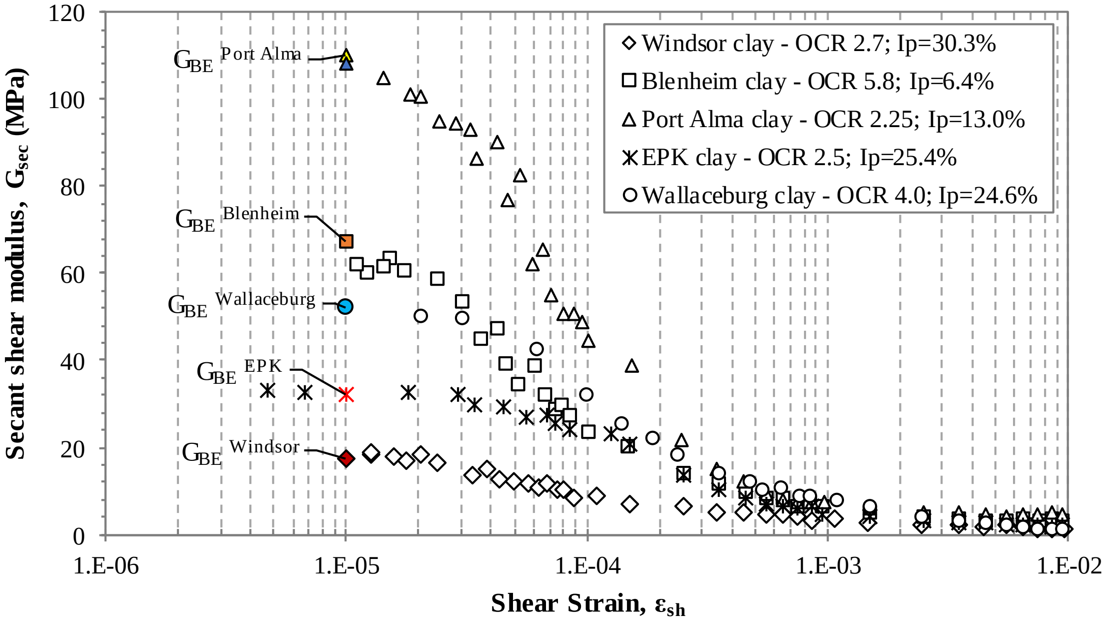

Figure D.4: Secant shear modulus degradation curves from different cohesive materials tested using local instrumentation during CIU triaxial tests

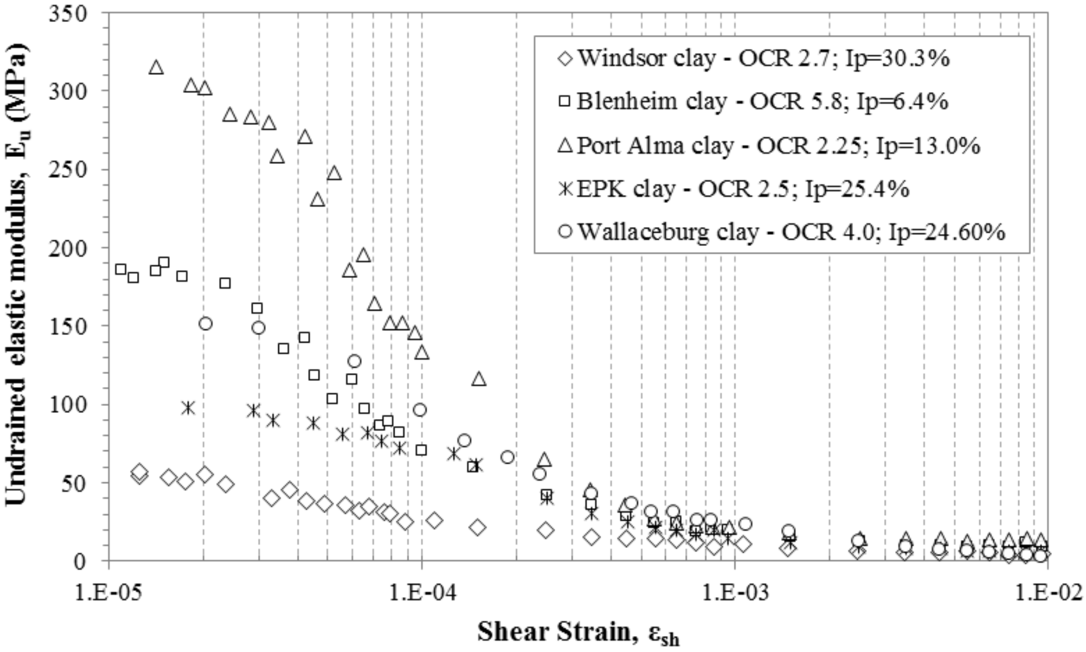

Figure D.5: Undrained Young's modulus degradation curves from different cohesive materials tested using local instrumentation during CIU triaxial tests

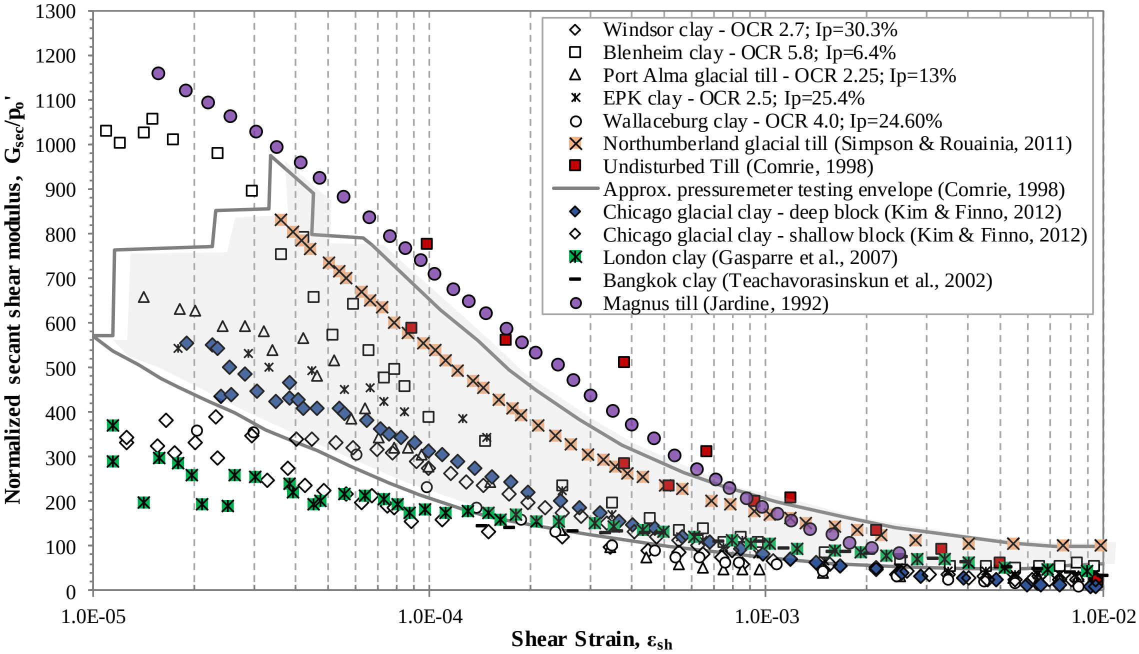

Figure D.6: Comparison of obtained normalized secant shear modulus with increasing of strain for tested cohesive materials with published data

D.2 Results from bender element (BE) tests

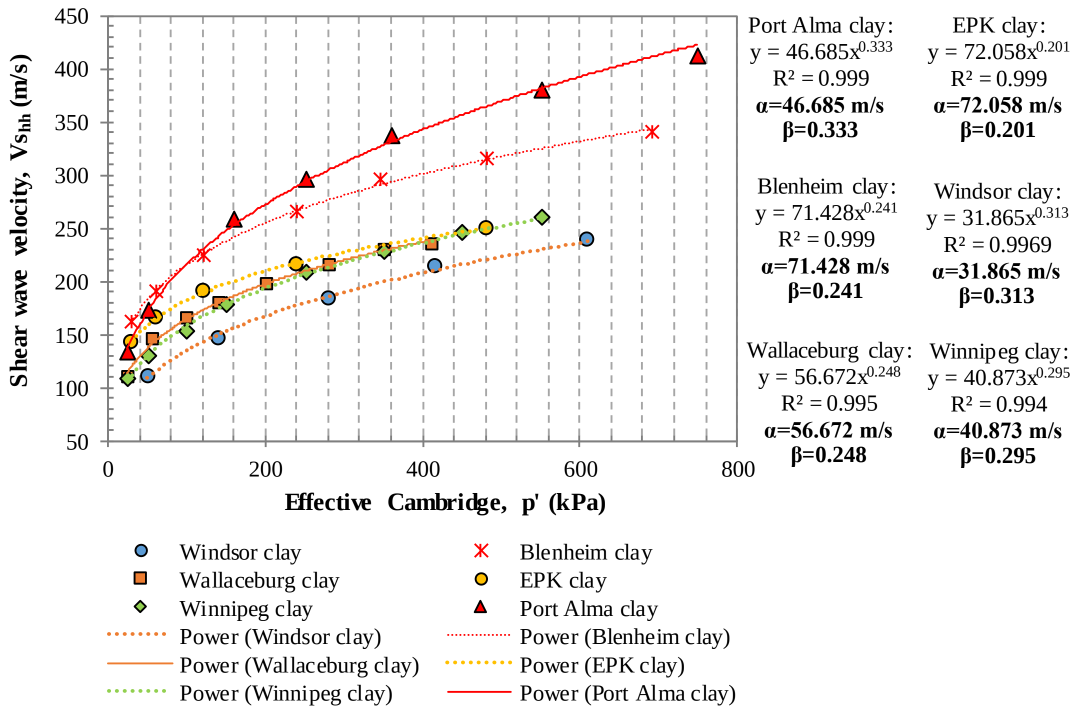

Port Alma clay:
$y = 46.685x^{0.333}$
$R^2 = 0.999$
α=46.685 m/s
β=0.333

EPK clay:
$y = 72.058x^{0.201}$
$R^2 = 0.999$
α=72.058 m/s
β=0.201

Blenheim clay:
$y = 71.428x^{0.241}$
$R^2 = 0.999$
α=71.428 m/s
β=0.241

Windsor clay:
$y = 31.865x^{0.313}$
$R^2 = 0.9969$
α=31.865 m/s
β=0.313

Wallaceburg clay:
$y = 56.672x^{0.248}$
$R^2 = 0.995$
α=56.672 m/s
β=0.248

Winnipeg clay:
$y = 40.873x^{0.295}$
$R^2 = 0.994$
α=40.873 m/s
β=0.295

Figure D.7: Measured horizontally polarized-horizontally propagating shear waves (Vs_{hh}) with increasing effective pressure

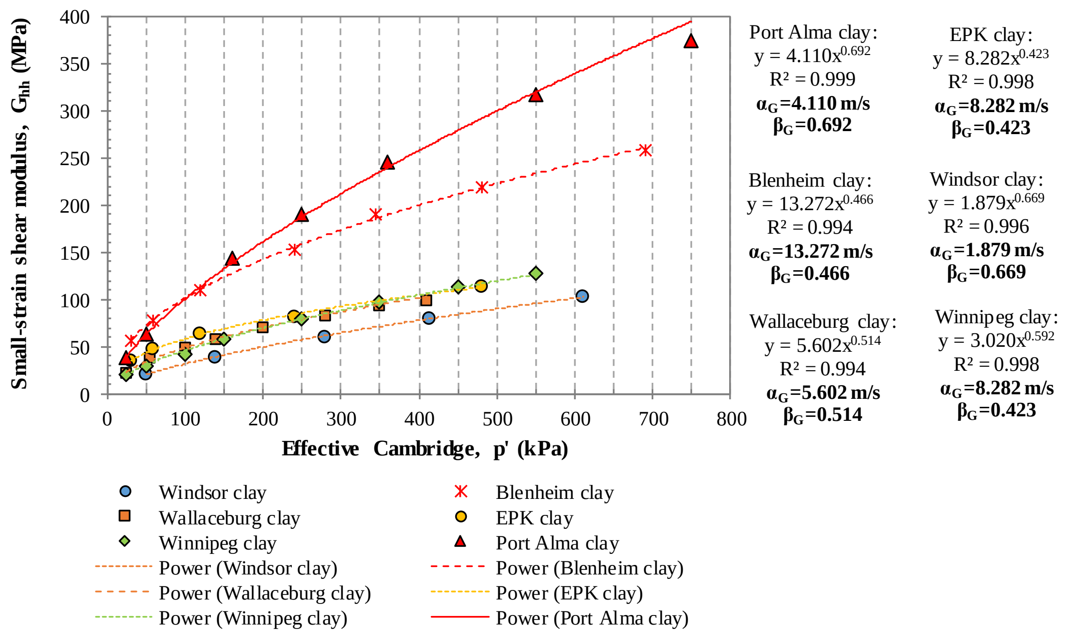

Port Alma clay:
$y = 4.110x^{0.692}$
$R^2 = 0.999$
α_G=4.110 m/s
β_G=0.692

EPK clay:
$y = 8.282x^{0.423}$
$R^2 = 0.998$
α_G=8.282 m/s
β_G=0.423

Blenheim clay:
$y = 13.272x^{0.466}$
$R^2 = 0.994$
α_G=13.272 m/s
β_G=0.466

Windsor clay:
$y = 1.879x^{0.669}$
$R^2 = 0.996$
α_G=1.879 m/s
β_G=0.669

Wallaceburg clay:
$y = 5.602x^{0.514}$
$R^2 = 0.994$
α_G=5.602 m/s
β_G=0.514

Winnipeg clay:
$y = 3.020x^{0.592}$
$R^2 = 0.998$
α_G=8.282 m/s
β_G=0.423

Figure D.8: Small-strain shear modulus measured in the horizontal direction (G_{hh}) with increasing effective pressure for different cohesive materials

D.2.1 BE test results on Windsor clay:

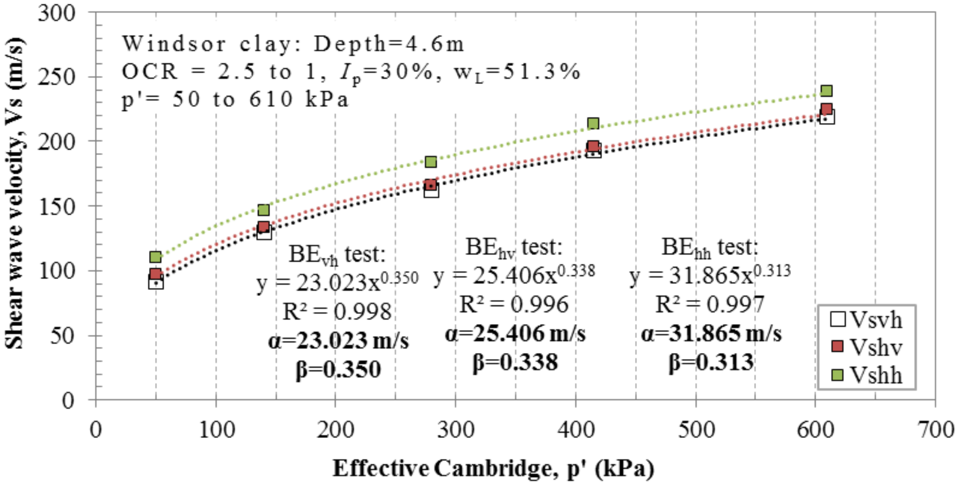

Figure D.9: Shear wave velocities measured from propagated shear waves with increasing effective pressure on Windsor clay

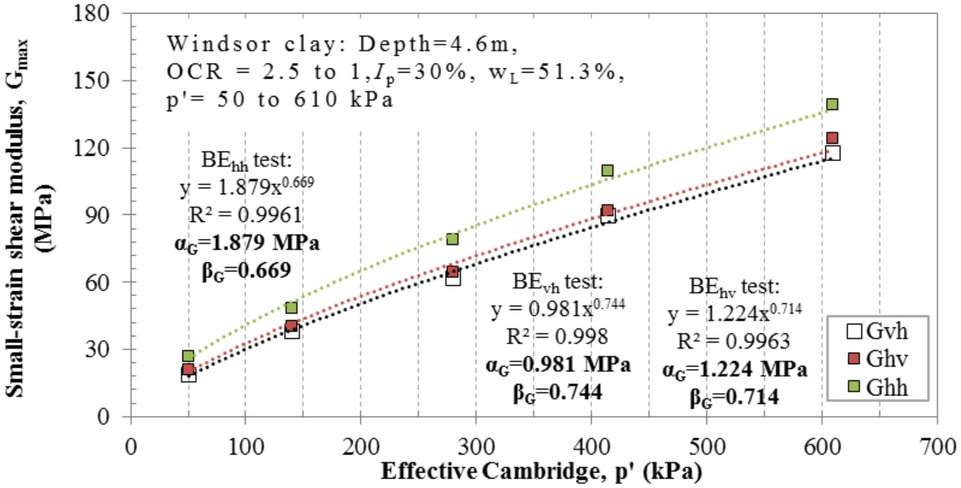

Figure D.10: Small-strain shear modulus with increasing effective pressure of Windsor clay

D.2.2 BE test results on Blenheim clay:

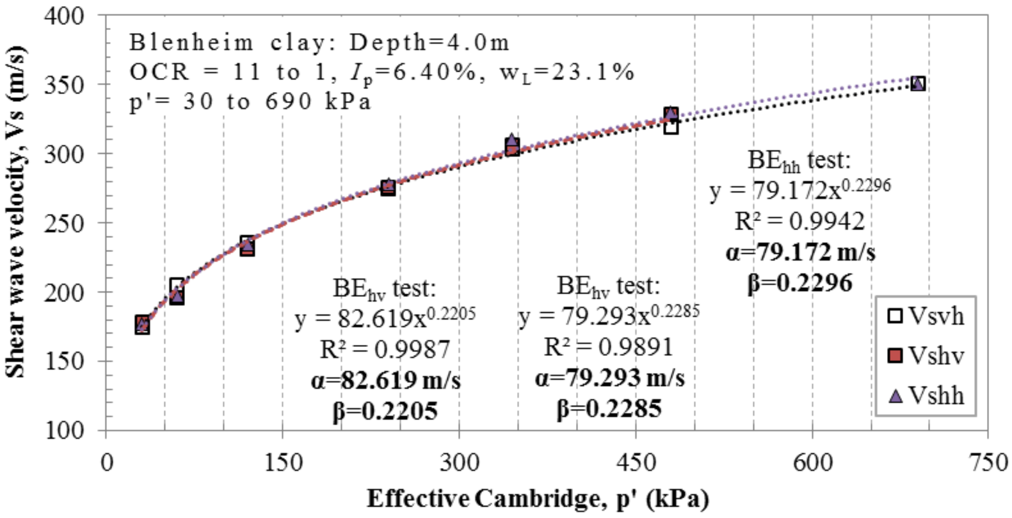

Figure D.11: Shear wave velocities measured from propagated shear waves with increasing effective pressure on Blenheim clay

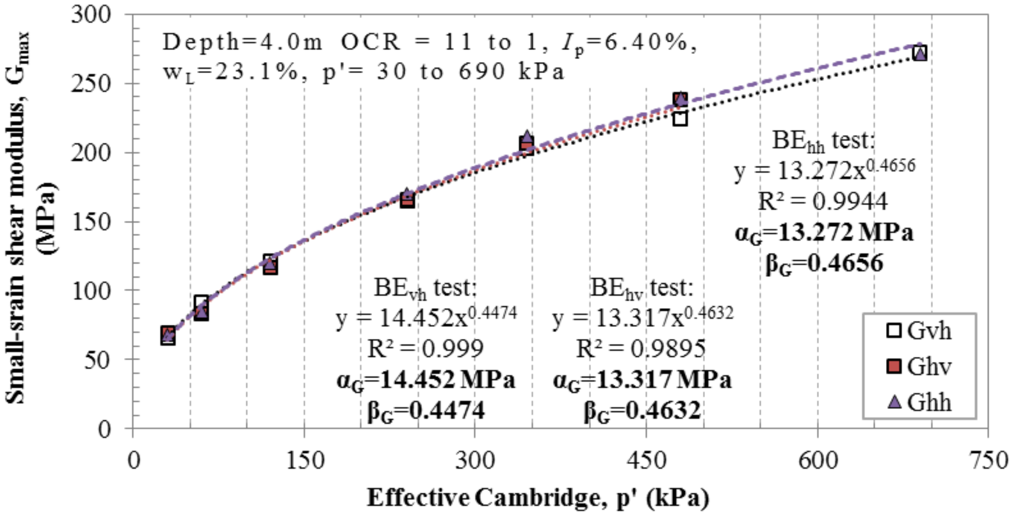

Figure D.12: Small-strain shear modulus with increasing effective pressure of Blenheim clay

D.2.3 BE test results on Wallaceburg clay:

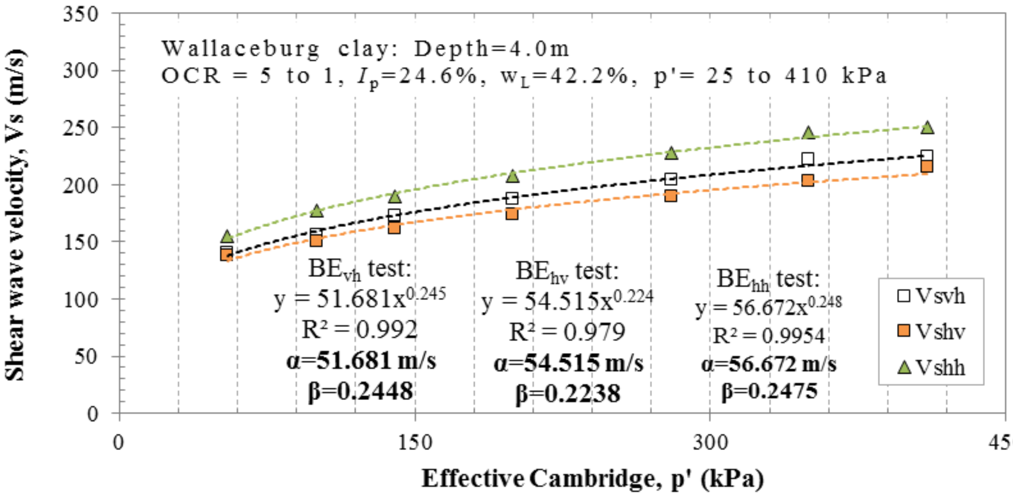

Figure D.13: Shear wave velocities measured from propagated shear waves with increasing effective pressure of Wallaceburg clay

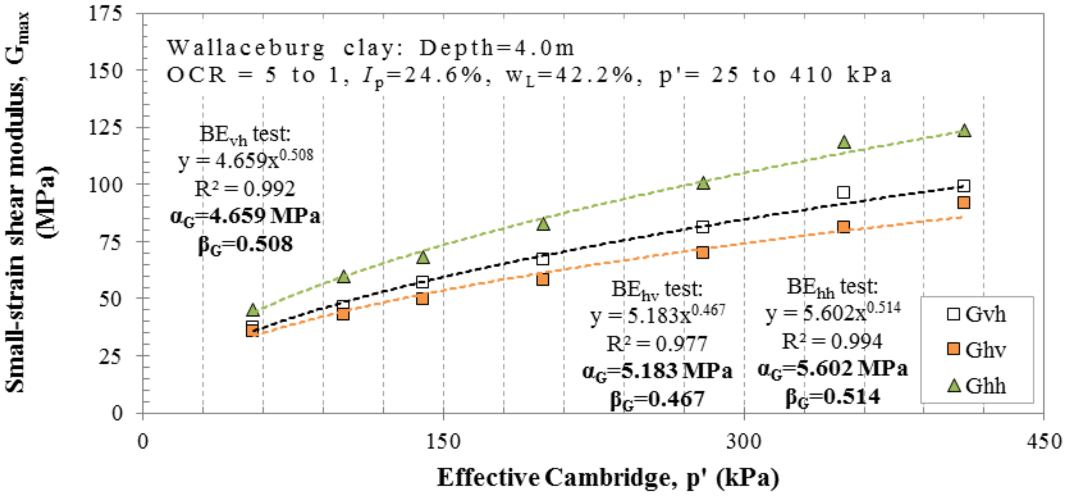

Figure D.14: Small-strain shear modulus with increasing effective pressure of Wallaceburg clay

D.2.4 BE test results on EPK Kaolin clay:

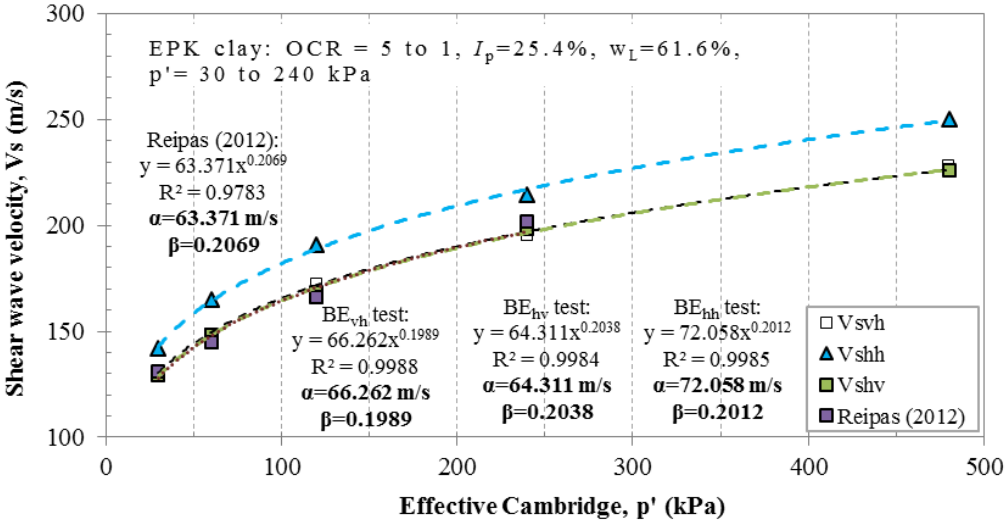

Figure D.15: Shear wave velocities measured from propagated shear waves with increasing effective pressure on EPK clay

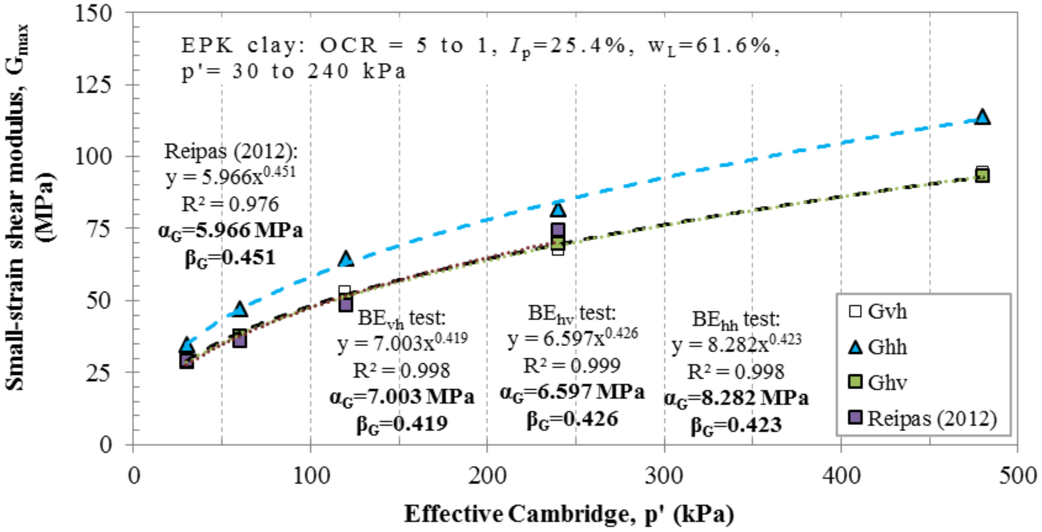

Figure D.16: Small-strain shear modulus with increasing effective pressure of EPK clay

D.2.5 BE test results on Winnipeg clay:

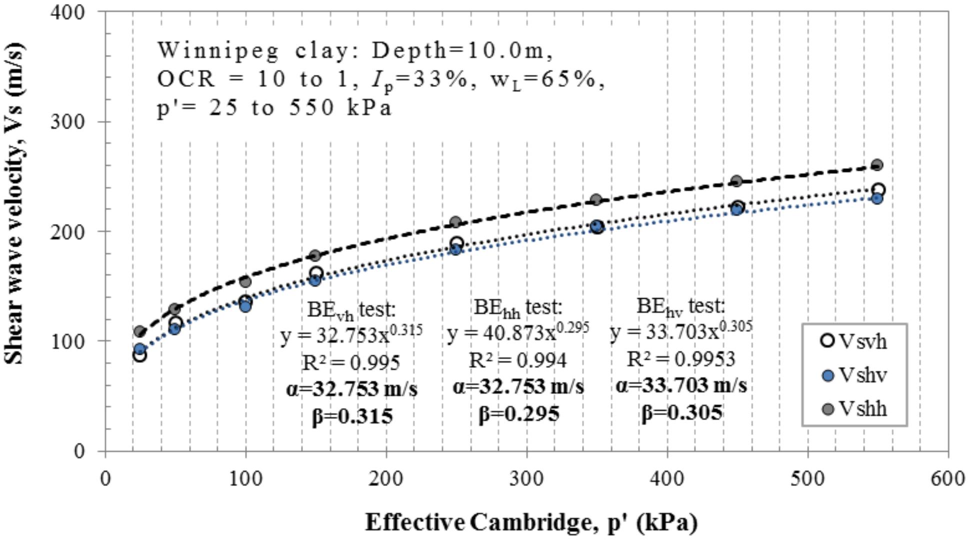

Figure D.17: Shear wave velocities measured from propagated shear waves with increasing effective pressure on Winnipeg clay

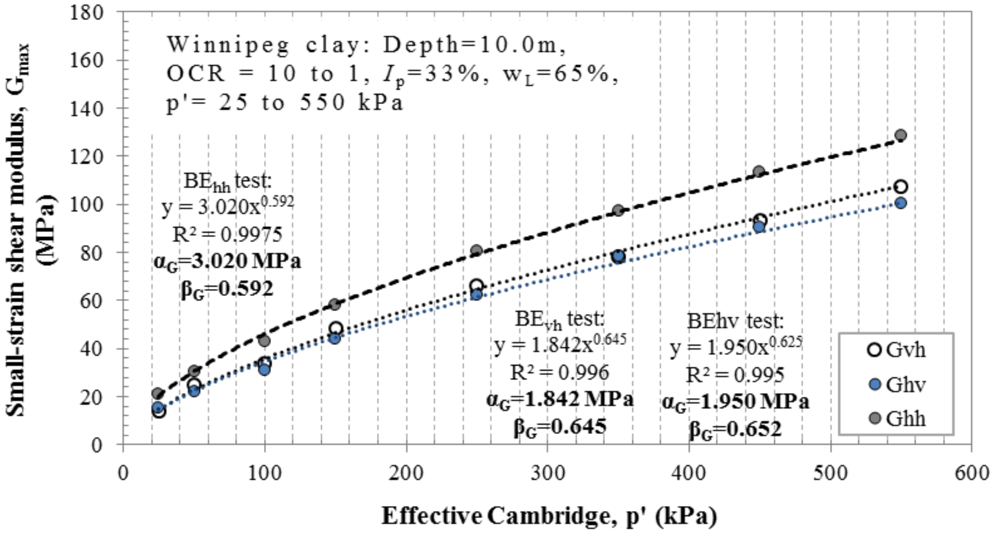

Figure D.18: Small-strain shear modulus with increasing effective pressure of Winnipeg clay

D.3 Results from resonant column (RC) tests

Table D.1: Summary of results from resonant column testing on 0° rotation samples of different cohesive soils

Soil	Effective pressure, p' (kPa)	V_s^v (m/s)	G_v (MPa)	V_{rod}^v (m/s)	E_v (MPa)	D^v (%)
Port Alma clay	40	151.58	48.81	242.50	123.24	2.80
OCR 9 to 1	80	191.55	78.54	288.03	174.46	2.35
I_p = 13.0%	160	225.17	109.11	362.62	278.36	2.10
Sample depth: 21 m	220	250.28	135.40	409.62	356.48	2.00
	320	280.69	171.09	470.14	471.79	1.71
	460	317.50	220.33	512.59	563.75	1.45
Blenheim clay	30	172.81	65.03	255.33	141.95	2.38
OCR 11 to 1	60	197.68	85.73	301.24	199.09	1.94
I_p = 6.40%	120	229.54	115.94	361.07	286.89	1.75
Sample depth: 4.0 m	240	266.49	156.96	414.74	380.15	1.50
	345	296.02	194.11	470.52	490.42	1.34
	480	318.71	225.66	514.48	588.04	1.27
	690	345.08	265.57	563.92	709.22	1.16
Windsor clay	55	99.33	18.20	187.15	62.85	2.45
OCR 9 to 1	140	121.65	27.95	243.83	109.71	2.34
I_p = 30.3%	280	157.43	47.19	309.79	182.25	2.15
Sample depth: 4.6 m	415	188.98	69.49	354.37	244.36	1.70
	610	215.72	92.73	419.74	351.10	1.60
Wallaceburg clay	55	132.51	32.73	221.34	91.20	2.57
OCR 5 to 1	140	154.20	44.71	261.89	128.35	2.30
I_p = 24.60%	280	184.33	65.40	307.78	181.06	2.04
Sample depth: 4.0 m	410	214.52	90.53	360.80	251.64	1.93
EPK clay	55	129.14	28.59	184.99	58.67	2.33
OCR 5 to 1	140	151.46	39.60	216.06	80.59	2.19
I_p = 24.60%	280	168.14	50.79	252.35	114.42	1.90
Sample depth: 4.0 m	410	201.96	74.58	294.74	158.83	1.75

V_s^v: shear wave velocity vertical direction; G_v: shear modulus in the vertical direction;

V_{rod}^v: rod wave velocity vertical direction; E_v: elastic modulus in the vertical direction;

D^v: damping ratio in the vertical direction (at shear strain ≈ 1×10^{-5})

Table D.2: Summary of results from resonant column testing on 90° rotation samples of different cohesive soils

Soil	Effective pressure, p' (kPa)	V_s^h (m/s)	G_h (MPa)	V_{rod}^h (m/s)	E_h (MPa)	D^h (%)
Port Alma clay	40	158.75	53.95	262.89	147.96	2.35
OCR 9 to 1	80	209.41	93.89	318.58	218.08	2.20
I_p = 13.0%	160	242.05	126.93	386.70	323.98	2.01
Sample depth: 21 m	220	278.15	168.69	441.51	425.00	1.78
	320	312.27	213.92	496.08	539.87	1.45
	460	361.41	287.81	549.28	664.82	1.30
Blenheim clay	30	153.80	50.25	250.40	133.20	2.36
OCR 11 to 1	60	186.10	73.69	295.57	185.88	1.93
I_p = 6.40%	120	217.82	101.19	348.46	258.98	1.66
Sample depth: 4.0 m	240	261.01	145.89	402.99	347.75	1.43
	345	290.13	180.72	449.72	434.23	1.33
	480	310.26	218.60	491.97	522.32	1.23
	690	340.96	260.68	541.24	634.35	1.15
Windsor clay	55	115.06	23.94	213.66	81.90	2.36
OCR 9 to 1	140	136.31	34.13	288.60	149.43	2.26
I_p = 30.3%	280	175.07	58.48	357.76	235.08	1.99
Sample depth: 4.6 m	415	200.23	78.03	407.31	322.89	1.65
	610	227.82	102.66	481.82	459.20	1.56
Wallaceburg clay	55	141.99	37.43	271.64	137.00	2.30
OCR 5 to 1	140	167.20	52.03	329.00	200.98	2.20
I_p = 24.6%	280	202.57	77.61	383.10	272.51	1.65
Sample depth: 4 m	410	231.03	103.02	448.41	373.34	1.58

V_s^h: shear wave velocity horizontal direction; G_h: shear modulus in the horizontal direction;

V_{rod}^h: rod wave velocity horizontal direction; E_h: elastic modulus in the horizontal direction;

D^h: damping ratio in the horizontal direction (at shear strain ≈ 1×10^{-5})

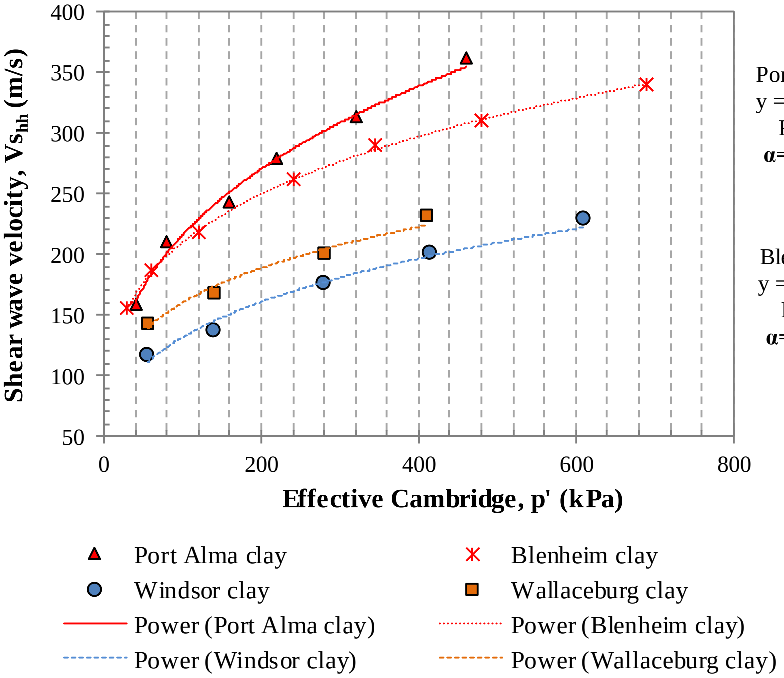

Port Alma clay:
$y = 48.493x^{0.324}$
$R^2 = 0.993$
α=48.493 m/s
β=0.324

Windsor clay:
$y = 34.568x^{0.291}$
$R^2 = 0.981$
α=34.568 m/s
β=0.291

Blenheim clay:
$y = 66.218x^{0.250}$
$R^2 = 0.999$
α=66.218 m/s
β=0.250

Wallceburg clay:
$y = 53.519x^{0.238}$
$R^2 = 0.977$
α=48.493 m/s
β=0.324

Figure D.19: Summary measured shear wave velocity in the vertical plane (Vs_{hh}) with increasing effective pressure for 90° rotation samples

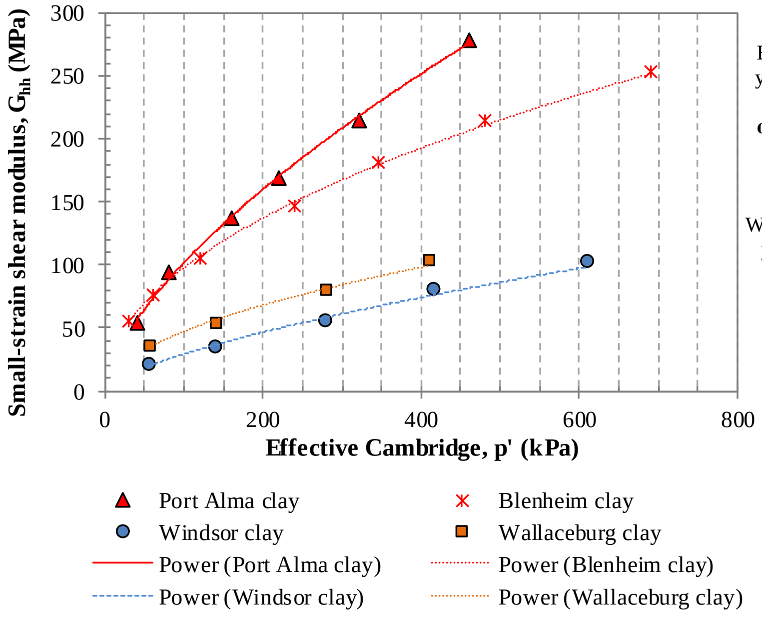

Blenheim clay:
$y = 10.258x^{0.489}$
$R^2 = 0.999$
α_G=10.258 m/s
β_G=0.489

Port Alma clay:
$y = 5.038x^{0.653}$
$R^2 = 0.997$
α_G=5.038 m/s
β_G=0.653

Wallaceburg clay:
$y = 4.252x^{0.523}$
$R^2 = 0.994$
α_G=4.252 m/s
β_G=0.523

Windsor clay:
$y = 1.345x^{0.669}$
$R^2 = 0.992$
α_G=5.038 m/s
β_G=0.653

Figure D.20: Summary of estimated small-strain shear modulus in the horizontal plane (G_{hh}) with increasing effective pressure for 90° rotation samples

D.3.1 RC results on Windsor clay:

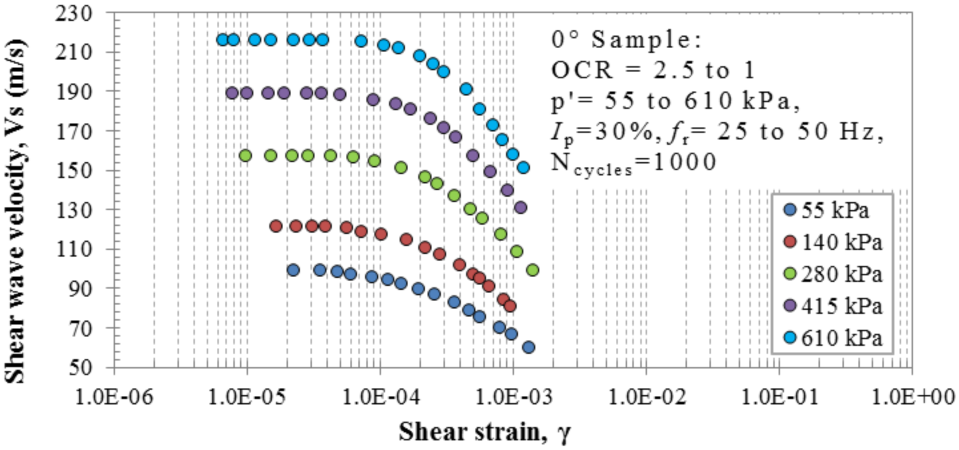

Figure D.21: Shear wave velocity variation with strain amplitude for Windsor clay (0° rotation sample)

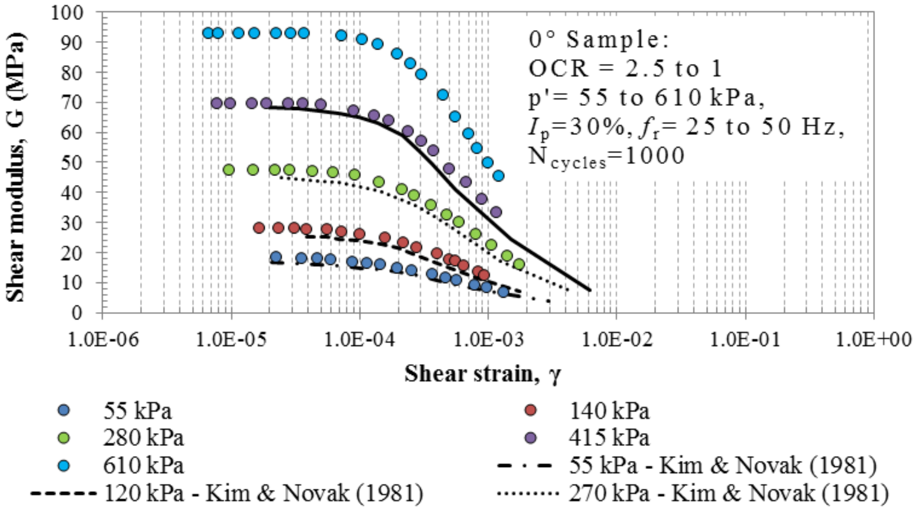

Figure D.22: Shear modulus variation with strain amplitude for Windsor clay (0° rotation sample)

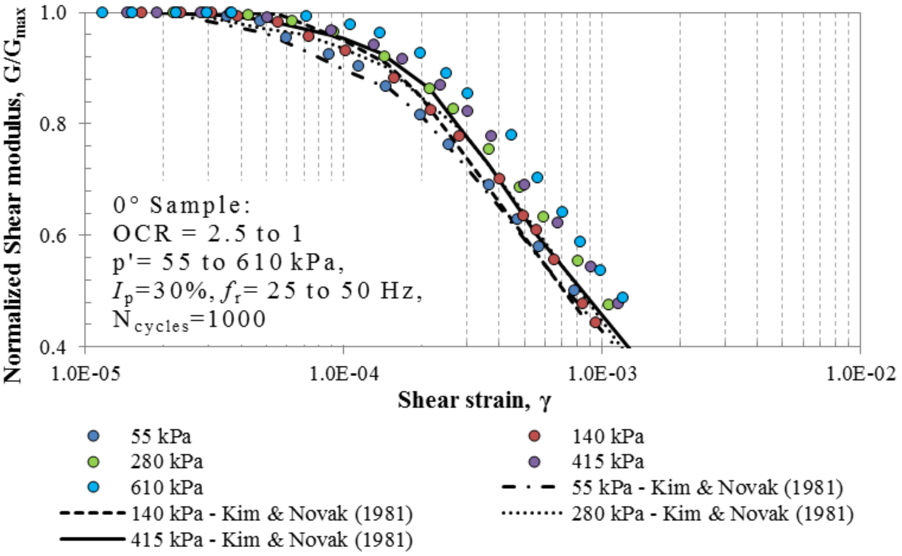

Figure D.23: Normalized shear modulus variation with strain amplitude for Windsor clay (0° rotation sample)

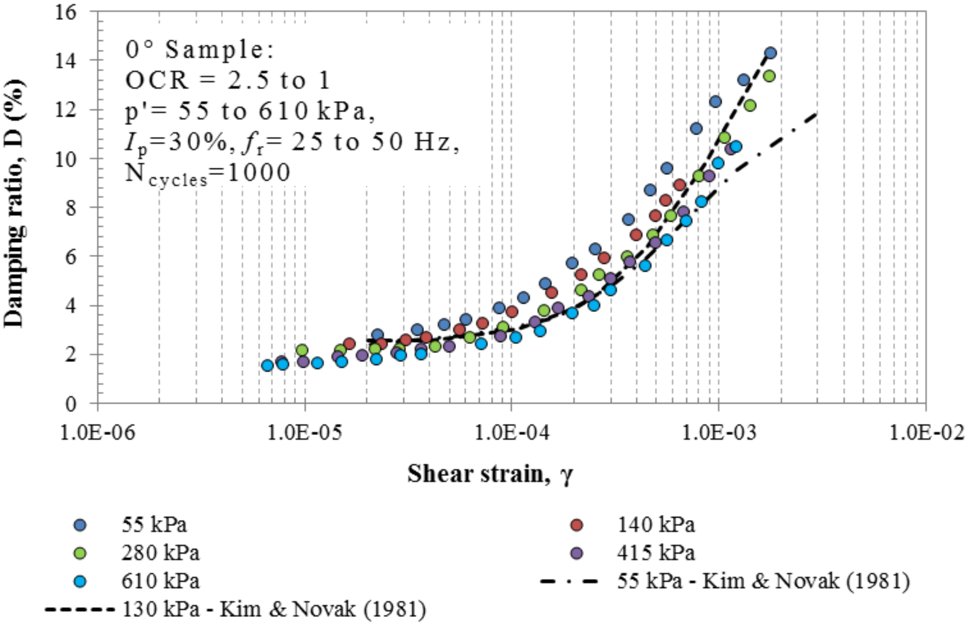

Figure D.24: Damping ratio variation with strain amplitude for Windsor clay (0° rotation sample)

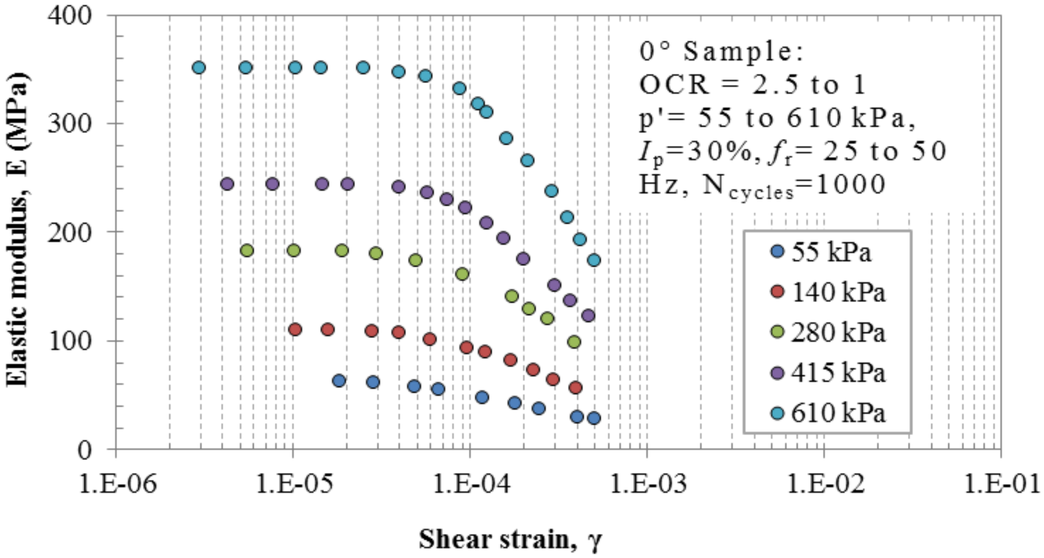

Figure D.25: Elastic modulus variation with strain amplitude of Windsor clay (0° rotation sample)

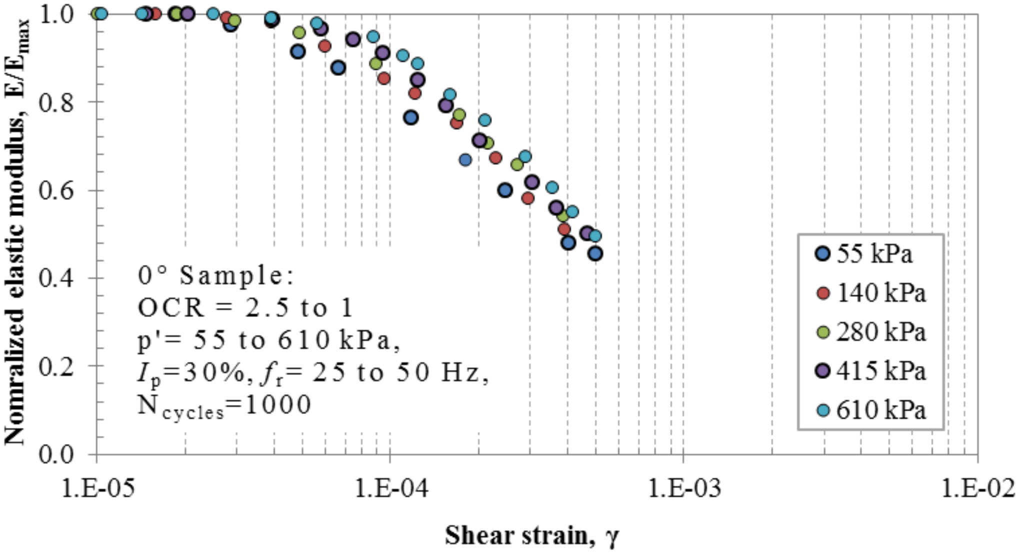

Figure D.26: Normalized elastic modulus variation with strain amplitude of Windsor clay (0° rotation sample)

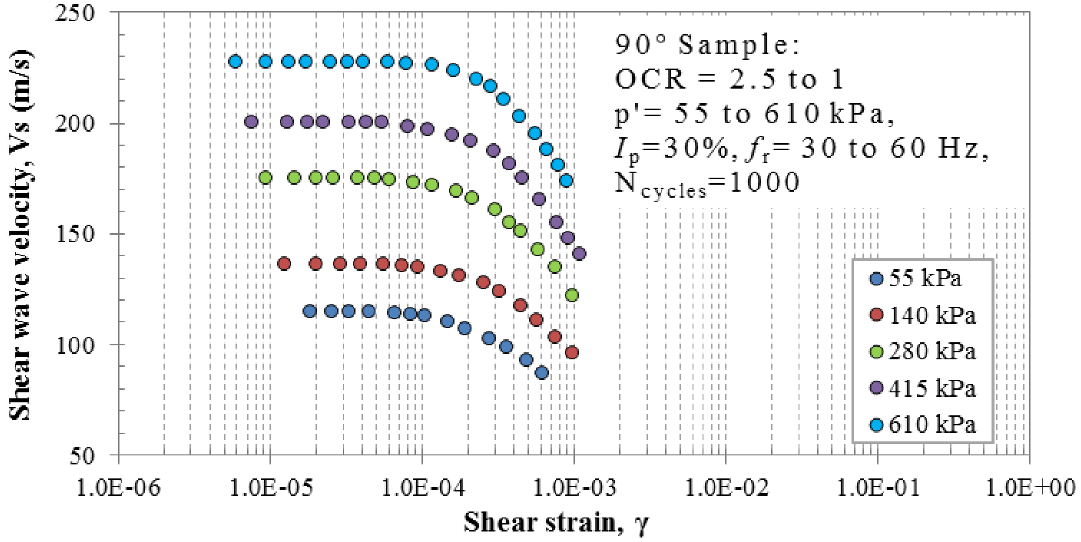

Figure D.27: Shear wave velocity variation with strain amplitude for Windsor clay (90° rotation sample)

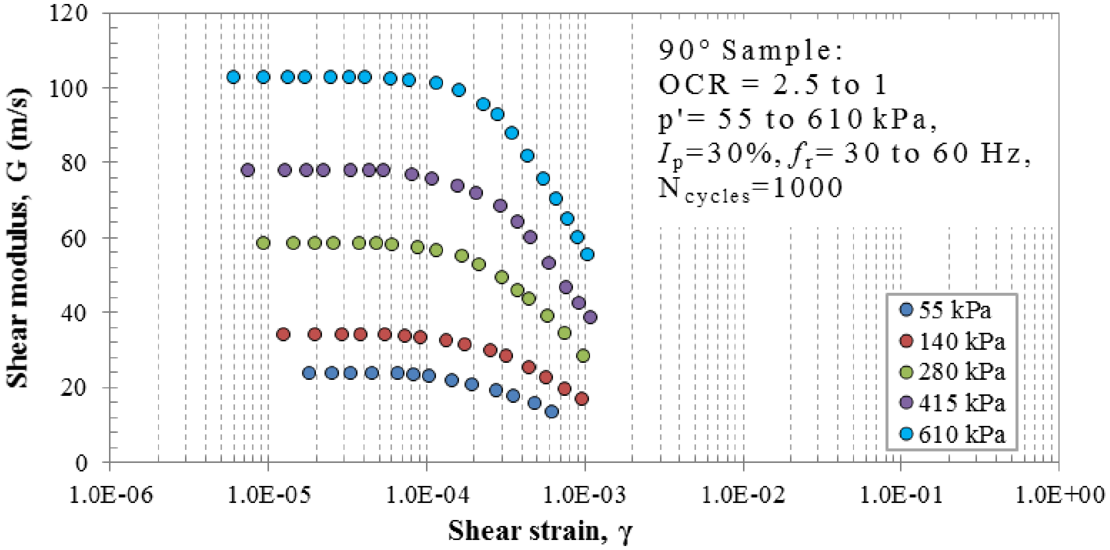

Figure D.28: Shear modulus variation with strain amplitude for Windsor clay (90° rotation sample)

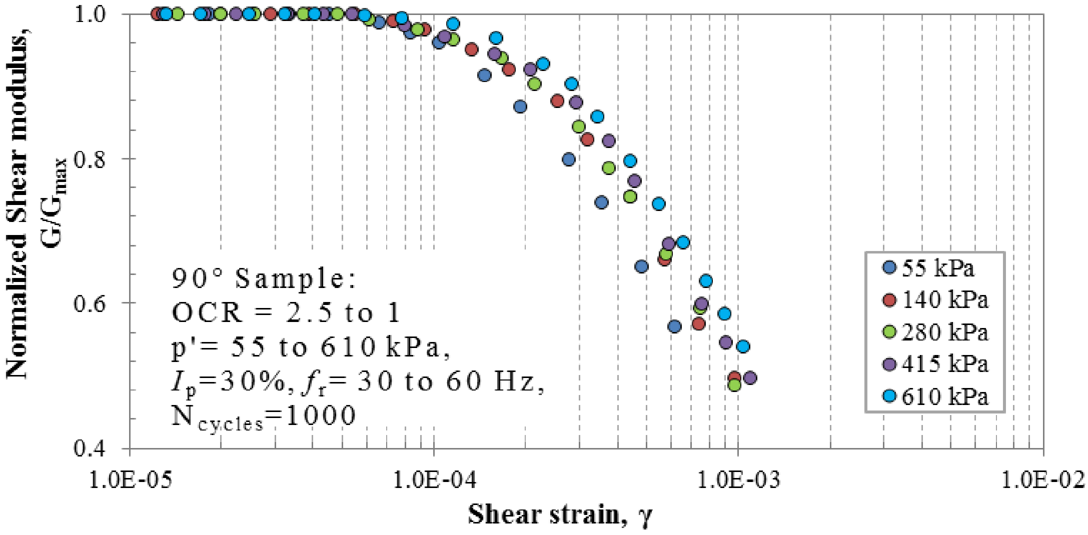

Figure D.29: Normalized shear modulus variation with strain amplitude for Windsor clay (90° rotation sample)

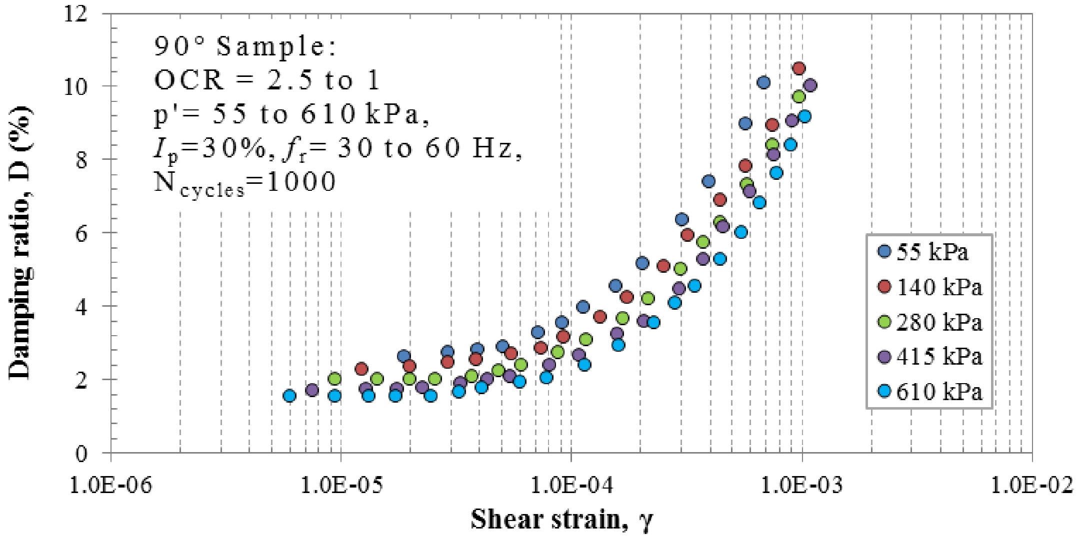

Figure D.30: Damping ratio variation with strain amplitude for Windsor clay (90° rotation sample)

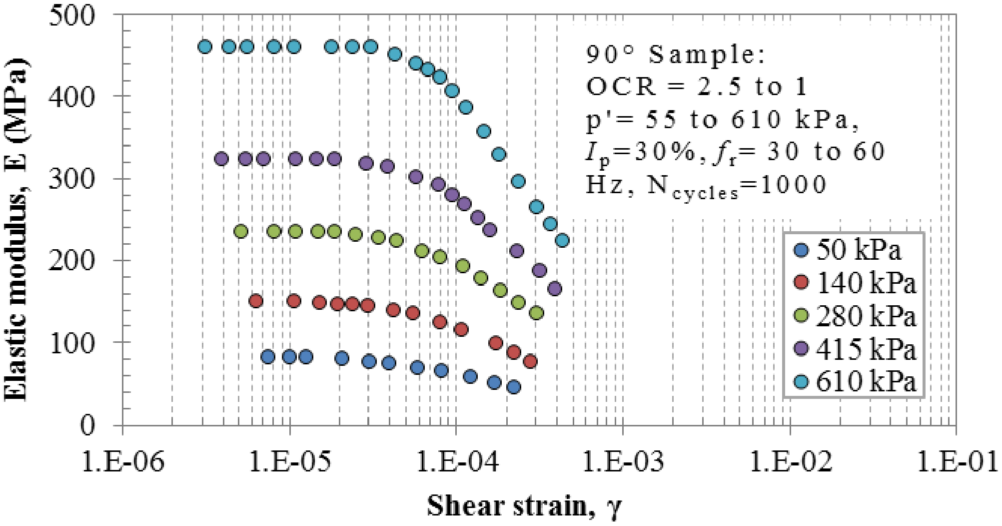

Figure D.31: Elastic modulus variation with strain amplitude of Windsor clay (90° rotation sample)

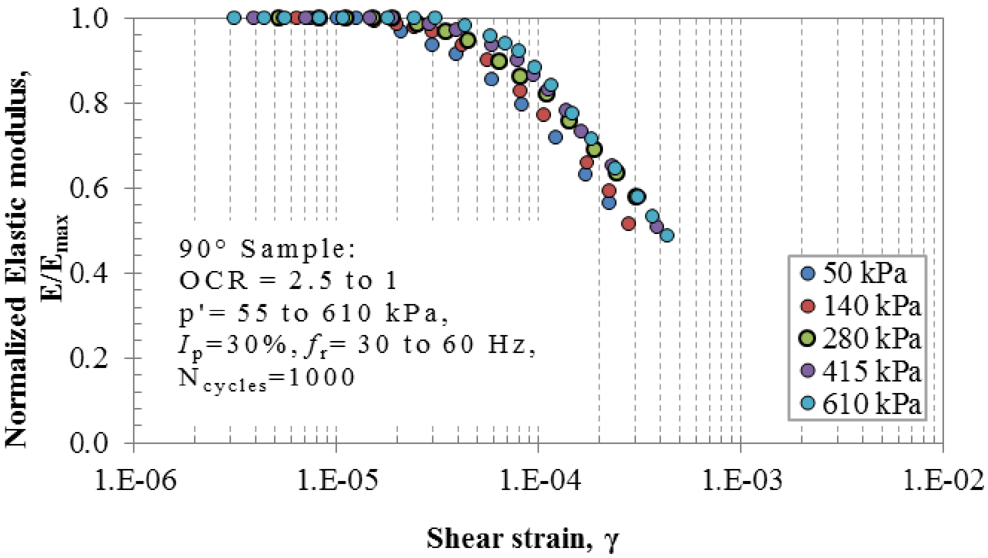

Figure D.32: Normalized elastic modulus variation with strain amplitude of Windsor clay (90° rotation sample)

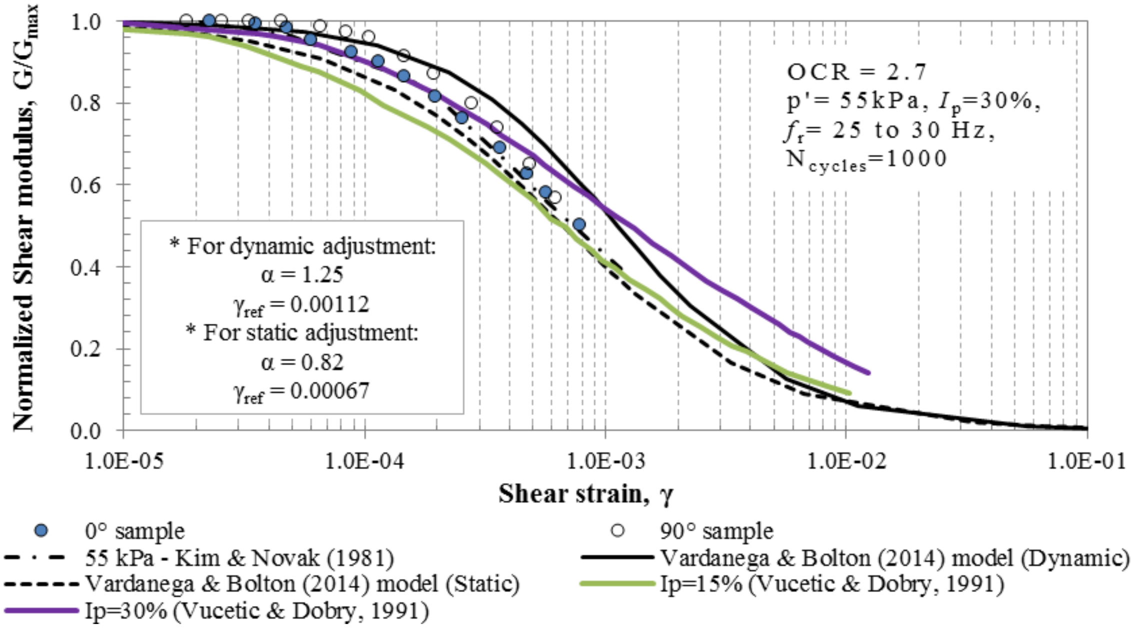

Figure D.33: G/G_{max} from RC test at p'=55 kPa for 0° and 90° samples of Windsor clay, compared to empirical models

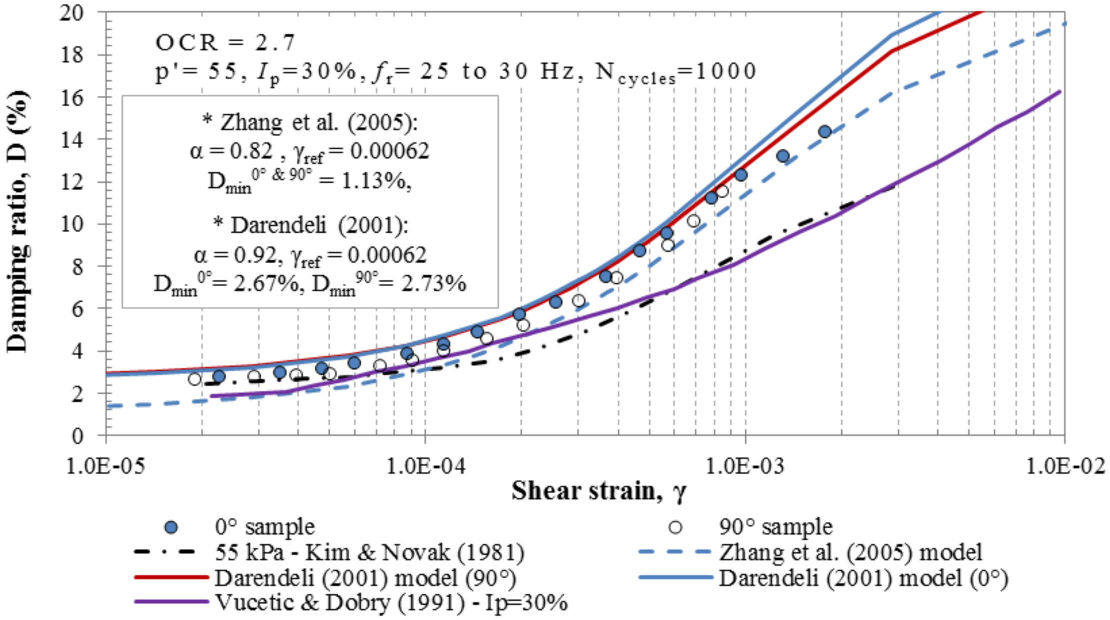

Figure D.34: Damping ratio from RC test at p'=55 kPa for 0° and 90° samples of Windsor clay, compared to empirical models

D.3.2 RC results of Blenheim clay

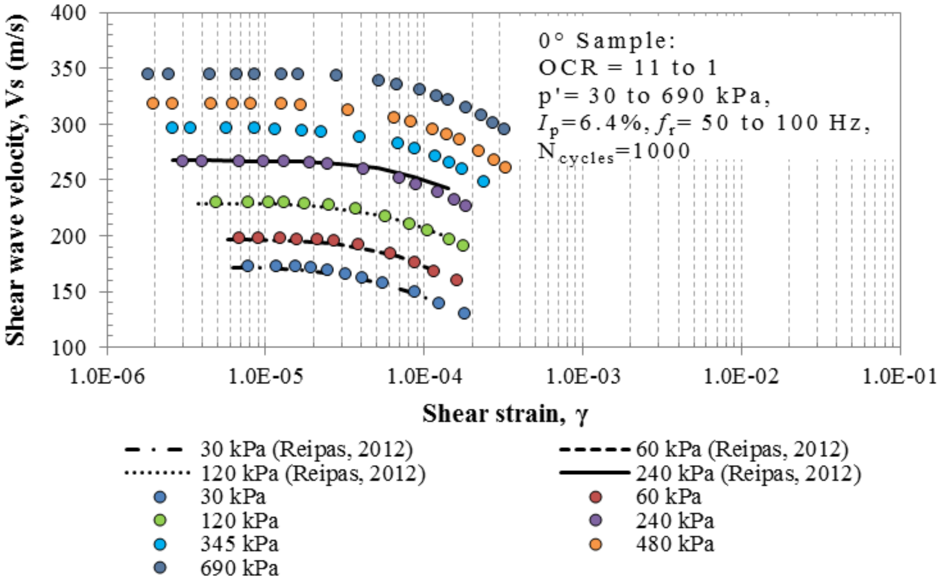

Figure D.35: Shear wave velocity variation with strain amplitude of Blenheim clay (0° rotation sample)

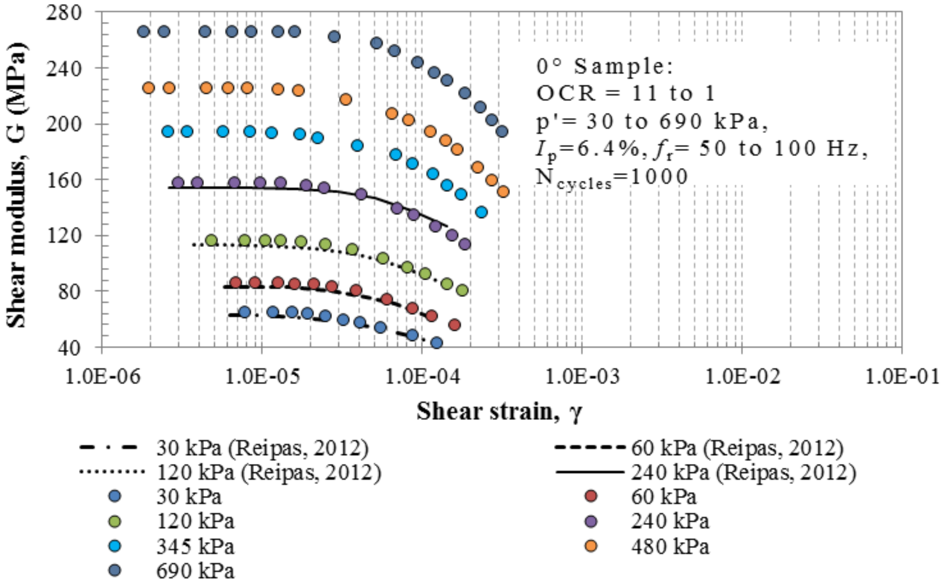

Figure D.36: Shear modulus variation with strain amplitude of Blenheim clay (0° rotation sample)

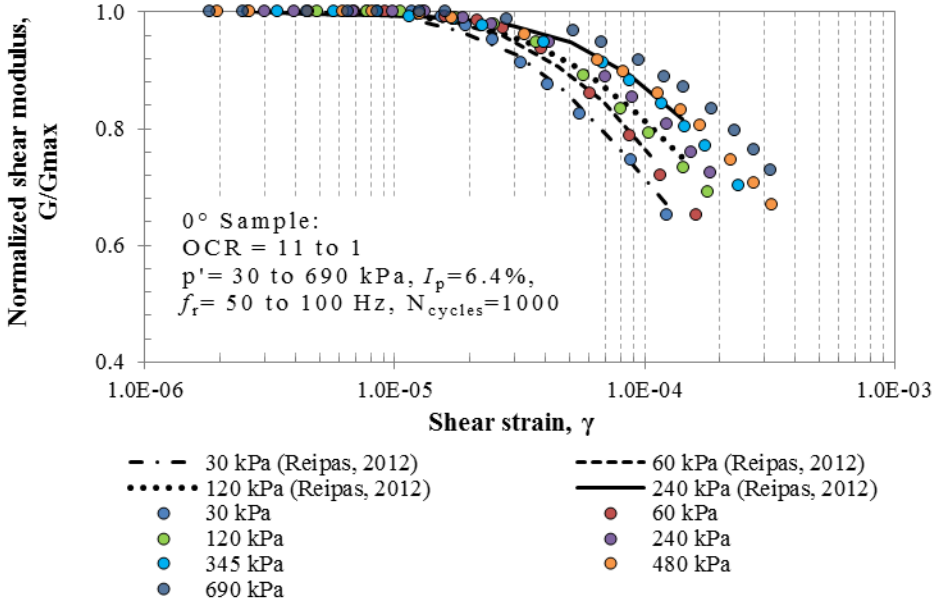

Figure D.37: Normalized shear modulus variation with strain amplitude of Blenheim clay (0° rotation sample)

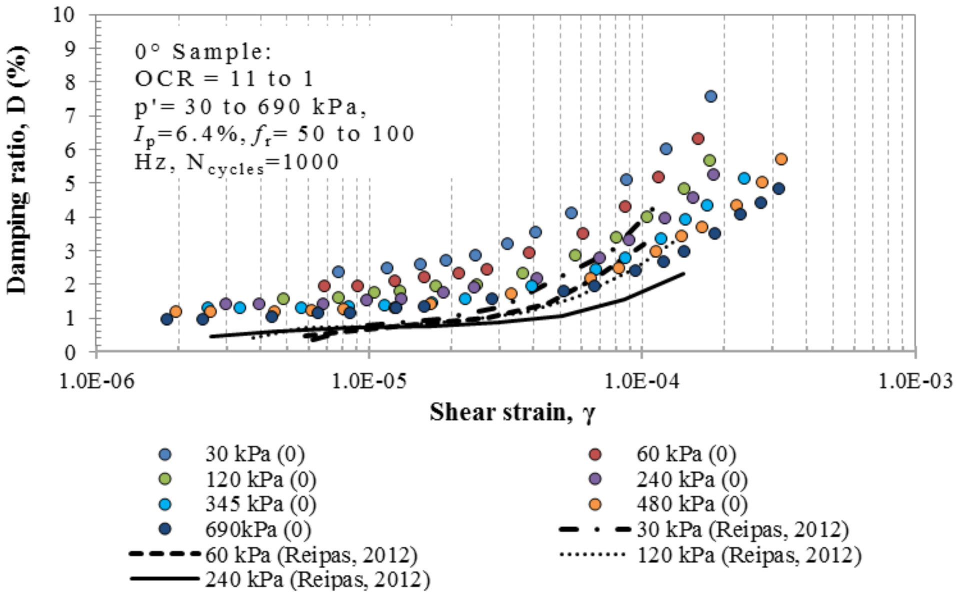

Figure D.38: Damping ratio variation with strain amplitude of Blenheim clay (0° rotation sample)

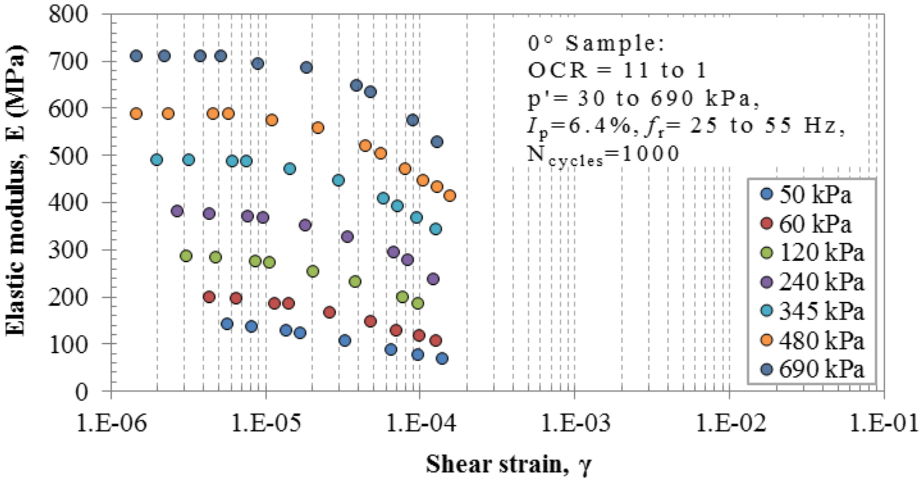

Figure D.39: Elastic modulus variation with strain amplitude of Blenheim clay (0° rotation sample)

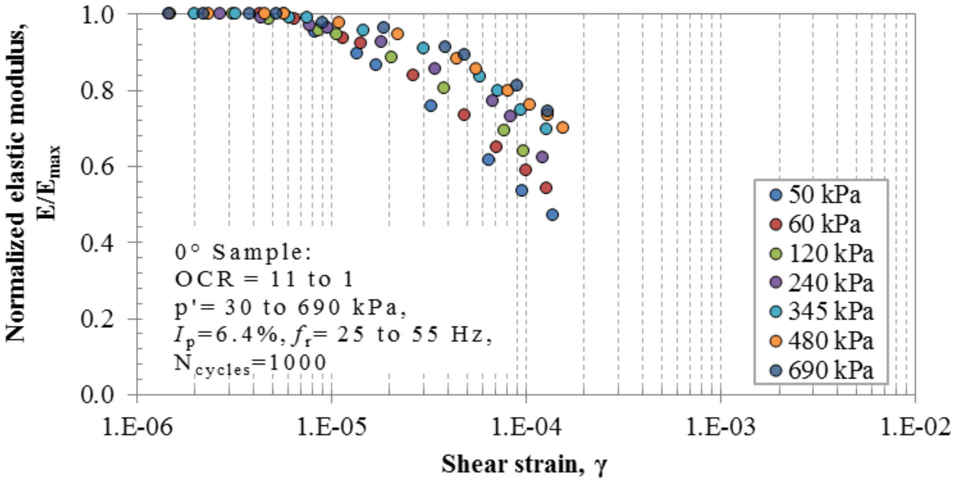

Figure D.40: Normalized elastic modulus variation with strain amplitude of Blenheim clay (0° rotation sample)

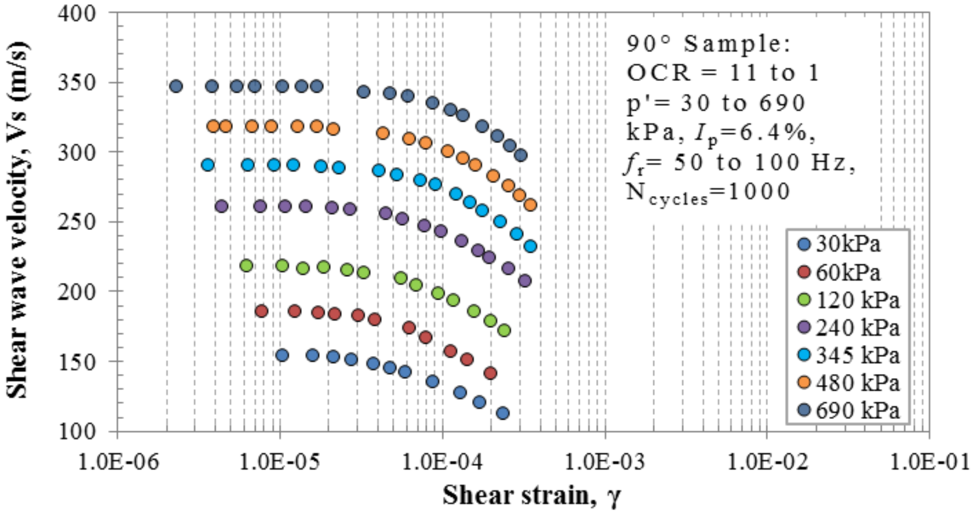

Figure D.41: Shear wave velocity variation with strain amplitude of Blenheim clay (90° rotation sample)

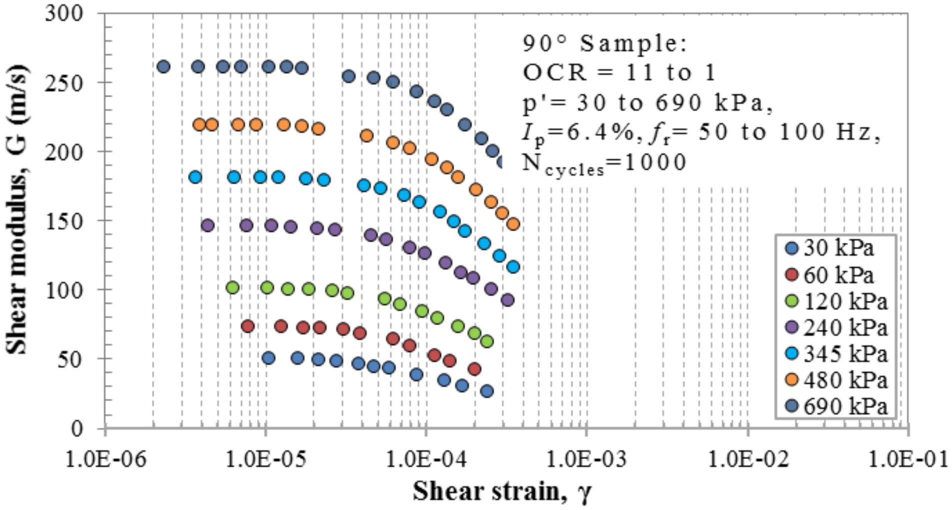

Figure D.42: Shear modulus variation with strain amplitude of Blenheim clay (90° rotation sample)

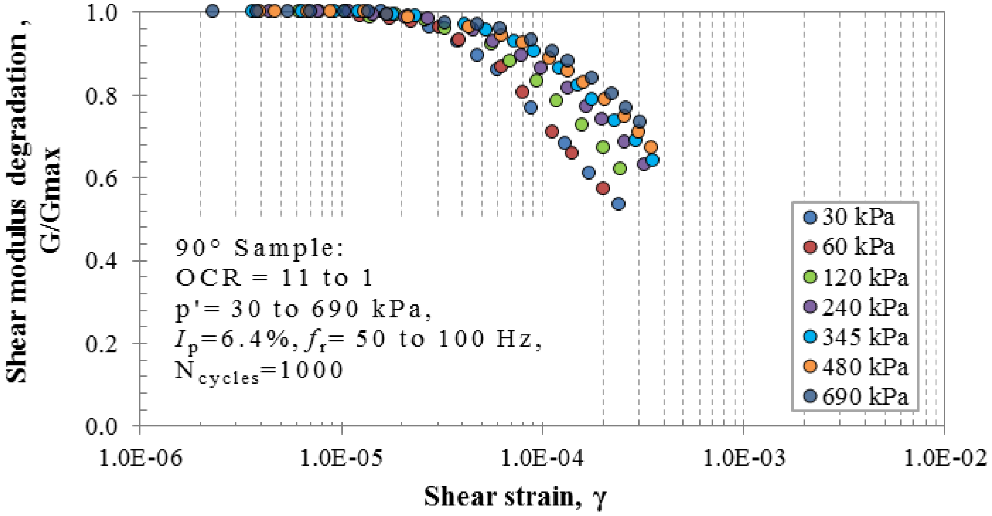

Figure D.43: Normalized shear modulus variation with strain amplitude of Blenheim clay (90° rotation sample)

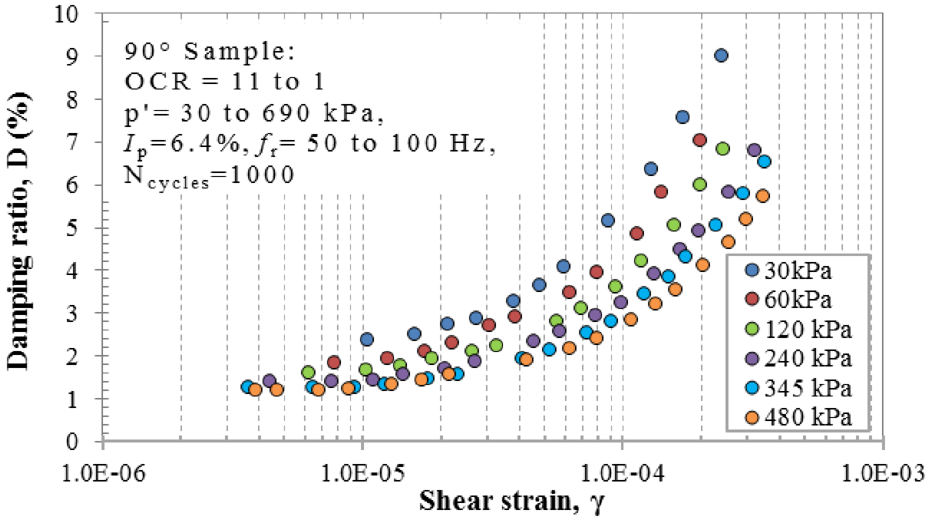

Figure D.44: Damping ratio variation with strain amplitude of Blenheim clay (90° rotation sample)

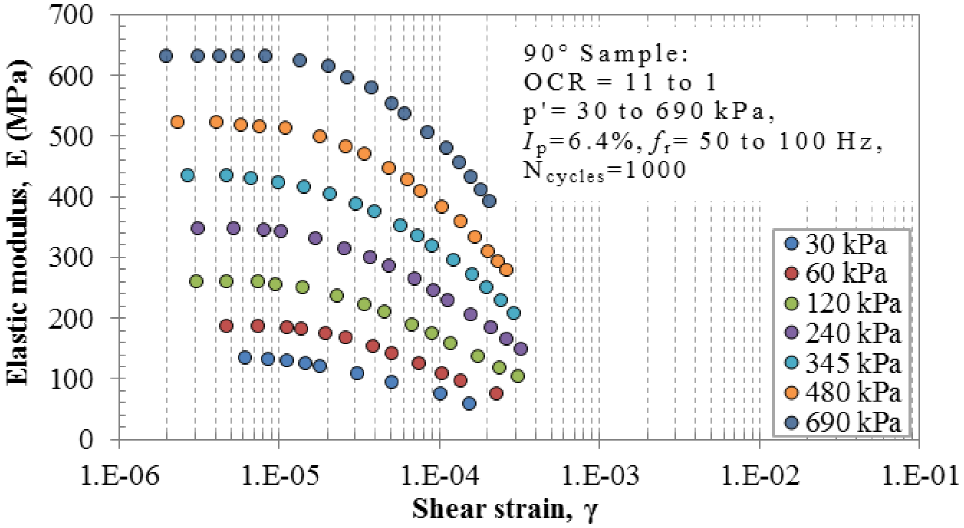

Figure D.45: Elastic modulus variation with strain amplitude of Blenheim clay (90° rotation sample)

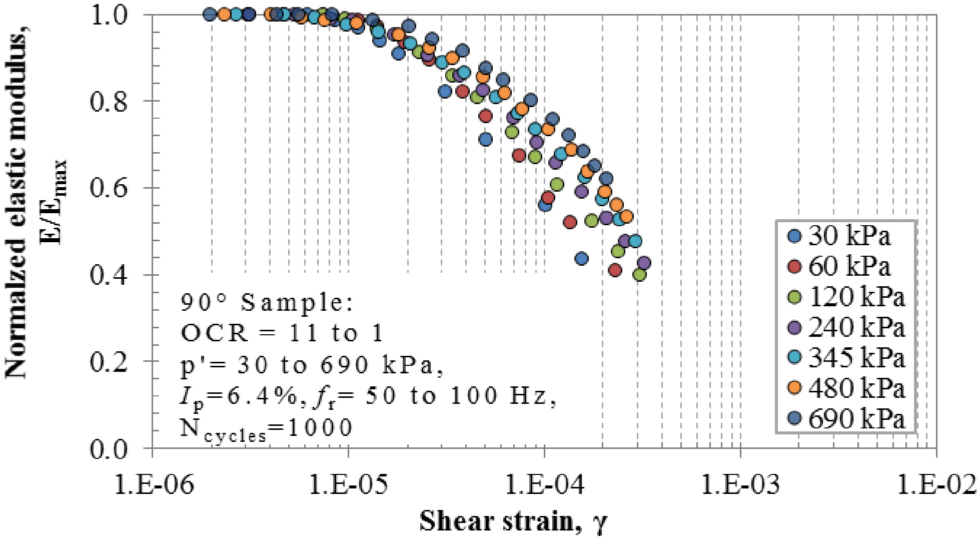

Figure D.46: Normalized elastic modulus variation with strain amplitude of Blenheim clay (90° rotation sample)

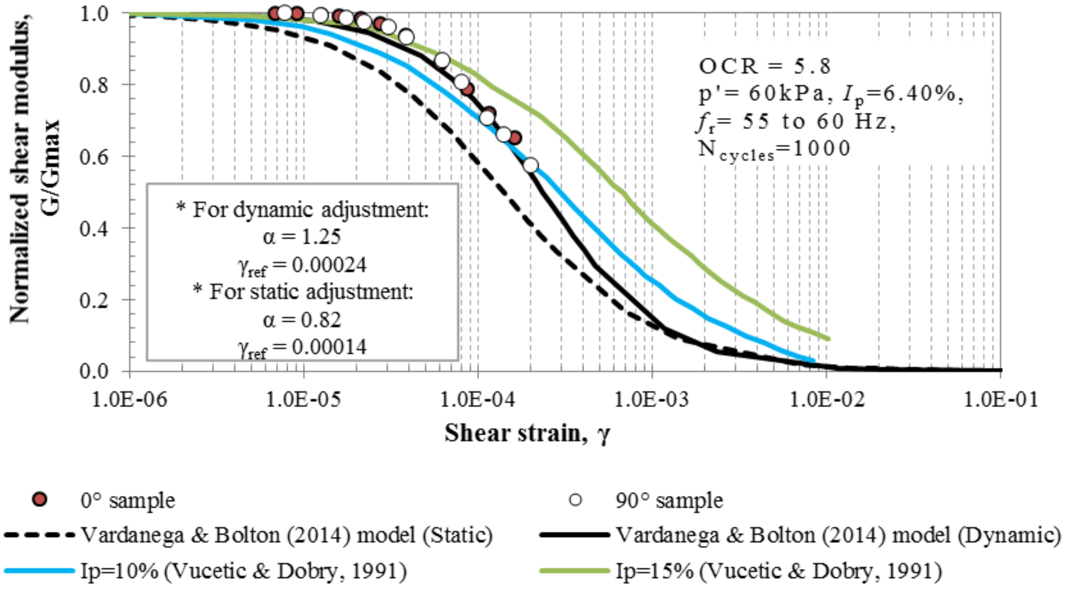

Figure D.47: G/G$_{max}$ from RC test at p'=60 kPa for 0° and 90° samples of Blenheim clay, compared to empirical models

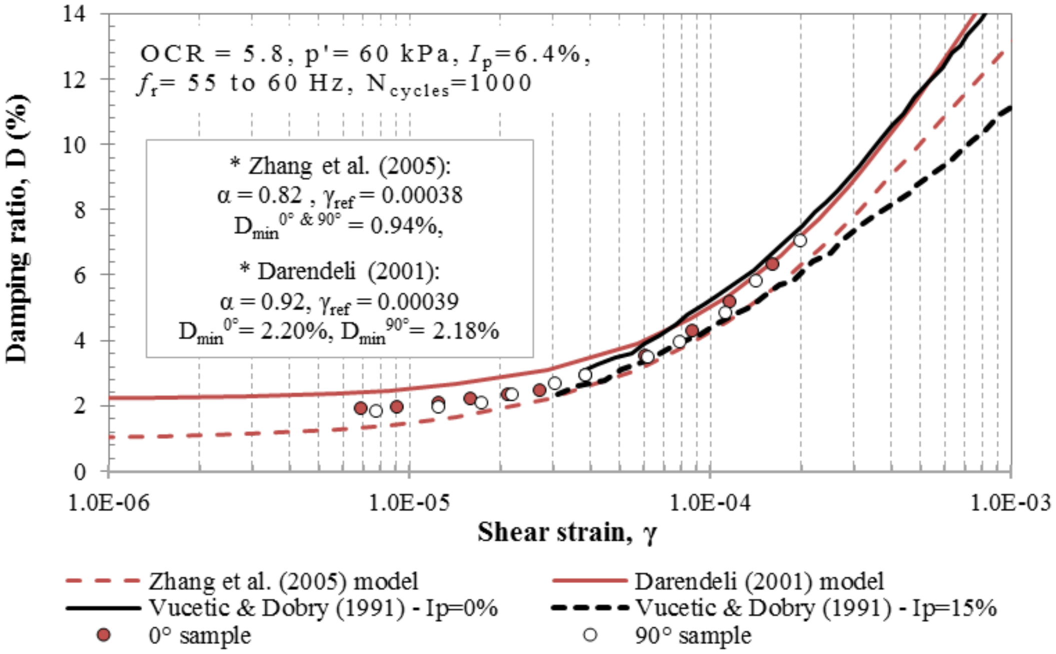

Figure D.48: Damping ratio from RC test at p'=60 kPa for 0° and 90° samples of Blenheim clay, compared to empirical models

D.3.3 RC results on Wallaceburg clay

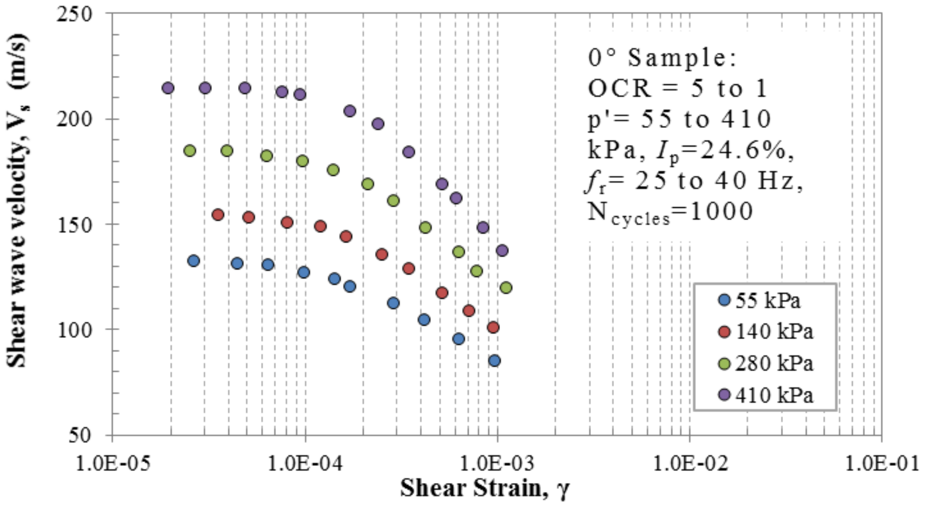

Figure D.49: Shear wave velocity variation with strain amplitude of Wallaceburg clay (0° rotation sample)

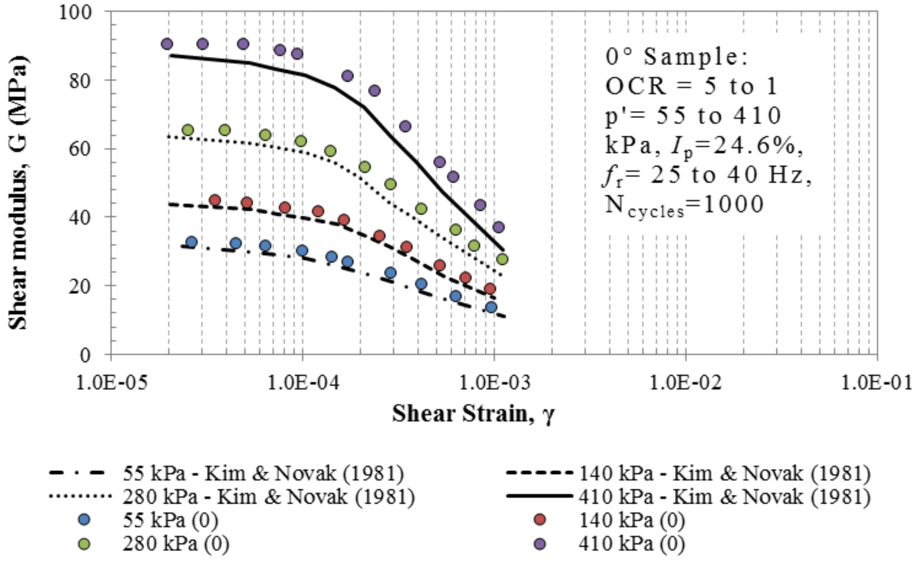

Figure D.50: Shear modulus variation with strain amplitude of Wallaceburg clay (0° rotation sample)

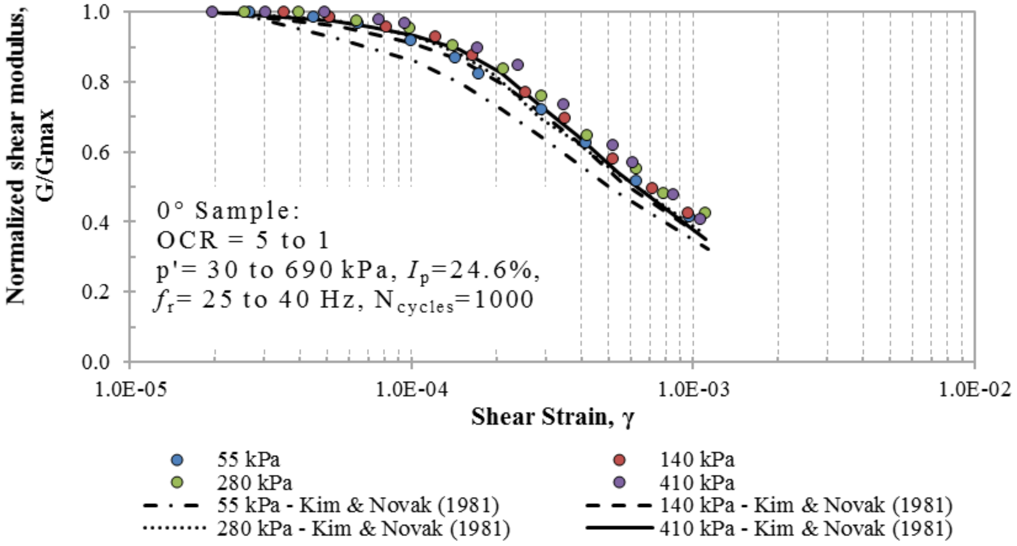

Figure D.51: Normalized shear modulus variation with strain amplitude of Wallaceburg clay (0° rotation sample)

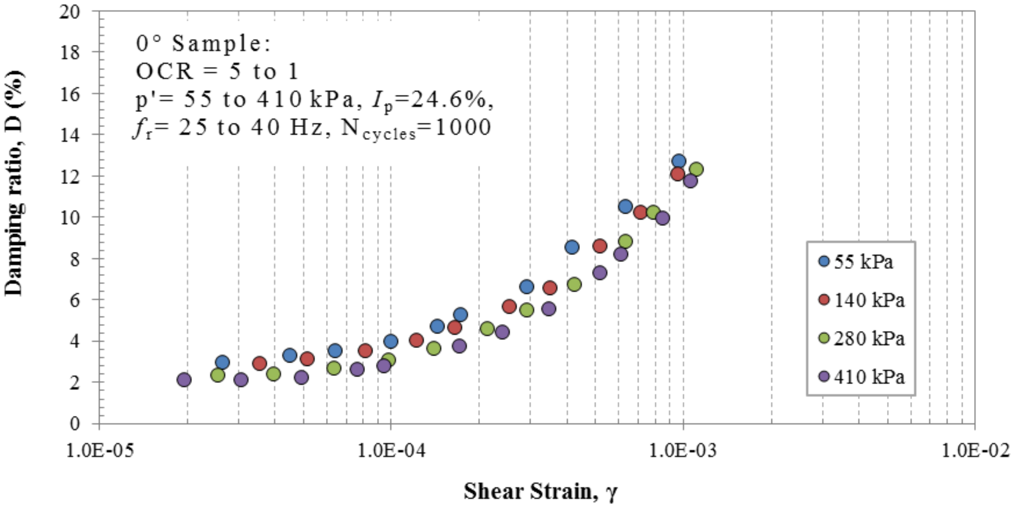

Figure D.52: Damping ratio variation with strain amplitude of Wallaceburg clay (0° rotation sample)

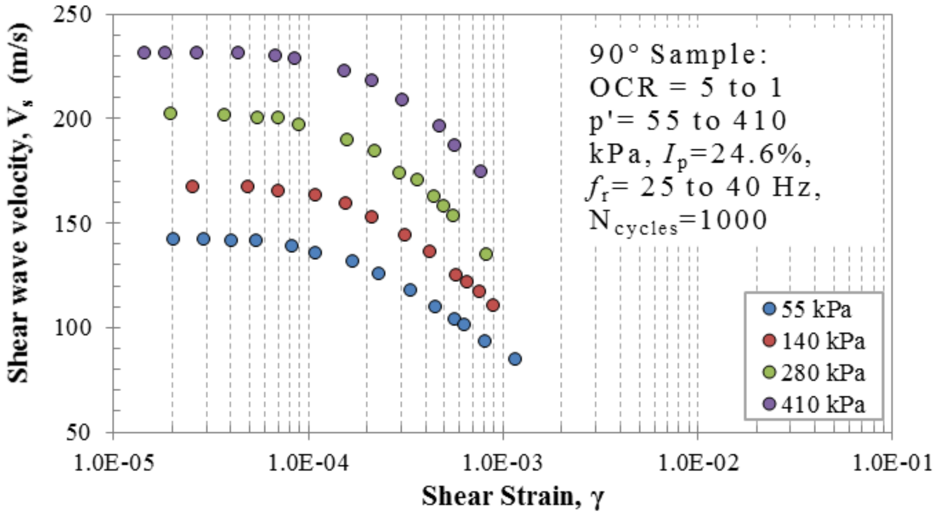

Figure D.53: Shear wave velocity variation with strain amplitude of Wallaceburg clay (90° rotation sample)

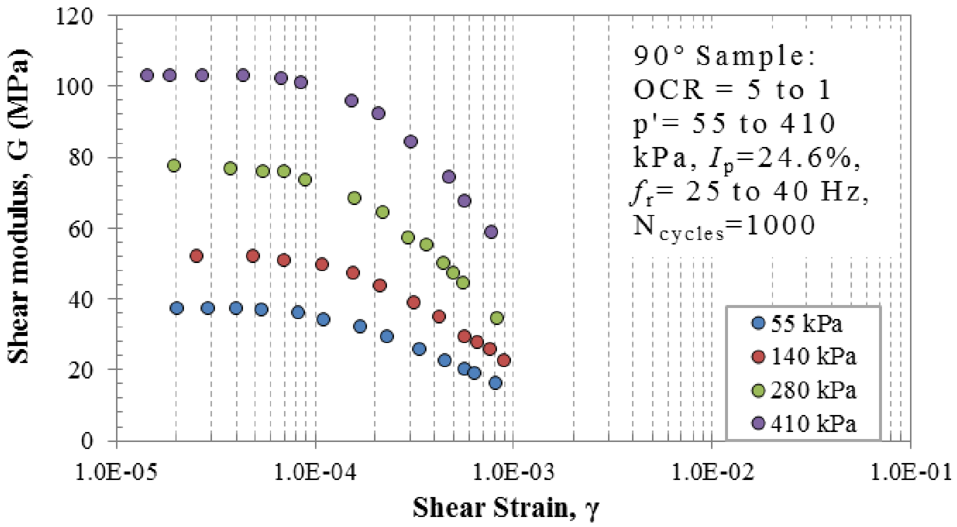

Figure D.54: Shear modulus variation with strain amplitude of Wallaceburg clay (90° rotation sample)

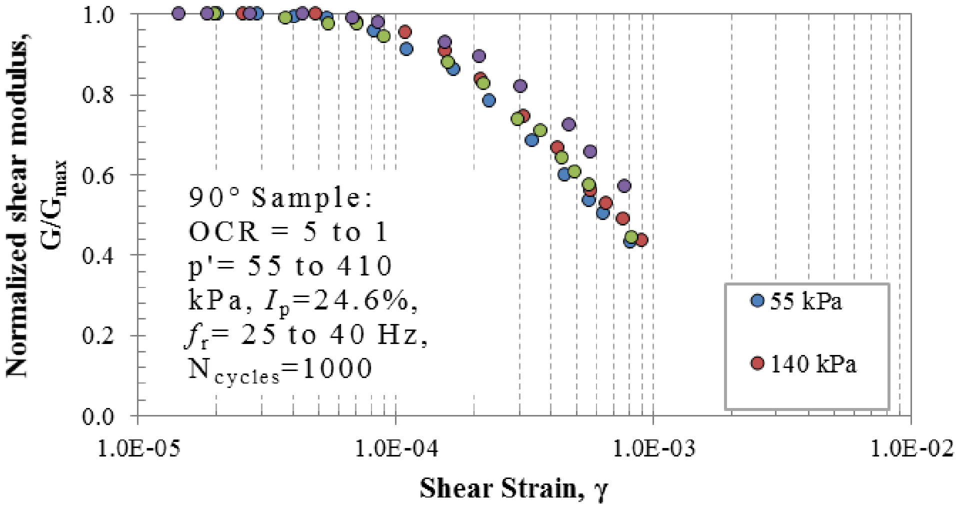

Figure D.55: Normalized shear modulus variation with strain amplitude of Wallaceburg clay (90° rotation sample)

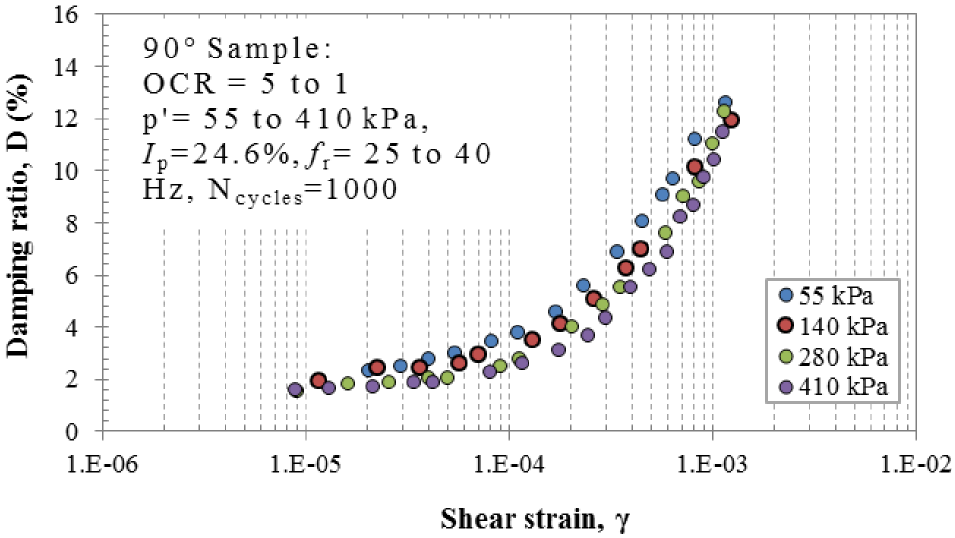

Figure D.56: Damping ratio variation with strain amplitude of Wallaceburg clay (90° rotation sample)

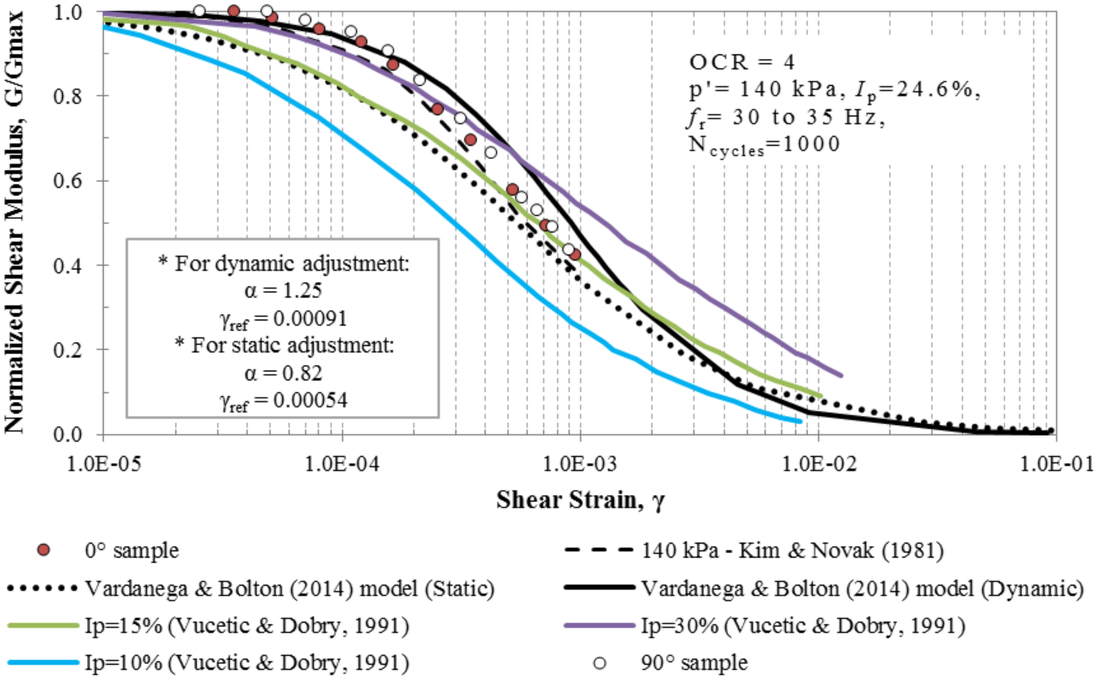

Figure D.57: G/Gmax from RC test at p'=140 kPa for 0° and 90° samples of Wallaceburg clay, compared to empirical models

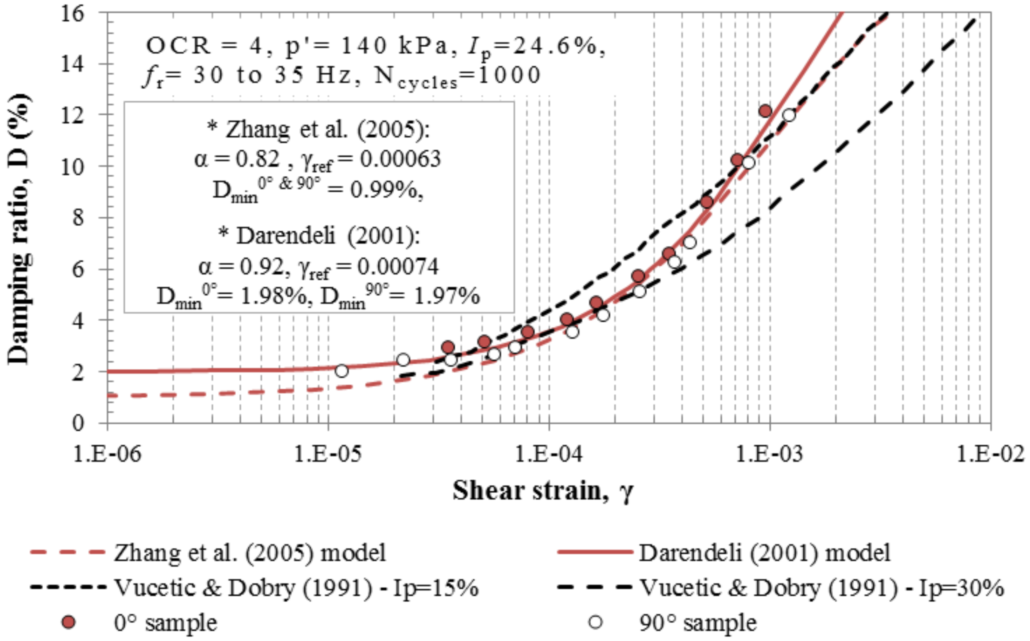

Figure D.58: Damping ratio from RC test at p'=140 kPa for 0° and 90° samples of Wallaceburg clay, compared to empirical models

D.3.4 RC results on EPK Kaolin clay

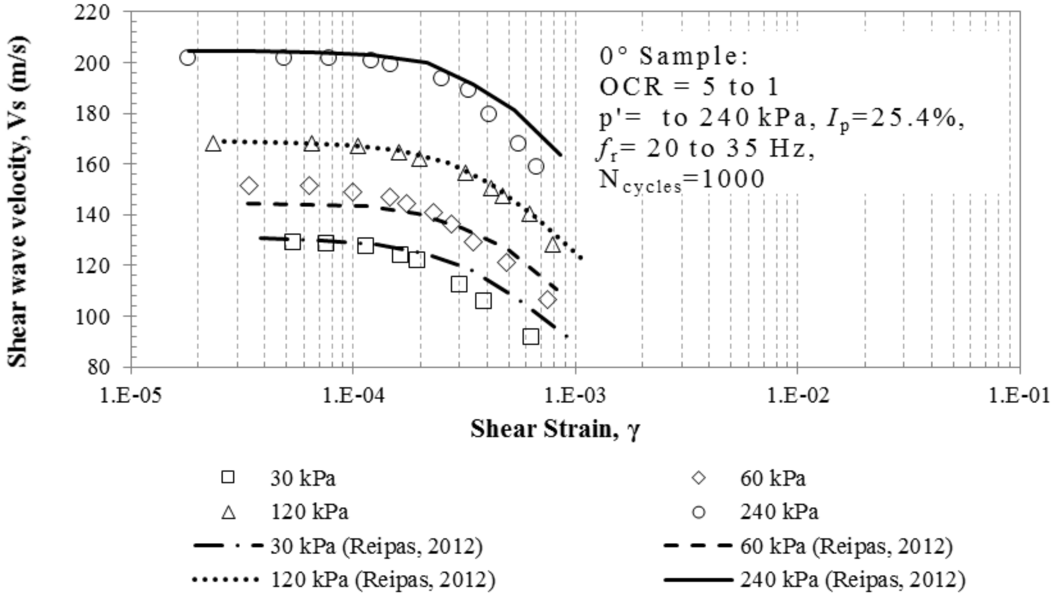

Figure D.59: Shear wave velocity variation with strain amplitude of EPK clay (0° rotation sample)

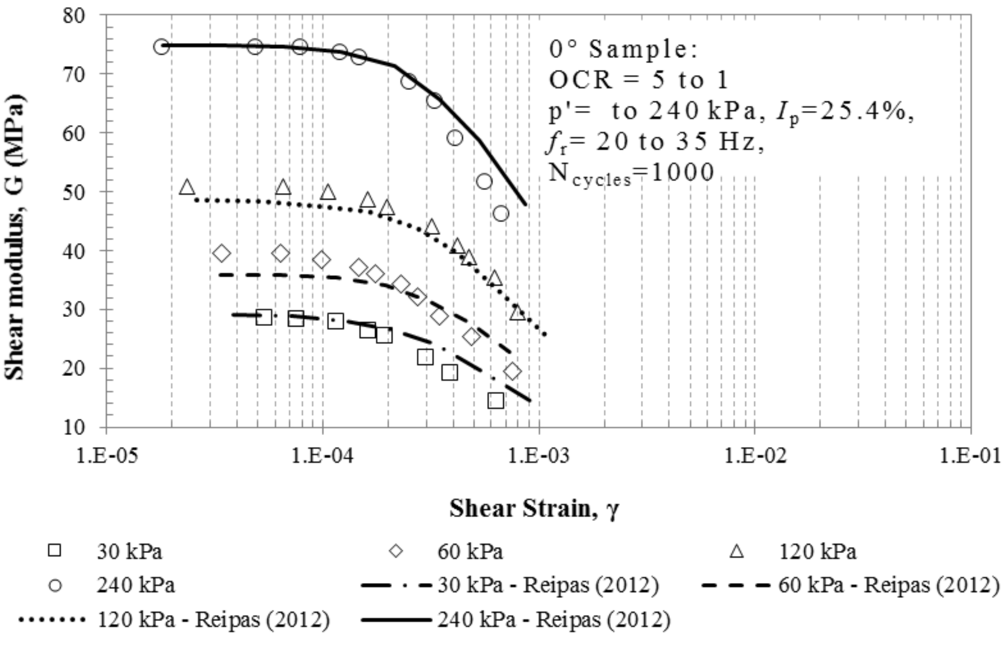

Figure D.60: Shear modulus variation with strain amplitude of EPK clay (0° rotation sample)

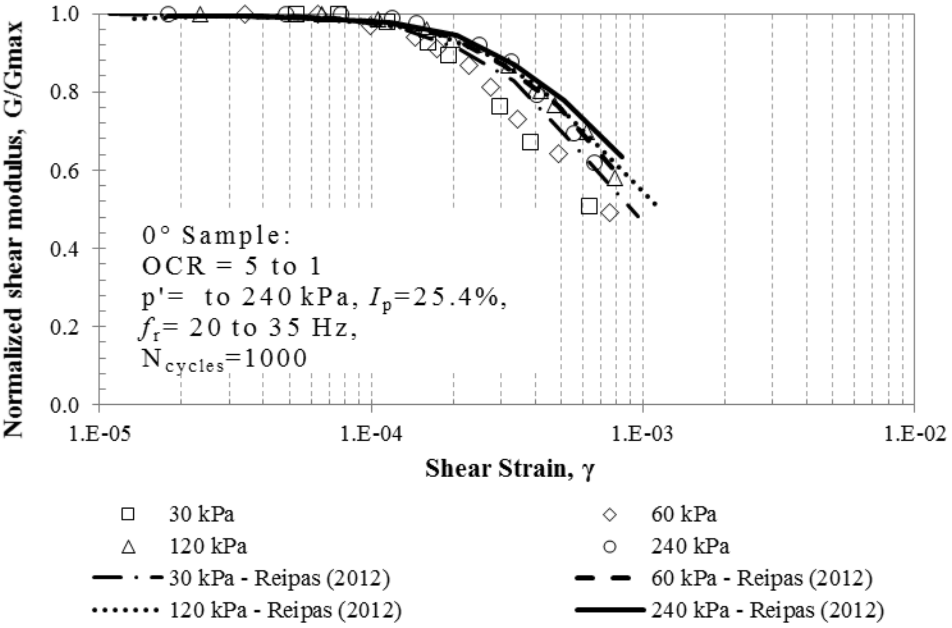

Figure D.61: Normalized shear modulus variation with strain amplitude of EPK clay (0° rotation sample)

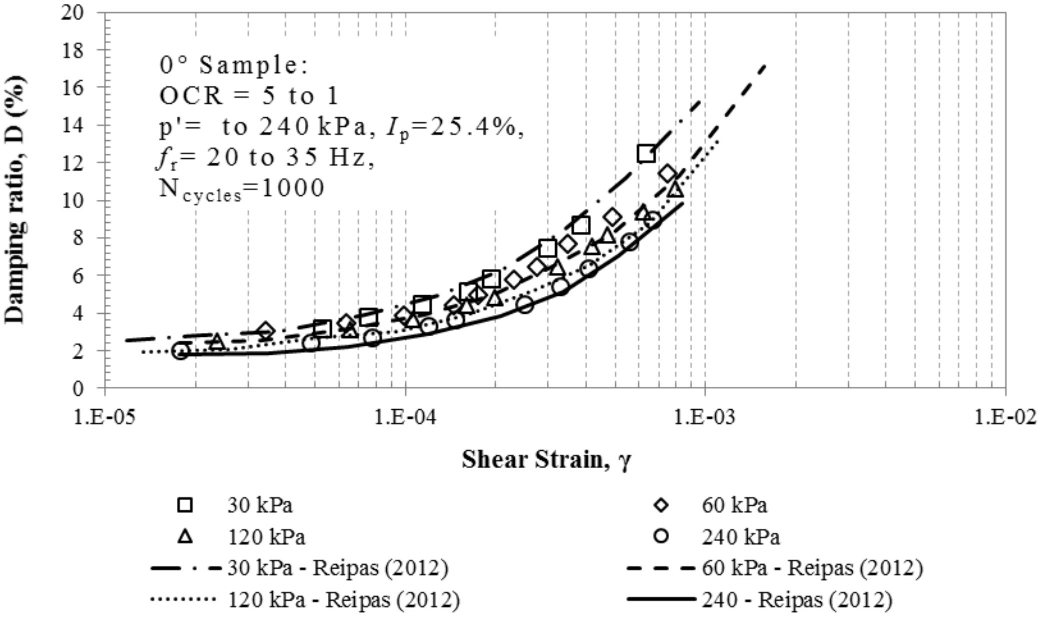

Figure D.62: Damping ratio variation with strain amplitude of EPK clay (0° rotation sample)

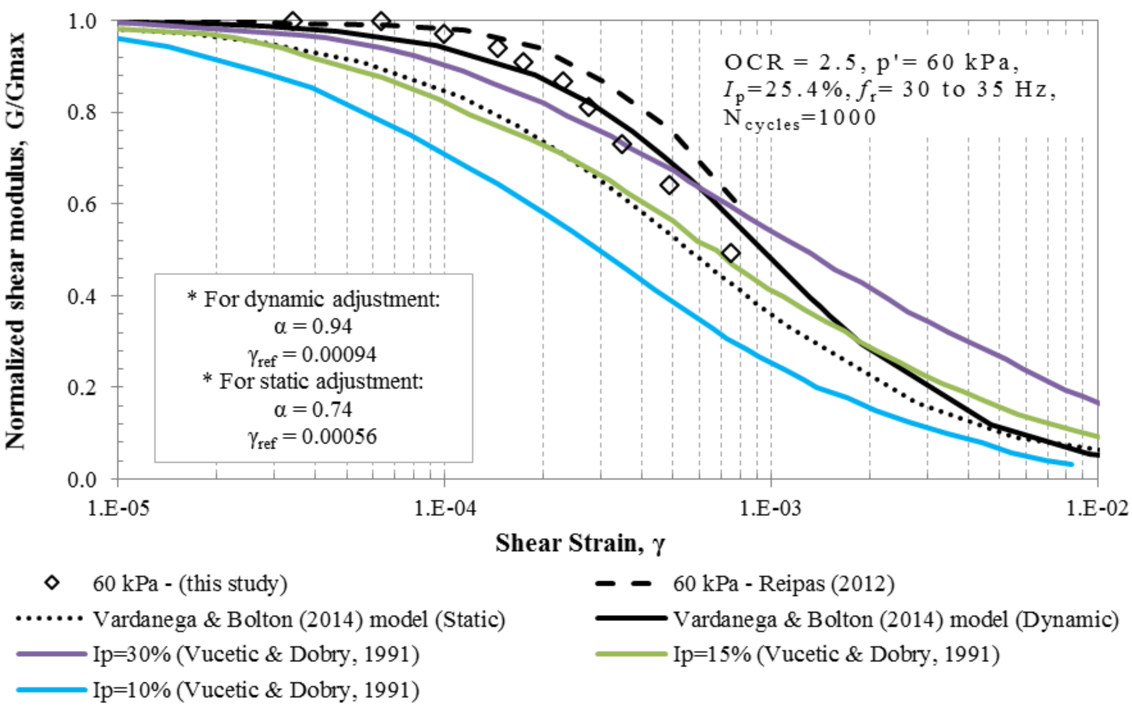

Figure D.63: G/Gmax from RC test at p'=60 kPa for 0° samples of EPK clay, compared to empirical models

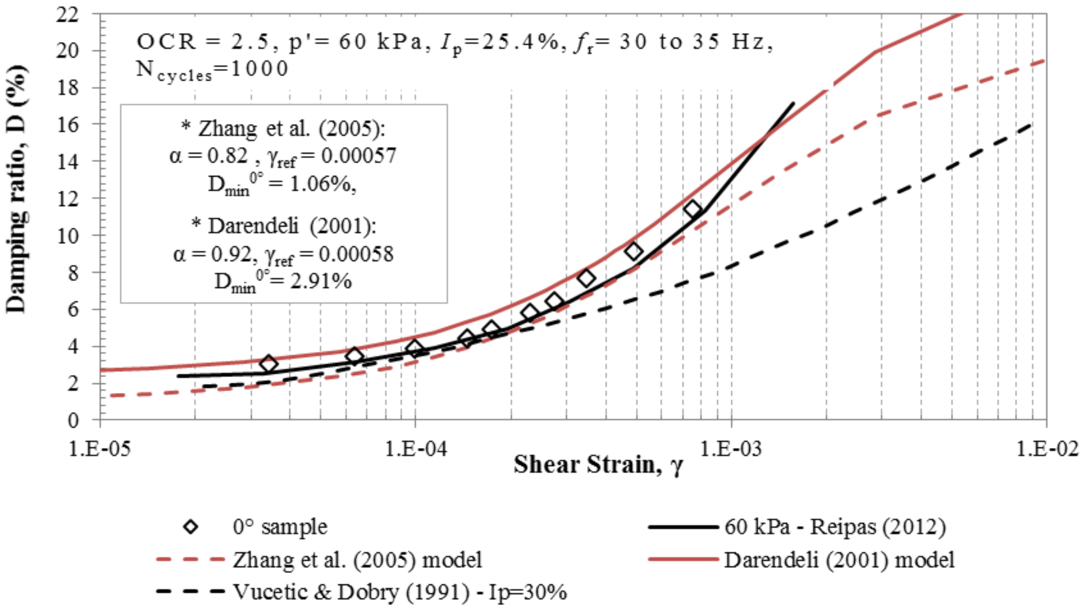

Figure D.64: Damping ratio from RC test at p'=60 kPa for 0° samples of EPK clay, compared to empirical models

D.4 Further analysis on the measured shear wave velocities

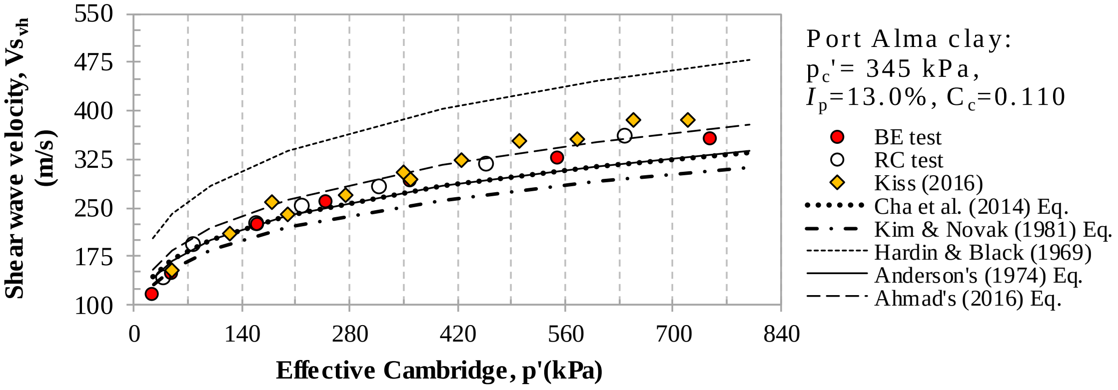

Figure D.65: Shear wave velocity (Vs_{vh}) with increasing of effective pressure for Port Alma clay

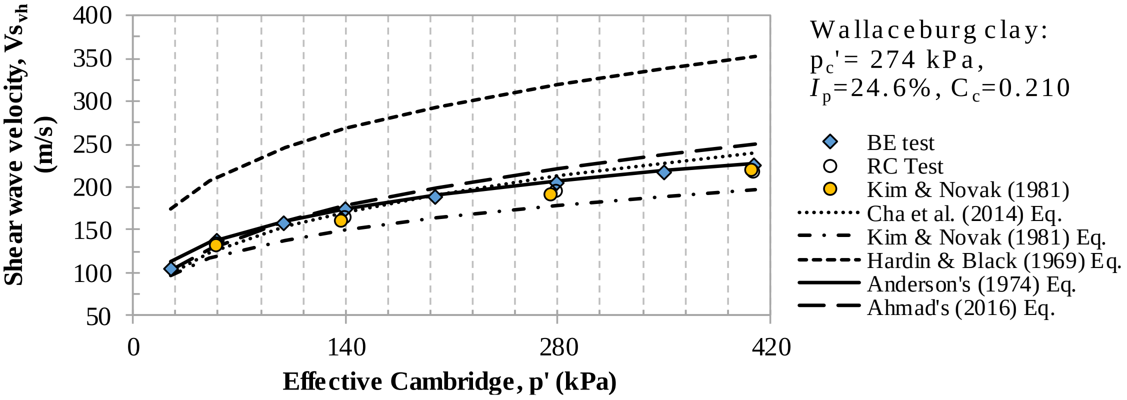

Figure D.66: Shear wave velocity (Vs_{vh}) with increasing of effective pressure for Wallaceburg clay

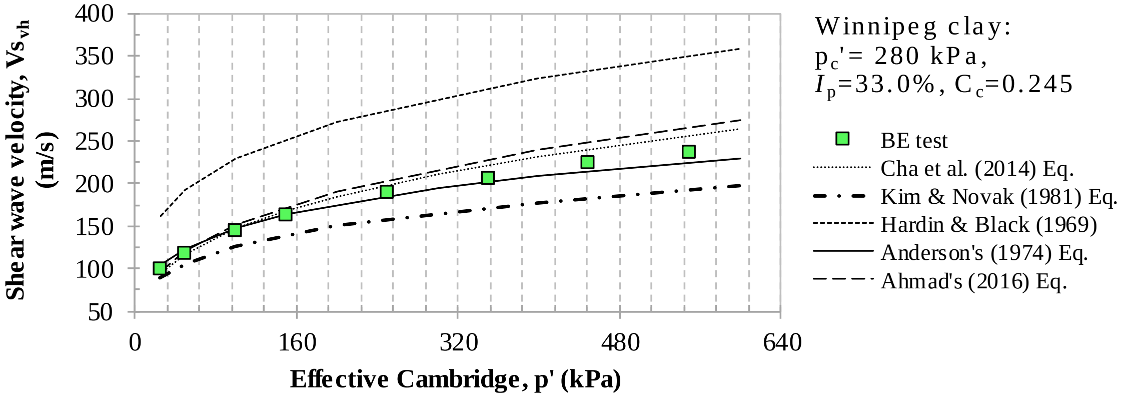

Figure D.67: Shear wave velocity (Vs_{vh}) with increasing of effective pressure for Winnipeg clay

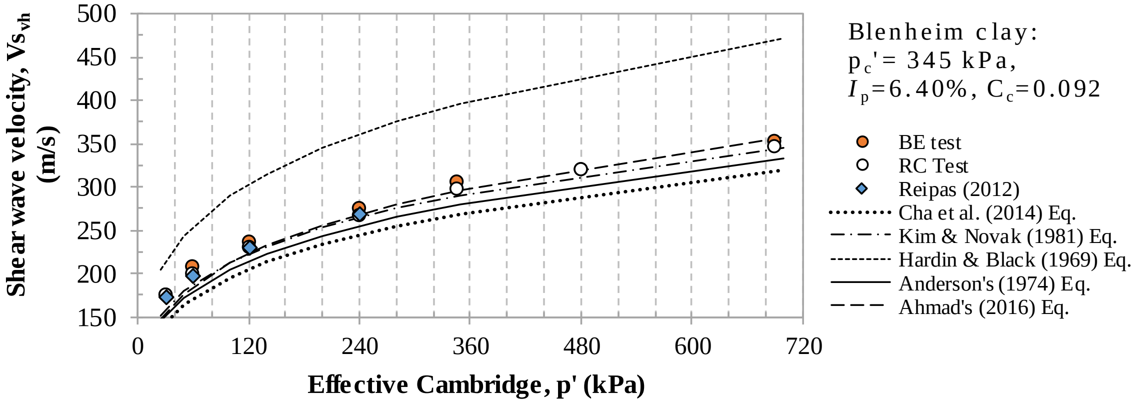

Figure D.68: Shear wave velocity (Vs_{vh}) with increasing of effective pressure for Blenheim clay

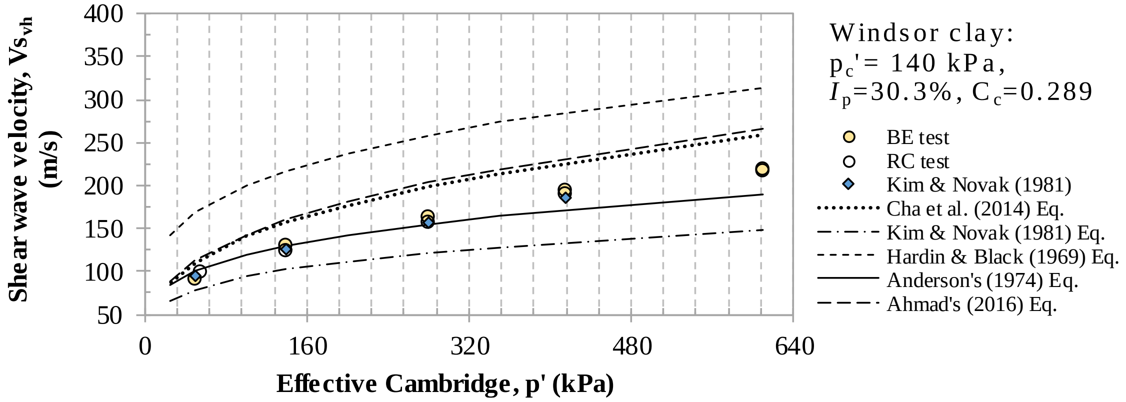

Figure D.69: Shear wave velocity (Vs_{vh}) with increasing of effective pressure for Windsor clay

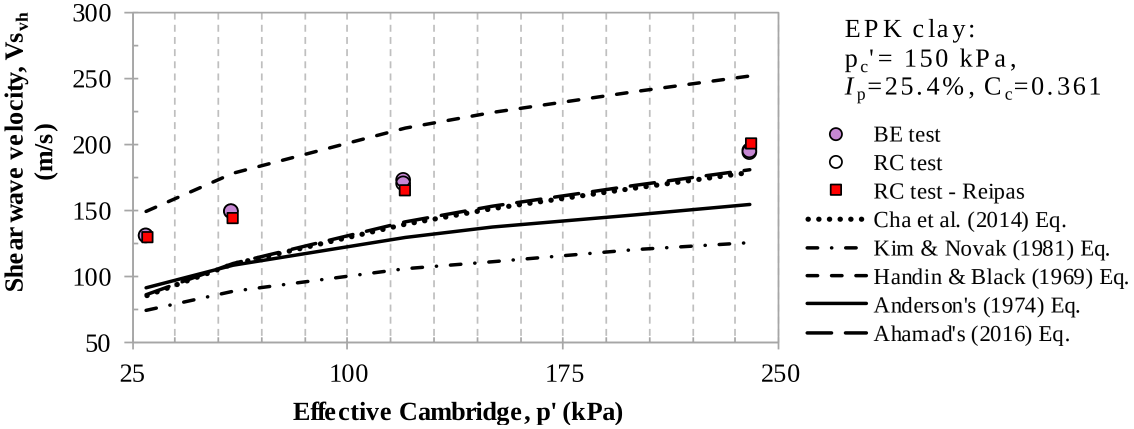

Figure D.70: Shear wave velocity (Vs_{vh}) with increasing of effective pressure for EPK clay

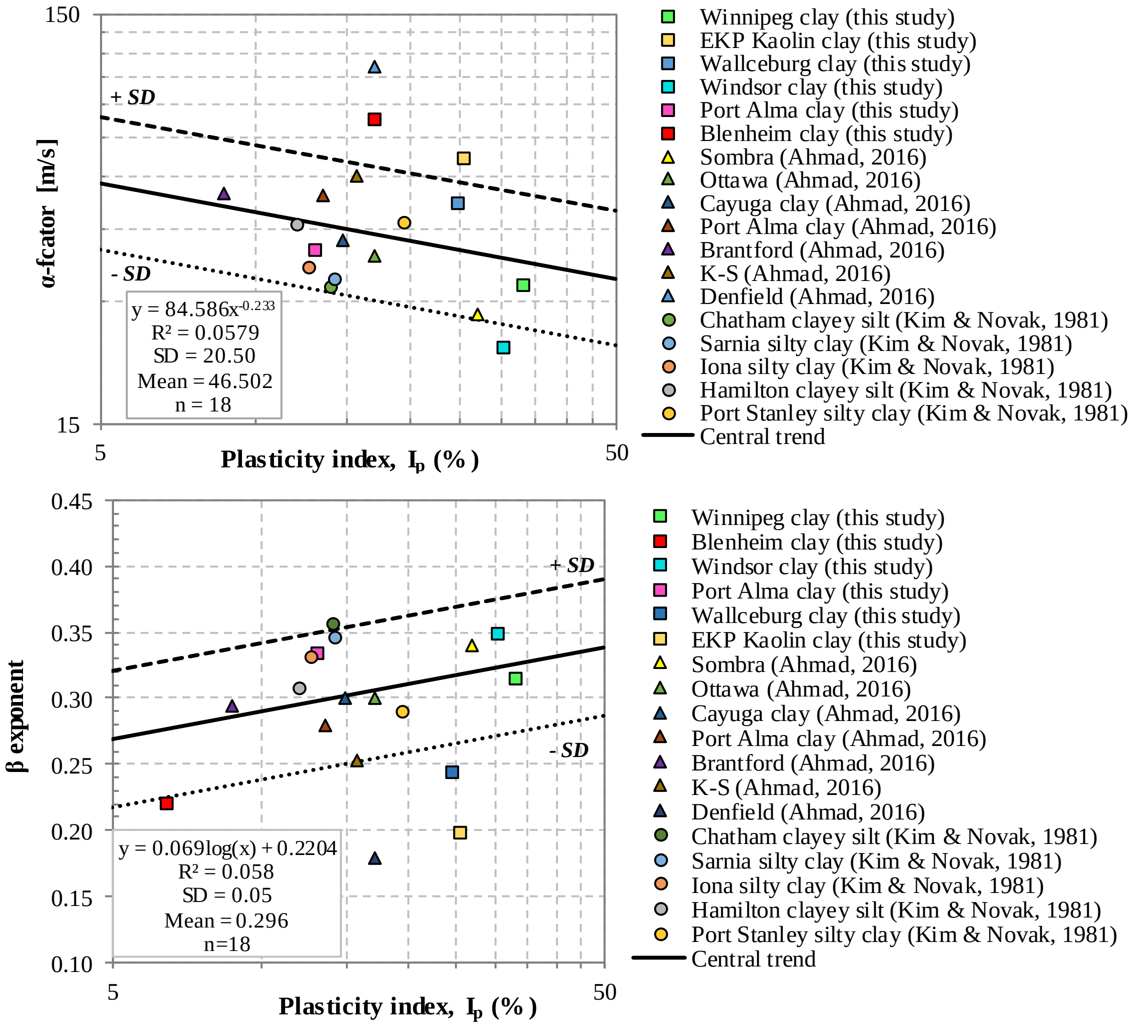

Figure D.71: Relationship between: a) the α-factor and plasticity index (I_P) and b) the β exponent and plasticity index (I_P) for different glacial and cohesive materials

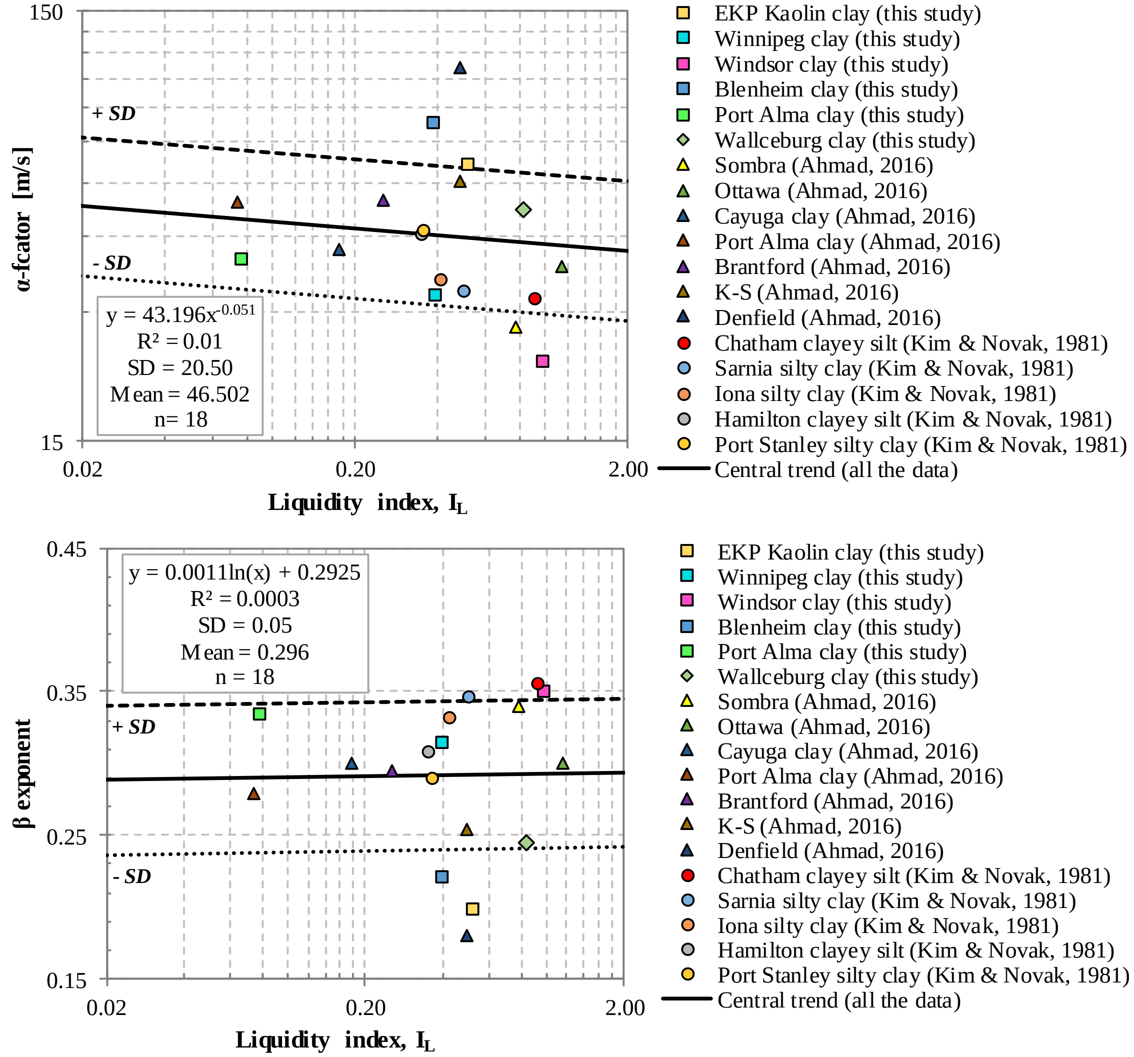

Figure D.72: Relationship between: a) the α-factor and liquidity index (I_L) and b) the β exponent and liquidity index (I_L) for different glacial and cohesive materials

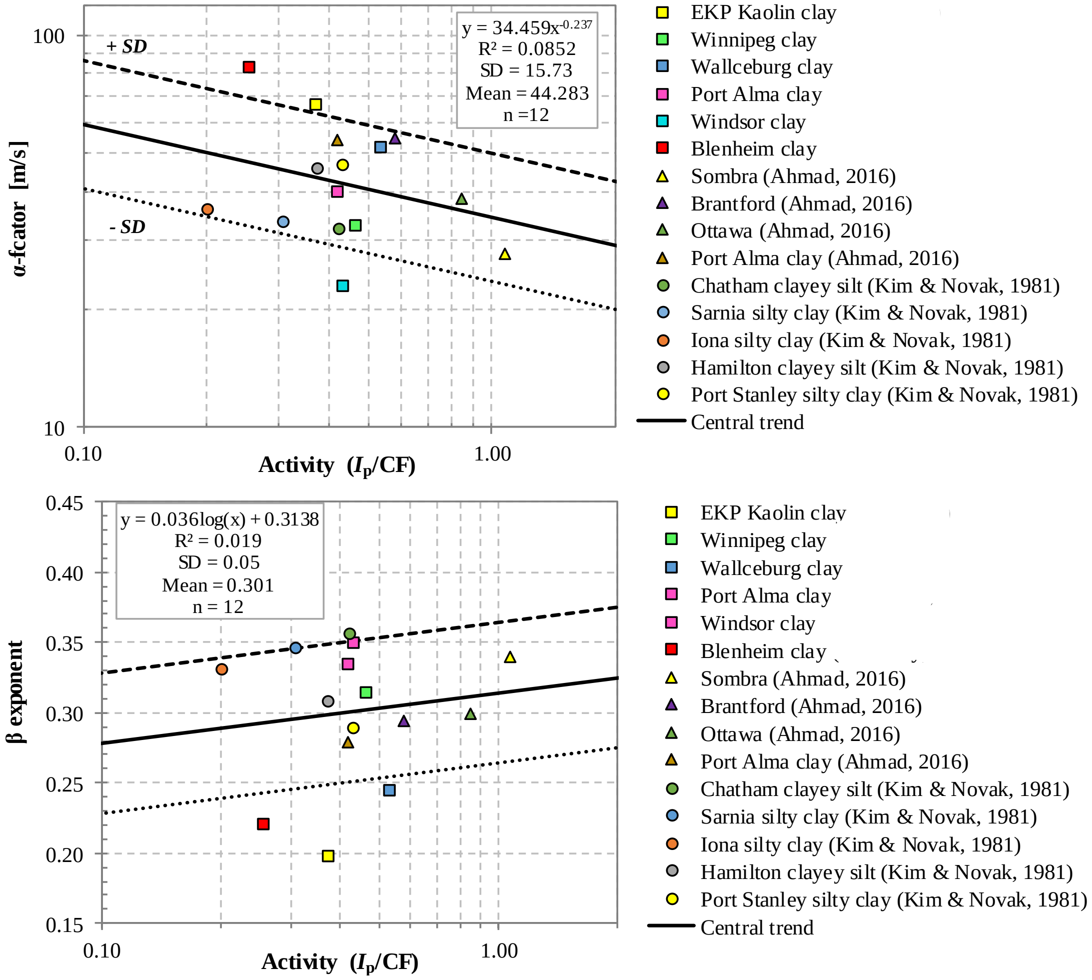

Figure D.73: Relationship between: a) the α-factor and activity and b) the β exponent and activity for different glacial and cohesive materials

D.5 Horizontal shear modulus from resonant column test

Sultaniya et al. (2010) reported findings from a series of numerical analyses of physical tests in the resonant column apparatus performed to model the apparatus, and isotropic and cross-anisotropic soil specimens. Among their findings, Sultaniya et al. (2010) observed that the shear modulus in the horizontal plane of the sample (G_{hh}) was not the same as estimated after inducing torsional vibration on horizontal-cut samples (90° degrees rotation samples). Based on their analyses, they proposed Equation D-1 to calculate G_{hh} using the estimated shear modulus in the vertical and horizontal direction:

$$G_{hh} = \frac{{G_{hc}}^2}{G_{vh}} \qquad \text{(D.1)}$$

where G_{hc} = shear modulus from horizontal-cut sample RC test; G_{vh} = shear modulus from vertical-cut sample RC test.

Equation D.1 was applied to the results reported in Section 6.2.2 and the results are presented in Table 6.4. The shear modulus obtained for the horizontal-cut samples that was assumed as G_{hh} for the calculation of α before, was assumed here as G_{hc} to adopt the same nomenclature used by Sultaniya et al. (2010). Thus, new values of G_{hh} were obtained for each soil through Equation D.1. These values are in some cases 8 to 15% higher to the estimated values directly from the resonant column tests (see Figure D.74). Those percentages of increase (or reduction) are also reflected in the calculation of α using the G_{hh} from Equation D.1.

Table D.3: Estimation of stiffness parameters using data from resonant column and Sultaniya et al. (2010) equation

	Port Alma clay	Blenheim clay	Wallaceburg clay	Windsor clay
G_v (MPa)	109.11	82.73	47.71	19.20
G_{hc} (MPa)	126.93	75.69	54.03	20.80
G_{hh} (MPa)	147.66	69.25	61.19	22.53
if $\alpha=G_{hc}/G_v$	1.16	0.91	1.13	1.08
if $\alpha=G_{hh}/G_v$	1.35	0.84	1.28	1.17

Values of shear modulus were obtained at p' equal to the original in-situ condition of soil material and at shear strain ≈ 1x10-5

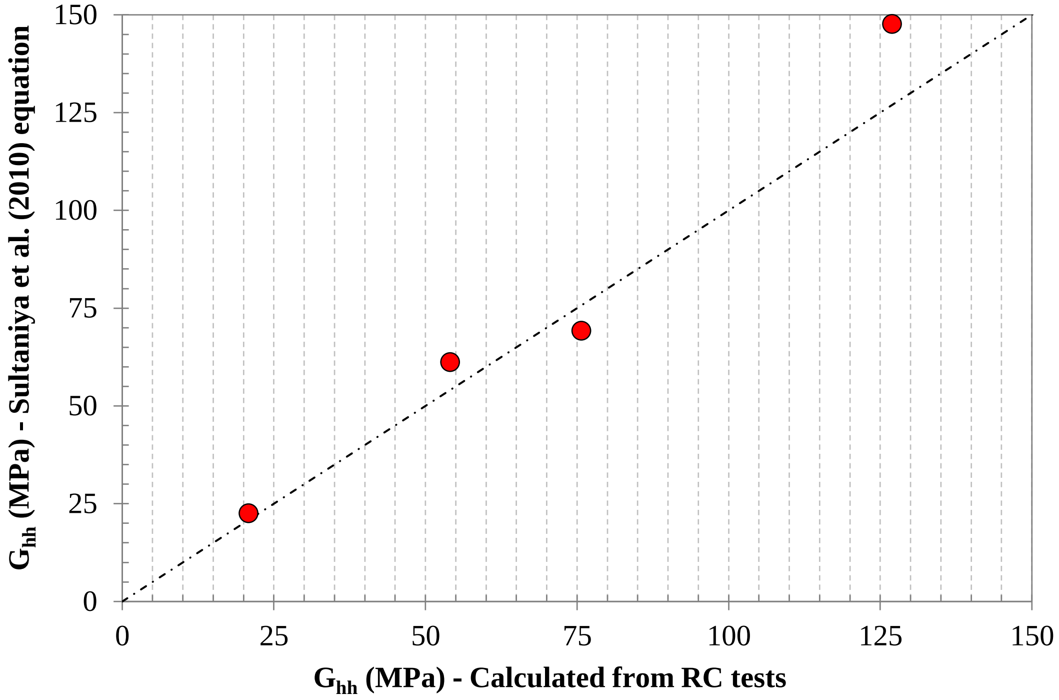

Figure D.74: Comparison between horizontal shear modulus (Ghh) estimated from Sultaniya et al. (2010) equation and obtained from RC test

The changes in the anisotropy ratio introduced by the calculation of a new G_{hh} through Sultaniya et al. (2010) equation did not affect the results reported in Chapter 5 and 6 with respect of the anisotropic behaviour exhibited by the Canadian soils investigated. The new G_{hh} values indicate that the materials could be much stiffer in their horizontal direction as is the case for Windsor, Wallaceburg and Port Alma clays, while for the case of Blenheim clays the results suggest that such materials could be much stiffer in its vertical direction than what was previously estimated. All these translates in an increase of the small-strain stiffness anisotropy ratio (α).

Appendix E

E.1 Estimated soil parameters used in the numerical model

This appendix shows graphical representations of the estimations of the anisotropy ratio (α), the variation of the shear modulus (G_{vh}) with depth and the slope of the stiffness increase with depth for the Port Alma glacial clay till material. The results shown in Figure E.1 were presented and discussed previously in Chapters 2, 3 and 5. An average value of α was deduced from Figure E.1(a) from the field and laboratory measurements. An average value of G_{vh} was obtained from the laboratory and field measurements as shown in Figure E.1(b), and a value of k was obtained from the slope of the linear regression of the average value of G_{vh} with depth.

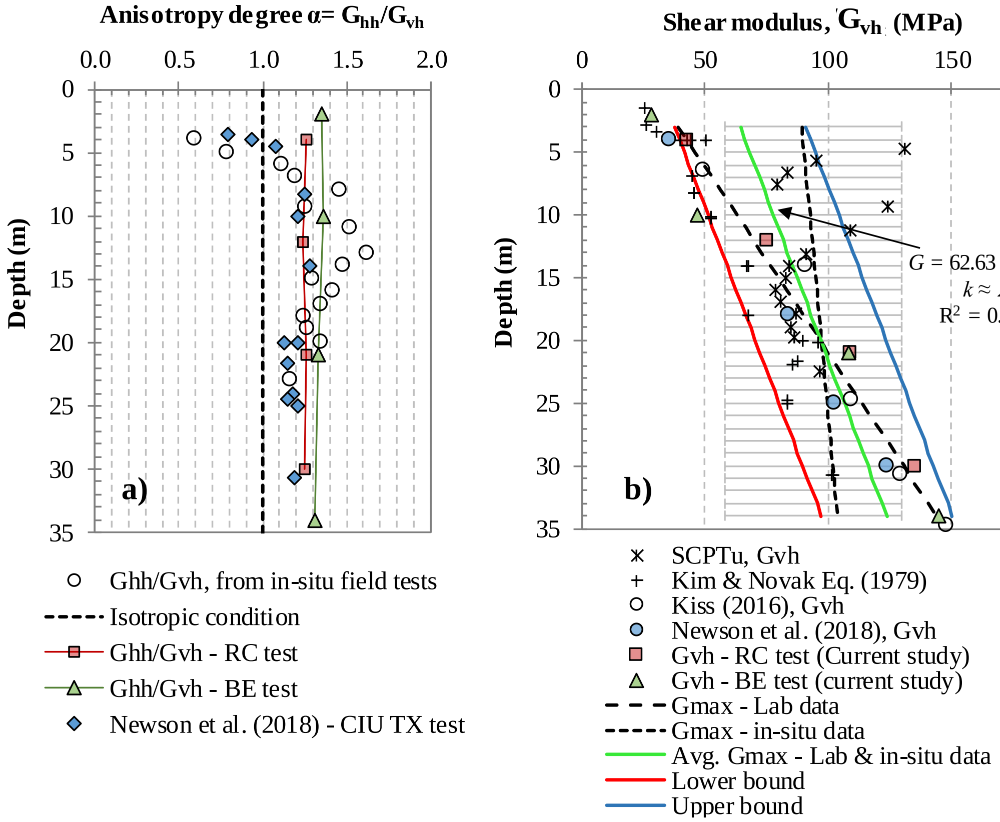

Figure E.1: Anisotropy degree (α) and small-strain shear modulus (G_{vh}) variation with depth of Port Alma glacial till deposit

E.2 Basic stiffness equations for surface foundation on homogeneous soil

A finite element model was developed and a series of parametric studies were carried out to derive coupled anisotropic elastic stiffness equations. A summary of the methods used for the numerical model development, material modelling and assumptions, and the approach for analysis were presented and discussed in Section 7.2 of Chapter 7. An example of the derivation of the proposed equations for K_V and K_{HH} is presented here; further details may be found elsewhere (He, 2019; Gonzalez-Hurtado et al., 2019)

E.2.1 Vertical stiffness (K_V)

If K_V is normalized by G_{hv} then: $K_V = \frac{V}{u_V R \cdot G_{hv}}$. The expression $\frac{1}{K_V(1.1-\mu_{hh})}$ can be considered to be independent of μ_{hh}, i.e. $\frac{1}{K_V(1.1-\mu_{hh})}$ is function of $f(\alpha)$, as shown in Figure E.2.

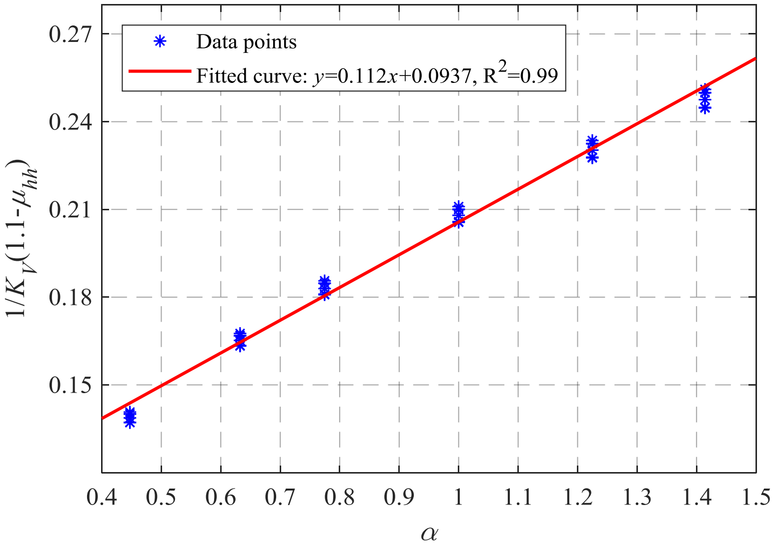

Figure E.2: Relationship between $\boldsymbol{\frac{1}{K_V(1.1-\mu_{hh})}}$ and $\boldsymbol{f(\alpha)}$

Curve fitting of the data in Figure E.2 using the least square method shows that, selected independent expression can be best represented by a linear function of the anisotropy parameter α:

$$\frac{1}{K_V(1.1-\mu_{hh})}=0.112\alpha+0.0937 \tag{E-1}$$

Rearranging Equation E-1, K_V can be evaluated through Equation E-2:

$$K_V=\frac{1}{(1.1-\mu_{hh})(0.112\alpha+0.0937)} \tag{E-2}$$

E.2.2 Horizontal stiffness (K_{HH})

If K_{HH} is normalized by G_{hv} then: $K_{HH}=\frac{H}{u_H R\cdot G_{hv}}$. The expression of $K_{HH}(2.4-\mu_{hh})$ can be considered to be independent of the Poisson's ratio μ_{hh}, i.e. $K_{HH}(2.4-\mu_{hh})$ is a function of $f(\alpha)$ as shown in Figure E.3.

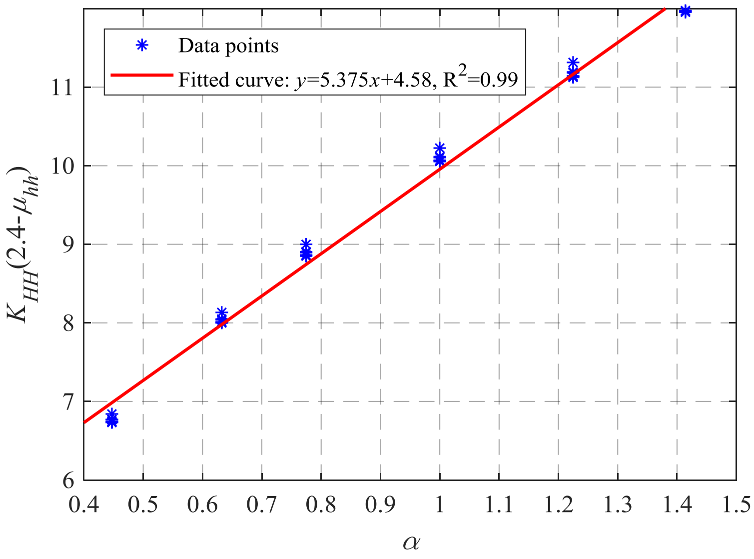

Figure E.3: Relationship between $K_{HH}(2.4-\mu_{hh})$ and $f(\alpha)$

Performing least squares curve fitting of the data in Figure E.3, the selected independent expression can be best represented by the following linear function of the anisotropy parameter α:

$$K_{HH}(2.4-\mu_{hh})=5.375\alpha+4.58 \tag{E-3}$$

Rearranging Equation E-3, K_{HH} can be evaluated through Equation E-4:

$$K_{HH} = \frac{5.375\alpha + 4.58}{2.4 - \mu_{hh}} \tag{E-4}$$

E.3 Gibson correction factors

E.3.1 For vertical stiffness - K_V

The dimensionless Gibson correction factor for vertical stiffness is defined as:

$$C_{\beta,V} = \frac{K_{V,1/\beta}}{K_{V,1/\beta=0}} = 1 + f\left(\frac{1}{\beta}\right) \tag{E-5}$$

where $1/\beta$ is the Gibson factor, defined as $1/\beta = \frac{k_s D_f}{E_{v0}}$; E_{v0} is the elastic soil modulus at ground level; k_s is the rate of increase of modulus with depth (units of E_{vo} per unit depth); D_f is the foundation diameter. The relationship between $\left(C_{\beta,V} - 1\right)$ and $f\left(\frac{1}{\beta}\right)$ is shown in Figure E.4.

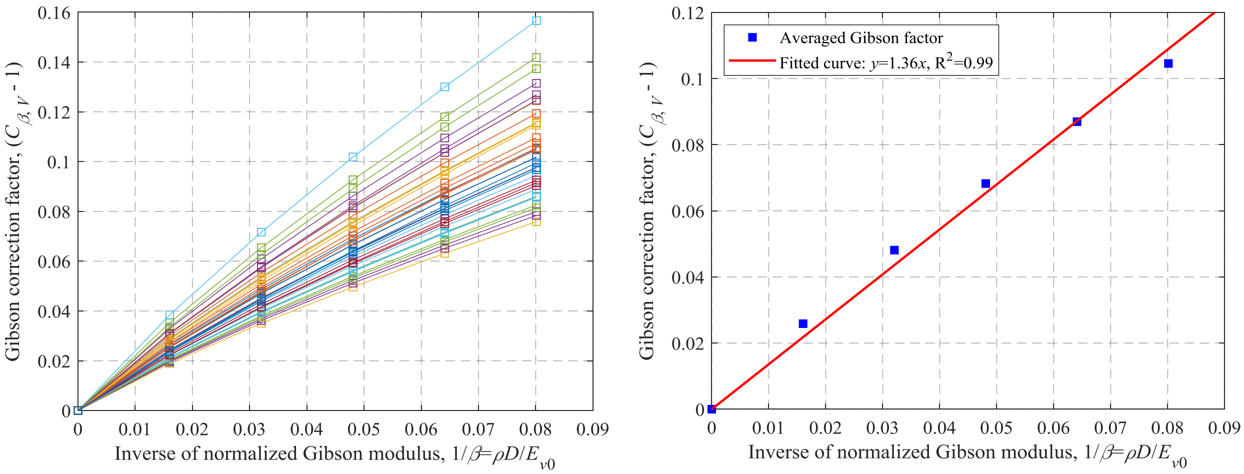

(a) Gibson factors

(b) Averaged Gibson factors

Figure E.4: Relationship between $\left(C_{\beta,V} - 1\right)$ with $f\left(\frac{1}{\beta}\right)$

For each $\frac{1}{\beta} = \frac{k_s D_f}{E_{vo}}$, there are 36 points (i.e. 6 anisotropic ratios * 6 Poisson's ratios), as shown in Figure E.4(a). Taking an average of the 36 points for each $\frac{1}{\beta}$ and fitting with a linear function passing through the origin, gives (as shown in Figure E.4(b)):

$$C_{\beta,V} = \frac{1.36}{\beta} + 1 \tag{E-6}$$

E.3.2 For horizontal stiffness - K_{HH}

Similar to $C_{\beta,V}$, the relationship of $\left(C_{\beta,HH} - 1\right)$ with $f\left(\frac{1}{\beta}\right)$ is shown in Figure E.5.

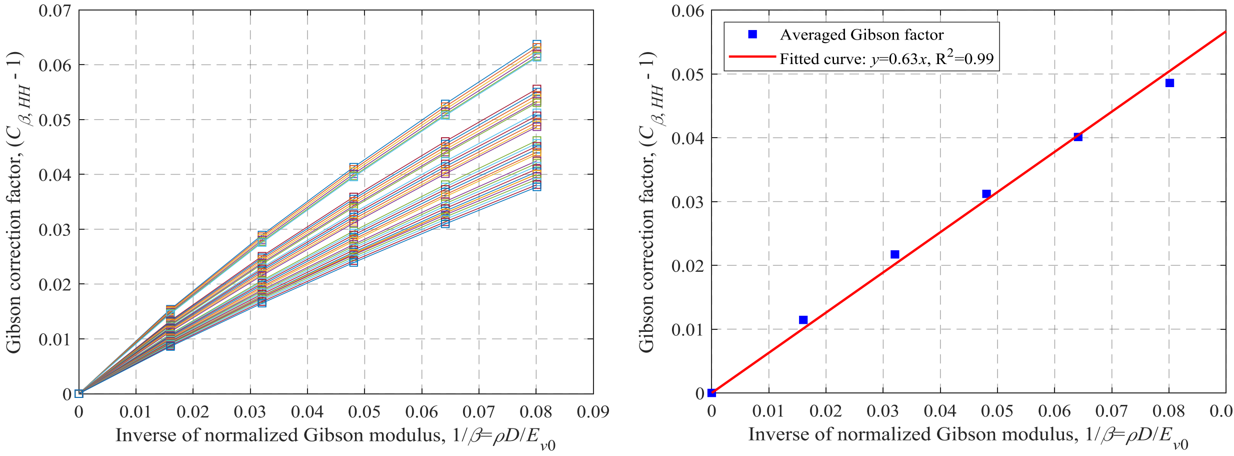

(a) Gibson factors (b) Averaged Gibson factors

Figure E.5: Relationship between $\left(C_{\beta,HH} - 1\right)$ with $f\left(\frac{1}{\beta}\right)$

Therefore,

$$C_{\beta,HH} = \frac{0.63}{\beta} + 1 \tag{E-7}$$

E.4 Embedment correction factor

E.4.1 For vertical stiffness - K_V

The dimensionless embedment correction factor for vertical stiffness is defined as:

$$C_{e,V} = \frac{K_{V,e}}{K_{V,e=0}} = 1 + f(e) \tag{E-8}$$

where e is the embedment ratio, defined as $e = \frac{d}{D_f}$. The relationship of $\left(C_{e,V} - 1\right)$ with $f(e)$ is shown in Figure E.6.

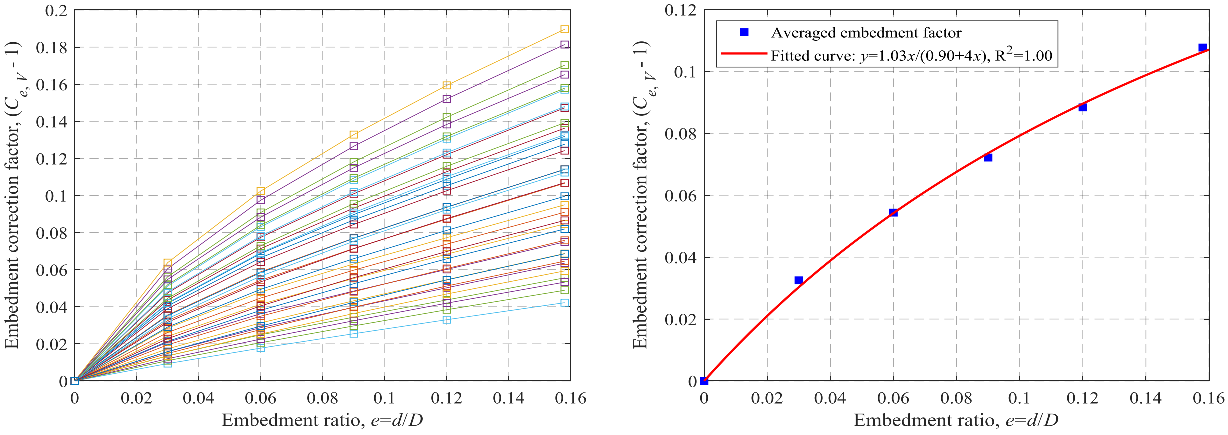

(a) Embedment factors (b) Averaged embedment factors

Figure E.6: Relationship between $\left(C_{e,V} - 1\right)$ and $f(e)$

For each $e = \frac{d}{D_f}$, there are 36 points (i.e. 6 anisotropic ratios * 6 Poisson's ratios), as shown in Figure E.6a. The average of the 36 points for each e was taken and fitted with a linear function passing through the origin, as shown in Figure E.6(b).

$$C_{e,V} = \frac{1.03e}{0.90 + 4e} + 1 \quad \text{(E-9)}$$

E.4.2 For horizontal stiffness - K_{HH}

Similar to $C_{e,V}$, the relationship between $\left(C_{e,HH} - 1\right)$ and $f(e)$ is shown in Figure E.7.

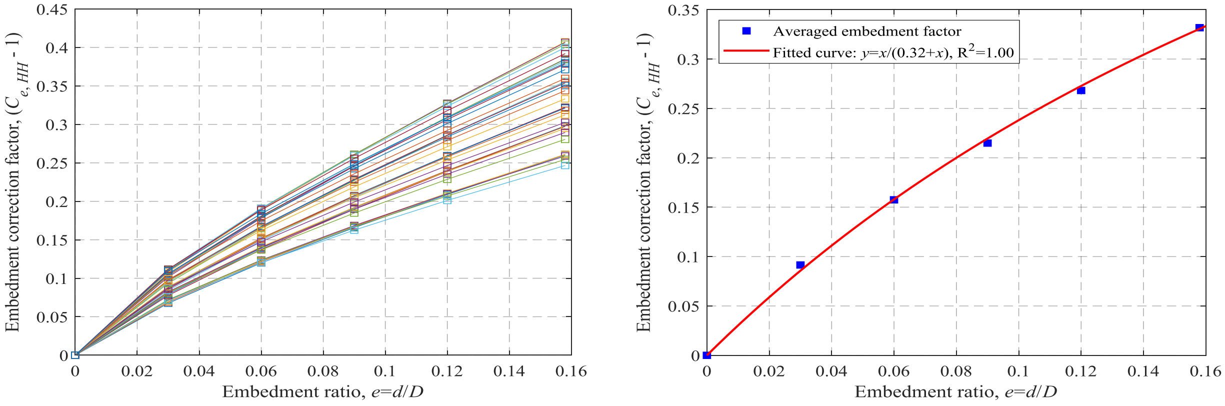

(a) Embedment factors (b) Averaged embedment factors

Figure E.7: Relationship between $\left(C_{e,HH} - 1\right)$ and $f(e)$

Therefore,

$$C_{e,HH} = \frac{e}{0.32+e} + 1 \quad \text{(E-10)}$$

E.5 Summary of obtained coupled anisotropic elastic stiffness equations

The complete set of anisotropic, coupled stiffness equations for surface and embedded foundations are therefore:

$$K_V = \left[\frac{1}{(1-\mu_{hh})(0.112\alpha + 0.0937)}\right] \cdot \left[\left(\frac{1}{\beta}\right) \cdot 0.36 + 1\right] \cdot \left[\frac{1.03e}{0.90 + 4e} + 1\right] \tag{E-11a}$$

$$K_{HH} = \left[\frac{5.37\alpha + 4.58}{2.4 - \mu_{hh}}\right] \cdot \left[\left(\frac{1}{\beta}\right) \cdot 0.63 + 1\right] \cdot \left[\frac{e}{0.32 + e} + 1\right] \tag{E-11b}$$

$$K_{MH} = K_{HM} = \left[\frac{-1.5(0.5 - \mu_{hh})}{1 - \mu_{hh}}\right] \cdot [-6.49e + 1] \tag{E-11c}$$

$$K_{MM} = \left[\frac{1}{(1.2-\mu_{hh})(0.145\alpha + 0.125)}\right] \cdot \left[\left(\frac{1}{\beta}\right) \cdot 0.30 + 1\right] \cdot \left[\frac{1.93e}{0.88 + e} + 1\right] \tag{E-11d}$$

where α is the square root of the anisotropic ratio, $\alpha = \sqrt{\frac{E_h}{E_v}}$; $1/\beta$ is the Gibson factor, $1/\beta = \frac{k_s D_f}{E_{v0}}$ (for $0 \leq 1/\beta \leq 0.08$); e is the embedment ratio, $e = \frac{d}{D_f}$.

E.6 Stiffness equations proposed by Gazetas (1983) and Gazetas (1991)

Gazetas (1983):

$$K_V = \frac{4}{1-\mu}(1 + e) \tag{E-12a}$$

$$K_{HH} = \frac{8}{2-\mu}\left(1 + \frac{4}{3}e\right) \tag{E-12b}$$

$$K_{MH} = K_{HM} = 0.80 K_{HH} \cdot e \tag{E-12c}$$

$$K_{MM} = \frac{8}{3(1-\mu)}(1 + 4e) \tag{E-12d}$$

Gazetas (1991):

$$K_V = \frac{4}{1-\mu}(1 + 1.1e) \tag{E-13a}$$

$$K_{HH} = \frac{8}{2-\mu}(1 + 2e) \tag{E-13b}$$

$$K_{MH} = K_{HM} = \frac{2}{3} K_{HH} \cdot e \tag{E-13c}$$

$$K_{MM} = \frac{8}{3(1-\mu)}(1 + 4e) \tag{E-13d}$$

E.7 Contour plots from typical finite element analysis

Figures E.8 to E.11 show contour plots obtained from some of the finite element analysis carried out in Chapter 7 for the pseudo-static normal operation design loads provided by the manufacturer of KEPA 4 wind turbine (see Table 7.4). These plots show estimations of the volumetric strain (ε_v), equivalent shear strain (ε_s), deviatoric stress (q) and mean stress (p) at the centerline of the foundation to a depth equal to the foundation radius, and the high stress/strain at the corner of the foundation.

Figure E.8: Volumetric strain (ε_v) with depth

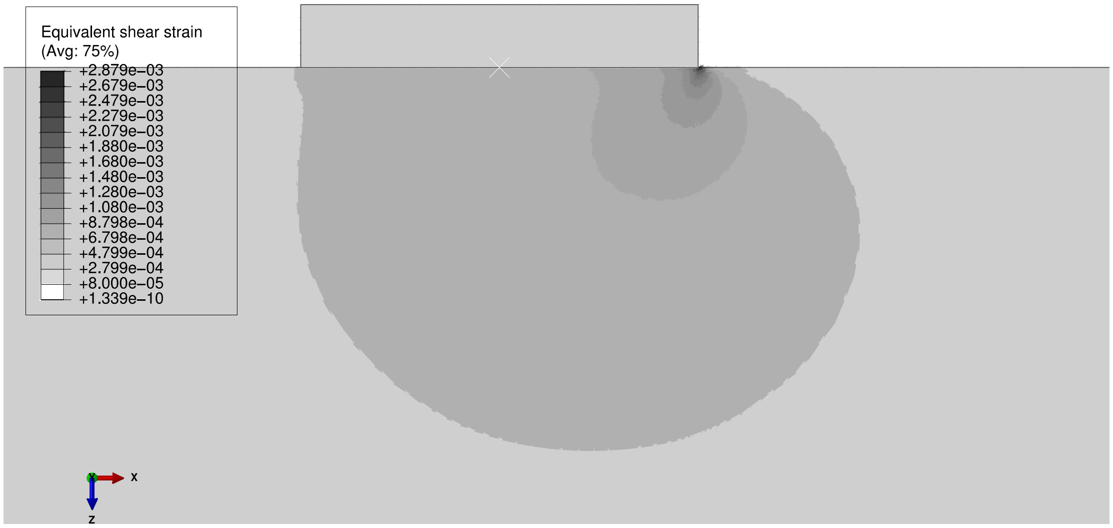

Figure E.9: Equivalent shear strain (ε_s) with depth

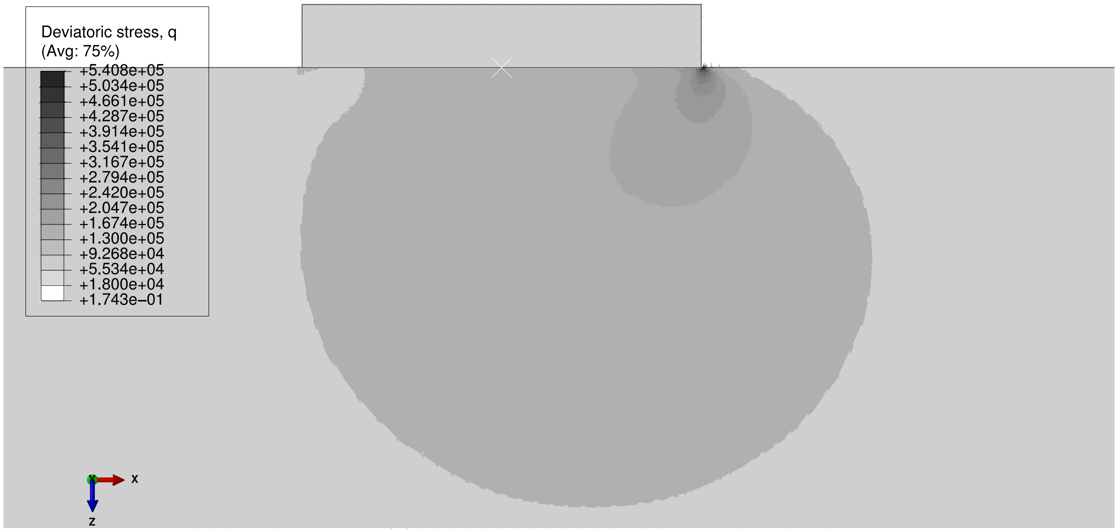

Figure E.10: Deviatoric stress (q) with depth

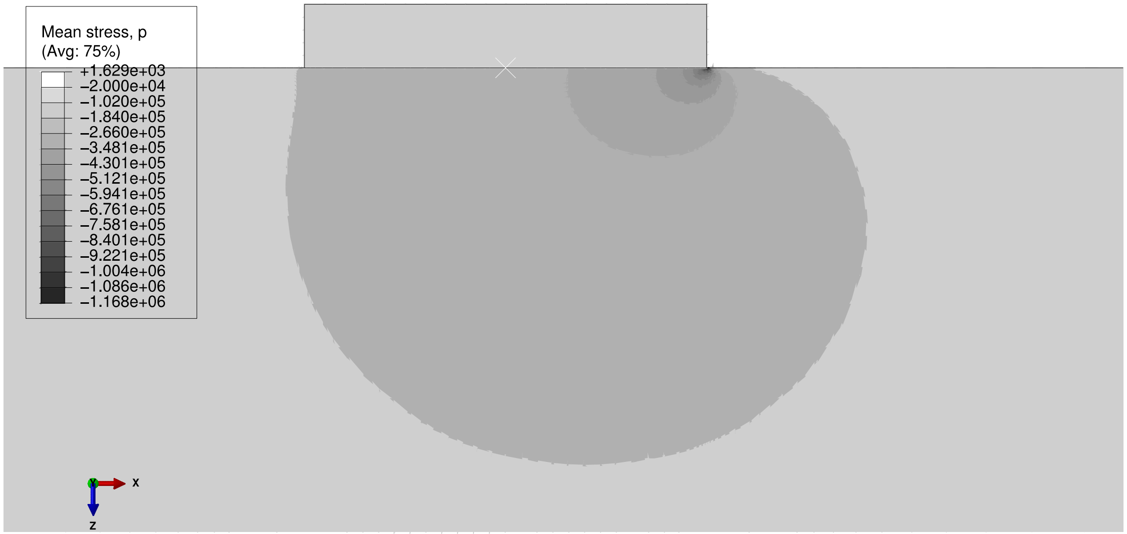

Figure E.11: Mean stress (p) with depth

E.8 Results from parametric study of embedded foundations on soil with linear increase of stiffness with depth

The following plots show the results from a parametric study carried out on an embedded foundation with an embedment ratio of 0.16 and soil stiffness gradient of 2. More details of the implementation and interpretation of the parametric study can be found in Section 7.4.

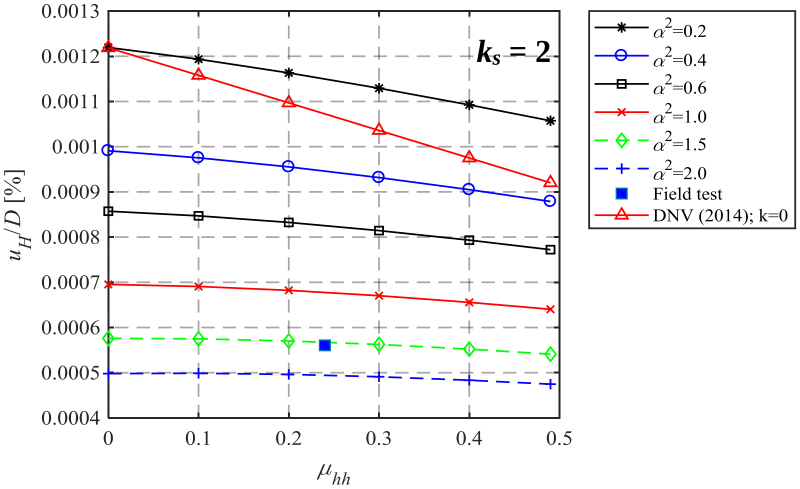

Figure E.12: Normalized horizontal translation (u_H/D_f) for the embedded foundation as a function of different soil parameters

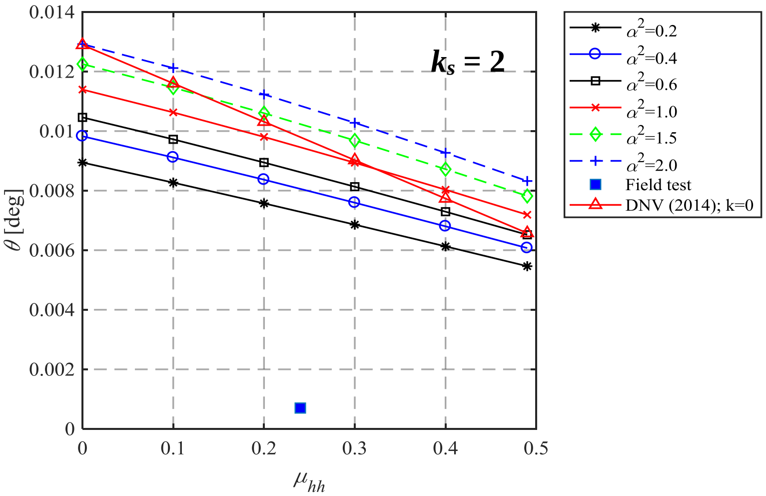

Figure E.13: Foundation rotation (θ) for the embedded foundation as a function of different soil parameters

Curriculum Vitae

Name: **Jesús A. <u>González-Hurtado</u>**

Post-secondary Education and Degrees:

Universidad de Carabobo
Valencia, Carabobo, Venezuela
Bachelor of Engineering Science (B.E.Sc.) in Civil Engineering
2004 - 2009

The University of Western Ontario
London, Ontario, Canada
Master of Engineering (M.Eng.) in Civil & Environmental Eng.
2012 - 2013

Honours and Awards:

Recipient of the prestigious **William E. & Ruth Lardner Award**
Geotechnical Research Centre (GRC)
The University of Western Ontario, 2017

Western Graduate Research Scholarship (WGRS)
Department of Civil & Environmental Engineering
The University of Western Ontario,
2013 - 2017

Related Work Experience

Geotechnical *Engineer-in-Training* (E.I.T.)
Golder Associates Ltd.
London, Ontario, Canada
2018 – Present

Teaching and Research Assistant
Department of Civil & Environmental Engineering
The University of Western Ontario,
London, Ontario, Canada
2013 – 2017

Field Engineer
Construcciones Civiles y Metálicas C.A
Maracay, Aragua, Venezuela
2009 - 2012

Publications:

Gonzalez-Hurtado, J. and Newson, T. (2019). “Measuring the small-strain stiffness anisotropy of clayey glacial tills in Southern Ontario”. XVI Pan-American Conference on Soil Mechanics and Geotechnical Engineering at Cancun, Mexico.

Gonzalez-Hurtado, J., He, P, and Newson, T. (2019). “The effect of stiffness anisotropy on elastic solutions of circular foundations under complex loading”. 2nd International Conference on Natural Hazards and Infrastructure at Chania, Greece.

Kiss, J., Boone, S., Gonzalez-Hurtado, J., and Newson, T. (2019) “Measurement of ground-borne vibrations at two operational wind turbine facilities”. Canadian Geotechnical Society: Geo St. John’s, Newfoundland, Canada.

Newson, T., He, P., Gonzalez-Hurtado, J. and Kiss, J. (2018). “Shallow foundation design for onshore turbines”. Research Report GEOT-18-02, ISSN: 08470626.

Postman, M., Molnar, S., Gonzalez-Hurtado, J., He, P., Newson, T. and Hong, H-P (2017). “Vibration monitoring at a wind turbine site in Port Alma”. Research Report GEOT-17-01, ISSN: 08470626.

Gonzalez-Hurtado, J., He, P., Newson, T., Hong, H., Postman, M., and Molnar, S. (2017). “Field monitoring and analysis of an onshore wind turbine shallow foundation system”. Canadian Geotechnical Society: Geo Ottawa, Ottawa, Canada. Paper # 406.

Gonzalez-Hurtado, J. and Newson, T. (2016). “Small-strain behaviour of a carbonate clay till underlying a wind turbine shallow foundation by different in-situ and laboratory tests”. Canadian Geotechnical Society: Geo Vancouver, Vancouver, Canada. Paper # 3653

Gonzalez-Hurtado, J. and Newson, T. (2015). “Measuring the small-strain elastic modulus of gap-graded soils using an effective-medium model and the resonant column apparatus”. Canadian Geotechnical Society: Geo Quebec, Quebec, Canada. Paper # 449

Gonzalez-Hurtado, J., Newson, T., and Tyldesley, M. (2014). “Determination of rigidity index for a shallow foundation on a carbonate clay till”. Canadian Geotechnical Society: Geo Regina, Regina, Canada. Paper # 227